Transactions of the ASME, Journal of Heat Transfer (ISSN 0022-1481) is published monthly by The American Society of Mechanical Engineers, Three Park Avenue, New York, NY 10016. Periodicals postage paid at New York, NY and additional mailing offices. POSTMASTER: Send address changes to Transactions of the ASME, Journal of Heat Transfer, c/o THE AMERICAN SOCIETY OF MECHANICAL ENGINEERS, 22 Law Drive, Box 2300, Fairfield, NJ 07007-2300. **CHANGES OF ADDRESS** must be received at Society headquarters seven weeks before they are to be effective. Please send old label and new address. **STATEMENT from By-Laws.** The Society shall not be responsible for statements or opinions advanced in papers or ... printed in its publications (B7.1, Para. 3).

Journal of Heat Transfer

Published Monthly by ASME

VOLUME 131 • NUMBER 11 • NOVEMBER 2009

RESEARCH PAPERS

(**Contents continued on inside back cover**)

This journal is printed on acid-free paper, which exceeds the ANSI Z39.48-1992 specification for permanence of paper and library materials. ♾™
♻ 85% recycled content, including 10% post-consumer fibers.

Journal of Heat Transfer **Volume 131, Number 11** **NOVEMBER 2009**

The ASME Journal of Heat Transfer is abstracted and indexed in the following:

Applied Science and Technology Index, Chemical Abstracts, Chemical Engineering and Biotechnology Abstracts (Electronic equivalent of Process and Chemical Engineering), Civil Engineering Abstracts, Compendex (The electronic equivalent of Engineering Index), Corrosion Abstracts, Current Contents, E & P Health, Safety, and Environment, Ei EncompassLit, Engineered Materials Abstracts, Engineering Index, Enviroline (The electronic equivalent of Environment Abstracts), Environment Abstracts, Environmental Engineering Abstracts, Environmental Science and Pollution Management, Fluidex, Fuel and Energy Abstracts, Index to Scientific Reviews, INSPEC, International Building Services Abstracts, Mechanical & Transportation Engineering Abstracts, Mechanical Engineering Abstracts, METADEX (The electronic equivalent of Metals Abstracts and Alloys Index), Petroleum Abstracts, Process and Chemical Engineering, Referativnyi Zhurnal, Science Citation Index, SciSearch (The electronic equivalent of Science Citation Index), Theoretical Chemical Engineering

An Experimental Study of the Effects of Platinum on Methane/Air and Propane/Air Mixtures in a Stagnation Point Flow Reactor

James T. Wiswall

Margaret S. Wooldridge

Hong G. Im

Department of Mechanical Engineering,
University of Michigan,
2350 Hayward Street,
Ann Arbor, MI 48109

A stagnation-flow burner facility was used to study the catalytic surface reactions of premixed combustion systems at atmospheric pressure. The configuration serves as an important platform to investigate the interaction between homogeneous and heterogeneous reactions with independent control of the characteristic chemical and physical residence time scales. Methane/oxygen/nitrogen and propane/oxygen/nitrogen mixtures were examined with and without the presence of a platinum catalyst located at the stagnation surface. The effects of oxidizer composition and nitrogen dilution were investigated. Lean flame extinction limits were determined for the two fuels and were found to be unaffected by the presence of the catalytic surface. The flame extinction data indicated that the systems were controlled by gas phase combustion with negligible contributions from heterogeneous reactions. The catalytic activity of the heated surface in response to the direct impingement of fuel/air mixtures onto the stagnation surface, without the presence of a flame, was quantified by the increase in the surface temperature. The methane/air mixtures demonstrated no catalytic activity for these conditions, whereas propane/air mixtures demonstrated temperature increases of over 100 K. The data indicate that the surface reaction was transport limited for the propane/air system.
[DOI: 10.1115/1.3156788]

Keywords: catalytic combustion, platinum, propane, methane, lean extinction limit

1 Introduction

Catalytically assisted combustion can greatly improve the performance of combustion devices and aid the development of new energy generation technologies. For the past 3 decades, over 85% of the global energy demand has been supplied by combustion sources [1]. Considering such large usage, improvements in combustion efficiencies and pollutant emissions will have a dramatic impact on our efforts toward extending existing fuel resources and transitioning to sustainable energy while reducing environmental impact. Catalysts can allow lower-temperature combustion, which directly reduces some pollutants, such as nitric oxides (NO_x), as well as improve the overall conversion efficiency, stability, and range of operating conditions [2].

Catalysts are particularly important to the development of small scale combustion devices. Despite the large energy density of hydrocarbon fuels, combustion at small dimensions with high surface-to-volume ratios often suffers from excessive heat losses that prevents sustained exothermic reactions. Surface reactions can overcome these challenges by increasing reaction rates at lower temperatures and by extending the range of stable combustion. However, the quantitative benefit of surface reactions on combustion properties, such as extending flammability limits for practical device operating conditions, remains uncertain primarily due to the uncertainties in the homogeneous and heterogeneous reaction rate chemistries. Catalyst chemistry also introduces uncertainties due to variability in surface properties.

The overall objective of this research program is thus to broaden our fundamental understanding of the interactions between gas-phase and surface combustion in a well defined combustion system and to use such knowledge to improve combustion performance. This work specifically explored the feasibility of using catalysts to extend the lean extinction limits of methane and propane fueled flames and to quantify the surface reactivity for conditions when no flame is present.

The stagnation-flow reactor used in this work is particularly well suited to fundamental studies of catalyst performance, as the stagnation-flow reactor allows independent control of the characteristic time scales for chemical reaction and flow. The stagnation-flow reactor simplifies temperature and species profiles to nominally one dimension where the thermal and concentration gradients occur in the axial direction only. The gas residence time on the surface and surface reaction rate can be independently controlled by the flow velocity and surface heating, respectively. The stagnation surface also provides a physical support, which can be used to examine a broad range of catalyst materials and properties, and many types of catalyst/fuel combinations can be tested in such a system. In the present study, the stagnation plane was chosen to be either platinum or silicon, so the effects of surface reactions can be quantitatively compared relative to two levels of surface reactivity (where the silicon surface is considered as a reference condition with negligible surface reaction). The lean extinction limits and surface reactivity were examined for a range of parametric conditions of surface heating, mixture equivalence ratio, and strain rates. For each set of experimental conditions, both catalytically active and baseline systems were examined.

Contributed by the Heat Transfer Division of ASME for publication in the JOURNAL OF HEAT TRANSFER. Manuscript received November 20, 2008; final manuscript received April 2, 2009; published online August 25, 2009. Review conducted by Walter W. Yuen. Paper presented at the 2007 ASME International Mechanical Engineering Congress (IMECE2007), Seattle, WA, November 10–16, 2007.

2 Scientific Background

There are two processes (surface reaction kinetics and gas-phase species diffusion) that can limit the heterogeneous reaction rate. Pfefferle and Pfefferle [3] among many other sources discussed the relative contributions of these processes. The transition from surface-kinetics-limited to diffusion-limited operation of a catalyst sometimes yields an observable step change in behavior. For example, as the temperature of the inlet reactant flow on a catalytic reactor is increased, the catalyst temperature may show a large increase in temperature as the reaction limitation transitions from surface kinetically limited to diffusion limited. Consistent with other studies (e.g., Ref. [4]), this transition is called "light-off" or heterogeneous ignition in the current work. Further heating will eventually lead to homogeneous ignition of the gas-phase reactants.

In general, both homogeneous and heterogeneous reactions contribute to extinction and ignition phenomena when a catalyst is present. As described earlier, this coupling can yield two distinct ignition events: heterogeneous and homogeneous ignitions. This often causes catalyst performance metrics to be intertwined with the parameters of the specific facility used to study the catalyst (e.g., the flow geometry, the form of the catalyst (e.g., foil, wash-coat, etc.), the heat transfer properties of the catalyst support, etc.). Thus, it is often difficult to compare results between different experimental facilities, and it is critical to establish clear baselines for conditions where a catalytic surface is not present.

The stagnation-flow configuration has served as a canonical geometry to investigate catalyst phenomena for many years. Researchers have used such experimental methods to develop and validate heterogeneous reaction mechanisms [4,5], to investigate light-off and the effects of catalysts on homogeneous flammability limits and ignition phenomena [4,6,7], to quantify fuel conversion efficiencies [8], and to compare catalyst properties, to name a few research topics. Among the most relevant papers, Veser and Schmidt [6] experimentally studied ignition of methane, ethane, propane, and isobutane flames in a stagnation flow. Williams et al. [7] studied methane and propane light-off and homogeneous ignition in a stagnation flow. In these studies, each fuel was found to have different ignition characteristics when the catalyst ignition temperature was considered as a function of fuel-air ratio. Ethane had the lowest homogeneous ignition temperature at 950°C, and methane had the highest at 1200°C. Law et al. [9] examined the lean extinction limits of propane/air flames in stagnation-point-flow subjected to different boundary conditions on the stagnation surface, including a platinum catalyst. They found that the catalyst did not affect the lean extinction limits at the conditions they considered.

More recent studies by Li and Im [10,11] specifically focused on the catalytic extension of lean extinction limit. Their numerical studies of methane/platinum stagnation-point-flow reactor revealed that lean extinction limit can be extended provided the characteristic time scales of the surface reactions are faster than those of the gas-phase reactions, as would be the case if the catalytic surface retains a high temperature with lower heat loss or if the gas-phase mixture is diluted. It remains to be seen, however, if the observed catalytic benefit of flammability extension can be realized experimentally.

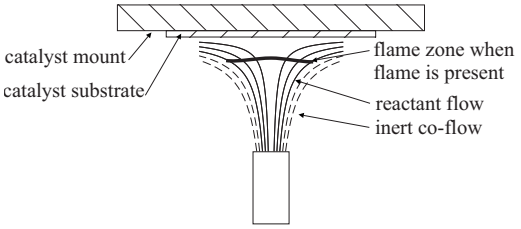

Fig. 1 Schematic of the stagnation-point-flow reactor configuration

Therefore, the goal of the present experimental study is to identify the practical extent to which heterogeneous reaction can alter and improve reactor performance and thereby verify the findings from the earlier modeling studies [10,11]. In particular, we investigate the effects of platinum catalyst on lean extinction limits of methane and propane in air, with and without the presence of gas-phase premixed flames. The consideration of different fuels, as well as the nonreacting and catalytic surfaces, allows comprehensive coverage of conditions at which gas-phase and heterogeneous reactions interact at varying degrees of relative dominance. For reference, a schematic of the flow configuration is shown in Fig. 1. A stream of gas-phase reactant mixture impinges onto a solid surface, which can be nonreacting (bare silicon) or catalytic (platinum). First, we consider the cases in which a gas-phase flame is present initially, such that the flow impinging on the stagnation surface consists predominantly of the combustion products. The lean extinction limits are then determined by varying the reactor conditions, such as the fuel/air equivalence ratio. In the second part of experiments, a fuel/air mixture at room temperature and pressure is directed onto the heated surface of the stagnation plane, such that surface-only reaction modes are investigated. For these experiments, the rate of heat release at the surface is monitored by measuring the time dependent temperature of the stagnation surface.

3 Experimental Approach

3.1 Experimental Facility. The experimental facility is schematically shown in Fig. 2. A mixture of fuel, oxygen (O_2), and nitrogen (N_2) was impinged on a flat plate to achieve a stagnation flow. The flow was directed upward with the fuel, O_2 and N_2 mixture in the inner tube, and nitrogen flowing through the outer

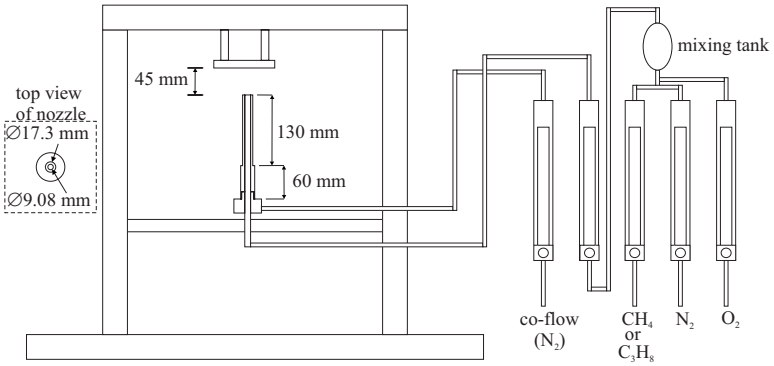

Fig. 2 Schematic showing gas flow measurement, control, and important reactor dimensions

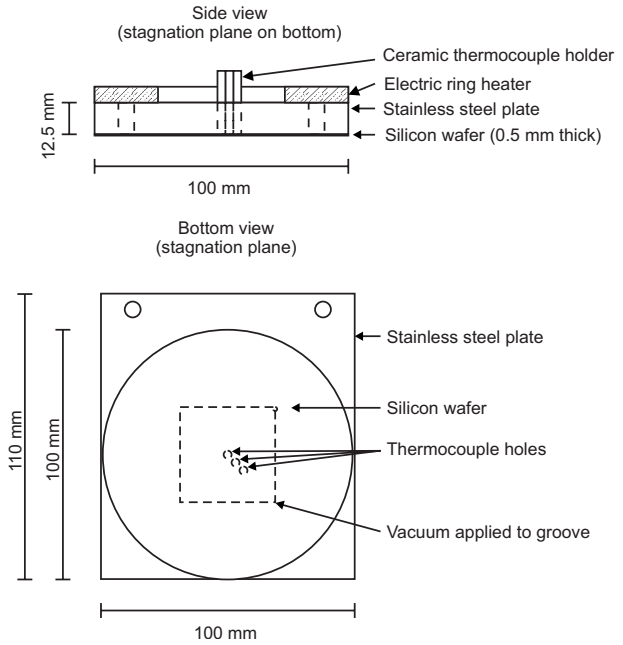

Fig. 3 Dimensions of stagnation plane and support

coflow tube. The nitrogen coflow minimizes the entrainment of the ambient air into the reactant mixture in the inner tube. The volume flow rates of the fuel, O_2 and N_2, and the total mixture were regulated using calibrated rotameters. The relative levels of the flow rates were used to set the stoichiometric ratios and levels of nitrogen dilution of the combustible mixtures. The total mixture rotameter was used to adjust the overall exit velocity from the nozzle, and the coflow rotameter was used to adjust the exit velocity of shroud flow of N_2. Each rotameter had an uncertainty of $\pm 2\%$ of the reading.

The coflow nozzle consists of the inner tube (reactant mixture) with 9.08 mm inner diameter and 0.265 mm wall thickness. The coflow tube was 17.3 mm inner diameter. The length of the coflow tube was 130 mm. Type 304 stainless steel was used for all tubing. Dry compressed air (79% N_2, 21% O_2) was used for some experiments instead of mixing O_2 and N_2.

Figure 3 shows the dimensions of the stagnation plane and the support. The support for the stagnation plane was constructed from type 304 stainless steel and was located 45.5 mm above the nozzle exit such that the stagnation plane was 45 mm above the nozzle exit. The plate was mounted on a translation stage, which had a 60 mm range and dimensions of 100×110 mm^2, by 12.5 mm thick. A 0.5 mm thick wafer of silicon with a diameter of 100 mm was used as the stagnation surface. The silicon wafer was mounted on the supporting stainless steel plate using a vacuum seal. Insulating washers made from ceramic were placed between the supporting structure and the stainless steel plate to reduce heat loss by conduction.

Platinum was used as the catalyst and was deposited on the silicon wafer by physical vapor deposition (PVD). To achieve a stable deposition of platinum, a 30 nm layer of titanium was first deposited on the silicon. A layer of platinum 100 nm thick was then deposited on the titanium. A bare silicon wafer was used as the reference nonreactive case of a surface with no catalytic activity. The platinum was deposited by PVD to ensure similar heat transfer parameters would exist between the catalytic and nonreactive cases.

A 0.2 mm diameter B-type thermocouple (Pt/30%Rh–Pt/6%Rh, Omega Engineering Inc.) was used to measure the stagnation plane temperature (T_s). It was possible to measure T_s in three locations radially outward from the centerline of the flow (see Fig. 3), and the variation over the radial measurement locations was less than 20 K. The thermocouples were in physical contact with the nonstagnation plane side of the silicon wafer, leaving no part of the thermocouples exposed to the reactant flow. The thermocouple bead temperature was considered equivalent to that of the stagnation plane and surrounding support. The thermocouple voltage was measured using a multimeter (Fluke 45) and was recorded at a rate of 2.5 Hz, using a data acquisition system (LABVIEW 8). T_s was calculated using the polynomial fit for B-type thermocouples [12].

Table 1 Uncertainty of the experimental parameters

Uncertainty
$U\phi = \pm 0.028\phi$
$U\chi_{N_2} = \pm 0.0057\chi_{N_2}$
$Uv_{ave} = \pm 0.036v_{ave}$
$U\phi_{min} = \pm 0.04\phi$
$UT_s = \pm 15$ K

The equivalence ratio (ϕ) is determined based on the measured flow rates for the fuel and O_2 flow rates (Eq. (1)). The dilution with N_2 is defined relative to the total N_2+O_2 flow rates (Eq. (2)). The nozzle exit velocity (v_{ave}) is the calculated average exit velocity of the total flow exiting the nozzle (Eq. (3)).

$$\phi = \frac{(\dot{Q}_{fuel}/\dot{Q}_{O_2})}{(\dot{Q}_{fuel}/\dot{Q}_{O_2})_{stoich}} \tag{1}$$

$$\chi_{N_2} = \frac{\dot{Q}_{N_2}}{\dot{Q}_{N_2} + \dot{Q}_{O_2}} \tag{2}$$

$$v_{ave} = \frac{\dot{Q}_{fuel} + \dot{Q}_{O_2} + \dot{Q}_{N_2}}{A_n} \tag{3}$$

The parameters ϕ, χ_{N_2}, and v_{ave} are controlled independently. Each flow meter was calibrated and corrected for atmospheric pressure variations during each experiment. The temperature in the laboratory varied by less than 10°C. The uncertainty in each flow meter was determined to be two standard deviations based on the calibration testing, to give a 95% confidence level. The reported uncertainty for ϕ, χ_{N_2}, and v_{ave} was determined using the square root of the sum of the uncertainty of each flow meter squared. The minimum equivalence ratio ϕ_{min} and stagnation plane temperature T_s were determined for each extinction experiment. The uncertainty in T_s was the uncertainty reported by the manufacturer of the thermocouple. The uncertainty in ϕ_{min} was based on the variability in results obtained from identical test conditions and the uncertainty in the measurement of ϕ. Table 1 shows the independent and dependent parameters and the associated uncertainties.

Each fuel was studied with and without an ignited gas-phase flame. For the flame extinction experiments, the fuel/air mixture was ignited using an external premixed propane/air flame brought into the proximity of the stagnation plane. The starter flame was removed after the stagnation flame was ignited. To measure the lean extinction limit (ϕ_{min}), the average nozzle exit velocity (v_{ave}) and the nitrogen mole fraction in the oxidizer (χ_{N_2}) were held constant while ϕ was decreased until extinction occurred. The lean extinction limit, ϕ_{min}, was defined as the average between the lowest measured ϕ yielding a stable flame and the slightly lower ϕ yielding an unstable condition. The resolution of controlling ϕ in the experimental setup was 0.008. The surface temperature (T_s) was recorded for each stable flame condition. In the studies of extinction limit, the independent parameters were v_{ave}, ϕ, and χ_{N_2},

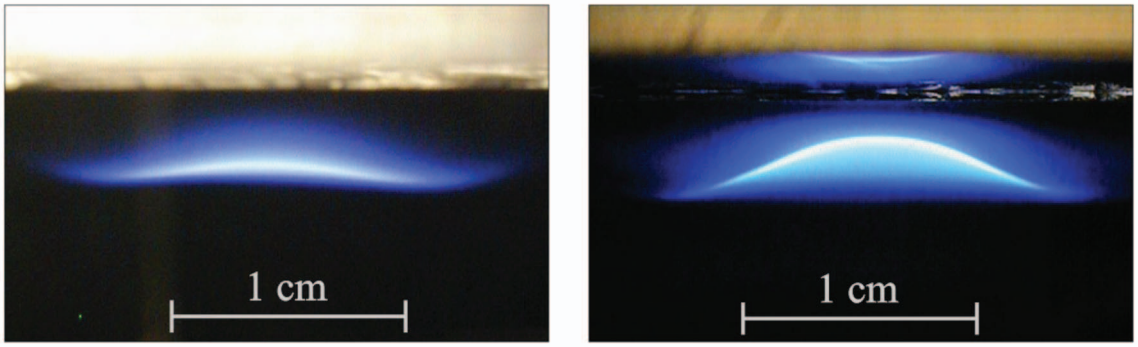

(a) CH_4/air ($\phi = 0.62$; $v_{ave} = 0.5$ m/s) (b) C_3H_8/air ($\phi = 0.77$; $v_{ave} = 0.8$ m/s)

Fig. 4 Typical methane and propane stagnation-flow flames

and the dependent parameters were $\phi_{\min}$ and T_s.

To measure the catalytic activity in the absence of a gas-phase flame, the air and coflow were impinged on the heated plate until a steady state temperature was reached. For these experiments, the back side of the plate was insulated using an alumina fiber based insulation paper (Cotronics Corp.). After the steady state temperature was reached (T_{s0}), the fuel was added to the mixture and the plate temperature was monitored until a steady state temperature with the fuel mixture was reached (T_{sf}). A change in surface temperature after the fuel was introduced indicates heat release due to the reaction of the fuel on the catalyst. For unburned reactants impinging on the heated plate, the independent parameters were v_{ave}, ϕ, χ_{N_2}, and the initial plate temperature T_{s0}, and the dependent parameter was the increase in the plate temperature $\Delta T_s = T_{sf} - T_{s0}$.

4 Experimental Results and Discussion

4.1 Extinction Limits for $CH_4/O_2/N_2$/Air and $C_3H_8/O_2/N_2$/Air Flames. Figure 4 shows the images of typical premixed flames for the methane/air and propane/air systems. The blue emission at the top of Fig. 4 is a reflection from the stagnation surface. For the conditions presented here, the distance from the stagnation surface to the center of the flame was approximately 4 mm for methane/air flames and 2 mm for propane/air flames. The propane/air flames in general have higher flame speeds; hence they required higher nozzle exit velocities to establish stable flames. The higher curvature of the propane/air flames is attributed to the fact that the higher nozzle exit velocity leads to a more nonuniform velocity profile in the radial direction.

For the stagnation-point-flow configuration under study, the impinging gases decelerate as they approach the stagnation plane, and the flame stabilizes at a location where the flame speed balances with the local gas velocity. A larger flame speed for a given v_{ave} will cause the flame to be farther away from the plate. Starting with a stabilized flame at a given condition, the extinction limits were measured by gradually decreasing the mixture equivalence ratio until the flame is extinguished on the stagnation surface.

4.1.1 Premixed $CH_4/O_2/N_2$ Stagnation-Flow Flames on Pt and Si. The experimental results for the methane extinction limits are presented in Figs. 5 and 6, while the raw data values are shown in Table 2. Figure 5 shows the minimum equivalence ratio at extinction and the corresponding surface temperature as a function of v_{ave}, while holding χ_{N_2} constant at 0.79 (as in air). The results for both unheated (filled symbols) and heated (open symbols) surface conditions are shown. It is evident that both $\phi_{\min}$ and T_s increase as v_{ave} increases, implying that the flame can be more easily extinguished due to the decreased residence time for complete combustion. The higher T_s at extinction for higher v_{ave} further confirms that faster chemical reactions are needed in order to sustain combustion under reduced flow residence time. The range of velocities presented here were practical limitations of the experimental facility used in this study: A lower flow rate would result in flashback and a higher flow rate would yield flame quenching.

Figure 6 shows $\phi_{\min}$ and corresponding T_s as a function of χ_{N_2}, while holding v_{ave} constant at 0.74 m/s. Results for the heated condition (open symbols) are shown. As χ_{N_2} increases, the flame speed is decreased due to dilution, causing a larger $\phi_{\min}$ at extinction. However, the plate temperature, T_s, is relatively constant

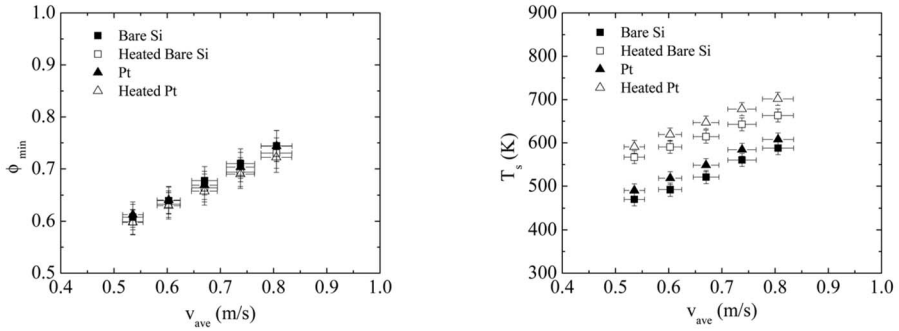

(a) ϕ_{min} as a function of v_{ave} (χ_{N_2}=0.79) (b) T_s at ϕ_{min} as a function of v_{ave} (χ_{N_2}=0.79)

Fig. 5 Lean extinction limits of CH_4 flames as a function of the nozzle exit velocity for fixed dilution level

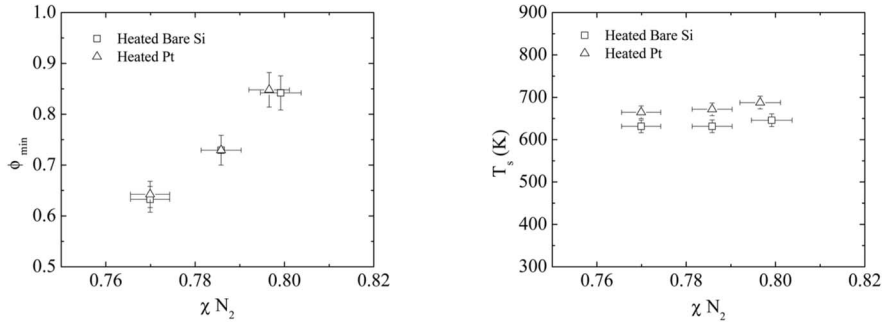

(a) ϕ_{min} as a function of χ_{N_2} (v_{ave}=0.74 m/s) (b) T_s at ϕ_{min} as a function of χ_{N_2} (v_{ave}=0.74 m/s)

Fig. 6 Lean extinction limits for CH_4 flames as a function of dilution for fixed levels of stretch

with respect to increasing χ_{N_2}, unlike the results shown in Fig. 5. This is expected because, for a given v_{ave} with the same residence time, extinction occurs at the same chemical reactivity. The decreased enthalpy of the reactants for increased dilution is offset by the increased enthalpy at higher equivalence ratio to achieve the same chemical reactivity at the extinction condition. The range of dilution with χ_{N_2} was limited at high concentrations by the lack of stable conditions and at low concentrations by flashback. The overall results in Figs. 5 and 6 suggest that the combustion characteristics at these conditions are primarily controlled by the gas-phase combustion.

Table 2 Measured extinction limits for methane flames

v_{ave} (m/s)	χ_{N_2}	ϕ_{min}	T_s (K)
	Bare Si wafer		
0.54	0.79	0.62	470
0.61	0.79	0.64	492
0.67	0.79	0.68	521
0.74	0.79	0.71	560
0.81	0.79	0.74	588
	Heated bare Si wafer		
0.54	0.79	0.60	567
0.61	0.79	0.63	590
0.67	0.79	0.66	614
0.74	0.79	0.69	642
0.81	0.79	0.73	663
0.74	0.77	0.63	631
0.74	0.79	0.73	632
0.75	0.80	0.84	646
	Pt coated wafer		
0.54	0.79	0.61	490
0.61	0.79	0.64	518
0.67	0.79	0.67	548
0.74	0.79	0.70	584
0.81	0.79	0.74	607
	Heated Pt coated wafer		
0.54	0.79	0.60	591
0.61	0.79	0.63	619
0.67	0.79	0.66	647
0.74	0.79	0.69	678
0.81	0.79	0.72	701
0.74	0.77	0.64	665
0.74	0.79	0.73	672
0.74	0.80	0.85	688

Figures 5(*b*) and 6(*b*) further show that T_s is slightly higher for the platinum surface case compared with that for the bare silicon surface case. The magnitude of the temperature difference was clearly greater than the experimental uncertainty. The increase in the temperature for the platinum case is attributed to the difference in the radiative heat loss associated with the two surface conditions, which is primarily attributed to differences in surface emissivity. Within the observed temperature range, the emissivities of platinum, silicon wafer, and stainless steel are estimated to be 0.26 [13], 0.76 [14], and 0.9 [15], respectively. There are also visible variations in the surface finish with aging of the catalyst, which can further modify the emissivity. Consistent temperature increases with platinum surfaces were observed regardless of the surface heating conditions, suggesting that surface reactions were not activated significantly in all cases.

Despite the small differences in the surface temperature, the presence of platinum hardly affected the lean extinction limits for the methane flames. There is a slight decrease in ϕ_{min} as the plate is heated, as shown in Fig. 5(*a*), which is attributed to the enhanced gas-phase reactions. However, the overall effect was found to be insignificant compared with the difference in T_s between the heated and unheated conditions (Fig. 5(*b*)). Therefore, for the conditions studied, catalytic activities were negligible, and the combustion and surface heating behavior were dictated by gas-phase reaction and transport.

4.1.2 Premixed $C_3H_8/O_2/N_2$ *Stagnation-Flow Flames on Pt and Si*. Anticipating that surface reactions can be more active with propane/air mixtures, we also conducted experiments to measure the lean extinction limits of propane/air impinging on the platinum surface. The results for the lean extinction limits are presented in Fig. 7 and Table 3. Figure 7 shows ϕ_{min} and corresponding T_s as a function of v_{ave} for χ_{N_2}=0.79. Only heated surface conditions were considered at a comparable heating level as in the methane flame cases. Similar to the methane results, T_s increases with increasing v_{ave}, while the difference in T_s, as well as in ϕ_{min}, between different surface conditions is very small. These results indicate that the extinction process for the propane flames was also dictated by the gas-phase reactions.

The results for the propane lean extinction limits are found to be consistent with the results by Law et al. [9], in which the effects of platinum on the extinction limits of premixed propane/air stagnation flames were investigated. They also found that the propane air flames stabilized on the heated stagnation surface (T_s=630–800 K) were insensitive to the presence or the absence of platinum of the stagnation surface. If the characteristic value for flame stretch is defined as $S_L=v_a vg/d$, where d is the distance from the luminous flame sheet to the stagnation surface, the values for S_L for the current work range from 2651/s to 3351/s for the

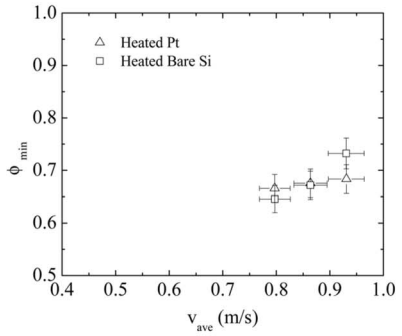

(a) ϕ_{min} as a function of v_{ave} (χ_{N_2}=0.79)

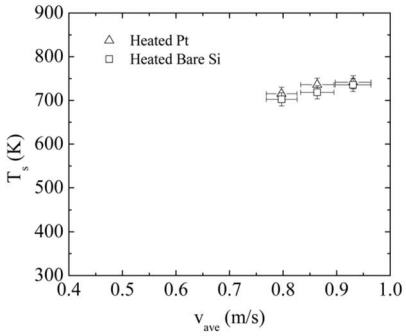

(b) T_s at ϕ_{min} as a function of v_{ave} (χ_{N_2}=0.79)

Fig. 7 Lean extinction limits for C_3H_8 flames as a function of the nozzle exit velocity for fixed dilution level

propane flames (where d=3 mm). The stretch values for the study by Law et al. [9] range from 1401/s to 11301/s. The results for the lean extinction limits as a function of the average nozzle exit velocity are plotted in Fig. 8 along with the experimental results by Law et al. [9]. The results agree well in the low velocity range considered in the present study. Law et al. [9] also studied the location of the flame at extinction. They found the flame location at extinction was slightly farther from the stagnation plane with decreasing mixture velocity. For the experimental conditions tested in the current work, the flame location at extinction was approximately constant; however, note that the range of velocities considered is much smaller than that of Law et al. [9].

Table 3 Measured extinction limits for propane flames

v_{ave} (m/s)	χ_{N_2}	ϕ_{min}	T_s (K)
	Bare Si wafer		
0.80	0.79	0.65	702
0.87	0.79	0.67	718
0.93	0.79	0.73	735
0.87	0.80	0.76	678
0.94	0.80	0.76	671
	Pt coated Si wafer		
0.80	0.79	0.67	715
0.87	0.79	0.68	735
0.93	0.79	0.68	741
0.87	0.80	0.76	678
0.94	0.80	0.79	702

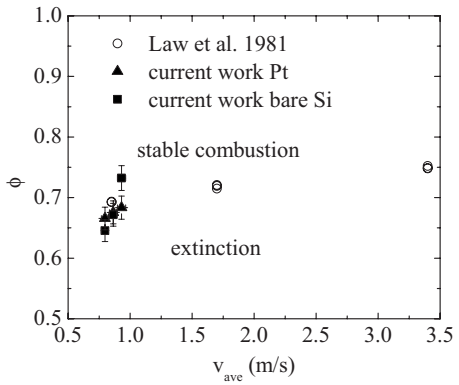

Fig. 8 Comparison between the C_3H_8 extinction limits as a function of the nozzle exit velocity measured in the present study and the results of Law et al. [9]

4.2 Catalytic Reactivity for Fuel/Air Mixtures Impinging on Heated Pt. In the subsequent set of experiments, a fresh fuel/air mixture stream at ambient conditions was impinged onto a nonreactive and catalytic surface at different heating conditions in order to identify if significant surface reactions were observed. All conditions tested had a nozzle exit velocity of v_{ave}=0.92. Initially, only air is supplied onto a heated plate, and then the fuel supply is started at the prescribed equivalence ratio. Activation of surface reactions is then identified by an additional increase in the surface temperature. As expected, no additional temperature increase was observed with bare silicon surfaces, and the results with platinum surfaces are reported in Secs. 4.2.1 and 4.2.2.

4.2.1 CH_4*/Air Mixtures Impinging on Heated Pt.* First, methane/air was supplied to the heated catalytic surface. The surface temperature, T_s, was varied from 300 K to 700 K, the average nozzle exit velocity v_{ave} was 0.92 m/s for all experiments, and ϕ was varied from 0 to 3. For all conditions considered, no increase in surface temperature was observed, indicating that catalytic reactions were not activated. The observed low methane/air/platinum activity agrees with previous studies. For example, Dupont et al. [16] reported that the conversion of methane was below 5% when the surface temperature was below 750 K. Williams et al. [7] and Veser and Schmidt [6,7] further showed that heterogeneous ignition of lean methane air mixtures on a heated platinum foil occurs in the range of 820–870 K, which was computationally confirmed by Deutschmann et al. [17]. Such high surface temperatures could not be achieved with the current experimental facility.

4.2.2 C_3H_8*/Air Mixtures Impinging on Heated Pt.* Unlike the methane/air system, however, significant surface reactions were observed with the propane/air system. Table 4 presents the results for the catalytic response of the three equivalence ratios ϕ=1, 1.8, and 3.5 that were investigated for a range of initial plate temperatures. The average nozzle exit velocity v_{ave} was 0.92 m/s for all experiments. Figure 9 shows the plate temperature as a function of time for a typical experiment where ϕ=1.8 and the initial surface temperature was T_{s0}=614 K. For each experiment the plate was initially heated until a steady temperature condition was achieved (about 60 min), after which the reactant mixture was supplied through the nozzle. The surface temperature then increased gradually until it reached a second steady condition (about 120 min). When the fuel supply was stopped, the temperature decreased to recover the initial heated temperature condition, T_{s0}. The return to T_{s0} confirms that the second temperature rise in Fig. 9 results from heat release from the surface reactions of the propane/oxygen/platinum system.

Table 4 Platinum surface temperature in response to the heated initial surface temperature, T_{s0}, with the propane/air mixture impinging on the surface. The average nozzle exit velocity was 0.92 m/s.

T_{s0}	T_{sf}	ΔT_s	ϕ
725	877	152	1.00
719	857	137	1.00
665	813	147	1.00
610	769	159	1.00
552	747	194	1.80
588	746	159	1.80
614	830	216	1.80
727	905	178	1.80
608	830	222	3.50
619	825	206	3.50
721	893	172	3.50
635	837	203	3.50

The temperature increase due to catalytic reaction is a valuable metric of the catalyst performance, as it indicates the strength of the catalytic effects. We define $\Delta T_s = T_{sf} - T_{s0}$, where T_{sf} and T_{s0} are indicated in Fig. 9, as the measure of the intensity of the catalytic reactions. This quantity was measured for different T_{s0} by changing the heat input to the surface.

Figure 10 shows ΔT as a function of the initial surface temperature T_{s0} for various ϕ conditions. Within the experimental uncertainties, ΔT_s appears to remain almost constant for the range of conditions. This suggests that the catalytic reactions on the platinum surface have reached the diffusion-limited mode. In other words, the catalytic activity is sufficiently high such that the overall heat release rate is determined by the transport rate of the reactant gases to the surface, which is fixed constant here. Nevertheless, there is a tendency that ΔT_s increases as the mixture equivalence ratio increases.

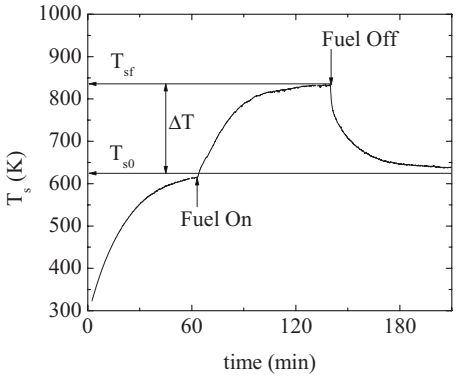

Fig. 9 Typical temperature evolution in time for unburned propane air mixture impinging on the heated stagnation surface (ϕ=1.8 and v_{ave}=0.92 m/s)

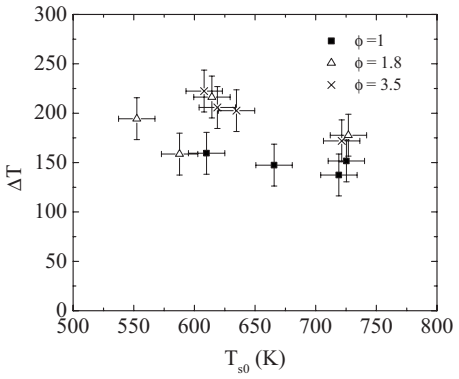

Fig. 10 Catalytic response, ΔT_s, of heated Pt surface to C_3H_8/air mixture as a function of surface heating (T_{s0}) for various equivalence ratios. The average nozzle exit velocity was 0.92 m/s.

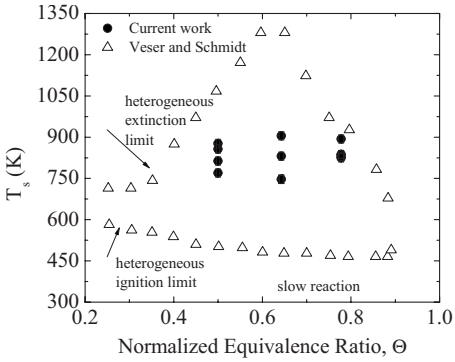

Fig. 11 Comparison between the Pt catalyst response to C_3H_8/air mixtures of the current work to Veser and Schmidt [6]

The steady state surface temperature with catalytic reaction, T_{sf}, measured in the present study is compared with the results by Veser and Schmidt [6], who investigated heterogeneous ignition and extinction characteristics of propane air mixtures on an electrically heated platinum foil. Figure 11 shows the results as a function of the normalized equivalence ratio, $\Phi = \phi/(1+\phi)$, such that the lean and rich limit is bounded between 0 and 1. The flow velocity in Veser and Schmidt [6] was 0.025 m/s, whereas in the present work the average velocity was 0.92 m/s. Note that the present experimental results show stable operating conditions in a region where Veser and Schmidt [6] found no stable operating conditions. This may be attributed to a number of factors. The present experimental setup has large heat loss associated with a large surface area and surface emissivity, unlike the case of the electrically heated foil employed by Veser and Schmidt [6]. In addition, the flow residence time is significantly lower in the present study due to the high nozzle exit velocity. The steady surface reaction temperature depends strongly on these conditions for heat and mass transport. Further studies may provide more quantitative assessment of these effects.

5 Conclusions

Experimental studies were conducted using a stagnation-point-flow combustor configuration in order to assess the feasibility of lean flammability extension by catalytic reaction. Platinum versus bare silicon surfaces were compared, while methane/air and propane/air at various mixture compositions were considered for gas-phase reactants. An additional heat supply to the catalytic surface was attempted to enhance the activity of surface chemistry. For all of the conditions considered, the lean flame extinction limits were predominantly governed by gas-phase combustion, and the presence of the catalytic surface hardly affected the extinction limits. The catalytic surface temperature at the extinction limits showed a slight, yet consistent, increase with the catalytic surface, due likely to the differences in the surface heat transfer properties. In contrast to the computational studies conducted by Li and Im [10,11], the present experimental facilities are characterized by large heat losses, resulting in catalytic surface temperatures much lower than those predicted by the modeling studies.

The extent of catalytic activity was also investigated by supplying a fuel/air mixture stream onto a heated platinum plate. For the heated surface temperature range obtained in the present study, methane/air mixtures failed to activate catalytic reaction, consistent with previous experimental findings. On the other hand, the propane/air mixtures did activate surface chemistry at a significant

level, by raising the surface temperature by a few hundred degrees. The results demonstrate that stable heterogeneous reaction conditions can be achieved with propane/air at relatively low temperatures and moderate flow rates. For the conditions under study, the magnitude of the additional surface temperature increase due to catalytic reactions was insensitive to the initial surface temperature, suggesting that the observed heterogeneous reaction was transport limited.

The present study provides useful new data on near-extinction characteristics of platinum/methane and platinum/propane reaction systems. There was clear evidence that propane can yield stronger catalytic activities. However, the benefit of catalytic reaction in achieving leaner and lower-temperature combustion in compact reactors with high surface-to-volume ratios should be carefully assessed by accounting for the fact that most such devices are likely subject to significant heat losses. Therefore, careful design and integration to ensure maximum thermal insulation are essential in acquiring the benefit of catalytic reactions. To this end, it is also of interest to investigate alternative novel catalyst materials with substantially lower activation temperatures.

Acknowledgment

This work was supported by the National Science Foundation, Grant No. CTS-0134128.

Nomenclature

A_n = nozzle exit area
$\dot{Q}$ = volumetric flow rate
T_s = surface temperature
T_{s0} = initial surface temperature
T_{sf} = final surface temperature
ΔT_s = difference in surface temperature
U_{param} = uncertainty in a given parameter
v_{ave} = average nozzle exit velocity
χ_{N_2} = nitrogen mole fraction in oxidizer
ϕ = equivalence ratio
ϕ_{min} = lean extinction limit
Φ = normalized equivalence ratio

References

[1] Boyer, R., 2006, "Annual Energy Review 2005," Energy Information Administration, Technical Report No. DOE/EIA-0384.
[2] Law, C. K., and Sivashinsky, G. I., 1982, "Catalytic Extension of Extinction Limits of Stretched Premixed Flames," Combust. Sci. Technol., **29**(3), pp. 277–286.
[3] Pfefferle, L. D., and Pfefferle, W. C., 1987, "Catalysis in Combustion," Catal. Rev. - Sci. Eng., **29**(2–3), pp. 219–267.
[4] McDaniel, A. H., Lutz, A. E., Allendorf, M. D., and Rice, S. F., 2002, "Effects of Methane and Ethane on the Heterogeneous Production of Water From Hydrogen and Oxygen Over Platinum in Stagnation Flow," J. Catal., **208**(1), pp. 21–29.
[5] Ljungstrom, S., Kasemo, B., Rosen, A., Wahnstrom, T., and Fridell, E., 1989, "An Experimental Study of the Kinetics of OH and H_2O Formation on Pt in the H_2+O_2 Reaction ," Surf. Sci., **216**(1–2), pp. 63–92.
[6] Veser, G., and Schmidt, L. D., 1996, "Ignition and Extinction in the Catalytic Oxidation of Hydrocarbons Over Platinum," AIChE J., **42**, pp. 1077–1087.
[7] Williams, W., Stenzel, M., Song, X., and Schmidt, L., 1991, "Bifurcation Behavior in Homogeneous-Heterogeneous Combustion: I. Experimental Results Over Platinum," Combust. Flame, **84**(3–4), pp. 277–291.
[8] Dupont, V., Zhang, S. H., and Williams, A., 2000, "Catalytic and Inhibitory Effects of Pt Surfaces on the Oxidation of $CH_4/O_2/N_2$ Mixtures," Int. J. Energy Res., **24**(14), pp. 1291–1309.
[9] Law, C. K., Ishizuka, S., and Mizomoto, M., 1981, "Lean-Limit Extinction of Propane/Air Mixtures in the Stagnation-Point Flow," Symposium (International) on Combustion, pp. 1791–1798.
[10] Li, J., and Im, H. G., 2006, "Extinction Characteristics of Catalyst-Assisted Combustion in a Stagnation-Point Flow Reactor," Combust. Flame, **145**(1-2), pp. 390–400.
[11] Li, J., and Im, H. G., 2007, "Effects of Dilution on the Extinction Characteristics of Strained Lean Premixed Flames Assisted by Catalytic Reaction," Proc. Combust. Inst., **31**, pp. 1189–1195.
[12] Croarkin, M. C., Guthrie, W. F., Burns, G. W., Kaeser, M., and Strouse, G. F., 1993, "Temperature-Electromotive Force Reference Functions and Tables for the Letter-Designated Thermocouple Types Based on the ITS-90," National Institute of Standards and Technology Monograph 175.
[13] Goard, R., 1966, "Application of Hemispherical Surface Pyrometers to the Measurement of the Emissivity of Platinum (A Low-Emissivity Material)," J. Sci. Instrum., **43**(4), pp. 256–258.
[14] Timans, P., 1993, "Emissivity of Silicon at Elevated Temperatures," J. Appl. Phys., **74**(10), pp. 6353–64.
[15] Incropera, F. P., Dewitt, D. P., Bergman, T. L., and Lavine, A. S., 2006, *Fundamentals of Heat and Mass Transfer*, 6th ed., Wiley, New York.
[16] Dupont, V., Zhang, S. H., and Williams, A., 2001, "Experiments and Simulations of Methane Oxidation on a Platinum Surface," Chem. Eng. Sci., **56**, pp. 2659–2670.
[17] Deutschmann, O., Behrendt, F., and Warnatz, J., 1994, "Modelling and Simulation of Heterogeneous Oxidation of Methane on a Platinum Foil," Catal. Today, **21**(2–3), pp. 461–470.

On the Analysis of Short-Pulse Laser Heating of Metals Using the Dual Phase Lag Heat Conduction Model

K. Ramadan
e-mail: rkhalid@mutah.edu.jo

W. R. Tyfour
e-mail: tyfour@mutah.edu.jo

Department of Mechanical Engineering,
Mu'tah University,
P.O. Box 7,
Karak 61710, Jordan

M. A. Al-Nimr
Department of Mechanical Engineering,
Jordan University of Science and Technology,
P.O. Box 3030,
Irbid 22110, Jordan
e-mail: malnimr@just.edu.jo

Transient heat conduction in a thin metal film exposed to short-pulse laser heating is studied using the dual phase lag heat conduction model. The initial heat flux distribution in the film, resulting from the temporal distribution function of the laser pulse, together with the zero temperature gradients at the boundaries normally used in literature with the presumption that they are equivalent to negligible boundary heat losses is analyzed in detail in this paper. The analysis presented here shows that using zero temperature gradients at the boundaries within the framework of the dual phase lag heat conduction model does not guarantee negligible boundary heat losses unless the initial heat flux distribution is negligibly small. Depending on the value of the initial heat flux distribution, the presumed negligible heat losses from the boundaries can be even way larger than the heat flux at any location within the film during the picosecond laser heating process. Predictions of the reflectivity change of thin gold films due to a laser short heat pulse using the dual phase lag model with constant phase lags are found to deviate considerably from the experimental data. The dual phase lag model is found to overestimate the transient temperature in the thermalization stage of the laser heating process of metal films, although it is still superior to the parabolic and hyperbolic one-step models. [DOI: 10.1115/1.3153580]

Keywords: dual phase lag, non-Fourier heat conduction, short-pulse laser heating, reflectivity change

1 Introduction

Short-pulse laser heating processes have made tremendous impacts in microelectronics and material processing, such as laser patterning, micromachining, and laser surface treatment processes [1,2].

Short-laser heating of metals involves deposition of radiation energy on electrons, resulting in energy increase in electrons; energy is transferred to lattice through electron-lattice interaction and propagates through media. Theoretical models in literature that are used to describe this nonequilibrium energy transport during the short-pulse laser heating are the classical parabolic one-step model [1,3], the hyperbolic one-step model [1], the parabolic two-step model and hyperbolic two-step model [1,4], and the dual phase lag (DPL) model developed by Tzou [4]. As reported in Refs. [1,4], the one-step models are considered inapplicable for the theoretical analysis of short-pulse laser heating of metals. The parabolic two-step model captures the heating and thermalization processes of the electron temperature in short-pulse laser heating of thin metal films fairly well, although it fails to predict finite speed of energy propagation [1,4]. The hyperbolic two-step model is found to agree well with the experimental data in subpicosecond laser heating processes of thin metal films [1]. Recently, a semiclassical two-temperature model was formulated to account for the effects of electron drifting and electron kinetic pressure [5].

The dual phase lag model was developed to account for both the temporal and spatial effects of heat transfer in one-temperature formulation [4,6] and takes the form

$$\boldsymbol{q}(\boldsymbol{r}, t + \tau_q) = -k \nabla T(\boldsymbol{r}, t + \tau_T)$$

The quantities τ_q and τ_T in this model are the phase lag of the heat flux and the phase lag of the temperature gradient, respectively. In the DPL model framework, τ_q captures the fast transient effect of thermal inertia and τ_T captures the time delay due to the microstructural interaction effect [4,6]. The DPL model reduces to classical Fourier's heat diffusion, thermal wave, phonon-electron interaction, and phonon scattering models when values of τ_q and τ_T are changed [4,6]. The phonon-electron interaction model is obtained with nonzero values of both τ_q and τ_T with $\tau_q < \tau_T$ [4]. The parabolic two-step heating model with temperature-independent thermophysical properties was reformulated in Ref. [4] to derive two identical equations governing transient energy transport in both the electron gas and the metal lattice. These two equations are identical in form to the energy equation utilizing the linearized form of the dual phase lag constitutive relation. The phase lags τ_q and τ_T are hence related to the thermophysical quantities appearing in the two-step parabolic model and are estimated for different metals [4]. The phase lags in Ref. [4] are, however, adjusted to account for the strong dependency on temperature of thermal conductivity and heat capacity of the electron gas. The formulation is detailed in Ref. [4] and is thus not repeated here. With this equivalency between the energy equation based on the DPL model and the two-step parabolic model with temperature-independent thermophysical properties, the problem of short-pulse laser heating of a thin gold film was studied in Ref. [4] using the DPL model to explain the transient energy transport in terms of the lagging thermal behavior. Theoretical predictions of the reflectivity change at the front surface of a thin gold film irradiated by a short laser heat pulse based on this model are found to agree well with the experimental data available, whereas it fails to give acceptable results on the rear surface.

Contributed by the Heat Transfer Division of ASME for publication in the JOURNAL OF HEAT TRANSFER. Manuscript received April 16, 2008; final manuscript received May 1, 2009; published online August 19, 2009. Review conducted by Cholik Chan.

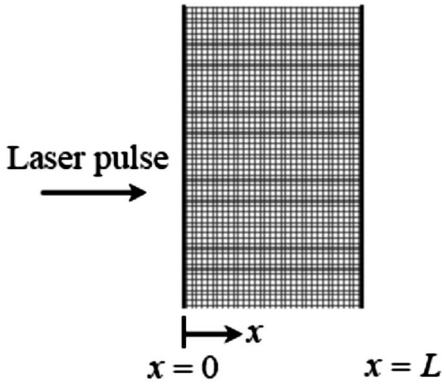

Fig. 1 Problem geometry: a thin metal film exposed to a short laser pulse

The problem of short-pulse laser heating on a thin gold film using the DPL model with constant phase lags is revisited in this work. The problem formulation using the DPL model is first presented in general form and is then used to rederive the solution obtained in Ref. [4] within the context of the present work. A discussion of the results obtained from this solution in terms of the laser pulse profile together with the initial and boundary conditions implemented in the solution of Ref. [4] is presented, followed by a discussion of the results obtained with a laser pulse almost identical to the one used in Ref. [1] but does give negligible heat losses at the boundaries. A comparison between the two solutions is made in terms of the temperature and heat flux distributions, as well as the reflectivity change at the front surface of a thin gold film. Based on the results presented, concluding remarks on the use of the DPL model in short-pulse laser heating processes of metals are then stated.

2 Problem Formulation

The problem geometry in this study is simply a thin metal film exposed to a short-laser heat pulse at the front surface [1,4] (left boundary), as shown in Fig. 1. The heat conduction equation and the linearized form of the dual phase lag model [4] take the form

$$q + \tau_q \frac{\partial q}{\partial t} + k\frac{\partial T}{\partial x} + k\tau_T \frac{\partial^2 T}{\partial t\,\partial x} = 0 \tag{1}$$

$$\frac{k}{\alpha}\frac{\partial T}{\partial t} + \frac{\partial q}{\partial x} = S(x,t) \tag{2}$$

The source term $S(x,t)$ is the laser energy absorption rate given in general form as

$$S(x,t) = S_o F(x) G(t) \tag{3}$$

where S_o is the intensity of the laser absorption and is a constant, $G(t)$ is the light intensity of the laser beam, and

$$F(x) = e^{-x/\delta} \tag{4}$$

with δ being the laser penetration depth.

3 Laplace Transform Solution

The above problem was solved in Ref. [4] using the temperature representation of the energy equation obtained by manipulating Eqs. (1) and (2). However, the mixed temperature-heat flux formulation was used [4] for multilayered films. The problem here is solved using the mixed formulation given by Eqs. (1) and (2) to give the same solution as that obtained in Ref. [4].

Taking the Laplace transform of Eqs. (1) and (2) with p as the Laplace transform parameter gives

$$\bar{q}(x;p) + U\frac{d\bar{T}(x;p)}{dx} = Hq_o(x) + W\frac{dT_o(x)}{dx} \tag{5}$$

$$\frac{d\bar{q}(x;p)}{dx} + \frac{pk}{\alpha}\bar{T}(x;p) = \frac{k}{\alpha}T_o(x) + \bar{S}(x;p) \tag{6}$$

where

$$\bar{S}(x;p) = S_o F(x)\bar{G}(p), \quad U = \frac{k(1+p\tau_T)}{1+p\tau_q}, \quad H = \frac{\tau_q}{1+p\tau_q},$$

$$W = \frac{k\tau_T}{1+p\tau_q} \tag{7}$$

Differentiating Eq. (5) and substituting the result in Eq. (6) give

$$\frac{d^2\bar{T}}{dx^2} - B^2\bar{T} = \frac{H}{U}\frac{dq_o}{dx} + \frac{W}{U}\frac{d^2T_o}{dx^2} - \frac{k}{\alpha U}T_o - \frac{1}{U}\bar{S} \tag{8}$$

where

$$B = \sqrt{\frac{p(1+\tau_q p)}{\alpha(1+\tau_T p)}} \tag{9}$$

Next, defining the reduced temperature gives

$$\theta(x,t) = T(x,t) - T(x,0) = T(x,t) - T_o(x) \tag{10}$$

Equations (5) and (8) are rewritten as

$$\bar{q} + U\frac{d\bar{\theta}}{dx} = Hq_o(x) + \left(W - \frac{U}{p}\right)\frac{dT_o}{dx} \tag{11}$$

$$\frac{d^2\bar{\theta}}{dx^2} - B^2\bar{\theta} = \frac{H}{U}\frac{dq_o}{dx} + \left(\frac{W}{U} - \frac{1}{p}\right)\frac{d^2T_o}{dx^2} - \frac{1}{U}\bar{S} \tag{12}$$

The above problem is solved in Ref. [4] with the following initial and boundary conditions:

$$T(x,0) = T_o(x) = T_\infty = \text{const}, \quad \frac{\partial T(x,0)}{\partial t} = 0 \tag{13}$$

Using Eq. (13) in Eq. (2),

$$\frac{\partial q(x,0)}{\partial x} = S(x,0) = S_o F(x) G(0) \tag{14}$$

and the initial heat flux distribution [4] is found by integrating Eq. (14):

$$q(x,0) = -\delta S_o F(x) G(0) = q_o(x) \tag{15}$$

The nonzero initial heat flux distribution associated with a constant initial temperature (i.e., zero initial temperature gradient), as given by Eqs. (13) and (15), are physically meaningful within the framework of the DPL model only when $\tau_q < \tau_T$ where the temperature gradient lags behind the heat flux, which is indeed the case for metals in general. However, for $\tau_q \geq \tau_T$, the heat flux lags behind the temperature gradient and a nonzero initial heat flux distribution associated with an initial zero temperature gradient is physically not possible in this case.

The boundary conditions used in Ref. [4] assuming negligible heat losses at the boundaries are

$$\frac{\partial T(0,t)}{\partial x} = \frac{\partial T(L,t)}{\partial x} = 0 \tag{16}$$

or in the Laplace transform domain

$$\frac{d\bar{\theta}(0,p)}{dx} = \frac{d\bar{\theta}(L,p)}{dx} = 0 \tag{17}$$

In this work, we use the same boundary conditions (Eqs. (16) and (17)) used in Ref. [4]. The governing equations (Eqs. (11) and (12)) with the above conditions are reduced to

$$\bar{q} + U\frac{d\bar{\theta}}{dx} = Hq_o(x) \tag{18}$$

$$\frac{d^2\bar{\theta}}{dx^2} - B^2\bar{\theta} = \frac{H}{U}\frac{dq_o}{dx} - \frac{1}{U}\bar{S} \tag{19}$$

Using Eq. (15) in Eq. (19),

$$\frac{d^2\bar{\theta}}{dx^2} - B^2\bar{\theta} = \gamma F(x) \tag{20}$$

where

$$\gamma = \frac{S_o[HG(0) - \bar{G}]}{U} \tag{21}$$

The general solution of Eq. (20) is given as

$$\bar{\theta}(x;p) = A_1 e^{Bx} + A_2 e^{-Bx} + A_3 F(x) \tag{22}$$

where the constant A_3 is found by using Eq. (22) in Eq. (20):

$$A_3 = \frac{S_o}{1/\delta^2 - B^2}\left(\frac{HG(0) - \bar{G}}{U}\right) = \frac{\gamma\delta^2}{1 - B^2\delta^2} \tag{23}$$

Using the boundary conditions (17) in Eq. (22), the constants A_1 and A_2 [4] are evaluated as

$$A_1 = \frac{A_3}{\delta B}\frac{e^{-L/\delta} - e^{-BL}}{e^{BL} - e^{-BL}}, \quad A_2 = A_1 - \frac{A_3}{\delta B} \tag{24}$$

The governing equation for the heat flux in the Laplace transform domain (not computed in Ref. [4]) can be found by differentiating Eq. (22) and substituting the result in Eq. (18), which gives

$$\bar{q}(x,p) = Hq_o(x) - U\left[A_1 Be^{Bx} - A_2 Be^{-Bx} - \frac{A_3}{\delta}F(x)\right] \tag{25}$$

The laser heat pulse used in Ref. [4] takes the following form:

$$S(x,t) = \frac{2}{\sqrt{\pi/\ln(2)}}J\left(\frac{1-R}{t_p\delta}\right)e^{-x/\delta}e^{-a|t/t_p|} = S_o F(x)G(t) \tag{26}$$

while the original laser heat source term used in Ref. [1] using one- and two-step heat conduction models is given as

$$S(x,t) = \frac{2}{\sqrt{\pi/\ln(2)}}J\left(\frac{1-R}{t_p\delta}\right)e^{-x/\delta}e^{-(4\ln 2)(t/t_p)^2} = S_o F(x)G^*(t) \tag{27}$$

where R is the reflectivity of the surface layer, J is the laser fluence, δ is the laser penetration depth, t_p is the Laser pulse full-width-at-half-maximum (FWHM) duration, and a is a constant parameter.

As stated in Ref. [4], Eq. (26) is used instead of Eq. (27) to avoid the complexity of the Laplace transform inversion of error functions and it better fits the experimental results. The difference between the two laser pulses (Eqs. (26) and (27)) is only in the temporal Gaussian distribution as is clear from the above two equations. Following the analysis presented in Ref. [4], the temporal Gaussian distribution is shifted in time by $-2t_p$ so that Eqs. (26) and (27) become

$$S(x,t) = \frac{2}{\sqrt{\pi/\ln(2)}}J\left(\frac{1-R}{t_p\delta}\right)e^{-x/\delta}e^{-a|t-2t_p|/t_p} = S_o F(x)G(t) \tag{28}$$

$$S(x,t) = \frac{2}{\sqrt{\pi/\ln(2)}}J\left(\frac{1-R}{t_p\delta}\right)e^{-x/\delta}e^{-(4\ln 2)(t/t_p - 2)^2} = S_o F(x)G^*(t) \tag{29}$$

As stated in Ref. [4], the factor $(t-2t_p)$ in Eqs. (28) and (29) results from shifting the initial time from zero to $-2t_p$ in correspondence with the analysis of Qiu and Tien [1] using the parabolic two-step model, where the laser heating of the electron-lattice starts from a thermalization state. The time shift in Eqs. (28) and (29) also simplifies the implementation of the Laplace transform solution method used in this work.

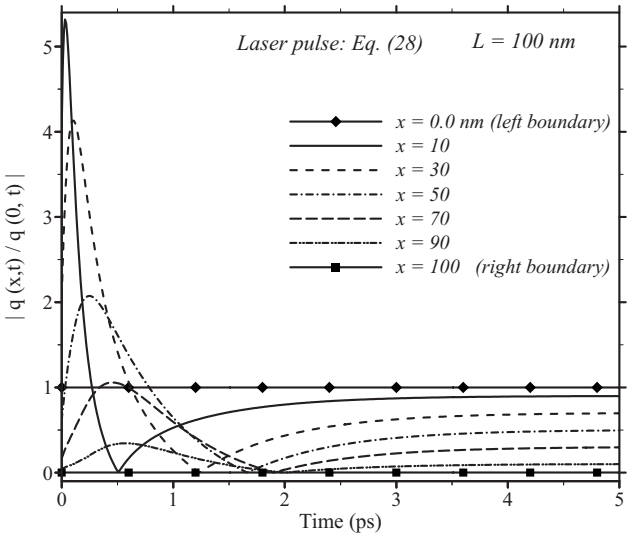

Fig. 2 Variation in the normalized heat flux with time at different locations in gold film with the laser pulse given by Eq. (28)

Comparing Eqs. (28) and (29) with Eq. (3), it follows that

$$S_o = \frac{2}{\sqrt{\pi/\ln(2)}}J\left(\frac{1-R}{t_p\delta}\right) \tag{30}$$

$$G(t) = e^{-a|t-2t_p|/t_p} \tag{31}$$

$$G^*(t) = e^{-(4\ln 2)(t/t_p - 2)^2} \tag{32}$$

and the Laplace transform of $G(t)$ (Eq. (31)) [4] is given as

$$\bar{G}(p) = \int_0^\infty e^{-pt}G(t)dt = t_p\left[\frac{e^{-2a} - e^{-2pt_p}}{pt_p - a} + \frac{e^{-2pt_p}}{pt_p + a}\right] \tag{33}$$

The temperature and heat flux distributions in the metal film (Fig. 1) are calculated by inverting the Laplace transformed Eqs. (22) and (25) to the physical time domain using the Reimann sum method detailed in Ref. [4].

4 Results and Discussion

The presumption of negligible boundary heat losses supposed to result from setting the temperature gradients at the boundaries to zero (Eq. (16)) in the above solution is first assessed by computing the heat flux at the boundaries and comparing it with the heat flux at different times and locations in the metal film during the heating process of the metal film. The same parameters used in Ref. [4] to theoretically predict the reflectivity change of a thin gold film are used in this work: $J = 13.4$ W/m^2, $\delta = 15.3 \times 10^{-9}$ m, $a = 1.992$, $t_p = 100 \times 10^{-15}$ s, and $R = 0.93$. The thermal properties of gold are taken as $k = 315$ W/m K and $\alpha = 1.2 \times 10^{-4}$ m^2/s, while the phase lags are taken as $\tau_q = 8.5 \times 10^{-12}$ s and $\tau_T = 90 \times 10^{-12}$ s.

Figure 2 shows the variation in the absolute value of the normalized heat flux with time at different locations within the film including the left and right boundaries. Figure 3 also shows the variation in the normalized heat flux with distance at different times. The heat flux $q(x,t)$ at any location in the domain is normalized via dividing it by the heat flux at the left boundary $q(0,t)$ and the absolute value of this ratio is taken since the magnitude of

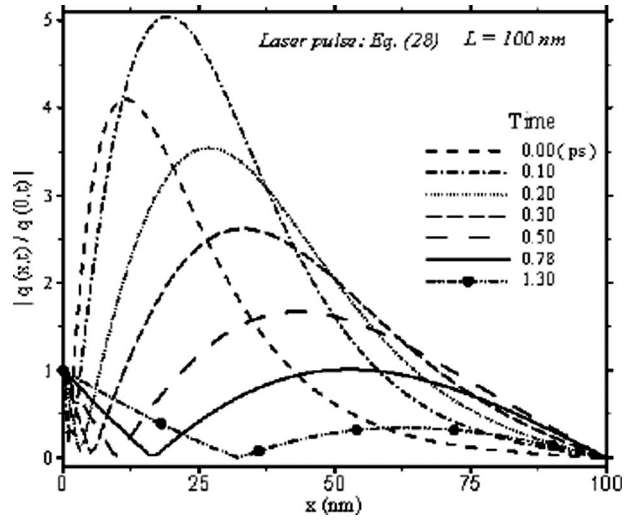

Fig. 3 Variation in the normalized heat flux with distance at different times with the laser pulse given by Eq. (28)

the heat flux rather than its direction is most important to the discussion. These two figures clearly show that the heat flux at the left boundary (heat loss) is even higher than the heat flux at any location in the film for $t>0.78$ ps. The heat flux at locations $x=10$, 30, and 50 nm for $t<0.78$ ps is around 5, 4, and 2 times higher than that at the left boundary. Hence, the heat loss from the left boundary is considerably large at any time during both the heating and thermalization processes. Thus, within the framework of the problem formulation above, setting the temperature gradient to zero at the boundaries does not give negligible heat losses from the film and the use of a laser pulse in the form of Eq. (28) gives a heat loss at the left boundary that is comparable to or even higher than the heat flux at any location within the film. This is also clear from Eq. (18), where setting $d\bar{\theta}/dx=0$ at a boundary implies a negligible heat loss only when the initial heat flux $q_o(x)\approx 0$.

The variation with time of the temperature in the film at different locations corresponding to Figs. 2 and 3 is shown in Fig. 4. The temperature at all locations and after sometime continually decreases with time with the highest rate of decrease being at the left boundary due to the high heat losses there. The temperature variation in Fig. 4 is shown for a duration of 10 ps. After around 10 ps, the temperature in the whole film indeed drops below its initial value. This unrealistic behavior results from the large heat losses due to the implementation of zero temperature gradient condition together with the initial heat flux distribution resulting from the laser pulse as given by Eq. (28) and raises a question in terms of the time interval during which the solution above is valid.

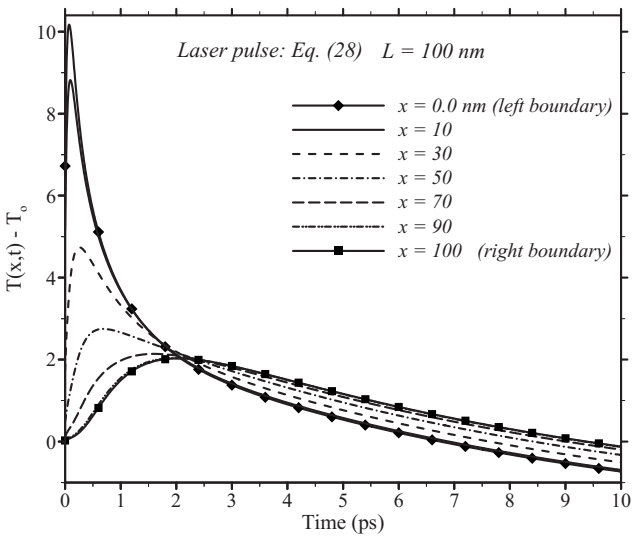

Fig. 4 Temperature variation with time at different locations in gold film with the laser pulse given by Eq. (28)

The boundary heat fluxes can, in fact, be evaluated using the governing equations and the initial and boundary conditions used in the solution. Applying the initial and boundary conditions (Eqs. (13)–(16)) to Eq. (1) at the boundaries result in

$$q(0,t)+\tau_q\frac{\partial q(0,t)}{\partial t}=0,\quad q(L,t)+\tau_q\frac{\partial q(L,t)}{\partial t}=0 \tag{34}$$

Likewise, Eq. (18) after applying the boundary conditions (Eq. (17)) is reduced at the boundaries to

$$\bar{q}(0;p)=Hq_o(0),\quad \bar{q}(L;p)=Hq_o(L) \tag{35}$$

The solutions of either of the above two equations give the boundary heat fluxes as

$$q(0,t)=-q_o(0)e^{-t/\tau_q}=-\delta S_o G(0)e^{-t/\tau_q} \tag{36}$$

$$q(L,t)=-q_o(L)e^{-t/\tau_q}=-\delta S_o G(0)e^{-L/\delta}e^{-t/\tau_q} \tag{37}$$

Even at the right boundary, where the heat flux is around three orders of magnitude less than that at the left boundary ($q(L,t)/q(0,t)=e^{-L/\delta}\approx 0.00145$), the heat flux there is not negligible compared with the heat flux at locations close to the right boundary during early times of the heating process and is, in fact, close to the heat flux at any location in the film for $t>1.5$ ps as is clear from Figs. 2 and 3. Moreover, with the formulation above and for $\tau_q=\tau_T=0$ (the parabolic one-step model), which is a special case of the DPL model, Eq. (34) or Eq. (35) with zero temperature gradients at the boundaries employed in the above solution reduces to $q(0,t)=q(L,t)=0$, which is in contradiction with Eq. (18) unless $q_o(x)=0$. In addition, a nonzero initial heat flux distribution associated with a constant initial temperature (i.e., zero initial temperature gradient) within the film presented by Eqs. (13) and (15) are physically meaningful within the framework of the DPL model only when $\tau_q<\tau_T$, where the temperature gradient lags behind the heat flux. However, for $\tau_q\geq\tau_T$, the temperature gradient is the cause of energy transport while the heat flux is the effect; hence the heat flux lags behind the temperature gradient so that an initial heat flux distribution associated with an initial zero temperature gradient is physically not possible in this case and the use of Eqs. (13) and (15) is not admissible unless the initial heat flux distribution is vanishingly small or zero.

From the above discussion and results, it is clear that the conditions of zero temperature gradients at the boundaries do not imply negligible boundary heat losses unless the initial heat flux distribution $q_o(x)$ that is determined from the laser heat source term is negligible (i.e., $q_o(x)\to 0$). This condition is clearly dependent on the temporal Gaussian distribution function $G(t)$. By inspecting Eqs. (31) and (32), one finds the ratio $G(0)/G^*(0)=e^{-2a}/e^{-16\ln 2}\cong 1220$. This means that using the laser heat source term of Eq. (28) results in an initial heat flux distribution $q_o(x)$ that is around three orders of magnitude higher than the initial heat flux that would be produced if Eq. (29) were used. To remedy this problem, and avoid the complexity of evaluating the Laplace inversion of the temporal Gaussian distribution function given by Eq. (32) but still have a reliable semi-analytical solution of the problem, the following temporal distribution function is used in the laser pulse:

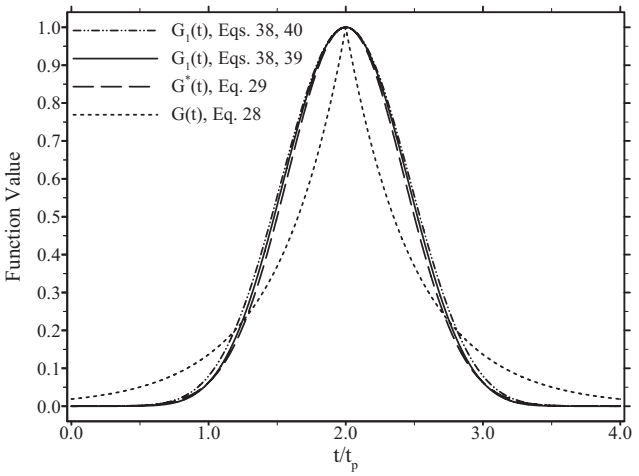

Fig. 5 Temporal Gaussian distribution of the laser pulses given by Eqs. (28), (29), and (38)–(40)

$$G_1(t) = \left[c_1 - c_2 \cos\left(\frac{\pi t}{2t_p} \right) \right]^4 \tag{38}$$

The function in Eq. (38) approximates Eq. (32) very closely with the proper choice of the constants c_1 and c_2. The constants c_1 and c_2 can be evaluated under the conditions that $G_1(0)=G^*(0)$ and $G_1(2t_p)=G^*(2t_p)=1$. This gives

$$c_1 = 0.5(1 + e^{-16 \ln 2})^{1/4}, \quad c_2 = 1 - c_1 \tag{39}$$

resulting in the same initial heat flux $q_o(x)$ as that given by Eq. (32), which is 1220 times less than that produced by Eq. (31). Also, the function given in Eq. (38) has the property $G_1(0)=0$ and its value is 1 at $t/t_p=2$ for

$$c_1 = c_2 = 0.5 \tag{40}$$

This results in a perfectly zero initial heat flux and constant initial temperature distributions so that in view of Eq. (18) the use of a zero temperature gradient at a boundary perfectly reduces to a zero boundary heat loss. The temporal Gaussian distributions given by Eqs. (28), (29), and (38) are all shown in Fig. 5. Clearly, the pulses given by Eq. (30) very closely approximate the laser pulse given by Eq. (29) for both $c_1 \neq c_2$ as given by Eq. (39) and $c_1=c_2=0.5$ (Eq. (40)), with a negligible initial zero heat flux in the first and perfectly zero initial heat flux in the second as explained above, while the pulse given by Eq. (28) is considerably different in shape and more importantly in terms of the function initial value.

The variation in the normalized heat flux distribution in both time and space in the gold film are shown in Figs. 6 and 7 using the laser pulse of Eqs. (38) and (39). These results show that the heat flux at the boundaries is in this case much smaller than the heat flux at any location within the film during the heating process opposing the results shown in Figs. 2 and 3 with the laser pulse given by Eq. (28). Thus, with the laser pulse of Eq. (38), setting the temperature gradients at the boundaries to zero does result in negligible heat losses from the boundaries. Figure 8 shows the temperature variation with time in the gold film at different locations corresponding to Figs. 6 and 7. The temperature rises due to the applied laser heat pulse and then tends to approach a steady value but does not continually decrease as was the case in Fig. 4. This is due to the fact that the heat flux at the boundaries is indeed negligible as clarified in Figs. 6 and 7.

Next, the normalized temperature change (reflectivity change) at the left surface of the gold film is investigated. Figures 9 and 10 show the reflectivity change at the front surface of gold films with widths $L=100$ nm and $L=200$ nm, respectively, using the laser pulse of Eqs. (38)–(40) that closely approximate Eq. (29) used in

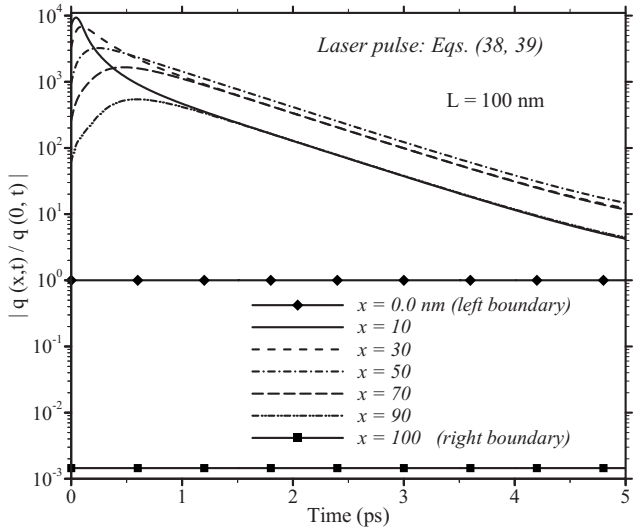

Fig. 6 Variation in the normalized heat flux with time at different locations in gold film with the laser pulse given by Eqs. (38) and (39)

Ref. [1] within the framework of one- and two-step heating models, together with the experimental results of Brorson et al. [7] and the solution of Ref. [4]. The present solution clearly deviates considerably from the experimental results and that given in Ref. [4] for the reasons explained above. However, the present solution and the experimental data both share the common feature that after around 2 ps the normalized temperature change tends to assume a near constant value, contrary to the solution in Ref. [4] that shows a continuous decrease in temperature as explained earlier in this section. The more sharp temperature drop in the solution of Ref. [4] that makes it better match the experimental results is due to the very large heat losses from the left boundary, as shown in Figs. 2 and 3. As reported in Ref. [4], the DPL model fails to predict the reflectivity change at the rear surface of the thin gold film; hence and from the analysis and results presented in this work, it should not be expected that the DPL model results in a good agreement with the experimental data or predictions of the two-step heating models. Figure 11 provides a comparison between predictions of the DPL, parabolic, and hyperbolic one-step

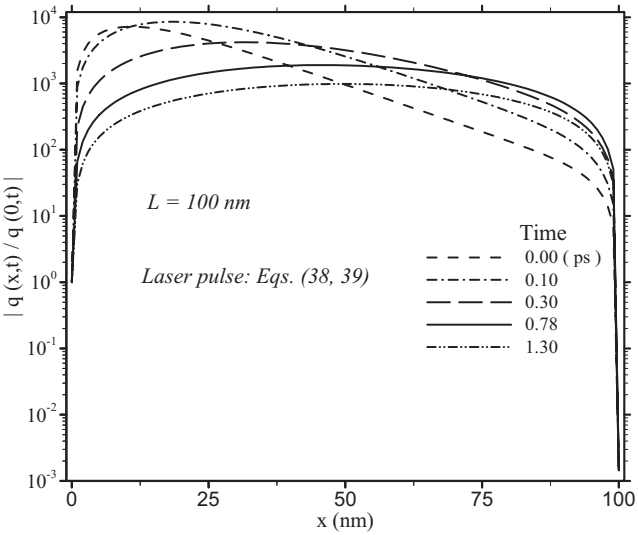

Fig. 7 Variation in the normalized heat flux with distance at different times with the laser pulse given by Eqs. (38) and (39)

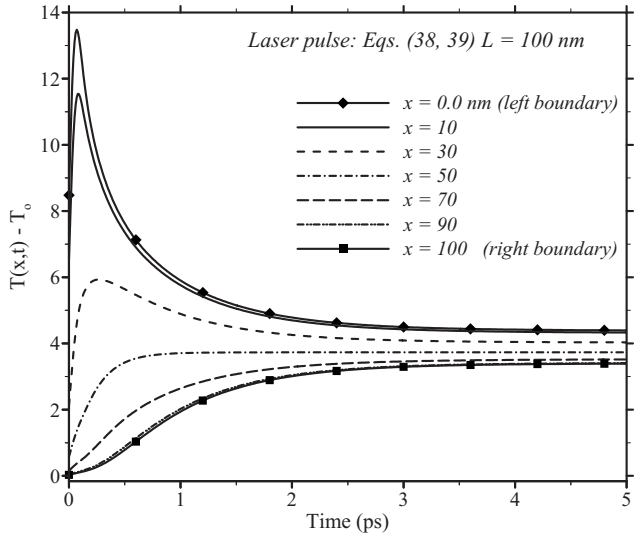

Fig. 8 Temperature variation with time at different locations in gold film with the laser pulse given by Eq. (28)

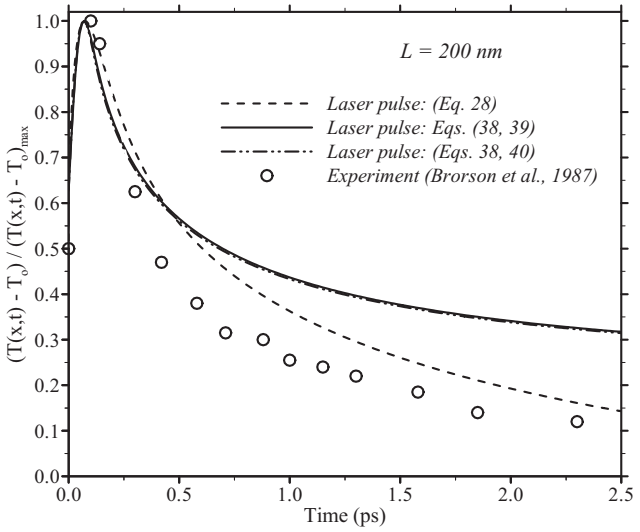

Fig. 10 Normalized temperature change at the left surface of gold film (L=200 nm) using laser pulses given by Eqs. (28) and (38)–(40) together with the experimental data

models in terms of the normalized temperature change at the front surface of gold film. These one-step models deviate considerably from the experimental results, although predictions of the DPL model are the closest to the experimental data.

Figures 12 and 13 present a comparison between the experimental data and predictions of the DPL model over a wide range of the phase lag ratios, including the values τ_q=8.5 ps and τ_T =90 ps estimated and used in Ref. [4] as well as in the present work (Figs. 2–11). The laser pulse in these two figures is as given by Eqs. (38) and (40) that give rise to zero boundary heat loss so that the zero heat flux and the zero temperature gradient at the boundaries are perfectly equivalent. Clearly the DPL model deviates considerably from the experimental data for any pair of τ_q and τ_T. Increasing the value of τ_q (with constant τ_T), as in Fig. 12, or decreasing the value of τ_T (with constant τ_q), as in Fig. 13, shifts the DPL more toward the parabolic one-step model shown in Fig. 11.

5 Conclusions

The problem of short-pulse laser heating of a thin gold film is investigated in this work using the DPL model with constant phase lags. The initial heat flux distribution in the thin film resulting from the temporal distribution function of the laser pulse together with the zero temperature gradients at the boundaries normally used in literature with the presumption that they result in negligible boundary heat losses are analyzed in detail in this paper. The analysis presented here show that using zero temperature gradients at the boundaries does not guarantee negligible boundary heat losses unless the initial heat flux distribution is negligibly small. Depending on the value of the initial heat flux distribution, the presumed negligible heat losses at the boundaries can be even way larger than the heat flux at any location within the film during the short-pulse laser heating process. The mathematical representation of the laser pulse together with the resulting initial heat flux

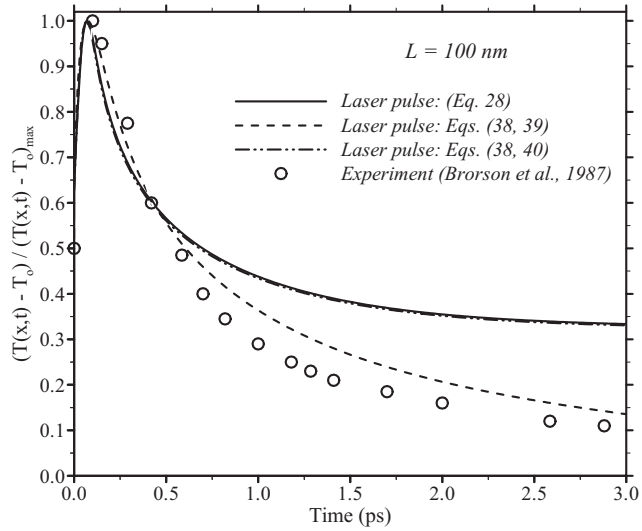

Fig. 9 Normalized temperature change at the left surface of gold film (L=100 nm) using laser pulses given by Eqs. (28) and (38)–(40) together with experimental data

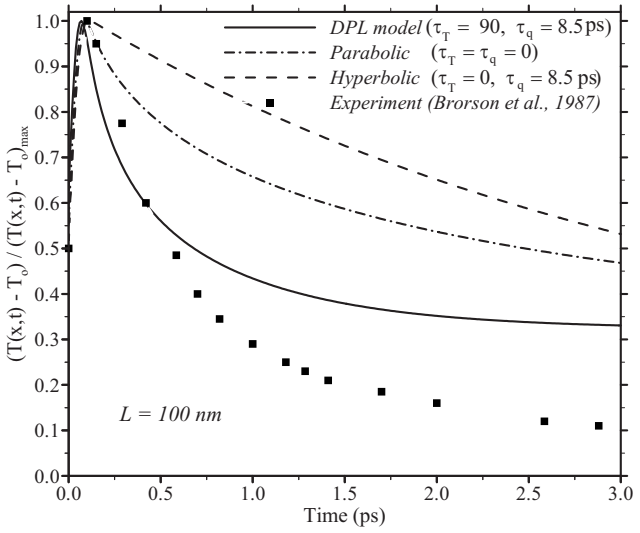

Fig. 11 Normalized temperature change at the left surface of gold film (L=100 nm) with negligible boundary heat losses (Eqs. (38) and (39)): a comparison between predictions of the DPL, parabolic, and hyperbolic models together with experimental data

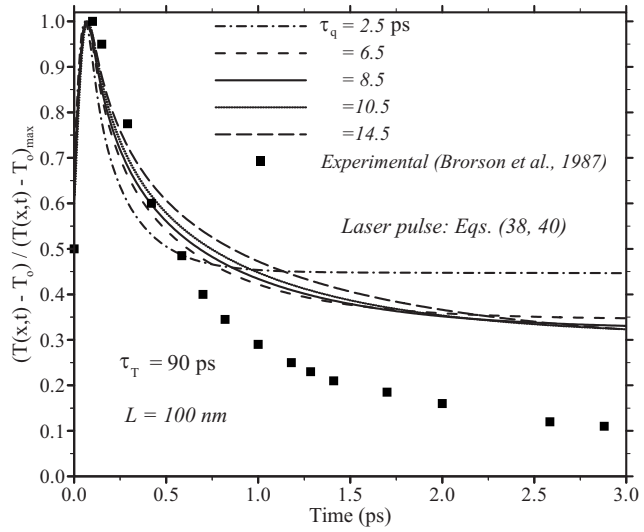

Fig. 12 Normalized temperature change at the left surface of gold film (L=100 nm) with zero boundary heat losses (Eqs. (38) and (40)): a comparison between experimental data and predictions of the DPL for τ_T=90 ps and a range of τ_q

distribution and the zero temperature gradients at the boundaries is thus very critical to the thermal analysis of thin films exposed to short-pulse laser heating. Contrary to what has been reported in literature, predictions of the reflectivity change of a thin gold film

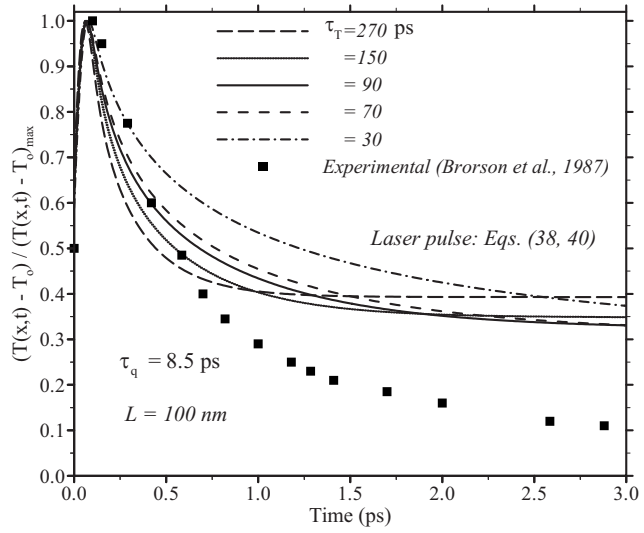

Fig. 13 Normalized temperature change at the left surface of gold film (L=100 nm) with zero boundary heat losses (Eqs. (38) and (40)): a comparison between experimental data and predictions of the DPL model for τ_q=8.5 ps and a range of τ_T

due to a laser short heat pulse using the dual phase lag model are found to deviate considerably from the experimental data. The dual phase lag model is found to overestimate the transient temperature in the thermalization stage of the heating process of metal films. The seemingly good agreement between the experimental data and theoretical predictions using the DPL model with constant phase lags in the thermalization stage seem to be a result of the very large heat losses from the boundary. The DPL model with constant phase lags is hence incapable of giving acceptable predictions not only on the rear surface of thin gold film as reported in Ref. [4] but also on the front surface, though it is still superior to the parabolic and hyperbolic one-step models.

Nomenclature

J = laser fluence (J/m^2)
k = thermal conductivity ($W/m\,K$)
L = film width (m)
p = Laplace transform parameter
$\boldsymbol{q}$ = heat flux vector (W/m^2)
q = heat flux (W/m^2)
q_o = initial heat flux (W/m^2)
$\bar{q}$ = Laplace transform of q
$\boldsymbol{r}$ = position vector (m)
R = radiative reflectivity
T = temperature (K)
T_o = initial temperature (K)
t = time (s)
t_p = laser pulse full-width-at-half-maximum duration (s)
x = x-coordinate

Greek Symbols

α = thermal diffusivity (m^2/s)
θ = reduced temperature ($T-T_o$)
$\bar{\theta}$ = Laplace transform of θ
τ_q = phase lag of the heat flux (s)
τ_T = phase lag of the temperature gradient (s)
δ = penetration depth of laser radiation (m)

References

[1] Qiu, T. Q., and Tien, C.-L., 1993, "Heat Transfer Mechanisms During Short-Pulse Laser Heating of Metals," ASME J. Heat Transfer, **115**, pp. 835–841.
[2] Al-Nimr, M. A., and Arpaci, V. S., 1999, "Picosecond Thermal Pulses in Thin Metal Films," J. Appl. Phys., **85**, pp. 2517–2521.
[3] Burzo, M. G., Komarov, P. L., and Raad, P. E., 2003, "Thermal Transport Properties of Gold-Covered Thin-Film Silicon Dioxide," IEEE Trans. Compon. Packag. Technol., **26**, pp. 80–88.
[4] Tzou, D. Y., 1997, *Macro- to Microscale Heat Transfer: The Lagging Behavior*, Taylor & Francis, Washington, DC, pp. 111–146.
[5] Chen, J. K., Tzou, D. Y., and Beraun, J. E., 2006, "A Semiclassical Two-Temperature Model for Ultrafast Laser Heating," Int. J. Heat Mass Transfer, **49**, pp. 307–316.
[6] Wang, L. Q., Zhou, X. S., and Wei, X. H., 2008, *Heat Conduction: Mathematical Models and Analytical Solutions*, Springer-Verlag, Berlin, pp. 21–55.
[7] Brorson, S. D., Fujimoto, J. G., and Ippen, E. P., 1987, "Femtosecond Electron Heat Transport Dynamics in Thin Gold Film," Phys. Rev. Lett., **59**, pp. 1962–1965.

Analysis of a Hyperbolic Heat Conduction-Radiation Problem With Temperature Dependent Thermal Conductivity

Subhash C. Mishra[1]
e-mail: scm_iitg@yahoo.com

T. B. Pavan Kumar[2]

Department of Mechanical Engineering,
Indian Institute of Technology Guwahati,
Guwahati, Assam 781039, India

This article deals with the analysis of a hyperbolic conduction and radiation heat transfer problem in a planar participating medium. Thermal conductivity of the medium is temperature dependent. Hyperbolic conduction is due to non-Fourier effect. The boundaries of the medium can be either at prescribed temperatures and/or fluxes. With both boundaries insulated, effects of a short pulse internal heat source in the medium are also considered. The problem is analyzed using the lattice Boltzmann method. The finite volume method is employed to compute the radiative information required. Transient temperature distributions in the medium are studied for the effects of various parameters.
[DOI: 10.1115/1.3154621]

Keywords: non-Fourier conduction, radiation, temperature dependent thermal conductivity

1 Introduction

The analysis of radiation along with Fourier conduction finds applications in the design of many engineering devices. The assumption of an infinite speed of conduction wave front made in Fourier heat conduction is not applicable for extremely short time levels, at normal time levels near the absolute zero temperature, and in the processed meat/skin [1]. This limitation with infinite propagation speed in the Fourier's law of heat conduction was pointed out by Cattaneo [2] and Vernotee [3], and they proposed a modified form of the conduction equation called the non-Fourier heat conduction equation.

Following the proposition by Cattaneo [2] and Vernotee [3] in the past two decades, a good amount of work [4–7] has been devoted in studying the non-Fourier effects in many thermal systems. Problems involving non-Fourier conduction combined with radiation have been investigated in simple to complex geometries [1]. Problems were analyzed with various numerical methods. Conduction-radiation problems in a 1D planar medium considering non-Fourier effects have been studied by many [5,6]. Recently, Mishra et al. [7] solved non-Fourier conduction-radiation problem in a planar medium. They used the lattice Boltzmann method (LBM) combined with the finite volume method (FVM) for the radiative information.

In many heat transfer problems, temperature varies over a wide range, and thus in such problems, the assumption of constant thermal conductivity leads to inaccurate results [6,8,9]. However, with consideration of temperature dependent thermal conductivity, the energy equation becomes nonlinear and its solution thus becomes difficult. Transient conduction-radiation problems with temperature dependent thermal conductivity have been reported in Refs. [8,9].

Because of the hyperbolic nature, solutions of heat transfer problems with non-Fourier effect are relatively difficult [5–7]. Consideration of temperature dependent thermal conductivity in such problems brings additional difficulty. Chen [6] studied effects of temperature dependent thermal conductivity in a non-Fourier heat conduction problem in a 1D planar finite, and also a semi-infinite medium. However, he did not consider the effect of radiation. The present work is, therefore, aimed at solving a 1D conduction-radiation problem considering non-Fourier effect in conduction and temperature dependent thermal conductivity. The problem is solved using the LBM in which unlike conventional numerical methods, nonlinearity does not manifest in the solution methodology. Radiative information is computed using the FVM. The medium boundaries can be maintained at constant temperatures, and/or fluxes. A pulse heat generation may remain present in a specific region in the medium. For the effects of the temperature dependent thermal conductivity, temperature distributions in the medium are studied for different values of the extinction coefficient, the scattering albedo, and the conduction-radiation parameter.

2 Formulation

Consideration is given to a 1D planar participating medium having initial temperature T_E. For time $t>0$, its west boundary is raised to temperature T_W, while its east boundary is kept either at temperature T_E or heat flux q_E. Both boundaries can also be insulated when the medium contains a localized pulse energy source g^*. Except thermal conductivity, all other properties of the medium are constant. Thermal conductivity k is assumed to vary as

$$k = k_0(1 + \gamma' T) \tag{1}$$

where γ' is the measure for the variation of thermal conductivity with temperature.

For the problem under consideration, the governing energy equation is given by

$$\rho c_p \frac{\partial T}{\partial t} = -\frac{\partial q_C}{\partial x} - \frac{\partial q_R}{\partial x} + g^* \tag{2}$$

where ρ, c_p, q_C, and q_R are density, specific heat, conductive flux, and radiative flux, respectively.

Assuming finite propagation speed of the conduction wave front q_C, heat conduction equation is given by [2,3]

[1]Corresponding author.
[2]Mr. Kumar contributed to this work when he was an MTech student at IIT Guwahati from July 2006 to July 2008.

Contributed by the Heat Transfer Division of ASME for publication in the JOURNAL OF HEAT TRANSFER. Manuscript received June 12, 2008; final manuscript received April 28, 2009; published online August 19, 2009. Review conducted by Ofodike A. Ezekoye.

$$\Gamma\frac{\partial q_C}{\partial t} + q_C = -k\frac{\partial T}{\partial x} \tag{3}$$

where with temperature dependent thermal conductivity, the thermal relaxation time $\Gamma = \alpha/C^2 = k_0(1+\gamma' T)/\rho c_p C^2 = \Gamma_0(1+\gamma' T)$.

From Eqs. (2) and (3), we get

$$(\rho c_p)\left(\Gamma\frac{\partial^2 T}{\partial t^2} + \frac{\partial T}{\partial t}\right) = k_0(1+\gamma' T)\frac{\partial^2 T}{\partial x^2} + k_0\gamma'\left(\frac{\partial T}{\partial x}\right)^2 - \frac{\partial q_R}{\partial x} + g^* - \Gamma\left[\frac{\partial}{\partial t}\left(\frac{\partial q_R}{\partial x} - g^*\right)\right] \tag{4}$$

It is to be noted that because of the non-Fourier effect, in one hand, the problem becomes hyperbolic, and because of temperature dependent thermal conductivity (Eq. (1)), the problem is highly nonlinear.

The divergence of radiative heat flux $\partial q_R/\partial x$ in Eq. (4) is given by

$$\frac{\partial q_R}{\partial x} = \beta(1-\omega)\left(4\pi\frac{\sigma T^4}{\pi} - G^*\right) \tag{5}$$

where β is the extinction coefficient, ω is the scattering albedo, and G^* is the incident radiation.

In dimensionless form, defining time ξ, distance η, temperature θ, coefficient of temperature dependent thermal conductivity γ, radiative heat flux Ψ_R, conduction-radiation parameter N, volumetric energy source g, and incident radiation G in the following way:

$$\xi = \frac{Ct}{X} \quad \eta = \frac{x}{X} \quad \theta = \frac{T}{T_{\text{ref}}} \quad \gamma = \gamma' T_{\text{ref}}$$
$$\Psi_R = \frac{q_R}{\sigma T_{\text{ref}}^4} \quad N = \frac{k_{\text{ref}} C}{4\alpha\sigma T_{\text{ref}}^3} \quad g = \frac{X^2\alpha g^*}{k_{\text{ref}} T_{\text{ref}} C^2} \quad G = \frac{G^*}{\sigma T_{\text{ref}}^4/\pi} \tag{6}$$

In dimensionless form Eq. (4) is written as

$$\frac{1}{2}\frac{\partial^2\theta}{\partial\xi^2}(1+\gamma\theta) + \frac{\partial\theta}{\partial\xi} = (1+\gamma\theta)\frac{\partial^2\theta}{\partial\eta^2} + \gamma\left(\frac{\partial\theta}{\partial\eta}\right)^2 - \frac{1}{4N}\left[\frac{\partial\Psi_R}{\partial\eta} + \frac{1}{2}(1+\gamma\theta)\frac{\partial}{\partial\xi}\left(\frac{\partial\Psi_R}{\partial\eta}\right)\right] + \frac{1}{2}\frac{\partial g}{\partial\xi} + g \tag{7}$$

In dimensionless form $\partial\Psi_R/\partial\eta$ appearing in Eq. (5) is written as

$$\frac{\partial\Psi_R}{\partial\eta} = \left(\frac{X\beta(1-\omega)}{\pi}\right)(4\pi\theta^4 - G) \tag{8}$$

By considering the effect of radiation $\partial\Psi_R/\partial\eta$, volumetric heat generation g, and non-Fourier heat conduction, the equivalent form of Eq. (7) in the LBM is given as [7]

$$f_i(\boldsymbol{\eta} + \mathbf{e}_i\Delta\xi, \xi + \Delta\xi) = f_i(\boldsymbol{\eta},\xi) - \frac{\Delta\xi}{\tau}[f_i(\boldsymbol{\eta},\xi) - f_i^{(0)}(\boldsymbol{\eta},\xi)] - 2\Delta\xi y_i e_i\Psi - \left(\frac{\Delta\xi w_i}{4N}\right)\frac{\partial\Psi_R}{\partial\eta} + \frac{w_i}{2}\Delta\xi g \qquad i = 1,2,\ldots b \tag{9}$$

where f_i is the particle distribution function, $e_i = \Delta\eta/\Delta\xi$ is the velocity, τ is the relaxation time, $f_i^{(0)}$ is the equilibrium distribution function, and b is the number of particle distribution functions considered in a lattice. For the 1D planar medium problem under consideration, with D1Q2 lattice, with temperature dependent thermal conductivity, the relaxation time τ is given by [9]

$$\tau = \frac{1}{e_i^2}(1+\gamma\theta) + \frac{\Delta\xi}{2} \tag{10}$$

Temperature and heat flux Ψ are computed from the following [7]:

$$\theta = \sum_{i=1}^{2} f_i \tag{11}$$

$$\Psi = \sum_{i=1}^{2} e_i f_i(1+\gamma\theta) \tag{12}$$

In Eq. (9), the equilibrium distribution function is given by [7]

$$f_i^{(0)} = w_i\theta + y_i e_i\Psi \tag{13}$$

where w_i and y_i are the weights corresponding to the ith direction, and they are given by

$$w_1 = w_2 = y_1 = y_2 = \tfrac{1}{2} \tag{14}$$

Solution procedure for a conduction-radiation problem using the LBM can be found in the work [7,9] of the group of the lead author. The procedure for computing radiative information has been discussed in Ref. [7]. Interested readers can refer to references given in Refs. [7,9].

3 Results and Discussion

To validate results of the present work for non-Fourier conduction with temperature dependent thermal conductivity ($\gamma \neq 0.0$), Figs. 1(*a*)–1(*c*) compare results with those given by Chen [6]. With constant thermal conductivity ($\gamma = 0.0$), for a conduction-radiation problem, in Figs. 1(*d*)–1(*f*) results are compared with those given by Chu et al. [5]. For comparisons made in Figs. 1(*a*) and 1(*b*), the medium is semi-infinite, while for other cases, the medium thickness is unity. While comparing results of the present work with those given in Refs. [5,6], in the LBM-FVM, 100 lattice/control volumes were found sufficient, and in the FVM, no significant change was observed beyond 12 rays.

In all three cases considered in Figs. 1(*a*)–1(*c*), initially the entire system is at temperature $\theta = \theta_E = 0.0$. For the cases considered in Figs. 1(*a*) and 1(*c*), for time $\xi > 0.0$, the west boundary is raised to $\theta_W = 1.0$; whereas in the case of the results in Fig. 1(*b*), the west boundary is subjected to a nonlinear boundary condition having radiative cooling. The boundary condition for this case is represented as

$$\psi_0 = -E_r\theta_W^4 + \psi_w \tag{15}$$

In Eq. (15), the first and second terms on the right-hand side represent heat dissipation by thermal radiation and prescribed heat flux, respectively. In the above equation, the dimensionless $E_r = \alpha_s\sigma\alpha^4 q_r^3/k^4 C^4$ and the wall heat flux $\psi_w = q_w/q_{\text{ref}}$ and its magnitude were taken as unity. In the E_r formula, α_s is the surface absorptivity. For the results given in Fig. 1(*c*), east boundary is insulated ($\Psi_E = 0.0$).

For the comparison made in Figs. 1(*d*)–1(*f*), for non-Fourier heat conduction with constant thermal conductivity ($\gamma = 0.0$) along with radiation, initially $\theta = \theta_E = 0.0$. After time $\xi > 0.0$, the west boundary is raised to $\theta_W = 1.0$. The results are compared for different values of ω, β, and N. From Figs. 1(*a*)–1(*f*), it is observed that results of the present work compare well with those of Refs. [5,6], which have considered different solution methodologies.

In the following pages (Figs. 2–4), we present results for the effect of radiation along with non-Fourier conduction having temperature dependent thermal conductivity in a finite medium with unity thickness. For the purpose of validation, in Figs. 1(*a*)–1(*c*), results of the present work were compared for $\gamma = -0.1, 0.0, +0.1$. From these figures, it is observed that for $\gamma = -0.1, 0.0, +0.1$, no significant change in θ distributions occurred. Therefore, in the

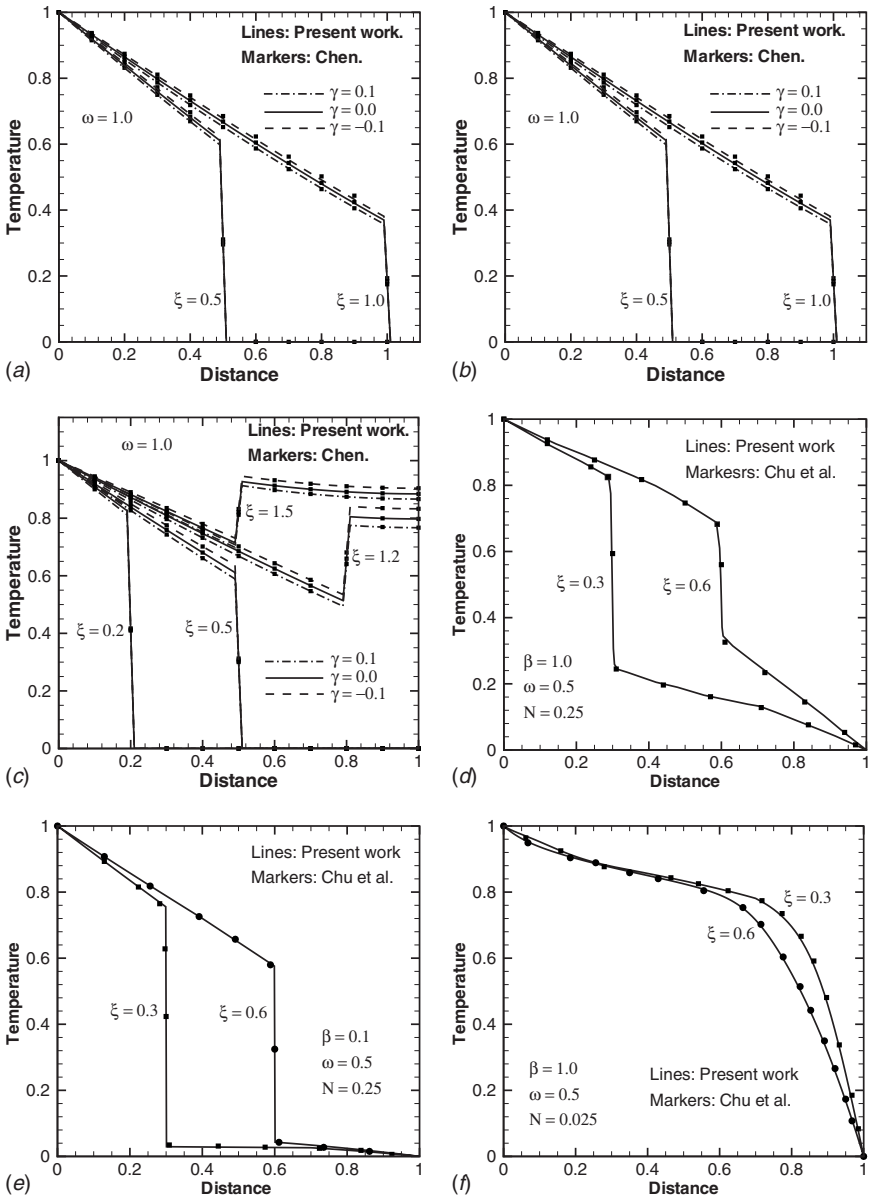

Fig. 1 Validation of results for dimensionless temperature θ distribution in a pure conducting medium (ω=1.0) with three values of γ (=−0.1, 0.0, and 0.1) for (*a*) a temperature boundary condition problem, (*b*) a nonlinear boundary condition (surface radiative cooling) problem with E_r=0.0, and (*c*) a mixed boundary condition problem. Validation of results for θ distribution in a non-Fourier conducting-radiating medium with constant thermal conductivity (γ=0.0) for (*d*) β=1.0, N=0.25, (*e*) β=0.1, N=0.25, and (*f*) β=1.0, N=0.025.

following pages, while considering the effects of the variable thermal conductivity, we present results for γ=−0.25, 0.0, and +0.25.

First we consider the case of a finite medium, which is initially at $\theta=\theta_E=0.0$, and for time $\xi>0$, its west boundary is maintained at $\theta_W=1.0$. In Fig. 2, we present results for this case.

With extinction coefficient $\beta=1.0$ and conduction-radiation parameter $N=1.0$, θ distributions for scattering albedo $\omega=0.0$ and 0.5 are given in Figs. 2(*a*) and 2(*b*), respectively. It is observed from these figures that for a lower value of ω, the effect of γ is less. It is further observed that the effect of γ is significant in the upstream of the wave front. In the downstream, its effect is almost negligible. In the upstream of the wave front, θ is much higher than the downstream, and thus the effect of γ on θ becomes relatively much less in the downstream of the thermal wave front.

With $\omega=0.5$ and $\beta=1.0$, for two values of the conduction-radiation parameter $N=2.5$ and 0.25, effects of γ on θ distributions have been given in Figs. 2(*c*) and 2(*d*), respectively. By considering results given in Fig. 2(*b*) for $N=1.0$, we can compare results for three values of $N=0.25$, 1.0, and 2.5. It is observed from Figs. 2(*b*)–2(*d*) that in a radiation dominated case ($N=0.25$) (Fig. 2(*d*)), the effect of γ manifests in the downstream of the thermal wave front. This effect is relatively more at an early stage ($\xi=0.3$). In the upstream, the effect of γ is more in the conduction dominated case ($N=2.5$) (Fig. 2(*c*)). From these figures, it is also observed that the difference between the maximum and the minimum temperatures at the thermal wave front decreases with a decrease in N. With a decrease in N at the wave front, the maximum and the minimum temperatures also increase. The above trend is owing to the fact that when radiation domi-

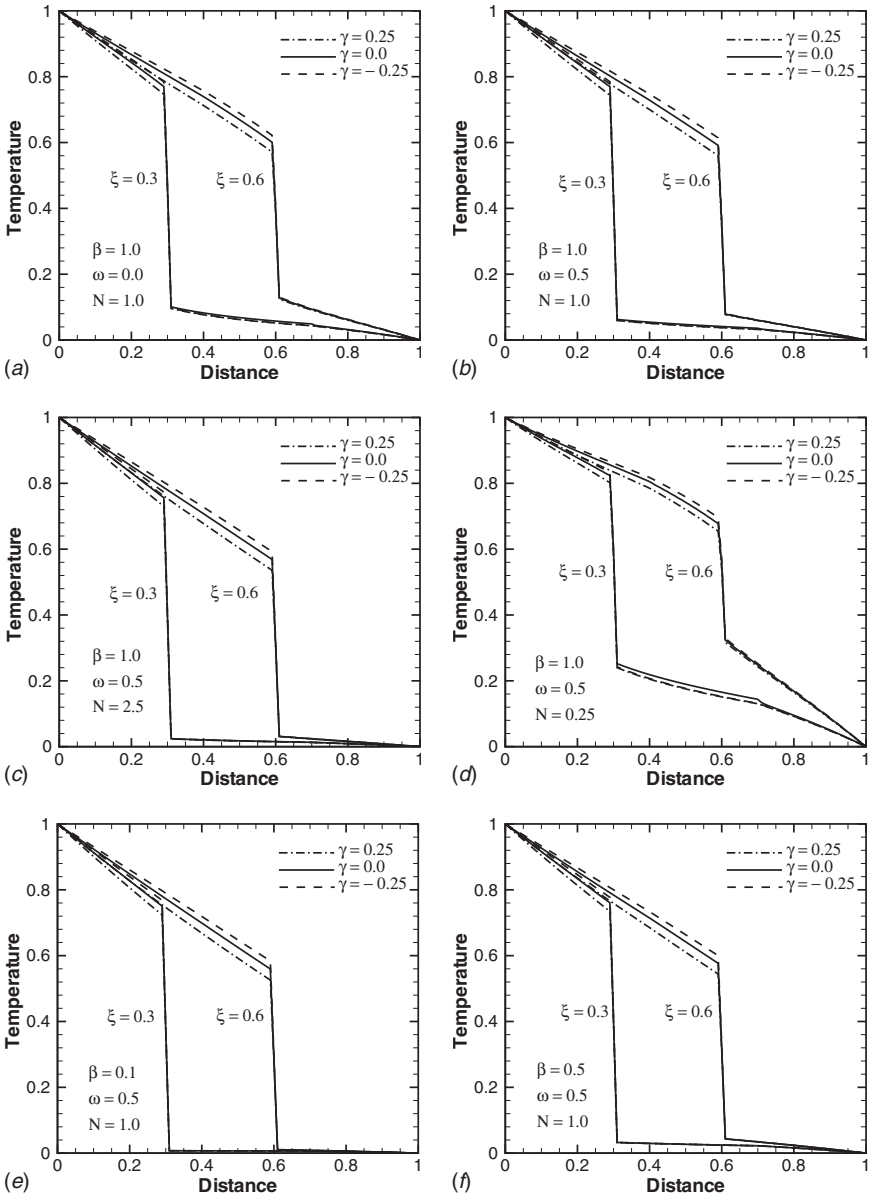

Fig. 2 Dimensionless temperature θ distribution in the medium for temperature boundary conduction problem for (*a*)ω=0.0, (*b*) ω=0.5, (*c*) N=2.5, (*d*) N=0.25, (*e*) β =0.1, and (*f*) β=0.5

nates over conduction (for a lower value of N) during a particular time, because radiation propagates faster than conduction, the overall effect on augmentation of temperature will be more pronounced, and only for this reason the effect of γ becomes visible on θ distributions in the downstream of the thermal wave front (Fig. 2(*d*)).

For the three values of γ, in Figs. 2(*e*) and 2(*f*) along with Fig. 2(*b*), we study the effect of the extinction coefficient β on temperature θ distributions in the medium. It is observed from these figures that for an optically thicker medium (higher values of β), both in the upstream and downstream of the thermal wave fronts, temperatures are more (Fig. 1(*b*)). Because θ in the downstream of the thermal wave front is less, the effect of γ is not visible. For a lower value of β (Fig. 2(*e*)), θ distributions are similar to pure conduction cases.

In Figs. 3(*a*)–3(*f*), we present results for a finite medium in which for time $\xi > 0.0$, its west boundary is subjected to a constant temperature $\theta_W = 1.0$, and its east boundary is insulated $\Psi_E = 0.0$. Initially ($\xi = 0.0$), the system is at temperature $\theta = 0.0$. For three values of γ (=−0.25, 0.0, and +0.25), in these figures, θ distributions have been shown at four time ξ levels.

In Figs. 3(*a*) and 3(*b*), the effect of γ on temperature θ distributions have been studied for the scattering albedo $\omega = 0.0$ and 0.5, respectively. It is seen from these figures that with the passage of time, the difference between the maximum and the minimum temperatures at the thermal wave front decreases. When the medium scatters less energy, the rate of energy distribution is fast such that the change in temperature is also fast.

In Figs. 3(*c*) and 3(*d*), the effects of conduction-radiation parameter N on θ distributions have been studied for three values of γ. From these figures, it is observed that in the radiation dominated case (lower values of N), the temperature difference between the upstream, and the downstream points of the thermal wave front is reducing. This is due to effect of faster energy distribution in a radiation dominated case, and because of this, at a particular time, temperature is more for lower values of N. Although temperature is more in a radiation dominated case, the effect of γ is less. This is because of the dominance of radiation

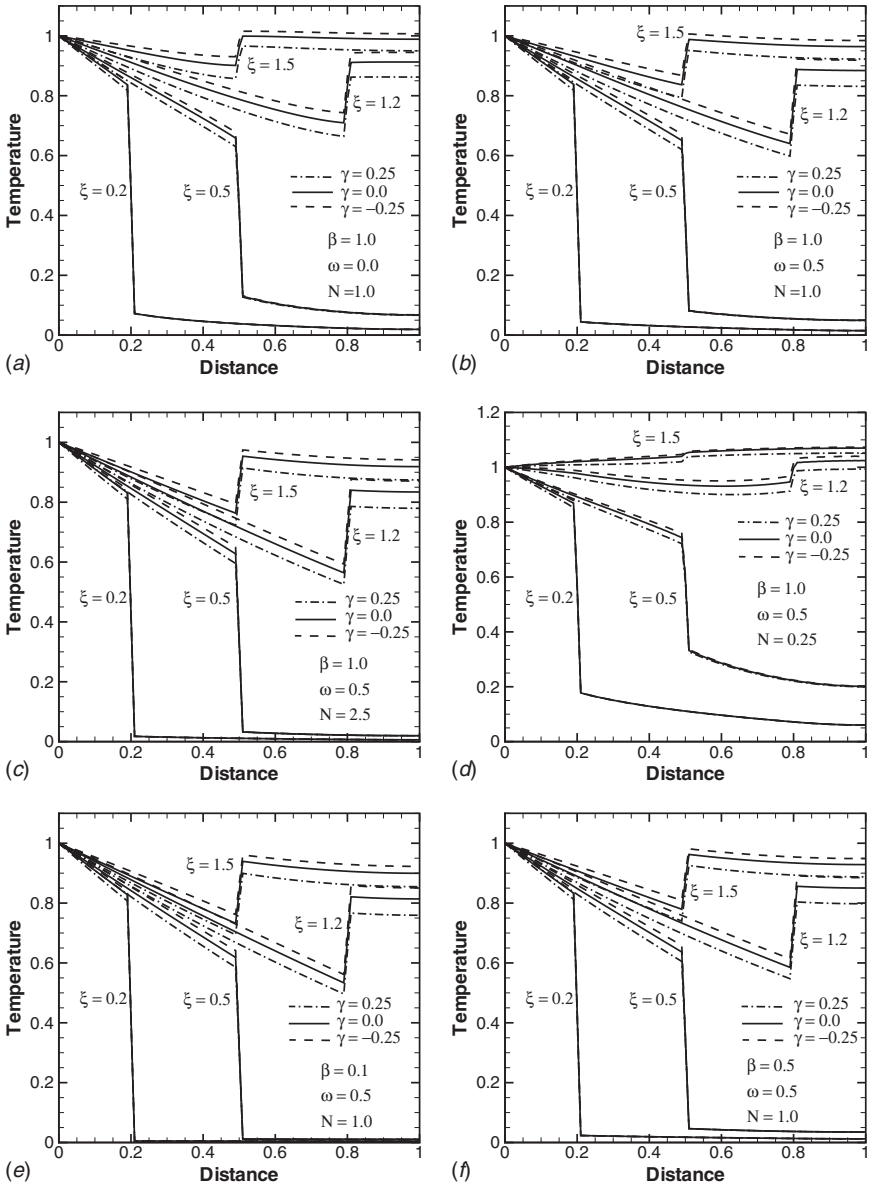

Fig. 3 Dimensionless temperature θ distribution in the medium for mixed boundary conduction problem for (*a*) ω=0.0, (*b*) ω=0.5, (*c*) N=2.5,(*d*) N=0.25, (*e*) β=0.1, and (*f*) β=0.5

over the effect of γ on energy distribution. This is evident from Fig. 3(*d*) in which, with the passage of time, the results of γ =0.25 is found to coincide with the results of γ=0.0.

For three values of γ, in Figs. 3(*e*) and 3(*f*), results are presented to study the effect of β on θ distributions. From these figures, it is clearly observed that at lower values of β, the medium is conduction dominated. The drop in temperature at the thermal wave front is observed to be more for lower values of β (=0.1), and this drop is found to reduce as the value of β increases. Although the magnitude of temperature is high for higher values of β, the effect of γ on θ distribution is less. This is because for higher values of β, the effect of radiation on energy distribution is more than that of γ.

For three values of γ (=−0.25, 0.0, +0.25), in Figs. 4(*a*)–4(*f*), we present results for a finite medium in which for time $0<\xi\leq\Delta\xi$, near its west boundary in the region $0.0\leq l\leq\Delta\eta$, an instantaneous volumetric heat source (g=500) is applied. In this case, initially the entire system is at θ=0.0, and for time $\xi>0$, both the boundaries are kept insulated. Effects of radiative parameters, namely, ω, N, and β on θ distributions, are presented for three different values of γ.

It is observed from Figs. 4(*a*)–4(*f*) that the energy source, which was applied in the region $0.0\leq l\leq\Delta\eta$ near the west boundary during the unit time step $0<\xi\leq\Delta\xi$, propagates in the medium, and its spatial range $0.0\leq l\leq\Delta\eta$ remains constant. With the passage of time, however, its energy content decreases.

In Figs. 4(*a*) and 4(*b*), results are given for ω=0.0 and 0.5, respectively. From these figures, it is observed that the slope of temperature in the region of heat source is very high for ω=0.0 (Fig. 4(*a*)). For ω=0.0, in the spatial range of the heat source, the slope of θ is positive until ξ=1.0, the time by which the heat source reaches the east boundary. After that, it reflects back toward the west boundary, and its slope becomes negative. This change in slope takes place after every reflection from the boundary. γ is found to have effects on θ distribution in the spatial range of the heat source and with the passage of time, since θ decreases,

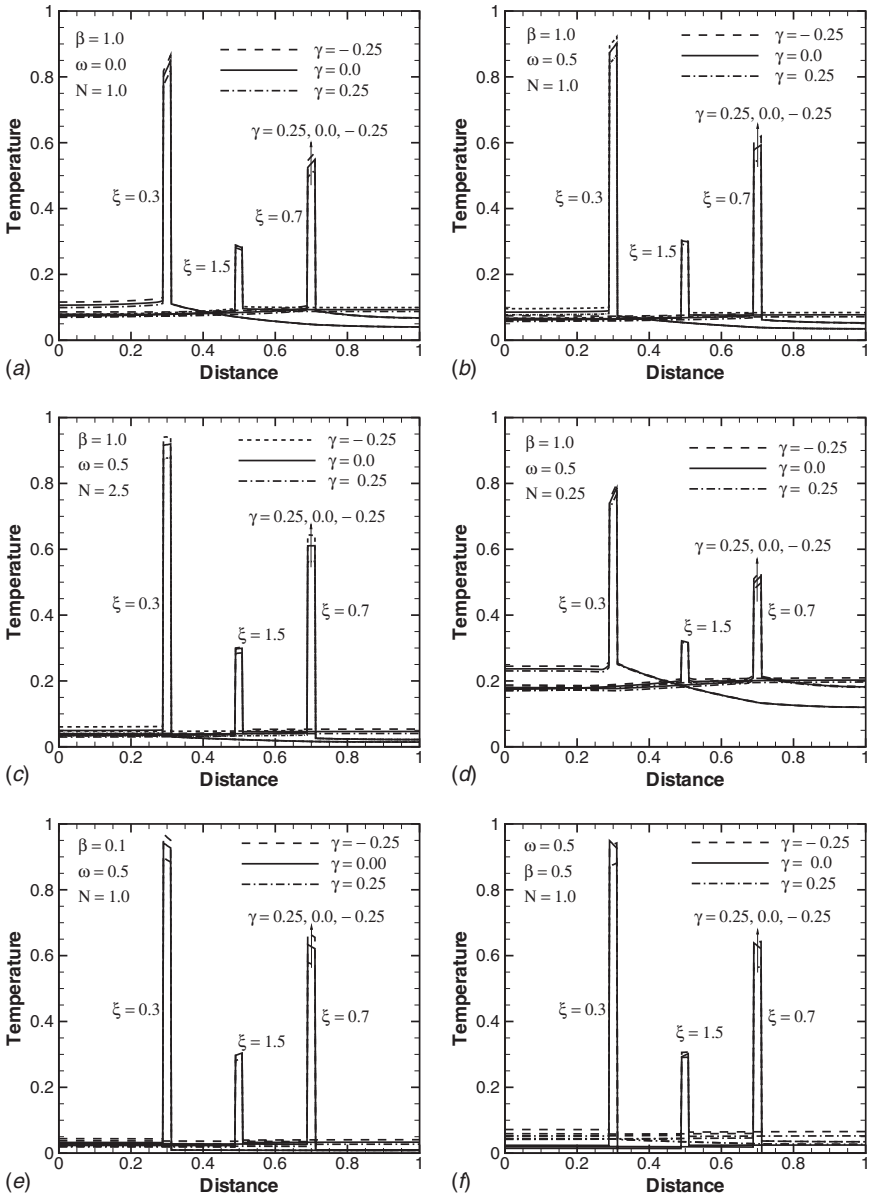

Fig. 4 Dimensionless temperature θ distribution in the medium for a pulsed internal heat source problem for (*a*) ω=0.0, (*b*) ω=0.5, (*c*) N=2.5, (*d*) N=0.25, (*e*) β=0.1, and (*f*) β=0.5

this effect also decreases. With an increase in ω, at any time, the magnitude of θ is found to increase in the spatial range of the heat source, and in other region it is found to decrease. This is because in the radiation dominated case (for a lower values of ω), energy distribution from the spatial region of the heat source is fast.

In Figs. 4(*c*) and 4(*d*) along with Fig. 4(*b*), the effects of N on θ distributions for three different values of γ are studied. From these three figures, it is observed that in a radiation dominated case (Fig. 4(*c*)), the slope of θ profiles at the heat source is positive until time ξ=1.0, and after reflection, the slope changes its sign. In a conduction dominated case (N=2.5) (Fig. 4(*c*)), the slope of θ is almost zero, and at any time the effect of γ is more. At any time, the magnitude of θ in the spatial range of heat source is more in the conduction dominated case. This is again owing to the fact that in a conduction dominated case, energy distribution from the heat source zone is slower. The effect of γ is also more in a conduction dominated case.

In Figs. 4(*e*) and 4(*f*) along with Fig. 4(*b*), the effect of β on θ distributions for three values of γ are shown. It is observed that at lower values of β(=0.1), the medium is conduction dominated, and the slope of θ profile at the heat source is negative. At higher values of β(=1.0), the medium is radiation dominated, and in this case, the slope of θ profile at the heat source is positive. From these three figures, it is observed that the slope is changing from negative to positive between β=0.0 and 1.0. For low values of β(=0.1), the effect of γ on θ distribution is more because the medium is conduction dominated, and θ is also high. At higher values of β(=1.0), due to the influence of radiation, the effect of γ on θ distribution reduces, and the profile of θ for γ=0.25 is found to match with that for γ=0.0 in Fig. 4(*b*).

4 Conclusions

Non-Fourier conduction and radiation problem with temperature dependent thermal conductivity was studied. Thermal conductivity was assumed to vary linearly with temperature. The analysis was made for a 1D planar absorbing, emitting and isotropically scattering, radiating, and conducting medium. Three dif-

ferent sets of boundary conditions were considered. The case of pulse localized volumetric heat source in the medium was also taken up. The problem was analyzed using the LBM in which the radiative information was computed using the FVM. Cases for which results were available in the literature, results of the present work were found to compare well. For three values of the coefficient of thermal conductivity γ, temperature distributions in the medium were studied for the effects of the extinction coefficient, the scattering albedo, and the conduction-radiation parameter. In all the cases, it was observed that in the radiation dominated case, temperature was more and the effect of γ on temperature was less. In the case of pulse heat source in the medium, in the radiation dominated case, temperature was less in the spatial range of the heat source and the effect of γ was less. At other locations, an opposite trend was observed.

Nomenclature

b = number of propagation directions in a lattice
c_p = specific heat at constant pressure
C = speed of thermal wave
e = propagation velocity $(\Delta\eta/\Delta\xi)$
E_r = dimensionless radiative parameter.
f_i = particle distribution function in the ith direction
f_i^{eq} = equilibrium particle distribution function in the ith direction
G = incident radiation
g = volumetric energy source
k = thermal conductivity
l = spatial length, where the energy pulse is applied
N = conduction-radiation parameter
q = heat flux
t = dimensional time
T = dimensional temperature
X = length of the geometry
x = space variable

Greek Symbols

α = thermal diffusivity
β = extinction coefficient
γ' = measure of variation of thermal conductivity with temperature
γ = coefficient of variation of thermal conductivity with temperature
η = dimensionless distance
ρ = density
σ = Stefan–Boltzmann constant, 5.67×10^{-8} W/m^2 K^4
τ = relaxation time in the LBM
Γ = thermal relaxation time in non-Fourier conduction
ω = scattering albedo
θ = nondimensional temperature
ξ = dimensionless time

Superscript

* = dimensional variable

Subscripts

C = conductive
R = radiative
ref = reference
E, W = east, west

References

[1] Xu, F., Seffen, K. A., and Lu, T. J., 2008, "Non-Fourier Analysis of Skin Biothermomechanics," Int. J. Heat Mass Transfer, **51**(9–10), pp. 2237–2259.
[2] Cattaneo, C. A., 1958, "Form of Heat Conduction Equation Which Eliminates the Paradox of Instantaneous Propagation," Compt. Rend., **247**, pp. 431–433.
[3] Vernotee, P., 1958, "Les Paradoxes de la Theorie Continue de 1 Equation del la Chaleur," Compt. Rend., **246**, pp. 3154–3155.
[4] Tang, D. W., and Araki, N., 1996, "Analytical Solution of Non-Fourier Temperature Response in a Finite Medium Under Laser-Pulse Heating," Heat Mass Transfer, **31**, pp. 359–363.
[5] Chu, H. S., Lin, S., and Lin, C. H., 2002, "On Non-Fourier Heat Conduction With Radiation in an Absorbing, Emitting, and Isotropically Scattering Medium," J. Quant. Spectrosc. Radiat. Transf., **73**, pp. 571–582.
[6] Chen, T. -M., 2007, "Numerical Solution of Hyperbolic Heat Conduction in Thin Surface Layers," Int. J. Heat Mass Transfer, **50**, pp. 4424–4429.
[7] Mishra, S. C., Kumar, T. B. P., and Mondal, B., 2008, "Lattice Boltzmann Method Applied to the Solution of Energy Equation of a Radiation and Non-Fourier Heat Conduction Problem," Numer. Heat Transfer, Part A, **54**, pp. 798–818.
[8] Talukdar, P., and Mishra, S. C., 2002, "Transient Conduction and Radiation Heat Transfer With Variable Thermal Conductivity," Numer. Heat Transfer, Part A, **41**(8), pp. 851–867.
[9] Gupta, N., Chaitanya, G. R., and Mishra, S. C., 2006, "Lattice Boltzmann Method Applied to Variable Thermal Conductivity Conduction and Radiation Problems," J. Thermophys. Heat Transfer, **20**(4), pp. 895–902.

Shiping Zhou
Department of Mathematics,
Harbin Institute of Technology,
Weihai, Shandong 264209, P.R.C.;
School of Computer Science and Technology,
Yantai University,
Yantai, Shandong 264005, P.R.C.
e-mail: shipingzh@hotmail.com

Minggen Cui[1]
School of Computer Science and Technology,
Yantai University,
Yantai, Shandong 264005, P.R.C.
e-mail: cmgyfs@263.net

Determination of Unknown Coefficients in Parabolic Equations

In this paper, we consider solving for a coefficient inverse problem in the parabolic equation. A new numerical method for the identification of the space-dependent coefficient is developed in a reproducing kernel space. The coefficients can be solved by a lower triangle linear system. Some numerical experiments are presented to show the efficiency of the proposed method. [DOI: 10.1115/1.3154627]

Keywords: parabolic equations, coefficient inverse problem, reproducing kernel space

1 Introduction

We consider the numerical solution to the coefficient inverse problem in a parabolic equation with the initial value and boundary value

$$\frac{\partial}{\partial x}\left(k(x)\frac{\partial u(x,t)}{\partial x}\right)-\frac{\partial u(x,t)}{\partial t}=f(x,t)\quad (x,t)\in[0,1]\times[0,1]$$

$$u(x,0)=h(x) \tag{1.1}$$

$$u(0,t)=0\quad \frac{\partial u(1,t)}{\partial x}=0$$

subject to the additional specification

$$u(x^*,t)=g(t)\quad t\in[0,1] \tag{1.2}$$

where $x^*\in(0,1)$.

Such problems arise, for example, while modeling the flow in homogeneous and isotropic porous media. The solution function $u(x,t)$ can be interpreted as a pressure head, the coefficient $k(x)$ may be interpreted as a hydraulic conductivity for the porous medium [1–4]. The existence and uniqueness of the solution to such problems are discussed [5,6]. A new method, which is established in reproducing kernel spaces, is presented to solve such problems of identifying the unknown coefficient $k(x)$. By using special techniques, the identification of the space-dependent coefficient $k(x)$ is formulated as a lower triangular linear system, which is not ill-posed. In detail we explain the method in Secs. 2–6.

2 Several Reproducing Kernel Spaces

In this section we define several reproducing kernel spaces based on smoothness requirements on the solution function $u(x,t)$, and the given boundary value condition in Eq. (1.1).

The inner product space $W_1[0,1]$ is defined as follows:

$$W_1[0,1]=\{\,u(x)|u \text{ is an absolutely continuous function, } u'\in L^2[0,1]\}$$

endowed with the inner product

$$\langle u(x),v(x)\rangle_{W_1}=u(0)v(0)+\int_0^1 u'(x)v'(x)dx$$

and with the norm $\|u\|_{W_1}=\sqrt{(u,u)_{W_1}}$.

It is proved that $W_1[0,1]$ is a complete reproducing kernel space [7], that is, for every $u(\xi)\in W_1[0,1]$, and every fixed $x\in[0,1]$, there exists $P_x(\xi)\in W_1[0,1]$ such that

$$\langle u(\xi),P_x(\xi)\rangle_{W_1}=u(x)$$

where

$$P_x(\xi)=\begin{cases}1+\xi, & \xi\le x\\ 1+x, & \xi>x\end{cases} \tag{2.1}$$

$P_x(\xi)$ is called the reproducing kernel of $W_1[0,1]$. Other reproducing kernel spaces are described similar to $W_1[0,1]$.

$$W_2[0,1]=\{u(t)|u' \text{ is an absolutely continuous function, } u''\in L^2[0,1]\}$$

The inner product and norm are defined by

$$\langle u(t),v(t)\rangle_{W_2}=\sum_{i=0}^{1}u^{(i)}(a)v^{(i)}(a)+\int_0^1 u''(t)v''(t)dt$$

and $\|u\|_{W_2}=\sqrt{(u,u)_{W_2}}$.

$$W_3[0,1]=\{u(x)|u'' \text{ is absolutely continuous function, } u'''\in L^2[0,1],\ u(0)=u'(1)=0\}$$

It is endowed with the inner product

$$\langle u(x),v(x)\rangle_{W_3}=\sum_{i=0}^{2}u(0)v(0)+\int_0^1 u^{(3)}(x)v^{(3)}(x)dx$$

and norm $\|u\|_{W_3}=\sqrt{(u,u)_{W_3}}$.

$$V[0,1]=\{u(x)|u' \text{ is an absolutely continuous function, } u''\in L^2[0,1],\ u'(0)=0\}$$

In Ref. [8], the author gives the general methods of solving reproducing kernels. We can use the methods to prove that $W_2[0,1]$ and $W_3[0,1]$ are reproducing spaces, and solve their reproducing kernels. We denote the reproducing kernels of $W_2[0,1]$ and $W_3[0,1]$ by $Q_t(s)$ and $R_x(y)$, respectively.

[1]Corresponding author. Also at the Department of Mathematics, Harbin Institute of Technology, Weihai, Shandong, P.R.China.

Contributed by the Heat Transfer Division of ASME for publication in the JOURNAL OF HEAT TRANSFER. Manuscript received November 6, 2008; final manuscript received May 13, 2009; published online August 19, 2009. Review conducted by Gautam Biswas.

$$Q_t(\eta)=\begin{cases}1-\dfrac{t^3}{6}+\dfrac{1}{2}t\eta(2+t) & t\le\eta\\ 1-\dfrac{s^3}{6}+\dfrac{1}{2}t\eta(2+\eta) & t>\eta\end{cases} \tag{2.2}$$

$$R_x(\xi)=\begin{cases}\dfrac{x\xi}{7}(\xi+x\xi)-\dfrac{x\xi}{14}(3x+3\xi+x^2+\xi^2)+\dfrac{x^4\xi}{56}-\dfrac{x^3\xi^2}{28}+\dfrac{x^2\xi^2}{112}+\dfrac{x^2\xi^3}{21}-\dfrac{x^3\xi^3}{84}+\dfrac{x^3\xi^3}{336}(x+\xi)-\dfrac{x\xi^4}{42}-\dfrac{x^4\xi^4}{1344}+\dfrac{\xi^5}{120}, & \xi\le x\\ \dfrac{x\xi}{7}(x+x\xi)-\dfrac{x\xi}{14}(3x+3\xi+x^2+\xi^2)+\dfrac{x\xi^4}{56}-\dfrac{x^2\xi^3}{28}+\dfrac{\xi^2\xi^2}{112}+\dfrac{x^3\xi^2}{21}-\dfrac{x^3\xi^3}{84}+\dfrac{x^3\xi^3}{336}(x+\xi)-\dfrac{x^4\xi}{42}-\dfrac{x^4\xi^4}{1344}+\dfrac{x^5}{120}, & \xi>x\end{cases} \tag{2.3}$$

Since the inner product space $V[0,1]$ is a subspace of $W_2[0,1]$, it is also a reproducing space. We denote the reproducing kernel by $G_t(\eta)$.

Now we consider a reproducing kernel space $W(D)$ based on the region $D=[0,1]\times[0,1]$. Suppose that $\{p_i(x)\}_{i=1}^{\infty}$ and $\{q_i(t)\}_{i=1}^{\infty}$ are the complete normal orthogonal system of $W_3[0,1]$ and $W_2[0,1]$, respectively. In Ref. [9], $W(D)$ and its inner product are defined by

$$W(D)=\left\{u(x,t)\middle|u(x,t)=\sum_{i,j=1}^{\infty}c_{ij}p_i(x)q_j(t),\{c_{ij}\}\in l^2\right\}$$

and

$$\langle u(x,t),v(x,t)\rangle_W=\sum_{i,j=1}^{\infty}c_{ij}d_{ij},\|u\|_W=\sqrt{\langle u,u\rangle_W}$$

where $u(x,t)=\Sigma_{i,j=1}^{\infty}c_{ij}p_i(x)q_j(t)$ and $v(x,t)=\Sigma_{i,j=1}^{\infty}d_{ij}p_i(x)q_j(t)$. We have the following Propositions 2.1 and 2.2 for the inner product space $W(D)$, see Ref. [9].

PROPOSITION 2.1. *If* $u(x,t)=u_1(x)u_2(t), v(x,t)=v_1(x)v_2(t)\in W(D)$, *then*

$$\langle u(x,t),v(x,t)\rangle_W=\langle u_1(x),v_1(x)\rangle_{W_3}\langle u_2(t),v_2(t)\rangle_{W_2} \tag{2.4}$$

PROPOSITION 2.2. *$W(D)$ is a reproducing kernel space and the reproducing kernel is*

$$K_{(x,t)}(\xi,\eta)=R_x(\xi)Q_t(\eta) \tag{2.5}$$

where $Q_t(\eta)$ and $R_x(\xi)$ are given in Eqs. (2.2) and (2.3), respectively.

We have imposed the two boundary conditions in Eq. (1.1) on the reproducing kernel space $W_3[0,1]$. Therefore, any function $u(x,t)\in W(D)$ automatically satisfies the boundary conditions of Eq. (1.1).

3 Transformation of the Coefficient Inverse Problem

In this section, we discuss the inverse problem in the reproducing kernel space $W(D)$, on which the boundary conditions in Eq. (1.1) have been imposed. Integrating both sides of Eq. (1.1) from x to 1, applying the initial and boundary conditions and letting $t=0$, it follows that

$$-k(x)\frac{\partial u(x,0)}{\partial x}-\int_x^1\frac{\partial u(\xi,0)}{\partial t}d\xi=\int_x^1 f(\xi,0)d\xi \tag{3.1}$$

Note that $h'(1)=0$. Now we define an operator $L:W(D)\to W_1[0,1]$ as follows:

$$(Lu)(x)=\int_x^1\frac{\partial u(\xi,0)}{\partial t}d\xi \tag{3.2}$$

LEMMA 3.1. *The operator $L:W(D)\to W_1[0,1]$ defined in Eq. (3.2) is a bounded operator.*

Proof.

$$\|(Lu)(x)\|_{W_1}^2=\left(\int_0^1\frac{\partial u(\xi,0)}{\partial t}d\xi\right)^2+\int_0^1\left(\frac{\partial u(x,0)}{\partial t}\right)^2dx\le 2\int_0^1\left(\frac{\partial u(x,0)}{\partial t}\right)^2dx \tag{3.3}$$

Since $R_x(\xi)Q_t(\eta)$ is the reproducing kernel of $W(D)$, it is known that

$$u(x,t)=\langle u(\xi,\eta),R_x(\xi)Q_t(\eta)\rangle_W$$

$$\frac{\partial u(x,t)}{\partial t}=\left\langle u(\xi,\eta),R_x(\xi)\frac{\partial Q_t(\eta)}{\partial t}\right\rangle_W$$

$$\frac{\partial u(x,0)}{\partial t}=\left\langle u(\xi,\eta),R_x(\xi)\left.\frac{\partial Q_t(\eta)}{\partial t}\right|_{t=0}\right\rangle_W$$

$$\left|\frac{\partial u(x,0)}{\partial t}\right|\le\|u\|_W\|R_x(\xi)\|_{W_3}\left\|\left.\frac{\partial Q_t(\eta)}{\partial t}\right|_{t=0}\right\|_{W_2}$$

$\|R_x(\xi)\|_{W_3}$ is a continuous function on the interval [0,1], that is, it holds that $\|R_x(\xi)\|_{W_3}\le M_1$. Assume that

$$\left\|\left.\frac{\partial Q_t(\eta)}{\partial t}\right|_{t=0}\right\|_{W_1}=M_2$$

then we have

$$\left\|\frac{\partial u(x,0)}{\partial t}\right\|\le\|u\|_W M_1M_2$$

Hence, we get

$$\|(Lu)(x)\|_{W_1}\le 2M_1M_2\|u\|_W M_1M_2$$

Hence, the original inverse problem is transferred into the following operator equation in the reproducing spaces $W(D)$:

$$(Lu)(x)=F(x)\quad u\in W(D) \tag{3.4}$$

subject to the initial condition in Eq. (1.1) and additional condition (1.2), where

$$F(x)=-k(x)h'(x)-\int_x^1 f(\xi,0)d\xi \tag{3.5}$$

4 Space Decomposition

In this section the technique space decomposition used for the method is described in detail. For a dense set $\{x_i\}_{i=1}^{\infty}$ of interval [0,1], let

$$\varphi_i(x) = P_{x_i}(x) \tag{4.1}$$

where $P_x(\xi)$ is given in Eq. (2.1). For every $u(x) \in W_1[0,1]$, it follows that

$$\langle u(x), \varphi_i(x)\rangle_{W_1} = u(x_i) \quad i = 1,2,\ldots \tag{4.2}$$

Let L^* denote the conjugate operator of L, and we use the following notation:

$$\psi_i(x,t) = (L^*\varphi_i)(x,t) \quad i = 1,2,\ldots \tag{4.3}$$

LEMMA 4.1. *L^* is a bounded operator from $W_1[0,1]$ to $W(D)$, and $\psi_i(x,t)$ can be expressed in the form*

$$\psi_i(x,t) = \frac{\partial Q_t(0)}{\partial \eta}\int_{x_i}^1 R_x(\xi)d\xi \quad i = 1,2,\ldots \tag{4.4}$$

$$\langle \psi_i(x,t), \psi_j(x,t)\rangle_W = C_1\int_{x_i}^1 dx\int_{x_j}^1 R_x(\xi)d\xi \tag{4.5}$$

where

$$C_1 = \frac{\partial^2 Q_t(0)|_{t=0}}{\partial t\,\partial \eta} = \frac{\partial^2 Q_0(0)}{\partial t\,\partial \eta} \tag{4.6}$$

Proof. Since L is bounded, it is natural to expect that L^* is bounded. By the properties of the reproducing kernels $P_x(\xi)$, $R_x(\xi)$, $Q_t(\eta)$, and $K_{x,t}(\xi,\eta)$, we have

$$\begin{aligned}\psi_i(x,t) &= \langle(\psi_i(\xi,\eta), K_{x,t}(\xi,\eta)\ \rangle_W = \langle (L^*\varphi_i)(\xi,\eta), R_x(\xi)Q_t(\eta)\rangle_W\\ &= \langle \varphi_i(x), L(R_x(\xi)Q_t(\eta))(x)\rangle_{W_1} = \ L(R_x(\xi)Q_t(\eta)))(x_i)\\ &= \frac{\partial Q_t(0)}{\partial \eta}\int_{x_i}^1 R_x(\xi)d\xi\end{aligned}$$

$$\begin{aligned}\langle \psi_i(x,t), \psi_j(x,t)\rangle_W &= \left\langle (L^*\varphi_i)(x,t), \frac{\partial Q_t(0)}{\partial \eta}\int_{x_j}^1 R_x(\xi)d\xi\right\rangle_W\\ &= \left\langle \varphi_i(\cdot), \left(L\left[\frac{\partial Q_t(0)}{\partial \eta}\int_{x_j}^1 R_x(\xi)d\xi\right]\right)(\cdot)\right\rangle_{W_1}\\ &= L\left(\frac{\partial Q_t(0)}{\partial \eta}\int_{x_j}^1 R_x(\xi)d\xi\right)(x_i)\\ &= \frac{\partial^2 Q_0(0)}{\partial t\,\partial \eta}\int_{x_i}^1 dx\int_{x_j}^1 R_x(\xi)d\xi\\ &= C_1\int_{x_i}^1 dx\int_{x_j}^1 R_x(\xi)d\xi\end{aligned}$$

Let $\{\bar{\psi}_i(x,t)\}_{i=1}^\infty$ denote an orthonormal system that derives from the Gram–Schmidt orthonormalization process of $\{\psi_i(x,t)\}_{i=1}^\infty$. Therefore we can express $\bar{\psi}_i(x,t)$ in the following form:

$$\bar{\psi}_i(x,t) = \sum_{k=1}^{i}\beta_{ik}\psi_k(x,t) \quad i = 1,2,\ldots \tag{4.7}$$

where β_{ik} are coefficients of orthonomalization.

LEMMA 4.2. *$\bar{\psi}_i(x,0)$ is an orthogonal system in $W_3[0,1]$ and*

$$\langle \bar{\psi}_i(x,0), \bar{\psi}_j(x,0)\rangle_{W_3} = \frac{C_2^2}{C_1}\langle \bar{\psi}_i(x,t), \bar{\psi}_j(x,t)\rangle_W \tag{4.8}$$

where C_1 is defined in Eq. (4.6) and

$$C_2 = \left.\frac{\partial Q_t(0)}{\partial \eta}\right|_{t=0} = \frac{\partial Q_0(0)}{\partial \eta} \tag{4.9}$$

Proof. In Eq. (4.4),

$$\begin{aligned}&\langle \psi_i(x,0), \psi_j(x,0)\rangle_{W_3}\\ &\quad= \left\langle \frac{\partial Q_0(0)}{\partial \eta}\int_{x_i}^1 R_x(\xi)d\xi, \frac{\partial Q_0(0)}{\partial \eta}\int_{x_j}^1 R_x(\xi)d\xi\right\rangle_{W_3}\\ &\quad= C_2^2\left\langle \int_{x_i}^1 R_x(\xi)d\xi, \int_{x_j}^1 R_x(\xi)d\xi\right\rangle_{W_3}\end{aligned} \tag{4.10}$$

On the other hand,

$$\begin{aligned}&\langle \psi_i(x,t), \psi_j(x,t)\rangle_W\\ &\quad= \left\langle \frac{\partial Q_t(0)}{\partial \eta}\int_{x_i}^1 R_x(\xi)d\xi, \frac{\partial Q_t(0)}{\partial \eta}\int_{x_j}^1 R_x(\xi)d\xi\right\rangle_W\\ &\quad= \left\langle \frac{\partial Q_t(0)}{\partial \eta}, \frac{\partial Q_t(0)}{\partial \eta}\right\rangle_{W_2}\left\langle \int_{x_i}^1 R_x(\xi)d\xi, \int_{x_j}^1 R_x(\xi)d\xi\right\rangle_{W_3}\end{aligned} \tag{4.11}$$

Note that

$$\begin{aligned}\left\langle \frac{\partial Q_t(0)}{\partial \eta}, \frac{\partial Q_t(0)}{\partial \eta}\right\rangle_{W_2} &= \left\langle \frac{\partial Q_t(0)}{\partial \eta_1}, \frac{\partial Q_t(0)}{\partial \eta}\right\rangle_{W_2}\\ &= \frac{\partial}{\partial \eta_1}\left\langle Q_t(\eta_1), \frac{\partial Q_t(0)}{\partial \eta}\right\rangle_{W_2}\Bigg|_{\eta_1=0}\\ &= \left.\frac{\partial R_{\eta_1}^{\{2\}}(0)}{\partial \eta_1\,\partial \eta}\right|_{\eta_1=0} = \frac{\partial^2 Q_0(0)}{\partial t\,\partial \eta} = C_1\end{aligned} \tag{4.12}$$

From Eqs. (4.10)–(4.12), we can conclude that

$$\langle \psi_i(x,0), \psi_j(x,0)\rangle_{W_3} = \frac{C_2^2}{C_1}\langle \psi_i(x,t), \psi_j(x,t)\rangle_W \tag{4.13}$$

Since $\{\bar{\psi}_i(x,t)\}_{i=1}^\infty$ is an orthonormal system of $W(D)$, we further obtain Eq. (4.8).

Let

$$S = \text{span}(\{\bar{\psi}_i(x,t)\}_{i=1}^\infty) = \left\{u(x,t)\middle| u(x,t) = \sum_{i=1}^\infty c_i\bar{\psi}_i(x,t), c_i \in l^2\right\}$$

and $S^\perp$ denotes the orthcomplement space of S in $W(D)$. So $W(D) = S \oplus S^\perp$.

LEMMA 4.3.

$$S^\perp = \text{Null}(L) \tag{4.14}$$

where Null(L) *denotes the null space of* L.

Proof. For every $u(x,t) \in S^\perp$, we find

$$(Lu)(x_i) = \langle (Lu)(x), \varphi_i(x)\rangle_{W_1} = \langle u(x,t), \psi_i(x,t)\rangle_W = 0 \quad i = 1,2,\ldots$$

since $\{x_i\}_{i=1}^\infty$ is dense in the interval [0,1], then

$$(Lu(x,t))(x) = 0$$

for arbitrary $x \in [0,1]$. That proved $u(x,t) \in \text{Null}(L)$. On the other hand, if $u(x,t) \in \text{Null}(L)$, that is, it satisfies $(Lu(x,t))(x) = 0$, we can conclude that

$$\langle u(x,t), \psi_i(x,t)\rangle_W = ((Lu)(x_i)) = 0$$

Thus $u(x,t) \in S^\perp$.

LEMMA 4.4. *$u(x,t) \in S^\perp$ if and only if $\partial u(x,t)/\partial t|_{t=0} = 0$.*

Proof. For any $u(x,t) \in S^\perp$, there exists

$$\int_x^1 \frac{\partial u(\xi,t)}{\partial t} d\xi = 0 \tag{4.15}$$

by Lemma 4.3 and the definition of the operator L in Eq. (3.2). Differentiating Eq. (4.15), we get $\partial u(x,t)/\partial t|_{t=0}=0$.

If $\partial u(x,t)/\partial t|_{t=0}=0$, on the other hand, then $(Lu)(x)=0$ for any $x\in[0,1]$. Furthermore, we have $u(x,t)\in S^{\perp}$ by Lemma 4.3.

Thus we have $S^{\perp}=W_3[0,1]\otimes V[0,1]$. Take a set of points $Z=\{(\xi_1,\eta_1),(\xi_2,\eta_2),\ldots\}$ as a dense set of region $D=[0,1]\times[0,1]$ and put

$$\rho_j(x,t)=R_{\xi_j}(x)G_{\eta_j}(t) \quad j=1,2,\ldots$$

Therefore, $\{\rho_j(x,t)\}_{j=1}^{\infty}$ is the basis of $S^{\perp}$. The orthonormal basis $\{\bar{\rho}_j(x,t)\}_{j=1}^{\infty}$ can be derived from the Gram–Schmidt orthogonalization process of $\{\rho_j(x,t)\}_{j=1}^{\infty}$.

$$\bar{\rho}_j(x,t)=\sum_{l=1}^{j}\beta_{jl}^{*}\rho_l(x,t) \quad j=1,2,\ldots$$

Note that $W(D)=S\oplus S^{\perp}$, hence, $\{\bar{\psi}_i(x,t)\}_{i=1}^{\infty}\cup\{\bar{\rho}_i(x,t)\}_{j=1}^{\infty}$ is an orthonormal basis of $W(D)$.

5 The Numerical Method

In this section, the method of solving the operator equation (3.4) is explained in detail.

THEOREM 5.1. *Assume that* $(k(x),u(x,t))$ *be the solution of* Eq. (3.4), *then*

$$u(x,t)=\sum_{i=1}^{\infty}\sum_{l=1}^{i}\beta_{il}\left(-k(s_l)h'(s_l)-\int_{s_l}^{1}f(\xi,0)d\xi\right)\bar{\psi}_i(x,t)+\sum_{i=1}^{\infty}\alpha_i\bar{\rho}_i(x,t) \tag{5.1}$$

where $\bar{\psi}_i(x,t),\bar{\rho}_i(x,t)$ *and* β_{il} *are defined in Sec. 4,* $k(s_l)$ *and* α_i *are to be solved according to the initial and additional conditions.*

Proof. Since $\{\psi_i(x,t)\}_{i=1}^{\infty}\cup\{\rho_i(x,t)\}_{j=1}^{\infty}$ is an orthonormal basis of $W(D)$, we have

$$\begin{aligned}u(x,t)&=\sum_{i=1}^{\infty}\langle u,\bar{\psi}_i\rangle_W\bar{\psi}_i(x,t)+\sum_{i=1}^{\infty}\langle u,\bar{\rho}_i\rangle_W\bar{\rho}_i(x,t)\\&=\sum_{i=1}^{\infty}\sum_{l=1}^{i}\beta_{il}\langle u,\psi_l\rangle_W\bar{\psi}_i(x,t)+\sum_{i=1}^{\infty}\langle u,\bar{\rho}_i\rangle_W\bar{\rho}_i(x,t)\\&=\sum_{i=1}^{\infty}\sum_{l=1}^{i}\langle Lu,\varphi\rangle_{W_1}\bar{\psi}_i(x,t)+\sum_{i=1}^{\infty}\langle u,\bar{\rho}_i\rangle_W\bar{\rho}_i(x,t)\end{aligned}$$

let $\alpha_i=\langle u,\bar{\rho}_i\rangle_W$ and apply Eq. (3.5), hence,

$$u(x,t)=\sum_{i=1}^{\infty}\sum_{l=1}^{i}\beta_{il}F(s_l)\bar{\psi}_i(x,t)+\sum_{i}^{\infty}\alpha_i\bar{\rho}_i(x,t) \tag{5.2}$$

therefore, Eq. (5.1) is obtained.

In terms of the unknowns α_i, we can get them by applying the additional specification (1.2).

$$g(t)=\frac{\partial Q_t(0)}{\partial\eta}\sum_{i=1}^{\infty}\left(\sum_{l=1}^{i}\beta_{il}F(s_l)\right)\sum_{l=1}^{i}\beta_{il}\int_{s_l}^{1}R_{x^*}(\xi)d\xi+\sum_{i=1}^{\infty}\alpha_i\bar{\rho}_i(x^*,t) \tag{5.3}$$

we use $C(k)$ to denote

$$C(k)=\sum_{i=1}^{\infty}\left(\sum_{l=1}^{i}\beta_{il}F(s_l)\right)\sum_{l=1}^{i}\beta_{il}\int_{s_l}^{1}R_{x^*}(\xi)d\xi \tag{5.4}$$

which is a linear combination of unknown values $k(s_l)$. So

$$g(t)=C(k)\frac{\partial Q_t(0)}{\partial\eta}+\sum_{i=1}^{\infty}\alpha_i\bar{\rho}_i(x^*,t) \tag{5.5}$$

Let $t=0$ in Eq. (5.5), we then have

$$g(0)=C(k)\frac{\partial Q_0(0)}{\partial\eta}+\sum_{i=1}^{\infty}\alpha_i\bar{\rho}_i(x^*,0) \tag{5.6}$$

Dividing the difference in Eqs. (5.5) and (5.6) by t, we get

$$\frac{g(t)-g(0)}{t}=C(k)\frac{\dfrac{\partial Q_t(0)}{\partial\eta}-\dfrac{\partial Q_0(0)}{\partial\eta}}{t}+\sum_{i=1}^{\infty}\alpha_i\frac{\bar{\rho}(x*,t)-\bar{\rho}(x^*,0)}{t} \tag{5.7}$$

Finding the limit at $t=0$, and noticing that the limit of the second term on the right is equal to 0 since $G_t(\eta)\in V[0,1]$ and $\partial Q_t(0)/\partial t|_{t=0}\neq 0$, we thus have demonstrated that $C(k)=C_3$ is a constant irrelevant to $k(s_l)$. So we have

$$\sum_{i=1}^{\infty}\alpha_i\bar{\rho}_i(x^*,t)=g(t)-C_3\frac{\partial Q_t(0)}{\partial\eta}$$

Taking $t_l\in[0,1]$ $l=1,2,\ldots$, we get the infinite linear system about α_i

$$\sum_{i=1}^{\infty}\alpha_i\bar{\rho}_i(x^*,t_l)=g(t)-C_3\left.\frac{\partial Q_t(0)}{\partial\eta}\right|_{t=t_l} \tag{5.8}$$

THEOREM 5.2. *The coefficients* $k(s_l)$ *can be solved by the following lower triangular system:*

$$\frac{C_2^2}{C_1}\sum_{l=1}^{i}\beta_{il}\left(-k(s_l)h'(s_l)-\int_{s_l}^{1}f(\xi,0)d\xi\right)=\langle h(x),\bar{\psi}_i(x,0)\rangle_{W_3}-\sum_{i=1}^{\infty}\alpha_i\langle\bar{\rho}_i(x,0),\bar{\psi}_j(x,0)\rangle_{W_3} \tag{5.9}$$

Proof. Setting $t=0$ in Eq. (5.2) and applying the initial condition gives us

$$h(x)=\sum_{i=1}^{\infty}\sum_{l=1}^{i}\beta_{il}F(s_l)\bar{\psi}_i(x,0)+\sum_{i=1}^{\infty}\alpha_i\bar{\rho}_i(x,0) \tag{5.10}$$

Simplifying the above formula, we have

Table 1 The error of coefficient $k(x)$ (with eight items in each series)

x	True solution	Approximate solution	Absolute error	Relative error
$\frac{1}{8}$	4.984375	4.984301041435037	0.00007395856496295039	0.000014838302170780775
$\frac{2}{8}$	4.9375	4.937419317929127	0.00008068207087319479	0.000016340939603856617
$\frac{3}{8}$	4.859375	4.859288628808751	0.0000863711912488796	0.000017774451745224567
$\frac{4}{8}$	4.75	4.749908974073891	0.00009102592610865656	0.00001916372010611093
$\frac{5}{8}$	4.609375	4.609280353724557	0.00009464627544275572	0.000020533850878972076
$\frac{6}{8}$	4.4375	4.437402767760745	0.00009723223925472979	0.00002191197066021489
$\frac{7}{8}$	4.234375	4.234276216182457	0.00009878381754280241	0.000023329563896958997

Table 2 The error of coefficient $k(x)$ (with 16 items in each series)

x	True solution	Approximate solution	Absolute error	Relative error
$\frac{1}{16}$	4.99609375	4.996080272577284	0.000013477422715624243	$2.697599313926108\times10^{-6}$
$\frac{3}{16}$	4.96484375	4.964828882640552	0.000014867359447556794	$2.9945361258149875\times10^{-6}$
$\frac{5}{16}$	4.90234375	4.902327691266218	0.000016058733781854073	$3.2757365058365314\times10^{-6}$
$\frac{7}{16}$	4.80859375	4.80857669845436	0.00001705154564035638	$3.54606918214226e\times10^{-6}$
$\frac{9}{16}$	4.68359375	4.683575904205057	0.000017845794943127657	$3.8102926712696508\times10^{-6}$
$\frac{11}{16}$	4.52734375	4.527325308518295	0.000018441481705266938	$4.073372344277703\times10^{-6}$
$\frac{13}{16}$	4.33984375	4.339824911393927	0.00001883860607332366	$4.340867767237367\times10^{-6}$
$\frac{15}{16}$	4.12109375	4.121074712831783	0.000019037168216939904	$4.61946689723045\times10^{-6}$

Table 3 The error of coefficient $k(x)$ (with 16 items in each series and an artificial error $10^{(-4)}$ to the right end)

x	True solution	Approximate solution	Absolute error	Relative error
$\frac{1}{16}$	4.99609375	4.996085272577282	$8.477422717589889\times10^{-6}$	$1.6968130556380039\times10^{-6}$
$\frac{3}{16}$	4.96484375	4.964833882640548	$9.867359452186975\times10^{-6}$	$1.987450070925438\times10^{-6}$
$\frac{5}{16}$	4.90234375	4.902332691266211	0.000011058733789148789	$2.2558105468546766\times10^{-6}$
$\frac{7}{16}$	4.80859375	4.808581698454347	0.000012051545652980167	$2.5062578549625084\times10^{-6}$
$\frac{9}{16}$	4.68359375	4.683580904205	0.000012845795000160365	$2.742729390801638\times10^{-6}$
$\frac{11}{16}$	4.52734375	4.527330308518159	0.000013441481841347525	$2.9689642516379724\times10^{-6}$
$\frac{13}{16}$	4.33984375	4.339829911393702	0.00001383860629822209	$3.188743932542262\times10^{-6}$
$\frac{15}{16}$	4.12109375	4.121079712831503	0.000014037168496905394	$3.4061870856802146\times10^{-6}$

Table 4 The error of coefficient $k(x)$ (with 16 items in each series and an artificial error $10^{(-4)}$ to the additional condition)

x	True solution	Approximate solution	Absolute error	Relative error
$\frac{1}{16}$	4.99609375	4.996085575289186	$8.174710814046193\times10^{-6}$	$1.636223137265422\times10^{-6}$
$\frac{3}{16}$	4.96484375	4.964834732225137	$9.01777486284061\times10^{-6}$	$1.8163293139062916\times10^{-6}$
$\frac{5}{16}$	4.90234375	4.902334009598814	$9.740401186064673\times10^{-6}$	$1.9868905641665543\times10^{-6}$
$\frac{7}{16}$	4.80859375	4.808583407410293	0.000010342589707335037	$2.1508599999318996\times10^{-6}$
$\frac{9}{16}$	4.68359375	4.683582925659638	0.000010824340361814677	$2.3111238839205932\times10^{-6}$
$\frac{11}{16}$	4.52734375	4.527332564346846	0.000011185653153944486	$2.4706939450466964\times10^{-6}$
$\frac{13}{16}$	4.33984375	4.339832323471773	0.000011426528226721189	$2.632942329343317\times10^{-6}$
$\frac{15}{16}$	4.12109375	4.121082203034261	0.000011546965739128723	$2.8019256035773686\times10^{-6}$

$$\sum_{i=1}^{\infty}\sum_{l=1}^{i}\beta_{il}F(s_l)\bar{\psi}_i(x,0)=h(x)-\sum_{i=1}^{\infty}\alpha_i\bar{\rho}_i(x,0) \tag{5.11}$$

Making inner product with $\bar{\psi}_j(x,0)$ on both sides of Eq. (5.11) and applying Lemma 4.2, the lower triangular system of equations has been built.

6 Numerical Examples and Conclusion

In this section we present some results of numerical experiments using the numerical method described above. The following is a parabolic equation with initial, boundary, and additional conditions.

$$\frac{\partial}{\partial x}\left(k(x)\frac{\partial u(x,t)}{\partial x}\right)-\frac{\partial u(x,t)}{\partial t}=f(x,t)\quad (x,t)\in[0,1]\times[0,1]$$

$$u(x,0)=h(x)$$

$$u(0,t)=0\quad \frac{\partial}{\partial x}u(1,t)=0$$

subject to

$$u(x^*,t)=g(t)$$

where $h(x)=10(x^2-2x)$, $f(x,t)=100+42x-61x^2+t(10+4x-6x^2)$, and $x^*=0.6$, $g(t)=-0.84(t+10)$. The true coefficient $k(x)=5-x^2$, and the true solution of the parabolic equation $u(x,t)=(x^2-2x)(t+10)$.

The results of determination of $k(x)$ illustrated in Tables 1–4 are obtained by truncating the two series in Eq. (5.1). Table 1 is the result of choosing the first eight terms in both series. Table 2 shows the results of choosing the first 16 terms in both series. As seen from the tables, approximation is improved by increasing the number of nodes. The last two examples have been done to control the sensitivity of the method to errors. Artificial errors 10^{-4} were introduced into the right end in the third example and conditional condition in the fourth example. As seen in Tables 3 and 4, the error almost never affects the results of the method. The method of solving the problem was tried on different tests, and the results we observed indicate that the method is stable and gives excellent approximation to the solution.

7 Conclusions

In this paper, we consider solving one-dimensional inverse parabolic problem. We presented a stable numerical algorithm for identifying the space-dependent coefficient in a parabolic equation. Numerical results show that the proposed method is effective. It will be very interesting to expand our work to higher dimensional cases.

Nomenclature

$W_i[0,1]$ = reproducing kernel spaces on the interval [0,1] ($i=1,2,3$)
$W(D)$ = reproducing kernel space on the region $D=[0,1]\times[0,1]$
$P_\xi(x)$ = reproducing kernel of $W_1[0,1]$
$Q_t(s)$ = reproducing kernel of $W_2[0,1]$
$R_x(y)$ = reproducing kernel of $W_3[0,1]$
$K_{x,t}(\xi,\eta)$ = reproducing kernel of $W(D)$
L = the operator of the operator equation transferred from the original equation
L^* = the conjugate operator of L
$\{x_i\}_{i=1}^{\infty}$ = a dense set of the interval [0,1]
$\varphi_i(x)$ = the value of $P_\xi(x)$ at $\xi=x_i$
$\psi_i(x,t)$ = $(L^*\varphi_i)(x,t)$
$\{\bar{\psi}_i\}_{i=1}^{\infty}$ = an orthonormal system of $\{\psi_i\}_{i=1}^{\infty}$
β_{ik} = coefficients of orthonomalization
S = span$\{\bar{\psi}_i(x,t)\}_{i=1}^{\infty}$
$S^{\perp}$ = the orthcomplement space of S in $W(D)$
$\{\rho_j\}_{j=1}^{\infty}$ = the basis of $S^{\perp}$

References

[1] Duchateau, P. C., 1995, "Monotonicity and Invertibility of Coefficients-to-Data Mapping for Parabolic Inverse Problems," SIAM J. Math. Anal., **26**, pp. 1473–1487.
[2] Shidfar, A., and Azary, H., 1997, "An Inverse Problem for a Nonlinear Diffusion Equation," Nonlinear Anal. Theory, Methods Appl., **28**, pp. 589–593.
[3] Cannon, J. R., and Duchateau, P. C., 1978, "Determination of Unknown Coefficients in Parabolic Operators From Overspecified Initial Boundary Data," ASME J. Heat Transfer, **100**, pp. 503–507.
[4] Muzylev, V., 1980, "Uniqueness Theorems for Some Converse Problems of Heat Conduction," USSR Comput. Math. Math. Phys., **20**, pp. 120–134.
[5] Alifanov, O. M., Artyukhin, E. A., and Rumyantsev, S. V., 1988, *Extreme Methods for Solving Ill-Posed Problems With Application to Inverse Heat Transfer Problems*, Nauka, Moscow, in Russian.
[6] Fatullayev, A. G., Can, E., and Gasilov, N., 2006, "Comparing Numerical Methods for Inverse Coefficient Problem in Parabolic Equation," Appl. Math. Comput., **179**, pp. 567–571.
[7] Chen, Z., and Lin, Y., 2008, "The Exact Solution of a Linear Integral Equation With Weakly Singular Kernel," J. Math. Anal. Appl., **344**, pp. 726–734.
[8] Cui, M., and Lin, Y., 2008, *Nonlinear Numerical Analysis in the Reproducing Kernel Space*, Nova Science, New York.
[9] Aronszajn, N., 1950, "Theory of Reproducing Kernels," Trans. Am. Math. Soc., **68**, pp. 337–404.

A Thermal Stability Criterion for Heat Conduction in Multilayer Composite Solids

Bingen Yang[1]
Professor
Fellow ASME
e-mail: bingen@usc.edu

Hang Shi
Graduate Student

Department of Aerospace and Mechanical Engineering,
University of Southern California,
3650 McClintock Avenue,
Room 430,
Los Angeles, CA 90089-1453

Excessive heat generation within a body can cause unbounded temperature or thermal instability. In this work, a new stability test is established for heat conduction in one-dimensional multilayer composite solids that have internal heat generation at a rate proportional to the interior temperature. In the development, a spatial state formulation in the Laplace transform domain and a root locus analysis yield a stability criterion. This criterion gives an upper bound of heat source for thermal stability and relates the degree of excessive heat production to the number of unstable (positive) eigenvalues. The proposed stability test does not need any information on system eigenvalues, requests minimum computational effort, and is applicable to composites with thermal resistance at layer interfaces and bodies with nonuniformly distributed parameters. The convenience and efficiency of the stability test are demonstrated in three numerical examples.
[DOI: 10.1115/1.3153581]

Keywords: heat conduction, multilayer composites, heat sources, temperature-dependent heat generation, thermal stability, unstable heat equation, state formulation, root locus, stability test

1 Introduction

Heat conduction in multilayer composite solids has a variety of engineering applications such as buildings, industrial furnaces, nuclear reactors, turbines, rockets, space craft, and high-tech devices and instruments, and thus has been a topic of continued research interest [1–10]. Excessive heat generation within a body can cause unbounded temperature or thermal instability. Heat can be generated in different ways. For heat generated by electric current passing through a solid or by radioactive decay in the region, the rate of hear generation is usually independent of temperature. However, in many chemical and physical processes, heat production taking place in a body can be a function of temperature. Examples are diverse, including high heat generation during cement polymerization [11,12], Ohmic heat generation in a composite superconductor [13] and dual-phase lag head conduction in a superconductor [14], temperature dependent heat sources in a stagnation point flow [15] and in a magnetohydrodynamic flow [16], heat generation in the earth's crust and upper mantel that is attributed to the radioactive decay of certain chemical elements such as U, Th, and K [17], and the ever-increasing temperature and power of a nuclear reactor when its temperature coefficient of reactivity is positive [18]. Heat generation rate in some cases can be modeled as a linear function of temperature (for example, see p. 404 of Ref. [1], and Refs. [13,14,16,17]). The stability and feedback control of heat conductions with temperature-dependent internal heat sources have also been studied by several authors [19–22].

The current study is concerned with the thermal stability of heat conduction in composite solids with heat generation that is at a rate proportional to the temperature. By stability we mean the temperature of a composite body in consideration is bounded. The stability of heat flow in single-layer finite slabs and rods has been well studied, and an upper bound of linear heat source has been derived. For instance, the nondimensional heat equation $u_{xx}+bu=u_t$ in region $0<x<1$ is stable if $b+s_1<0$, where s_1 is the largest eigenvalue of the heat equation with $b=0$ (see p. 405 of Ref. [1]). For multilayer composite solids, due to discontinuous distributions of material properties, stability analysis is difficult. One direct way to examine stability is to compute the eigenvalues of the related heat equation. This approach obtains a stability bound by trial and error, and is numerically intensive. In Ref. [19], a stability test without computation of system eigenvalues is presented. This method applies Nyquist criterion to a composite solid based on a virtual feedback-loop formulation. Because the gains of heat source are embedded in the transcendental open-loop transfer function, determination of a stability bound inevitably relies on numerical simulation of a sequence of Nyquist plots.

In this work, a new stability test is proposed for heat conduction in one-dimensional multilayer composite solids. In the development, a spatial state formulation [23,24] is first used to derive a characteristic equation for system eigenvalues; a root locus analysis is then applied to the characteristic equation, yielding a stability criterion. This criterion gives an upper bound of heat source for thermal stability and relates the degree of excessive heat generation to the number of unstable (positive) eigenvalues. The stability test requires minimum numerical effort, does not need information about the eigenvalues of the composite solid, and is applicable to various spatial distributions of inner heat sources. The convenience and efficiency of the proposed method are demonstrated in three examples.

2 Problem Statement

Consider a one-dimensional n-layer composite solid shown in Fig. 1, where x_j is the spatial coordinate of the interface between the jth and $(j+1)$th layers, and x_0 and x_n denote the left and right boundaries of the body, respectively. Here $x_0=0$ and $x_j=l_1+l_2+\cdots+l_j$, where $j=1,2,\ldots,n$, with $l_j=x_j-x_{j-1}$ being the thickness of the jth layer. The heat conduction in the jth layer is governed by the partial differential equation

[1]Corresponding author.

Contributed by the Heat Transfer Division of ASME for publication in the JOURNAL OF HEAT TRANSFER. Manuscript received May 24, 2008; final manuscript received April 29, 2009; published online August 25, 2009. Review conducted by Cholik Chan.

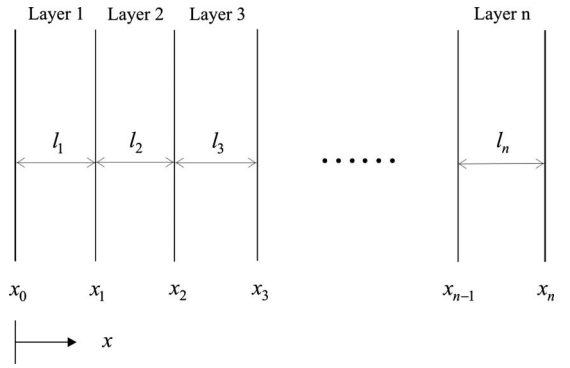

Fig. 1 An *n*-layer composite body

$$\lambda_j \frac{\partial^2 T_j(x,t)}{\partial x^2} + B_j T_j(x,t) = \frac{\lambda_j}{\alpha_j}\frac{\partial T_j(x,t)}{\partial t}, \quad x \in [x_{j-1}, x_j],$$
$$j = 1,2,\ldots,n \tag{1}$$

where $T_j(x,t)$, λ_j, and α_j are the temperature, thermal conductivity, and thermal diffusivity of the layer, respectively, and B_j is a non-negative parameter describing heat generation within the layer. In the literature linear heat generation rate usually takes the form $A_j + B_j T_j(x,t)$, where A_j is a constant (for example, see p. 404 of Ref. [1] or Ref. [17]). The A_j is dropped from Eq. (1) for simplicity in analysis as it does not affect the stability results.

With the perfect thermal contact assumption, the matching conditions at the layer interfaces are given by

$$T_j(x_j,t) = T_{j+1}(x_j,t)$$
$$-\lambda_j \frac{\partial T_j(x_j,t)}{\partial x} = -\lambda_{j+1}\frac{\partial T_{j+1}(x_j,t)}{\partial x} \tag{2}$$

for $j = 1,2,\ldots,n-1$. Partial thermal contact at the layer interfaces will be addressed in Sec. 4.1. The boundary conditions of the body are of the following general forms:

$$\text{at } x = x_0, \quad a_1 \frac{\partial T_1(x_0,t)}{\partial x} + a_0 T_1(x_0,t) = 0 \tag{3a}$$

$$\text{at } x = x_n, \quad b_1 \frac{\partial T_n(x_n,t)}{\partial x} + b_0 T_n(x_n,t) = 0 \tag{3b}$$

where constants a_0, a_1, b_0, and b_1 are assigned to characterize different types of boundaries.

The objectives of this work are to investigate the stability of heat flow in the above composite body and to determine the stability bound of linear heat source.

3 Approach

For convenience in stability analysis, the heat equation (1) is revised as

$$\lambda_j \frac{\partial^2 T_j(x,t)}{\partial x^2} + \mu B_j T_j(x,t) = \frac{\lambda_j}{\alpha_j}\frac{\partial T_j(x,t)}{\partial t}, \quad x \in [x_{j-1}, x_j],$$
$$j = 1,2,\ldots,n \tag{4}$$

where μ is a nondimensional and non-negative parameter, which shall be called heat gain. When $\mu = 0$ there is no heat generation inside the composite body, and when $\mu = 1$ Eq. (4) becomes the original Eq. (1). In sequel, a spatial state formulation in the s domain [23,24] and a root locus analysis are applied to obtain an upper bound of μ for the thermal stability of the body.

3.1 Spatial State Equations. Laplace transform of Eqs. (2), (3*a*), (3*b*), and (4) with respect to time gives

$$\frac{\partial^2 \bar{T}_j(x,s)}{\partial x^2} = \left(\frac{s}{\alpha_j} - \mu\frac{B_j}{\lambda_j}\right)\bar{T}_j(x,s), \quad x \in [x_{j-1}, x_j] \tag{5}$$

$$\bar{T}_j(x_j,s) = \bar{T}_{j+1}(x_j,s)$$
$$-\lambda_j \frac{\partial \bar{T}_j(x_j,s)}{\partial x} = -\lambda_{j+1}\frac{\partial \bar{T}_{j+1}(x_j,s)}{\partial x} \tag{6}$$

$$a_1 \frac{\partial \bar{T}_1(x_0,s)}{\partial x} + a_0 \bar{T}_1(x_0,s) = 0$$
$$b_1 \frac{\partial \bar{T}_1(x_n,s)}{\partial x} + b_0 \bar{T}_n(x_n,s) = 0 \tag{7}$$

where the overbar stands for Laplace transform, s is the Laplace transform parameter, and zero initial temperature has been assumed. For the jth layer, defining the spatial state vector

$$\{\hat{\eta}_j(x,s)\} = \begin{pmatrix} \bar{T}_j(x,s) \\ \lambda_j \dfrac{\partial \bar{T}_j(x,s)}{\partial x} \end{pmatrix} \tag{8}$$

which automatically satisfies the matching conditions (6), i.e.,

$$\{\hat{\eta}_j(x_j,s)\} = \{\hat{\eta}_{j+1}(x_j,s)\}, \quad j = 1,2,\ldots,n-1 \tag{9}$$

and reduces Eq. (5) to the first-order state equation

$$\frac{\partial}{\partial x}\{\hat{\eta}_j(x,s)\} = [F_j(s)]\{\hat{\eta}_j(x,s)\}, \quad x \in [x_{j-1}, x_j] \tag{10}$$

where

$$[F_j(s)] = \begin{bmatrix} 0 & \dfrac{1}{\lambda_j} \\ \lambda_j \beta_j^2 & 0 \end{bmatrix} \quad \text{with } \beta_j = \sqrt{\frac{s}{\alpha_j} - \mu\frac{B_j}{\lambda_j}} \tag{11}$$

The boundary conditions (7) are also cast in the matrix form

$$[M_b]\{\hat{\eta}_1(x_0,s)\} + [N_b]\{\hat{\eta}_n(x_n,s)\} = 0 \tag{12}$$

with

$$[M_b] = \begin{bmatrix} a_0 & a_1/\lambda_1 \\ 0 & 0 \end{bmatrix}, \quad [N_b] = \begin{bmatrix} 0 & 0 \\ b_0 & b_1/\lambda_n \end{bmatrix} \tag{13}$$

The heat conduction problem is now described by the equivalent state form, Eqs. (10) and (12).

3.2 Characteristic Equation. The characteristic equation of the composite body is derived through the use of a formulation given in Refs. [23,24]. The solution of the state in Eq. (10) is

$$\{\hat{\eta}_j(x,s)\} = e^{[F_j(s)](x-x_{j-1})}\{\hat{\eta}_{j-1}(x_j,s)\}, \quad x \in [x_{j-1}, x_j] \tag{14}$$

where the exponential matrix, according to p. 326 of Ref. [1], is given by

$$e^{[F_j(s)]x} = \begin{bmatrix} \cosh(\beta_j x) & \dfrac{1}{\lambda_j \beta_j}\sinh(\beta_j x) \\ \lambda_j \beta_j \sinh(\beta_k x) & \cosh(\beta_j x) \end{bmatrix} \tag{15}$$

Successive use of Eqs. (9) and (14) leads to

$$\{\hat{\eta}_n(x_n,s)\} = [\Phi(s,\mu)]\{\hat{\eta}_1(x_0,s)\} \tag{16}$$

where

$$[\Phi(s,\mu)] = e^{[F_n(s)]l_n}\cdots e^{[F_2(s)]l_2}e^{[F_1(s)]l_1} \tag{17}$$

Substitute Eq. (16) into the boundary condition in Eq. (12) to obtain

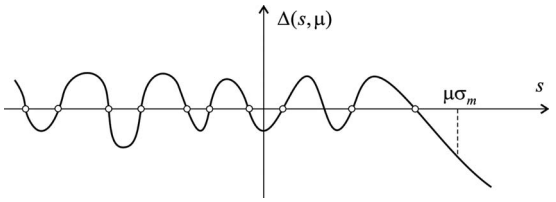

Fig. 2 Schematic of the characteristic function $\Delta(s,\mu)$ versus s; σ_m is a parameter defined in Eq. (21); circles (○) are the eigenvalues of the composite body

$$([M_b]+[N_b][\Phi(s,\mu)])\{\hat{\eta}_1(x_0,s)\}=0 \tag{18}$$

A characteristic equation then is

$$\Delta(s,\mu)\equiv \det([M_b]+[N_b][\Phi(s,\mu)])=0 \tag{19}$$

whose roots are the eigenvalues of the composite body.

The characteristic function $\Delta(s,\mu)$ has the following two properties.

(P1) function $\Delta(s,\mu)$ is continuous for $-\infty<s<\infty$ and $\mu\geq 0$, and is bounded in any finite region of s and μ. The function at $s=0$ and $\mu=0$ has a finite value

$$\Delta(0,0)=a_0b_0\sum_{j=1}^{n}\frac{l_j}{\lambda_j}+\frac{a_0b_1}{\lambda_n}-\frac{a_1b_0}{\lambda_1} \tag{20}$$

(P2) Define a parameter

$$\sigma_m\equiv \max_{1\leq j\leq n}\left(\frac{B_j\alpha_j}{\lambda_j}\right) \tag{21}$$

Let μ (≥ 0) be fixed. For $s<\mu\sigma_m$, some of β_j in Eq. (11) are imaginary and the exponential matrices in Eq. (15) contain sinusoidal functions. As such, $\Delta(s,\mu)$ is oscillatory in the region $-\infty<s<\mu\sigma_m$. For $s>\mu\sigma_m$, all β_j are real and $\Delta(s,\mu)$ is nonoscillatory. This indicates that $\Delta(s,\mu)$ is infinite as $s\to+\infty$. Thus, given a finite μ, $\Delta(s,\mu)$ has an infinite number of roots in the negative region $s<0$, and a finite number of roots in the positive region $s>0$.

A schematic of the characteristic function $\Delta(s,\mu)$ versus s is shown in Fig. 2, where the circles are the eigenvalues of the composite body.

3.3 Root Locus Analysis. Denote the eigenvalues of the composite body by $s_k(\mu)$, where $k=1,2,\ldots$, which are the roots of the characteristic equation (19) and are dependent on the heat gain μ in Eq. (4). As μ varies from zero to infinity, an eigenvalue makes a trajectory in the complex plane, which is called root locus. The body is said to be thermally unstable if at least one eigenvalue has positive real part, which renders the temperature of the body unbounded. The body is thermally stable if all the eigenvalues have negative real parts.

Claim 1. For any $\mu\geq 0$, all eigenvalues $s_k(\mu)$ of the composite body described by Eqs. (4), (2), and (3) are real.

Proof. The eigenvalue problem for the composite body is described by

$$\lambda_j\frac{d^2v_j(x)}{dx^2}=\left(\frac{\lambda_j s}{\alpha_j}-\mu B_j\right)v_j(x),\quad x\in[x_{j-1},x_j] \tag{22}$$

$j=1,2,\ldots,n$, where s is an eigenvalue and $v_j(x)$ is the associate eigenfunction that also satisfies the matching and boundary conditions (6) and (7). By Eq. (22), write

$$\sum_{j=1}^{n}\lambda_j\int_{x_{j-1}}^{x_j}\bar{v}_j(x)\frac{d^2v_j(x)}{dx^2}dx=\sum_{j=1}^{n}\int_{x_{j-1}}^{x_j}\left(\frac{\lambda_j s}{\alpha_j}-\mu B_j\right)\bar{v}_j(x)v_j(x)dx \tag{23}$$

where $\bar{v}_j(x)$ is the complex conjugate of $v_j(x)$. Integral by part and application of the matching and boundary conditions eventually reduce Eq. (23) to

$$-\sum_{j=1}^{n}\lambda_j\int_{x_{j-1}}^{x_j}\left|\frac{dv_j(x)}{dx}\right|^2dx-J_0-J_n=\sum_{j=1}^{n}\left(\frac{\lambda_j s}{\alpha_j}-\mu B_j\right)\int_{x_{j-1}}^{x_j}|v_j(x)|^2dx \tag{24}$$

where J_0 and J_n are real and non-negative numbers arising from the boundary conditions. Because every integral in Eq. (24) is real, so must be s. □

According to Claim 1, all the root loci lie on the real axis as μ varies. Arrange the root loci in a descending order ($s_1(\mu)>s_2(\mu)>s_3(\mu)>\cdots$). It can be shown from Eq. (18) that the eigenvalues of the current problem are distinct. The root loci start at the eigenvalues of the body with no heat source ($\mu=0$), in which case $0\geq s_1(0)>s_2(\mu)>s_3(\mu)>\cdots$. The equality $s_1(0)=0$ holds only when the composite body is insulated ($a_0=b_0=0$). Physically, the negative eigenvalues are due to the nature of heat conduction through a body without any thermal input. This can also be seen from Eq. (24) with $\mu=0$.

Now increase μ from zero. By Property P2 in Sec. 3.2, function $\Delta(s,\mu)$ becomes oscillatory in the positive region $0\leq s<\mu\sigma_m$ (see Fig. 2). This implies that $\Delta(s,\mu)$ starts to have some positive roots if μ is large enough. Further increasing μ will expand the region $0\leq s<\mu\sigma_m$, and as a result produce more positive characteristic roots. The larger the μ, the more positive roots. This leads to Claim 2.

Claim 2. The root loci $s_k(\mu)$ start at the eigenvalues of the body with no internal heat source ($\mu=0$). As μ continues to increase, root loci $s_k(\mu)$ travel rightward along the real axis, cross the origin one by one, and migrate into the positive region $s>0$.

By Claim 2, there is a critical value μ_{cr} of μ at which the first root locus arrives at the origin, namely, $s_1(\mu_{cr})=0$. For $\mu<\mu_{cr}$, all eigenvalues lie on the negative real axis ($s_k<0$). A μ that is slightly larger than μ_{cr} will push the first eigenvalue into the positive region ($s_1>0$) and cause thermal instability. Because $s_1=0$ and μ_{cr} satisfy the characteristic equation (19), the following stability criterion is in order.

THEOREM 1. *The composite body described by Eqs. (4), (2), and (3) is thermally stable if the heat gain μ satisfies $\mu<\mu_{cr}$, where the upper bound μ_{cr} is the minimum non-negative root of the transcendental equation*

$$\Delta(0,\mu)=0 \tag{25}$$

The composite body is thermally unstable with at least one positive eigenvalue if $\mu>\mu_{cr}$.

For an insulated body ($a_0=b_0=0$), $\mu_{cr}=0$ by Eq. (20). In this case the body is thermally unstable when it has any inner heat production ($\mu>0$). This of course is well known from an energy balance viewpoint.

It can be shown that for $\mu>0$,

$$\Delta(0,\mu)=a_0b_0\frac{\phi_{12}(\mu)}{\sqrt{\mu}}+\frac{a_0b_1}{\lambda_n}\phi_{22}(\mu)-\frac{a_1b_0}{\lambda_1}\phi_{11}(\mu)+\frac{a_1b_1}{\lambda_1\lambda_n}\sqrt{\mu}\phi_{21}(\mu) \tag{26}$$

where the functions ϕ_{ij} are given by

$$\begin{bmatrix} \phi_{11} & \phi_{12} \\ \phi_{21} & \phi_{22} \end{bmatrix} = [D_n] \cdots [D_2][D_1] \tag{27}$$

with

$$[D_j] = \begin{bmatrix} \cos(\sqrt{\mu B_j/\lambda_j}\, l_j) & \dfrac{1}{\sqrt{B_j \lambda_j}} \sin(\sqrt{\mu B_j/\lambda_j}\, l_j) \\ -\sqrt{B_j \lambda_j}\, \sin(\sqrt{\mu B_j/\lambda_j}\, l_j) & \cos(\sqrt{\mu B_j/\lambda_j}\, l_j) \end{bmatrix} \tag{28}$$

If $B_j = 0$ (no heat source in the jth layer),

$$[D_j] = \begin{bmatrix} 1 & \sqrt{\mu} l_j/\lambda_j \\ 0 & 1 \end{bmatrix} \tag{29}$$

Because ϕ_{ij} only contain sinusoidal functions of $\sqrt{\mu}$, $\Delta(0,\mu)$ is continuous and bounded in any finite region of μ. Thus, Eq. (25) can be easily solved by standard root-searching techniques.

According to Claim 2, all root loci $s_k(\mu)$ move in the positive direction of the real axis as μ increases. The transcendental function $\Delta(0,\mu)$ has infinitely many roots. Each time when μ reaches one of the roots, one more root locus crosses the origin and moves into the positive region. This gives the following result on the number of unstable eigenvalues.

THEOREM 2. *Let μ_k be the non-negative roots of $\Delta(0,\mu)=0$ arranged in an ascending order, $(0 \le \mu_1 < \mu_2 < \mu_3 < \cdots)$. The composite body has m unstable (positive) eigenvalues if the heat gain μ in Eq. (4) is such that $\mu_m < \mu < \mu_{m+1}$. If $\mu < \mu_1 = \mu_{cr}$, the body has no unstable eigenvalue.*

In summary, the root locus analysis presented in this section yields an upper bound μ_{cr} of heat gain, which can be computed according to Theorem 1. The number of unstable eigenvalues for a given value of μ can be obtained by Theorem 2. Because Eq. (26) is given in an explicit analytical form, the stability bound and the correlation between excessive heat generation and the number of unstable eigenvalues can be easily determined, without the need for system eigenvalues and intensive computation.

4 Extension of Stability Analysis

The stability analysis in Sec. 3 is extended to composite solids with thermal resistance at layer interfaces and continua with nonuniformly distributed parameters.

4.1 Partial Thermal Contact at Layer Interfaces. For a composite body with partial thermal contact at its layer interfaces, the heat equation and boundary conditions are the same as Eqs. (4) and (3), respectively. The matching conditions at the layer interfaces are modified as

$$\begin{aligned} -\lambda_j \frac{\partial T_j(x_j,t)}{\partial x} &= h_j (T_j(x_j,t) - T_{j+1}(x_j,t)) \\ -\lambda_j \frac{\partial T_j(x_j,t)}{\partial x} &= -\lambda_{j+1} \frac{\partial T_{j+1}(x_j,t)}{\partial x} \end{aligned} \tag{30}$$

where h_j is a conductance coefficient, with its reciprocal describing the thermal resistance at the interfaces [25–27]. For a finite h_j, the temperature is discontinuous at the layer interface. As $h_j \to \infty$, the temperature becomes continuous and perfect thermal contact is resumed.

The matching conditions (30) are written in a spatial state form:

$$\{\hat{\eta}_{j+1}(x_j,s)\} = [C_j]\{\hat{\eta}_j(x_j,s)\} \tag{31}$$

where

$$[C_j] = \begin{bmatrix} 1 & 1/h_j \\ 0 & 1 \end{bmatrix} \tag{32}$$

Matrix $[C_j]$ reduces to an identity matrix when the interface has perfect thermal contact. The characteristic equation of the body is of the same form as Eq. (19), but with

$$[\Phi(s,\mu)] = e^{[F_n(s)]l_n}[C_{n-1}]e^{[F_{n-1}(s)]l_{n-1}} \cdots [C_2]e^{[F_2(s)]l_2}[C_1]e^{[F_1(s)]l_1} \tag{33}$$

Because $[C_j]$ are constant matrices, the characteristic function has the same properties P1 and P2, as given in Sec. 3.2. Hence, Theorems 1 and 2 are directly applicable here. In estimation of the upper bound μ_{cr} and system eigenvalues, one only needs to modify matrix $[\Phi(s,\mu)]$ according to Eq. (33).

4.2 Nonuniformly Distributed Continua. The heat conduction in a nonuniform body is described by

$$\frac{\partial}{\partial x}\left(\lambda(x)\frac{\partial}{\partial x}T(x,t)\right) + \mu B(x) T(x,t) = \rho(x) c(x) \frac{\partial T(x,t)}{\partial t}, \quad x \in (0,L) \tag{34}$$

where L is the length of the region, the physical parameters λ, ρ, and c are functions of x that are positive in $(0,L)$, function $B(x)$ has non-negative values and is piecewise continuous, and μ is a nondimensional non-negative heat gain. Because exact solutions are difficult to obtain for such a nonuniformly distributed system, a semi-analytical method is introduced. Following Refs. [23,24], the nonuniform body is approximated as an n-layer composite solid as described by Eqs. (4), (2), and (3), with the layer parameters given by

$$\begin{aligned} \lambda_j &= \frac{\lambda(x_{j-1}) + \lambda(x_j)}{2}, \quad B_j = \frac{B(x_{j-1}) + B(x_j)}{2} \\ \frac{\lambda_j}{\alpha_j} &= \frac{\rho(x_{j-1})c(x_{j-1}) + \rho(x_j)c(x_j)}{2} \end{aligned} \tag{35}$$

One may also use other formulas like $\lambda_j = \lambda(x_{j-1})$, $B_j = B(x_{j-1})$, $\lambda_j/\alpha_j = \rho(x_{j-1})c(x_{j-1})$, or $\lambda_j = \lambda(x_j)$, $B_j = B(x_j)$, $\lambda_j/\alpha_j = \rho(x_j)c(x_j)$. The spatial space formulation and stability analysis given in Sec. 3 are valid for the approximated system. As the number n of the layers increases, the computed stability bound and eigenvalues should converge to those of the original system (34).

5 Numerical Examples

To demonstrate the stability results, three examples are considered: a three-layer composite body, the same three-layer composite body with partial thermal contact at a layer interface, and a nonuniform body. In numerical simulation, all physical parameters are assigned nondimensional values. In solving transcendental equations (19) and (25), the Newton–Raphson method is applied.

5.1 Example 1: A Three-Layer Body. Consider a three-layer composite body with an inner heat source in the middle layer. The layer parameters of the body are chosen as follows:

$$\text{Layer } 1{:}\lambda_1 = 1, \quad \alpha_1 = 1, \quad B_1 = 0, \quad l_1 = 1$$

$$\text{Layer } 2{:}\lambda_2 = 2, \quad \alpha_2 = 1, \quad B_2 = 1, \quad l_2 = 1$$

$$\text{Layer } 3{:}\lambda_3 = 3, \quad \alpha_3 = 1, \quad B_3 = 0, \quad l_1 = 1$$

The body has convection boundary conditions at both ends:

$$\lambda_1 \frac{\partial T_1(x_0,t)}{\partial x} - h_L T_1(x_0,t) = 0$$

$$\lambda_3 \frac{\partial T_3(x_3,t)}{\partial x} + h_R T_3(x_3,t) = 0$$

with $h_L = 2$ and $h_R = 0.75$, which in the form of Eq. (3) give $a_0 = -2$, $a_1 = 1$, $b_0 = 0.75$, and $b_1 = 3$. A plot of characteristic function $\Delta(0,\mu)$ versus μ is given in Fig. 3. Listed in Table 1 are the first eight roots of $\Delta(0,\mu)=0$. By Theorem 1, the upper bound of μ for

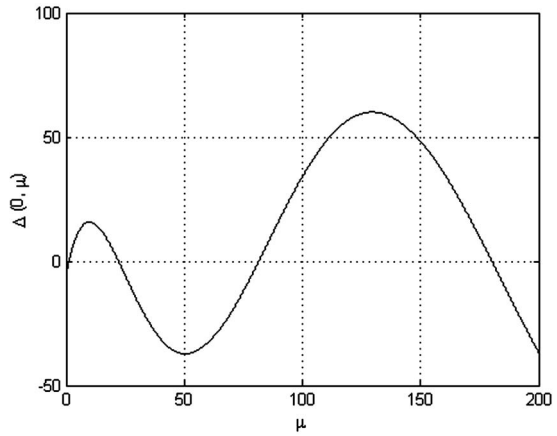

Fig. 3 Characteristic function $\Delta(0,\mu)$ versus heat gain μ

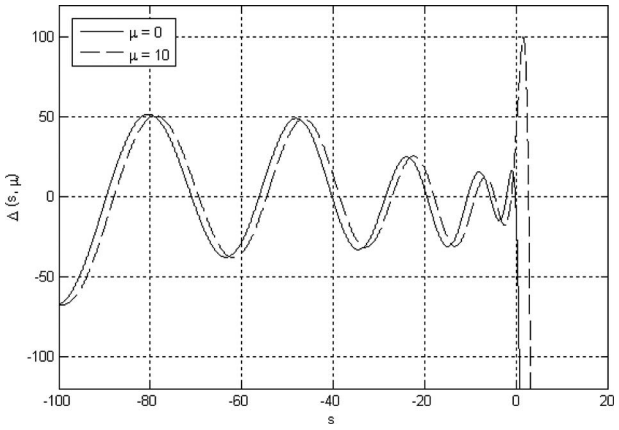

Fig. 4 Characteristic function $\Delta(s,\mu)$ versus s for heat gain $\mu=0$ and 10

thermal stability is $\mu_{cr}=\mu_1$. Thus, the heat conduction in the composite body is stable if $\mu<1.2021$.

Although not needed in stability prediction, the eigenvalues of the composite body are computed for the purpose of validation. Listed in Table 2 are the first ten eigenvalues s_k for $\mu=0$, 1, 10, 50, 100, and 200, which are obtained by solving Eq. (19). The table reveals the trend of the root locus of the body. As μ increases, all the eigenvalues moves rightward along the real axis. For a large enough μ, one or more positive eigenvalues appear. The number of unstable (positive) eigenvalues confirms Theorem 2. For instance, for $\mu=100$ that falls between μ_3 and μ_4, the body has three unstable eigenvalues. Additionally, the characteristic function $\Delta(s,\mu)$ are plotted against s for $\mu=0$ and 10 in Fig. 4, which shows the rightward migration of the eigenvalues as the heat gain μ increases.

Table 1 Roots of $\Delta(0,\mu)=0$ in Example 1

k	μ_k
1	1.20210
2	22.1930
3	81.4684
4	180.176
5	318.355
6	496.010
7	713.142
8	969.753

5.2 Example 2: A Three-Layer Body With Thermal Resistance at Layer Interface. Consider the same composite body as in Example 1, except that there is partial thermal contact between the second and third layers:

$$-\lambda_2\frac{\partial T_2(x_2,t)}{\partial x}=h_c(T_2(x_2,t)-T_3(x_2,t))$$

By Eq. (33), $[\Phi(s,\mu)]=e^{F_3(s)l_3}[C_2]e^{F_2(s)l_2}e^{F_1(s)l_1}$. Listed in Table 3 are the first four roots of Eq. (25), with the conductance $h_c=1$, 10, 100, 1000, and ∞. The body has perfect thermal contact when $h_c=\infty$. From the table, μ_1 decreases from 1.20210 to 0.98902 as h_c varies from ∞ to 1. Therefore, thermal resistance $(1/h_c)$ at the layer interface reduces the stability bound $(\mu_{cr}=\mu_1)$. Listed in Table 4 are the eigenvalues of the composite body for $\mu=1$ and 50, and for $h_c=10$, 100, and ∞. The thermal resistance at the layer interface increases the eigenvalues, which in turn makes the system less stable.

5.3 Example 3: A Nonuniform Body. A body of unit length $(L=1)$ is governed by Eq. (34), with parameters

Table 2 The first ten eigenvalues s_k of the composite body in Example 1

k	$\mu=0$	$\mu=1$	$\mu=10$	$\mu=50$	$\mu=100$	$\mu=200$
1	−0.2385	−0.1510	2.7327	20.6032	44.6630	93.7723
2	−2.1562	−2.0261	−1.1819	7.2606	27.9873	74.5171
3	−5.6959	−5.5517	−4.6698	−2.1565	3.6423	42.2897
4	−10.7207	−10.5565	−9.0279	−5.2032	−3.3913	3.8288
5	−19.569	−19.4099	−18.0005	−12.1648	−5.9491	−3.6309
6	−28.5951	−28.4346	−27.1371	−23.1984	−18.2255	−6.0320
7	−40.3761	−40.2102	−38.6953	−31.8227	−26.5585	−20.8427
8	−56.267	−56.1034	−54.6258	−48.1408	−40.1633	−27.4989
9	−71.0105	−70.8464	−69.4428	−64.5230	−59.3149	−46.1921
10	−89.7344	−89.5681	−88.0607	−81.0916	−72.8471	−63.8146

Table 3 Roots μ_k of $\Delta(0,\mu)=0$ in Example 2

h_c	1	10	100	1000	∞
μ_1	0.98902	1.17088	1.19883	1.20177	1.20210
μ_2	21.7676	22.1292	22.1863	22.1924	22.1930
μ_3	81.0254	81.4017	81.4614	81.4677	81.4684
μ_4	179.730	180.109	180.169	180.176	180.176

Table 4 The first ten eigenvalues s_k of the composite body in Example 2

	$\mu=1$		$\mu=50$	
s_k	$h_c=10$	$h_c=\infty$	$h_c=100$	$h_c=\infty$
1	−0.03801	−0.0428	20.7108	20.6032
2	−1.72100	−2.0261	7.45899	7.2606
3	−5.21472	−5.5517	−2.08328	−2.1565
4	−10.5537	−10.5565	−5.17314	−5.2032
5	−16.8146	−19.4099	−12.1391	−12.1648
6	−26.6087	−28.4346	−22.8286	−23.1984
7	−40.2061	−40.2102	−31.5414	−31.8227
8	−49.2996	−56.1034	−47.7111	−48.1408
9	−66.7514	−70.8464	−63.7899	−64.5230
10	−89.5637	−89.5681	−80.7003	−81.0916

$$\lambda(x) = 2(1 + 0.25x^2), \quad \rho(x)c(x) = 5(1 + 0.1x), \quad 0 \le x \le 1$$

$$B(x) = \begin{cases} 10[(0.25)^2 - (x - 0.5)^2], & 0.25 \le x \le 0.75 \\ 0 & \text{otherwise} \end{cases}$$

Here the inner heat source has a parabolic distribution within the region $0.25 \le x \le 0.75$. Let the boundary conditions of the body be of convective type

$$\lambda(0)\frac{\partial T(0,t)}{\partial x} - h_0 T(0,t) = 0$$

$$\lambda(1)\frac{\partial T(1,t)}{\partial x} + h_1 T(1,t) = 0$$

where $h_0=4$ and $h_1=0.625$. In use of the semi-analytical method given in Sec. 4.2, equally spaced interfaces are considered: $x_j = jL/n$, where $j=0,1,\ldots,n$. In computation, the number of layers is chosen as $n=8$, 20, 40, 60, and 100. Table 5 lists the first three roots of $\Delta(0,\mu)=0$, which shows fast convergence as n increases. According to the computed results, the body is thermally stable if the heat gain $\mu < \mu_1 = 2.51419$. The eigenvalues of the body with $\mu=2$ and 100 are given in Table 6, which also indicates fast convergence as n increases. For $\mu=2$, which is in the stable region, all the eigenvalues are negative. For $\mu=100$, which falls between roots μ_2 and μ_3 of $\Delta(0,\mu)$, there are two positive eigenvalues (s_1 and s_2). This supports the prediction by Theorem 2.

It is observed from the numerical simulation that a larger n does not significantly increase the computation time needed to determine μ_k and s_k. Two special features of the proposed method attribute to this computational efficiency: (i) function $\Delta(s,\mu)$ is smooth and bounded in any finite region and (ii) the computation by Eqs. (19) and (33) only involves simple manipulation of 2×2 matrices, regardless of the number of layers.

6 Conclusions

The stability analysis performed in this study yields the following two main results.

(a) To maintain thermal stability of heat conduction in a composite or nonuniform solid, the gain μ of a linear heat source must be below a bound μ_{cr}, which is the minimum non-negative root of the transcendental equation (25). Different from single-layer bodies, the stability bound μ_{cr} of a multilayer body may not necessarily be related to any eigenvalue of the body without internal heat source.

(b) The number of unstable eigenvalues of a composite solid with excess internal heat production is determined by the roots of function $\Delta(0,\mu)$. The body has m unstable eigenvalues if the heat gain μ falls between the mth and $(m+1)$th roots of $\Delta(0,\mu)$.

Table 5 Roots of $\Delta(0,\mu)=0$ in Example 3 (n=number of layers)

n	μ_1	μ_2	μ_3
8	3.11273	67.4651	216.5746
20	2.67916	52.3663	185.4359
40	2.57182	48.1362	169.9793
60	2.53922	46.8487	165.0628
100	2.51419	45.8615	161.2592

Table 6 The first four eigenvalues of the nonuniform body in Example 3 (n=number of layers)

n	s_1	s_2	s_3	s_4
		$\mu=2(0<\mu<\mu_1)$		
8	−0.21772	−5.48221	−17.6024	−38.0190
20	−0.15499	−5.44622	−17.5574	−37.8772
40	−0.13602	−5.42997	−17.5539	−37.8454
60	−0.12993	−5.42407	−17.5535	−37.8374
100	−0.12514	−5.41919	−17.5533	−37.8320
		$\mu=100(\mu_2<\mu<\mu_3)$		
8	31.3460	4.43624	−8.28007	−22.7821
20	35.5886	9.59739	−7.95949	−20.1226
40	36.3522	11.3568	−7.51631	−19.9047
60	36.5489	11.8962	−7.31233	−19.8763
100	36.6873	12.3068	−7.12843	−19.8633

The numerical simulation leads to two observations. First, a thermally unstable composite body usually has one or two positive eigenvalues. To have many positive eigenvalues, the heat gain μ of an inner heat source has to enlarge by several orders of magnitude. Second, thermal resistance at layer interfaces increases system eigenvalues, which in turn lowers the stability bound μ_{cr}.

The new stability test does not need any information on system eigenvalues. Function $\Delta(0,\mu)$ is smooth, which makes root searching (for determination of stability bound) straightforward, as has been shown in the numerical examples. Because only simple operations of 2×2 matrices are involved in computation, the proposed method is highly efficient for thermal stability analysis of composite solids with any number of layers and various distributions of heat source. The results presented in this paper should provide important information and useful guidance for control of unstable heat flows in multilayer composite solids in many engineering problems.

References

[1] Carslaw, H. S., and Jaeger, J. C., 1959, *Conduction of Heat in Solids*, 2nd ed., Oxford University Press, Oxford.

[2] Ozisik, M. N., 1980, *Heat Conduction*, Wiley, New York, pp. 294–334.

[3] Huang, S. C., and Chang, Y. P., 1990, "Heat Conduction in Unsteady, Periodic and Steady States in Laminated Composites," ASME J. Heat Transfer, **102**, pp. 742–748.

[4] Jin, M., and Sadhal, S. S., 1996, "Thermal Boundary Conditions for Heterogeneous Solids," TMS Annual Meeting, Properties of Composites Session, Anaheim, CA, Feb. 4–8.

[5] Aviles-Ramos, C., Haji-Sheikh, A., and Beck, J. V., 1998, "Exact Solution of Heat Conduction in Composite Materials and Application to Inverse Problems," ASME J. Heat Transfer, **120**, pp. 592–599.

[6] Siegel, R., 1999, "Transient Thermal Analysis of Parallel Translucent Layers by Using Green's Functions," J. Thermophys. Heat Transfer, **13**, pp. 10–17.

[7] Kantor, B. Ya., Smetankina, N. V., and Shupikov, A. N., 2001, "Analysis of Non-Stationary Temperature Fields in Laminated Strips and Plates," Int. J. Solids Struct., **38**, pp. 8673–8684.

[8] Sutradhar, A., Paulino, G. H., and Gray, L. J., 2002, "Transient Heat Conduction in Homogeneous and Non-Homogeneous Materials by the Laplace Transform Galerkin Boundary Element Method," Eng. Anal. Boundary Elem., **26**, pp. 119–132.

[9] Fredman, T. P., 2003, "An Analytical Solution Method for Composite Layer

Diffusion Problems With an Application in Metallurgy," Heat Mass Transfer, **39**, pp. 285–295.
[10] Wang, Z.-H., and Tan, K. H., 2006, "Green's Function Solution for Transient Heat Conduction in Concrete-Filled CHS Subjected to Fire," Eng. Struct., **28**, pp. 1574–1585.
[11] Baliga, B. R., Rose, P. L., and Ahmed, A. M., 1992, "Thermal Modeling of Polymerizing Polymethylmethacrylate, Considering Temperature-Dependent Heat Generation," ASME J. Biomech. Eng., **114**, pp. 251–259.
[12] Stańczyk, M., and van Rietbergen, B., 2004, "Thermal Analysis of Bone Cement Polymerisation at the Cement-Bone Interface," J. Biomech., **37**, pp. 1803–1810.
[13] Malinowski, L., 1994, "Relaxation Equation of Heat Conduction and Generation—An Analytical Solution by Laplace Transforms Method," Heat Mass Transfer, **29**, pp. 265–269.
[14] Al-Odat, M., Al-Nimr, M. A., and Hamdan, M., 2002, "Superconductor Thermal Stability Under the Effect of the Dual-Phase-Lag Conduction Model," Int. J. Thermophys., **23**, pp. 855–868.
[15] Sparrow, E. M., and Cess, R. D., 1961, "Temperature-Dependent Heat Sources or Sinks in a Stagnation Point Flow," Journal Applied Scientific Research, **10**, pp. 185–197.
[16] Taneja, R., and Jain, N. C., 2004, "MHD Flow With Slip Effects and Temperature-Dependent Heat Source in a Viscous Incompressible Fluid Confined Between a Long Vertical Wavy Wall and a Parallel Flat Wall," Def. Sci. J., **54**, pp. 21–29.
[17] Negi, J. G., and Singh, R. N., 1968, "Heat Transfer in Multi-Layered Media With Temperature Dependent Sources," Pure Appl. Geophys., **69**, pp. 110–118.
[18] Lamarsh, J. R., 1975, *Introduction to Nuclear Engineering*, Addion-Wesley, Reading, MA, pp. 273–274.
[19] Vajta, M., 2001, "Stability Test for a Parabolic Partial Differential Equation," Ninth Mediterranean Conference, Dubrovnik, Croatia, Jun. 27–29.
[20] Vajta, M., 2003, "Stability of a Heat Process With Exponential Internal Source," 11th Mediterranean Conference, Rhodes, Greece, Jun. 18–20.
[21] Balogh, A., and Krstic, M., 2001, "Infinite-Step Backstepping for a Heat Equation-Like PDE With Arbitrarily Many Unstable Eigenvalues," *Proceedings of the American Control Conference*, Arlington, VA, Jun. 25–27.
[22] Qian, L., and Tian, L., 2007, "Boundary Control of an Unstable Heat Equation," International Journal of Nonlinear Science, **3**, pp. 68–73.
[23] Yang, B., and Fang, H., 1994, "Transfer Function Formulation of Non-Uniformly Distributed Parameter Systems," ASME J. Vibr. Acoust., **116**, pp. 426–432.
[24] Yang, B., 2005, *Stress, Strain, and Structural Dynamics: An Interactive Handbook of Formulas, Solutions, and MATLAB Toolboxes*, Elsevier Science, Boston, p. 913.
[25] Tio, K.-K., and Sadhal, S. S., 1992, "Thermal Constriction Resistance: Effect of Boundary Conditions and Contact Geometries," Int. J. Heat Mass Transfer, **35**, pp. 1533–1544.
[26] Yin, H. M., Paulino, G. H., Buttlar, W. G., and Sun, L. Z., 2008, "Effective Thermal Conductivity of Functionally Graded Particulate Nanocomposites With Interfacial Thermal Resistance," ASME J. Appl. Mech., **75**, p. 051113.
[27] Matt, C. F., and Cruz, M. E., 2008, "Effective Thermal Conductivity of Composite Materials With 3-D Microstructures and Interfacial Thermal Resistance," Numer. Heat Transfer, Part A, **53**, pp. 577–604.

Boubaker Polynomials Weak Solutions to a Robin Boundary Conditioned Dynamic-State Heat Transfer Problem

K. ben Mahmoud Boubaker
ESSTT/Laboratoire de Physique de la Matière Condensée,
UPDS,
Faculté des Sciences de Tunis,
2092 Tunis, Tunisia

In this paper we are concerned with the solution of a Robin boundary conditioned problem associated with the local heat transfer equation. The results are obtained using both symmetrical system features and expansions of a Boubaker polynomial subsequence. The yielded profile is compared with some recently proposed models.
[DOI: 10.1115/1.3154623]

1 Introduction

With advances in techniques to deal with problems of heat transfer in physics, these problems have generated increasing interest over a wide range of areas, including microwave heating, kinetics in diffusion processes, biophysics, and welding investigations [1–4].

In recent studies, Masood and Zaman [1] tried to investigate inverse problem method in order to solve general heat transfer equations in some particular cases. Vynnycky et al. [2], Haji-Sheikh et al. [3], and Pacheco-Vega et al. [4] yielded different numerical solutions to heat transfer problems taking into account several boundary condition formulations.

In this paper we consider a targeted surface, which receives a single-pulse from a Gaussian heat source. The resolution of the heat transfer problem is based on introducing Robin boundary conditions apart from the main equation. In fact, an appropriate expression is attributed to the temperature expression in the manner that the major part of the boundary conditions is verified in advance to main equation resolution. This feature is enabled by the Boubaker polynomial properties [5–19].

2 Theoretical Investigations

2.1 Problem Geometrical Features. The problem is studied in a cylindrical coordinate system where the targeted surface represents the Z-plane ($Z=0$).

The Gaussian source propagation axis is also the Z-axis (Fig. 1).

The simplified main system of the heat equation under Robin boundary conditions is

$$\begin{gathered}\frac{\partial T(r,t)}{\partial t} = D\frac{\partial^2 T(r,t)}{\partial r^2}, \quad t>0, \;\; 0<r<R:\{\text{Domain}(\Omega)\} \\ T(0,t) = T_0 \\ T(R,t) + L\times\frac{\partial T(R,t)}{\partial t} = 0:\{\text{Domain}(d\Omega)\} \\ T(r,0) = T_0\times f(r)\end{gathered} \tag{1}$$

where L is a constant, D is the thermal diffusivity, and $f(r)$ is a real function that verifies the spatial conditions

$$\begin{gathered}\frac{\partial f(r)}{\partial r}\le 0 \quad \text{for} \quad 0<r<R \\ f(0)=1 \\ f(R)=0 \\ \left.\frac{\partial f(r)}{\partial r}\right|_{r=0} = 0\end{gathered} \tag{2}$$

System (2) corresponds to many common functions (Gaussian, cosine, polynomial, etc.).

Solutions for particular expressions of $f(r)$ have been proposed [20–24].

2.2 Analytic Calculations. For resolution purposes, $f(r)$ is first expressed as an infinite expansion of Boubaker polynomials [19] whose interesting properties are detailed in Appendix A.

$$f(r) = \lim_{N\to+\infty}\left[\frac{1}{2N}\sum_{n=1}^{N}\zeta_n\cdot\hat{B}_{4n}\left(r\frac{\alpha_n}{R}\right)\right] \tag{3}$$

where α_n are the minimal positive roots of the $4n$-order Boubaker polynomials $\hat{B}_{4n}$, R is the maximum radial range (where the temperature is supposed to be the room one), and ζ_n are the coefficients to be determined using the expression of $f(r)$.

In fact, the Boubaker $4n$-order polynomials $\hat{B}_{4n}$ have the particular properties

$$\begin{gathered}\hat{B}_{4n}(r)|_{r=0} = -2, \quad \forall\, n>0 \\ \left.\frac{\partial\hat{B}_{4n}(r)}{\partial r}\right|_{r=0} = 0, \quad \forall\, n>0 \\ \left.\frac{\partial^2\hat{B}_{4n}(r)}{\partial r^2}\right|_{r=0} = 4n(n-1), \quad \forall\, n>0\end{gathered} \tag{4}$$

These properties induce the system

$$f(0) = \lim_{N\to+\infty}\left[\frac{1}{2N}\sum_{n=1}^{N}\zeta_n\hat{B}_{4n}\left(r\frac{\alpha_n}{r_m}\right)\right]\Bigg|_{r=0} = -\frac{1}{N}\sum_{n=1}^{N}\xi_n$$

$$f(R) = \lim_{N\to+\infty}\left[\frac{1}{2N}\sum_{n=1}^{N}\zeta_n\hat{B}_{4n}\left(r\frac{\alpha_n}{r_m}\right)\right]\Bigg|_{r=r_m} = 0$$

Contributed by the Heat Transfer Division of ASME for publication in the JOURNAL OF HEAT TRANSFER. Manuscript received July 10, 2008; final manuscript received May 6, 2009; published online August 25, 2009. Review conducted by He-Ping Tan.

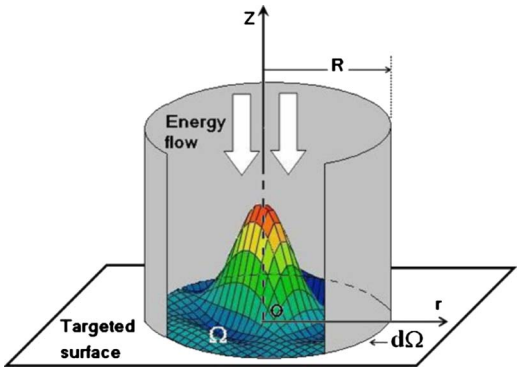

Fig. 1 Geometrical features. The simplified main system of the heat equation under Robin boundary conditions.

$$\left.\frac{\partial f(r)}{\partial r}\right|_{r=0} = \lim_{N\to+\infty}\left[\frac{1}{2N}\sum_{n=1}^{N}\zeta_n\frac{\partial\left(\hat{B}_{4n}\left(r\frac{\alpha_n}{r_m}\right)\right)}{\partial r}\right]\Bigg|_{r=0} = 0 \quad (5)$$

with the constraint

$$\sum_{n=1}^{N}\xi_n = -N \quad (6)$$

By the same way, the temperature expression is expressed as a polynomial expansion

$$g(r) = T_0 \times \lim_{N\to+\infty}\left[\frac{1}{2N}\sum_{n=1}^{N}\xi_n' \cdot B_{4n}\left(r\frac{\alpha_n}{R}\right)\right] \quad (7)$$

by writing $T(r,t)=g(r)\times h(t)$, the main heat equation gives

$$\frac{h'(t)}{h(t)} = D\frac{g''(r)}{g(r)} \quad (8)$$

Since the left term is independent of x and the right one is independent of t, it follows that the two expressions must be a constant. In Appendix B, we demonstrate that this constant is negative (denoted $-k_n^2$, $n=1,2,\ldots,N$).

$$\begin{gathered} h'(t) = -k_n^2 h(t), \quad h(t)|_{r=R} + L \times h'(t)|_{r=R} = 0 \\ g''(r) = -\frac{k_n^2}{D} \times g(r) \end{gathered} \quad (9)$$

The first equation is compatible with the second (expressing Robin condition) and has a simple solution

$$h(t) = Ae^{-k_n^2 t}$$

where A is a constant.

The second equation, along with the initial condition, is written as

$$\begin{aligned} &\lim_{N\to+\infty}\left[\frac{1}{2N}\sum_{n=1}^{N}\xi_n' \cdot \left(\frac{\alpha_n}{R}\right)^2 \hat{B}_{4n}''\left(r\frac{\alpha_n}{R}\right)\right] \\ &= -\frac{1}{D} \times \lim_{N\to+\infty}\left[\frac{1}{2N}\sum_{n=1}^{N}k_n^2\xi_n' \cdot \hat{B}_{4n}\left(r\frac{\alpha_n}{R}\right)\right] \\ &\lim_{N\to+\infty}\left[\frac{1}{2N}\sum_{n=1}^{N}\xi_n' \cdot \hat{B}_{4n}\left(r\frac{\alpha_n}{R}\right)\right] \\ &= A \times e^{-k^2 t} \lim_{N\to+\infty}\left[\frac{1}{2N}\sum_{n=1}^{N}\xi_n \cdot \hat{B}_{4n}\left(r\frac{\alpha_n}{R}\right)\right]\Bigg|_{t=0} \end{aligned} \quad (10)$$

by taking into account the initial conditions we have the system

$$\begin{aligned} &\lim_{N\to+\infty}\left[\frac{1}{2N}\sum_{n=1}^{N}\xi_n' \cdot \left(\frac{\alpha_n}{R}\right)^2 4n(n-1)\right] \\ &= -\frac{1}{D} \times \lim_{N\to+\infty}\left[\frac{1}{2N}\sum_{n=1}^{N}k_n^2\xi_n' \times (-2)\right] \\ &\lim_{N\to+\infty}\left[\frac{1}{2N}\sum_{n=1}^{N}\xi_n' \times (-2)\right] \\ &= A \times e^{-k^2 t} \lim_{N\to+\infty}\left[\frac{1}{2N}\sum_{n=1}^{N}\xi_n \times (-2)\right]\Bigg|_{t=0} \end{aligned} \quad (11)$$

System (11) has as a weak solution

$$\begin{gathered} k_n = \frac{\alpha_n}{R}\sqrt{[2n(n-1)] \times D} \\ \sum_{n=1}^{N}\xi_n' = A \times \sum_{n=1}^{N}\xi_n \end{gathered} \quad (12)$$

Oppositely to the t-dependent solution, the spatial solution is not unique. Among possible solutions we chose the vector $[\zeta]$ as follows:

$$[\zeta] = \begin{pmatrix} \zeta_1 \\ \zeta_2 \\ \cdots \\ \zeta_N \end{pmatrix} \quad (13)$$

which minimizes the functional H_{MS} as follows:

$$H_{MS} = \left[\sum_{n=1}^{N}(\xi_n' - A\xi_n)^2\right] \quad (14)$$

The final solution is hence

$$T(r,t) = T_0\sum_{n=1}^{N}\xi_n' \times B_{4n}\left(r\frac{\alpha_n}{R}\right) \times e^{-(\alpha_n/R\sqrt{[2n(n-1)]\times D})^2 t} \quad (15)$$

3 Solutions and Discussion

As mentioned in Eqs. (3), (13), and (14), the solution depends on the chosen initial vector $[\zeta]$. The optimal vector $[\zeta]_{\text{opt}}$ is associated with the Gaussian excitation, and its terms are being calculated in another study. For the actual model we tried our model on two elementary sets of initial conditions, expressed by vectors

$$[\zeta]_1 = \begin{pmatrix} 0 \\ \cdots \\ -N \times \delta(n-N) \\ 0 \end{pmatrix} \quad (16)$$

$$[\zeta]_2 = \begin{pmatrix} -N/2 \\ -N/2^2 \\ \cdots \\ -N/2^N \end{pmatrix} \quad (17)$$

Table 1 Numerical values (case of the initial vector $[\zeta]_2$)

$4n$	α_{4n}	$(k_n)^2$	ζ'_n
4	1.1894	0 (invalid)	0.02188
8	0.5078	0.01031	0.01094
12	0.3114	0.01164	0.00547
16	0.2236	0.012	0.00273
20	0.1742	0.01214	0.00137
24	0.1428	0.01224	0.00068
28	0.1208	0.01226	0.00034

The vectors $[\zeta]_1$ and $[\zeta]_2$ verify both the condition (6).

In Table 1, the relevant numerical solutions corresponding to the case of the initial vector $[\zeta]_2$ are given. It was noted that the error introduced by truncating was less than 6.5%. It was also noted that the relative contribution of terms with indices beyond ($4n=24$) was less than 1/100 (see last terms in Table 1). Truncating at $4n=20$ or $4n=28$ is hence justified.

The temperature radial dynamic profile is yielded for the initial vector $[\zeta]_1$, associated with the respective values $N=2$ (Fig. 2), $N=3$ (Fig. 3), and $N=4$ (Fig. 4).

A more appropriate time-space representation of the solution corresponding to the initial vector $[\zeta]_2$ is yielded in Fig. 5.

4 Conclusion

The obtained t-dependent and spatial temperature profiles are agreeing with many recently yielded results [21–25]. Comparison of the extinguishing time (≈ 1.075 s) with several models [24–26] was also satisfactory. Actually the model is prepared to be applied with a quasi-Gaussian excitation term. This step is expected to solve the intriguing problem of obtaining non-Gaussian responses to Gaussian excitations.

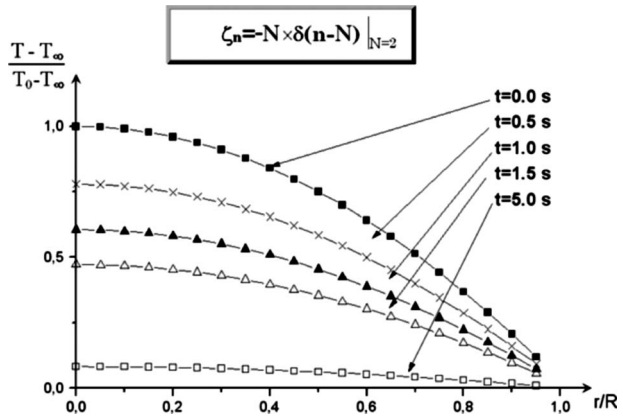

Fig. 2 Evolution of temperature profile versus time ($N=2$)

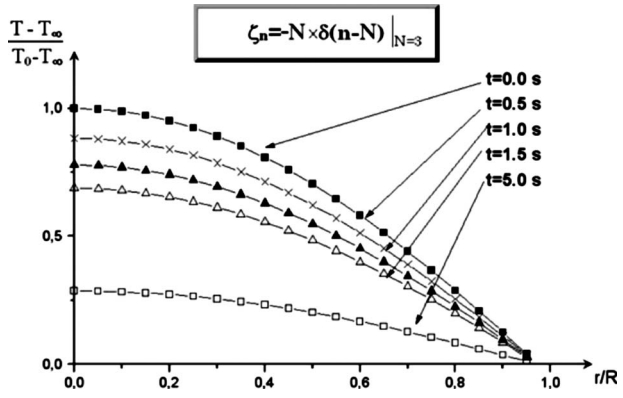

Fig. 3 Evolution of temperature profile versus time ($N=3$)

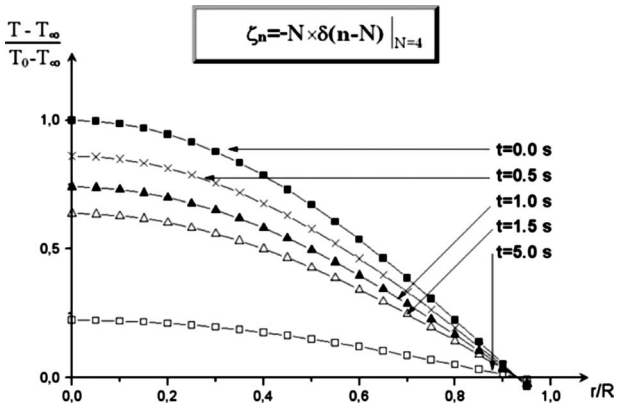

Fig. 4 Evolution of temperature profile versus time ($N=4$)

Appendix A

In this appendix, we present the $4q$-Boubaker polynomial subsequence.

The Boubaker polynomials' $B_n(X)$ explicit monomial form evoked, while prospected, some singularities for $m=4,8,12$, etc. In fact, for the general case, $m=4q$, the $2q$ rank monomial term is removed from the explicit form so that the whole expression contains only $2q$ effective terms. Correspondent $4q$-order Boubaker polynomials have as a general form

$$\hat{B}_{4q}(X) = 4\sum_{p=0}^{2q}\left[\frac{(q-p)}{(4q-p)}C_{4q-p}^{p}\right]\cdot(-1)^p\cdot X^{2(2q-p)}$$

The few $4q$-order Boubaker polynomials have some interesting properties

$$\hat{B}_{4(q+1)} = (X^4 - 4X^2 + 2)\times\hat{B}_{4(q)} - \hat{B}_{4(q-1)}, \quad \forall\, q > 1$$

$$\hat{B}_{4n}(0) = -2, \quad \hat{B}'_{4n}(0) = 0, \quad \hat{B}''_{4n}(0) = 4n(n-1)$$

and

$$\hat{B}^2_{4q}(X) - \hat{B}_{4(q-1)}(X)\times\hat{B}_{4(q+1)}(X) = X^2(X^2-1)^2(3X^2+4)$$

$$\forall\, q > 1$$

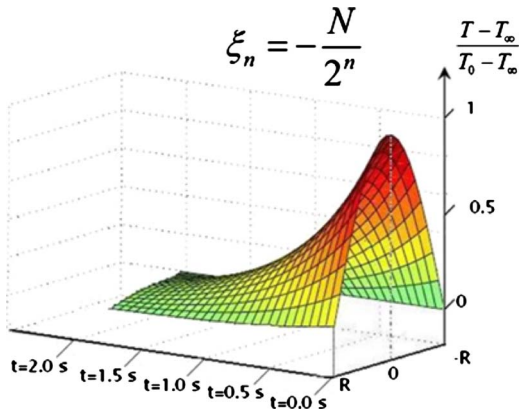

Fig. 5 Time-space temperature evolution (case of the initial vector $[\zeta]_2$)

Appendix B

In this appendix, we demonstrate that the problem

$$\frac{h'(t)}{h(t)} = D\frac{g''(r)}{g(r)} = \theta$$

has convergent solutions only for negative values of θ.

Let us suppose $\theta=0$, the t-dependent solution will be

$$h(t) = a$$

with $a=$const.

This solution is convergent but physically invalid since it imposes a time-constant temperature in all points. The problem cannot have non-null solutions when $\theta=0$.

Let us suppose $\theta=k^2>0$, the main equation will give

$$g''(r) - \frac{k^2}{D} \times g(r) = 0$$

which has solutions

$$g(r) = M\cosh\left(\frac{k\sqrt{D}}{D}r\right) + N\sinh\left(\frac{k\sqrt{D}}{D}r\right)$$

with M and N as constants. Derivative conditions at boundaries $(r=0)$ and $(r=R)$ give the trivial but unique result $M=N=0$.

The problem cannot have any convergent or physically valid solution when $\theta\geq 0$.

References

[1] Masood, K., and Zaman, F. D., 2004, "Investigation of the Initial Inverse Problem in the Heat Equation," ASME J. Heat Transfer, **126**, pp. 294–296.

[2] Vynnycky, M., Ferrari, J., and Lior, N., 2003, "Some Analytical and Numerical Solutions to Inverse Problems Applied to Optimizing Phase-Transformation Tracking in Gas Quenching," ASME J. Heat Transfer, **125**, pp. 1–10.

[3] Haji-Sheikh, A., Minkowycz, W. J., and Sparrow, E. M., 2002, "Certain Anomalies in the Analysis of Hyperbolic Heat Conduction," ASME J. Heat Transfer, **124**, pp. 307–319.

[4] Pacheco-Vega, A., Pacheco, J. R., and Rodić, T., 2007, "A General Scheme for the Boundary Conditions in Convective and Diffusive Heat Transfer With Immersed Boundary Methods," ASME J. Heat Transfer, **129**, pp. 1506–1516.

[5] Boubaker, K., Chaouachi, A., Amlouk, M., and Bouzouita, H., 2007, "Enhancement of Pyrolysis Spray Disposal Performance Using Thermal Time-Response to Precursor Uniform Deposition," Eur. Phys. J.: Appl. Phys., **37**, pp. 105–109.

[6] Ghanouchi, J., Labiadh, H., and Boubaker, K., 2008, "An Attempt to Solve the Heat Transfer Equation in a Model of Pyrolysis Spray Using 4*q*-Order Boubaker Polynomials," International Journal of Heat and Technology, **26**(1), pp. 49–53.

[7] Awojoyogbe, O. B., and Boubaker, K., 2009, "A Solution to Bloch NMR Flow Equations for the Analysis of Homodynamic Functions of Blood Flow System Using *m*-Boubaker Polynomials," Curr. Appl. Phys., **9**(1), pp. 278–283.

[8] Boubaker, K., 2007, "On Modified Boubaker Polynomials: Some Differential and Analytical Properties of the New Polynomials Issued From an Attempt for Solving Bi-Varied Heat Equation," Trends in Applied Science Research, **2**(6), pp. 540–544.

[9] The Boubaker–Tuki polynomials (or modified Boubaker polynomials), PlanetMath Encyclopedia, The Mathematics Worldwide Encyclopedia, http://planetmath.org/encyclopedia/BoubakerTurkiPolynomials.html.

[10] Labiadh, H., and Boubaker, K., 2007, "A Sturm-Liouville Shaped Characteristic Differential Equation as a Guide to Establish a Quasi-Polynomial Expression to the Boubaker Polynomials," Journal of Differential Equations and Control Processes, **2**, pp. 117–133.

[11] Boubaker, K., 2007, "Les Polynômes de Boubaker, une classe polynomiale qui émane d'un essai de résolution de l'équation de la chaleur," Deuxièmes Journées Méditerranéennes de Math. App., Monastir, Tunisie, March.

[12] Slama, S., Bessrour, J., Boubaker, K., and Bouhafs, M., 2008, "Investigation of A3 Point Maximal Front Spatial Evolution During Resistance Spot Welding Using 4*q*-Boubaker Polynomial Sequence," *Proceedings of COTUME 2008*, pp. 79–80.

[13] Boubaker, K., Labiadh, H., and Bannour, A., 2008, "Establishment of a Homogenous Characteristic Differential Equation for the Applied Physics Canonical Formulation-Related Boubaker Polynomials," Journal of Analysis and Computation, **4**(2), pp. 14–18.

[14] Ghrib, T., Boubaker, K., and Bouhafs, M., 2008, "Investigation of Thermal Diffusivity-Microhardness Correlation Extended to Surface-Nitrured Steel Using Boubaker Polynomials Expansion," Mod. Phys. Lett. B, **22**, pp. 2893–2907.

[15] Boubaker, K., 2008, "A Boubaker-Turki Polynomials Solution to Pancreatic Islet Blood Flow Biophysical Equations in the Case of a Preset Monitored Spatial Rotating Field," Research and Reviews in BioSciences, **2**, pp. 78–81.

[16] Dada, M., Awojoyogbe, O. B., Hasler, M., Boubaker Ben Mahmoud, K., and Bannour, A., 2008, "Establishment of a Chebyshev-Dependent Inhomogeneous Second Order Differential Equation for the Applied Physics-Related Boubaker-Turki Polynomials," International Journal of Applications and Applied Mathematics, **3**, pp. 329–336.

[17] Boubaker, K., 2008, "A New Polynomial Sequence as a Guide to Numerical Solutions for Applied-Physics-Related Partial Differential Equations Under Dirichlet-Newman-Type Exogenous Boundary Conditions," Numer. Methods Partial Differ. Equ., **21**(2), pp. 171–177.

[18] Labiadh, H., and Boubaker, K., 2008, "A New Analytic Expression as a Guide to Establish a Characteristic Differential Equation to the Heat Equation-Related Boubaker Polynomials," International Journal of Applied Mathematics, **21**(2), pp. 171–177.

[19] Karem, B., Tinggang, Z., and Zhuosheng, W., 2008, "Limit and Uniqueness of the Boubaker-Zhao Polynomials Single Imaginary Root Sequence," International Journal of Mathematics and Computation, **1**(9), pp. 13–16.

[20] Richardson, G., and Rubinstein, J., 2000, "The Mixed Boundary Condition for the Ginzburg-Landau Model in Thin Films," Appl. Math. Lett., **13**, pp. 97–99.

[21] Polking, J. A., and Bogges, D. A., 2002, *Differential Equations*, Prentice-Hall, Englewood Cliffs, NJ.

[22] Calvo, E., and Garcia, L., 2001, "Shape Design Sensitivity Analysis in Elasticity Using the Boundary Element Method," Eng. Anal. Boundary Elem., **25**, pp. 887–896.

[23] Kraus, A., Aziz, A., and Welty, J., 2001, *Extended Surface Heat Transfer*, Wiley, New York.

[24] Takaoka, H., and Tsutsumi, Y., 2004, "Well-Posedness of the Cauchy Problem for the Modified KdV Equation With Periodic Boundary Condition," Int. Math. Res. Notices, **2004**, pp. 3009–3040.

[25] Beale, S. B., 2007, "Use of Streamwise Periodic Boundary Conditions for Problems in Heat and Mass Transfer," ASME J. Heat Transfer, **129**, pp. 601–605.

[26] Grigoriu, M., 2000, "A Monte Carlo Solution of Heat Conduction and Poisson Equations," ASME J. Heat Transfer, **122**, pp. 40–45.

Cooling Performance of Arrays of Vibrating Cantilevers

Mark Kimber

Suresh V. Garimella[1]
e-mail: sureshg@purdue.edu

NSF Cooling Technologies Research Center,
School of Mechanical Engineering,
Purdue University,
585 Purdue Mall,
West Lafayette, IN 47907-2088

Piezoelectric fans are vibrating cantilevers actuated by a piezoelectric material and can provide heat transfer enhancement while consuming little power. Past research has focused on feasibility and performance characterization of a single fan, while arrays of such fans, which have important practical applications, have not been widely studied. This paper investigates the heat transfer achieved using arrays of cantilevers vibrating in their first resonant mode. This is accomplished by determining the local convection coefficients due to the two piezoelectric fans mounted near a constant heat flux surface using infrared thermal imaging. The heat transfer performance is quantified over a wide range of operating conditions, including vibration amplitude (7.5–10 mm), distance from heat source (0.01–2 times the fan amplitude), and pitch between fans (0.5–4 times the amplitude). The convection patterns observed are strongly dependent on the fan pitch, with the behavior resembling a single fan for small fan pitch and two isolated fans at a large pitch. The area-averaged thermal performance of the fan array is superior to that of a single fan, and correlations are developed to describe this enhancement in terms of the governing parameters. The best thermal performance is obtained when the fan pitch is 1.5 times its vibration amplitude. [DOI: 10.1115/1.3153579]

Keywords: local heat transfer, piezoelectric fan, fan array, electronics cooling, vibrating cantilever, heat transfer enhancement

1 Introduction

A piezoelectric fan is a cantilever beam whose vibration is actuated by means of a piezoelectric element. This element is typically bonded near the clamped end of the beam and induces a bending moment at the interface between the cantilever beam and the piezo element when a voltage is applied. For an alternating voltage, the beam is set into an oscillatory motion, which in turn creates motion in the surrounding fluid. This fluid motion has been shown to provide heat transfer enhancements with low power consumption in an otherwise quiescent region. These devices can also be configured to meet the geometric constraints of applications where the limited available volume might preclude the use of traditional cooling techniques. The fan design can be tailored to operate at frequencies, which are inaudible to the human ear. Due to these attractive features, piezoelectric fans have been investigated in the literature for practical cooling applications.

Vibrating cantilever-type structures have been commonplace in engineering for decades. However, detailed studies of the motion induced in the surrounding fluid, and more importantly its effect on heat transfer, have only been recently undertaken. Flow field measurements around a cantilever vibrating in quiescent air at relatively small vibration amplitudes (less than 3 mm peak-to-peak tip vibration) were obtained by Kim et al. [1]. They observed a pair of counter-rotating vortices from each oscillation cycle. These vortices were shed from the fan tip as it passed the position of zero displacement. The maximum velocity occurred in the region between these two vortices and just beyond the cantilever tip, and was measured to be approximately four times the maximum tip velocity. Kimber et al. [2] experimentally measured the local heat transfer characteristics of piezoelectric fans and developed heat transfer correlations based on applicable dimensionless numbers.

Numerical modeling of the fluid flow and heat transfer induced by a piezoelectric fan was also conducted [3]. The flow field generated by these fans was found to be extremely complex and highly dependent on the distance from the fan tip to the heat source, as well as other boundary conditions. A single piezoelectric fan vibrating near a small heat source was also experimentally investigated to determine the conditions under which the average heat transfer could be optimized. The factors considered were fan length, vibration amplitude, frequency offset, and distance from the heat source. Optimal conditions occurred when the fan operated at resonance and was oriented normal to the heat source. Under these conditions, an enhancement of over 375% in the heat transfer coefficient was obtained when compared with natural convection alone.

A number of studies have demonstrated the potential of these fans as cooling solutions and explored implementation and feasibility issues [4–7]. Most of these studies have considered single fans, and a more complete review of the literature is available in Ref. [2]. The present work considers the practically important configuration in which multiple fans are used in arrays, and where the complexity increases substantially in describing the structural, fluidic, and heat transfer behavior.

The two-dimensional flow field generated from two flexible cantilevers was analyzed experimentally by Ihara and Watanabe [8]. They investigated the behavior for in-phase and out-of-phase vibration at three different pitches. The cantilevers were sandwiched between two large plates, thereby approximating a two-dimensional flow field. The results were compared with the flow field generated by a single cantilever in the same experimental setup, and the volumetric flow rate for in-phase vibration of two cantilevers was found to be approximately double that of a single cantilever. Pumping capabilities of an array of vibrating beams were analyzed by Linderman et al. [9]. Flow rates produced by micromachined cantilevers in a channel were measured for both a single cantilever and a linear array of cantilevers. The flow rate for the single cantilever varied linearly with frequency, length, and vibration amplitude. Three fans placed in series resulted in a nearly tripled flow rate. The fan pitch was not considered as a variable, and the interaction between neighboring fans was not captured. Mass transfer measurements were obtained by Schmidt

[1]Corresponding author.

Contributed by the Heat Transfer Division of ASME for publication in the JOURNAL OF HEAT TRANSFER. Manuscript received February 15, 2008; final manuscript received April 21, 2009; published online August 19, 2009. Review conducted by Roger Schmidt.

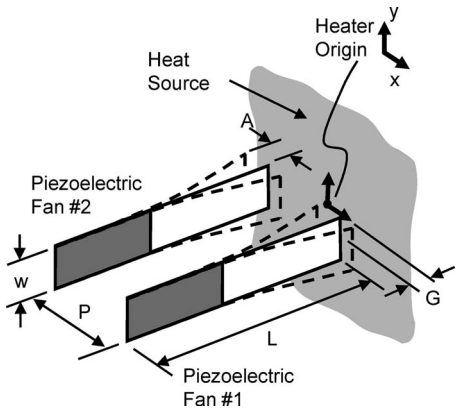

Fig. 1 Experimental parameters: vibration amplitude (*A*), gap from heat source (*G*), and fan pitch (*P*). Also shown is the piezoelectric fan length (*L*) and width (*w*).

[10] on a vertical surface mounted near two piezoelectric fans. The fan blades vibrated out of phase and the fan pitch was kept constant. Power-law correlations were found to reasonably describe both maximum and surface-averaged Sherwood numbers for three different distances from the vertical surface. In each case the Sherwood numbers formed contours that were symmetric about the midpoint of fan separation.

Changes in fan vibration parameters influence the flow field and heat transfer performance. A number of studies [11–13] have shown that the vibration characteristics of a vibrating cantilever are altered by the presence of a second oscillating beam. Hosaka and Itao [11] and Basak and Raman [12] showed that fluidic loading on an array of vibrating beams is greatly altered depending on the vibration amplitude as well as the pitch and phase difference between neighboring cantilevers. This was confirmed experimentally by Kimber et al. [13] who observed fluidic coupling between multiple piezoelectric fans. They measured resonance frequency and quality factors for fans vibrating in air and observed a decrease in viscous drag when the fans vibrated in phase, which allowed the fans to achieve larger vibration amplitudes for a given input signal relative to a single fan.

In the present work, local and area-averaged heat transfer characteristics of arrays of piezoelectric fans are investigated. This work follows previous work by the authors [2] in which the thermal performance of a single fan was studied in detail. Of particular interest in this work is the increase in performance obtained with the addition of a second fan, as well as the coupling conditions under which the overall heat transfer rate can be maximized.

2 Experimental Setup and Procedures

The experiments in this work are performed using the setup and procedures described in Ref. [2] and only salient details are provided here.

2.1 Experimental Setup. A flat constant heat flux surface is mounted in a vertical position on an optical table and coated on both sides with a thin layer of Krylon 1602 black paint having a known emissivity of 0.95 [14]. Positioned normal to this surface are piezoelectric fans on two linear stages. This fan orientation with respect to the heater is identical to that used in Ref. [2] and is illustrated in Fig. 1. One linear stage controls the distance from the fan tip to the heated surface, while the other controls the separation between the fans or the pitch. The side of the heated surface opposite the fans is also exposed to ambient conditions and provides access for the infrared camera (ThermaCAM Merlin) with which full-field temperature measurements are captured, thereby enabling convection coefficients to be computed on a point-by-point basis. Two laser displacement sensors (Keyence LK-G157) are positioned near the fan tip to capture the vibration amplitude for each fan independently. Only in-phase vibration is considered based on past results [8,13], which suggested that in-phase vibration creates constructive interference within the fluid domain while the opposite is true for out-of-phase vibration. As the resonance frequencies of any two fans cannot be matched exactly, a phase difference exists between their motions even with identical input signals. Therefore, a two-channel phase-controlled function generator (Tektronix AFG3022) is employed to ensure in-phase vibration of the fans in all experiments. A plexiglass enclosure is built around the entire setup to isolate it from extraneous air currents within the laboratory.

The constant-flux heat source design is described in Ref. [2] and consists of an electrically heated thin stainless steel (type 302) foil stretched over two 25.4 mm diameter copper rods acting as busbar terminals. The foil is 0.051 mm thick and 101.6 mm wide. The required potential drop across the copper rods is achieved with a high-current power supply. Spring-loaded bolts are used to accommodate thermal expansion and maintain the heated foil in tension. A 25.4-mm-thick plexiglass frame holds the heater assembly together and also provides electrical isolation between the two ends of the heater. The copper rods are separated by a distance of 203.2 mm, thereby providing a heated surface area of 101.6×203.2 mm^2.

As the thermal conductivity of the copper busbars is much larger than that of the stainless steel, the busbars can act as a local heat sink. This localized cooling effect is experimentally found to be confined to a region close to the busbars; therefore, all the heat transfer results are obtained for the portion of the heated foil remote from the busbars. A span of the foil 25.4 mm in length adjacent to each copper rod is excluded from the analysis, leaving a heated surface area of 101.6×152.4 mm^2 that is considered in the measurements.

2.2 Local Heat Transfer Calculations. The electrically generated heat flux (q''_{gen}) is uniform across the entire heated surface and is computed according to

$$q''_{\text{gen}} = \frac{V_s \cdot I_s}{A_{\text{heat}}} \tag{1}$$

A local flux balance is employed to determine the convection coefficient due to the piezoelectric fans. Radiation losses (q''_{rad}) occur on both sides of the heater and are quantified from the measured temperature field and known surface emissivity. As losses due to natural convection (q''_{nc}) must also be quantified, a number of experiments are conducted in the absence of fans. Natural convection temperature maps are analyzed at multiple levels of power input to the heat source, thereby yielding the experimental dependency of the natural convection coefficients on position and surface temperature. This information is used during the forced convection experiments to account for natural convection losses present on the side opposite the fans. After subtracting these losses (natural convection and radiation), the remaining component of the heat generated is dissipated as q''_{mixed} by mixed convection with contributions from both forced convection (due to the piezoelectric fans) and natural convection. The relationship in such a regime can be approximated as [15]

$$\text{Nu}_{\text{mixed}}{}^3 = \text{Nu}_{\text{pz}}{}^3 + \text{Nu}_{\text{nc}}{}^3 \tag{2}$$

Taking each of these Nusselt numbers to be based on the same length scale, the convection coefficient attributed to the piezoelectric fan (h_{pz}) can be extracted according to

$$h_{\text{pz}} = (h_{\text{mix}}{}^3 - h_{\text{nc}}{}^3)^{1/3} \tag{3}$$

where h_{mixed} is directly found from

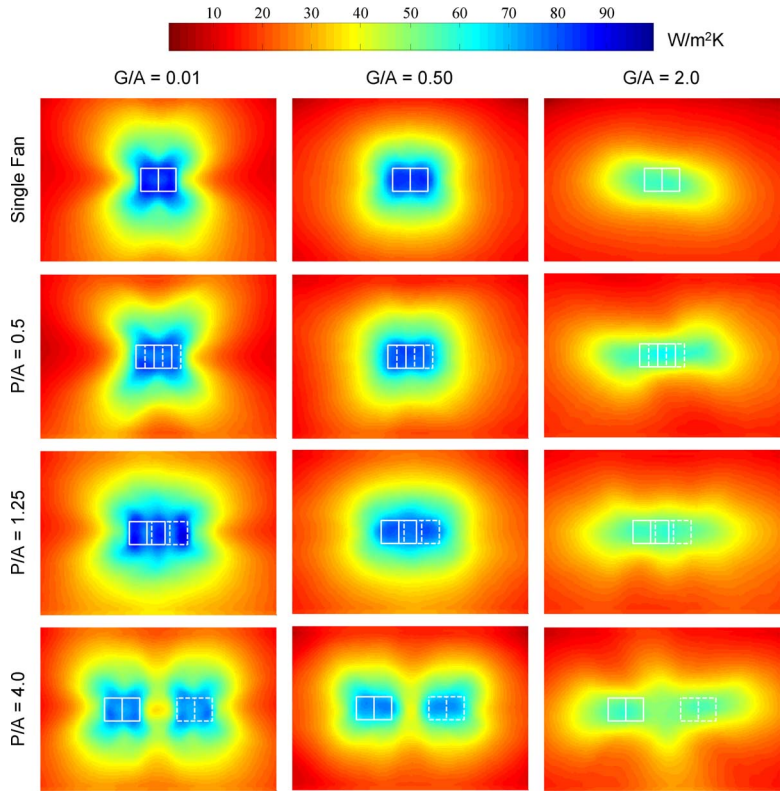

Fig. 2 Experimental convection coefficient contours (h_{pz}) for $A=10$ mm and $G/A=0.01$ (first column), $G/A=0.50$ (second column), and $G/A=2.0$ (last column). The first row illustrates single-fan performance at the same gaps, while the remaining rows are the results from array experiments with each row representing a different pitch corresponding to $P/A=0.5,1.25,4.0$. The heater size shown is 101.6×152.5 mm^2. Vibration envelopes are superimposed to show location of fans with solid and dashed lines depicting the first and second fans, respectively.

$$h_{\text{mixed}} = \frac{q''_{\text{gen}} - 2 \cdot q''_{\text{rad}} - q''_{\text{nc}}}{T_s - T_\infty} \tag{4}$$

The convection coefficients reported in the results below exclusively represent the forced convective contribution due to the piezoelectric fans (h_{pz}).

2.3 Experimental Parameters. The commercially available fans used in the experiments are made from a flexible Mylar blade. As shown in Fig. 1, the overall fan length (L) is 64.0 mm, the width (w) is 12.7 mm, and the fundamental resonance frequency of the fan is 60 Hz, which is used as the excitation frequency for all experiments. Also illustrated in the figure are the experimental parameters: vibration amplitude (A), which is half the peak-to-peak amplitude, pitch (P), and gap (G) from the fan tip to the heated surface. To explore the effect of each of these parameters on the heat transfer performance, multiple values of each are considered. Three amplitudes of vibration are investigated ($A=7.5$, 8.5, and 10 mm) and are achieved by adjusting the magnitude of the input voltage signal until the desired amplitude is reached. It should be noted that this adjustment is also dependent on the proximity of the second fan, as well as the distance of the fans from the heated surface. These separation distances govern the viscous drag, an increase or decrease in which causes the amplitude to change significantly [13]. As the viscous drag is reduced for fans vibrating in phase, this can result in a large increase (30%) in vibration amplitude without the need for additional input power. The current investigation, however, is aimed at the underlying physics responsible for heat transfer. Thus, comparisons are made for specified amplitudes, rather than for given input signal voltages. It should be noted that the total power consumption for the two-fan configuration at a particular amplitude is generally less than double to that needed for a single isolated fan. For example, the total power consumption ranges from 27 mW to 44 mW for the array, whereas the corresponding single fan power consumption is approximately 22 mW for the largest amplitude ($A=10$ mm). The remaining two parameters varied in the experiments (gap and pitch) are expressed as dimensionless quantities normalized by the vibration amplitude. They range from 0.01 to 2.0 and 0.5 to 4.0 for G/A and P/A, respectively. The uncertainty associated with the determination of convection coefficients was estimated in Ref. [2] and is approximately $\pm 8\%$.

3 Results and Discussion

In this section, the experimental results for local convection coefficients are presented, followed by an analysis of the stagnation and area-averaged heat transfer rates. Comparison is made to a single fan to illustrate the relative performance of arrays of fans.

3.1 Distribution of Local Convection Coefficients. Determination of the forced convection coefficient due exclusively to the piezoelectric fans requires a thorough analysis of the setup in natural convection conditions. Full details of natural convection experiments using this setup can be found in Ref. [2] and are not repeated here; the measured natural convection coefficients were found to be in satisfactory agreement with predictions from established correlations [16] for natural convection from a vertical constant flux heat source. Local forced convection coefficient (h_{pz}) maps are presented in Fig. 2; the same scale is used in all the

images to enable direct qualitative and quantitative comparison between the different cases. Each column represents a change in gap ranging from small ($G/A=0.01$) to large ($G/A=2$) gaps from left to right. Maps of single-fan experiments from Ref. [2] are reproduced as the first row in Fig. 2 to further facilitate comparison. For the three images in the first row, the fan is located at the center of the heat source and the vibration envelope is superimposed. The solid vertical line in the center of the vibration envelope represents the fan at its zero (undisplaced) position, while the remaining lines trace the extent of the vibration envelope whose overall dimensions are twice the vibration amplitude in the horizontal direction and equal to the width of the fan in the vertical direction. The heater size for all images in Fig. 2 is 101.6 $\times 152.4$ mm^2.

For a single fan, a lobed pattern is generated when the fan vibrates close to the surface; these lobes appear to be symmetric in both the vertical and horizontal directions, suggesting that the fluid agitation is roughly similar in the vibration direction, as well as its orthogonal direction. This behavior transitions to a nearly circular (or rounded-square) shape for the intermediate gaps, while the largest gap results in elliptical contours. The cooling effect is felt over a larger area in the horizontal direction in contrast to the somewhat localized behavior seen at small gaps. Although the magnitude of the heat transfer coefficients is lower for the largest gap, the horizontal extent over which the influence of the fan is felt is greater.

The remaining three rows in Fig. 2 are nine unique cases selected from the experiments conducted when a second fan is present, with each row representing a different pitch. The vibration envelopes of the two fans are illustrated with solid and dashed lines for the first and second fans, respectively. In-phase vibration allows overlapping vibration envelopes, as in the case of small or intermediate pitch (rows 2 and 3 of Fig. 2). The results for the smallest pitch ($P/A=0.5$, second row of Fig. 2) exhibit remarkably similar trends to those observed over the range of gaps for a single fan. In particular, when the fans are located close to the heated surface ($G/A=0.01$), a lobed pattern is once again realized. This pattern transitions to circular and eventually to a somewhat elliptical pattern. One difference that may be noted is the lower magnitude of the convection coefficients for these cases compared with their single-fan counterparts. For a small gap, this suggests that adding a second fan at such a small pitch has a mildly negative effect on the overall performance. However, the opposite appears to be the case for large gaps as seen in the last column of Fig. 2, where the magnitude is quite comparable to that of a single fan but the horizontal coverage has now increased.

As the fan pitch is increased to $P/A=1.25$ (third row of Fig. 2), the behavior exhibits some notable differences from that of a single fan. For the small gap, there now appear to be three zones of enhanced cooling: two at the extreme horizontal ends of the combined vibration envelope and one at the center of the two fans. This is consistent with the findings in Ref. [8], where constructive interference was observed under certain conditions for two cantilevers vibrating in phase. A similar trend can also be seen at the largest gap ($G/A=2$), where the elliptical contours also show enhanced cooling in these three zones.

Maps for the largest pitch ($P/A=4$) are shown in the last row of Fig. 2. Contours at the small gap reveal regions where the behavior is similar to two isolated fans, yielding four distinct lobes surrounding each vibration envelope. However, the convection coefficients are somewhat reduced when compared with a single fan at the same gap. In the limit of a sufficiently large fan pitch, two separate sets of contours identical to single-fan behavior would be expected, but it is apparent from the results that this condition is not fully satisfied for $P/A=4$. Although the contours are similar, the presence of the second fan causes the overall performance to decrease; the same is observed for the intermediate gap ($G/A=0.5$). A possible reason for this behavior is discussed in more detail at the end of this section. The largest gap ($G/A=2$) does not seem to share these characteristics, and the additional region of cooling between the fans has become more pronounced. It is also interesting to note the similarities between the $G/A=2$ maps at the different fan pitches (far right column of Fig. 2). The general shape and magnitude of the convection coefficient maps are similar, regardless of pitch. This is an important consideration for actual implementation of these fans in arrays. The performance decreases as the gap increases, but a greater fan pitch can be used under these conditions without sacrificing any additional performance; this implies that a smaller number of fans can be used in an array under these conditions.

To facilitate a quantitative analysis of the important trends, convection coefficients are presented along the horizontal centerline of the heat source ($y=0$) in Fig. 3 for a number of gaps and four different pitches. In each case, corresponding profiles for a single fan ($G/A=0.01$) and for natural convection alone (in the absence of fan operation) are also shown for comparison; the vibration envelopes are illustrated by vertical solid and dashed lines for the first and second fans, respectively. Profiles for $P/A=0.5$ are shown in Fig. 3(a), which again illustrates the decrease in performance of a fan array compared with a single fan. However, it is interesting to note that the profiles for all gaps less than $G/A=1$ are nearly identical in the stagnation region. Two fans at this pitch appear to be insensitive to relatively large changes in gap (up to G/A of 1).

An increase in pitch to $P/A=1$ in Fig. 3(b) reveals the constructive interference previously mentioned. Compared with a single fan, the stagnation performance has increased by over 10%, and for the three smallest gaps shown is roughly constant over a large portion of the combined vibration envelope of both fans. A further increase in pitch (to $P/A=1.25$, Fig. 3(c)) shows the three zones of enhanced cooling. This is most apparent for G/A less than 0.25, but the effect persists at $G/A=0.5$. As the gap is increased to $G/A=2$, the shape and magnitude of the profile approach the results seen at this same gap and smaller pitch ($G/A=2$ and $P/A=0.5$ of Fig. 3(a)).

For the largest pitch considered ($P/A=4$, Fig. 3(d)), the profiles start to take the general shape of two isolated fans. However, as previously mentioned, the magnitude of the convection coefficients is somewhat lower when compared with that from the single fan, suggesting that truly isolated conditions are not achieved at $P/A=4$. Additional experiments conducted at larger pitches not covered in Fig. 3 yielded profiles with magnitudes approaching that of a single fan as expected, but the size of the experimental heat source prevented a pitch large enough to yield completely isolated conditions. The observed decrease in performance of two fans relative to a single fan could be attributed localized "trapping" of heated air close to the heat source in the case of the two fans. The ambient temperature in the test setup is measured approximately 10 cm from the heat source, and localized increases in air temperature near the surface are not captured in the ambient temperature measurement.

3.2 Stagnation and Area-Averaged Heat Transfer Coefficients. Correlations for the area-averaged heat transfer for a single fan were presented in an earlier study [2] in terms of dimensionless quantities involving vibration amplitude and distance from the heat source. The calculation of average heat transfer coefficients depends on the geometry of the heat source over which the averaging is performed. In the case of fan arrays, a rectangular target area is most appropriate for averaging. The applicable dimensionless parameters in this correlation process are first defined, after which the stagnation heat transfer coefficient for fan arrays is considered. The area-averaged heat transfer characteristics of fan arrays are then explored.

3.2.1 Nondimensional Parameters. As discussed in Ref. [2], the length scale employed in the applicable dimensionless numbers is the hydraulic diameter of the vibration envelope given as

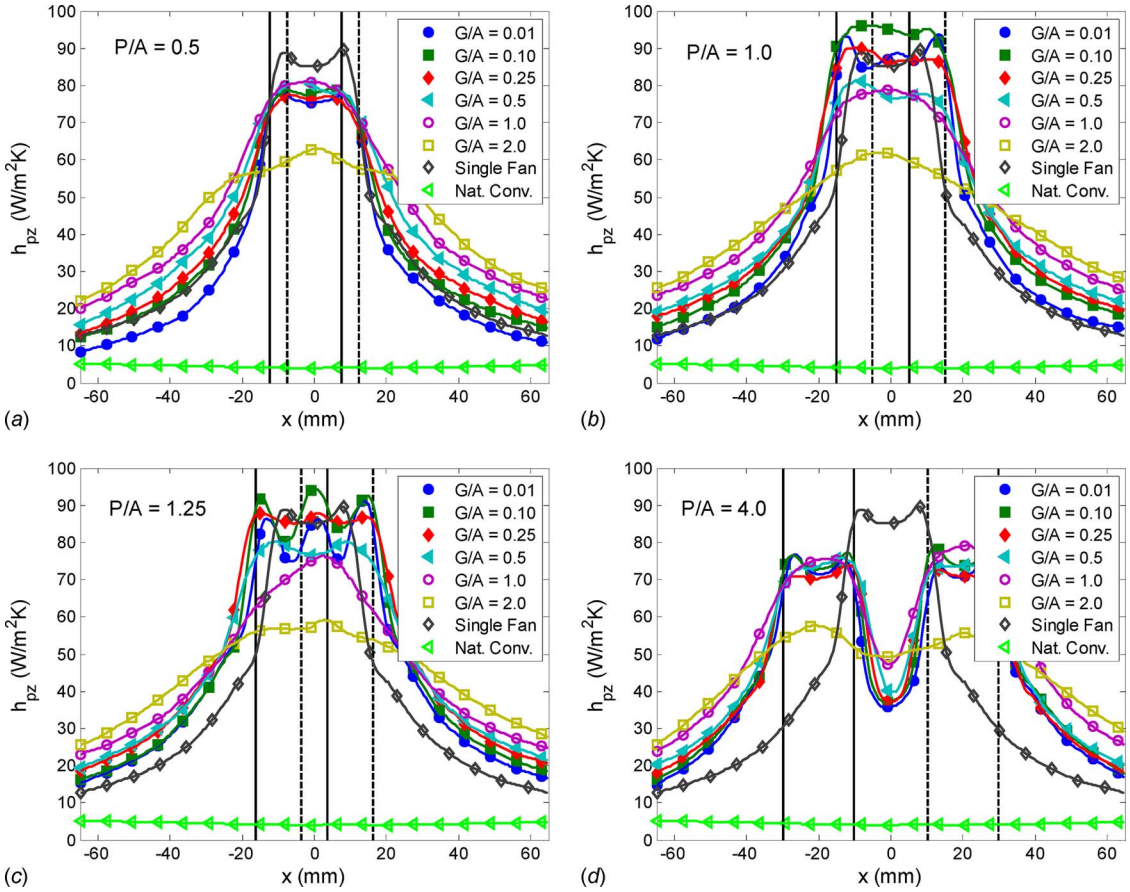

Fig. 3 Convection coefficients (h_{pz}) along the horizontal centerline of the heat source ($y=0$) over a range of nondimensional gaps ($G/A=0.01, 0.1, 0.25, 0.5, 1.0, 2.0$) for (*a*) $P/A=0.5$, (*b*) $P/A=1.0$, (*c*) $P/A=1.25$, and (*d*) $P/A=4.0$. For comparison, the single-fan ($G/A=0.01$) and natural convection profiles are also shown. The solid and dashed vertical lines represent the vibration envelopes of the first and second fans, respectively.

$$D_{pz} = \frac{4Aw}{2A + w} \tag{5}$$

The stagnation, local, and area-averaged heat transfer is depicted by Nusselt numbers based on this length scale and the corresponding heat transfer coefficients as follows:

$$\mathrm{Nu}_0 = \frac{h_0 \cdot D_{pz}}{k}, \quad \mathrm{Nu} = \frac{h_{pz} \cdot D_{pz}}{k}, \quad \overline{\mathrm{Nu}} = \frac{\bar{h}_{pz} \cdot D_{pz}}{k} \tag{6}$$

where h_0 is the local convection coefficient at the center of the vibration envelope. The average heat transfer coefficient is dependent on the area of the heat source and can be expressed for an arbitrary geometry as

$$\bar{h}_{pz} = \frac{1}{A_{eq}} \int \int_{A_{eq}} h_{pz} dA_{eq} \tag{7}$$

The influence of vibration amplitude is captured with a piezoelectric fan Reynolds number based on the maximum tip velocity (ωA) and the hydraulic diameter of the vibration envelope according to

$$\mathrm{Re}_{pz} = \frac{\omega A D_{pz}}{\nu} \tag{8}$$

3.2.2 Stagnation Nusselt Number for Fan Arrays. The following correlation for stagnation Nusselt number developed in Ref. [2] is independent of heat source geometry and is expected to apply for fan arrays as well

$$\mathrm{Nu}_0 = (\mathrm{Re}_{pz})^{q_1} \left[C_1 \left(\frac{G}{A} \right)^{q_2} + C_2 \right] \tag{9}$$

Here, $q_1=0.440$, $q_2=1.451$, $C_1=-0.168$, and $C_2=1.358$. Experimental results for stagnation Nusselt number for the fan array are compared with predictions from this correlation in Fig. 4 for $\mathrm{Re}_{pz}=3640$, 2920, and 2430, corresponding to $A=10$, 8.5, and 7.5

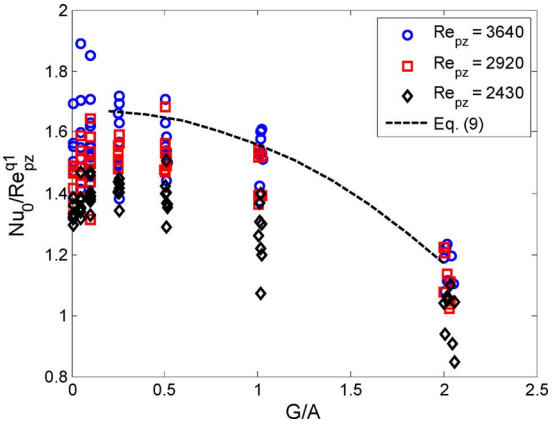

Fig. 4 Stagnation Nusselt number for fan arrays at $\mathrm{Re}_{pz}=3640$, 2920, and 2430 corresponding to $A=10$, 8.5, and 7.5 mm. These are compared with the single fan correlation in Eq. (9).

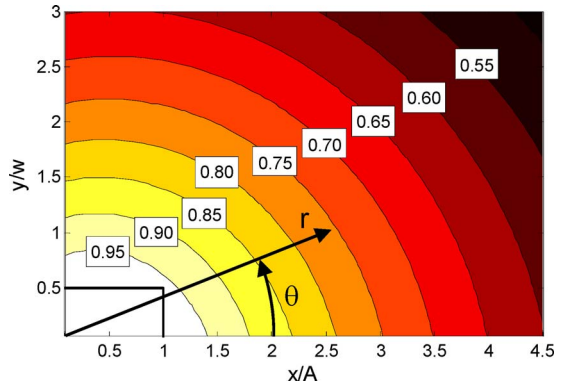

Fig. 5 Map of $\overline{Nu}/Nu_0$ (values in boxes) for a single fan from the correlation in Eq. (10). Also illustrated are polar coordinates (r, θ) as defined in Eq. (11).

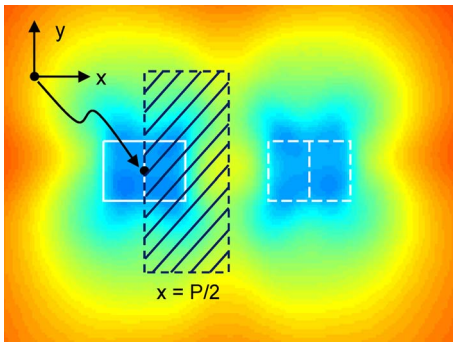

Fig. 6 Illustration of unit cell area used in computing $\overline{Nu}$. The horizontal dimension is always equal to half the pitch ($x=P/2$), while the vertical dimension can vary depending on the size of the heat source.

mm, respectively. Data from the largest Re_{pz} value (3640) agree well with the single-fan correlation but the results diverge as the amplitude (Reynolds number) is decreased. As explained earlier, this deviation is likely due to higher air temperatures near the heater surface for the fan arrays, especially at low fan velocities (low amplitudes) when the heated air is not as effectively transported away. Nonetheless, the single-fan stagnation correlation may be used to estimate stagnation Nusselt numbers in fan arrays to a first approximation.

3.2.3 Area-Averaged Array Nusselt Number. A predictive correlation developed for Nusselt numbers averaged over a circular area in Ref. [2] for a single fan is adjusted here to account for a rectangular averaging area and takes the following form:

$$\overline{Nu} = Nu_0(1 + [a(\theta)\exp\{b(\theta)r\}]^{-P(\theta)})^{-1/P(\theta)} \tag{10}$$

where

$$r = \left[\left(\frac{x}{A}\right)^2 + \left(\frac{y}{w}\right)^2\right]^{1/2}, \quad \theta = a\tan\left(\frac{y/w}{x/A}\right) \tag{11}$$

The horizontal and vertical distances that define the heat source geometry are normalized by the vibration amplitude and fan width, respectively. The heat source geometry defined by x/A and y/w was transformed in Eq. (10) to polar coordinates using Eq. (11). The three parameters (a, b, and P) in Eq. (10) are well represented by the following curvefits:

$$a(\theta) = 1.181 - 0.054\theta, \quad b(\theta) = -0.150 - 0.017\theta,$$

$$P(\theta) = 39.26 - 6.62\theta \tag{12}$$

The correlation in Eq. (10) yields a two-dimensional map for the normalized Nusselt number ($\overline{Nu}/Nu_0$) for a single fan and is shown in Fig. 5. The point (x/A, y/w) of (0, 0) equals the stagnation Nusselt number ($\overline{Nu}/Nu_0=1$); other points in the map show $\overline{Nu}/Nu_0$ values, which represent the cumulative average from the stagnation point to the (x/A, y/w) at that location (e.g., $\overline{Nu}$ is approximately half of Nu_0 for (x/A, y/w)=(4.5, 3)). It should be noted that the correlation given in Eq. (10) is based on single-fan experiments performed in Ref. [2], but only covers the results for $G/A \leq 0.5$ (unlike the correlation in Ref. [2], which is valid up to $G/A=2$). It is necessary to use the adjusted correlation in order for direct comparison to experimental data from arrays, as explained earlier. The convection contours from an array would repeat from one fan to the next, and therefore a unit cell can be employed to gauge the average thermal performance of the entire array, regardless of the number of fans. This unit cell is illustrated in Fig. 6 and has a horizontal dimension of $x=P/2$ (independent of vibration amplitude). The vertical extent of this unit cell depends on the size of the heat source and is considered a variable in the analysis that follows.

The area-averaged Nusselt numbers for fan arrays are first normalized by their respective experimental stagnation values. The results from $G/A \leq 0.5$ are then averaged for each pitch and compared with the single-fan contours of Fig. 5. A series of constant x/A profiles for a single fan and arrays are shown in Figs. 7(a) and 7(b), respectively. Each curve represents a different value of x/A,

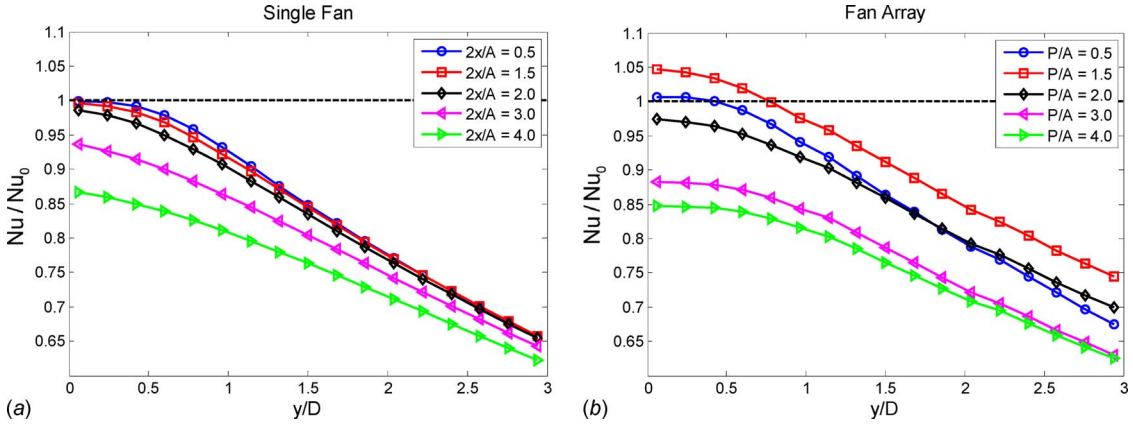

Fig. 7 Profiles of $\overline{Nu}/Nu_0$ at different x/A locations: (a) single-fan correlation results from Fig. 5 and (b) experimental array data at the largest amplitude ($Re_{pz}=3640$). In the case of fan arrays, $2x$ is better represented as P so that the two sets of data correspond to the same area on the heat source.

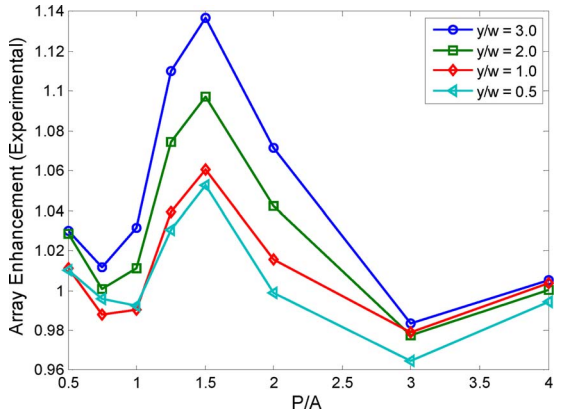

Fig. 8 Experimental enhancement observed with arrays at the largest amplitude (Re_{pz}=3640) over the full range of pitches considered. The horizontal dimension of the targeted heat source is $x=P/2$, while the vertical dimension varies with y/w (values of 3.0, 2.0, 1.0, and 0.5 are shown).

with $P=2x$ shown in the legend for the array curves (Fig. 7(*b*)). Note that for the curves in Fig. 7(*a*) with $2x/A \leq 2.0$, the average Nusselt number is approximately equal to the stagnation value ($\overline{Nu}/Nu_0=1$) at $y/w=0$, and falls to 65% of the stagnation value ($\overline{Nu}/Nu_0=0.65$) at $y/w=3$. The increase (or decrease) in performance through implementing an array can be found by comparing results from Fig. 7(*a*) with those from Fig. 7(*b*). The smallest pitch ($P/A=0.5$) yields little enhancement over its single-fan counterpart ($2x/A=0.5$ in Fig. 7(*a*)). Likewise, the two largest pitches ($P/A=3,4$) do not increase the performance over a single fan. In fact, for small y/w values ($y/w<1$), these results suggest a decrease in performance for the array configuration. The most notable difference occurs for the intermediate pitch ($P/A=1.5$), which shows a substantial increase in thermal performance over the entire range of y/w shown. The average Nusselt number in this case is 5% higher than the stagnation value ($\overline{Nu}/Nu_0=1.05$) at $y/w=0$ and falls to 75% of the stagnation value ($\overline{Nu}/Nu_0=0.75$) at $y/w=3$. Therefore, the enhancement in this case over the single fan is 5% for small y/w and 15% ($\overline{Nu}/Nu_0=0.75$ compared with $\overline{Nu}/Nu_0=0.65$) for large y/w.

The enhancement is further illustrated in Fig. 8 for discrete values of y/w and is plotted against fan pitch. The figure reveals an optimum pitch of $P/A=1.5$, with the enhancement dropping off (or becoming negative) for very large or very small pitches. This behavior can be approximated using the following Gaussian-like profile:

$$\text{Enhancement} = \left\{ C_1 Z \exp\left(-\left[\left(\frac{P}{A} - C_2 \right) C_3 \right]^2 \right) \right\} + 1 \quad (13)$$

In this equation, the function Z represents the dependence of the enhancement factor on the vertical extent of the heat source (y/w) over which the Nusselt number is averaged, as well as on fan amplitude. It should be noted that only results for the largest amplitude (Re_{pz}=3640) are included in Figs. 7 and 8. The experimental results from additional amplitudes revealed similar behavior with the optimum pitch in the same range. The observed enhancement is seen to decrease with amplitude, suggesting an additional dependence on Reynolds number. The dependence on these two parameters (y/w and amplitude) is captured with the following power-law relationship:

Table 1 Correlation coefficients for estimation of array enhancement (Eqs. (13) and (14)). Errors are determined by comparing estimated results with those from Fig. 7 and similar results for smaller amplitudes.

Parameter	Value
C_1	6.12×10^{-3}
C_2	1.5
C_3	1.667
m	1.5
n	1.0
Average deviation	2.5%
Maximum deviation	6.0%

$$Z = \left(\frac{Re_{pz}}{1000} \right)^m \left(\frac{y}{w} \right)^n \quad (14)$$

with exponents m and n being greater than or equal to unity so that as either variable (Re_{pz} or y/w) increases, the enhancement will also increase.

The variables C_1, C_2, C_3, m, and n are all determined from a least-squares analysis of the data. The results are listed in Table 1 and yield average and maximum errors of 2.5% and 6.0% in accounting for the normalized experimental data. The recommended correlation for heat transfer coefficients with fan arrays is thus the product of Eq. (10) (where Nu_0 is found from the single-fan correlation developed in Ref. [2]) and Eq. (13). The enhancement factor (Eq. (13)) is presented in Fig. 9 for three Re_{pz} values (3640, 2920, and 2430) and two y/w values (3.0 and 0.5).

4 Conclusions

Local heat transfer coefficients are obtained experimentally for arrays of piezoelectric fans and compared with the performance of a single fan. The interaction between neighboring fans is observed in analyzing both the stagnation and area-averaged thermal performance. A modest decrease in stagnation heat transfer for arrays is attributed to an increase in effective ambient temperature, as fans in the array feed heated air to their neighboring fans. For area-averaged results, conditions exist where the heat transfer in fan arrays is enhanced relative to the performance of single fans. The extent of enhancement is found to depend on the vibration amplitude and pitch, as well as the size of the heat source over which the heat transfer coefficient is averaged. Correlations are developed, which describe heat transfer characteristics of fan arrays over a range of operating conditions; a pitch of $P/A=1.5$ yields the largest increase in area-averaged thermal performance

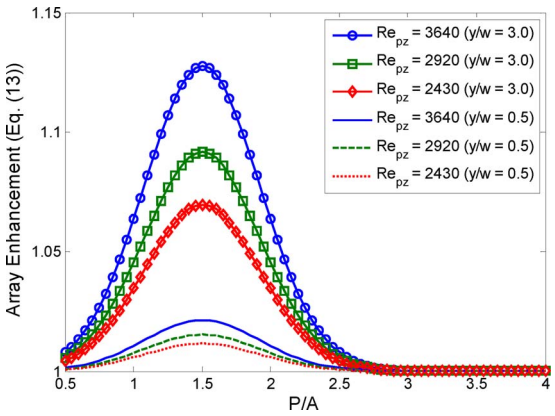

Fig. 9 Expression for array enhancement over single-fan performance (Eq. (13)) at three amplitudes (Re_{pz}=3640, 2920, and 2430) and two values for y/w (3.0 and 0.5)

(approximately 15%) when compared with a single fan. As the pitch becomes smaller or larger, the relative enhancement is found to decrease.

The present study was conducted at prescribed vibration amplitudes for the fans and not at a specified power input to drive the fans. For an array of N fans operating at the optimal pitch, the required power is less than N times the power required for one fan. Therefore, an experiment performed with the input power fixed would yield even further increases in thermal performance than that reported in this work. The optimal value of dimensionless pitch holds true regardless of gap or vibration amplitude and provides a guideline for use in the design of such fan arrays.

Acknowledgment

The authors acknowledge the financial support from members of the Cooling Technologies Research Center (www.ecn.purdue.edu/CTRC), a National Science Foundation Industry/University Cooperative Research Center and Purdue University.

Nomenclature

A = vibration amplitude (1/2 of peak-to-peak amplitude)
A_{heat} = area of heat source
D_{pz} = hydraulic diameter of vibration envelope
G = gap
h = local convection coefficient
$\overline{h}$ = area-averaged convection coefficient
h_0 = stagnation forced convection coefficient
I_s = current from power supply
k = thermal conductivity
L = piezoelectric fan length
$\underline{\mathrm{Nu}}$ = local Nusselt number
$\overline{\mathrm{Nu}}$ = area-averaged Nusselt number
Nu_0 = stagnation Nusselt number
P = fan pitch
q'' = heat flux
Re_{pz} = Reynolds number for vibrating cantilever
T_s = surface temperature
T_∞ = ambient temperature
V_s = voltage drop across heater
r = radial location on heat source
w = piezoelectric fan width
x = horizontal location on heat source
y = vertical location on heat source

Greek Symbols

ε = surface emissivity
ν = kinematic viscosity
θ = polar angle from horizontal on heat source
σ = Stefan–Boltzmann constant
ω = vibration frequency

Subscripts

gen = energy generation
mixed = mixed regime convection
nc = natural convection
pz = forced convection (under piezoelectric actuation)
rad = radiation

References

[1] Kim, Y., Wereley, S. T., and Chun, C., 2004, "Phase-Resolved Flow Field Produced by a Vibrating Cantilever Plate Between Two Endplates," Phys. Fluids, **16**(1), pp. 145–162.
[2] Kimber, M., Garimella, S. V., and Raman, A., 2007, "Local Heat Transfer Coefficients Induced by Piezoelectrically Actuated Vibrating Cantilevers," ASME J. Heat Transfer, **129**(9), pp. 1168–1176.
[3] Açıkalın, T., Garimella, S. V., Raman, A., and Petroski, J., 2007, "Characterization and Optimization of the Thermal Performance of Miniature Piezoelectric Fans," Int. J. Heat Fluid Flow, **28**(4), pp. 806–820.
[4] Toda, M., 1979, "Theory of Air Flow Generation by a Resonant Type PVF_2 Bimorph Cantilever Vibrator," Ferroelectrics, **22**, pp. 911–918.
[5] Toda, M., 1981, "Voltage-Induced Large Amplitude Bending Device—PVF_2 Bimorph—Its Properties and Applications," Ferroelectrics, **32**, pp. 127–133.
[6] Açıkalın, T., Wait, S. M., Garimella, S. V., and Raman, A., 2004, "Experimental Investigation of the Thermal Performance of Piezoelectric Fans," Heat Transfer Eng., **25**(1), pp. 4–14.
[7] Yoo, J. H., Hong, J. I., and Cao, W., 2000, "Piezoelectric Ceramic Bimorph Coupled to Thin Metal Plate as Cooling Fan for Electronic Devices," Sens. Actuators, A, **79**(1), pp. 8–12.
[8] Ihara, A., and Watanabe, H., 1994, "On the Flow Around Flexible Plates, Oscillating With Large Amplitude," J. Fluids Struct., **8**, pp. 601–619.
[9] Linderman, R. J., Nilsen, O., and Bright, V. M., 2005, "Electromechanical and Fluidic Evaluation of the Resonant Microfan Gas Pump and Aerosol Collector," Sens. Actuators, A, **118**(1), pp. 162–170.
[10] Schmidt, R. R., 1994, "Local and Average Transfer Coefficients on a Vertical Surface Due to Convection From a Piezoelectric Fan," International Society Conference on Thermal Phenomena, Washington DC, pp. 41–49.
[11] Hosaka, H., and Itao, K., 2002, "Coupled Vibration of Microcantilever Array Induced by Airflow Force," ASME J. Vibr. Acoust., **124**(1), pp. 26–32.
[12] Basak, S., and Raman, A., 2007, "Hydrodynamic Coupling Between Micromechanical Beams Oscillating in Viscous Fluids," Phys. Fluids, **19**(1), p. 017105.
[13] Kimber, M., Garimella, S. V., and Raman, A., 2006, "An Experimental Study of Fluidic Coupling Between Multiple Piezoelectric Fans," International Society Conference on Thermal Phenomena, San Diego, CA, pp. 333–340.
[14] NASA Jet Propulsion Laboratory Website, http://masterweb.jpl.nasa.gov/reference/paints.htm.
[15] Incropera, F., and DeWitt, D., 2002, *Fundamentals of Heat and Mass Transfer*, 5th ed., Wiley, New York.
[16] Vliet, G. C., and Ross, D. C., 1975, "Turbulent Natural Convection on Upward and Downward Facing Inclined Constant Heat Flux Surfaces," ASME J. Heat Transfer, **97**(4), pp. 549–555.

Single-Phase Microscale Jet Stagnation Point Heat Transfer

Gregory J. Michna[1]
e-mail: michng@rpi.edu

Eric A. Browne

Yoav Peles

Michael K. Jensen

Department of Mechanical, Aerospace, and Nuclear Engineering,
Rensselaer Polytechnic Institute,
Troy, NY 12180

An investigation of the pressure drop and impingement zone heat transfer coefficient trends of a single-phase microscale impinging jet was undertaken. Microelectromechanical system (MEMS) processes were used to fabricate a device with a 67-μm orifice. The water jet impinged on an 80-μm square heater on a normal surface 200 μm from the orifice. Because of the extremely small heater area, the conjugate convection-conduction heat transfer process provided an unexpected path for heat losses. A numerical simulation was used to estimate the heat losses, which were quite large. Pressure loss coefficients were much higher in the range $Re_{d,o}<500$ than those predicted by available models for short orifice tubes; this behavior was likely due to the presence of the wall onto which the jet impinged. At higher Reynolds numbers, much better agreement was observed. Area-averaged heat transfer coefficients up to 80,000 W/m^2 K were attained in the range $70<Re_d<1900$. This corresponds to a 400 W/cm^2 heat flux at a 50°C temperature difference. However, this impingement zone heat transfer coefficient is nearly an order-of-magnitude less than that predicted by correlations developed from macroscale jet data, and the dependence on the Reynolds number is much weaker than expected. Further investigation of microjet heat transfer is needed to explain the deviation from expected behavior. [DOI: 10.1115/1.3154750]

Keywords: electronics cooling, microscale jet heat transfer, microjet, orifice pressure loss coefficient

1 Introduction

Due to the increasing power consumption and decreasing size of electronic chips, cooling of these devices is becoming increasingly difficult. Heat fluxes seen in processors and power electronics are quickly approaching levels that cannot be easily accommodated by forced air convection over finned heat sinks. Therefore, more effective heat transfer cooling methods will be necessary to meet heat rejection needs within the next few years. One approach being investigated is liquid cooling, which takes advantage of a liquid's high (compared with air) conductivity, Prandtl number, density, and specific heat; because of these advantages, there have been many recent investigations of the use of liquid microchannel flows for electronics cooling.

Another possible liquid cooling method is microscale jet impingement cooling. Jet impingement cooling offers high heat transfer coefficients and has been used effectively in conventional-scale applications such as turbine blade cooling and the quenching of metals. Many studies investigating the performance of circular macroscale jets are available in the literature. Reviews of the single-phase heat and mass transfer performance of circular macroscale jets were given by Martin [1] and Jambunathan et al. [2].

Less information is available concerning the heat transfer performance of microscale jets. There have been several investigations of the performance of arrays of microscale jets [3–8] but very few published studies describing the heat transfer performance of a single circular microscale impinging jet.

Wu et al. [9] performed experiments investigating the heat transfer characteristics of a single confined submerged compressed-air jet with diameters between 500 μm and 1500 μm. They reported a heat transfer coefficient of 320 W/m^2 K for a 500-μm diameter jet with a standoff (the distance from orifice exit to heated surface) of 750 μm and a pressure drop of 5 psi. Reynolds numbers were not reported. The heat transfer coefficient was very small because the entire 2 cm $\times$ 2 cm chip was taken to be the heat transfer area, and the 500-μm diameter jet had little influence over most of this area.

Patil and Narayanan [10] performed an experimental study of a confined submerged 125-μm circular air jet. Spatially resolved heat transfer data were obtained using an infrared radiometer to measure the temperature of the heated thin foil onto which the jet impinged. Reynolds numbers in these experiments were in the range $700<Re_d<1800$. Standoff-to-diameter ratios of 2, 4, and 6 were tested, and the heat transfer coefficients were determined to be insensitive to this ratio in that range. The stagnation point Nusselt number varied from about $Nu_d=15$ at $Re_d=700$ to $Nu_d=55$ at $Re_d=1800$. The area-averaged Nusselt number results were compared with those predicted by the correlation given by Martin [1]. The observed area-averaged Nusselt numbers were approximately 40% lower than predicted at Reynolds numbers (based on orifice diameter) less than 1000, and approximately 25% higher than predicted at Reynolds numbers greater than 1700.

The pressure drop across the microjet orifice is also of interest to obtain a better understanding of the overall system and when considering pumping requirements. The microjet papers discussed above do not contain detailed information about the pressure drops across the orifices; however, there are several recent investigations of the pressure drop of flow through short microtubes or orifice tubes [11–13], the conclusions of which may be applicable to microjet orifice flows. Jankowski et al. [13] developed a model to predict the pressure drop for incompressible flows through orifices, including micro-orifices, with length-to-diameter ratios in the range $0<L/d<15$ and Reynolds numbers in the range $0<Re_{d,o}<3000$.

In this work, we examine the performance of a single-phase 67-μm diameter confined submerged impinging jet of water. The pressure drops and heat transfer coefficients are studied using a device fabricated using standard microelectromechanical system (MEMS) procedures. The pressure loss coefficients across the orifice are investigated. Using a heated section that measures only

[1]Corresponding author.

Contributed by the Heat Transfer Division of ASME for publication in the JOURNAL OF HEAT TRANSFER. Manuscript received January 16, 2009; final manuscript received May 4, 2009; published online August 26, 2009. Review conducted by Jayathi Murthy.

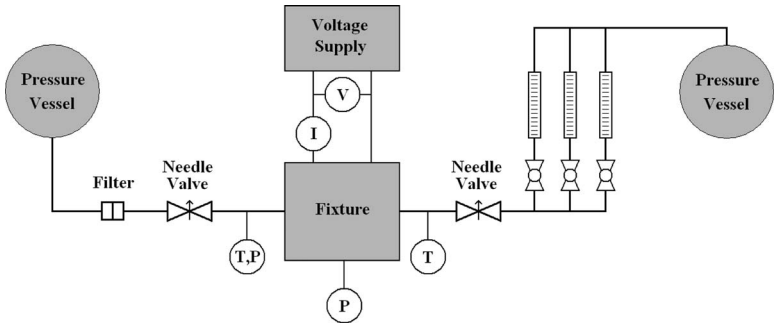

Fig. 1 Schematic of the flow loop used in the experiments

80 μm $\times$ 80 μm, area-averaged Nusselt numbers are determined. These area-averaged Nusselt numbers correspond to the so-called impingement zone, a region very close to the jet stagnation point.

2 Experimental Apparatus and Method

2.1 Apparatus. The experimental apparatus consisted of an open flow loop delivering water to and from a microdevice. A fixture was designed and built to incorporate the microdevice, fabricated using MEMS fabrication processes in a clean room environment, into the flow loop as well as to provide electrical contact. The working fluid was degassed de-ionized water.

The flow loop (Fig. 1) contains two tanks: one that supplies fluid to the device and one that collects fluid from the device exit. The flow traveled from the supply tank through a filter and needle valve before entering the fixture and microdevice. After exiting the microdevice, the flow traveled through another needle valve to one of three rotameters used to measure the flow rate before being discarded in the receiving tank. Three rotameters with different flow ranges were used to allow for a wide range of flow conditions; valves were used to direct all of the flow through each rotameter as needed. Type-T thermocouples were located before and after the fixture. Absolute pressure transducers were connected to the fluid entrance of the fixture and the chamber pressure port in the device.

A fixture (Fig. 2) was designed to integrate the device into the experimental apparatus. The fixture was fabricated with a computer numerical control (CNC) mill to ensure an accurate fit with the microdevice. A pocket was cut into the top surface of a Delrin block to hold the microdevice. Fluid channels were drilled into the Delrin fixture in the locations of the orifice, the pressure tap, and the device fluid exits. These locations were sealed with rubber o-rings seated in recesses in the fixture. Two spring-loaded pins were press fit into the fixture from below and were extended above the mating surface to the contact pads on the device. These pins were connected to an Instek PSP-405 power supply. Two HP 3457A multimeters were connected to measure the current and voltage supplied to the heater. A thin aluminum plate was bolted to the top of the fixture to hold the device in place and to ensure proper sealing of the fluid ports and good electrical contact between the pins and the contact pads.

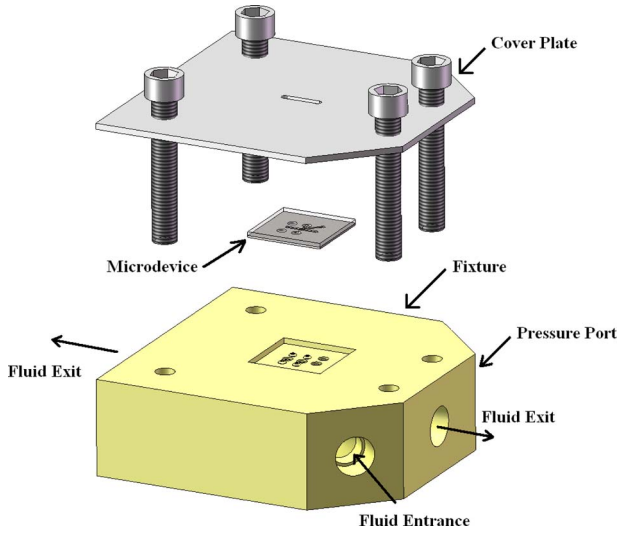

Fig. 2 Schematic of the assembly of the fixture, the microdevice and the cover plate

The microdevice was fabricated by anodically bonding and dicing two processed wafers. The two wafers were a silicon wafer etched using a deep reactive ion etcher (DRIE) to form the geometry of the channel and a Pyrex wafer with a thin-film metallic heater deposited on it. The fabrication of both wafers used photolithography carried out on a tool capable of back-side alignment.

The silicon wafer was first etched with a photoresist mask to a depth of 5 μm to create clearance for the heater vias and alignment marks. Next, 2 μm of oxide were deposited on both sides of the wafer in two separate steps providing oxide for hardmasks. DRIE was then performed on the top side using an oxide mask creating the channel 200 μm in depth. The orifice, fluid exit holes, and pass-through holes for the electrical contact pins were then etched from the bottom until they met the channel above.

The heater on the 1-mm thick Pyrex wafer was fabricated by depositing and patterning of metal layers and an oxide layer. First, 100 nm of titanium and 1 μm of aluminum were deposited without breaking vacuum. The 1-μm thick aluminum film was used to create vias and contact pads, while the underlying titanium existed in both those areas and the heater area. To electrically isolate and physically protect the heater, 1 μm of silicon oxide was deposited. The patterned silicon oxide film covers the heater and the vias but not the contact pads. In this way, the heater and the vias were electrically isolated from the water in the chamber, but electrical contact could be made with the spring-loaded contact pins outside of the chamber. Finally, the Pyrex and silicon wafers were anodically bonded together to form the completed microdevice.

The microdevice (Figs. 3 and 4) housed a channel 1.0 mm wide, 200 μm high, and 8.0 mm long into which the microjet flowed and impinged upon the heater from below. The microjet orifice was 67 μm in diameter, 250 μm long, and was positioned in the center of the bottom surface of the channel (silicon). The heater on the top surface of the channel (Pyrex) was square, measuring 80 μm on a side, and the center of the heater was aligned to the centerline of the microjet. This jet orientation (impingement on the heater from below) is different from most previous macroscale jet experiments, where the jet impinged on the heated surface from above. However, since the experiments presented here involved submerged jets, where the entire channel is flooded, in a channel only 200 μm tall and 1 mm wide, orientation is not expected to have a significant effect on performance.

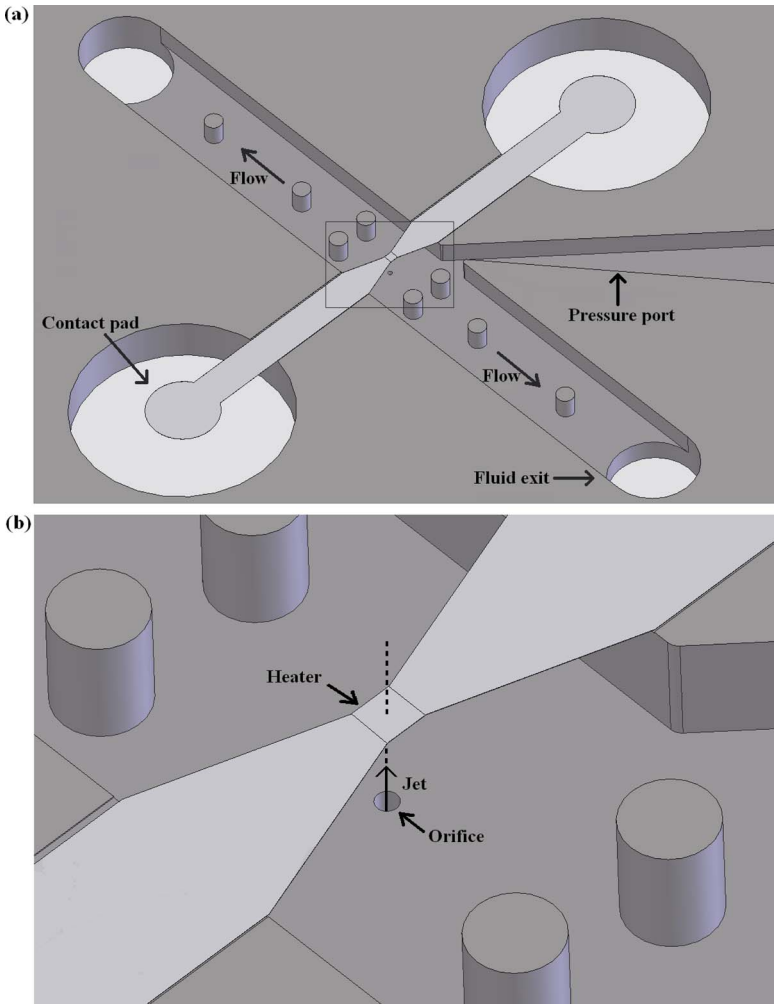

Fig. 3 (*a*) **Schematic of the microdevice and** (*b*) **a close up view of the orifice and the heater. The jet issues from the orifice in the center of the bottom surface of the channel. It impinges upon the heater 200** μ**m above (on the bottom surface of the Pyrex wafer), and the fluid exits down from either end of the channel.**

Fluid exited the channel at both ends through 1.0 mm holes in the bottom of the channel. During the experiments, the entire channel was flooded, creating a submerged jet. A pressure tap was located on a side wall in the middle of the channel to allow for measurement of chamber pressure. To enhance the structural integrity of the channel and to minimize deflection, several supporting pillars were fabricated in the channel starting more than 1 mm away from the orifice, such that their effect on the microjet was negligible.

2.2 Experimental Procedure. In addition to supplying heat to the system, the titanium heater also served as a thermistor. Before experiments were performed, the heater was placed in an oven, and its resistance was measured at 5°C intervals in the range 25–110°C. The temperature during this procedure was measured by a 36-gauge type-T thermocouple inserted into one of the fluid exit holes, positioning the thermocouple as close to the heater as possible. This thermocouple had previously been calibrated in a thermostatic bath with a precision resistance temperature detector (RTD) over the entire temperature range to an accuracy of ± 0.2°C. A third-order polynomial curve was fit to these data to provide a relationship between resistance and average heater temperature. The measured data and curve fit are shown in Fig. 5.

The device was then placed into the fixture. The chamber in the

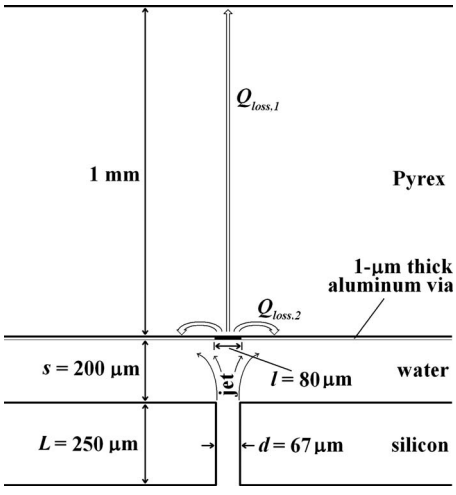

Fig. 4 Schematic showing the paths from the heater through which heat is lost. Most of the heat is lost through the path labeled $Q_{loss,2}$**, which cannot be measured independently or calculated without knowledge of local heat transfer coefficients.**

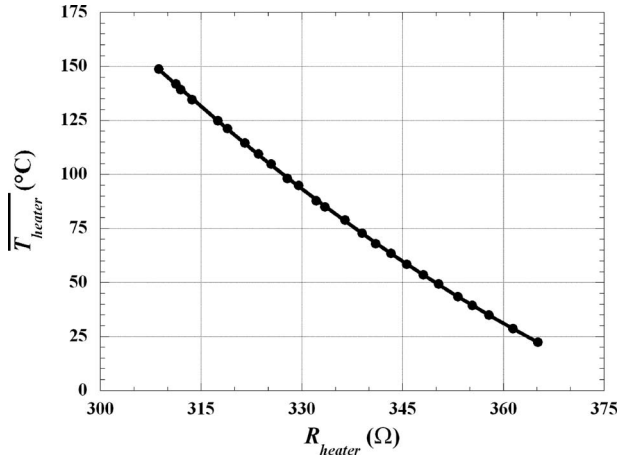

Fig. 5 Relationship between the resistance of the heater and average heater surface temperature. The error bars are smaller than symbol size.

device was evacuated, and power was supplied to the heater. The supplied voltage and current were measured, and an estimate of the heat lost through the fixture was obtained over the expected range of operating temperatures.

The supply tank was kept at a very low pressure with a vacuum pump for several days to ensure very low dissolved gas content in the de-ionized water used in the experiments. When water that had not been degassed as described above was used in earlier experiments, some gas bubbles could be seen on the downstream side of the orifice when large pressure drops were used. Immediately before the experiments were performed, the supply tank was pressurized with helium. Experiments were run at jet Reynolds numbers in the range $70 < \mathrm{Re}_d < 1900$ by controlling the flow rate through the system with the upstream needle valve and the pressure in the supply tank. At jet Reynolds numbers less than $\mathrm{Re}_d = 70$, the uncertainty in flow rate became very large. At $\mathrm{Re}_d = 1900$, the upstream pressure was 700 kPa absolute and higher jet Reynolds numbers were not attempted to prevent breakage of the device. Once a steady flow rate had been attained, a fixed voltage (~ 3 V) from the power supply was provided to the heater. Voltage and current were measured, and inlet pressure, inlet temperature, and chamber pressure were measured and recorded by a National Instruments data acquisition system.

2.3 Data Reduction. The jet Reynolds numbers were calculated according to

$$\mathrm{Re}_d = \frac{\rho \cdot V \cdot d}{\mu} \tag{1}$$

In this equation, ρ is the density, V is the average velocity at the orifice exit, d is the orifice diameter, and μ is the dynamic viscosity. The thermophysical properties of water were evaluated at the film temperature, which was calculated using

$$T_{\mathrm{film}} = \frac{T_s + T_{\mathrm{in}}}{2} \tag{2}$$

The orifice Reynolds numbers ($\mathrm{Re}_{d,o}$) were also calculated using Eq. (1). However, for the orifice Reynolds numbers, the thermophysical properties of water were evaluated at the orifice inlet temperature, which was approximately 22 °C for all of the experiments. Two different Reynolds numbers are necessary because the fluid properties at the orifice are relevant for the pressure drop behavior, and the fluid properties at the film temperature are used for the heat transfer behavior, consistent with previous work.

From the inlet and chamber pressures measured in the experiments, the pressure drop across the orifice was calculated. The relationship between pressure drop and flow rate through orifices can be presented in two ways: using the pressure loss coefficient K or the discharge coefficient C_d. The relationship between these parameters, flow velocity and pressure drop, is given by

$$K = \frac{(1-\beta^4)}{C_d^2} = \frac{\Delta P}{\frac{1}{2}\rho \cdot V^2} \tag{3}$$

where ΔP is the pressure drop across the orifice, and β is the ratio of the orifice diameter to the upstream tube diameter, which is effectively zero in the experiments presented here. The results presented in Sec. 3.1 are in terms of the pressure loss coefficient K, which, as can be seen in Eq. (3), is directly proportional to the pressure drop across the orifice.

The voltage and current supplied to the heater were used to calculate both the power dissipated by the heater and its resistance. The relationship between the electrical resistance of the heater and its average temperature was well characterized by calibration. The average surface temperature $\overline{T_s}$ was calculated from the total power supplied to the heater Q_{heater}, the heat loss estimate Q_{loss}, the heater area A_{heater}, the conductivity of silicon dioxide $k_{\mathrm{SiO_2}}$, the thickness of the silicon dioxide layer on the heater $t_{\mathrm{SiO_2}}$, and the average heater temperature $\overline{T_{\mathrm{heater}}}$ using

$$Q_{\mathrm{heater}} - Q_{\mathrm{loss}} = \frac{k_{\mathrm{SiO_2}} \cdot A_{\mathrm{heater}}(\overline{T_{\mathrm{heater}}} - \overline{T_s})}{t_{\mathrm{SiO_2}}} \tag{4}$$

From the total power supplied to the heater Q_{heater}, the heat loss estimate Q_{loss}, the heater area A_{heater}, the average heater surface temperature $\overline{T_s}$, and the inlet water temperature T_{in}, the area-averaged heat transfer coefficients over the heater $\bar{h}$ were calculated using

$$Q_{\mathrm{heater}} - Q_{\mathrm{loss}} = \bar{h} \cdot A_{\mathrm{heater}}(\overline{T_s} - T_{\mathrm{in}}) \tag{5}$$

Note that to comply with current practices in jet impingement heat transfer, we employed the commonly-used inlet temperature as the pertinent reference temperature in calculating the heat transfer coefficient and Nusselt number.

The area-averaged Nusselt numbers $\overline{\mathrm{Nu}_d}$ were calculated from the area-averaged heat transfer coefficient, the orifice diameter d, and the conductivity of water $k_{\mathrm{H_2O}}$ using

$$\overline{\mathrm{Nu}_d} = \frac{\bar{h} \cdot d}{k_{\mathrm{H_2O}}} \tag{6}$$

The conductivity of water used to calculate the Nusselt numbers was evaluated at the film temperature.

2.4 Heat Loss Estimation. As described above, before performing heat transfer experiments, the heat loss through the Pyrex wafer and the fixture was measured by completely evacuating the chamber and applying power to the heater. At steady state, the heater current and voltage were measured, and the power supplied to the heater and temperature of the heater were calculated. A polynomial was fit to these data to relate the heat lost from the back of the heater to its temperature. However, the path of heat losses (the amount of heat supplied which was not removed by convection over the surface of the heater) during the experiments is much different than the path present with the chamber evacuated. The heat loss measured in a vacuum neglects any heat lost by convection to the water from the surface of the Pyrex and the aluminum vias outside of the area covered by the heater. Therefore, the heat losses measured in a vacuum represent a best-case scenario.

To better understand heat losses during the experiment, a finite element analysis was performed using a commercially available software package, COMSOL MULTIPHYSICS. In this analysis, a 1-mm cube section of the Pyrex wafer was modeled. The 80-μm square heater was centered on the bottom face of this cube, and the

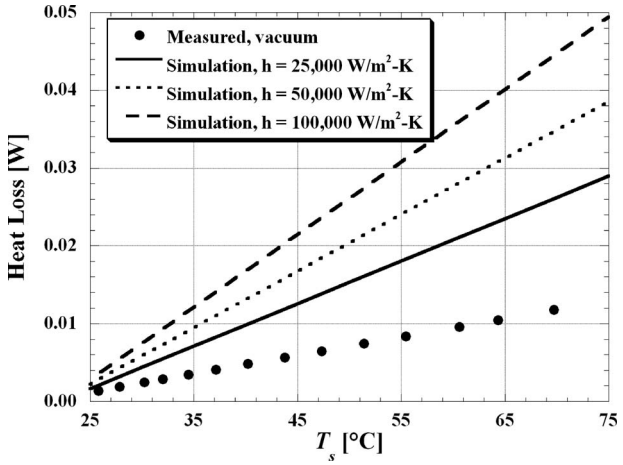

Fig. 6 Plot of the measured vacuum heat losses and the heat losses calculated using finite element analysis for several values of heat transfer coefficient. The error bars for the measured values are smaller than the symbol size.

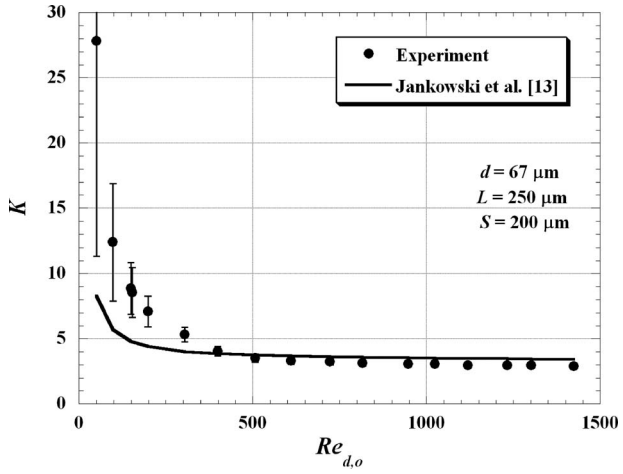

Fig. 7 The effect of Reynolds number on the pressure loss coefficient

aluminum vias and oxide layers were included in the model. A constant temperature boundary condition was applied to the heater, and a convection boundary condition was applied to the remainder of the surface exposed to the water, including the aluminum vias and exposed Pyrex sections. The inlet temperature of the water (which was the ambient temperature in these experiments, approximately 22°C) and a constant heat transfer coefficient were used in the simulation. To the remaining boundaries a constant temperature boundary condition at the ambient temperature was applied.

As shown in Fig. 6, the finite element analysis gave much higher estimated heat losses than were measured in the vacuum—more than double if the heat transfer coefficient is greater than 25,000 W/m^2 K. Moreover, the analysis showed that nearly all of the losses were not by conduction to the outside boundaries of the Pyrex ($Q_{loss,1}$ in Fig. 4), but rather by conduction from the back of the heater through the Pyrex to the surface of the Pyrex and aluminum vias, and then by convection to the water ($Q_{loss,2}$ in Fig. 4). Even though Pyrex is a very good insulator ($k=1.1$ W/m K), the heat flow needed to travel only miniscule distances (~ 10 μm) through the Pyrex to reach the surface just outside of the heater area, where the heat transfer coefficient is very large. Because of this low thermal resistance heat loss path, the calculated losses were on the order of the heat transfer from the heater directly to the fluid.

With the chosen boundary conditions, a worst-case estimate of the heat losses was obtained. In the actual experiments, the nonconvective boundaries of this volume were at some temperature above the ambient, reducing those conduction losses. The assumption of constant heat transfer coefficient on the surface of the Pyrex and vias also serves to give the worst-case estimate, since the literature on macroscale jets, as well as research of Wu et al. [9] and Patil and Narayanan [10] on microjets, suggest the heat transfer coefficient is greatest near the stagnation point and decreases with distance from the stagnation point. Therefore, the worst-case estimate overstates the losses, possibly significantly. The measured vacuum heat losses (best case) and the heat losses calculated using finite element analysis (worst case) are shown in Fig. 6.

The area-averaged Nusselt number results presented in the Sec. 3.2 are calculated using the assumption that the actual losses during the experiments, Q_{loss} in Eq. (5), are the arithmetic mean of the best and worst case losses described above. Since the worst case losses depend on the heat transfer coefficient, the solution is calculated iteratively. The uncertainty in the heat loss measurement is then taken to be one-half of the difference between the best case and worst case. This results in a quite large uncertainty in the area-averaged Nusselt number, but, as will be discussed below, the overall conclusion of the paper is not affected by this large value.

2.5 Uncertainties. The propagation of uncertainties for the reduced data followed standard methods [14]. The uncertainty in the Reynolds number (both jet and orifice) was less than $\pm 5\%$ for all experiments. The uncertainty in the area-averaged Nusselt number was approximately $\pm 85\%$ for the lowest Reynolds numbers and decreased to $\pm 65\%$ for the highest Reynolds numbers. This very large uncertainty is due almost entirely to the uncertainty in the heat losses described above. The large uncertainties reported in this investigation are inherent to the length scale of the heater. The heater was deposited on an excellent insulator with an extremely low thermal conductivity. However, due to the conjugate convection-conduction nature of the heat losses and the very small length scales involved, the heat losses are not experimentally measurable. A numerical simulation was undertaken to better understand these losses, but due to our very conservative approach (taking the uncertainty in heat losses to span the entire range from the best-to worst-case situations), the experimental uncertainty remained large. The uncertainty in the pressure loss coefficient was less than $\pm 35\%$ for all points except the smallest Reynolds number and less than $\pm 5\%$ for $Re_{d,o} > 400$.

3 Results and Discussion

3.1 Pressure Drop. The pressure loss coefficients determined from these experiments are shown in Fig. 7. For comparison purposes the correlation given by Jankowski et al. [13] is also shown. Error bars are included in the figure for all data points; however, the error bars are smaller than the symbol size for $Re_{d,o} > 500$. While the trend is the same, the experimentally determined pressure loss coefficients were larger than predicted by the model at low orifice Reynolds numbers. However, for $Re_{d,o} > 500$, the pressure loss coefficients were slightly less than predicted by the model.

The model of Jankowski et al. [13] assumes that the overall pressure drop in an orifice tube is the sum of the pressure drop due to friction in developing flow in a straight length of tube and the pressure drop due to flow through a sharp-edged (zero length) orifice, as shown by

$$\Delta P = K \cdot \frac{1}{2}\rho \cdot V^2 = (K_f + K_s) \cdot \frac{1}{2}\rho \cdot V^2 \tag{7}$$

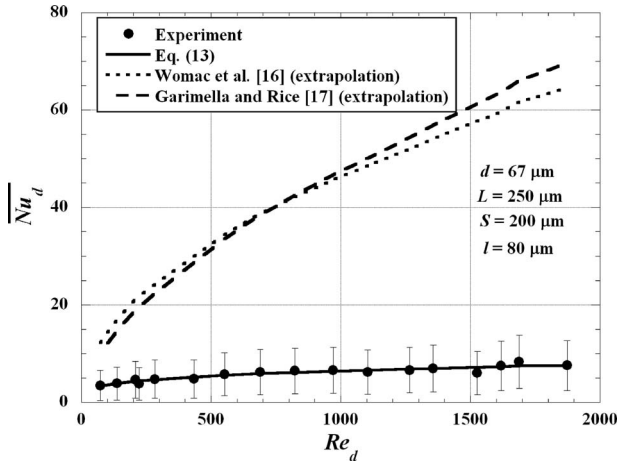

Fig. 8 The heat transfer performance of the microjet

The contribution due to flow friction was calculated using a correlation given by Shah [15], which is expressed as

$$K_f = f\frac{L}{d} = \frac{\Delta P_f}{\frac{1}{2}\rho \cdot V^2} = \frac{4}{\mathrm{Re}_{d,o}}\frac{L}{d}\left(\frac{3.44}{\sqrt{\xi}} + \frac{16 + 3.125/\xi - 3.44/\sqrt{\xi}}{1 + 0.000212/\xi^2}\right) \tag{8}$$

where f is the Darcy friction factor and $\xi = L/(d\ \mathrm{Re}_{d,o})$. Jankowski et al. [13] developed a correlation for the contribution due to flow through a sharp-edged orifice, expressed as

$$\frac{1}{\sqrt{K_s}} = C_{d,s} = 0.6\left[1 + \exp(-0.12\sqrt{\mathrm{Re}_{d,o}}) - 2.16\exp(-0.26\sqrt{\mathrm{Re}_{d,o}}) + 0.16\left(1 - \frac{\sqrt{\mathrm{Re}_{d,o}}}{1 + \sqrt{\mathrm{Re}_{d,o}}}\right)\right] \tag{9}$$

In the case of microjet flow, the presence of the impingement surface will also have an effect on the overall pressure drop. This effect is not represented in the model of Jankowski et al. [13]. The pressure loss coefficient from the experiment is larger than that predicted by the model at low orifice Reynolds numbers, suggesting that the pressure drop is increased due to the presence of the wall. At orifice Reynolds numbers in the range $\mathrm{Re}_{d,o} > 500$, however, the pressure loss coefficient is approximately 15% lower than the pressure drop for a sharp-edged orifice. The pressure drop for the impinging jet flow in this range is quite close to that predicted by the correlations for orifice flow. The presence of the wall onto which the jet impinges is likely to cause large recirculation zones and entrainment that are not present in typical orifice flows at low orifice Reynolds numbers. At higher orifice Reynolds numbers, both orifice and impinging jet flows are expected to cause recirculation zones and entrainment. This may explain why the pressure drop is not well predicted by the model at low orifice Reynolds numbers but agrees well for $\mathrm{Re}_{d,o} > 500$.

3.2 Heat Transfer. The observed Nusselt numbers are plotted in Fig. 8. For comparison purposes the correlations given by Womac et al. [16] and Garimella and Rice [17] have also been included in the figure. The experimental heat transfer coefficients ranged from 30,000 $\mathrm{W/m^2\,K}$ to 80,000 $\mathrm{W/m^2\,K}$. Both correlation curves shown in Fig. 8 are extrapolations, since they were developed from macroscale jet data. The 67-μm diameter is well outside of the geometrical range of these correlations. The Reynolds numbers investigated here are also below the range of data from which the correlations were developed. However, since no correlations for microscale jets exist in the literature, these correlations are the best available. The area-averaged Nusselt number correlation given by Womac et al. [16] for a jet is given by

$$\frac{\overline{\mathrm{Nu}_d}}{\mathrm{Pr}^{0.4}} = 0.785\ \mathrm{Re}_d^{0.5}A_r + 0.0257\ \mathrm{Re}_y^{0.8}\frac{d}{y}(1 - A_r) \tag{10}$$

where A_r is the ratio of the "impingement zone" area to the heater area given by the equation

$$A_r = \frac{\pi(1.9d)^2}{l^2} \tag{11}$$

and y is the average length of the wall-jet region. The authors state that A_r should be set to 1 when A_r as determined by Eq. (11) is greater than 1, as is the case with the geometry under investigation. Interestingly, Womac et al. divided the entire heat transfer area into two separate regions: the impingement zone, which is influenced directly by jet impingement and is taken to extend to a radius of $1.9d$, and the wall-jet region outside of the impingement zone. The impingement zone Nusselt number was taken to have a weaker dependence on the Reynolds number than did the wall-jet region. This correlation fit all of the data for which it was determined within $\pm 16\%$.

The correlation given by Garimella and Rice [17] is for the stagnation point Nusselt number, rather than an area-averaged Nusselt number, since the correlation given for area-averaged Nusselt numbers is specifically for a 10 mm $\times$ 10 mm area. Since the heater size is small in these experiments, the stagnation Nusselt number correlation is appropriate and is given by

$$\mathrm{Nu}_d = 0.492\ \mathrm{Re}_d^{0.585}\ \mathrm{Pr}^{0.4}\left(\frac{S}{d}\right)^{0.024}\left(\frac{L}{d}\right)^{-0.09} \tag{12}$$

The authors state that this correlation fit most of the data within $\pm 10\%$.

An extrapolation of the widely-used correlation given by Martin [1] could not be applied for this geometry. The Martin correlation is valid for area ratios (the ratio of orifice area to heater area) between 0.004 and 0.04. Because the area ratio investigated in these experiments is very large (0.55), the correlation gives a nonphysical negative value for Nusselt number.

Both correlations shown in Fig. 8 overpredict the area-averaged Nusselt number by 200–800%. The overprediction is not a result of the large uncertainties associated with the experiments. That is, even if the losses (which account for nearly all of the uncertainty) were assumed to be zero and all of the power provided to the heater was used to calculate the heat transfer coefficients, the correlations would still overpredict the area-averaged Nusselt numbers by up to 500%.

There could be several reasons for this disagreement. In the investigations of the performance of macroscale single jets, a long tube is usually used to provide the jet fluid. Because of the length of these tubes, the jet flow typically has the velocity profile of fully-developed flow in a tube. The L/d ratio of the orifice in this investigation is less than 4, and the flow in the orifice is not expected to be fully developed. The hydrodynamic entrance conditions of the jet are therefore different for this investigation than for the jet flows that have provided the data for the development of the correlations. The discrepancy reported here is, however, likely much larger than would be caused by differing entrance conditions.

The discrepancy in the size of the heater area relative to the area of the jet may explain some of the difference between the measured area-averaged Nusselt numbers and those predicted by the correlations. The jet in these experiments covered more than half of the heater area. In the two microjet investigations previously undertaken [9,10], the heat transfer coefficient was maximum at the stagnation point. However, several experimental studies of local jet impingement heat transfer at the macroscale have shown the existence of a local minimum of the heat transfer coefficient at the stagnation point [18–20]. In cases where this local minimum was observed, the heat transfer coefficient increased to a maximum at distances as large as 1.5 diameters away from the stagnation point (outside of the heater area in this experiment).

Since the area over which the area-averaged Nusselt numbers were measured in this experiment is small relative to the size of the jet, it is possible that the entire area was within the previously-observed zone of locally reduced heat transfer. Even if this were the case, however, this would account for only a small portion of the discrepancy between the measured area-averaged Nusselt numbers and the values predicted by the correlations.

Another possible cause for the disagreement between the experimental results and the correlations are some fundamental differences between jet flow at the microscale and at the macroscale. Since only orifice pressure drop and impingement zone heat transfer data have been collected in this experiment, this conclusion cannot be made on the basis of this work. Future work in which the fluid mechanics of the microscale jet flow is investigated should be undertaken.

The jet Reynolds numbers investigated here are smaller than those used to develop the correlations. Even though the velocities are large, the small diameter of the orifice in the microdevice leads to jet Reynolds numbers much lower than are typically seen in the macroscale jet flows that have been thoroughly studied. The correlations shown in Fig. 8 were therefore developed using data from almost exclusively turbulent jets, while the jets present in the microdevice under investigation were in the laminar regime. Therefore, the discrepancy may have been caused by flow regime differences between the experiment and the data used to develop the correlations. This is perhaps the most likely reason for the disagreement.

A curve fit to the experimentally obtained area-averaged Nusselt number is included in Fig. 8. The equation of this fit is given by

$$\overline{\mathrm{Nu}_d} = 0.635\ \mathrm{Re}_d^{0.245}\ \mathrm{Pr}^{0.4} \tag{13}$$

Only water was used in this experiment, so the Prandtl number exponent was set to 0.4, which is most often used in the jet literature [16,17]. This curve fit is valid only for the geometry studied here. Interestingly, this equation shows a much weaker dependence of the Nusselt number on the jet Reynolds number than is expected from earlier work. However, since the heater area is very close in size to the area of the orifice in this case, the area over which the Nusselt number is averaged is very close to the stagnation point. Some investigators, such as Womac et al. [16], Garimella and Rice [17], and Zhou and Ma [21] reported a weaker dependence on the jet Reynolds number for the stagnation point heat transfer coefficient than for the impingement surface far away from the stagnation point. The exponent reported here (0.245) is significantly lower than even those reported values (0.5, 0.585, and 0.5, respectively). Further research is required to determine the cause of this behavior.

4 Conclusions

An experimental investigation of the pressure drop and stagnation zone heat transfer coefficient of a single impinging microjet was undertaken. The pressure loss coefficients and area-averaged Nusselt numbers were reported over the range $50 < \mathrm{Re}_{d,o} < 1400$ and $70 < \mathrm{Re}_d < 1900$, respectively. The pressure loss coefficients obtained experimentally were much higher than predicted by the model of Jankowski et al. [13] at orifice Reynolds numbers less than 500 due to the presence of the impingement wall. At orifice Reynolds numbers higher than 500, the experimentally obtained pressure loss coefficients were well predicted by the model.

Even with the large experimental uncertainties taken into account, the observed area-averaged Nusselt numbers were significantly less than that predicted by Womac et al. [16] or Garimella and Rice [17]. The dependence of the area-averaged Nusselt number on the Reynolds number ($\mathrm{Nu}_d \propto \mathrm{Re}_d^{0.245}$) is also much weaker than has been previously observed. Additional experimentation should be undertaken to better understand whether the discrepancies noted above are due to the laminar flow regime investigated in these experiments or if the flow through microscale jets is fundamentally different from that through macroscale jets. In addition, we have initiated a numerical simulation project to explore these two issues, as well as the conjugate effects inherent with these very small length scales.

Acknowledgment

This work is supported by the Office of Naval Research (ONR) under the Multidisciplinary University Research Initiative (MURI) award No. GG10919. The authors would like to acknowledge the staff of the Micro and Nano Fabrication Clean Room (MNCR) at Rensselaer Polytechnic Institute for their assistance in fabrication of the test devices.

Nomenclature

English

A_{heater} = surface area of the heater (m^2)
A_r = ratio of impingement zone area to heater area
C_d = discharge coefficient of orifice
d = diameter of orifice (m)
f = Darcy friction factor
$\overline{h}$ = area-averaged convective heat transfer coefficient ($\mathrm{W/m^2\ K}$)
K = pressure loss coefficient
$k_{\mathrm{H_2O}}$ = thermal conductivity of water (W/m K)
$k_{\mathrm{SiO_2}}$ = thermal conductivity of silicon dioxide (W/m K)
L = length of orifice (m)
l = side length of heater (m)
Nu_d = Nusselt number
$\overline{\mathrm{Nu}_d}$ = area-averaged Nusselt number
ΔP = pressure drop (Pa)
Q_{heater} = total power supplied to the heater (W)
Q_{loss} = heat loss from heater other than convection directly to fluid (W)
$Q_{\mathrm{loss},1}$ = heat loss by conduction through the Pyrex to the ambient (W)
$Q_{\mathrm{loss},2}$ = heat loss by convection from the surface in contact with the water (W)
R_{heater} = resistance of the heater (Ω)
Re_d = jet Reynolds number
$\mathrm{Re}_{d,o}$ = orifice Reynolds number
Re_y = wall-jet Reynolds number
S = standoff (distance from orifice exit to heater surface) (m)
T_{in} = fluid inlet temperature (°C)
T_{film} = film temperature (°C)
$\overline{T_{\mathrm{heater}}}$ = average heater temperature (°C)
T_s = average surface temperature (°C)
$t_{\mathrm{SiO_2}}$ = thickness of silicon dioxide on heater (m)
y = average length of the wall-jet region (m)

Greek

β = ratio of orifice diameter to upstream tube diameter
μ = viscosity of water (kg/m s)
ξ = correlation parameter
ρ = density of water ($\mathrm{kg/m^3}$)

Subscripts

f = corresponding to developing flow in a tube
s = corresponding to flow through a sharp-edged orifice

References

[1] Martin, H., 1977, "Heat and Mass Transfer Between Impinging Gas Jets and Solid Surfaces," Adv. Heat Transfer, **13**, pp. 1–60.

[2] Jambunathan, K., Lai, E., Moss, M. A., and Button, B. L., 1992, "A Review of Heat Transfer Data for Single Circular Jet Impingement," Int. J. Heat Fluid Flow, **13**(2), pp. 106–115.
[3] Stefanescu, S., Mehregany, M., Leland, J., and Yerkes, K., 1999, "Micro Jet Array Heat Sink for Power Electronics," *Proceedings of the 12th IEEE International Conference on Micro Electro Mechanical Systems (MEMS)*, Orlando, FL, pp. 165–170.
[4] Fabbri, M., Jiang, S., and Dhir, V. K., 2003, "Experimental Investigation of Single-Phase Micro Jets Impingement Cooling for Electronic Applications," *Proceedings of the 2003 ASME Summer Heat Transfer Conference*, Las Vegas, NV, pp. 461–468.
[5] Wang, E. N., Zhang, L., Jiang, L., Koo, J.-M., Maveety, J. G., Sanchez, E. A., Goodson, K. E., and Kenny, T. W., 2004, "Micromachined Jets for Liquid Impingement Cooling of VLSI Chips," J. Microelectromech. Syst., **13**(5), pp. 833–842.
[6] Brunschwiler, T., Rothuizen, H., Fabbri, M., Kloter, U., Michel, B., Bezama, R. J., and Natarajan, G., 2006, "Direct Liquid Jet-Impingement Cooling With Micron-Sized Nozzle Array and Distributed Return Architecture," *Proceedings of the 10th Intersociety Conference on Thermal and Thermomechanical Phenomena and Emerging Technologies in Electronic Systems, iTherm 2006*, San Diego, CA, pp. 196–203.
[7] Sung, M. K., and Mudawar, I., 2008, "Single-Phase Hybrid Micro-Channel/Micro-Jet Impingement Cooling," Int. J. Heat Mass Transfer, **51**(17–18), pp. 4342–4352.
[8] Sung, M. K., and Mudawar, I., 2008, "Effects of Jet Pattern on Single-Phase Cooling Performance of Hybrid Micro-Channel/Micro-Circular-Jet-Impingement Thermal Management Scheme," Int. J. Heat Mass Transfer, **51**(19–20), pp. 4614–4627.
[9] Wu, S., Mai, J., Tai, Y. C., and Ho, C. M., 1999, "Micro Heat Exchanger by Using MEMS Impinging Jets," *Proceedings of the 12th IEEE International Conference on Micro Electro Mechanical Systems (MEMS)*, Orlando, FL, pp. 171–176.
[10] Patil, V. A., and Narayanan, V., 2005, "Spatially Resolved Heat Transfer Rates in an Impinging Circular Microscale Jet," Microscale Thermophys. Eng., **9**(2), pp. 183–197.
[11] Brutin, D., and Tadrist, L., 2003, "Experimental Friction Factor of a Liquid Flow in Microtubes," Phys. Fluids, **15**(3), pp. 653–661.
[12] Phares, D. J., Smedley, G. T., and Zhou, J., 2005, "Laminar Flow Resistance in Short Microtubes," Int. J. Heat Fluid Flow, **26**(3), pp. 506–512.
[13] Jankowski, T. A., Schmierer, E. N., Prenger, F. C., and Ashworth, S. P., 2008, "A Series Pressure Drop Representation for Flow Through Orifice Tubes," ASME J. Fluids Eng., **130**(5), p. 051204.
[14] Kline, S. J., and McClintock, F. A., 1953, "Describing Uncertainties in Single-Sample Experiments," Mech. Eng. (Am. Soc. Mech. Eng.), **75**(1), pp. 3–8.
[15] Shah, R. K., 1978, "Correlation for Laminar Hydrodynamic Entry Length Solutions for Circular and Noncircular Ducts," ASME J. Fluids Eng., **100**(2), pp. 177–179.
[16] Womac, D. J., Ramadhyani, S., and Incropera, F. P., 1993, "Correlating Equations for Impingement Cooling of Small Heat Sources With Single Circular Liquid Jets," ASME J. Heat Transfer, **115**(1), pp. 106–116.
[17] Garimella, S. V., and Rice, R. A., 1995, "Confined and Submerged Liquid Jet Impingement Heat Transfer," ASME J. Heat Transfer, **117**(4), pp. 871–877.
[18] Gardon, R., and Cobonpue, J., 1962, "Heat Transfer Between a Flat Plate and Jets of Air Impinging on It," International Developments in Heat Transfer, ASME, New York, pp. 454–460.
[19] Lytle, D., and Webb, B. W., 1994, "Air Jet Impingement Heat Transfer at Low Nozzle-Plate Spacings," Int. J. Heat Mass Transfer, **37**(12), pp. 1687–1697.
[20] Lee, J., and Lee, S.-J., 1999, "Stagnation Region Heat Transfer of a Turbulent Axisymmetric Jet Impingement," Exp. Heat Transfer, **12**(2), pp. 137–156.
[21] Zhou, D. W., and Ma, C. F., 2006, "Radial Heat Transfer Behavior of Impinging Submerged Circular Jets," Int. J. Heat Mass Transfer, **49**(9–10), pp. 1719–1722.

Gunnar Tamm[1]
e-mail: gunnar.tamm@usma.edu

Daisie D. Boettner

Bret P. Van Poppel

Michael J. Benson

A. Özer Arnas

Department of Civil and Mechanical Engineering,
United States Military Academy,
West Point, NY 10996

On the Similarity Solution for Condensation Heat Transfer

Analytical solutions for laminar film condensation on a vertical plate are integral to many heat transfer applications, and have therefore been presented in numerous refereed articles and in most heat transfer textbooks. Commonly made assumptions achieve the well known similarity solution for the Nusselt number, heat transfer coefficient, and film thickness. Yet in all of these studies, several critical assumptions are made without justifying their use. Consequently, for a given problem one cannot determine whether these restrictive assumptions are actually satisfied, and thus, how these conditions can be checked for validity of the results. This study provides a detailed solution that clarifies these points. [DOI: 10.1115/1.3154920]

Keywords: film condensation, similarity solution, vertical plate

1 Introduction

The engineering significance of condensation heat transfer stems from Watt's steam engine, and remains critical to power and refrigeration applications. Nusselt provided the first rigorous analytical studies on condensation a century ago [1,2], and most heat transfer textbooks in recent decades discuss the condensation phenomena [3–29]. All of these textbooks, along with several handbooks [30–32] and refereed articles, make assumptions to obtain the Nusselt number, heat transfer coefficient, and boundary layer thickness for film condensation problems. However, none of the works in print present a complete and detailed similarity solution to show how the problem is solved analytically because the restrictive assumptions are not appropriately justified. This article demonstrates in a rigorous, analytical fashion the similarity-based solution, the physical meaning of the assumptions, and the conditions that the student and others must verify, prior to using the results.

2 Governing Equations

Conservation of mass, momentum, and energy must be considered in order to describe the convection in the boundary layer. The full forms of the conservation laws can be reduced for flow that is steady, two-dimensional, with constant and uniform properties, and without thermal generation. Additionally, applying an order of magnitude analysis, the conservation of mass, x-momentum, y-momentum, and energy become Eqs. (1)–(4), respectively. The x-direction is in the vertical, and the y-direction is normal to the plate surface.

$$\frac{\partial u}{\partial x} + \frac{\partial v}{\partial y} = 0 \tag{1}$$

$$u\frac{\partial u}{\partial x} + v\frac{\partial u}{\partial y} = g - \frac{1}{\rho}\frac{\partial p}{\partial x} + \nu\frac{\partial^2 u}{\partial y^2} \tag{2}$$

$$\frac{\partial p}{\partial y} = 0 \tag{3}$$

$$u\frac{\partial T}{\partial x} + v\frac{\partial T}{\partial y} = \frac{u}{\rho c_p}\frac{\partial p}{\partial x} + \alpha\frac{\partial^2 T}{\partial y^2} + \frac{\nu}{c_p}\left(\frac{\partial u}{\partial y}\right)^2 \tag{4}$$

As a consequence of order of magnitude analysis, a restriction that $\mathrm{Re}_L \geq 100$ at the end of the plate is found. Additionally, the Eckert number is shown to have an order of magnitude of one and the Péclet number $\mathrm{Pé} \geq 100$

$$\mathrm{Ec} = \frac{U_\infty^2}{c_p(T_w - T_\infty)} = O(1) \tag{5}$$

For cases where there is negligible freestream velocity, the Eckert number has an order of magnitude of much less than one $\mathrm{Ec} \ll O(1)$, and the pressure and viscous terms drop out from conservation of energy, reducing Eq. (4) to Eq. (6) for energy conservation.

$$u\frac{\partial T}{\partial x} + v\frac{\partial T}{\partial y} = \alpha\frac{\partial^2 T}{\partial y^2} \tag{6}$$

3 Assumptions to Simplify Governing Equations

For the condensation problem, Hsu [16], Lienhard [22], and others provide the following general assumptions:

(1) The temperature of the vapor T_v is constant and equal to the saturation temperature.
(2) The condensate film is laminar.
(3) Since the kinematic viscosity of the vapor is much less than that of the liquid, there is no frictional resistance on the liquid at the interface with the vapor.
(4) The inertia terms for the liquid are negligible, or

$$u\frac{\partial u}{\partial x} + v\frac{\partial u}{\partial y} = 0 \tag{7}$$

(5) The convection term in the liquid film is also negligible, or

$$u\frac{\partial T}{\partial x} + v\frac{\partial T}{\partial y} = 0 \tag{8}$$

The key element in this article, which is neglected in similar derivations found in the literature, is to present the validity of assumptions 2, 4, and 5. Additionally, this article presents the complete and rigorous similarity solution so that one has a way of satisfying the assumptions, prior to using the results obtained for the film thickness, the Nusselt number, and the convective heat transfer coefficient.

Since there are vapor and liquid phases present at equilibrium, there must be two equations characterizing the physical problem:

[1]Corresponding author.

Contributed by the Heat Transfer Division of ASME for publication in the JOURNAL OF HEAT TRANSFER. Manuscript received January 5, 2009; final manuscript received April 24, 2009; published online August 26, 2009. Review conducted by Yogesh Jaluria. Paper presented at the 2004 ASME International Mechanical Engineering Congress (IMECE 2004), Anaheim, CA, November 13–19, 2004.

one for the liquid film and one for the vapor. However, assumption 1, stating that the vapor temperature is a constant, eliminates the energy equation for the vapor. Assumption 3 eliminates the inertia and frictional terms of the momentum balance in Eq. (2) for the vapor giving

$$-\frac{1}{\rho_v}\frac{dp}{dx}+g=0$$

or

$$-\frac{1}{\rho}\frac{dp}{dx}=-\frac{\rho_v}{\rho}g \tag{9}$$

Substituting Eq. (9) into the momentum equation for the liquid, Eq. (2) results in

$$u\frac{\partial u}{\partial x}+v\frac{\partial u}{\partial y}=\nu\frac{\partial^2 u}{\partial y^2}+g\left(\frac{\rho-\rho_v}{\rho}\right) \tag{10}$$

Rose [33,34] gave rather a detailed study of condensation heat transfer as is done here. However, the validity of the assumptions is not shown explicitly for the student, instructor, and the researcher. Fujii [35], in his textbook, went through a number of the steps presented here. These will be referred to as they become significant. White [29] actually gave the combination of Eqs. (7) and (10), and of Eqs. (6) and (8); however, he does not show the consequences of the limitations of negligible inertia (assumption 4) and convection (assumption 5). The material discussed by White [29] is available in a series of articles by Rohsenow [36], in which he neglects the momentum changes at the start, and never shows how one can calculate the validity of the assumption. Sparrow and Gregg [37] neglected then retained the inertia terms for the liquid, but did not show how one might check the conditions under which either case is valid. Chen [38] included "the effect of the drag to an initially stationary body of vapor." He obtained the solution using the integral method and a perturbation procedure for numerical results. He did not include methods to check the validity of assumptions made.

4 Simplified Governing Equations

Since at equilibrium, the densities of liquid (ρ) and vapor (ρ_v) are constants, the buoyancy body force is independent of the temperature. In most cases, the density of the liquid is much larger than that of the vapor. Thus, conservation of mass for the liquid is

$$\frac{\partial u}{\partial x}+\frac{\partial v}{\partial y}=0 \tag{11}$$

Conservation of momentum for the liquid reduces to

$$u\frac{\partial u}{\partial x}+v\frac{\partial u}{\partial y}=\nu\frac{\partial^2 u}{\partial y^2}+g \tag{12}$$

Conservation of energy for the liquid is

$$u\frac{\partial T}{\partial x}+v\frac{\partial T}{\partial y}=\alpha\frac{\partial^2 T}{\partial y^2} \tag{13}$$

As shown in Fig. 1, the boundary conditions are

$$\text{at}\quad y=0,\quad u=v=0,\quad \text{and}\quad T=T_w \tag{14}$$

$$\text{at}\quad y=\delta,\quad \frac{\partial u}{\partial y}=0,\quad \text{and}\quad T=T_v \tag{15}$$

$$\text{at}\quad x=0\quad \text{and}\quad \delta=0 \tag{16}$$

since at the top of the plate ($x=0$), T, u, and v have no physical meaning. Now there are three equations (Eqs. (11)–(13)) with four unknowns (T, u, v, and δ). Thus, a fourth equation is required for a mathematically solvable system of four equations and four unknowns.

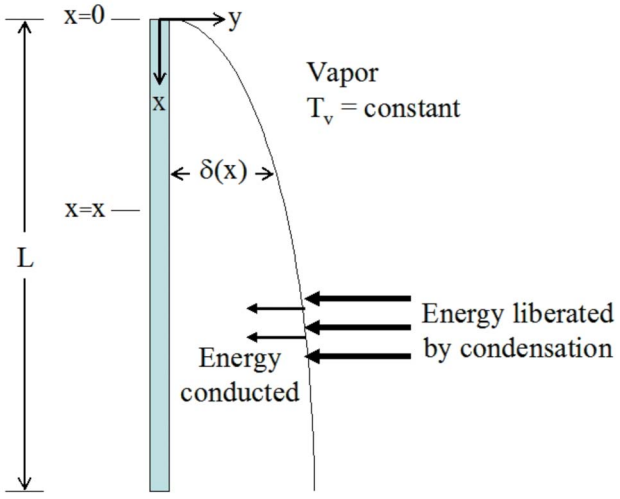

Fig. 1 Schematic of condensation film on a vertical plate

The fourth equation is obtained by introducing the latent heat of condensation i_{fg}, and performing an overall energy balance on the liquid film flowing down the plate, as shown in Fig. 1. In the region from $x=0$ to $x=x$, and at $y=\delta$, the mass flow rate per plate width is

$$\dot{m}=\rho\delta\bar{u}=\rho\delta\left[\frac{1}{\delta}\int_0^\delta u\,dy\right] \tag{17}$$

The total energy liberated at $y=\delta$ is $\dot{m}i_{fg}$, and is conducted into the liquid toward the wall. Thus, using Eq. (17) and Fourier's law

$$\rho i_{fg}\int_0^\delta u\,dy=k\int_0^x \left.\frac{\partial T}{\partial y}\right|_{y=\delta} d\xi \tag{18}$$

Equation (18) becomes the fourth equation since it is also in terms of T, u, v, and δ. Thus the problem of condensation is characterized by Eqs. (11)–(16) and (18).

5 Similarity Solution and Results

Using similarity transformations given as

$$\eta=\left(\frac{g}{4\nu^2 x}\right)^{1/4} y \tag{19}$$

$$\Psi(x,y)=(64g\nu^2x^3)^{1/4}f(\eta) \tag{20}$$

$$\Theta=\frac{T-T_v}{T_w-T_v} \tag{21}$$

conservation of mass Eq. (11) is identically satisfied, applying the normal definition of the stream function. Momentum in Eq. (12) transforms to Eq. (22)

$$f'''+3ff''-2(f')^2+1=0 \tag{22}$$

and energy Eq. (13) transforms to Eq. (23)

$$\Theta''+3\,\mathrm{Pr}\,f\Theta'=0 \tag{23}$$

Boundary conditions in Eqs. (14) and (15) become

$$\text{at}\quad \eta=0,\quad f=f'=0,\quad \text{and}\quad \Theta=1 \tag{24}$$

$$\text{at}\quad \eta=\eta_\delta,\quad f''=0,\quad \text{and}\quad \Theta=0 \tag{25}$$

where

Table 1 Physical descriptions of terms in untransformed and transformed equations

Physical description	Untransformed equation term	Transformed equation term
Viscous force	$\nu\frac{\partial^2 u}{\partial y^2}$	f'''
Inertia force	$u\frac{\partial u}{\partial x}+\nu\frac{\partial u}{\partial y}$	$3ff''-2(f')^2$
Body force	g	1
Conduction	$\alpha\frac{\partial^2 T}{\partial y^2}$	Θ''
Convection	$u\frac{\partial T}{\partial x}+\nu\frac{\partial T}{\partial y}$	$3\,\mathrm{Pr}\,f\Theta'$

$$\eta_\delta=\left(\frac{g}{4\nu^2 x}\right)^{1/4}\delta \tag{26}$$

Burmeister [9] goes through the similarity calculations and obtains Eqs. (22) and (23); however, the analysis is not carried out any further.

The physical descriptions of the terms in the transformed and untransformed equations are shown in Table 1. This physical meaning is important since various terms will be dropped, based on the assumptions made in the analysis that follows.

In order for similarity to hold, all equations and boundary conditions should be independent of the variable x. Equation (18) must be transformed using Eqs. (19)–(21). The right hand side of Eq. (19) (the term for conduction into the liquid layer) transforms to

$$k\int_0^x \left.\frac{\partial T}{\partial y}\right|_{y=\delta} d\xi=-k(T_v-T_w)\int_0^x \left.\frac{\partial\Theta}{\partial\eta}\right|_{\eta=\eta_\delta}\left(\frac{g}{4\nu^2\xi}\right)^{1/4}d\xi$$

$$=-k(T_v-T_w)\left(\frac{g}{4\nu^2}\right)^{1/4}\int_0^x \Theta'(\eta_\delta)\xi^{-1/4}d\xi$$

Assuming $\Theta'(\eta_\delta)$ is constant, a requirement if η_δ is constant, and integrating yields

$$k\int_0^x \left.\frac{\partial T}{\partial y}\right|_{y=\delta} d\xi=-\frac{4}{3}k(T_v-T_w)\Theta'(\eta_\delta)\left(\frac{gx^3}{4\nu^2}\right)^{1/4} \tag{27}$$

Similarly transforming the left hand side of Eq. (18) (the term for total energy liberated during condensation) and integrating yields

$$\rho i_{fg}\int_0^\delta u dy=\rho i_{fg}\int_0^{\eta_\delta} 2(gx)^{1/2}f'(\eta)\left(\frac{4\nu^2 x}{g}\right)^{1/4}d\eta$$

$$=\rho i_{fg}(64g\nu^2x^3)^{1/4}f(\eta_\delta) \tag{28}$$

since $f(0)=0$. Substituting Eqs. (27) and (28) into Eq. (18) yields

$$\frac{k(T_v-T_w)}{\nu\rho i_{fg}}=-3\frac{f(\eta_\delta)}{\Theta'(\eta_\delta)} \tag{29}$$

Multiplying Eq. (29) by the Prandtl number $\mathrm{Pr}=\frac{c_p\mu}{k}$ yields

$$\frac{c_p(T_v-T_w)}{i_{fg}}=-3\,\mathrm{Pr}\frac{f(\eta_\delta)}{\Theta'(\eta_\delta)} \tag{30}$$

which is a similar result obtained by Sparrow and Gregg [37]. Since x no longer appears in Eq. (29) or Eq. (30), then η_δ is either a constant or $\delta\approx x^{1/4}$ for similarity to hold.

Thus, for condensation heat transfer, the governing sets of equations are Eqs. (22)–(30), with boundary conditions given by Eqs. (24) and (25). The properties are those of the liquid since the vapor is at constant temperature, T_v is nonviscous, and has negligible density compared with that of the liquid. Equation (30) is obtained by Rohsenow and Choi [25] without going further with any discussion.

To obtain the exact solution, choose a value for η_δ for a given Prandtl number, and solve the momentum and energy equations simultaneously. Substitute the result into the energy balance equation. Repeat the process until the value converges to the value chosen for η_δ.

However, a meaningful approximate solution can be obtained using a power series that satisfy the boundary conditions at $\eta=0$ for both the velocity distribution

$$f=C_1\eta^2-\frac{1}{6}\eta^3+\frac{C_1^2}{30}\eta^5+\ldots \tag{31}$$

and for the temperature distribution

$$\Theta=1+C_2\eta-\mathrm{Pr}\frac{C_1C_2}{4}\eta^4+\ldots \tag{32}$$

where C_1 and C_2 are constants. For $\eta=1$, as an approximation

$$f=C_1\eta^2-\frac{1}{6}\eta^3 \tag{33}$$

$$\Theta=1+C_2\eta \tag{34}$$

These distributions, Eqs. (33) and (34), also satisfy

$$f'''+1=0 \tag{35}$$

for negligible inertia, and

$$\Theta''=0 \tag{36}$$

for negligible convection in the film, such that all energy transfer is by conduction from the outside film to the plate surface. Equations (35) and (36) are obtained by Fujii [35].

For these solutions to be valid, the condition $\eta<1$ must be satisfied. For the condition of negligible inertia

$$\frac{C_1^2}{30}\eta_\delta^5\ll\frac{1}{6}\eta_\delta^3 \tag{37}$$

or

$$\eta_\delta^2\ll\frac{5}{C_1^2} \tag{38}$$

must be satisfied. For the condition of negligible convection

$$\mathrm{Pr}\frac{C_1C_2}{4}\eta_\delta^4\ll C_2\eta_\delta \tag{39}$$

or

$$\eta_\delta^3\ll\frac{4}{C_1\,\mathrm{Pr}} \tag{40}$$

must be satisfied. The three conditions, Eqs. (38) and (40), and laminar flow, form the restrictions of the above solutions and, therefore, analyses. Differentiating Eq. (33) twice and evaluating at η_δ yields $f''(\eta_\delta)=2C_1-\eta_\delta$. Applying the boundary condition $f''(\eta_\delta)=0$ at $\eta=\eta_\delta$ (Eq. (25)) yields

$$C_1=\frac{\eta_\delta}{2} \tag{41}$$

Substituting back into Eq. (33) gives for the distribution

$$f=\frac{\eta_\delta^3}{2}\left[\left(\frac{\eta}{\eta_\delta}\right)^2-\frac{1}{3}\left(\frac{\eta}{\eta_\delta}\right)^3\right] \tag{42}$$

Since $\Theta=0$ at $\eta=\eta_\delta$, then $C_2=-1/\eta_\delta$, resulting in the temperature distribution

$$\Theta = 1 - \left(\frac{\eta}{\eta_\delta}\right) \tag{43}$$

Equations (41)–(43) are also obtained by Fujii [35]; however, ways on how to validate the assumptions are not presented.

The energy balance equation requires the values of $f(\eta_\delta)$ and $\Theta'(\eta_\delta)$. Thus, upon substitution of Eqs. (42) and (43) into Eq. (30)

$$\frac{c_p(T_v - T_w)}{i_{fg}} = \left[-3\,\mathrm{Pr}\left(\frac{\eta_\delta^3}{3}\right)\right] \Big/ \left[-\frac{1}{\eta_\delta}\right] = \mathrm{Pr}(\eta_\delta)^4$$

Solving for η_δ yields

$$\eta_\delta = \left[\frac{c_p(T_v - T_w)}{i_{fg}\,\mathrm{Pr}}\right]^{1/4} \tag{44}$$

Substituting for η_δ from Eq. (26) into Eq. (44) gives Eq. (45), which is the boundary layer thickness result given in almost all textbooks

$$\delta = \left[\frac{4c_p\nu^2 x(T_v - T_w)}{g i_{fg}\,\mathrm{Pr}}\right]^{1/4} \tag{45}$$

Substituting Eqs. (19) and (21) into the heat flux equation

$$q'' = k\left[\frac{\partial T}{\partial y}\right]_{y=0}$$

results in

$$q'' = -k(T_v - T_w)\Theta'(0)\left(\frac{g}{4\nu^2 x}\right)^{1/4} \tag{46}$$

As discussed by Seban in Ref. [37], for

$$\Theta'(0) = -\frac{1}{\eta_\delta} = -\left[\frac{i_{fg}\,\mathrm{Pr}}{c_p(T_v - T_w)}\right]^{1/4}$$

the heat flux reduces to

$$q'' = k(T_v - T_w)\left(\frac{g i_{fg}\,\mathrm{Pr}}{4\nu^2 x c_p(T_v - T_w)}\right)^{1/4}$$

Thus, applying Newton's Law of Cooling, the local Nusselt number $\mathrm{Nu}_x = h_x x/k$ can be obtained as

$$\mathrm{Nu}_x = \left(\frac{q''}{T_v - T_w}\right)\frac{x}{k}$$

or

$$\mathrm{Nu}_x = \left[\frac{g i_{fg}\,\mathrm{Pr}\,x^3}{4c_p(T_v - T_w)\nu^2}\right]^{1/4} \tag{47}$$

Using an alternate definition of the Prandtl number $\mathrm{Pr} = \nu\rho c_p/k$, the local Nusselt number, as found in most textbooks, becomes

$$\mathrm{Nu}_x = 0.70711\left[\frac{g\rho i_{fg}x^3}{k\nu(T_v - T_w)}\right]^{1/4} \tag{48}$$

Once the local Nusselt number is known, the local convective heat transfer coefficient is determined by

$$h_x = \frac{\mathrm{Nu}_x k}{x} \tag{49}$$

Prior to using the three results, Eqs. (45) and (47) or (48) and (49), the three restrictive conditions, Eqs. (7) and (8), and the laminar film condensate, must be validated.

6 Validation of Restrictive Conditions

The validation of this result is the most important aspect of this paper. Nowhere in literature does it exist so that the student can depend on the use of the results. Therefore, the range of applicability for this result is as follows:

(1) *Negligible inertia*. Using Eqs. (38) and (40),

$$\left[\frac{c_p(T_v - T_w)}{i_{fg}\,\mathrm{Pr}}\right] \ll 20$$

which implies

$$\left[\frac{c_p(T_v - T_w)}{i_{fg}\,\mathrm{Pr}}\right] < 2 \tag{50}$$

Sparrow and Gregg [37] reported this result but not as a limitation for the final solution. White [29] presented a similar result in the form of $\mathrm{Ja} \ll 1$; however, since no analysis is given, it is a mystery as to how it is obtained.

(2) *Negligible convection*. Using Eqs. (40) and (41),

$$\left[\frac{c_p(T_v - T_w)}{i_{fg}}\right] \ll 8$$

which implies

$$\left[\frac{c_p(T_v - T_w)}{i_{fg}}\right] < 0.8 \tag{51}$$

White [29] reported this result in the form $(\mathrm{Re}_\delta \mathrm{Ja}/\mathrm{Pr}) \ll 1$, again with no analysis.

Thus, both conditions, Eqs. (50) and (51), must hold in addition to the laminar film assumption before Eq. (45) for boundary layer thickness or Eq. (47) or Eq. (48) for Nu_x would have any validity. Nowhere in literature do these exist as an explicit equation, which can be utilized by the student, instructor, or the researcher.

For the range of applicability for the laminar film condition, and following Giedt [15],

$$\overline{\mathrm{Re}}_{D_H} = \frac{4\bar{u}\delta}{\nu} < 2000 \tag{52}$$

where D_H is the hydraulic diameter equal to the ratio of the cross-sectional area of the conduit to the wetted perimeter. Mean velocity is given by

$$\bar{u} = \delta\left[\frac{1}{\delta}\int_0^\delta u\,dy\right]$$

Upon transformation and substitution of Eqs. (19) and (20), mean velocity becomes

$$\bar{u} = \frac{(64g\nu^2x^3)^{1/4}}{\delta} f(\eta_\delta) \tag{53}$$

Using Eqs. (42), (45), and (53), Eq. (52) reduces to

$$\left[\frac{c_p(T_v - T_w)}{i_{fg}\,\mathrm{Pr}}\right] < 4293\left(\frac{\nu^2}{gx^3}\right)^{1/3} \tag{54}$$

Equations (50), (51), and (54) are the restrictive conditions. Therefore, in order to use Eqs. (45) and (47) or (48) and (49), the inequalities of Eqs. (50), (51), and (54) must be satisfied. If any of these conditions is not met, then the equations for the boundary layer thickness, the Nusselt number, and the local convective heat transfer coefficient, Eqs. (45) and (47) or (48) and (49), respectively, cannot be used.

7 Conclusions

Heat transfer analyses are important particularly in engineering design of devices involving condensation. Therefore, condensation results given in textbooks are integral to this design process. However, none of the textbooks in print go through the complete and analytically rigorous similarity analysis, showing the required restrictions on the applicability of the results to calculate the boundary layer thickness, the Nusselt number, or the convective heat transfer coefficient, Eqs. (45) and (47) or (48) and (49). This

article identifies and quantifies these critical three restrictive conditions, Eqs. (50), (51), and (54), that one must satisfy before using any of the results.

Nomenclature

C = constant
c = specific heat, (kJ/kg K)
D = substantial (material) derivative
e = internal energy, (kJ/kg)
Ec = Eckert number, $U_\infty^2/c_p(T_w-T_\infty)$
F = force vector per mass, (N/kg)
f = similarity velocity transform
g = gravitational acceleration, (m/s^2)
h = convective heat transfer coefficient, (W/(m^2 K))
i = enthalpy, (kJ/kg)
Ja = Jacob number, $c_p(T_v-T_w)/i_{fg}$
k = thermal conductivity, (W/m K)
m = mass, (kg)
p = pressure, (kPa)
Pé = Péclet number, (Re)(Pr)
Pr = Prandtl number, $c_p\mu/k=\nu/\alpha=c_p\rho\nu/k$
Re = Reynolds number, $\boldsymbol{V}x_c/\nu$
T = temperature, (K)
T = time, (s)
u = velocity component in the x direction, (m/s)
$\bar{u}$ = mean velocity, (m/s)
v = velocity component in the y direction, (m/s)
V = volume, (m^3)
$\boldsymbol{V}$ = velocity, (m/s)
w = velocity component in the z direction, (m/s)
x = direction, (m)
y = direction, (m)
z = direction, (m)

Subscripts

c = characteristic
D_H = hydraulic diameter, (m)
fg = liquid-vapor phase change
L = length
p = constant pressure
v = constant volume, vapor
w = wall
∞ = freestream
δ = evaluated at the boundary layer thickness

Superscripts

$'$ = derivative with respect to time

Greek Symbols

α = thermal diffusivity, (m^2/s)
δ = boundary layer thickness, (m)
∇ = vector operator
ϕ = viscous dissipation, (W/m^3)
η = similarity coordinate transform
Θ = nondimensional temperature
μ = dynamic viscosity, (N s/m^2)
ν = kinematic viscosity, (m^2/s)
ξ = dummy variable
ρ = density, (kg/m^3)
Ψ = stream function

References

[1] Nusselt, W., 1915, "Das Grundgesetz des Wärmeüberganges," Gesund.-Ing., **38**(42), pp. 477–482 and 490–496.
[2] Nusselt, W., 1916, "Die Oberflächenkondensation des Wasserdampfes," Z. Ver. Dtsch. Ing., **60**(28), pp. 541–546 and 569–575.
[3] Arpaci, V., and Larsen, P., 1984, *Convection Heat Transfer*, Prentice-Hall, Englewood Cliffs, NJ.
[4] Bayley, F. J., Owen, J. R., and Turner, A. B., 1972, *Heat Transfer*, Barnes & Noble, New York.
[5] Bejan, A., 1993, *Heat Transfer*, Wiley, New York.
[6] Bejan, A., 1995, *Convection Heat Transfer*, 2nd ed., Wiley, New York.
[7] Bennett, C. O., and Myers, J. E., 1974, *Momentum, Heat and Mass Transfer*, 2nd ed., McGraw-Hill, New York.
[8] Boelter, L. M. K., Cherry, V. H., and Johnson, H. A., 1965, *Heat Transfer Notes*, McGraw-Hill, New York.
[9] Burmeister, L. C., 1983, *Convective Heat Transfer*, Wiley, New York.
[10] Çengel, Y. A., 1998, *Heat Transfer: A Practical Approach*, McGraw-Hill, New York.
[11] Chapman, A. J., 1984, *Heat Transfer*, 4th ed., Macmillan, New York.
[12] Eckert, E. R. G., 1963, *Introduction to Heat and Mass Transfer*, McGraw-Hill, New York.
[13] Eckert, E. R. G., and Drake, R. M., Jr., 1972, *Analysis of Heat and Mass Transfer*, McGraw-Hill, New York.
[14] Gebhart, B., 1961, *Heat Transfer*, McGraw-Hill, New York.
[15] Giedt, W. H., 1957, *Principles of Engineering Heat Transfer*, Van Nostrand, Princeton, NJ.
[16] Hsu, S. T., 1963, *Engineering Heat Transfer*, Van Nostrand, Princeton, NJ.
[17] Incropera, F. P., DeWitt, D. P., Bergman, T. L., and Lavine, A. S., 2007, *Fundamentals of Heat and Mass Transfer Heat Transfer*, 6th ed., Wiley, New York, NY.
[18] Isachenko, V., Osipova, V., and Sukomel, A., 1969, *Heat Transfer*, MIR, Moscow.
[19] Janna, W. S., 1986, *Engineering Heat Transfer*, PWS, Boston, MA.
[20] Kays, W. M., and Crawford, M. E., 1993, *Convective Heat and Mass Transfer*, McGraw-Hill, New York.
[21] Kreith, F., and Bohn, M. S., 2001, *Principles of Heat Transfer*, 6th ed., Brooks-Cole, Pacific Grove, CA.
[22] Lienhard, J. H., 1981, *A Heat Transfer Textbook*, Prentice-Hall, Englewood Cliffs, NJ.
[23] McAdams, W. H., 1954, *Heat Transmission*, McGraw-Hill, New York.
[24] Mills, A. F., 1995, *Heat and Mass Transfer*, Richard D. Irwin, Inc., Boston, MA.
[25] Rohsenow, W. M., and Choi, H., 1961, *Heat, Mass, and Momentum Transfer*, Prentice-Hall, Englewood Cliffs, NJ.
[26] Thomas, L. C., 1999, *Heat Transfer*, 2nd ed., Capstone Publishing Corporation, Tulsa, OK.
[27] Welty, J. R., 1974, *Engineering Heat Transfer*, Wiley, New York, NY.
[28] Whitaker, S., 1977, *Fundamental Principles of Heat Transfer*, Pergamon, New York.
[29] White, F. M., 1984, *Heat Transfer*, Addison-Wesley, Reading, MA.
[30] Butterworth, D., 1983, "Film Condensation of Pure Vapor," *Heat Exchanger Design Handbook*, Vol. 2, Hemisphere, New York, 2.62-B.
[31] Hewitt, G. F., Shires, G. L., and Polezhaev, Y. V., eds., 1997, *International Encyclopedia of Heat and Mass Transfer*, CRC, Boca Raton, FL.
[32] Rohsenow, W. M., 1973, "Film Condensation," *Handbook of Heat Transfer*, Vol. 12A, McGraw-Hill, New York.
[33] Rose, J. W., 1988, "Fundamentals of Condensation Heat Transfer: Laminar Film Condensation," JSME Int. J., Ser. II, **31**(3), pp. 357–375.
[34] Rose, J. W., 1998, "Condensation Heat Transfer Fundamentals," Trans. Inst. Chem. Eng., Part A, **76**, pp. 143–152.
[35] Fujii, T., 1991, *Theory of Laminar Film Condensation*, Springer, New York.
[36] Rohsenow, W. M., 1956, "Heat Transfer and Temperature Distribution in Laminar-Film Condensation," Trans. ASME, **78**, pp. 1645–1648.
[37] Sparrow, E. M., and Gregg, J. L., 1959, "A Boundary Layer Treatment of Laminar-Film Condensation," Trans. ASME, Ser. C: J. Heat Transfer, **81**, pp. 13–18.
[38] Chen, M. M., 1961, "An Analytical Study of Laminar Film Condensation: Part 1—Flat Plates," Trans. ASME, Ser. C: J. Heat Transfer, **83**, pp. 48–60.

Periodic Fluid Flow and Heat Transfer in a Square Cavity Due to an Insulated or Isothermal Rotating Cylinder

Y.-C. Shih
Department of Energy and Refrigerating Air-Conditioning Engineering, National Taipei University of Technology, 1, Sec. 3, Chung-Hsiao, E. Road, Taipei, Taiwan 106, R.O.C.
e-mail: f10958@ntut.edu.tw

J. M. Khodadadi[1]
Department of Mechanical Engineering, 270 Ross Hall, Auburn University, AL 36849-5341
e-mail: khodajm@auburn.edu

K.-H. Weng
Department of Energy and Refrigerating Air-Conditioning Engineering, National Taipei University of Technology, 1, Sec. 3, Chung-Hsiao, E. Road, Taipei, Taiwan 106, R.O.C.

A. Ahmed
Department of Aerospace Engineering, Auburn University, AL 36849

The periodic state of laminar flow and heat transfer due to an insulated or isothermal rotating cylinder object in a square cavity is investigated computationally. A finite-volume-based computational methodology utilizing primitive variables is used. Various rotating objects (circle, square, and equilateral triangle) with different sizes are placed in the middle of a square cavity. A combination of a fixed computational grid and a sliding mesh was utilized for the square and triangle shapes. For the insulated and isothermal objects, the cavity is maintained as differentially heated and isothermal enclosures, respectively. Natural convection heat transfer is neglected. For a given shape of the object and a constant angular velocity, a range of rotating Reynolds numbers are covered for a $Pr=5$ fluid. The Reynolds numbers were selected so that the flow fields are not generally affected by the Taylor instabilities ($Ta<1750$). The periodic flow field, the interaction of the rotating objects with the recirculating vortices at the four corners, and the periodic channeling effect of the traversing vertices are clearly elucidated. The simulations of the dynamic flow fields were confirmed against experimental data obtained by particle image velocimetry. The corresponding thermal fields in relation to the evolving flow patterns and the skewness of the temperature contours in comparison to the conduction-only case were discussed. The skewness is observed to become more marked as the Reynolds number is lowered. Transient variations of the average Nusselt numbers of the respective systems show that for high Re numbers, a quasiperiodic behavior due to the onset of the Taylor instabilities is dominant, whereas for low Re numbers, periodicity of the system is clearly observed. Time-integrated average Nusselt numbers of the insulated and isothermal object systems were correlated with the rotational Reynolds number and shape of the object. For high Re numbers, the performance of the system is independent of the shape of the object. On the other hand, with lowering of the hydraulic diameter (i.e., bigger objects), the triangle and the circle exhibit the highest and lowest heat transfers, respectively. High intensity of the periodic channeling and not its frequency is identified as the cause of the observed enhancement. [DOI: 10.1115/1.3154620]

1 Introduction

Control and regulation of convective flows through active and passive means are extremely important to design of heat exchange systems. To this end, variations of both techniques in a simple square cavity addressing lid-driven flow [1], buoyancy-driven convection within a differentially heated cavity [2], and forced convection within a cavity with inlet and outlet ports [3] have been studied. In addition to the simplicity of the square cavity geometry, the observed cavity flows exhibited simultaneous existence of diverse regimes involving boundary layers, multiple cellular flow regions, and dynamic flow fields. Moreover, many practical problems can be simplified to a cavity model. These include design of mixing chambers, cooling of electronic components, ventilation of buildings, design of solar collectors, thermal storage units, lubrication of journal bearings, etc.

One technique for active regulation of heat transfer in convection-dominated heat exchange systems is through controlled movement of a wetted boundary. In order to assess the viability of this idea to a square cavity with rigid walls, a computational study of the flow and thermal fields due to a rotating object in a square cavity was undertaken. In light of the mathematical complexity of the analysis of unsteady flow of a noncircular rotating cylinder (triangle and rectangle) in a square cavity, no prior study with such a focus exists. Rotating circular cylinders within rectangular enclosures lend themselves to a steady formulation and were studied by Lewis [4] and Hellou and Coutanceau [5], respectively. A study of two rotating circular cylinders within a rectangle was reported by Hills [6]. Kimura et al. [7] provide experimental data for natural convection within a differentially heated square cavity that is affected by a rotating horizontal circular cylinder.

Undoubtedly, the classic problem of flow within the spacing of two concentric circular cylinders in relative motion is linked to the subject of this paper. In extending the applicability of this classic problem to oil drilling operations, a great number of investigations have reported the effects of eccentricity of the inner circular cylinder and behavior of non-Newtonian fluids. Most notably, the exhaustive list of references provided by Escudier et al. [8] can be a good starting point for those interested in this related problem.

In covering the spectrum of thermal boundary conditions and keeping in mind the limiting problems of nonrotating objects as benchmark states, results for the two cases of an insulated rotating object within a differentially heated square cavity and an isothermal rotating object within a square cavity with constant wall tem-

[1]Corresponding author.

Contributed by the Heat Transfer Division of ASME for publication in the JOURNAL OF HEAT TRANSFER. Manuscript received July 30, 2008; final manuscript received April 26, 2009; published online August 19, 2009. Review conducted by Minking Chyu. Paper presented at the 2007 ASME-JSME Thermal Engineering Conference and Summer Heat Transfer Conference (HT2007), Vancouver, BC, Canada, July 8–12, 2007.

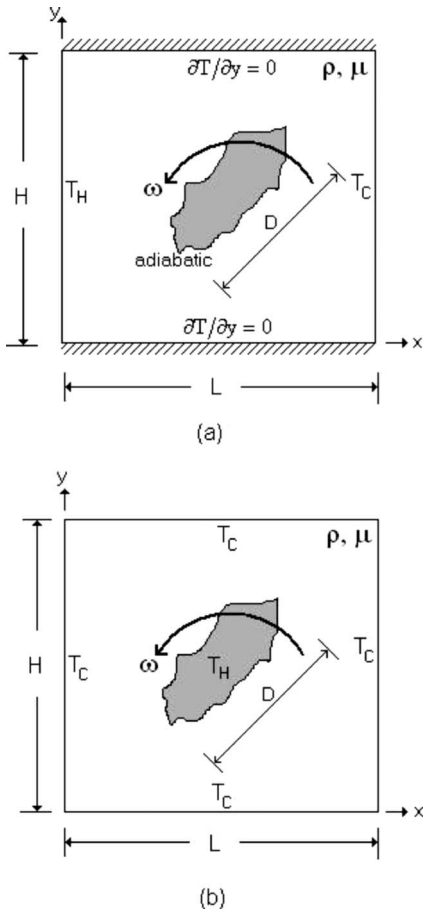

Fig. 1 Schematic diagrams of a rotating (*a*) insulated object within a differentially heated cavity and (*b*) isothermal object within a cavity with a different constant temperature

peratures are discussed in this paper. Analyses of noncircular rotating cylinders (square and triangle) stand out as a novel aspect of the present study.

2 Problem Formulation

The physical models for two 2D cavities (height H and length L) are shown in Figs. 1(a) and 1(b). For the present study, it is assumed that $H=L$ and four walls of the cavities are stationary. The fluid within the cavities is assumed to be incompressible with constant properties. An object is allowed to rotate within the cavities with the rotational speed ω. The axis of rotation passes through the centroid of the object that coincides with the center of the cavities. Three rotating objects, including circle, square, and equilateral triangle, are considered. The rotating object is assumed to be made of an insulated material in Fig. 1(a), whereas a highly conductive object (thus isothermal) is considered in Fig. 1(b). For the adiabatic object (Fig. 1(a)), the left and right walls are maintained at constant temperatures T_H and T_C, respectively, whereas the top and bottom walls are insulated. For the case of an isothermal object (Fig. 1(b)), its temperature is kept at a constant value (T_H) different from the remaining walls of the cavity (T_C). For both cases, the condition $T_H > T_C$ is assumed. The gravity effect and viscous dissipation are neglected. The scope of this study is only limited to the laminar flow regime. Moreover, in order to avoid Taylor instabilities, the Taylor number that is defined as

$$\mathrm{Ta} = \frac{R\rho^2(0.5H - R)^3\omega^2}{\mu^2} \tag{1}$$

needs to be below 1750 [9], with R being the radius of an equivalent object with a circular cross section. This equivalency issue will be clarified in Sec. 2.1.

2.1 Geometric and Dynamic Scaling of the Problem. The side of the cavity is a natural length scale for the geometric scaling of the problem. However, the dynamics of the flow field needs to be scaled with a meaningful length scale associated with the passageway available to the fluid. Such a hydraulic diameter is defined in studies of porous media and is expressed by Middleman [10]

$$D_h = 2\frac{\text{fluid volume}}{\text{wetted area}} \tag{2}$$

For a rotating cylinder with a circular cross section (diameter D), the hydraulic diameter is

$$D_{h,c} = 2\frac{H^2 - \pi D^2/4}{4H + \pi D} \tag{3}$$

Hydraulic diameter for a square (side ℓ) in the cavity is given by

$$D_{h,s} = 2\frac{H^2 - \ell^2}{4H + 4\ell} \tag{4}$$

whereas for an equilateral triangle (side S) in the cavity, it is

$$D_{h,t} = 2\frac{H^2 - \sqrt{3}/4S^2}{4H + 3S} \tag{5}$$

Using these relations to impose equivalency of the hydraulic diameters, one will be able to directly compare the benefits and drawbacks of various shapes. Note that for very small objects, the hydraulic diameter tends to $H/2$.

2.2 Dimensionless Form of the Governing Equations. The dimensionless form of the governing equations can be obtained via introducing the following dimensionless variables:

$$X = \frac{x}{H}, \quad Y = \frac{y}{H}, \quad U = \frac{u}{D_h\omega}, \quad V = \frac{v}{D_h\omega}$$
$$P = \frac{p}{\rho D_h^2\omega^2}, \quad \Theta = \frac{T - T_C}{T_H - T_C}, \quad t^* = \frac{D_h\omega t}{H} \tag{6}$$

The governing equations of continuity, momentum, and thermal energy are then written in dimensionless forms:

$$\frac{\partial U}{\partial X} + \frac{\partial V}{\partial Y} = 0 \tag{7}$$

$$\frac{\partial U}{\partial t^*} + U\frac{\partial U}{\partial X} + V\frac{\partial U}{\partial Y} = -\frac{\partial P}{\partial X} + \frac{D_h}{H}\frac{1}{\mathrm{Re}}\left(\frac{\partial^2 U}{\partial X^2} + \frac{\partial^2 U}{\partial Y^2}\right) \tag{8}$$

$$\frac{\partial V}{\partial t^*} + U\frac{\partial V}{\partial X} + V\frac{\partial V}{\partial Y} = -\frac{\partial P}{\partial Y} + \frac{D_h}{H}\frac{1}{\mathrm{Re}}\left(\frac{\partial^2 V}{\partial X^2} + \frac{\partial^2 V}{\partial Y^2}\right) \tag{9}$$

$$\frac{\partial \Theta}{\partial t^*} + U\frac{\partial \Theta}{\partial X} + V\frac{\partial \Theta}{\partial Y} = \frac{D_h}{H}\frac{1}{\mathrm{Re}\,\mathrm{Pr}}\left(\frac{\partial^2 \Theta}{\partial X^2} + \frac{\partial^2 \Theta}{\partial Y^2}\right) \tag{10}$$

with the Prandtl number defined as $\mathrm{Pr} = \nu/\alpha$ and the Reynolds number is based on the hydraulic diameter D_h:

$$\mathrm{Re} = \frac{\rho D_h^2\omega}{\mu} \tag{11}$$

The effect of natural convection is neglected, so that the ratio $\mathrm{Gr}/\mathrm{Re}^2$ is taken to be much smaller than 1. Consequently, this problem is dependent on the dimensionless parameter D_h/H, Pr,

Table 1 Number of cycles for three rotating isothermal objects to reach periodic or quasiperiodic states for nine size ratios

		Circle	Square	Triangle
Re=111	Ta=1244	1801	362	670
Re=92	Ta=1748	165	234	644
Re=74	Ta=1756	160	107	131
Re=58	Ta=1475	125	93	100
Re=44	Ta=1067	105	82	91
Re=31	Ta=655	90	47	86
Re=21	Ta=323	75	41	N/A
Re=12	Ta=109	70	37	N/A
Re=6	Ta=15	60	N/A	N/A

and Re; however, it must be noted that in this paper with ω =const, the hydraulic diameter to cavity side ratio and the Reynolds numbers are linked to each other. Thus, combinations of the Pr and Re numbers define this problem.

To simplify the numerical simulation, the rotating objects are assumed to be hollow. The flow boundary conditions on the cavity walls and on the surface of the rotating object satisfy the no-slip condition. For the insulated rotating objects, adiabatic condition ($\partial\Theta/\partial n=0$) is imposed on their surfaces, with n standing for the unit normal vector on that surface. The thermal boundary conditions of the left and right walls of the cavity are fixed at $\Theta=1$ and $\Theta=0$, respectively, and the remaining walls are insulated. For the isothermal rotating objects, $\Theta=1$ is imposed on their surfaces. The thermal boundary conditions of cavity walls are fixed at $\Theta=0$. Regardless of the thermal states of the solid boundaries, the initial conditions for velocity and temperature fields are zero velocity and $\Theta=0$, respectively.

In this study, the Prandtl number of the fluid is fixed to 5. The effect of the size of the rotating objects on the transient behavior of fluid flow and heat transfer within the cavity were studied by varying the Reynolds numbers between 6 and 111, while keeping the angular velocity constant (Table 1). For the case of a rotating circle, this was achieved by varying the diameter to side ratio (D/H) from 0.1 (Re=111) to 0.9 (Re=6) in 0.1 increments (a total of nine cases). As for the rotating square and triangle objects, their dimensions were computed by demanding an equivalent hydraulic diameter and utilizing Eqs. (4) and (5), respectively. For the square and triangle shapes, the viable number of cases that did not involve collision of the object and the cavity were eight and six, respectively. Therefore, a total of 23 cases were simulated for different shapes. The Taylor numbers for these runs were kept of the order of 1750 or lower.

2.3 Computational Details. The numerical technique adopted in this study is based on the finite volume method [11]. The unsteady governing equations including continuity, momentum, and thermal energy equations can be expressed in their conservative form and are solved by the computational fluid dynamics (CFD) software FLUENT [12]. In this study, a hybrid structured/unstructured staggered grid system is used. The diffusion-convection term of the conservative equation is discretized by the second-order upwind scheme and the second-order implicit method is used to discretize the transient term. By employing the iterative scheme of a point implicit (Gauss–Seidel) linear equation solver in conjunction with an algebraic multigrid (AMG) method, the pressure, velocity, and temperature fields can be solved. During the iterative procedure, the PISO algorithm is employed to solve the pressure-velocity coupling equations.

To simulate the flow field generated by a rotating circular object, a boundary condition of velocity magnitude equal to $R\omega$ is imposed on the surface of the circle. Regarding the flow induced by the rotating object with the shape of a square or an equilateral triangle, the method of sliding meshes is employed in view of its availability in the chosen commercial CFD code, thus favoring it over other existing methodologies for treating moving boundary problems (e.g., Behr and Tezduyar [13] and Tai et al. [14]). In utilizing a sliding mesh, one does not need to regrid at each time step, so that the grid number is always the same. The computational domain is divided into two parts. One is the rotating zone and the other is the stationary region. The rotating zone is defined as a circular region, part of which contains the square or equilateral triangle object. A grid interface to connect both regions needs to be defined. Once the simulation is started, the rotating zone slides along the grid interface thus causing the square or triangle object to spin, whereas the grids in the stationary region are kept motionless.

It takes a time period equal to $\tau=2\pi/\omega$ for a fixed point on an object to rotate one revolution. After conducting a time-step independence test, the time step for numerical simulation was chosen as $\tau/240$. Grid-independence tests for various objects were undertaken. For instance, a grid-independence test for a rotating circle at Re=111 was performed for five grid densities (6000, 12,900, 22,400, 34,500, and 49,200 cells) for an isothermal rotating object inside a constant temperature cavity. The numerical results revealed that the relative errors for both average skin friction coefficients and average Nusselt numbers on the surface of the rotating circle and cavity walls decrease with the increase in grid density. The difference between the numerical results based on the 34,500 and 49,200 cells was insignificant. The grid-independence test proved the numerical robustness of FLUENT in solving this problem and a grid density with 34,500 cells was employed for the production runs. The convergence criteria of each time step for the energy equation and other equations required that the normalized residuals become smaller than 10^{-6} and 10^{-3}, respectively. The numerical simulation of each case was stopped when the difference of the average Nusselt numbers on the high- and low-temperature walls were less than 0.01%. Given this criterion, the numbers of cycles for various isothermal rotating objects to reach their periodic or quasiperiodic states are summarized in Table 1. A similar procedure was followed for insulated rotating objects.

3 Flow Visualization and PIV

In order to validate the results of simulations, a transparent model of the flow system under consideration was built. The side of the square cavity was 7.62 cm and the test section had a height of 46.35 cm. The rotating objects with heights of 46.05 cm were machined from aluminum and painted black to minimize their interaction with the laser sheet. The working fluid was water. A variable-speed motor was utilized to achieve the desired speed of the rotation of the object. Flow visualization was carried out using silver-coated hollow glass spheres with a nominal diameter of 20 μm suspended in the fluid. These particles were also used as seeds for particle image velocimetry (PIV) measurements and were illuminated by a 5 W argon ion laser. The light sheet was generated using two OZ Optics fiber optic laser light sheet generators. An optical coupler with a built-in beam splitter was used to illuminate a horizontal field of view of the cross section of the cavity at the middle of the setup. Thickness of the laser sheet was 1 mm. The images were captured using a Dantec HiSense PIV/PLIF camera model C4742-53-12NR and were recorded on a JVC model BR-S622DXU professional video recorder.

A Dantec Dynamics PIV system consisting of 50 mJ dual-pulsed yttrium aluminum garnet (YAG) lasers, and 1000 $\times$1200 pixel cross-correlation camera was used to measure velocities on the planes of interest. The results were postprocessed using cross correlation and adaptive correlation of dual images taken at a separation time ranging from 120 μs to 1200 μs. Mean velocity and other statistics of the flow structures were computed using a set of 50 images for each case tested using 32 $\times$32 pixel interrogation window.

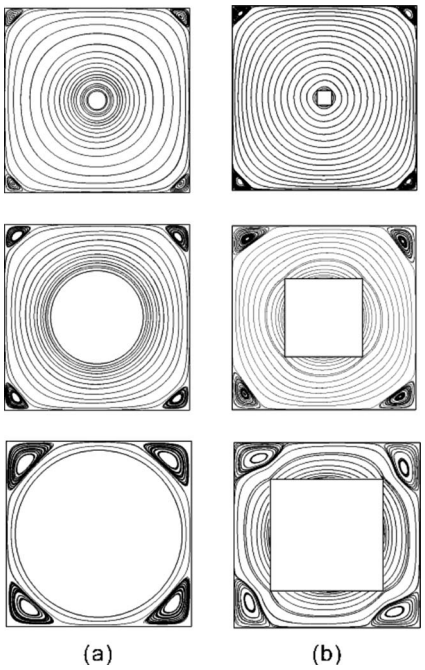

Fig. 2 Comparison of the (*a*) steady streamlines for a rotating circle and (*b*) instantaneous streamlines for a rotating square with Reynolds numbers of 111 (top), 44 (middle), 6 for the circle, and 21 for square (bottom) at the end of a cycle

4 Results and Discussion

The periodic flow and thermal fields for the posed problem are discussed now. Starting with the stated initial fields, the object was set in rotation at $t=0$. Upon attaining the periodic state, the periodicity of the flow and thermal fields for a fixed observer depends on the shape of the object and is equal to $2\pi/\omega N$, with N being the number of mirror symmetries of the object (i.e., 3, 4, and ∞ for triangle, square, and circle, respectively). All the results presented here correspond to the cases upon attaining the periodic state that were discussed in Sec. 2.3. In the absence of the buoyancy-driven convection, the flow field is independent of the imposed thermal boundary conditions and thus will be discussed first without regard to the specific thermal conditions.

4.1 Periodic Flow Field. The evolving flow field surrounding an object that starts to rotate at time $t=0$ will be dependent on the shape of the object, the imposed Reynolds number, and the radial pressure gradient. In general, upon setting the object into rotation, a thin, shear layer is formed adjacent to the surface of the object. This shearing layer will grow with time and eventually affects the fluid that is farthest from the object. The steady flow patterns attained by a rotating circle for the low, midrange, and high Reynolds numbers are shown in Fig. 2(*a*). The streamlines were perfectly circular in the close vicinity of the surface of the rotating circle; however, moving away from the surface of the object, the streamlines start deviating from circular patterns as the wall of the cavity was neared. This deviation becomes more marked as the Reynolds number was lowered that corresponds to lowering of the hydraulic diameter for this study (case of a bigger circle). It is clearly observed that the four recirculating vortices at the corners of the cavity for a rotating circle were identical. The sizes of these vortices were strengthened as the Reynolds number is lowered. Regardless of the Re, the streamline patterns within these identical vortices exhibited symmetry only about the center point of the square cavity. These observations of the flow fields due to a rotating circular cylinder in a square cavity were found to match the flow visualization and computational results of Lewis [4] and Hellou and Coutanceau [5] very well.

For comparison purposes, the instantaneous streamlines for the rotating squares with Re=111, 44, and 21 are shown in Fig. 2(*b*). Note that for the case of the biggest object, matching of the Re number between the circle and square objects is not possible due to the diagonal of the square becoming longer than the side of the cavity. The time instant shown is when the sides of the square are parallel to the walls of the cavity. For the highest Reynolds number case, the behavior of the streamlines and the corner vortices are similar to what was observed for a rotating circle with the same Reynolds number (Fig. 2(*a*)). As the side of the square is increased, the streamlines turn into noncircular closed curves and the recirculating vortices at the four corners grow in size. For the lowest Reynolds number of 21, the streamlines next to the cavity walls are more wrinkled and recirculation zones anchored to the four corners of the cavity are clearly observed. The observed symmetry of the shape of the vortices about the center point of the cavity (Fig. 2(*a*)) is still maintained. Even though these vortices are identical at the shown time instant, their individual dynamic characteristics within a cycle will be highlighted shortly. It must be noted that unlike classic corner Stokes vortices [15], each individual corner vortex observed in Fig. 2 does not possess mirror symmetry about its respective diagonal of the cavity and is clearly affected by the dynamic "stirring" force of the object.

The instantaneous streamlines for a rotating square with Re=31 during a quarter of a full period of revolution ($\tau/4=\pi/2\omega$) are shown at different phase angles (θ) in Fig. 3. The streamline patterns at the beginning of the cycle (Fig. 3(*a*)) possess the features discussed in Fig. 2(*b*). Upon turning of the square in the counterclockwise direction, the vortices and the circularlike streamline patterns evolve with time. Specifically, the corner vortices attain their smallest size at about $\tau/8$ (Figs. 3(*e*) and 3(*f*)). During the remainder of the cycle, the sizes of the vortices increase. Moreover, due to the even number of vertices of the square object, the symmetry of the streamlines within these vortices about the center of the cavity is clearly maintained. For a rotating triangle with the same Re, the instantaneous streamlines during one-third of a full period of revolution ($\tau/3=2\pi/3\omega$) are shown in Fig. 4. Due to the odd number of the vertices of the object, the corner vortices are of different sizes at any instant and no symmetry about the center of the cavity is expected. Marked asymmetry of the individual corner vortex about the bisector of each corner is observed when the vertex of the object is at the close proximity to that corner (e.g., top left corner of Figs. 4(*d*)–4(*f*)). One can also note that the flow patterns at time instants (t) and ($t+\tau/4$) are identical (e.g., time instants of Figs. 4(*a*) and 4(*j*)) if one considers a 90 deg rotation between the respective two images. The most interesting aspect of the dynamic flow fields of Figs. 3 and 4 has to do with the "periodic channeling" of the flow next to a cavity wall. In comparison to the steady flow counterpart offered by a rotating circle with the same Re, channeling will cause the fluid between the traversing vertex of the object and the fixed wall of the cavity to flow faster. This, in turn, will affect the thermal field, to be discussed in Secs. 4.2 and 4.3.

The instantaneous velocity vectors and streamlines that were determined using the PIV measurements for a rotating square and triangle are shown in Figs. 5 and 6, respectively, with Re=31. Depending on the shape of the object and its orientation, a certain region of the cavity is not accessible by the laser sheet and no data are shown in those zones. The general features of the unsteady flow fields that were discussed earlier in presenting Figs. 2–4 are clearly observed in the experimental PIV data, thus verifying the capabilities of the CFD code and the employed methodology to simulate this problem.

Having discussed the periodic flow field that is common to the two thermal boundary conditions, we now present results of the thermal fields for each specific systems of Figs. 1(*a*) and 1(*b*).

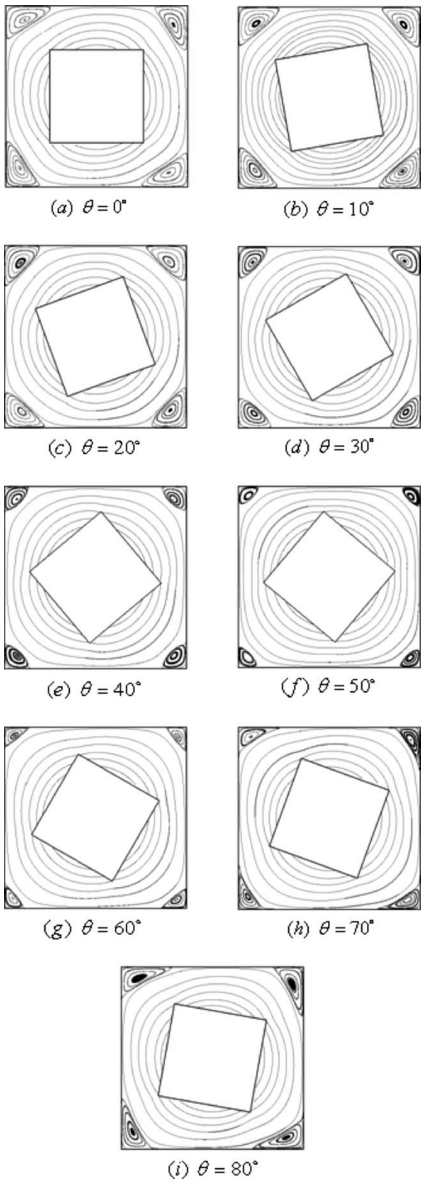

Fig. 3 Instantaneous streamlines under periodic conditions for a rotating square with Re=31 shown at 10 deg increments during a $\tau/4$ cycle

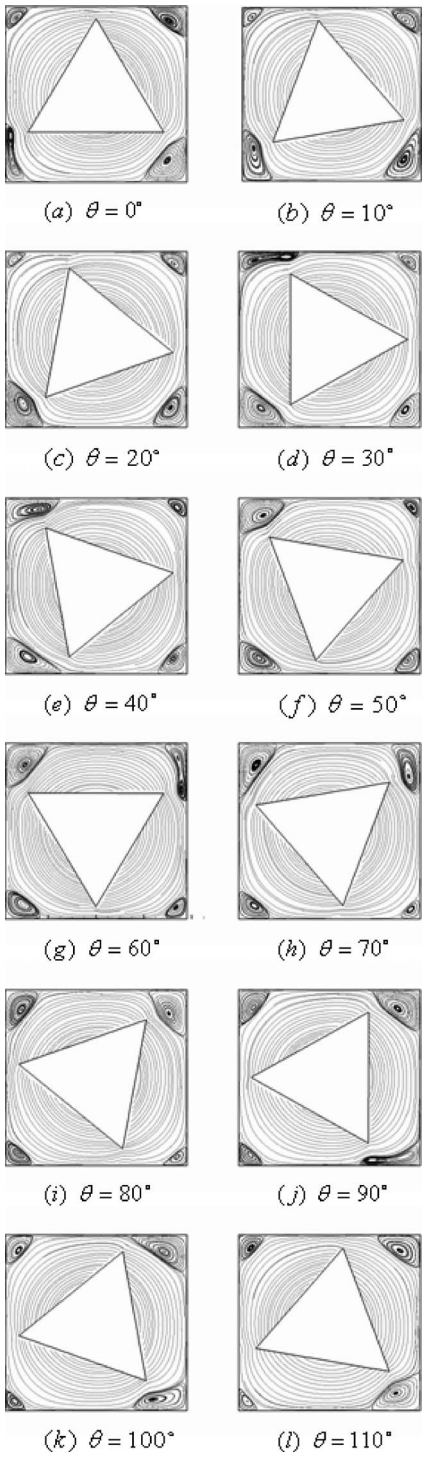

Fig. 4 Instantaneous streamlines under periodic conditions for a rotating triangle with Re=31 shown at 10 deg increments during a $\tau/3$ cycle

4.2 Periodic Heat Transfer for an Insulated Rotating Object. The temperature contours corresponding to the time instant exhibited in Fig. 2(*b*) for the rotating insulated squares with Re=111, 44, and 21 are shown in Fig. 7. Note that the contour level increment for the temperature field is 0.05. In the absence of the object and with no primer for convection, a pure conduction temperature field would have resulted (i.e., $\Theta = X$ leading to equally spaced vertical lines). It is observed that the rotational motion of the object greatly modifies the purely conductive mode of heat transfer and the temperature contours are skewed. The extent of skewness becomes more marked as the rotational Reynolds number is lowered. As Re is lowered, steep temperature gradients next to the active walls of the cavity indicate enhancement of heat transfer. These walls are also affected by the periodic "channeling" at other time instants. The temperature contours exhibit symmetry about the axis of rotation for the square object due to the even number of vertices. Instantaneous temperature contours during a full period of revolution are not shown here since the observed changes of this scalar field was not as varied of the dynamic streamline patterns.

4.2.1 Instantaneous Nusselt Numbers on the Active Walls. Transient variation in the instantaneous surface-averaged Nusselt numbers on the left and right walls (surface average of

$$\frac{D_h}{H}\left.\frac{\partial \Theta}{\partial X}\right|_{X=0}$$

or

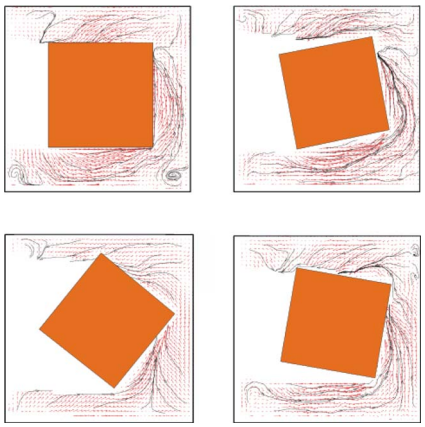

Fig. 5 Instantaneous measured velocity vectors and streamlines for a rotating square with Re=31 shown at four time instants

$$-\frac{D_h}{H}\left.\frac{\partial\Theta}{\partial X}\right|_{X=1}$$

respectively) during 5 cycles for the case of a rotating square with Re=111 and 31 are shown in Fig. 8. For Re equal to and less than 58 (e.g., bottom row of Fig. 8 with Re=31), the Taylor numbers are of the order of 1475 and lower. Taylor instabilities are not expected for this case (Re=31 and Ta=655) and the periodicity of the system is directly linked to the shape of the square object which exhibits a beating at 1/4 of τ. For this specific case, no noticeable phase shift between the Nusselt numbers on the left and right walls is observed. For cases with Re greater than or equal to 74, the Taylor numbers are of the order of 1200 and higher. For the specific case shown in Fig. 8 (top row with Re=111 and Ta =1244), quasiperiodic oscillations that do not reveal the nature of the square object are observed. This may be viewed as a signal indicating the onset of the Taylor instabilities.

Transient variation in the average Nusselt numbers on the left and right walls during 5 cycles for the case of a rotating triangle with Re=111 and 31 are shown in Fig. 9. For the case with Re =111 (top row of Fig. 9), quasiperiodic oscillation is exhibited with the dominant period of oscillations being about 1/3 of $\tau = 2\pi/\omega$. A low frequency oscillation with its period of the order of τ is also evident. For Reynolds numbers equal to and less than 74 (e.g., bottom row of Fig. 9), the periodicity of the system that distinctly beats at 1/3 of τ is observed. A phase shift between the Nusselt numbers on the left and right walls of the order of π is observed for the cases shown in Fig. 9.

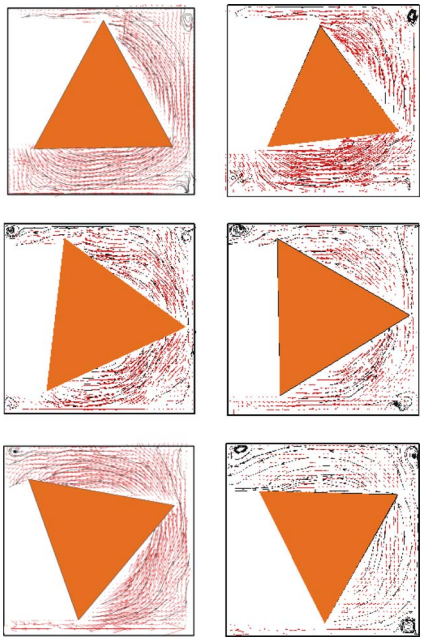

Fig. 6 Instantaneous measured velocity vectors and streamlines for a rotating triangle with Re=31 shown at six time instants

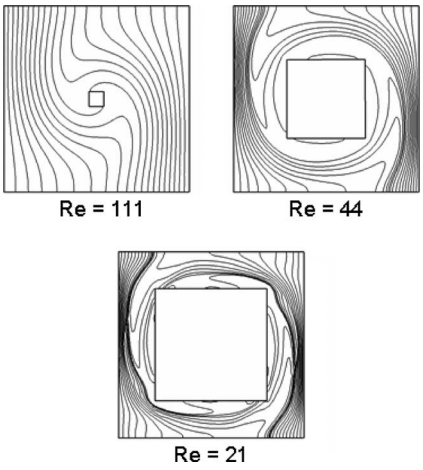

Fig. 7 Temperature contours for a rotating insulated square with Reynolds numbers of 111, 44, and 21 at the end of a cycle (contour level increment of 0.05)

4.2.2 Average Nusselt Number of the Insulated Object System. Time-integrated average Nusselt numbers on the left and right walls of the cavity were computed over the last 5 cycles and they were identical, as expected. The dependence of the time-averaged Nusselt number on the left wall of the cavity with the Reynolds number for three different rotating objects is shown in Fig. 10. Note that for the range of the Reynolds number studied, the system consistently exhibits higher heat transfer rates compared with the case associated with a conduction-only object-free condition ($\mathrm{Nu}=D_h/H=0.5$). As expected, the Nusselt number of the system for the highest Reynolds number studied (Re=111) is independent of the shape of the rotating object. One would expect that for higher values of the Reynolds number, the Nusselt number will asymptotically approach 1/2, irrespective of the shape of the object. The distinctions among the three rotating shapes become clear as the size of the object is increased and the Reynolds number is lowered. As the diameter of the circle is increased (keeping angular velocity constant), the heat transfer rate is raised reaching a maximum of about Re=44. Further increase in the diameter of the circle degrades the heat transfer rate since the adiabatic rotating circle acts as a resistance to heat transfer. However, the square and triangle objects behave differently by exhibiting monotonic rise of the heat transfer rate. This is due to the dynamic flow fields that were observed in Figs. 3 and 4, featuring the "periodic channeling" of the flow on the four sides. For the Reynolds number range $\mathrm{Re}\leq 80$, the rotating circle exhibits the lowest heat transfer among the three objects, whereas the triangle exhibits the highest heat transfer. The higher heat transfer of the triangle compared with the square can be explained by the greater intensity of the channeling (shorter distance between the wall and the vertex) as opposed to the greater frequency of channeling (4 for square versus 3 for a triangle in 1 cycle). It may be noted that there are no experimental heat transfer data against which our predictions can be benchmarked. However, the present results for a rotating circular object system are found to be of the same order of magni-

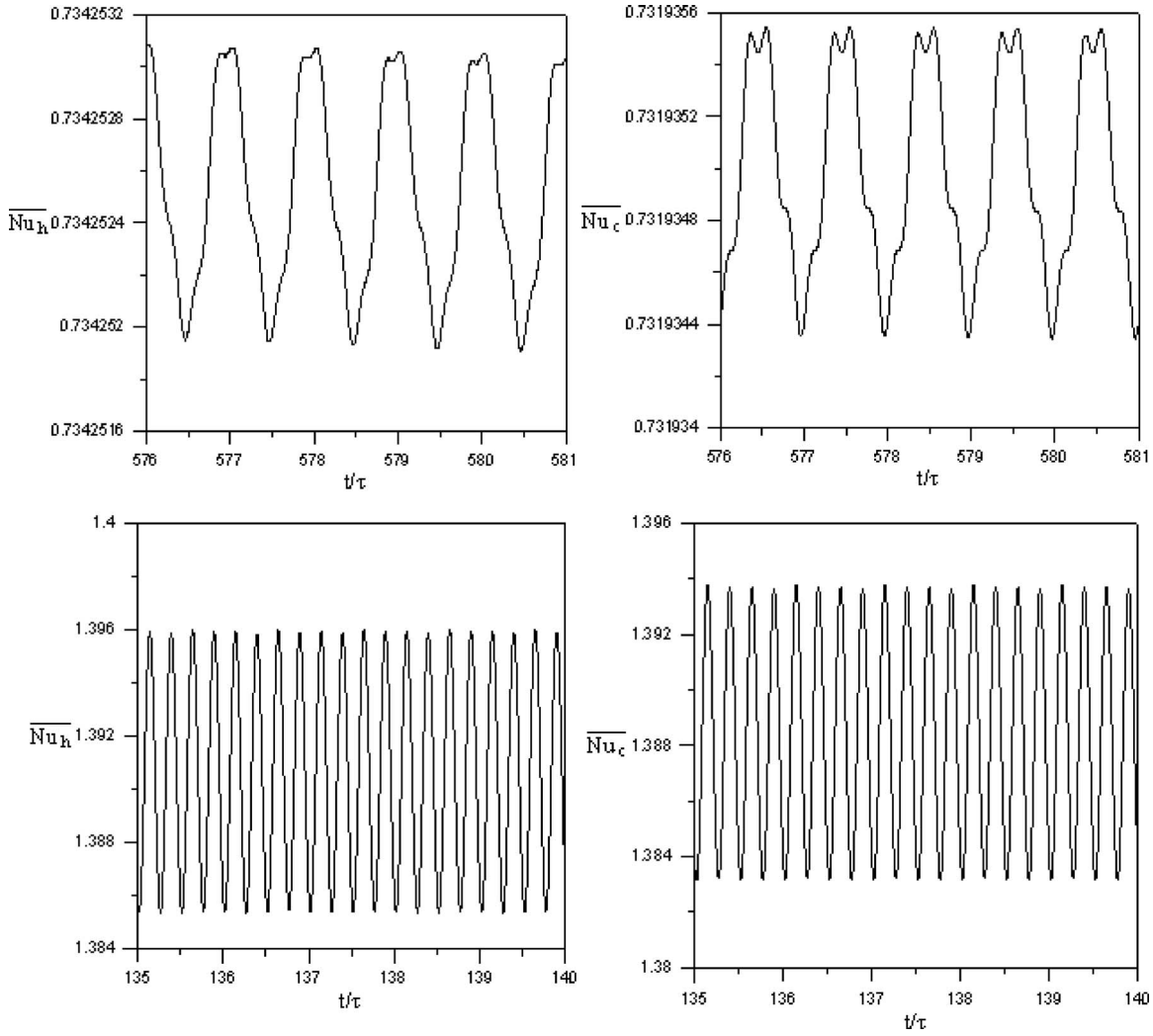

Fig. 8 Transient variation in the instantaneous average Nusselt numbers on the left wall (left column) and right wall (right column) for the case of a rotating insulated square with Re=111 (top row) and 31 (bottom row)

tude of the experimental data of Kimura et al. [7] that report higher heat transfer rates due to natural convection.

4.3 Periodic Heat Transfer for an Isothermal Rotating Object. At the beginning of rotation of an isothermal object, a thermal wave starts to spread from its surface toward the isothermal cavity walls. This is similar to the spreading of viscous effects generated from the surface of the rotating object into the fluid. The larger the hydraulic diameter is, the longer it takes for the temperature field to reach the periodic or quasiperiodic state. The steady temperature contours of a rotating circle for different Reynolds numbers are displayed in Fig. 11(*a*), which correspond to flow patterns of Fig. 2(*a*). Basically, the temperature contour patterns are symmetric about the axis of rotation. Similar to flow patterns, the isothermal lines for the cases with high Re are perfectly circular next to the surface of the rotating circle and they start deforming as the wall of the cavity is neared. However, for the case with Re=6, the rotating circle occupies a great portion of the cavity and isothermal lines are greatly distorted next to the four corners of cavity owing to the influence of strong corner vortices (Fig. 2(*a*)) in comparison to the smaller vortices for higher Re numbers. Also note the effect of the steady channeling on the thermal field at the narrow gap between the circle and the midpoints of the walls of the cavity, as indicated by the pronounced temperature gradient. For comparison purposes, the instantaneous temperature contours for the rotating squares with Re=111, 74, and 12 and triangles with Re=111, 74, and 31 are shown in Figs. 11(*b*) and 11(*c*), respectively. Similar to the discussion above in relation to Fig. 2, Re numbers on the low end cannot be matched for various objects. The time instant shown is when a side of the square and the bottom of the triangle are parallel to the bottom wall of the cavity. The isothermal lines near the square and triangle objects follow the shape of the object; however, they start conforming to the shape of the cavity wall as one nears those surfaces. For these cases, the isotherms are not greatly distorted by the corner vortices. For the low Re numbers associated with the square and triangle objects (bigger objects), it can be observed that marked temperature gradients occur near the vertices of the objects, owing to the strong shearing of the flow field near these points and periodic channeling. Simultaneously, strong temperature gradients are also observed next to the midpoints of the side walls of the cavity, which were already identified as sites where periodic channeling occurs. Appreciable distortions of isothermal lines are also observed for the low Re numbers associated with the square and triangle objects owing to the dominance of the corner vortices.

4.3.1 Instantaneous Nusselt Numbers on the Surface of the Rotating Object and Cavity Walls. Transient variation in the average Nusselt numbers on the surfaces of a rotating square and

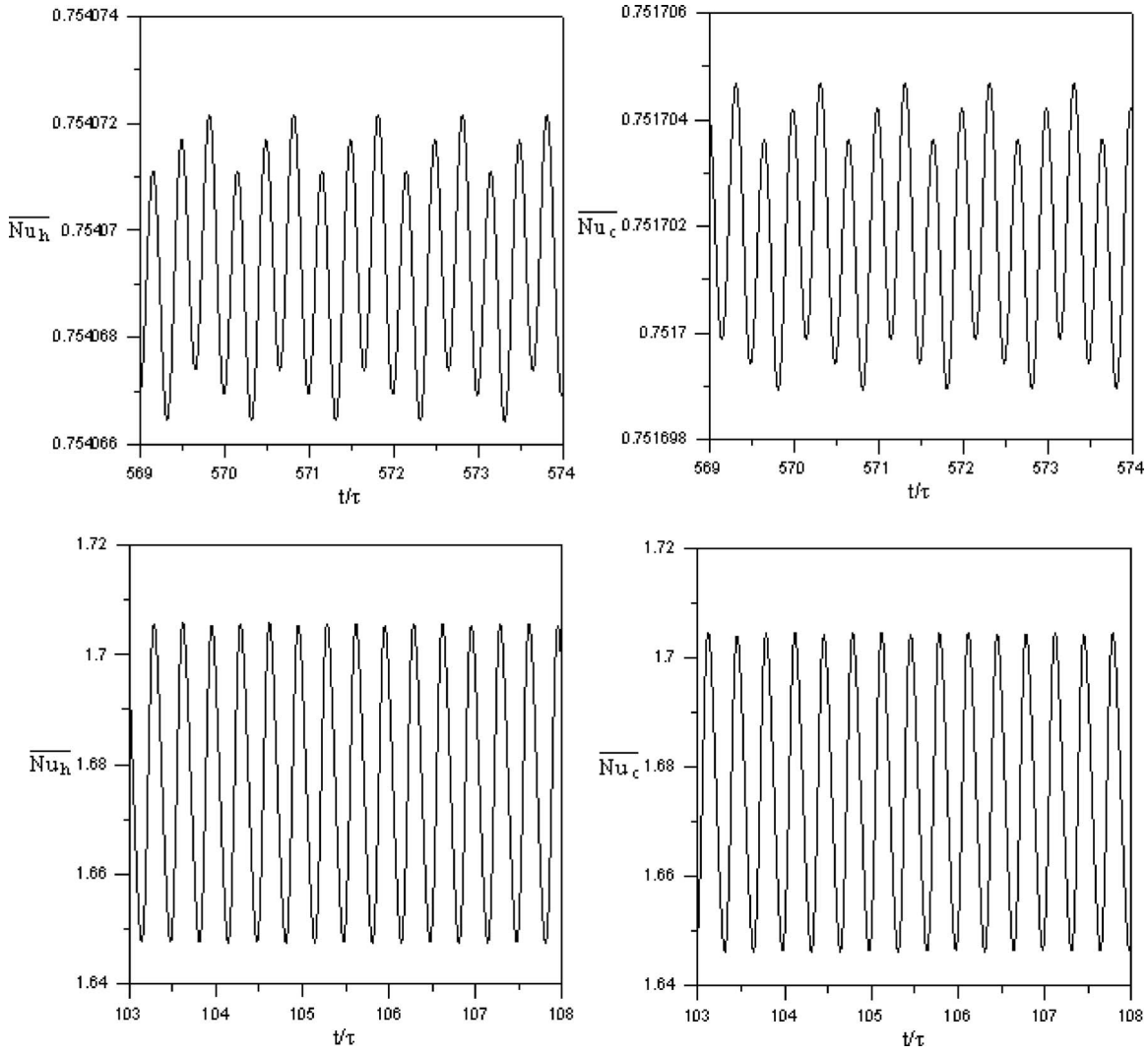

Fig. 9 Transient variation in the instantaneous average Nusselt numbers on the left wall (left column) and right wall (right column) for the case of a rotating insulated triangle with Re=111 (top row) and 31 (bottom row)

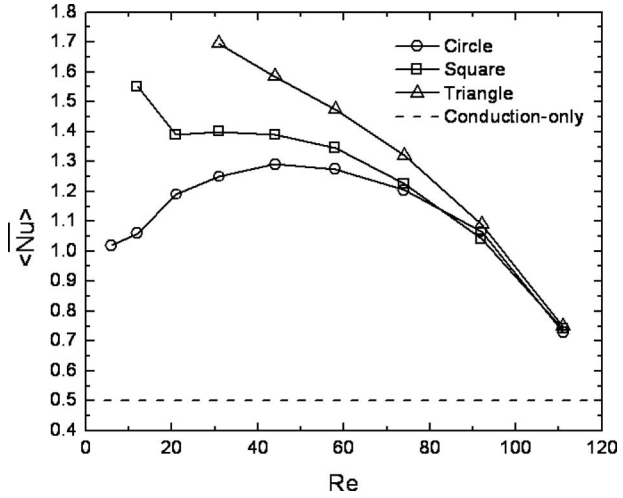

Fig. 10 Dependence of the time-averaged Nusselt number on the left wall with the Reynolds number for various insulated objects

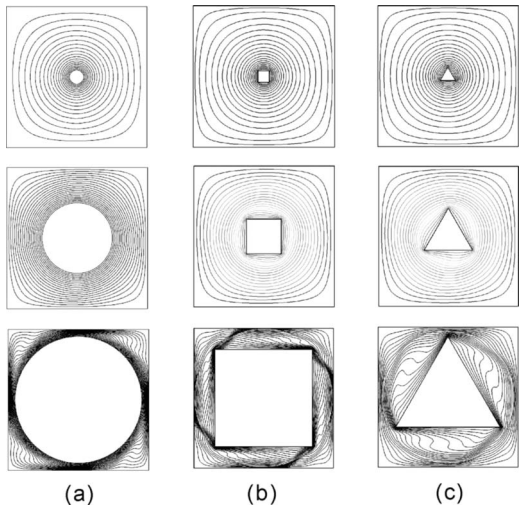

Fig. 11 Comparison of the temperature contours for (*a*) steady rotating circle, (*b*) rotating square, and (*c*) rotating triangle, with Reynolds numbers of 111 (top), 44 for circle, 74 for square and triangle (middle), 6 for circle, 12 for square, and 31 for triangle (bottom) at the end of a cycle (contour level increment of 0.05)

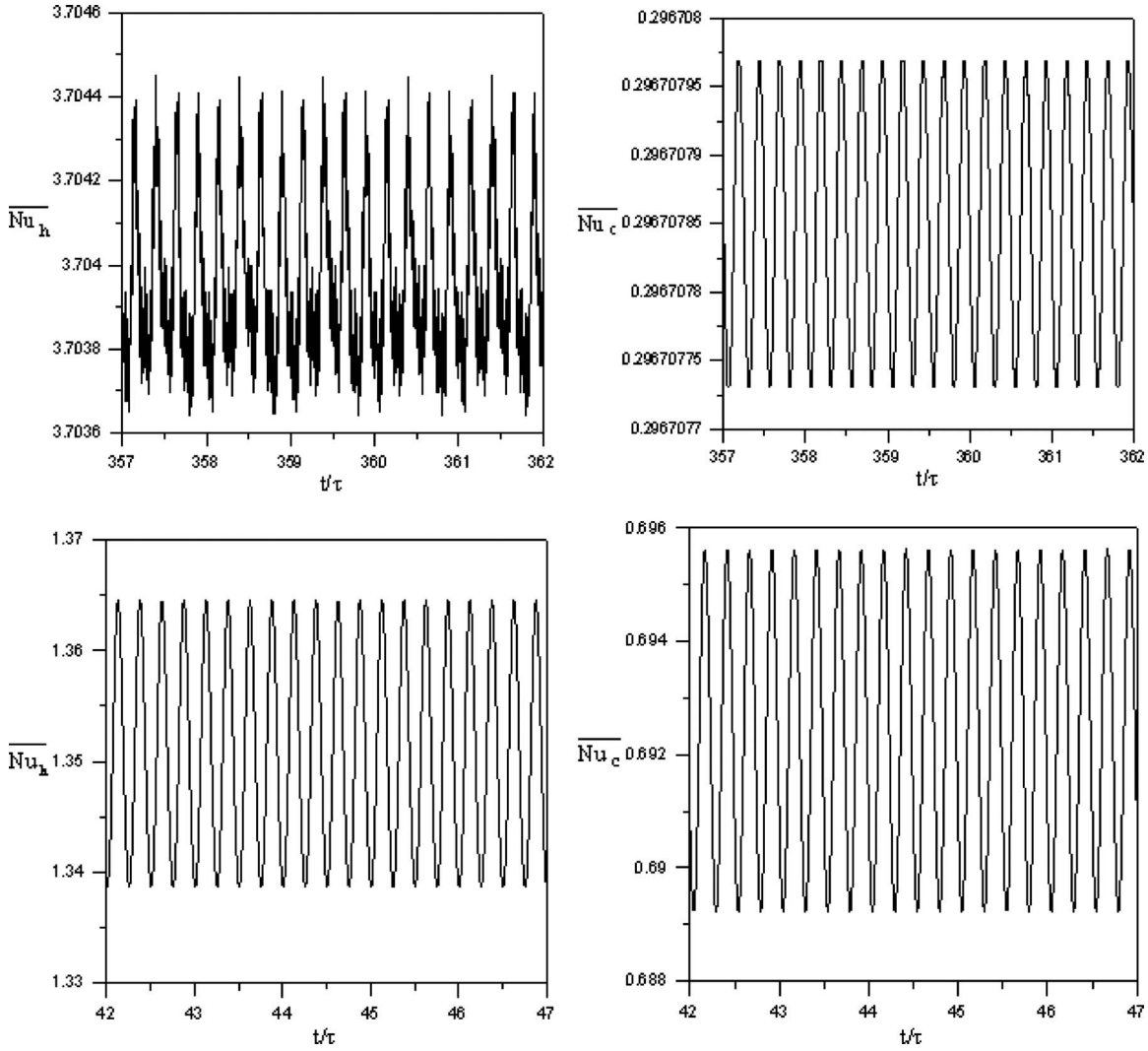

Fig. 12 Transient variation in the instantaneous average Nusselt numbers on the surface of a rotating square (left column) and cavity walls (right column) with Re=111 (top row) and 31 (bottom row)

cavity during 5 cycles with Re=111 and 31 are shown in Fig. 12. For the cases with Re greater than or equal to 74, the Taylor numbers are of the order of 1250 and higher. The onset of Taylor instabilities for these cases is observed and the resulting quasiperiodic signature on the surface of the rotating object with the dominant period of oscillations being equal to 1/4 of $\tau=2\pi/\omega$ is observed (e.g., top row and left column with Re=111). At the same time, high-frequency oscillations are also observed for these cases. On the other hand, for the same Reynolds number, a periodic variation in the instantaneous Nusselt numbers is exhibited on the walls of the cavity (e.g., top row and right column with Re=111). For Reynolds numbers equal to and less than 58 (e.g., bottom row of Fig. 12), periodicity of the system beating at $\tau/4$ is clearly observed on the surface of the object and walls of the cavity. For low Reynolds numbers, there is also a phase angle associated with the variations of instantaneous Nusselt numbers, with the wall values falling behind those on the object.

4.3.2 Average Nusselt Numbers of the Isothermal Object System. The time-averaged Nusselt numbers on the surface of the object and cavity were calculated for the last five periodic cycles. The time-averaged Nusselt numbers versus the Reynolds number on the surfaces of the rotating circle, square, and triangle, as well

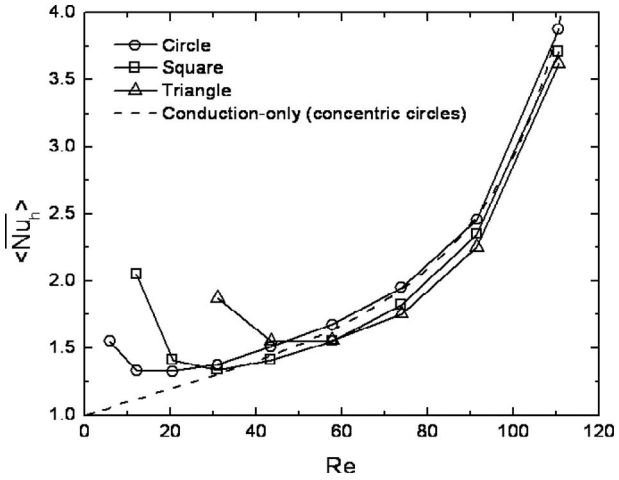

Fig. 13 Time-averaged Nusselt number versus Reynolds number on the surfaces of different isothermal rotating objects

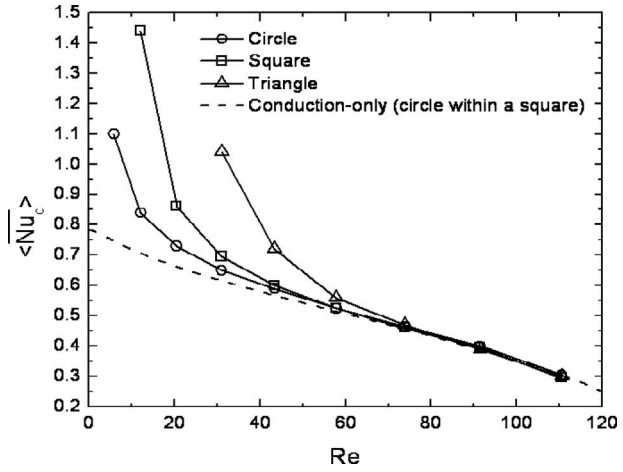

Fig. 14 Time-averaged Nusselt number versus Reynolds number on the cavity walls due to different isothermal rotating objects

as on the cavity walls are shown in Figs. 13 and 14, respectively. For comparison purposes, the analytic solution of steady conductive heat transfer between two concentric cylinders (inner and outer radii of R_1 and R_2 maintained at temperatures T_H and T_C with $T_H > T_C$) was obtained. The expressions for the Nusselt numbers on the rotating cylinder and the outer cylinder are

$$\langle \overline{\mathrm{Nu}_h} \rangle = \frac{\left(1 - \frac{1}{\beta}\right)}{\ln \beta} \tag{12}$$

and

$$\langle \overline{\mathrm{Nu}_c} \rangle = \frac{(\beta - 1)}{\ln \beta} \tag{13}$$

respectively, with $\beta = R_1/R_2 < 1$. Note that both Nusselt numbers approach unity for $\beta \to 1$, whereas $\langle \overline{\mathrm{Nu}_h} \rangle \to \infty$ and $\langle \overline{\mathrm{Nu}_c} \rangle \to 0$ for $\beta \to 0$. The expression for the Nusselt number on the surface of the inner rotating cylinder for the case of two concentric cylinders (Eq. (12)) is plotted in Fig. 13. For high Re values studied that correspond to cases of an object with a small diameter in comparison to the side of the cavity, the monotonic rise of heat transfer is observed for all three objects and the analytic solution perfectly matches the computed quantities for the case of a rotating cylinder. For these cases, heat transfer from surfaces of equivalent rotating squares and triangles were lower compared with the rotating circles. This can easily be explained by the increased wetted surface of the objects ($A_{\mathrm{cir}} < A_{\mathrm{sq}} < A_{\mathrm{tri}}$) that holds true for all the objects with identical hydraulic diameters. As the sizes of the objects are increased (i.e., the Reynolds number is lowered), heat transfer rates are always greater than the limiting analytic solution and it is observed that they start increasing at different values of the D_h/H ratios (thus corresponding to different Re numbers). This phenomenon is in contrast to the limiting analytic result for heat conduction between two concentric cylinders, thus suggesting that convective effects due to rotation of the object and the specific shape are contributing to this effect. The observed points of inflection for the circle, square, and triangle occurred at Re = 12, 31, and 44, respectively. Once again, periodic channeling explains these variations clearly. For bigger objects, the vertices of the triangle come closest to the wall of the cavity followed by the square, whereas the fixed position of the rotating circle is associated with the least effective channeling. Due to periodic channeling and the ensuing dense packing of temperature contours, enhancement of heat transfer is realized.

For a proper discussion of heat transfer on the walls of the cavity, the analytic expression for the Nusselt number on the surface of outer cylinder for the case of two concentric cylinders (Eq. (13)) was multiplied by $\pi/4$ and then plotted in Fig. 14. This approximation accounts for the bigger circumference of a square that has a side equal to the diameter of the circle that it touches and encloses simultaneously. Note that for high Re numbers, heat transfer on the wall of the cavity due to various rotating objects are identical to the approximated case of heat conduction between a circle enclosed by a square. In effect, since the rotating object is very small, its shape becomes immaterial to the temperature contours next to the walls of the cavity. As the Reynolds number is lowered, heat transfer rates are greatly enhanced due to the periodic channeling offered by different objects. The intense channeling supported by the triangle shape clearly exhibits superior heat exchange capability among the three objects, whereas the circle performs the weakest among the three objects.

Table 2 Constants of the correlation (Eq. (14)) for various objects (*R*-squared ranges of 0.9177 and 0.9926)

	a	*b*	Range of Re
Circle	3.5304	−0.4899	$21 < \mathrm{Re} \le 111$
	1.9748	−0.3318	$6 < \mathrm{Re} \le 21$
Square	6.7646	−0.6430	$31 < \mathrm{Re} \le 111$
	9.7397	−0.7794	$12 < \mathrm{Re} \le 31$
Triangle	31.9764	−0.9889	$58 < \mathrm{Re} \le 111$
	32.8666	−1.0064	$31 < \mathrm{Re} \le 58$

To provide the designer to adopt the proper shape of the object for a given application, the time-averaged Nusselt number of the cavity is correlated with the rotational Reynolds number and shape of the object of the form

$$\langle \overline{\mathrm{Nu}_c} \rangle = a\ \mathrm{Re}^b \tag{14}$$

The constants a and b in Eq. (14) for the three objects are tabulated in Table 2.

5 Conclusions

In relation to the periodic flow, the important conclusions of this study are as follows. For noncircular objects, dynamic recirculating vortices at the four corners of the cavity are formed. The instantaneous identical shape of the vortices for the cases of the rotating circle and square is compromised for the case of a triangle. For low Reynolds numbers, the vortices exhibit marked time-dependent spatial growth and decay. A distinct channeling effect is offered by the square and triangle where the vertices of these objects come in close proximity of the side walls. These observations were verified through comparison of the simulations against measured PIV data collected in a transparent model of the system.

For both insulated and isothermal rotating objects with high Re, surface-averaged Nusselt numbers suggest that due to the onset of the Taylor instabilities, quasiperiodic behavior is exhibited with the dominant period of oscillations being equal to $1/N$ of $\tau = 2\pi/\omega$ ($N = 4$ and 3 for square and triangle, respectively). High-frequency oscillations are also observed for these cases. For smaller Reynolds numbers, periodicity of the system oscillating with a period of $1/N$ of τ is clearly observed.

By comparing the time-averaged Nusselt numbers of the system for both insulated and isothermal objects, it is concluded that for high Re cases, heat transfer is independent of the shape of the object. However, as the hydraulic diameter of the object is lowered (i.e., bigger objects), the triangle and the circle give rise to the highest and lowest heat transfers, respectively. Periodic channeling and its high intensity for a triangle are identified as the cause of the observed enhancement.

Nomenclature

$\underline{D_h}$ = hydraulic diameter, defined by Eqs. (2)–(5)

$\underline{\mathrm{Nu}}$ = instantaneous surface-averaged Nusselt number

$\langle\overline{\mathrm{Nu}}\rangle$ = time- and surface-averaged Nusselt number

Re = Reynolds number, defined as $\rho D_h^2 \omega / \mu$

Ta = Taylor number, defined as $R\rho^2(0.5H-R)^3\omega^2/\mu^2$

Greek Symbol

ω = angular velocity, s^{-1}

References

[1] Shi, X., and Khodadadi, J. M., 2002, "Laminar Fluid Flow and Heat Transfer in a Lid-Driven Cavity Due to a Thin Fin," ASME J. Heat Transfer, **124**(6), pp. 1056–1063.

[2] Shi, X., and Khodadadi, J. M., 2003, "Laminar Natural Convection Heat Transfer in a Differentially Heated Square Cavity Due to a Thin Fin on the Hot Wall," ASME J. Heat Transfer, **125**(4), pp. 624–634.

[3] Saeidi, S. M., and Khodadadi, J. M., 2006, "Forced Convection in a Square Cavity With Inlet and Outlet Ports," Int. J. Heat Mass Transfer, **49**(11–12), pp. 1896–1906.

[4] Lewis, E., 1979, "Steady Flow Between a Rotating Circular Cylinder and Fixed Square Cylinder," J. Fluid Mech., **95**(3), pp. 497–513.

[5] Hellou, M., and Coutanceau, M., 1992, "Cellular Stokes Flow Induced by Rotation of a Cylinder in a Closed Channel," J. Fluid Mech., **236**, pp. 557–577.

[6] Hills, C. P., 2002, "Flow Patterns in a Two-Roll Mill," Q. J. Mech. Appl. Math., **55**(2), pp. 273–296.

[7] Kimura, T., Takeuchi, M., and Miyagawa, K., 1995, "Effects of Inner Rotating Horizontal Cylinder on Heat Transfer in a Differentially Heated Enclosure," Heat Transfer-Jpn. Res., **24**(6), pp. 504–516.

[8] Escudier, M. P., Olivieira, P. J., and Pinho, F. T., 2002, "Fully Developed Laminar Flow of Purely Viscous Non-Newtonian Liquids Through Annuli, Including the Effects of Eccentricity and Inner-Cylinder Rotation," Int. J. Heat Fluid Flow, **23**(1), pp. 52–73.

[9] White, F. M., 1991, *Viscous Fluid Flow*, 2nd ed., McGraw-Hill, New York, p. 368.

[10] Middleman, S., 1997, *An Introduction to Fluid Dynamics: Principles of Analysis and Design*, Wiley, New York, Chap. 10.

[11] Patankar, S. V., 1980, *Numerical Heat Transfer and Fluid Flow*, Hemisphere, Washington, DC.

[12] FLUENT Inc., 2004, FLUENT User's Guide, Version 6.2.

[13] Behr, M., and Tezduyar, T., 1999, "The Shear-Slip Mesh Update Method," Comput. Methods Appl. Mech. Eng., **174**(3–4), pp. 261–274.

[14] Tai, C. H., Zhao, Y., and Liew, K. M., 2005, "Parallel Computation of Unsteady Incompressible Viscous Flows Around Moving Rigid Bodies Using an Immersed Object Method With Overlapping Grids," J. Comput. Phys., **207**(1), pp. 151–172.

[15] Moffatt, H. K., 1964, "Viscous Eddies Near A Sharp Corner," Arch. Mech. Stosow., **2**, pp. 365–372.

An Integral Solution for Heat Transfer in Accelerating Turbulent Boundary Layers

James Sucec
Department of Mechanical Engineering,
University of Maine,
Orono, ME 04469-5711

An equilibrium thermal wake strength parameter is developed for a two-dimensional turbulent boundary layer flow and is then used in the combined thermal law of the wall and the wake to give an approximate temperature profile to insert into the integral form of the thermal energy equation. After the solution of the integral x momentum equation, the integral thermal energy equation is solved for the local Stanton number as a function of position x for accelerating turbulent boundary layers. A simple temperature distribution in the thermal "superlayer" is part of the present modeling. The analysis includes a dependence of the hydrodynamic and thermal wake strengths on the momentum thickness and enthalpy thickness Reynolds numbers, respectively. An approximate dependence of the turbulent Prandtl number, in the "log" region, on the strength of the favorable pressure gradient is proposed and incorporated into the solution. The resultant solution for the Stanton number distribution in accelerated turbulent flows is compared with experimental data in the literature. A comparison of the present predictions is also made to a finite difference solution, which uses the turbulent kinetic energy—turbulent dissipation model of turbulence, for a few cases of accelerating flows.
[DOI: 10.1115/1.3154649]

1 Introduction

Heat transfer to turbulent boundary layers subject to a favorable pressure gradient, an accelerating flow, occurs naturally in gas turbine blades and vanes and in nozzles. Extensive experimental data in moderately and in strongly accelerated turbulent boundary layers is available in Refs. [1–3]. Earlier attempts to predict the Stanton number distribution in accelerating turbulent boundary layers include the $k-\in$ finite difference solution by Jones and Launder [4] and a simpler integral approach by Sucec and Lu [5]. A more recent work [6] used temperature scalings from similarity analysis and a near asymptotic method, along with a number of constants determined from experimental data, to develop a detailed composite temperature distribution across the entire boundary layer for zero and adverse pressure gradients. This was then used to solve the integral thermal energy equation for the local Stanton number, but only in a zero pressure gradient flow.

In the present work, the equilibrium thermal wake strength parameter π_{teq} is found as a function of the Clauser parameter β and the turbulent Prandtl number in the log region Pr_t by using the earlier work of So [7]. Details of the procedure are given in Ref. [8]. The dependence of the velocity and thermal wake strengths π_{eq} and π_{teq} on the momentum thickness and enthalpy thickness Reynolds numbers is the one used in an earlier work for zero and adverse pressure gradients [9]. The proposed dependence of the turbulent Prandtl number in the log region on the pressure gradient draws heavily on the work of Blackwell [10]. As part of the present modeling, a simple linear temperature distribution is employed as the approximating sequence in the thermal superlayer $\delta<y<\delta_t$. After these effects are incorporated, the velocity and thermal laws of the wall and wake, together with the velocity and temperature profiles in the thermal superlayer, when it occurs, are used to solve the integral *x*-momentum equation for needed quantities, such as $C_f/2$, δ^+, etc., and then the integral thermal energy equation is solved for δ_t^+ (x), which leads to St_x. The predicted Stanton numbers are then compared with experimental data for a large number of cases and also to the predictions of Jones and Launder [4] for a few cases.

2 Analysis

The earlier fundamental work of So [7] was instrumental in enabling us to develop an expression for the equilibrium thermal wake strength parameter π_{teq} as a function of β and of the turbulent Prandtl number Pr_t. So solved for the effect of pressure gradient on heat transfer in constant property, turbulent, equilibrium, planar two-dimensional boundary layers, which is the thermal counterpart of the hydrodynamic problem solved earlier by Mellor and Gibson [11]. So's work was the base needed to develop π_{teq} (β, Pr_t) for favorable pressure gradients $\beta<0$ using procedures similar to those explained in Ref. [8]. The resultant expression for π_{teq} is given in graphical form as in Fig. 1.

2.1 Integral Equation and Profiles. The integral form of the low speed constant property thermal energy equation was derived and integrated for the case of specified surface heat flux q_w. The result, in inner variables, is given as follows:

$$\int_0^{\delta_t^+} u^+(T_s^+ - T^+)dy^+ = \frac{u^*(x)}{\nu q_w(x)}\int_{x_0}^{x} q_w dx + \frac{u^*(x)q_w(x_0)}{u^*(x_0)q_w(x)}\int_0^{\delta_{t_0}^+} u^+(T_s^+ - T^+)dy^+ \quad (1)$$

The velocity and temperature profiles needed in Eq. (1) are as follows, namely, the combined law of wall and wake for velocity and temperature.

$$u^+ = \frac{1}{K}\ln y^+ + B + \frac{2\pi(x)}{K}\left[3\left(\frac{y^+}{\delta^+}\right)^2 - 2\left(\frac{y^+}{\delta^+}\right)^3\right], \quad 0 < y^+ \le \delta^+$$
$$u^+ = u_s^+ = 1/\sqrt{C_f/2} \quad \text{for} \quad y^+ > \delta^+ \quad (2)$$

With $T^+=(T_w-T)\rho C_p u^*/q_w$, the temperature profile used in Eq. (1) is the combined thermal law of wall and wake, namely, for $\delta_t^+ \le \delta^+$,

Contributed by the Heat Transfer Division of ASME for publication in the JOURNAL OF HEAT TRANSFER. Manuscript received December 15, 2008; final manuscript received April 21, 2009; published online August 25, 2009. Review conducted by Frank Cunha.

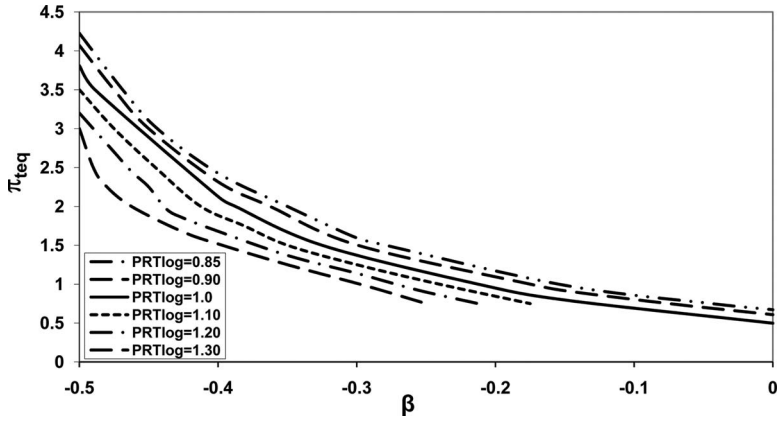

Fig. 1 Predicted thermal wake strength π_{teq} variation with β and Pr_t

$$T^+ = \frac{Pr_t}{K}\ln y^+ + C_t(Pr) + \frac{2Pr_t\pi_t(x)}{K}\left[3\left(\frac{y^+}{\delta_t^+}\right)^2 - 2\left(\frac{y^+}{\delta_t^+}\right)^3\right] \quad (3)$$

Before Eq. (1) can be solved for the general case, the dependence of the wake strengths, π (x) and π_t (x), on the momentum and enthalpy thickness Reynolds numbers are needed. Also, the turbulent Prandtl number and the temperature profile in the thermal superlayer must be modeled.

2.2 Wake Strength Expressions. These come from Ref. [9] where nonaccelerating flows were dealt with. The equilibrium velocity wake strength π_{eq} is from Ref. [12] and is shown next.

$$\beta = -0.5 + 0.76\pi_{eq} + 0.42\pi_{eq}^2 \quad (4)$$

The dependence of π on π_{eq} and the momentum thickness Reynolds number Re_θ is from Ref. [13].

$$\pi = 0 \quad 0 \le Re_\theta < 425$$

$$\pi = \pi_{eq}[1 - \exp(-0.243\sqrt{Z_1} - 0.298Z_1)] \quad 425 < Re_\theta < 15{,}000 \quad (5)$$

$$Z_1 = Re_\theta/425 - 1$$

π approaches π_{eq} asymptotically as Re_θ approaches about 6000. The dependence of π_t on π_{teq} and the enthalpy thickness Reynolds number Re_Δ resulted from curve fits to a numerical solution by Fridman [14] and are given as follows:

$$\pi_t = \pi_{teq}[0.000477\ Re_\Delta], \quad 0 < Re_\Delta < 348$$

$$\pi_t = \pi_{teq}[0.065 + 0.00029\ Re_\Delta], \quad 348 < Re_\Delta < 1000 \quad (6)$$

$$\pi_t = \pi_{teq}[1 - \exp(-0.00044109\ Re_\Delta)], \quad Re_\Delta > 1000$$

π_t approaches π_{teq} as Re_Δ approaches about 11,000. A more complete discussion of details associated with Eqs. (4)–(6) is available in Ref. [9].

2.3 Modeling of Turbulent Prandtl Number. There is some evidence that the turbulent Prandtl number in the log region increases in an accelerating flow, one with a favorable pressure gradient $\beta < 0$. This is discussed in Ref. [15] and limited experimental evidence is shown in Fig. 6.10 of Ref. [10], Figs. 4.2 and 4.4 of Ref. [2] and in Fig. 8 of Ref. [16]. An equation for the turbulent Prandtl number in the log region, developed by Blackwell [10], gives the correct qualitative trend of Pr_t with pressure gradient. A version of it, modified to give $Pr_t = 0.85$ at $\bar{K} = 0$, is used here as a conservative approximation to Pr_t because of the shortage of Pr_t data in accelerating flows.

$$Pr_t = 0.7556[\gamma + 2]^{0.17}$$

$$\gamma = 1000\bar{K}\ Re_\theta/(H - 1) \quad (7)$$

where $\bar{K}$ is the pressure gradient parameter used to characterize accelerating flows, $\bar{K} = (\nu/u_s^2)(du_s/dx)$, $H = \delta^*/\theta$, the usual "shape" factor, and Re_θ is the momentum thickness Reynolds number.

2.4 The Thermal Superlayer. Perhaps the most distinctive characteristic of an accelerating turbulent boundary layer is the depression of Stanton number values, below what might be expected, due to the suppression of turbulence caused by the acceleration when $\bar{K}$ values are large enough. As has been pointed out by many sources, if a value of $\bar{K}$ greater than about $(2.5-3) \times 10^{-6}$ is maintained over a long enough streamwise distance, retransition to a laminar flow is theoretically possible. Another less obvious state often found in accelerating boundary layers is the occurrence of long regimes of flow where the thermal boundary layer thickness δ_t is larger than the local hydrodynamic boundary layer thickness δ. The layer of thickness δ_t-δ when $\delta_t > \delta$ has been termed the "thermal superlayer" in Ref. [17]. The existence of such a layer was shown to be possible by Kays et al. [18]. This layer has essentially zero eddy conductivity and is a layer of molecular conduction. The x component of velocity in the layer is the local free stream velocity, u_s (x). It remains to model the temperature distribution across the thermal superlayer. A very simple linear in y temperature distribution was chosen. Cubic, in y, and a quartic, in y, temperature profiles were also investigated, but since the average difference in predicted St_x values differed only by about 1.5%, the simple linear profile was used in the predictions and is shown next.

$$T^+ = T^+_{\delta^+} + b(y^+ - \delta^+), \ \text{for} \ \delta_t^+ > \delta^+ \quad (8)$$

where b is dependent on δ^+, Pr_t, and Pr.

2.5 Solution of the Integral Equations. In order to solve for the local Stanton number as a function of surface position x, the integral form of the x momentum equation and the thermal energy equation must be solved for δ^+ (x) and δ_t^+ (x), respectively. In this constant property solution, the x momentum equation is solved first by using, as the velocity profile, the combined law of wall and wake given by Eq. (2). The solution procedure was described in an earlier work [12]. In the present work, the starting hydrodynamic condition was modeled as follows. At the location of the boundary layer "trips," the mixing process caused by the trips leads to the start of a new turbulent boundary layer with $\delta^+ = 0$. Very small nonzero values of δ^+ were actually used to avoid numerical problems. Another way of modeling the starting condition is to use laminar flow up to the boundary layer trips after which

the flow is turbulent and say that the momentum thickness θ is continuous at the trip, as suggested in Ref. [19], for natural transition. This led to results very close to those which used $\delta^+=0$ at the trips, less than 0.5% difference, on the average. However, since the transition at a trip is not a natural transition, the $\delta^+=0$ modeling was employed in the predictions.

The integral thermal energy equation (Eq. (1)) was solved next, now that the hydrodynamic solution for δ^+ and u^* are available. The velocity profile (Eq. (2)) and the temperature profiles (Eq. (3) and, when $\delta_t^+ > \delta^+$, Eq. (8)) were inserted into Eq. (1) and the integrations were performed analytically. The resultant nonlinear equation was solved by Newton's method using the same small lattice spacing in x (Δx) as was used in the hydrodynamic solution. The initial or starting condition, for the solution of the thermal boundary layer for δ_t^+ (x) is described next.

At the x location of the start of heating, $\delta_t^+=0$ or, equivalently, the local Stanton number was chosen to be very large to simulate St_x of ∞ at this point. To insure that the downstream solution was independent of the starting value of St_x used, runs were made with different starting values and it was found that a change in starting value from $\mathrm{St}_x=0.035$ to 0.010 caused a maximum change of 0.15% in the predicted downstream values of St_x.

2.6 Stanton Number Solution. With the solution of Eq. (1) for δ_t^+ (x) known, the local Stanton number is formed by setting $y^+=\delta_t^+$ to give T_s^+ from the temperature profiles, Eq. (3) when $\delta_t^+ < \delta^+$ or Eq. (8) for $\delta_t^+ > \delta^+$. The definition of T_s^+ leads to the following heat transfer relations:

$$\frac{\sqrt{C_f/2}}{\mathrm{St}_x} = \frac{\mathrm{Pr}_t}{K}\ln\,\delta_t^+ + C_t(\mathrm{Pr}) + 2\frac{\mathrm{Pr}_t}{K}\pi_t \quad \text{for} \quad \delta_t^+ < \delta^+ \tag{9}$$

$$\frac{\sqrt{C_f/2}}{\mathrm{St}_x} = \frac{\mathrm{Pr}_t}{K}\ln\,\delta^+ + C_t(\mathrm{Pr}) + 2\frac{\mathrm{Pr}_t}{K}\pi_t + b\frac{\mathrm{Pr}_t}{K}\left(\frac{\delta_t^+}{\delta^+}-1\right) \quad \text{for} \quad \delta_t^+ > \delta^+ \tag{10}$$

Lattice refinement studies were carried out to be sure that the predicted values of St_x were independent of the lattice size Δx used in the calculations. In a typical case, cutting Δx in half caused a maximum change in the predicted St_x values of 0.018% when $\Delta x=0.00065$ m was used. The expression and values needed in Eqs. (9) and (10) were $K=0.41$, $\mathrm{Pr}=0.71$, $B=5.0$ with C_t (Pr)=13.2 Pr-5.34, coming from Ref. [19].

3 Results and Discussion

The relationship for π_{teq} as a function of the Clauser parameter β and Pr_t is shown graphically in Fig. 1 for accelerating turbulent boundary layers $\bar{K}>0$. This was developed from the work of So [7] on equilibrium thermal boundary layers, as previously mentioned. Qualitatively, π_{teq} decreases as β increases and as Pr_t increases. Figure 1 does not show this, but, in fact, π_{teq} decreases almost linearly with increasing Pr_t.

Comparison of present predictions of St_x with the experimental data of several investigators is shown in Fig. 2. Run 1, in Fig. 2(a), is a zero pressure gradient ($\bar{K}=0$) baseline case with the solid curve being the present predictions and the experimental data are from Ref. [1] with $7.6\times10^5<\mathrm{Re}_x<2.2\times10^6$. The agreement with the data seems to be adequate. The present method was used earlier in Ref. [9] with many different cases of zero pressure gradient for isothermal and constant flux surfaces, both with and without unheated starting lengths, and the agreement with data from three different investigators was good.

Figure 2(b) displays experimental data (Run F-3) taken by Filetti and reported in Ref. [1]. The data reductions, which led to the Stanton numbers in Ref. [1], used as the driving potential difference ΔT, which is the wall temperature minus the freestream stagnation temperature. Some of the data just prior to the end of the acceleration was taken at high enough freestream velocity to cause appreciable viscous dissipation effects. Hence, the driving potential difference between wall and fluid that should be used is the wall temperature minus the adiabatic wall temperature. When this was done, in the present work, it led to slightly higher than reported experimental St_x values at some of the data points. However, the maximum correction to the data only raised St_x by 1.1%. In Run F-3, the boundary layer trip was located at about $X=1.17$, Re_x varied between 4.7×10^5 and 4.8×10^6, the acceleration region was between $X=0.65$ and about 0.90 with a maximum acceleration parameter $\bar{K}$ equal to 2.5×10^6, a very strong acceleration. The effective location of the step change in surface heating was taken to be $X=0.33$. Predictions, the solid curve, are pretty good except for a region just after the start of acceleration where the characteristic drop in St_x due to the acceleration is seen. This is due to the "lag" in the fluid flow in adjusting to the somewhat abrupt change in freestream velocity. The fluid flow and temperature fields in the fluid do not instantaneously change from the ones they had in the previous constant freestream velocity flow to those eventually appropriate to a more or less constant $\bar{K}$ flow. The integral predictions, on the other hand, do react right away to the abrupt change in $\bar{K}$. It will be seen later that even the $k-\in$ finite difference procedures have difficulty in this region. It can be seen from the figure that the present predictions do very well in the "recovery" region at, and after, the acceleration ends in the neighborhood of $X>0.90$. This tends to agree with the experimental observations in Ref. [20], where it was noted that there was a substantial lag in the overall response of the boundary layer at the beginning of acceleration and a considerably smaller lag at the end of acceleration.

The experimental Stanton number data in Fig. 2(c) come from Ref. [2], where the boundary layer trip was at the start of the test section for Run 091069-1. The local length Reynolds number Re_x varied from about 8.2×10^4 to 3.6×10^6, and $\bar{K}$ was held essentially constant at 2×10^{-6} from about $X=0.25$ to about 0.60. This was a strong acceleration, which started somewhat gradually, but ended quite abruptly. The present predictions follow the data very well in the entire acceleration region and do fairly well in the long recovery region ($X>0.60$).

The data in Thielbahr et al. [3], is shown in Fig. 2(d). his Run 072968-1, where Re_x ranged from 1.08×10^5 to 2.8×10^6. The data are for a moderately strong acceleration, the nominal value of $\bar{K}$ was 1.45×10^6, which started a gradual rise at $X=0.18$ and ends pretty abruptly at $X=0.62$. The predicted St_x values follow about the same trends as in Run 091069-1 of Kearney, good agreement with data in the acceleration region and reasonably good in the recovery region $X>0.62$.

Figure 3 continues comparison between experimental St_x data and the present predictions.

In Fig. 3(a), the data for Run 070869-1 is from Kearney, et al. [2] for Reynolds numbers, Re_x, varying from 6.5×10^4 to 2.8×10^6 with very strong acceleration, $\bar{K}=2.5\times10^{-6}$, occurring between $X=0.28$ and 0.43. The solid line, the predicted values, follows the data in the acceleration regions fairly well, though it overpredicts the St_x values near the end of that region and is seen to do very well in the long recovery region $X>0.43$.

Run F-2 data in Fig. 3(b) is from Ref. [1], ($3.9\times10^5<\mathrm{Re}_x<4\times10^6$) with $\bar{K}$ increasing, fairly abruptly, from 0 to a maximum value of 3×10^{-6} at $X=0.65$ followed by a gradual reduction to 0 at $X=0.94$. Surface heating began at $X=0.33$. The predictions are good in the flat plate region before the acceleration, but are not that good at the beginning of the acceleration because of the lag in response of the data. However, when the lag region has passed, the predictions in that section of the acceleration region are good again. There is a much smaller lag in the decreasing $\bar{K}$ region than

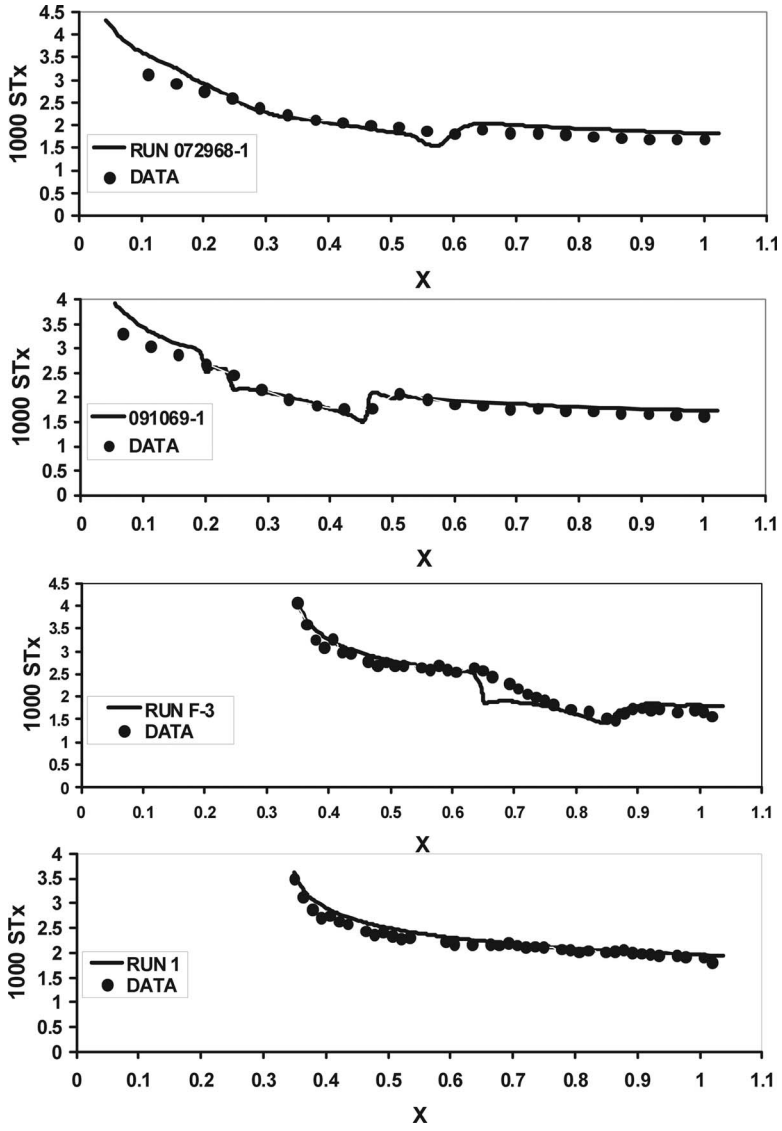

Fig. 2 Predictions and experimental data (•). Runs 1 and F-3 data [1]. Run 091069-1 data [2]: $L=1.83$ m (6.0 ft). Run 072968-1 data [3]: $L=2.29$ m (7.5 ft).

there was in the increasing $\bar{K}$ region due to the much more gradual decrease in $\bar{K}$ to 0 compared with its abrupt increase from $\bar{K}=0$. Agreement of predictions with data is again good for $X>0.90$.

Figure 3(*c*) contains some more data from Ref. [2], namely, Run 092469-1, $(6.4\times10^4<\mathrm{Re}_x<2.7\times10^6)$. The acceleration to $\bar{K}=2.5\times10^{-6}$ starts out at about $X=0.48$ and ends around 0.89. The predictions are reasonably good in the acceleration and recovery regions. Surprisingly, the predicted St_x values are poorest in the $\bar{K}=0$, flat plate region, $X<0.48$. The reason for this is not apparent since other flat plate initial region predictions, such as in Runs 1, F-3, F-2, and numerous other cases in Ref. [9], have been good to very good.

In Fig. 4 it is shown not only the comparison of present predictions to experimental data of three runs of Ref. [1], but also the predictions of Jones and Launder [4]. Their predictions came from a finite difference solution of the governing partial differential equations using a $k-\in$ (turbulent kinetic energy and dissipation) turbulence model. Figure 4(*a*) shows the data from Run F-3, previously discussed, compared with the solution of Jones and Launder [4], represented by the dashed curve and to the present solution, the solid curve. The present method is closer to the data in most of the strong acceleration region, between $X=0.65$ and 0.90, and in the recovery region $X>0.90$. It is seen that the finite difference solution also responds to the beginning of the acceleration before the data does, due to the lag in the physical process, but does not drop as abruptly or as low as the present integral method.

The experimental data in Fig. 4(*b*) is from Run 42 $(3.3\times10^5<\mathrm{Re}_x<3.4\times10^6)$. This is one of the more challenging data sets in Ref. [1], with a long initial constant $\bar{K}=0$ region to about $X=0.65$ followed by a rise to $\bar{K}=4.0\times10^{-6}$ at $X=0.68$ continuing to 0.75 where $\bar{K}$ decreases slightly to 3.6×10^{-6} before increasing again to 4.0×10^{-6} followed by a decrease to 0.0 between $X=0.83$ and $X=0.95$. Thus, this is a case of a very strongly accelerated flow. The present integral prediction comes closer to following the data in most of the initial flat plate region and most of the acceleration region than do the predictions of Jones and Launder [4]. Their predictions are somewhat better just after the start of acceleration and just after the decrease in $\bar{K}$ toward 0.0 while the present results are a little better in the recovery zone $X>0.95$.

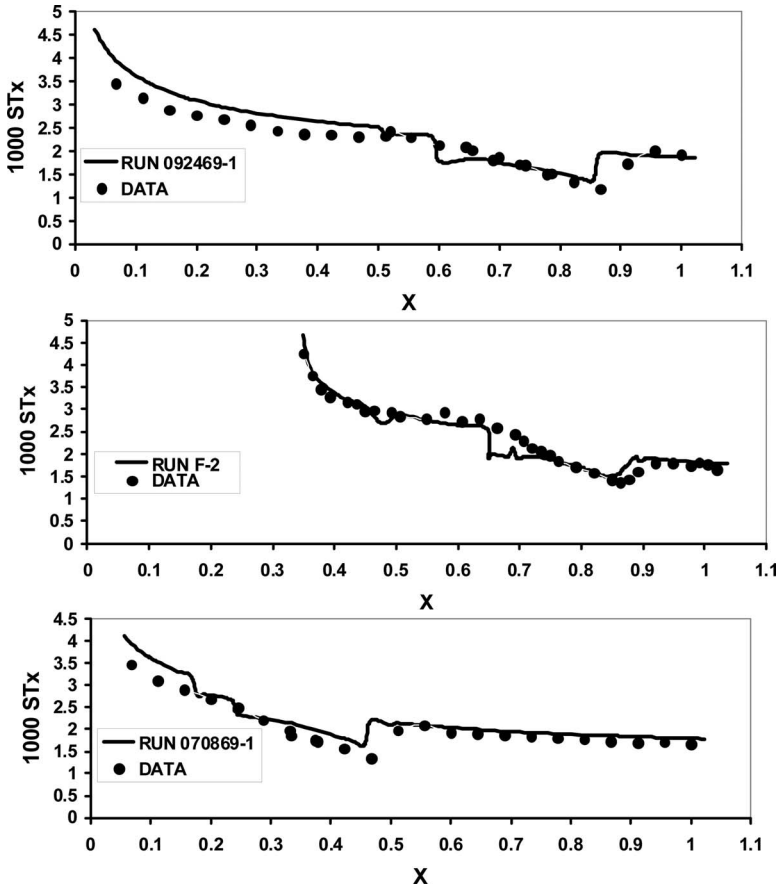

Fig. 3 Predictions and experimental data (•). Run 070869-1 data [2]. Run F-2 data [1]: $L=1.83$ m (6.0 ft). Run 092469-1, data [2]: $L=2.29$ m (7.5 ft).

This Run 42 has also been predicted by El-Hawary and Nicoll [21], who used a finite difference solution with a modified one equation model of turbulence. As can be seen from their Fig. 8, (their "flow 14" is Run 42) their predictions are better than those of Jones and Launder (also shown in their Fig. 8) in the initial flat plate region, about the same in the acceleration region, but are far below the data and the predictions of Jones and Launder in the region for $X>0.87$ where $\bar{K}$ decreases to zero and remains at zero. Overall, the present predictions are quite a bit better at tracking the data than those in [21]. They also show, in their Fig. 8, the predictions of Kreskovsky et al. [22], who also used a finite difference procedure with a turbulence kinetic energy equation. Their predictions for Run 42, however, very greatly underestimate the data everywhere except in the initial region of $\bar{K}=0.0$, the flat plate region.

Figure 4(*c*) has St_x data from Run 10 ($7.1\times10^5<Re_x<6.4\times10^6$) of Ref. [1]. In this run the acceleration parameter $\bar{K}$ increased for 0.0 at $X=0.81$, reached a maximum value of 3.6×10^{-6} at $X=0.88$ then immediately decreased from $X=0.88$ to 0.0 at about $X=0.95$. As was discussed in connection with Run F-3 in Fig. 2(*b*), slight corrections were made to some of the measured St_x data to account for viscous dissipation. The maximum change in their St_x values was only about 2.2%. Neither the present predictions nor those of Jones and Launder [4] are able to follow the lowest data points, which lag both predictions near the end of the acceleration region. Overall, though, the predictions of Jones and Launder [4] are better than those of the present method for Run 10 in Fig. 4(*c*).

Looking at the results in Figs. 4(*a*)–4(*c*), it seems as if some of the statements made in Ref. [21] still ring true, namely, that predictions of highly accelerating flows, generally speaking, are not as accurate as those for flows which are not strongly accelerated. These flows are so complex that even finite difference methods cannot predict these flows as accurately as one might wish. As more evidence of this, Shishov [23] used a modified $k-\in$ turbulence model to predict the cross-stream distribution of turbulent heat flux for three turbulent boundary layers, one had a zero pressure gradient, another was a strongly retarded flow (adverse pressure gradient), and the last was an accelerated flow. He found good agreement of his predictions with data for both the zero pressure gradient and the adverse pressure gradient flows, but not for the accelerated boundary layer. Hence another modification to his turbulence model was made specifically for accelerated flow which improved his predictions, but they still were not as good as for the zero and adverse pressure gradient flows as is seen in his Fig. 19.

The results of a sensitivity analysis are shown in Fig. 5. The experimental data is for Run 25 of Ref. [1], with Re_x ranging from 4×10^5 to 3.9×10^6 with $\bar{K}$ remaining approximately constant at 0.75×10^{-6} from $X=0.32$ to about 0.933 and then decreasing to about 0.0 at $X=1.0$. What is being studied here is how much the effect of three different effective locations of the start of heating has on the predicted downstream Stanton numbers. This was done because the experimental attempt at a "step" change to begin heating results, in actuality, in a range of $X=0.3015-0.3352$ for the step change to take place. Thus, calculations were carried out with the following three different effective start of heating locations: $X=0.3015$, 0.3245, and 0.3352, Runs 25a, 25, and 25b, respectively, in Fig. 5. As is evident from the figure, there is little difference in the predicted St_x values for Runs 25b and 25, which

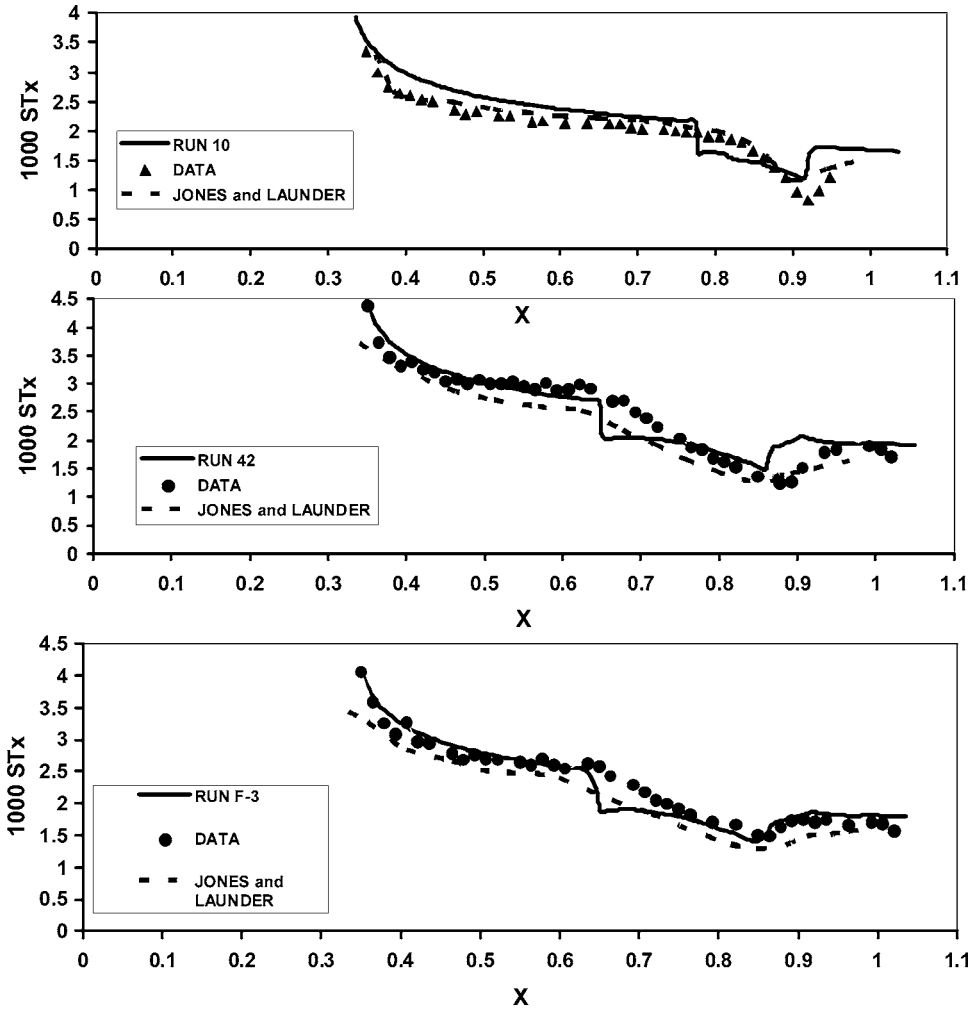

Fig. 4 Comparison of present predictions and those of Jones and Launder [4] with data (•). Runs 10, 42, and F-3 data [1]: $L=1.83$ m (6.0 ft).

have essentially merged already at $X=0.360$. Even the calculation using a somewhat extreme choice for the start of heating ($X=0.3015$) essentially coincides with the other two calculations by about $X=0.42$. Therefore, we find that the predictions certainly are not overly sensitive to the precise choice of the beginning of heating. The predictions for this case, at first, somewhat overpredict the data and underpredict the data in much of the acceleration region, but then shows good agreement with the data for the region, near the end, $X>0.93$, where K is being reduced to almost zero.

Additional comparisons of predictions with Stanton number data are given by Fig. 6. Figure 6(*a*) shows Run 100269-1 of

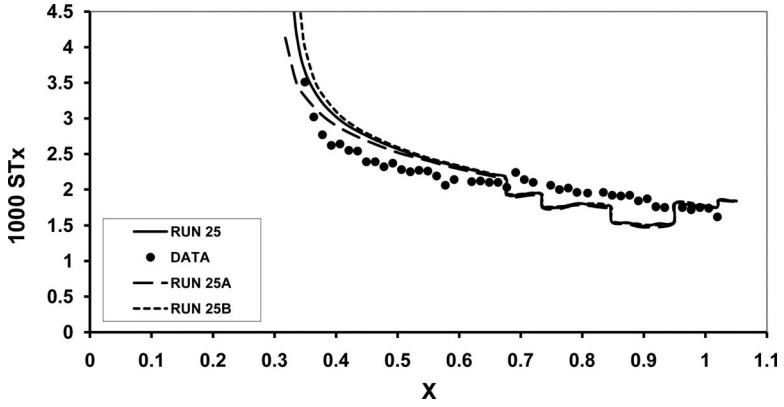

Fig. 5 Comparison of predictions with data (•) for different locations of the start of calculation. Run 25 data [1]: $L=1.83$ m (6.0 ft).

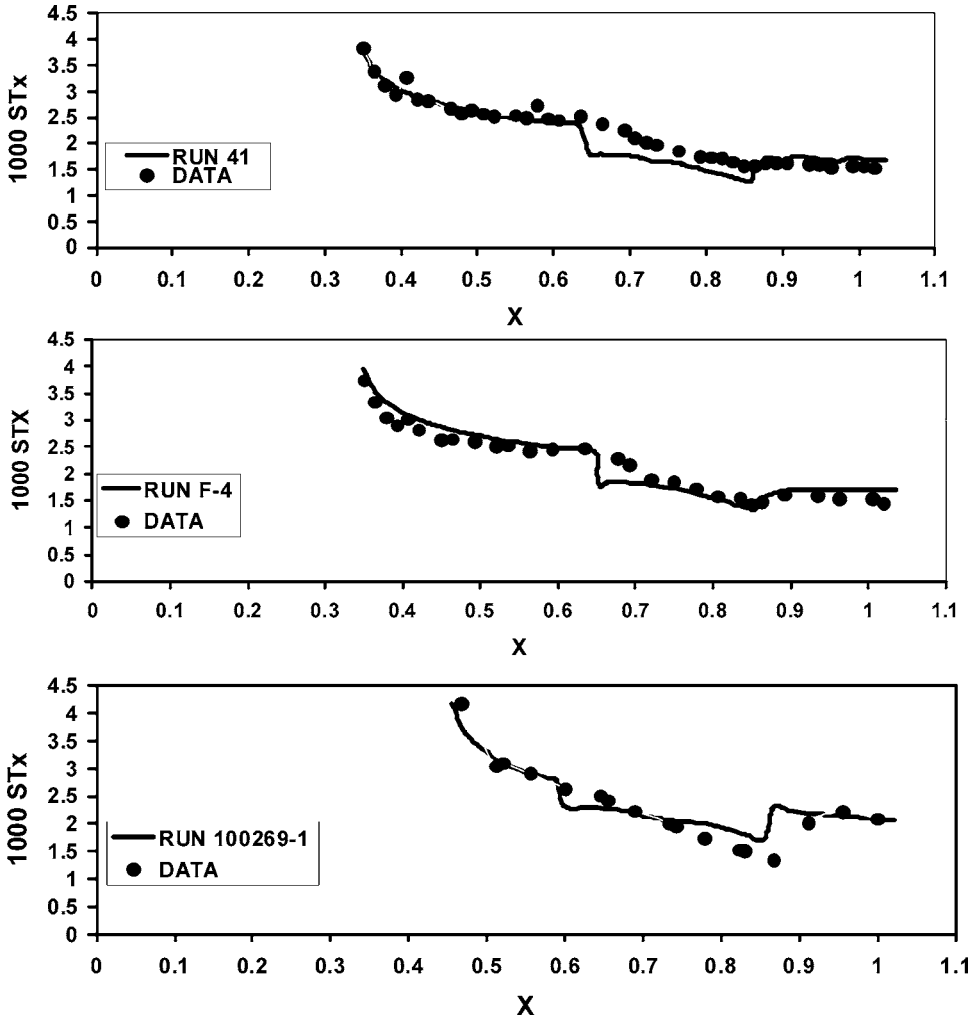

Fig. 6 Predictions and data (•). Runs 41 and F-4 data [1]: $L=1.83$ m (6.0 ft). Run 100269-1 data [2]: $L=2.29$ m (7.5 ft).

Ref. [2], ($4.4\times10^5<\mathrm{Re}_x<2.7\times10^6$) which has a long unheated starting length with heating beginning at $X=0.44$ and a very strong acceleration $\bar{K}=2.5\times10^{-6}$, from $X=0.70$ to about 0.84. $\bar{K}$ starts increasing at $X=0.55$ to 2.5×10^{-6} and decreases back to about zero around $X=0.93$. While the agreement between predictions and data is very good in the initial flat plate region and the recovery region, the present method overpredicts St_x in the later stages of acceleration.

Figure 6(*b*) contains data from Run F-4 of Ref. [1]; Re_x varies from about 5.4×10^5 to 5.45×10^6 while the acceleration parameter $\bar{K}$ ramps up, rather abruptly, from 0.0 to a maximum value of 2.2×10^{-6} before it starts decreasing, gradually, from this value at 0.83 to 0.0 at $X=0.92$. As with some previous runs, some of the experimental St_x data values were given a small correction, in the present work, to account, more rigorously, for viscous dissipation effects. The maximum correction in their St_x data values was only 1.6%. The present integral method's predictions do reasonably well everywhere except just after the start of the acceleration, which, due to the rapid increase in $\bar{K}$ in the very short distance discussed above, causes a significant lag in the physical processes causing the data to be higher than the predictions.

Data shown in Fig. 6(*c*) also comes from Ref. [1] (Run 41, where $6.5\times10^5<\mathrm{Re}_x<6.6\times10^6$). Acceleration begins at about $X=0.62$ and ends close to 0.90 with a maximum $\bar{K}=1.84\times10^{-6}$. Here again corrections were made to some of the data for viscous dissipation with the largest correction to St_x being 2%. Predictions are pretty good in the initial flat plate region where $\bar{K}=0.0$ for $X<0.62$, also in the region where $\bar{K}$ is being reduced to 0.0, $0.86<X<0.90$ and in the recovery region where $\bar{K}$ has returned to 0.0, for $X>0.90$. However, the predictions consistently underpredict the data in the bulk of the acceleration region ($0.62<X<0.86$).

4 Concluding Remarks

Values of the thermal wake strength parameter π_{teq} were calculated for accelerated equilibrium turbulent boundary layers. These π_{teq} values depend on the turbulent Prandtl number and the Clauser pressure gradient parameter and are given in graphical form. It was found that π_{teq} values decrease with both increasing values of β and increasing values of Pr_t for accelerated boundary layers.

Using the π_{teq} values, predictions of the dependence of the local Stanton number St_x with position x were made using an integral method. This integral method, which used inner variables u^+, T^+, and y^+, takes into approximate account the dependence of the wake strengths π and π_t on π_{eq} and π_{teq} and the momentum thickness and enthalpy thickness Reynolds numbers, respectively. Also, an approximate procedure to account for the turbulent Prandtl number's increase with increasing acceleration parameter was proposed and used in the calculations.

Comparison of predicted values of St_x with experimental data, from the literature, were made for a large number of cases ranging from zero acceleration to mild, moderate, strong, and very strong accelerations as the acceleration parameter $\bar{K}$ increased. On the whole, it seemed as if the comparison of predictions to data was satisfactory and reasonable for most of the cases. There was difficulty in making good predictions, for some cases, just after the start of acceleration when $\bar{K}$ increased from 0 to a much larger value in a very short distance in x. This is caused by the lag, in the response of the hydrodynamic and thermal boundary layers, which the present integral method fails to exhibit. However, it was seen that even the $k-\in$ two equation models of turbulence, in finite difference solutions of the governing partial differential equation, also failed to predict the lag of the actual physical processes.

Comparisons of the present integral method predictions with previous two equation finite difference solutions for a few cases were made and it was found that the integral method predictions of St_x were better than those of the finite difference methods in two of the three cases.

Arguments were made for concluding, as others also have previously, that accurate predictions of strongly accelerated turbulent boundary layers are quite a bit more difficult than for decelerated or zero acceleration flows. This is borne out by the present work in which the predicted St_x values are not as good as experienced in two previous works [8,9], which dealt with zero and adverse pressure gradient turbulent boundary layers.

Nomenclature

b = slope in the temperature profile, Eq. (8)
B = a constant in the velocity profile, Eq. (2)
C_f = $2\tau_w/\rho u_s^2$, skin friction coefficient
C_p = constant pressure specific heat
C_t = Prandtl number function in temperature profile, Eq. (3)
H = δ^*/θ shape factor
i = enthalpy per unit mass
K = von Karman constant, 0.41
$\bar{K}$ = $\nu/u_s^2\ (du_s/dx)$
L = reference length
P = local pressure
Pr = molecular Prandtl number
Pr_t = turbulent Prandtl number
q_w = surface heat flux
Re_x = $u_s x/\nu$, local Reynolds number
St_x = $h_x/\rho c_p u_s$, local Stanton number
T, T_w, T_s = local, wall, and freestream temperatures, respectively
T^+ = $(T_w-T)\rho C_p u^*/q_w$
T_s^+ = value of T^+ in freestream
$T_{\delta^+}^+$ = value of T^+ at δ^+
u, u_s = local and freestream x velocity components
u^* = $\sqrt{\tau_w/\rho}$, friction velocity
u^+ = u/u^*, inner velocity
u_s^+ = freestream value of u^+
X = x/L nondimensional x coordinate
x = space coordinate along surface
x_0 = x value at the start of calculations
y = space coordinate normal to surface
y^+ = yu^*/ν, inner coordinate

Greek Symbols

β = $\delta^*(dP/dx)/\tau_w$, Clauser parameter
γ = defined in Eq. (7)
δ, δ_t = local thickness of velocity and thermal boundary layer, respectively
δ^* = displacement thickness, $\int_0^\infty(1-\rho u/\rho_s u_s)dy$
δ^+, δ_t^+ = value of y^+ at $y=\delta$ and δ_t
Δ = local enthalpy thickness, $\int_0^\infty(\rho u/\rho_s u_s)[(i-i_s)/(i_w-i_s)]dy$
θ = local momentum thickness, $\int_0^\infty(\rho u/\rho_s u_s)(1-u/u_s)dy$
ν = kinematic viscosity
ρ = mass density
τ_w = surface shear stress

References

[1] Moretti, P. M., and Kays, W. M., 1964, "Heat Transfer Through an Incompressible Turbulent Boundary Layer With Varying Free-Stream Velocity and Varying Surface Temperature," Thermosciences Division Report No. PG-1, Stanford University, Stanford, CA.
[2] Kearney, D. W., Moffat, R. J., and Kays, W. M., 1970, "The Turbulent Boundary Layer: Experimental Heat Transfer With Strong, Favorable Pressure Gradients and Blowing," Thermosciences Division Report No. HMT-12, Stanford University, Stanford, CA.
[3] Thielbahr, W. H., Kays, W. M., and Moffat, R. J., 1972, "The Turbulent Boundary Layer on a Porous Plate: Experimental Heat Transfer With Uniform Blowing and Suction, With Moderately Strong Acceleration," ASME J. Heat Transfer, **94**, pp. 111–118.
[4] Jones, W. P., and Launder, B. E., 1972, "The Prediction of Laminarization With a Two-Equation Model of Turbulence," Int. J. Heat Mass Transfer, **15**, pp. 301–314.
[5] Sucec, J., and Lu, Y., 1990, "Heat Transfer Across Turbulent Boundary Layers With Pressure Gradient," ASME J. Heat Transfer, **112**, pp. 906–912.
[6] Wang, X., Castillo, L., and Araya, G., 2008, "Temperature Scalings and Profiles in Forced Convection Turbulent Boundary Layers," ASME J. Heat Transfer, **130**, pp. 021701-01–021701-17.
[7] So, R. M. C., 1994, "Pressure Gradient Effects on Reynolds Analogy for Constant Property Equilibrium Turbulent Boundary Layers," Int. J. Heat Mass Transfer, **37**, pp. 27–41.
[8] Sucec, J., 2005, "Calculation of Turbulent Boundary Layers Using Equilibrium Thermal Wakes," ASME J. Heat Transfer, **127**, pp. 159–164.
[9] Sucec, J., 2006, "Modern Integral Method Calculation of Turbulent Boundary Layers," J. Thermophys. Heat Transfer, **20**, pp. 552–557.
[10] Blackwell, B. F., 1972, "The Turbulent Boundary Layer on a Porous Plate: An Experimental Study of the Heat Transfer Behavior With Adverse Pressure Gradients," Ph.D. thesis, Department of Mechanical Engineering, Stanford University, Stanford, CA.
[11] Mellor, G. L., and Gibson, D. M., 1966, "Equilibrium Turbulent Boundary Layers," J. Fluid Mech., **24**, pp. 255–274.
[12] Sucec, J., and Oljaca, M., 1995, "Calculation of Turbulent Boundary Layers With Transpiration and Pressure Gradient Effects," Int. J. Heat Mass Transfer, **38**, pp. 2855–2862.
[13] Cebeci, T., and Bradshaw, P., 1984, *Physical and Computational Aspects of Convective Heat Transfer*, Springer-Verlag, New York, p. 188.
[14] Fridman, E., 1997, "Heat Transfer and Temperature Distribution in a Turbulent Flow Over a Flat Plate With an Unheated Starting Length," *Proceedings of the 1997 National Heat Transfer Conference*, HTD-Vol. 346, Chap. 8, pp. 127–132.
[15] Kays, W. M., 1994, "Turbulent Prandtl Number—Where Are We?" ASME J. Heat Transfer, **116**, pp. 284–295.
[16] Roganov, P. S., Zabolotsky, V. P., Shishov, E. V., and Leontiev, A. I., 1984, "Some Aspects of Turbulent Heat Transfer in Accelerated Flows on Permeable Surfaces," Int. J. Heat Mass Transfer, **27**, pp. 1251–59.
[17] Launder, B. E., and Lockwood, F. C., 1969, "An Aspect of Heat Transfer in Accelerating Turbulent Boundary Layers," ASME J. Heat Transfer, **91**, pp. 229–234.
[18] Kays, W. M., Moffat, R. J., and Thielbahr, W. H., 1970, "Heat Transfer to the Highly Accelerated Turbulent Boundary Layer With and Without Mass Addition," ASME J. Heat Transfer, **92**, pp. 499–505.
[19] Kays, W. M., Crawford, M. E., and Weigand, B., 2005, *Convective Heat and Mass Transfer*, 4th ed., McGraw-Hill, New York.
[20] Kearney, D. W., Kays, W. M., and Moffat, R. J., 1973, "Heat Transfer to a Strongly Accelerated Turbulent Boundary Layer: Some Experimental Results, Including Transpiration," Int. J. Heat Mass Transfer, **16**, pp. 1289–1305.
[21] El-Hawary, M. A., and Nicoll, W. B., 1979, "The Prediction of Highly Accelerating Flows Near Smooth Walls," *Proceedings of the Joint ASME-CSME Applied Mechanics, Fluids Engineering and Bioengineering Conference*, H. E. Weber, ed., pp 93–106.
[22] Kreskovsky, J. P., Shamroth, S. J., and McDonald, H., 1975, "Application of a General Boundary Layer Analysis to Turbulent Boundary Layers Subjected to Strong Favorable Pressure Gradients," ASME J. Fluids Eng., **97**, pp. 217–224.
[23] Shishov, E. V., 1991, "Turbulent Heat and Momentum Transfer in Boundary Layers Under Strong Pressure Gradient Conditions: Analysis of Experimental Data and Numerical Predictions," Exp. Therm. Fluid Sci., **4**, pp. 389–398.

Analytic Approximations for a Strongly Nonlinear Problem of Combined Convective and Radiative Cooling of a Spherical Body

A. El-Nahhas
Department of Mathematics,
Helwan Faculty of Science,
Helwan University,
Helbawy Street,
Cairo 11795, Egypt
e-mail: aasayed35@yahoo.com

In this paper, a nonlinear problem for combined convective and radiative cooling of a spherical body is considered. This problem represents a strong nonlinearity in both the governing equation and the boundary condition. Analytic approximations for the solution of this problem are obtained using the homotopy analysis method and via a polynomial exponential basis. Also, the effect of the radiation-conduction parameter N_{rc} and the Biot number Bi for the temperature on the surface of the spherical body is investigated and discussed. [DOI: 10.1115/1.3154625]

Keywords: partial differential equations, boundary value problems, unsteady nonlinear heat-conduction problems, combined convective and radiative cooling, homotopy analysis method

1 Introduction

Problems of transient heat-conduction in a solid with combined convective and radiative cooling on the solid surface have many applications such as glass manufacturing, nuclear reactor thermo-hydraulics, and aerothermodynamic heating of spaceships and satellites. The solution for heat-conduction problems, using probability methods applied to a plate subjected to simultaneous boundary convection and radiation, was introduced by Haji-Sheikh and Sparrow [1]. Crosbie and Viskanta [2] studied transient heating or cooling of a plate by combined convection and radiation. Davies [3] discussed the cooling of a plate by combined thermal-radiation using the heat balance integral technique. Sunden [4,5] handled, respectively, the problem of transient heat-conduction in a composite slab by a timevarying incident heat-flux, combined with convective and radiative cooling, and the problem of transient conduction in a cylindrical-shell with a timevarying incident surface heat-flux and convective and radiative surface cooling. Parang et al. [6] studied the problem of inward solidification of a liquid in cylindrical and spherical geometries due to combined convective and radiative cooling by the regular perturbation method. Siegel [7] studied transient heat transfer in a semitransparent radiating layer with boundary convection and surface reflections. Su [8] investigated the transient radiative cooling of a spherical body by using improved lumped models. We consider, here, the problem of combined convective and radiative cooling of a spherical body. This problem has a strong nonlinearity in both the governing equation and the boundary condition, and so encounters difficulties in obtaining exact solutions. The homotopy analysis method presented by Liao [9–12] is a powerful tool to treat such complicated nonlinearity. This method does not depend on the existence of small or large parameters in the studied problem such as the perturbation methods [13–17], and, unlike other methods, such as Lyapunov's small parameter method [18], the δ-expansion method [19], and the Adomian decomposition method [20–23], it has the ability to control convergence for the obtained solutions. Liao and other authors [24–30] applied this method in a successful manner to many nonlinear applications in science and engineering. To show the basic ideas of this method, let us consider the nonlinear equation

$$N[g(r,t)] = 0 \tag{1}$$

where N is a nonlinear operator, g is an unknown function, r is a vector of spatial variables, and t is the time. By means of the traditional concept of homotopy, Liao [12] constructed the so-called zero-order deformation equation

$$(1-q)L[\phi(r,t,q) - g_0(r,t)] = qhN[\phi(r,t,q)] \tag{2}$$

where $q\varepsilon$ [0,1] is an embedding parameter, L is an auxiliary linear operator, g_0 is an initial guess for the unknown function g, and h is an auxiliary parameter. As q varies from 0 to 1, the solution of Eq. (2) varies from the initial guess g_0 to the exact solution g of the nonlinear equation (1) as follows:

$$\phi(r,t,0) = g_0(r,t), \quad \phi(r,t,1) = g(r,t) \tag{3}$$

Expanding $\phi(r,t,q)$ in the Taylor series, with respect to q, one has

$$\phi(r,t,q) = g_0(r,t) + \sum_{m=1}^{\infty} g_m(r,t)q^m \tag{4}$$

$$g_m(r,t) = \frac{1}{m!} \left. \frac{\partial^m \phi(r,t,q)}{\partial q^m} \right|_{q=0} \tag{5}$$

If the parameter h is properly chosen, such that the series (4) is convergent at $q=1$, then from Eq. (3)

$$g(r,t) = g_0(r,t) + \sum_{m=1}^{\infty} g_m(r,t) \tag{6}$$

Differentiating the zero-order deformation equation (2), m times with respect to q, setting $q=0$, and finally dividing by $m!$, we obtain the mth order deformation equation

$$L[g_m(r,t) - \chi_m g_{m-1}(r,t)] = hP_m(r,t), \quad m \geq 1 \tag{7}$$

Contributed by the Heat Transfer Division of ASME for publication in the JOURNAL OF HEAT TRANSFER. Manuscript received December 23, 2008; final manuscript received May 4, 2009; published online August 26, 2009. Review conducted by Cholik Chan.

$$P_m(r,t) = \frac{1}{(m-1)!} \left. \frac{\partial^{m-1} N[\phi(r,t,q)]}{\partial q^{m-1}} \right|_{q=0} \tag{8}$$

$$\chi_m = \begin{cases} 0, & m = 1 \\ 1, & m > 1 \end{cases} \tag{9}$$

The solutions $g_m(r,t)$, where $m \geq 1$, of Eq. (7) are called the mth deformations, and can be computed by any symbolic software. The homotopy analysis method provides a freedom to choose L and g_0, and control the convergence by the aid of the parameter h to obtain analytic approximations in terms of suitable basis of functions.

2 Mathematical Formulation

In the problem of combined convective and radiative cooling of a spherical body, it is assumed that the spherical body is homogeneous, isotropic, opaque, and at the time $t=0$, it is suddenly exposed to a constant fluid temperature T_f and a constant radiation sink temperature T_s.

The mathematical model for this problem has the form

$$\rho c_\rho \frac{\partial T}{\partial t} = \frac{1}{r^2}\frac{\partial}{\partial r}\left[r^2 k(T) \frac{\partial T}{\partial r} \right] \quad \text{in} \quad r < R \quad \text{and} \quad \text{for} \quad t > 0 \tag{10}$$

and subject to the conditions

$$T(r,0) = T_i \quad \text{in} \quad r \leq R \quad \text{and} \quad \text{at} \quad t = 0 \tag{11}$$

$$-k(T)\frac{\partial T}{\partial r} = h_t(T - T_f) + \varepsilon\sigma(T^4 - T_s^4) \quad \text{at} \quad r = R \quad \text{and} \quad \text{for} \quad t > 0 \tag{12}$$

$$\frac{\partial T}{\partial r} = 0 \quad \text{at} \quad r = 0 \quad \text{and} \quad \text{for} \quad t > 0 \tag{13}$$

where ρ (const) is the density, c_ρ (const) is the specific heat, T is the temperature, t is the time, r is the spatial coordinate, $k(T)$ is the thermal conductivity, R is the radius of the spherical body, T_i is the initial uniform temperature for the spherical body, h_t is the convective heat transfer coefficient, ε is the surface emissivity, and σ is the Stefan–Boltzmann constant.

Introducing the concept of the adiabatic surface temperature T_a by the equation

$$h_t(T_a - T_f) + \varepsilon\sigma(T_a^4 - T_s^4) = 0 \tag{14}$$

we then have

$$h_t T_f + \varepsilon\sigma T_s^4 = h_t T_a + \varepsilon\sigma T_a^4 \tag{15}$$

and Eq. (12) takes the form

$$-k(T)\frac{\partial T}{\partial r} = h_t(T - T_a) + \varepsilon\sigma(T^4 - T_a^4) \quad \text{at} \quad r = R \quad \text{and} \quad \text{for} \quad t > 0 \tag{16}$$

Also, using the dimensionless parameters

$$\theta = \frac{T}{T_i}, \quad \eta = \frac{r}{R}, \quad \tau = \frac{\alpha_0 t}{R^2}, \quad \lambda = \frac{k}{k_0}$$

$$\theta_a = \frac{T_a}{T_i}, \quad \alpha_0 = \frac{k_0}{\rho c_\rho}, \quad \mathrm{Bi} = \frac{h_t R}{k_0}, \quad N_{\mathrm{rc}} = \frac{\varepsilon\sigma R T_i^3}{k_0} \tag{17}$$

Equations (10)–(13) are transformed to the form

$$\frac{\partial\theta}{\partial\tau} = \frac{1}{\eta^2}\frac{\partial}{\partial\eta}\left[\eta^2 \lambda(\theta) \frac{\partial\theta}{\partial\eta} \right] \quad \text{in} \quad \eta < 1 \quad \text{and} \quad \text{for} \quad \tau > 0 \tag{18}$$

with the conditions

$$\theta(\eta,0) = 1 \quad \text{in} \quad \eta \leq 1 \quad \text{and} \quad \text{at} \quad \tau = 0 \tag{19}$$

$$-\lambda(\theta)\frac{\partial\theta}{\partial\eta} = \mathrm{Bi}(\theta - \theta_a) + N_{\mathrm{rc}}(\theta^4 - \theta_a^4) \quad \text{at} \quad \eta = 1 \quad \text{and} \quad \text{for} \quad \tau > 0 \tag{20}$$

$$\frac{\partial\theta}{\partial\eta} = 0 \quad \text{at} \quad \eta = 0 \quad \text{and} \quad \text{for} \quad \tau > 0 \tag{21}$$

where k_0 is a reference thermal conductivity and α_0 is a reference thermal diffusivity. The parameters Bi and N_{rc} are known as the Biot number and the radiation-conduction parameter, respectively.

Considering the case for which the thermal conductivity has a linear form in the temperature

$$k = k_0[1 + bT], \quad b(\text{const}) \tag{22}$$

we have

$$\lambda(\theta) = 1 + \beta\theta, \quad \beta = \frac{bT_i}{k_0} \tag{23}$$

and Eqs. (18)–(21) can be written as

$$\frac{\partial\theta}{\partial\tau} = \frac{1}{\eta^2}\frac{\partial}{\partial\eta}\left[\eta^2(1 + \beta\theta)\frac{\partial\theta}{\partial\eta} \right] \quad \text{in} \quad \eta < 1 \quad \text{and} \quad \text{for} \quad \tau > 0 \tag{24}$$

with the conditions

$$\theta(\eta,0) = 1 \quad \text{in} \quad \eta \leq 1 \quad \text{and} \quad \text{at} \quad \tau = 0 \tag{25}$$

$$-(1 + \beta\theta)\frac{\partial\theta}{\partial\eta} = \mathrm{Bi}(\theta - \theta_a) + N_{\mathrm{rc}}(\theta^4 - \theta_a^4) \quad \text{at} \quad \eta = 1 \quad \text{and} \quad \text{for} \quad \tau > 0 \tag{26}$$

$$\frac{\partial\theta}{\partial\eta} = 0 \quad \text{at} \quad \eta = 0 \quad \text{and} \quad \text{for} \quad \tau > 0 \tag{27}$$

Finally, by means of the time transformation

$$\xi = 1 - \exp(-\tau) \tag{28}$$

Eqs. (24)–(27) have the form

$$\frac{\partial^2\theta}{\partial\eta^2} + \beta\theta\frac{\partial^2\theta}{\partial\eta^2} + \frac{2}{\eta}\beta\theta\frac{\partial\theta}{\partial\eta} + \beta\left[\frac{\partial\theta}{\partial\eta}\right]^2 + \frac{2}{\eta}\frac{\partial\theta}{\partial\eta} - (1 - \xi)\frac{\partial\theta}{\partial\xi} = 0 \tag{29}$$

with the conditions

$$\theta(\eta,0) = 1 \quad \text{in} \quad \eta \leq 1 \quad \text{and} \quad \text{at} \quad \xi = 0 \tag{30}$$

$$-(1 + \beta\theta)\frac{\partial\theta}{\partial\eta} = \mathrm{Bi}(\theta - \theta_a) + N_{\mathrm{rc}}(\theta^4 - \theta_a^4) \quad \text{at} \quad \eta = 1, \quad 0 < \xi \leq 1 \tag{31}$$

$$\frac{\partial\theta}{\partial\eta} = 0 \quad \text{at} \quad \eta = 0, \quad 0 < \xi \leq 1 \tag{32}$$

Equations (29)–(32) represent strong nonlinearity, not only in the governing equation (29), but also in the boundary condition (31). Liao et al. [31] applied the homotopy analysis method to give analytic approximations to the problems (29)–(32), via a polynomial basis. Here, we apply the same method to obtain analytic

approximations to Eqs. (29)–(32), but via a polynomial exponential basis.

3 Application of the Homotopy Analysis Method

Applying the homotopy analysis method on Eqs. (29)–(32), we use the basis

$$\eta^n e^{m\eta}, \quad n,m \geq 0 \tag{33}$$

Also, we express the solution by the rule of expression

$$\theta(\eta,\xi) = \sum_{m=0}^{\infty} A_{m0} e^{m\eta} + \sum_{m=0}^{\infty}\sum_{n=2}^{\infty} A_{mn}\eta^n e^{m\eta} \tag{34}$$

where A_{m0} and A_{mn} are functions of the dimensionless time ξ.

Viewing Eqs. (29)–(34), we chose an initial approximation and an auxiliary linear operator for the governing Eq. (29) as follows:

$$\theta_0(\eta,\xi) = 1 + (\theta_a - 1)\xi - \xi(1-\xi)\eta^2 e^{\eta} \tag{35}$$

$$L_1 = \frac{1}{(\eta+1)} e^{-\eta}\left[\frac{\partial^2}{\partial\eta^2} - \frac{\partial}{\partial\eta}\right] \tag{36}$$

Also, we choose the following auxiliary linear operator, for the nonlinear boundary condition (31), at $\eta=1$ and $0<\xi\leq 1$:

$$L_2 = \frac{\partial}{\partial\eta} + \mathrm{Bi} \tag{37}$$

We construct the so-called zero-order deformation equation

$$(1-q)L_1[\phi(\eta,\xi,q) - \theta_0(\eta,\xi)] = qh_1 N_1[\phi(\eta,\xi,q)] \tag{38}$$

with the conditions

$$\phi(\eta,0,q) = 1 \quad \text{in} \quad \eta \leq 1 \quad \text{and} \quad \text{at} \quad \xi = 0 \tag{39}$$

$$(1-q)L_2[\phi(\eta,\xi,q) - \theta_0(\eta,\xi)] = qh_2 N_2[\phi(\eta,\xi,q)],$$

$$\eta = 1, \quad 0 < \xi \leq 1 \tag{40}$$

$$\frac{\partial\phi(\eta,\xi,q)}{\partial\eta} = 0 \quad \text{at} \quad \eta = 0, \quad 0 < \xi \leq 1 \tag{41}$$

where h_1 and h_2 are auxiliary parameters, and q is an embedding parameter from 0 to 1. As q varies from 0 to 1, the solution of Eqs. (38)–(41) varies from the initial approximation to the exact solution of Eqs. (29)–(32).

Thus we have

$$\phi(\eta,\xi,0) = \theta_0(\eta,\xi), \quad \phi(\eta,\xi,1) = \theta(\eta,\xi) \tag{42}$$

The nonlinear operators N_1 and N_2 in Eqs. (38) and (40) are defined as

$$\begin{aligned} N_1[\phi(\eta,\xi,q)] = {} & \frac{\partial^2\phi(\eta,\xi,q)}{\partial\eta^2} + \beta\phi(\eta,\xi,q)\frac{\partial^2\phi(\eta,\xi,q)}{\partial\eta^2} \\ & + \frac{2}{\eta}\beta\phi(\eta,\xi,q)\frac{\partial\phi(\eta,\xi,q)}{\partial\eta} + \beta\left[\frac{\partial\phi(\eta,\xi,q)}{\partial\eta}\right]^2 \\ & + \frac{2}{\eta}\frac{\partial\phi(\eta,\xi,q)}{\partial\eta} - (1-\xi)\frac{\partial\phi(\eta,\xi,q)}{\partial\xi} \end{aligned} \tag{43}$$

$$\begin{aligned} N_2[\phi(\eta,\xi,q)] = {} & [1+\beta\phi(\eta,\xi,q)]\frac{\partial\phi(\eta,\xi,q)}{\partial\eta} + \mathrm{Bi}[\phi(\eta,\xi,q) - \theta_a] \\ & + N_{\mathrm{rc}}[\phi^4(\eta,\xi,q) - \theta_a^4] \quad \text{at} \quad \eta = 1, 0 < \xi \leq 1 \end{aligned} \tag{44}$$

By Taylor's series at $q=0$, we have

$$\phi(\eta,\xi,q) = \phi(\eta,\xi,0) + \sum_{m=1}^{\infty}\theta_m(\eta,\xi)q^m \tag{45}$$

where

$$\theta_m(\eta,\xi) = \frac{1}{m!}\left.\frac{\partial^m\phi(\eta,\xi,q)}{\partial q^m}\right|_{q=0} \tag{46}$$

If the parameters h_1 and h_2 are properly chosen, such that the series (45) converges at $q=1$, then from Eq. (42)

$$\theta(\eta,\xi) = \theta_0(\eta,\xi) + \sum_{m=1}^{\infty}\theta_m(\eta,\xi) \tag{47}$$

Differentiating the zero-order deformation in Eqs. (38)–(41), m times with respect to q, setting $q=0$, and finally dividing by $m!$, we obtain the mth order deformation equation

$$L_1[\theta_m(\eta,\xi) - \chi_m\theta_{m-1}(\eta,\xi)] = h_1 P_m(\eta,\xi) \tag{48}$$

with the conditions

$$\theta_m(\eta,0) = 0 \quad \text{in} \quad \eta \leq 1 \quad \text{and} \quad \text{at} \quad \xi = 0 \tag{49}$$

$$L_2[\theta_m(\eta,\xi) - \chi_m\theta_{m-1}(\eta,\xi)] = h_2 Q_m(\xi) \quad \text{at} \quad \eta = 1, \quad 0 < \xi \leq 1 \tag{50}$$

$$\frac{\partial\theta_m(\eta,\xi)}{\partial\eta} = 0 \quad \text{at} \quad \eta = 0, \quad 0 < \xi \leq 1 \tag{51}$$

where

$$\begin{aligned} P_m(\eta,\xi) = {} & \frac{\partial^2\theta_{m-1}(\eta,\xi)}{\partial\eta^2} + \beta\sum_{n=0}^{m-1}\theta_n(\eta,\xi)\frac{\partial^2\theta_{m-1-n}(\eta,\xi)}{\partial\eta^2} \\ & + \frac{2}{\eta}\beta\sum_{n=0}^{m-1}\theta_n(\eta,\xi)\frac{\partial\theta_{m-1-n}(\eta,\xi)}{\partial\eta} \\ & + \beta\sum_{n=0}^{m-1}\frac{\partial\theta_n(\eta,\xi)}{\partial\eta}\frac{\partial\theta_{m-1-n}(\eta,\xi)}{\partial\eta} + \frac{2}{\eta}\frac{\partial\theta_{m-1}(\eta,\xi)}{\partial\eta} - (1 \\ & - \xi)\frac{\partial\theta_{m-1}(\eta,\xi)}{\partial\xi} \end{aligned} \tag{52}$$

$$\begin{aligned} Q_m(\xi) = {} & \frac{\partial\theta_{m-1}(\eta,\xi)}{\partial\eta} + \beta\sum_{n=0}^{m-1}\theta_n(1,\xi)\frac{\partial\theta_{m-1-n}(\eta,\xi)}{\partial\eta} + \mathrm{Bi}\ \ \theta_{m-1}(1,\xi) \\ & + N_{\mathrm{rc}}\sum_{n=0}^{m-1}\left(\sum_{j=0}^{n}\theta_j(1,\xi)\theta_{n-j}(1,\xi)\right) \\ & \times\left(\sum_{j=0}^{m-1-n}\theta_j(1,\xi)\theta_{m-1-n-j}(1,\xi)\right) \\ & - \mathrm{Bi}(1-\chi_m)\theta_a - N_{\mathrm{rc}}(1-\chi_m)\theta_a^4 \quad \text{at} \quad \eta = 1 \end{aligned} \tag{53}$$

The deformations $\theta_m(\eta,\xi)$, where $m\geq 1$, for Eqs. (48)–(51) can be obtained by a symbolic software such as MATHEMATICA and can be taken as

$$\theta_m(\eta,\xi) = \sum_{i=0}^{2m+1}\sum_{j=0}^{2m+1} a_{mi}^j \eta^{2j} e^{i\eta} \tag{54}$$

where a_{mi}^j are functions of ξ.

For a best choice of h_1 and h_2, the mth order approximation for the solution of Eqs. (29)–(32) is then

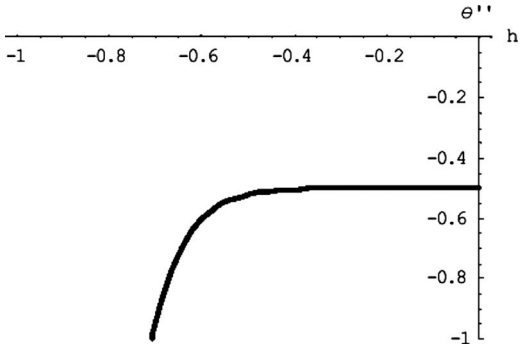

Fig. 1 The *h*-curve of $\theta''=\partial^2\theta(\eta,\xi)/\partial\eta^2|_{\eta=0}$ for $\xi=0.5$, $\beta=0$, Bi =1, $N_{rc}=0$, and $\theta_a=0$

$$\theta(\eta,\xi)=\theta_0(\eta,\xi)+\sum_{m=1}^{m}\sum_{i=0}^{2m+1}\sum_{j=0}^{2m+1}a_{mi}^{j}\eta^{2j}e^{i\eta} \tag{55}$$

The corresponding *m*th order approximations for the solution of Eqs. (24)–(27) can be obtained via the relation (28). The best values of the parameters h_1 and h_2, which control the convergence of the approximation (55) can be deduced by plotting the *h*-curve of $\theta''=\partial^2\theta(\eta,\xi)/\partial\eta^2|_{\eta=0}$ for fixed values of ξ and reasonable choices of the parameters. This curve takes a horizontal line through the position of convergence.

4 Results of the Application

On applying the homotopy analysis method for Eqs. (29)–(32), it is essential that the solution series (47) is convergent. This method gives us freedom to choose the values of the auxiliary parameters h_1 and h_2, which provide us with an easy way to adjust and control the convergence region for the obtained approximations. For the application up to the 30th order approximation, we choose simply $h_1=h_2=h$. Plotting the *h*-curve of $\theta''=\partial^2\theta(\eta,\xi)/\partial\eta^2|_{\eta=0}$ for the values $\xi=0.5$, $\beta=0$, Bi=1, $N_{rc}=0$, and $\theta_a=0$, we choose $h=-0.3$ as indicated in Fig. 1. Figure 2 indicates also the *h*-curve of $\theta''=\partial^2\theta(\eta,\xi)/\partial\eta^2|_{\eta=0}$, but for $\xi=0.5$, $\beta=1$, Bi=0.5, $N_{rc}=0.5$, and $\theta_a=0.5$, the appropriate choice for this case is $h=-0.2$. Figure 3 investigates the 30th order approximation analytic homotopy solution for the temperature θ as a function of the dimensionless time τ, and at the boundary $\eta=1$ for the parametric values $\beta=0$, Bi=1, $N_{rc}=0$, $\theta_a=0$, and $h=-0.3$. Figure 4 views a comparison between the homotopy solution in Fig. 3 and the exact solution for θ, which is possible for this case ($\beta=0$, Bi=1, $N_{rc}=0$, $\theta_a=0$), in which Eqs. (29)–(32) are linear. This comparison shows that the 30th order homotopy solution, for this case, agrees with the exact solution for the dimensionless time $0.35\leq\tau<\infty$, which tests the validation of the application of the homotopy analysis method for the nonlinear case. Figure 5 describes the temporal variations in the temperature θ on the surface of the spherical body, at the boundary $\eta=1$ for different values of the Biot number Bi (Bi=0.5,1,2) and the values $\beta=1$, $N_{rc}=0$, $\theta_a=0$, and $h=-0.3$. This figure shows that the temperature decreases as the Biot number enlarges, and also, decays more quickly for large values of the Biot number. Figure 6 also describes the temporal variations in the temperature θ on the surface of the spherical body, at the boundary $\eta=1$ for different values of the radiation-conduction parameter N_{rc}($N_{rc}=0.25,0.5$) and the values $\beta=1$, Bi=0.5, $\theta_a=0.5$, and $h=-0.2$, and also shows that the temperature decreases as the radiation-conduction enlarges. Figure 7 views the spatial variations in the temperature θ of the spherical body through different values of τ($\tau=0.05,0.10,0.20,0.35,0.50,1$), for the Biot number Bi=1, and for $\beta=1$, $N_{rc}=0$, $\theta_a=0$, and $h=-0.3$. Figure 8 also views the spatial variations in

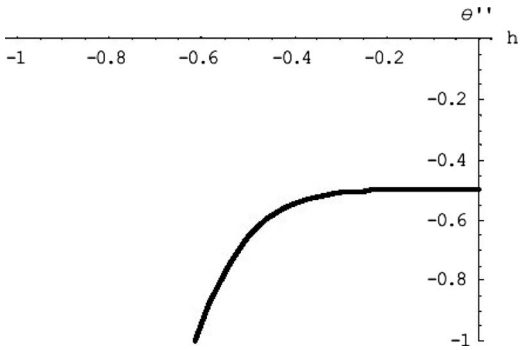

Fig. 2 The *h*-curve of $\theta''=\partial^2\theta(\eta,\xi)/\partial\eta^2|_{\eta=0}$ for $\xi=0.5$, $\beta=1$, Bi =0.5, $N_{rc}=0.5$, and $\theta_a=0.5$

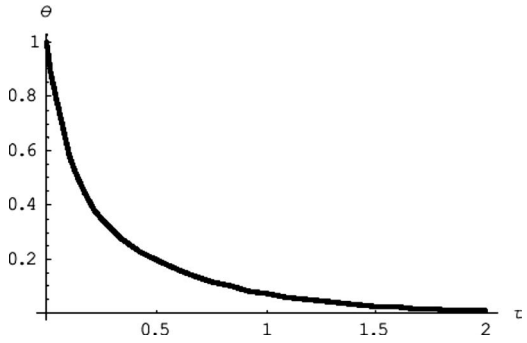

Fig. 3 The 30th order analytic homotopy solution θ (as a function of τ) at $\eta=1$, and for $\beta=0$, Bi=1, $N_{rc}=0$, $\theta_a=0$, and $h=-0.3$

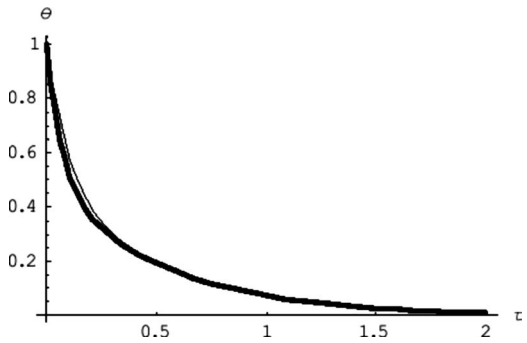

Fig. 4 A comparison between the 30th order analytic homotopy solution (thin line) and the exact solution (solid line) at $\eta=1$, and for $\beta=0$, Bi=1, $N_{rc}=0$, $\theta_a=0$, and $h=-0.3$

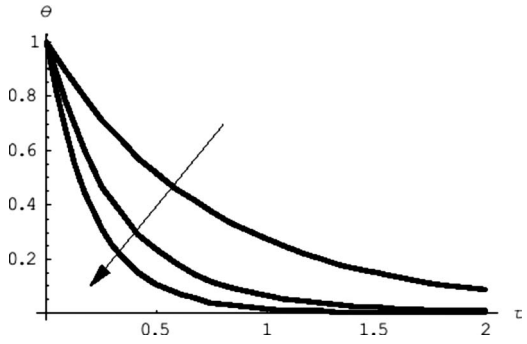

Fig. 5 The variation in the temperature θ on the surface of the spherical body ($\eta=1$) for different values of the Biot number Bi(Bi=0.5,1,2) and $\beta=1$, $N_{rc}=0$, $\theta_a=0$, and $h=-0.3$

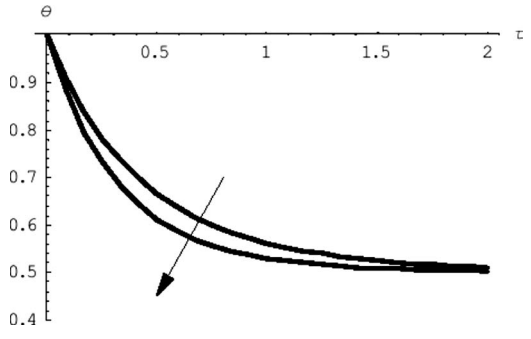

Fig. 6 The variation in the temperature θ on the surface of the spherical body (η=1) for different values of the radiation-conduction parameter N_{rc}(N_{rc}=0.25,0.5) and β=1, Bi=0.5, θ_a=0.5, and h=−0.2

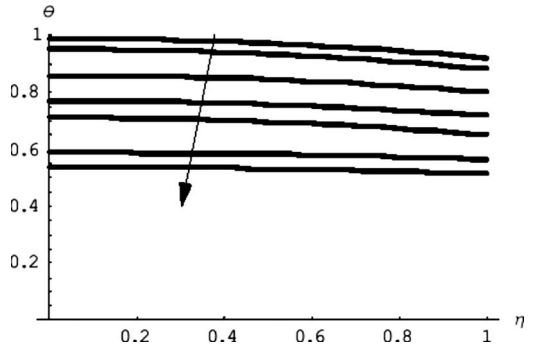

Fig. 9 The variation in the temperature θ on the surface of the spherical body through different values of τ(τ=0.05,0.10,0.20,0.35,0.50,1,1.5) for the radiation-conduction parameter (N_{rc}=0.25) and β=1, Bi=0.5, θ_a=0.5, and h=−0.2

the temperature θ of the spherical body through the same values of τ and for the Biot number Bi=2, and the same values of β, N_{rc}, θ_a, and h. Figures 7 and 8 investigate that the temperature generally decreases as the Biot number Bi enlarges, and for the case η=1, that is, on the surface of the spherical body, the temperature decays more rapidly for large values of the Biot number. Figure 9 views the spatial variations in the temperature θ of the spherical body through different values of τ(τ=0.05,0.10,0.20, 0.35,0.50,1,1.5), for the radiation-conduction parameter N_{rc} =0.25, and for the values β=1, Bi=0.5, θ_a=0.5, and h=−0.2, while Fig. 10 also views the spatial variations in the temperature θ of the spherical body, through the same values of τ, for N_{rc}=0.5, and for the same values of β, Bi, θ_a, and h. Figures 9 and 10 investigate that the temperature of the spherical body generally decreases as the radiation-conduction parameter N_{rc} increases, and for the case η=1, that is, on the surface of the spherical body, the temperature decays more rapidly for large values of this parameter.

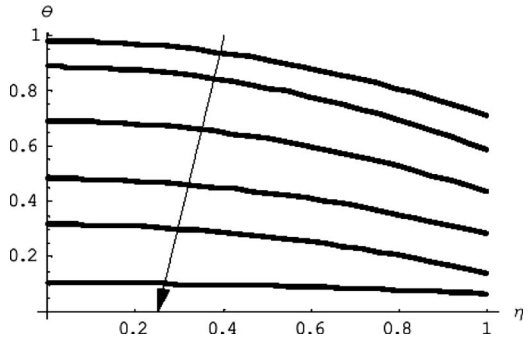

Fig. 7 The variation in the temperature θ on the surface of the spherical body through different values of τ(τ=0.05,0.10,0.20,0.35,0.50,1) and for (Bi=1), β=1, N_{rc}=0, θ_a=0, and h=−0.3

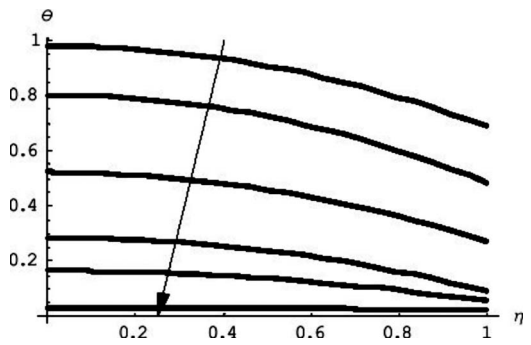

Fig. 8 The variation in the temperature θ on the surface of the spherical body through different values of τ(τ=0.05,0.10,0.20,0.35,0.50,1) and for (Bi=2), β=1, N_{rc}=0, θ_a=0, and h=−0.3

5 Conclusion

This paper treated the application of the homotopy analysis method for a strongly nonlinear problem in both the governing equation and the boundary condition. The nonlinear problem describes the combined convective and radiative cooling of a spherical body. The obtained homotopy analytic solution gives accurate spatial and temporal variations in the temperature, which indicate that, for the nonlinear model of combined convective and radiative cooling of a spherical body, the temperature on the surface of the body decays rapidly for large values of the Biot number Bi and the radiation-conduction parameter N_{rc}. This analytic approach of the homotopy analysis method gives us a new tool to obtain analytic approximations for unsteady nonlinear heat transfer problems, which are valid for all dimensionless times. The treatment proved the ability and flexibility of this method to handle such kinds of problems for different bases, and give convergent analytic approximations in a direct effective scheme.

Acknowledgment

The author thanks the anonymous reviewers for their comments and suggestions to enhance this work.

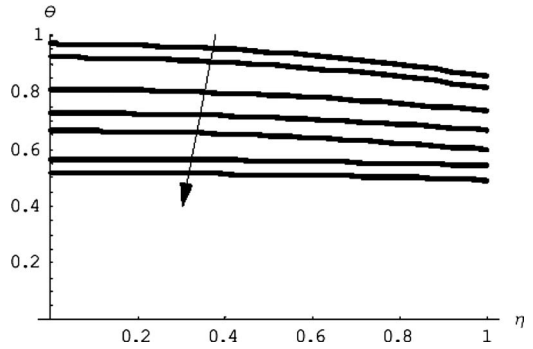

Fig. 10 The variation in the temperature θ on the surface of the spherical body through different values of τ(τ=0.05,0.10,0.20,0.35,0.50,1,1.5) for the radiation-conduction parameter (N_{rc}=0.5) and β=1, Bi=0.5, θ_a=0.5, and h=−0.2

References

[1] Haji-Sheikh, A., and Sparrow, E. M., 1967, "Solution of Heat Conduction Problems by Probability Methods," Trans. ASME, Ser. C: J. Heat Transfer, **89**, pp. 121–131.

[2] Crosbie, A. L., and Viskanta, R., 1968, "Transient Heating or Cooling of a Plate by Combined Convection and Radiation," Int. J. Heat Mass Transfer, **11**, pp. 305–317.

[3] Davies, T. W., 1985, "The Cooling of a Plate by Combined Thermal-Radiation and Convection," Int. Commun. Heat Mass Transfer, **12**, pp. 405–415.

[4] Sunden, B., 1986, "Transient Heat-Conduction in a Composite Slab by a Time Varying Incident Heat-Flux Combined With Convective and Radiative Cooling," Int. Commun. Heat Mass Transfer, **13**, pp. 515–522.

[5] Sunden, B., 1989, "Transient Conduction in a Cylindrical-Shell With a Time Varying Incident Surface Heat-Flux and Convective and Radiative Surface Cooling," Int. J. Heat Mass Transfer, **32**, pp. 575–584.

[6] Parang, M., Crocker, D. S., and Haynes, B. D., 1990, "Perturbation Solution for Spherical and Cylindrical Solidification by Combined Convective and Radiative Cooling," Int. J. Heat Fluid Flow, **11**, pp. 142–148.

[7] Siegel, R., 1996, "Transient Heat Transfer in a Semitransparent Radiating Layer With Boundary Convection and Surface Reflections," Int. J. Heat Mass Transfer, **39**, pp. 69–79.

[8] Su, J., 2004, "Improved Lumped Models for Transient Radiative Cooling of a Spherical Body," Int. Commun. Heat Mass Transfer, **31**, pp. 85–94.

[9] Liao, S. J., 1992, "The Proposed Homotopy Analysis Technique for the Solutions of Nonlinear Problems," Ph.D. thesis, Shanghai Jiao Tong University, Shanghai.

[10] Liao, S. J., 1999, "An Explicit Totally Analytic Approximate Solution for Blasius Viscous Flow Problems," Int. J. Non-Linear Mech., **34**, pp. 759–769.

[11] Liao, S. J., 2002, "An Analytic Approximation of the Drag Coefficient for the Viscous Flow Past a Sphere," Int. J. Non-Linear Mech., **37**, pp. 1–18.

[12] Liao, S. J., 2003, *Beyond Perturbation: Introduction to Homotopy Analysis Method*, Chapman and Hall, London/CRC, Boca Raton, FL.

[13] Cole, J. D., 1968, *Perturbation Methods in Applied Mathematics*, Blaisdell, Waltham.

[14] Nayfeh, A. H., 1981, *Introduction to Perturbation Techniques*, Wiley, New York.

[15] Murdock, J. A., 1991, *Perturbations: Theory and Methods*, Wiley, New York.

[16] Bush, A. W., 1992, *Perturbation Methods For Engineers and Scientists*, CRC, Library of Engineering Mathematics, Boca Raton, FL.

[17] Nayfeh, A. H., 2000, *Perturbation Methods*, Wiley, New York.

[18] Lyapunov, A. M., 1992, *General Problem on Stability of Motion*, Taylor & Francis, London.

[19] Karmishin, A. V., Zhukov, A. T., and Kolosov, V. G., 1990, *Methods of Dynamics Calculation and Testing for Thin-Walled Structures*, Mashinostroyenie, Moscow.

[20] Adomian, G., 1988, "A Review of the Decomposition Method in Applied Mathematics," J. Math. Anal. Appl., **135**, pp. 501–544.

[21] Adomian, G., 1991, "A Review of the Decomposition Method and Some Recent Results for Nonlinear Equations," Comput. Math. Appl., **21**, pp. 101–127.

[22] Adomian, G., 1994, "Solution of Physical Problems by Decomposition," Comput. Math. Appl., **27**, pp. 145–154.

[23] Adomian, G., 1994, *Solving Frontier Problems of Physics: The Decomposition Method*, Kluwer Academic, Boston, MA.

[24] Liao, S. J., 2003, "An Explicit Analytic Solution to the Thomas-Fermi Equation," Appl. Math. Comput., **144**, pp. 495–506.

[25] Liao, S. J., 2003, "On the Analytic Solution of Magnetohydrodynamic Flows of Non-Newtonian Fluids Over a Stretching Sheet," J. Fluid Mech., **488**, pp. 189–212.

[26] Liao, S. J., 2003, "An Analytic Approximate Technique for Free Oscillations of Positively Damped Systems With Algebraically Decaying Amplitude," Int. J. Non-Linear Mech., **38**, pp. 1173–1183.

[27] Xu, H., Liao, S. J., and Pop, I., 2006, "Series Solutions of Unsteady Boundary Layer Flow of a Micropolar Fluid Near the Forward Stagnation Point of a Plane Surface," Acta Mech., **184**, pp. 87–101.

[28] Liao, S. J., and Tan, Y., 2007, "A General Approach to Obtain Series Solutions of Nonlinear Differential Equations," Stud. Appl. Math., **119**, pp. 297–355.

[29] Bouremel, Y., 2007, "Explicit Series Solution for the Glauert-Jet Problem by Means of the Homotopy Analysis Method," Commun. Nonlinear Sci. Numer. Simul., **12**, pp. 714–724.

[30] Hayat, T., and Sajid, M., 2007, "On Analytic Solution for Thin Film Flow of a Fourth Grade Fluid Down a Vertical Cylinder," Phys. Lett. A, **361**, pp. 316–322.

[31] Liao, S. J., Su, J., and Chwang, A. T., 2006, "Series Solutions for a Nonlinear Model of Combined Convective and Radiative Cooling of a Spherical Body," Int. J. Heat Mass Transfer, **49**, pp. 2437–2445.

Thermal Response of Supersonic Airflow to a Fin Protrusion Situated on a Curved Surface

Majid Molki
e-mail: mmolki@siue.edu

David W. Fasig

Department of Mechanical Engineering,
Southern Illinois University Edwardsville,
Edwardsville, IL 62025

Aerodynamic heating of an airfoil with a short fin attached to its surface is computationally investigated. This research is motivated by the fact that the gap fillers inserted between the insulation tiles of the space shuttle thermal protection system may sometimes get loose and extend beyond the surface and cause an uneven aerodynamic heating of the surface. It is often difficult for engineers to determine whether the protruded gap filler would cause an undesirable effect in the boundary layer including early turbulence transition or shockwaves that could cause an unsafe increase in surface temperature. In this investigation, the supersonic flow over NACA 0012 airfoil on which a short fin is attached is studied using a computational approach. The method is validated by the experimental data available in published literature. The results indicate a significant increase in the surface temperature in the vicinity of the fin. This elevated temperature extends downstream beyond the location of the fin and covers a large portion of the airfoil downstream of the fin. The fin induces an oblique shockwave followed by an expansion wave. [DOI: 10.1115/1.3155003]

Keywords: aerodynamic heating, gap filler, supersonic, space shuttle, shockwave, fin

1 Introduction

In supersonic flights, a bow shockwave appears upstream of the flying objects. Air decelerates as it flows through the nose of the bow shockwave and reaches the stagnation point on the leading edge of the airfoil. On either side of the bow shockwave, the flow decelerates but it remains supersonic downstream of the oblique shockwave. Supersonic flights experience aerodynamic heating. The presence of even a small protrusion on the surface disturbs the flow, breaks the partial insulating effect of the boundary layer, and exposes the surface to higher levels of aerodynamic heating. In this study, we examine the interaction between a short fin positioned on the surface of an airfoil and the supersonic flow.

The present research was motivated by the news a few years ago that NASA authorized a spacewalk to remove two sections of gap filler that protruded between the insulation tiles of the space shuttle Discovery [1]. The gap fillers, which are made of ceramic-coated fabrics, are placed between the shuttle's insulation tiles to provide flexibility for the tiles and also to prevent hot gases from entering the gap between the tiles, protecting the internal super structure of the space shuttle against aerodynamic heating.

In this work, we consider a short fin as a model of gap filler, attached to the surface of a NACA 0012 airfoil flying at supersonic speeds (Fig. 1). The fin length is 0.833% of airfoil chord length. This is obtained by scaling the exposed length of the actual gap filler, namely, 27.94 mm (1.1 in.) [2], to a near unit chord length used in the present computations. The fin is perpendicular to the airfoil surface. In our computations, the fin is positioned on the surface at $x/c=0.15$, 0.30, or 0.80, where $x=0$ indicates the nose position.

Despite the importance of the problem, aerodynamic heating due to protruding gap fillers, or alternatively fins, have not been studied widely in open literature. One of the earlier space-related research works dealing with aerodynamic heating is presented in Ref. [3]. In this report, cylinders with cone heads are positioned streamwise in a supersonic flow and the effect of aerodynamic heating is documented in terms of heat recovery factor. Later in this paper, we shall compare our computational results with those reported in this reference.

In an attempt to study the effect of protruding gap fillers, a number of researchers modeled the problem with a forward- or a backward-facing step [4,5]. Although a step model may be a good representation of protruding gap filler on a surface, such models do not capture the full effect of the protrusion. A more recent work [6] studied the deflection or bending of gap fillers. The pressure load during re-entry was considered and the likelihood of gap filler extraction caused by the reentry pressures was examined.

The present research is focused on the impact of a protruding fin on a surface in supersonic flow. The fin is mounted on NACA 0012 airfoil with a Mach number of 2.5. The results are presented for pressure, skin friction, Mach number, and temperature recovery factor. The aerodynamic heating, which is demonstrated with the aid of the temperature recovery factor, is compared with experimental data of other investigators.

2 Mathematical Formulation

The flow over airfoil is formulated by writing governing equations for mass, momentum, and thermal energy.

$$\text{Continuity} \quad \partial_i(\rho u_i) = 0 \tag{1}$$

$$\text{Momentum} \quad \partial_j(\rho u_i u_j) = -\partial_i p + \partial_j\{\mu[\partial_j u_i + \partial_i u_j - (2/3)\delta_{ij}\partial_\ell u_\ell]\} + \partial_j(-\rho\overline{u_i' u_j'}) \tag{2}$$

$$\text{Energy} \quad \partial_i[u_i(\rho E + p)] = \partial_j[(k + c_p\mu_t/\mathrm{Pr}_t)\partial_j T + u_i(\tau_{ij})_{\text{eff}}] \tag{3}$$

where $(\tau_{ij})_{\text{eff}} = \mu_{\text{eff}}(\partial_i u_j + \partial_j u_i) - (2/3)\mu_{\text{eff}}\partial_k u_k \delta_{ij}$.

The turbulence is modeled by the Spalart–Allmaras model [7]. Reynolds stresses are based on the Boussinesq hypothesis (see Ref. [8]):

$$-\rho\overline{u_i' u_j'} = \mu_t(\partial_j u_i + \partial_i u_j) - (2/3)(\rho k + \mu_t\partial_k u_k)\delta_{ij} \tag{4}$$

Turbulent viscosity, μ_t, is computed from the modified turbulent kinematic viscosity, $\tilde{\nu}$ (see Eq. (6)). The transport equation for the modified turbulent kinematic viscosity is

Contributed by the Heat Transfer Division of ASME for publication in the JOURNAL OF HEAT TRANSFER. Manuscript received January 22, 2009; final manuscript received May 7, 2009; published online August 26, 2009. Review conducted by Frank Cunha.

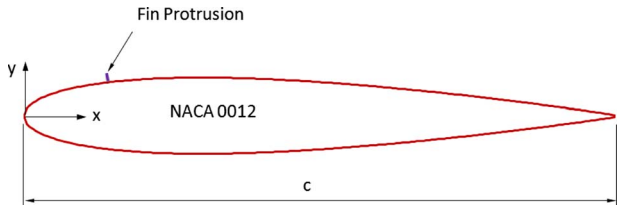

Fig. 1 The NACA 0012 airfoil with a fin protrusion

$$\partial_i(\rho\tilde{\nu}u_i) = G_\nu + (1/\sigma_{\tilde{\nu}})\{\partial_j[(\mu + \rho\tilde{\nu})\partial_j\tilde{\nu}] + C_{b2}\rho(\partial_j\tilde{\nu})^2\} - Y_\nu \quad (5)$$

In this equation, G_ν and Y_ν are the production and destruction of turbulent viscosity, respectively. These terms are given in Ref. [8]. The symbols $\sigma_{\tilde{\nu}}$ and C_{b2} represent the constant values given in Ref. [8]. It is to be noted that, in Spalart–Allmaras model, the turbulent kinetic energy, k, is not calculated. Therefore, the corresponding term in Eq. (4) is ignored for the evaluation of Reynolds stresses.

Once the modified turbulent kinematic viscosity is evaluated from Eq. (5), the turbulent viscosity, μ_t, is determined from (see Sec. 12.3.3 of Ref. [8])

$$\mu_t = \rho\tilde{\nu}f_{v1} \quad (6)$$

In this equation, $f_{v1} = \chi^3/(\chi^3 + C_{v1}^3)$, $\chi = \tilde{\nu}/\nu$, and $C_{v1} = 7.1$. Ideal gas equation is used for air density and the Sutherland law for viscosity [8].

Boundary conditions for the governing equations are as follows. Fluid velocity is zero on airfoil and fin surfaces. At the outer boundary, defined as pressure far field, the absolute pressure is 15761.5 Pa and the Mach number is 2.5. The surface of the airfoil is adiabatic (zero temperature gradient) and air temperature on the outer boundary is 221.0 K. At the walls, the modified turbulent kinematic viscosity, $\tilde{\nu}$, is set equal to zero. The present simulation was chosen as a representative supersonic case of an actual flight condition of the shuttle orbiter system. The landing phase is called the *terminal area energy management* and is conducted at an altitude of about 25,000 m. The speed of the orbiter during this phase of landing puts the shuttle at Mach 2.5.

3 Computational Approach and Validation

The outer boundary of the computational domain is constructed from a semicircle in front of the airfoil, while it is rectangular on the backside. This domain extends horizontally from $x = -5.49$ m to $x = 10$ m and vertically from $y = -6.5$ m to $y = 6.5$ m. The chord length of the airfoil is 1.009 m and it is positioned in such a way that its leading edge is at the origin, namely, $(x,y) = (0,0)$. The domain is discretized using a structured mesh consisting of nearly radial and circular lines in the semicircular section and horizontal and vertical straight lines downstream. The mesh was clustered near the walls to resolve the steep gradients of the dependent variables.

The computations are performed using FLUENT 6.3 [8]. The pressure-based method, which is a new feature in FLUENT 6.3, is used for the computations. Spalart–Allmaras one-equation turbulence model is used with the strain/vorticity-based production option and viscous heating. The pressure-velocity coupling is selected as *coupled* with a Courant number of 200 and an explicit relaxation factor of 0.5 for both momentum and pressure. Underrelaxation factors for density, body force, modified turbulent viscosity, turbulent viscosity, and energy are 0.5, 1, 0.9, 1, and 0.8, respectively. Although the Courant-Friedrichs-Lewy (CFL) condition allows using a higher Courant number in implicit methods, at the onset of the computations, these factors and the Courant number needed to be reduced to control the stability and convergence of the solution. All the computations are based on the second-order upwind discretization scheme. The iterations were continued until mass and momentum residuals were below 10^{-5} and energy residual was below 10^{-6}.

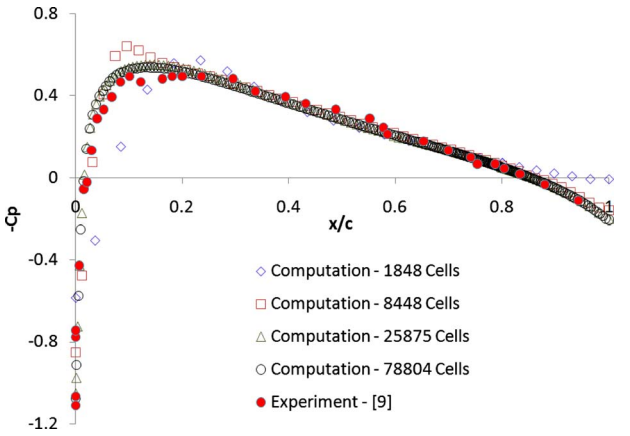

Fig. 2 Grid refinement study and validation of the computational results for NACA 0012 airfoil. The experimental data are taken from Fig. 1 of Ref. [9].

A number of preliminary runs were performed to ensure that the computations were independent of the mesh size. Figure 2 is a plot of surface pressure coefficient versus dimensionless distance along the chord line. It is clear from the figure that as the number of mesh cells increases the pressure coefficient approaches the final solution. The solid circles in the figure are the experimental data taken from Fig. 1 of Ref. [9]. Although the experimental uncertainty is not given in this reference, the data scatter seen in the figure is indicative of a reasonable uncertainty in the measurements. The good agreement between the computations and experimental data confirm the present approach.

4 Results and Discussion

Contours of the Mach number for the flow over NACA 0012 at $M = 2.5$ are presented in Fig. 3. The fin protrusion is mounted on the upper surface of the airfoil at $x/c = 0.15$, 0.30, and 0.80. A bow shockwave is standing in front of the airfoil. The flow decelerates as it goes through the shockwave. Downstream of the shockwave, flow is subsonic in a small neighborhood between the shockwave and nose of the airfoil. However, on either side of the airfoil, the flow Mach number is reduced to below $M = 2.5$, but it is still supersonic.

Careful examination of the contour lines indicates that the fin generates an oblique shockwave followed by an expansion wave. Flow deceleration and acceleration through these fin-induced waves are clearly seen from the intensity change of the contour lines. The expansion wave near the fin tip is reminiscent of flow acceleration to a Mach number close to that of the freestream, namely, $M = 2.5$. Also noted in the figure is a subsonic region in the neighborhood of the fin.

The fin effect is better understood when the contour lines above the airfoil are compared with those below. The presence of the fin has two prominent effects. One is to disturb the boundary layer, and the other is the formation of a secondary shockwave and an expansion wave. With regard to the first effect, the fin disturbs the boundary layer and slightly pushes the high-speed flow away from the surface of the airfoil. This is seen as a thicker layer on the upper surface from the location of the fin all the way to the trailing edge. As to the second effect, as the fin is moved downstream, namely, a shift in fin position in $+x$ direction, the aforementioned shockwave and expansion wave also move downstream and become weaker in strength. The weaker strength of the fin-induced waves is evident from the wave angle.

The information conveyed in the pressure contours of Fig. 4 is a confirmation of the contour lines of Mach number in Fig. 3. The

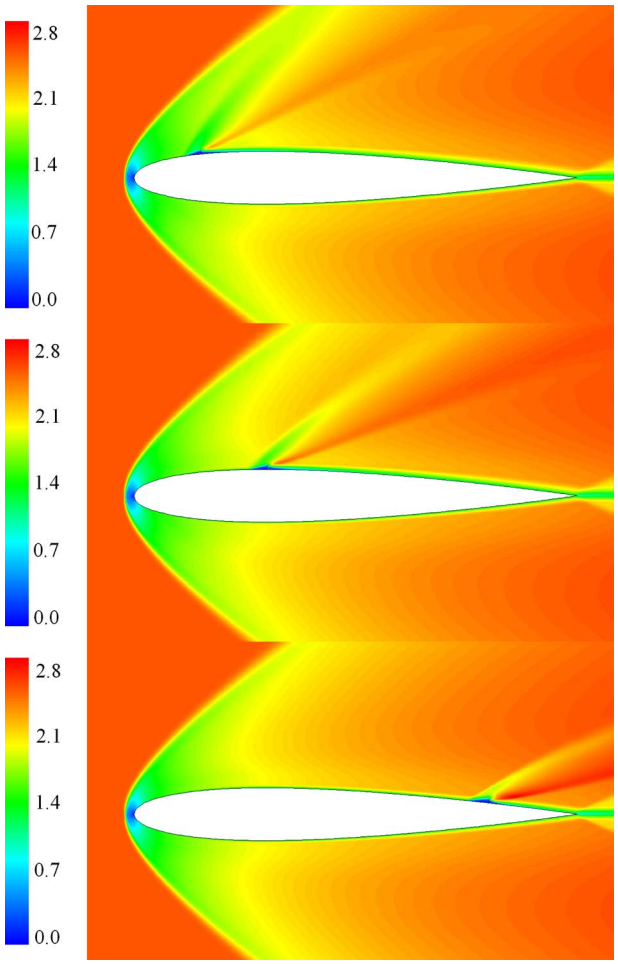

Fig. 3 Contours of Mach number for supersonic flow over NACA 0012 airfoil at M=2.5. Flow is from left to right. The fin is located at x/c=0.15, 0.30, and 0.80.

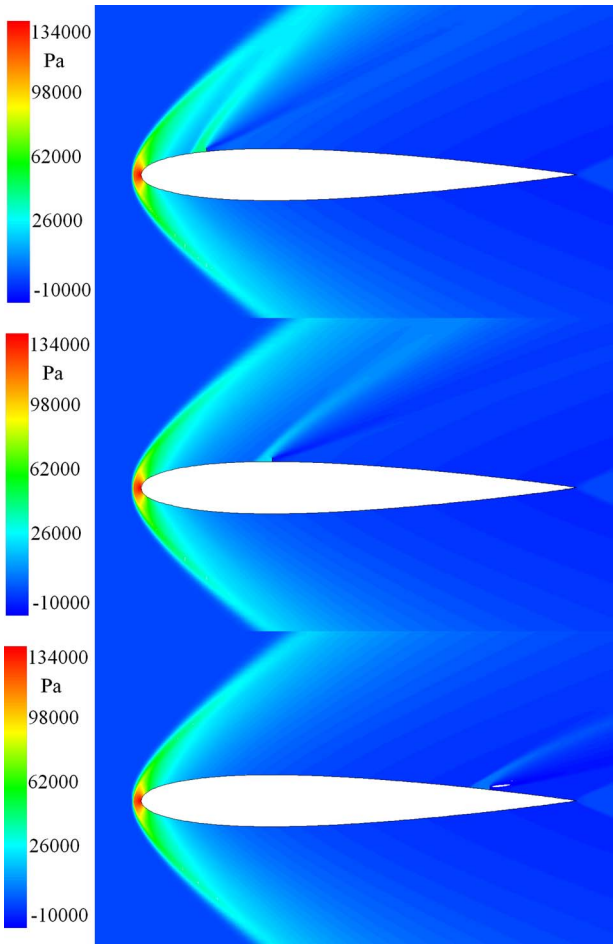

Fig. 4 Contours of pressure for supersonic flow over NACA 0012 airfoil at M=2.5. Flow is from left to right. The fin is located at x/c=0.15, 0.30, and 0.80.

highest pressure is just after the bow shockwave on the nose of the airfoil. The contour lines in the vicinity and above the fin confirm the presence of the shockwave followed by an expansion wave. The disturbance caused by the fin is more clearly recognized when flow above the airfoil is compared with that below. As the fin location is shifted further downstream, the disturbed flow is also shifted downstream to the neighborhood of the fin location. The pressure contours of Fig. 4 confirm the previous observation in Fig. 3 that the fin-induced shockwave becomes weaker when the fin is shifted downstream.

Pressure distribution on the airfoil surface is presented in terms of pressure coefficient in Fig. 5. The open symbols are for the top surface, which has the fin, while the solid symbols are for the bottom surface of the airfoil. The points deviating from the smooth trend are for the neighborhood of the fin positions. Pressure upstream of the fin is higher and that for the immediate downstream of the fin is lower than the undisturbed pressure trend of the lower surface. The extent of pressure disturbance is larger for the fins located further upstream. The pressure disturbance caused by the presence of the fin is expected to have an adverse effect on the drag force of the airfoil.

Skin friction coefficients of the upper and lower surfaces of the airfoil are shown in Fig. 6. Since the lower surface does not have a fin, the distribution of the skin friction coefficient is smooth on this surface. For the upper surface, however, the fin disturbs the flow and skin friction coefficient has deviated from the smooth trend. The deviations caused by the presence of the fin are relatively large and extend downstream up to the trailing edge. In this respect, the impact of the protruded fin on skin friction coefficient is more significant than that seen for the pressure coefficient. It should be noted that the skin friction coefficient depends on the velocity gradient at the wall, which is a more sensitive parameter to near-surface disturbances than pressure.

Contours of static temperature are shown in Fig. 7. Air temperature rises across the bow shockwave. The largest temperature rise

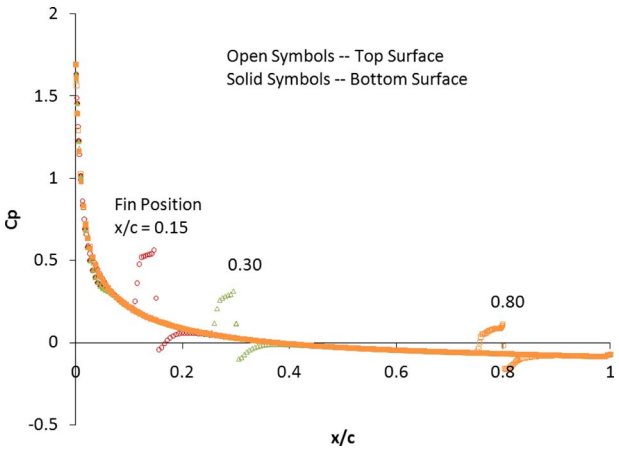

Fig. 5 Distribution of pressure coefficient on the upper and lower surfaces of the airfoil; NACA 0012; M=2.5

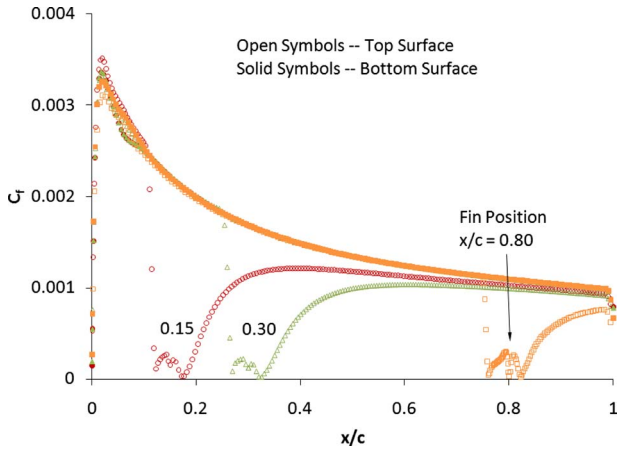

Fig. 6 Distribution of skin friction coefficient on the upper and lower surfaces of the airfoil; NACA 0012; M=2.5

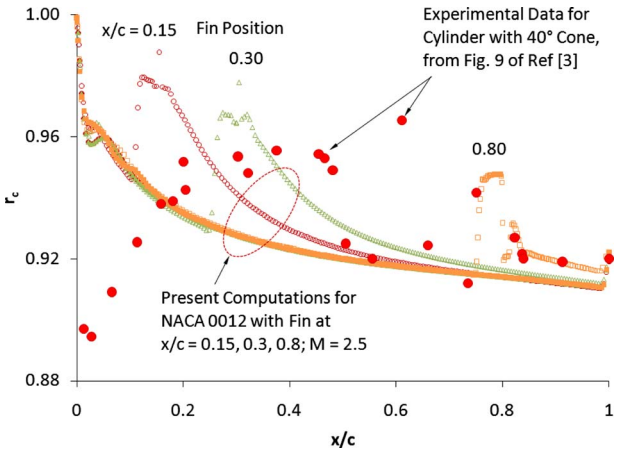

Fig. 8 Distribution of the temperature recovery factor on the upper and lower surfaces of the airfoil; NACA 0012; M=2.5. The experimental data are from Fig. 9 of Ref. [3].

occurs through the normal section of the shockwave just in front of the nose. The highest surface temperature is at the stagnation point on the nose.

It is clear from the figure that the presence of the fin generates an aerodynamic heating that is spread over the fin neighborhood. Judged from the intensity of the contour lines, the aerodynamic heating of the fin is comparable to the highest surface temperature at the stagnation point on the airfoil nose. This is also evident from the temperature recovery factors to be discussed next.

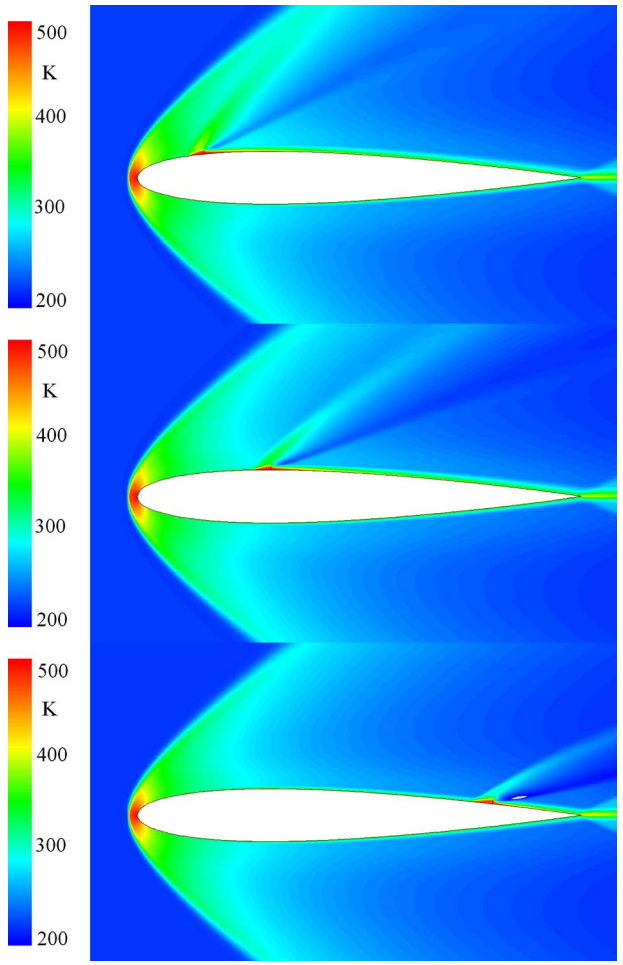

Fig. 7 Contours of static temperature for supersonic flow over NACA 0012 airfoil at M=2.5. Flow is from left to right. The fin is located at $x/c=0.15$, 0.30, and 0.80.

Temperature recovery factor, $r_c=(T_{aw}-T_\infty)/(U_\infty^2/2c_p)$, is an indication of the aerodynamic heating of the surface. Figure 8 presents the distribution of recovery factor for the upper and lower surfaces of the airfoil. In addition to the present computational values, the experimental data for streamwise cylinders having a 40 deg cone for M=2.87 are also shown for comparison.

The highest attainable value of temperature recovery factor is 1, which occurs at the stagnation point. Therefore, as seen in Fig. 8, the recovery factor decreases from the stagnation value of 1 to around 0.91 at the trailing edge. The range of experimental data is close to that of computational values. Although the two problems are not exactly the same, they have many common features that make this comparison relevant and supportive of the present computations.

It is seen in Fig. 8 that the temperature recovery factor increases in the vicinity of the fin location. The higher recovery factors at such points indicate higher surface temperatures. As the fin is placed further downstream, the corresponding increase in the recovery factor is also shifted downstream. Furthermore, it is seen in the figure that the enhancing effect of the fin on the recovery factor extends beyond the fin location to far downstream, covering a considerable area of the airfoil. These results indicate that removing the fin, or extended gap filler, will considerably reduce the aerodynamic heating of the surface.

In the classical problems of high-speed convective heat transfer, the temperature recovery factor is often expressed as a function of Prandtl number. For example, for laminar boundary layer on a flat plate, $r_c \approx \mathrm{Pr}^{1/2}$, and for turbulent boundary layer, $r_c \approx \mathrm{Pr}^{1/3}$ (see Ref. [10]). In an attempt to see any possible correlation between temperature recover factor and Prandtl number for the present work, we present Fig. 9 in which the recovery factor of the airfoil with the fin position at $x/c=0.15$ is plotted as a function of Prandtl number. Also shown in this figure is the range of experimental data for various geometries taken from Table 2 of Ref. [3]. It is to be noted that the vertical line in this figure is intended to show only the range of experimental data, and not the trend.

It is seen that the heat recovery factor obtained from the present computations is well within the range of experimental values. Although the recovery factor may not correlate well with Prandtl number, the increasing trend with Pr is reminiscent of the trends depicted by the 1/2 and 1/3 powers of Pr for the laminar and turbulent boundary layers.

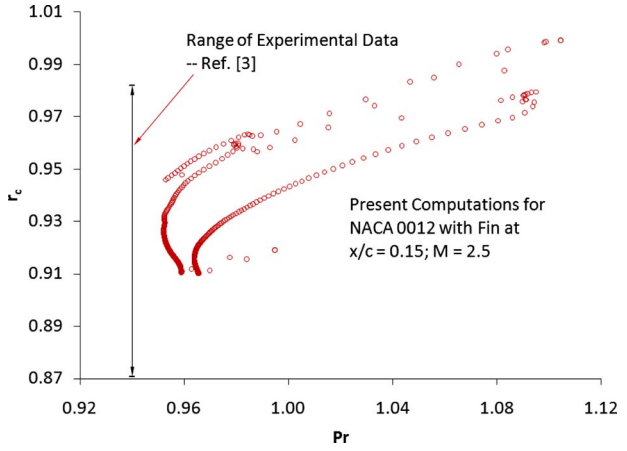

Fig. 9 Distribution of the temperature recovery factor on the upper and lower surfaces of the airfoil as a function of Prandtl number; NACA 0012; M=2.5. The range of experimental data is from Table 2 of Ref. [3].

5 Concluding Remarks

This computational work studied the impact of protruded gap filler on the aerodynamic heating of the surface of an airfoil. The gap filler was modeled by considering a short fin attached perpendicularly to the surface of NACA 0012 airfoil.

The computations indicated the formation of an oblique shockwave around the fin, which was followed by an expansion wave. As a result, the airflow over the fin decelerated through the shockwave and subsequently accelerated through the expansion wave to near the freestream Mach number.

The presence of the fin enlarged the boundary layer downstream along the surface of the airfoil. The enlargement of the boundary layer became evident when the flow downstream of the fin was compared with the undisturbed flow on the lower surface of the airfoil.

The fin disturbed both the surface pressure and the skin friction coefficient in the neighborhood of the fin. It was noticed that pressure disturbance was limited to a small region around the fin, while the skin friction disturbance extended downstream and its effect was noticeable over a major portion of the airfoil.

The fin also enhanced the aerodynamic heating of the surface. Like skin friction coefficient, aerodynamic heating caused by the fin elevated the surface temperature not only in the neighborhood of the fin but it also elevated temperature over a major portion of the airfoil surface downstream of the fin.

Aerodynamic heating was expressed in terms of temperature recovery factor. The presence of the fin increased the heat recovery factor to a maximum value at the fin location. As the fin was positioned further downstream, the maximum value of temperature recovery factor at the fin location decreased. It appears that, for the range of parameters and the specific geometry of this investigation, the effect of fin on enhancement of aerodynamic heating is more pronounced when the fin is located further upstream.

Nomenclature

C = Courant number ($u\Delta t/\Delta x$)
C_{b2} = constant (0.622)
$C_{\nu 1}$ = constant (7.1)
c = chord length
c_p = specific heat; pressure coefficient ($(p-p_\infty)/(0.5\rho_\infty U_\infty^2)$)
E = total energy
G_ν = production of turbulent viscosity
k = thermal conductivity; turbulent kinetic energy
M = Mach number
Pr_t = turbulent Prandtl number
p = pressure
r_c = temperature recovery factor ($(T_{aw}-T_\infty)/(U_\infty^2/2c_p)$)
T = temperature
T_{aw} = adiabatic wall temperature
T_∞ = freestream temperature
u_i = velocity component
x = coordinate along the chord line
y = coordinate perpendicular to chord line
Y_ν = destruction of turbulent viscosity

Greek Symbols

δ_{ij} = Kronecker delta
μ = molecular viscosity
μ_{eff} = effective viscosity ($\mu+\mu_t$)
μ_t = turbulent viscosity
ν = kinematic viscosity
$\tilde{\nu}$ = modified turbulent kinematic viscosity
ρ = density
$\sigma_{\tilde{\nu}}$ = constant (2/3)
$(\tau_{ij})_{\mathrm{eff}}$ = deviatoric stress tensor
∂_j = $\partial(\,)/\partial x_j$

References

[1] Pellerin, C., 2008, "NASA Authorizes Spacewalk to Fix Shuttle Problem Astronaut to Remove Protruding Gap Fillers From Discovery's Heat Shield," The Bureau of International Information Programs, U.S. Department of State, http://www.america.gov/st/washfile-english/2005/August/20050802141006lcnirellep0.5377161.html.
[2] New Scientist, 2008, "Dimensional Picture of Protruding Gap Filler," http://space.newscientist.com//data/images/ns/cms/dn7767/dn7767-1_475.jpg.
[3] Gruenewald, K. H., 1953, "Temperature Recovery Factors in the Transitional and Turbulent Boundary Layer on a 40-Degree Cone Cylinder at Mach Number 2.9," Naval Ordnance Laboratory, NAVORD Report No. 2742.
[4] Petley, D. H., Smith, D. M., and Edwards, C. L. W., 1983, "Filler Bar Heating Due to Stepped Tiles in the Shuttle Orbiter Thermal Protection System," *NASA Conference Publication*, NASA, Scientific & Technical Information Branch, Washington, DC, Part 2, pp. 891–911.
[5] Loth, E., Kailasanth, K., and Lohner, R., 1992, "Supersonic Flow Over an Axisymmetric Backward-Facing Step," J. Spacecr. Rockets, **29**(3), pp. 352–359.
[6] Campbell, C. H., Driver, D. M., and Alter, S. J., 2007, "Orbiter Gap Filler Bending Model for Re-Entry," AIAA Paper No. AIAA-2007-413, pp. 1–3.
[7] Spalart, P. R., and Allmaras, S. R., 1994, "One-Equation Turbulence Model for Aerodynamic Flows," Rech. Aerosp., (1), pp. 5–21.
[8] Fluent Inc., FLUENT 6.3 User's Guide, Lebanon, NH.
[9] Tenaud, C., and Loc, T. P., 1995, "Numerical Simulation of Unsteady Compressible Viscous Flow NACA 0012 Airfoil—Vortex Interaction," *Lecture Notes in Physics*, Vol. 453, Springer, Berlin/Heidelberg, pp. 562–567.
[10] Kays, W., Crawford, M., and Weigand, B., 2005, *Convective Heat and Mass Transfer*, McGraw-Hill, New York.

Flow Maldistribution and Performance Deteriorations in Membrane-Based Heat and Mass Exchangers

Li-Zhi Zhang[1]
Key Laboratory of Enhanced Heat Transfer and Energy Conservation of Education Ministry, School of Chemistry and Chemical Engineering, South China University of Technology, Guangzhou 510640, China
e-mail: lzzhang@scut.edu.cn

Heat mass exchangers are crucial for the prevention of epidemic respiratory diseases such as H1N1 (swine flu). The flow maldistribution affects their performance seriously. The flow maldistribution and the consequent performance deteriorations in heat and mass exchangers are investigated. The focus is on moisture effectiveness deteriorations. As a first step, a computational fluid dynamics (CFD) code is used to calculate the flow distribution, by treating the plate-fin core as a porous medium. Then a coupled heat and moisture transfer model between the two air flows in the plate-fin channels is set up with slug flow assumption in the channels. Using the CFD predicted core face flow distribution data, the sensible heat and moisture exchange effectiveness and the performance deterioration factors are calculated with finite difference scheme. The results indicate that under current core to whole exchanger pressure drop ratio, when the channel pitch is below 2.0 mm, the flow distribution is quite homogeneous and the sensible and latent performance deteriorations due to flow maldistribution can be neglected. However, when the channel pitch is larger than 2 mm, the maldistribution is quite large and a 10–15% thermal deterioration factor and a 20–25% latent deterioration factor could be found. Mass transfer deteriorates much more than heat transfer does due to larger mass transfer resistance through membranes.
[DOI: 10.1115/1.3154832]

Keywords: heat transfer, moisture transfer, swine flu, flow maldistribution, heat and mass exchangers

1 Introduction

Heat and mass exchangers (enthalpy exchangers, or the so-called energy recovery ventilators) [1,2] could save a large fraction of energy for cooling and dehumidifying the fresh air since cool and dryness would be recovered from the exhaust stream to the fresh air in summer. Besides energy conservation, the heat and mass exchangers have the additional benefits of ensuring sufficient fresh air supply, which is crucial for the prevention of epidemic respiratory diseases such as H1N1 (swine flu), SARS, and bird flu.

Besides exchanger cores, ducts, inlet/outlet vents, and fans are necessary to assemble a commercial product. Figure 1 shows the schematic of typical commercialized heat and mass exchangers. As seen, the whole exchanger is composed of inlets, outlets, exchanger shells, separating plates, and most importantly, the core. When installed, the exchanger core is rotated 45 deg and inserted into the exchanger shell, forming two parallel air ducts with the separating plates in the rectangular shell box. Fresh air is sucked into the exchanger by a fan (not shown in the figure) through the fresh air inlet. Exhaust air is sucked into the exchanger by another fan through the exhaust air inlet. The two air streams are drawn through the exchanger core in a cross-flow arrangement. The plate-fin core structure is popular due to its high mechanical strength and large packing density. The core material is vapor permeable membranes that could transfer both the sensible heat and moisture simultaneously. Thus the sensible heat and the latent heat (moisture) could be recovered through this equipment.

Fluid flow and heat and mass transfer in such an exchanger are of interest to predict heat and moisture recovery efficiencies. The effectiveness–number of transfer units (ε-NTU) method has been the most convenient methodology to predict sensible and latent performances [3]. Fluid flow and heat mass transfer in a single core channel provide the basic transport data for effectiveness-NTU methodology. There have been numerous investigations of the heat transfer and fluid flow in a single plate-fin channel with infinite fin conductance [4–11]. Besides fundamental studies in a plate-fin channel, there have been several studies on heat and moisture transfer in heat and mass exchangers [12,13]. In these studies, a uniform flow distribution on core face was assumed. It should be noted that, considering the complex ducting work inside a practical enthalpy exchanger shell, it is anticipated that the flow would undergo turnarounds, expansions, and contractions, which would finally lead to flow maldistribution across the core face. This issue has not been mentioned at all before.

The flow maldistribution effects have been well recognized and presented for sensible-only heat exchangers [14–19]. The flow maldistribution is generated by the velocity profiles in the inlet ducts. Their effects on heat transfer were estimated. However, the effects of flow maldistribution on heat and mass exchangers, which have simultaneous heat and mass transfer, were not considered before. Further, previous studies have serious problems in estimating flow maldistribution [20].

This problem will be investigated in this study. The influences of inlet duct, the core, and the outlet duct will be considered simultaneously. The first objective is to predict the flow maldistribution on the core face. Then their effects on both the thermal performance and the latent performance will be discussed.

[1]Corresponding author.

Contributed by the Heat Transfer Division of ASME for publication in the JOURNAL OF HEAT TRANSFER. Manuscript received December 23, 2008; final manuscript received April 28, 2009; published online August 26, 2009. Review conducted by S. A. Sherif.

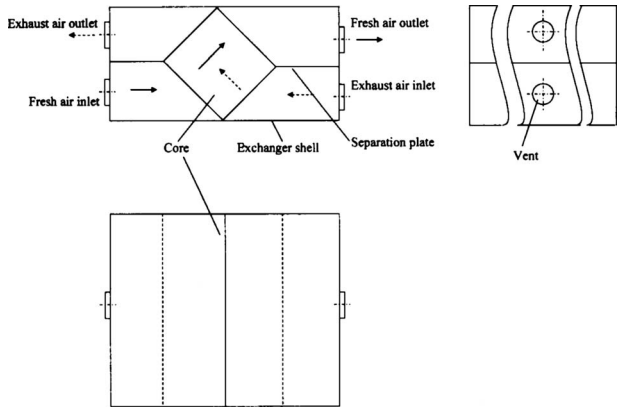

Fig. 1 Schematic of a cross-flow enthalpy exchanger with a membrane core

2 Experimental Work

To measure the heat and moisture exchange effectiveness, several experiments were done. A schematic of the test-rig is shown in Fig. 2. Two air ducts are assembled. One is for fresh air, and the other is for exhaust air. Each duct comprises of a variable speed blower downstream from the core, a wind tunnel, a set of nozzles, wind straighteners, and temperature sensors before and after the exchanger. The exchanger is connected to the two ducts with flanges. The whole test-rig is established in a constant temperature and constant humidity room, so the inlet temperature and humidity of the exhaust air, which equals to the room air, can be controlled and maintained very well even under very hot and humid ambient weather conditions. Additional electric heating circuits and humidifiers are installed for the fresh air duct. The heating and humidification power currents can be adjusted according to the fresh air set points' temperature. A 10 mm thick plastic foam insulation layer is pasted on the outer surfaces of the ducts and the exchanger shells to prevent heat dissipation from the system to the surroundings. The heat or moisture loss from the system is below 0.5%. Air leakage is prevented.

The uncertainties are temperature $\pm 0.1\,^{\circ}\mathrm{C}$; humidity $\pm 2\%$, and volumetric flow rate $\pm 1\%$. The final uncertainty is $\pm 4.5\%$ for exchanger effectiveness. The fresh air and exhaust air temperatures or humidity differences are controlled to be less than 0.1%. From these preparatory works, the test-rig is considered to be reliable. In addition, heat and mass balance between the fresh air and the exhaust air are checked.

After the measurement of the mean inlet and outlet temperatures and humidities, the exchanger effectiveness can be calculated with the following equations. These are the experimentally obtained effectiveness.

For sensible effectiveness,

Table 1 Structural and transport parameters of the three cores

Symbol	Unit	Core A	Core B	Core C
n		57	92	127
$x_F,\ y_F$	mm	185	185	185
z_F	mm	460	460	460
$\delta_{\mathrm{fin}},\ \delta_p$	μm	100	100	100
$\lambda_{\mathrm{fin}},\ \lambda_p$	W m^{-1} K^{-1}	0.44	0.44	0.44
θ	deg	60	60	60
$2a$	mm	4.0	2.5	1.8
D_h	mm	3.72	2.33	1.67
A_p	m^2	3.90	6.30	8.69
$A_f,\ A_e$	m^2	8.39	13.55	18.68
Ω_s		0.42	0.67	0.93
Ω_L		0.0019	0.0031	0.0043
Nu		1.413	1.582	1.618
Sh		0.595	0.597	0.603
$f\cdot\mathrm{Re}$		53.3	53.3	53.3
$D_p,\ D_{\mathrm{fin}}$	m^2/s	5.15×10^{-10}	5.15×10^{-10}	5.15×10^{-10}
k_p	kg/kg	0.58	0.58	0.58
Inlet/outlet duct length	mm	262	262	262
Inlet/outlet vent diameter	mm	60	60	60

$$\varepsilon_s = \frac{(Gc_p)_f(T_{fi}-T_{fo})}{(Gc_p)_{\min}(T_{fi}-T_{ei})} = \frac{(Gc_p)_e(T_{eo}-T_{ei})}{(Gc_p)_{\min}(T_{fi}-T_{ei})} \tag{1}$$

and for latent effectiveness,

$$\varepsilon_L = \frac{(G)_f(\omega_{fi}-\omega_{fo})}{(G)_{\min}(\omega_{fi}-\omega_{ei})} = \frac{(G)_e(\omega_{eo}-\omega_{ei})}{(G)_{\min}(\omega_{fi}-\omega_{ei})} \tag{2}$$

where T and ω are temperature (°C) and humidity ratio (kg moisture/kg dry air), respectively. Subscripts f, e, i, and o refer to fresh air, exhaust air, inlet, and outlet, respectively. Subscripts s and L refer to sensible and latent, respectively. The sensible effectiveness and the latent effectiveness are the key performance indices to evaluate an enthalpy exchanger.

When the two streams have the same mass flow rate

$$\varepsilon_s = \frac{(T_{fi}-T_{fo})}{(T_{fi}-T_{ei})} = \frac{(T_{eo}-T_{ei})}{(T_{fi}-T_{ei})} = T^*_{eo} \tag{3}$$

$$\varepsilon_L = \frac{(\omega_{fi}-\omega_{fo})}{(\omega_{fi}-\omega_{ei})} = \frac{(\omega_{eo}-\omega_{ei})}{(\omega_{fi}-\omega_{ei})} = \omega^*_{eo} \tag{4}$$

Three membrane cores are built and tested. They are plate-fin structure with triangular duct cross sections. Both the plates and the fins are made with hydrophilic polymer membranes. The core depths are the same: 460 mm. The geometrical and transport properties are listed in Table 1. As seen, the outer dimensions of the three cores are the same, so they can be inserted into the same exchanger cell. However, the channel pitches are different. Core A

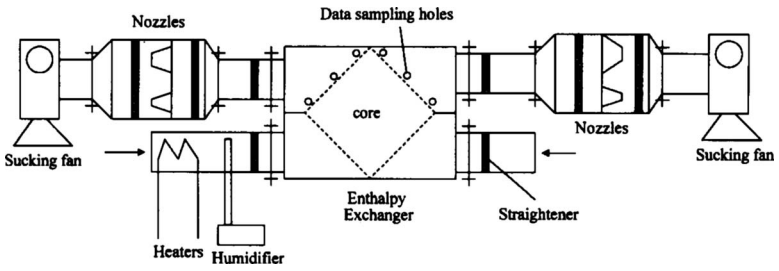

Fig. 2 Experimental setup of the enthalpy exchanger with a membrane core

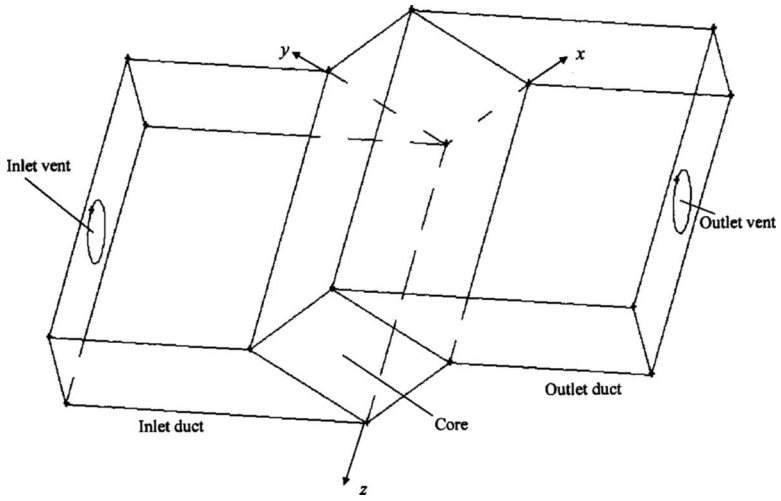

Fig. 3 The calculating domain for fresh air flow

has 57 channels for each of the two flows, Core B has 92 channels, and Core C has 127 channels. Core C is the most compact one.

3 Heat and Moisture Transfer Model

The fluid flow in the exchanger was numerically calculated [20]. The fresh air duct and the exhaust air duct are in symmetry. So only the fresh air duct as shown in Fig. 3 is selected as the calculating domain. There have been several numerical studies concerning the modeling of flow maldistribution in plate heat exchangers, on a channel to channel basis [21,22]. However, due to the limit in computer capacity and speed, the number of channels that can be modeled directly is quite small. The large number of channels prohibits the direct simulation of flow on a channel to channel basis. To solve this problem, this study simulates the core as a porous medium, which only permits one-dimensional air flow along the channel length [20]. The methodology is reasonable, considering the small channel pitch (1.5–5 mm) in the core. The honeycomb type core structure permits the assumption of unmixed flow for both of the fluids, in other words, cross or transverse mixing of fluids is not considered. When modeling the fluid flow, heat and mass transfer is not considered. In other words, only the flow in one stream is considered.

After the flow distribution on the core face is known, the convective heat and mass transfer between the fresh air and the exhaust air can be studied. To aid in the model setup, the following assumptions are made: (1) The flow distribution inside a channel is taken to be uniform giving a "slug flow" of fluid inside each channel. It can be justified as the channel gap is small. A steady slug flow assumption has been usually used in a single phase flow in a duct. (2) The flow in channels is fully developed both hydrodynamically, thermally, and concentrationally. For fully developed laminar flow in ducts with highly conductive walls, the Nusselt and Sherwood numbers are constants once the cross section is determined. Therefore the convective heat transfer and mass transfer coefficients are also constants. (3) The plates are considered to be thin enough so that axial conduction in them in the direction of flow can be neglected. (4) The thermophysical and transport properties of the fluids are considered to be independent of temperature and pressure.

A mesoscopic model is set up. Each channel cross section is represented by one temperature or humidity. The temperature or humidity varies along flow directions (x for fresh air and y for exhaust air) and the corresponding perpendicular directions (y for fresh air and x for exhaust air) simultaneously. On each channel cross section, though temperature or humidity is two-dimensionally different locally, in this study for the whole exchanger, they are represented by a lumped parameter for each channel cross section. It can be considered as a semilumped parameter model. The two air streams, one hot and humid (fresh air), and the other cool and dry (exhaust air), exchange heat and moisture in the exchanger in a cross-flow arrangement. Two-dimensional heat and mass transfer model can be set up to govern the energy and mass conservations in the following two air streams:

$$\frac{\partial T_f^*}{\partial x^*} = \mathrm{NTU}_{sf}(T_{pf}^* - T_f^*) \tag{5}$$

$$\frac{\partial T_e^*}{\partial y^*} = \mathrm{NTU}_{se}(T_{pe}^* - T_e^*) \tag{6}$$

$$\frac{\partial \omega_f^*}{\partial x^*} = \mathrm{NTU}_{Lf}(\omega_{pf}^* - \omega_f^*) \tag{7}$$

$$\frac{\partial \omega_e^*}{\partial y^*} = \mathrm{NTU}_{Le}(\omega_{pe}^* - \omega_e^*) \tag{8}$$

where x is flow direction for fresh stream and y is flow direction for exhaust stream. Certainly since the local mass flow rate is variant with both core height (y direction) and core depth (z direction), the local number of transfer units is different from point to point on the core surface. Subscript f refers to the fresh side and e refers to the exhaust side; s refers to sensible and L refers to latent; and pf refers to membrane surface on the fresh side and pe refers to membrane surface on the exhaust side.

The dimensionless temperature and humidity are defined by

$$T^* = \frac{T - T_{ei}}{T_{fi} - T_{ei}} \tag{9}$$

$$\omega^* = \frac{\omega - \omega_{ei}}{\omega_{fi} - \omega_{ei}} \tag{10}$$

The boundary conditions are as follows.

For the fresh side,

$$T_f^*|_{x^*=0} = 1 \tag{11}$$

$$\omega_f^*|_{x^*=0} = 1 \tag{12}$$

and for the exhaust side,

$$T_e^*|_{y^*=0} = 0 \tag{13}$$

$$\omega_e^*|_{y^*=0} = 0 \tag{14}$$

The dimensionless coordinates are defined by

$$x^* = \frac{x}{x_F} \tag{15}$$

$$y^* = \frac{y}{y_F} \tag{16}$$

$$z^* = \frac{z}{z_F} \tag{17}$$

where x_F and y_F are the channel lengths for fresh air and exhaust air (m). Here $x_F = y_F$. The core depth, which determines the total number of channels, is z_F. The air side local number of transfer units is defined by

$$\mathrm{NTU}_{sf} = \frac{1}{\beta}\frac{(hA)_f}{(Gc_p)_f} \tag{18}$$

$$\mathrm{NTU}_{se} = \frac{1}{\beta}\frac{(hA)_e}{(Gc_p)_e} \tag{19}$$

$$\mathrm{NTU}_{Lf} = \frac{1}{\beta}\frac{(\rho_a kA)_f}{(G)_f} \tag{20}$$

$$\mathrm{NTU}_{Le} = \frac{1}{\beta}\frac{(\rho_a kA)_e}{(G)_e} \tag{21}$$

where k and h are the air side convective mass transfer coefficient (m/s) and convective heat transfer coefficient (kW m^{-2} s^{-1}), respectively; G is air mass flow rate (kg/s); A is total transfer area including plates and fins (m^2) for each stream; and c_p is specific heat (kJ kg^{-1} K^{-1}).

As seen in Eqs. (18)–(21), the last term in the right hand side is the overall number of transfer units for a stream. The local number of transfer unit is equal to the overall number of transfer units divided by the local to overall mass flow ratio. Therefore the local number of transfer units is inversely proportional to mass flow ratio. The local number of transfer units increases with decreased mass flow rate.

The convective heat transfer coefficient and mass transfer coefficient can be calculated from established Nusselt and Sherwood numbers [20]. For plate-fin channels of finite fin conductance, the fully developed Nusselt and Sherwood numbers are influenced by the aspect ratios (a/b) or apex angle for triangular duct, and fin conductance parameters [10]. This is quite different from the simple classical data of a sensible-only heat exchanger with infinite fin conductance [13].

The fin conductance parameter for sensible heat transfer

$$\Omega_s = \frac{\lambda_{\mathrm{fin}}\delta_{\mathrm{fin}}}{\lambda_a(2a)} \tag{22}$$

where λ_{fin} is heat conductivity of fin, δ_{fin} is fin thickness (m), and $(2a)$ is channel height (m). When the plate and the fin use the same material, their heat conductivities are equal in Eq. (22).

The fin conductance parameter for moisture transfer

$$\Omega_L = \frac{\rho_{\mathrm{fin}}k_p D_{\mathrm{fin}}\delta_{\mathrm{fin}}}{\rho_a D_a(2a)} \tag{23}$$

where D_{fin} is water diffusivity in fin materials (m^2/s) and k_p is partition coefficient, which reflects the moisture sorption potential on fin materials. The value of k_p can be measured by adsorption isotherms as

$$\gamma = k_p \mathrm{RH} \tag{24}$$

where γ is water uptake in materials (kg moisture/kg material) and RH is relative humidity of moist air. The more hydrophilic the materials are, the higher the values of k_p are.

Heat conduction through the plate is in equilibrium with the convective heat transfer on both sides. The equilibrium can be expressed by

$$(hA)_f(T_f^* - T_{pf}^*) = \frac{A_p\lambda_p}{\delta_p}(T_{pf}^* - T_{pe}^*) \tag{25}$$

$$(hA)_e(T_e^* - T_{pe}^*) = -\frac{A_p\lambda_p}{\delta_p}(T_{pf}^* - T_{pe}^*) \tag{26}$$

where A_p is total transfer area (m^2) of plates, λ_p is heat conductivity of plate (kW m^{-1} K^{-1}), and δ_p is thickness of plate (m). In the above two equations, the right hand sides are heat conduction through plates. They have the same value, but different signs. In the left hand sides, the first equation represents convective heat transfer in the fresh air side, and the second equation represents convective heat transfer in the exhaust air side.

Moisture diffusion through the plate is in equilibrium with the convective mass transfer on two surfaces. The equations can be expressed by

$$\rho_a(kA)_f(\omega_f - \omega_{pf}) = \frac{\rho_p A_p D_p}{\delta_p}(\gamma_{pf} - \gamma_{pe}) \tag{27}$$

$$\rho_a(kA)_e(\omega_e - \omega_{pe}) = -\frac{\rho_p A_p D_p}{\delta_p}(\gamma_{pf} - \gamma_{pe}) \tag{28}$$

where D_p is water diffusivity in plate material (m^2/s) and ρ_p is plate density (kg/m^3).

The relation between humidity ratio and RH is [13]

$$\mathrm{RH} = \frac{\exp(5294/T)}{10^6}\omega \tag{29}$$

Moisture emission rate (kg s^{-1} m^{-2}) through the plate from the fresh air to the exhaust air

$$E = \frac{\rho_p D_p}{\delta_p}(\gamma_{pf} - \gamma_{pe}) \tag{30}$$

Combining the above equations, it is deduced that

$$E = \frac{\rho_p D_p k_p \exp(5294/T)}{10^6\delta_p}(\omega_{pf} - \omega_{pe}) \tag{31}$$

The total numbers of transfer units for sensible heat transfer and moisture transfer are

$$\mathrm{NTU}_{s,\mathrm{tot}} = \frac{(UA)_{\mathrm{tot}}}{(Gc_p)_{\min}} = \frac{(UA)_{\mathrm{tot}}}{(Gc_p)_{\min}} \tag{32}$$

$$\mathrm{NTU}_{L,\mathrm{tot}} = \frac{(kA)_{\mathrm{tot}}}{(Gc_p)_{\min}} = \frac{(kA)_{\mathrm{tot}}}{(Gc_p)_{\min}} \tag{33}$$

respectively, where

$$(UA)_{\mathrm{tot}}^{-1} = (hA)_f^{-1} + \left(\frac{A_p\lambda_p}{\delta_p}\right)^{-1} + (hA)_e^{-1} \tag{34}$$

$$(kA)_{\mathrm{tot}}^{-1} = (kA)_f^{-1} + \left(\frac{\rho_p A_p D_p}{\rho_a\delta_p}\right)^{-1} + (kA)_e^{-1} \tag{35}$$

In fact, the final sensible effectiveness and the latent effectiveness can be estimated from the total number of transfer units with established correlations [3], if a uniform flow distribution is realized. However, to know the details of heat and moisture transfer in the exchanger, detailed equations should be solved.

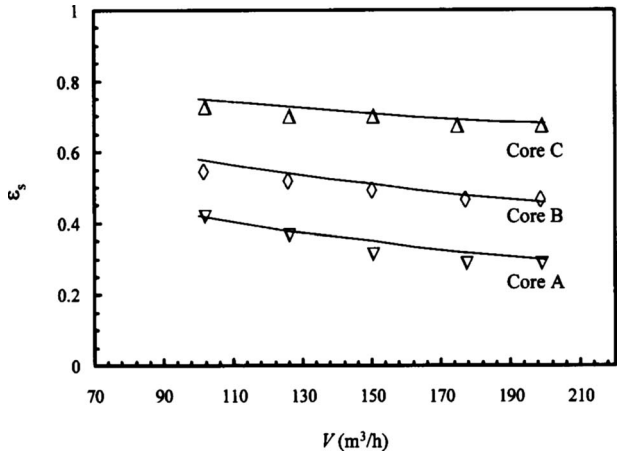

Fig. 4 Sensible effectiveness of the three plate-fin cores under various air flow rates. The solid line is the calculated values, and the discrete dots are the measured data.

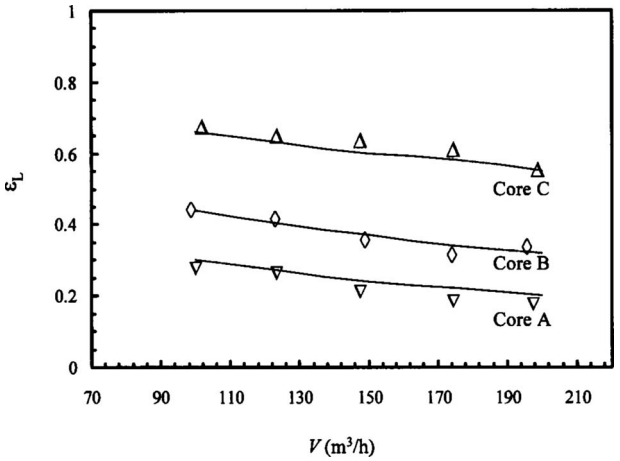

Fig. 5 Latent effectiveness of the three plate-fin cores under various air flow rates. The solid line is the calculated values, and the discrete dots are the measured data.

The exchanger thermal and latent performance deterioration factors are defined by

$$\tau_s = \frac{\varepsilon_{s,\text{uniform}} - \varepsilon_s}{\varepsilon_{s,\text{uniform}}} \tag{36}$$

$$\tau_L = \frac{\varepsilon_{L,\text{uniform}} - \varepsilon_L}{\varepsilon_{L,\text{uniform}}} \tag{37}$$

where $\varepsilon_{s,\text{uniform}}$ and $\varepsilon_{L,\text{uniform}}$ are exchanger sensible and latent effectiveness at uniform flow distribution, respectively.

4 Results and Discussion

4.1 Experimental Validation. A finite difference technique is used to discretize the partial differential equations developed for the air streams. The calculating domain of the core is divided into a number of discrete nodes. Each node represents a control volume. The numbers of calculating node are 50 in both x and y directions. Besides the discretization of energy and mass equations in x and y directions, the whole core depth is divided into 100 cells (z direction). Under this scheme, the whole core is divided into 100 mini cross-flow heat exchangers in core depth. For each mini cross-flow heat exchanger, the inlet velocity varies with the y direction for fresh air and x direction for exhaust air, respectively. The computational nodes match the physical nodes created by the intersection of the channel boundaries.

The sensible effectiveness of the three cores under various volumetric air flow rates are plotted in Fig. 4. The latent effectiveness of the three cores under various air flow rates are plotted in Fig. 5. The measured data are demonstrated by discrete dots. The calculated data are plotted by a solid line. The maximum deviation between the calculated value and the measured data is below 5%. Due to the compact structure and the high packing density, the heat transfer area is very large for such exchangers. Therefore the exchanger effectiveness is rather high. The outside dimensions are the same, but Core A has 57 passages, Core B has 92 passages, and Core C has 127 passages. The resulting channel pitches are Core A, 4.0 mm; Core B, 2.5 mm; and Core C, 1.8 mm. Core C is the most compact one; therefore its effectiveness is the highest among three. The sensible effectiveness is usually higher than latent effectiveness, because moisture resistance through membranes is much higher than thermal resistance through membranes. The fresh air duct and the exhaust air duct have the same flow distribution.

4.2 Flow Maldistribution. The effects of the core channel pitch on flow maldistribution are modeled. Three cores with different channel pitches are considered: A, 4.0 mm; B, 2.5 mm; and C 1.8 mm. The core dimensions and other structural parameters have been described in Table 1. The profiles of velocity nonuniformity (local to mean velocity ratio) on the core outlet face for the pitch 2.5 mm are plotted in Fig. 6. The total volumetric air flow rate for each stream is 150 m^3/h, which equals to a mean face velocity of 0.49 m/s or mean duct velocity of 0.98 m/s. The flow distributions on the core inlet face are the same as those on the outlet face, since only one-dimensional flow on channel length is permitted.

A general rule can be concluded: The larger the channel pitch is, the more serious the flow maldistribution is. The flow maldistribution is codetermined by the inlet duct, the core, and the outlet duct. The core itself plays a determinant role in the flow maldistribution. These components should be coupled together to predict the flow maldistribution. The incoming air impinges on the core face and some flow is driven by the core face to the remote areas at corners. There are swirls generated before the core face, which lead to flow redistribution. The flow in the core becomes somewhat uniform, due to this redistribution. The higher the core resistance is, the more serious the swirls are, and the more homogeneous the flow redistributes. The higher the total air flow rates are, the more inhomogeneous the flow becomes.

4.3 Thermal and Latent Performance Deteriorations. With the heat and mass transfer model, the local temperature and humidity on the outlet face of the core can be calculated. Let us assume that the whole exchanger is divided into a number of mini exchangers in z direction. Each mini enthalpy exchanger is an x-y

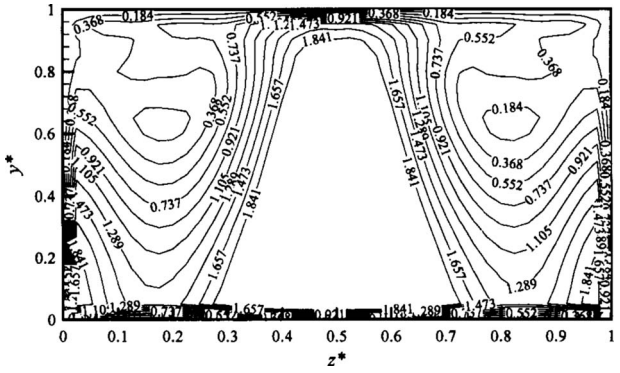

Fig. 6 Velocity nonuniformity on the core face, Core B with a channel pitch of 2.5 mm

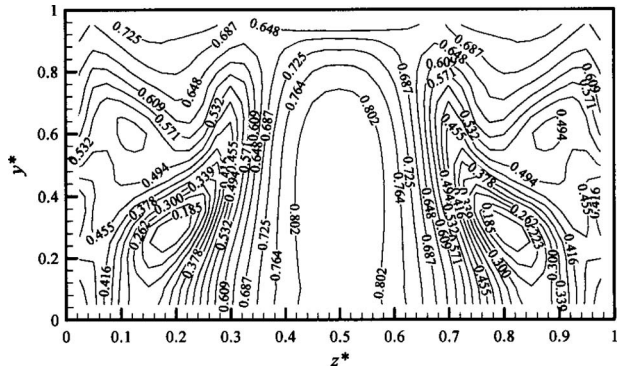

Fig. 7 Local dimensionless humidity of fresh air on the core outlet face ($x^*=1$), Core A with channel pitch of 4 mm

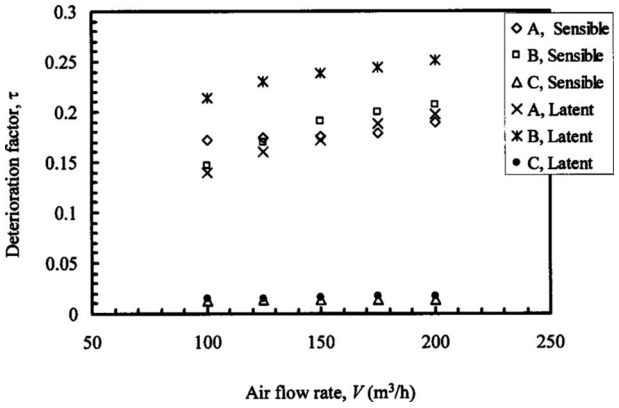

Fig. 9 Performance deterioration factors for the three cores under various air flow rates

cross-flow enthalpy exchanger. The outlet temperatures for each mini exchanger vary with x or y directions. Therefore, the outlet temperature and humidity for fresh air are two dimensional on the z-y face, while the outlet temperature and humidity for exhaust air is two dimensional on the z-x face.

Figures 7 and 8 show the local dimensionless humidity on the fresh air outlet face ($x^*=1$) on two cores. As seen, for the homogeneous flow distribution on Core C, the dimensionless humidity isolines are nearly parallel to plates, meaning the divided mini exchangers in core depth have the same heat or mass effectiveness. Both the flow and heat transfer are uniform in core depth. The moisture transfer is not as uniform as heat transfer, due to higher moisture resistance through membranes. The flow is uniform in the y direction, but the local temperature and humidity are in the opposite. This is due to the cross-flow character between the fresh air and the exhaust air, as in other common cross-flow heat exchangers.

When the maldistribution becomes serious with increased channel pitches, the local temperature and humidity become irregular. Generally, the higher the local velocity is, the higher the fresh air outlet temperatures and humidity, and the less the heat and mass effectiveness are. At the same time, the local temperature and humidity are also influenced by the temperature or humidity differences between the two neighboring fresh air and exhaust air. This results in a phenomenon that the local outlet temperature or humidity curves for Core A are more complex than those for Core C.

For engineering applications, the overall heat and moisture effectiveness of the whole exchanger is more significant than local values. Figure 9 depicts the exchanger thermal and latent performance deterioration factors under various air flow rates for the three cores. As can be seen, both the thermal and the latent performance deterioration factors for Core C are very small and the performance deterioration can be neglected. However, for the two cores with larger channel pitches, the performance deteriorations are substantial. The deterioration factors for Core B are the highest among the three. This is because the deterioration factors codetermined by flow maldistribution caused effectiveness reduction and the absolute values of effectiveness. The relative decreases in effectiveness for Core B are higher than Cores A and C. The sensible effectiveness is decreased by 15–20%, and the latent effectiveness is decreased by 20–25%. The higher deterioration factors for latent effectiveness are due to the higher moisture resistance through membranes. Compared with sensible-only heat exchangers, enthalpy exchangers should be paid more attention for flow maldistribution. Latent effectiveness of an enthalpy exchanger is usually small. A uniform flow distribution becomes more important because all the exchanger area should be equally and sufficiently employed to take part in moisture exchange.

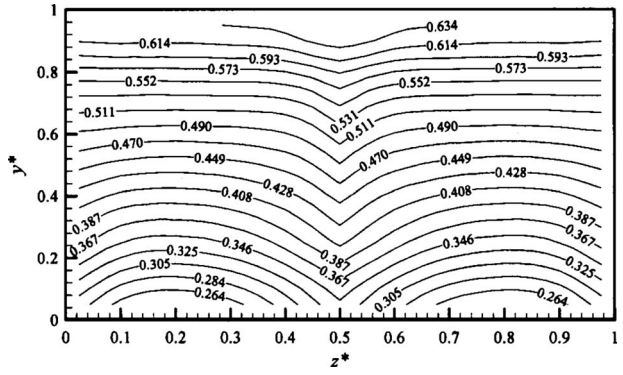

Fig. 8 Local dimensionless humidity of fresh air on the core outlet face ($x^*=1$), Core C with channel pitch of 1.8 mm

5 Conclusions

Flow maldistribution is a result of interactions between inlet duct flow, flow in cores, and flow in outlet duct. The core plays a determining role in flow distribution. Previous studies have failed to reflect this phenomenon. The following results can be found.

(1) For plate-fin compact heat exchanger cores, the channel pitch determines how serious the flow maldistribution is. For the current channel to whole exchanger pressure drop ratio, when the channel pitch is less than 2 mm, the flow maldistribution is very small and can be neglected. When the channel pitch is larger than 2 mm, the flow maldistribution becomes serious and the nonuniformity problem should be considered. This 2 mm limit would depend on the geometric details such as width and depth of the core. The cores of small pitches have larger pressure resistance, which could offset some degree of flow maldistribution that is generated by irregular duct geometries such as turnaround, expansion, and contraction.

(2) Heat and moisture exchange effectiveness are inversely proportional to local mass flow rate. For the cores with channel pitches less than 2 mm, both the thermal and the latent deterioration factors are less than 5%. When the channel pitches are larger than 2 mm, the thermal performance is deteriorated by 10–15%; while the latent performance is deteriorated by 20–25%. Compared with sensible-only heat exchangers, flow maldistribution has more impacts on enthalpy exchangers.

Acknowledgment

Project No. 50676034 is supported by the National Natural Science Foundation of China. The project is also supported by the National High Technology Research and Development Program of China (863), Grant No. 2008AA05Z206.

Nomenclature

a = half channel pitch (m)
A = area (m^2)
b = channel width (m)
c_p = specific heat ($kJ\ kg^{-1}\ K^{-1}$)
D = moisture diffusivity (m^2/s)
D_h = hydrodynamic diameter (m)
G = mass flow rate (kg/s)
h = convective heat transfer coefficient ($kW\ m^{-2}\ K^{-1}$)
k = convective mass transfer coefficient (m/s)
k_p = partition coefficient (kg/kg)
$\dot{m}$ = mass flow rate ($kg\ m^{-2}\ s^{-1}$)
n = number of channels for each flow
P = pressure (Pa)
Re = Reynolds number
RH = relative humidity
S = source term
T = temperature (K)
V = volumetric flow rate (m^3/h)
x = coordinate (m)
x_F = channel length (m)
y = coordinate (m)
y_F = channel length (m)
z = coordinate (m)
z_F = core depth (m)

Greek Letters

ρ = density (kg/m^3)
ε = effectiveness
β = flow nonuniformity
θ = half apex angle of channel (deg)
λ = heat conductivity ($W\ m^{-1}\ K^{-1}$)
ω = humidity ratio (kg/kg)
τ = thermal performance deterioration factor
δ = thickness (μm)
γ = water uptake in materials (kg moisture/kg material)
Ω = fin conductance parameter

Superscripts

* = dimensionless

Subscripts

a = air
e = exhaust air
f = fresh air
fin = fins
i = inlet
L = Latent
m = mean
o = outlet
p = plate
s = sensible

References

[1] Zhang, L. Z., 2008, *Total Heat Recovery: Heat and Moisture Recovery From Ventilation Air*, Nova Science, New York, Chap. 1, pp. 2–10.
[2] Kistler, K. R., and Cussler, E. L., 2002, "Membrane Modules for Building Ventilation," Chem. Eng. Res. Des., **80**, pp. 53–64.
[3] Zhang, L. Z., and Niu, J. L., 2002, "Effectiveness Correlations for Heat and Moisture Transfer Processes in an Enthalpy Exchanger With Membrane Cores," ASME J. Heat Transfer, **124**(5), pp. 922–929.
[4] Shah, R. K., and London, A. L., 1978, *Laminar Flow Forced Convection in Ducts*, Academic, New York, pp. 253–260.
[5] Incropera, F. P., and Dewitt, D. P., 1996, *Introduction to Heat Transfer*, 3rd ed., Wiley, New York, Chap. 8, p. 416.
[6] Shah, R. K., and Bhatti, M. S., 1987, "Laminar Convection Heat Transfer in Ducts," *Handbook of Single-Phase Convective Heat Transfer*, S. Kakac, R. K. Shah, and W. Aung, eds., Wiley, New York.
[7] Chen, S., Chan, T. L., and Leung, C. W., 2000, "Numerical Prediction of Laminar Forced Convection in Triangular Ducts With Unstructured Triangular Grid Method," Numer. Heat Transf., Part A: Applications, **38**(2), pp. 209–224.
[8] Baliga, B. R., and Azrak, R. R., 1986, "Laminar Fully Developed Flow and Heat Transfer in Triangular Plate-Fin Ducts," ASME J. Heat Transfer, **108**, pp. 24–32.
[9] Zhang, L. Z., 2007, "Thermally Developing Forced Convection and Heat Transfer in Rectangular Plate-Fin Passages Under Uniform Plate Temperature," Numer. Heat Transfer, Part A, **52**, pp. 549–564.
[10] Zhang, L. Z., 2007, "Laminar Flow and Heat Transfer in Plate-Fin Triangular Ducts in Thermally Developing Entry Region," Int. J. Heat Mass Transfer, **50**, pp. 1637–1640.
[11] Zhang, L. Z., 2008, "Heat and Mass Transfer in Plate-Fin Sinusoidal Passages With Vapor-Permeable Wall Materials," Int. J. Heat Mass Transfer, **51**, pp. 618–629.
[12] Zhang, L. Z., Liang, C. H., and Pei, L. X., 2008, "Heat and Moisture Transfer in Application-Scale Parallel-Plates Enthalpy Exchangers With Novel Membrane Materials," J. Membr. Sci., **325**, pp. 672–682.
[13] Zhang, L. Z., 2007, "Heat and Mass Transfer in a Cross Flow Membrane-Based Enthalpy Exchanger Under Naturally Formed Boundary Conditions," Int. J. Heat Mass Transfer, **50**, pp. 151–162.
[14] Bassiouny, M. K., and Martin, H., 1984, "Flow Distribution and Pressure Drop in Plate Heat Exchangers-I, U-Type Arrangement," Chem. Eng. Sci., **39**, pp. 693–700.
[15] Bassiouny, M. K., and Martin, H., 1984, "Flow Distribution and Pressure Drop in Plate Heat Exchangers-II, Z-Type Arrangement," Chem. Eng. Sci., **39**, pp. 701–704.
[16] Prabhakara Rao, B., Kumar, P. K., and Das, S. K., 2002, "Effect of Flow Distribution to the Channels on the Thermal Performance of a Plate Heat Exchanger," Chem. Eng. Process., **41**, pp. 49–58.
[17] Dwivedi, A. K., and Das, S. K., 2007, "Dynamics of Plate Heat Exchangers Subject to Flow Variations," Int. J. Heat Mass Transfer, **50**, pp. 2733–2743.
[18] Shah, R. K., 1985, "Flow Maldistribution-Compact Heat Exchangers," *Handbook of Heat Transfer Applications*, W. M. Rohsenow, P. J. Hartnett, and E. N. Ganic, eds., McGraw-Hill, New York, pp. 266–280.
[19] Ranganayakulu, Ch., Seetharamu, K. N., and Sreevatsan, K. V., 1997, "The Effects of Inlet Fluid Flow Nonuniformity on Thermal Performance and Pressure Drops in Crossflow Plate-Fin Compact Heat Exchangers," Int. J. Heat Mass Transfer, **40**, pp. 27–38.
[20] Zhang, L. Z., "Flow Maldistribution and Thermal Performance Deterioration in a Cross-Flow Air to Air Heat Exchanger With Plate-Fin Cores," Int. J. Heat Mass Transfer, in press; available online doi:10.1016/j.ijheatmasstransfer.2009.03.049.
[21] Galeazzo, F. C. C., Miura, R. Y., Gut, J. A. W., and Tadini, C. C., 2006, "Experimental and Numerical Heat Transfer in a Plate Heat Exchanger," Chem. Eng. Sci., **61**, pp. 7133–7138.
[22] Bansode, A. S., Patel, S., Kumar, T. R., Muralidhar, B., Sundararajan, T., and Das, S. K., 2007, "Numerical Simulation of Effects of Flow Maldistribution on Heat and Mass Transfer in a PEM Fuel Cell Stack," Heat Mass Transfer, **43**, pp. 1037–1047.

Heat Transfer During Deposition of Molten Aluminum Alloy Droplets to Build Vertical Columns

M. Fang

S. Chandra

C. B. Park

Department of Mechanical and Industrial Engineering,
University of Toronto,
Toronto, ON, M5S 3G8, Canada

To create functional metal parts by depositing molten metal droplets on top of each other, we have to obtain good metallurgical bonding between droplets. To investigate conditions under which such bonds are achieved, experiments were conducted in which vertical columns were formed by depositing molten aluminum alloy (A380) droplets on top of each other. A pneumatic droplet generator was used to create uniform, 0.8 mm diameter, molten aluminum droplets. The droplet generator was mounted on a stepper motor and moved constantly so as to maintain a fixed distance between the generator nozzle and the tip of the column being formed. The primary parameters varied in experiments were those found to have the strongest effect on bonding between droplets: substrate temperature (250–450°C) and deposition rate (1–8 Hz). Droplet temperature was constant at 620°C. To achieve metallurgical bonding between droplets, the tip temperature of the column should be maintained slightly below the melting temperature of the alloy to ensure remelting under an impacting drop and good bonding. The temperature cannot exceed the melting point of the metal; otherwise the column tip melts down. The temperature at the bottom of a column was measured while droplets were being deposited. An analytical one-dimensional heat conduction model was developed to obtain the transient temperature profile of the column, assuming the column and the substrate to be a semi-infinite body exposed to a periodic heat flux. From the model, the droplet deposition frequency required to maintain the tip temperature at the melting point of the metal was calculated. [DOI: 10.1115/1.3156782]

Keywords: droplet deposition, remelting, droplet-based manufacturing, aluminum droplet

1 Introduction

Rapid prototyping technology is used to fabricate solid objects, without using special tooling, molds, or dies, by depositing layers of the material in a controlled pattern. Being first developed in the 1980s, rapid prototyping techniques have been used in a wide range of applications to produce models and prototypes from virtual computer designs. A large number of competing technologies are now available in the marketplace, such as stereolithography, selective laser sintering, fused deposition modeling, laminated object manufacturing, and multijet modeling. All are additive technologies that create parts by applying the materials, layer by layer, in the form of liquid, powders, or sheets [1]. Some of these technologies can be used to directly manufacture parts that are required in small volumes [2].

Droplet-based manufacturing is an important branch of rapid prototyping technology, in which the material is melted, formed into small droplets, and deposited onto a moving substrate to fabricate three-dimensional components. Gao and Sonin [3] modified an inkjet printer head to dispense wax droplets in a predetermined pattern. Other researchers have used various droplet deposition techniques to build three-dimensional objects using polymers [4] or ice [5,6].

Parts made from nonmetallic materials are suitable for demonstration, test fit in assemblies, and as patterns to prepare molds for casting metal parts. Several experimental metal-droplet-based rapid prototyping systems have been developed in recent years to fabricate functional parts. Amon et al. [7] termed their technique "shape deposition manufacturing" in which a feedstock wire was located directly over the substrate and was melted using a plasma-welding torch. Droplets of 1–10 mm in diameter detached from the tip of the wire and fell onto a substrate whose movement was controlled, allowing the fabrication of objects through consecutive deposition of molten metal droplets. Orme and Huang [8] developed an alternate system termed precision droplet-based net-form manufacturing in which a stream of approximately 100 μm diameter droplets was generated by vibrating a molten metal jet, emerging out of a fine nozzle. Droplets were charged as they passed through a ring electrode and then deflected in an electric field applied such that droplets were delivered at the desired location on a substrate. Tseng et al. [9] developed a similar system.

To better understand the dynamics of individual molten metal droplets landing on a substrate, a number of experimental, analytical, and numerical studies have been carried out [10–15]. Much less work has been done on the interaction of droplets, landing sequentially on a surface and fusing with each other. Haferl and Poulikakos [16,17] conducted experiments and numerically modeled the deposition of two molten solder droplets, one on top of the other, and determined the effects of fluid mechanics and heat transfer during an impact on the final droplet shape. Xu et al. [18] numerically investigated the thermal behavior during a succession of droplets impinging onto a solid surface in the process of spray atomization and deposition. Ghafouri-Azar et al. [19] studied, using experiments and a numerical model, the impact of a molten tin droplet on a previously deposited and solidi-

Contributed by the Heat Transfer Division of ASME for publication in the JOURNAL OF HEAT TRANSFER. Manuscript received July 23, 2007; final manuscript received April 23, 2009; published online August 19, 2009. Review conducted by Yogesh Jaluria.

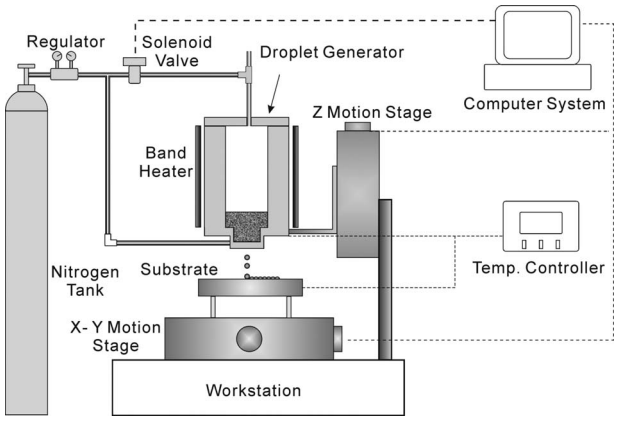

Fig. 1 Schematic diagram of the experimental apparatus

fied drop. Fang et al. [20] built columns by depositing up to 200 tin droplets on top of each other and determined conditions under which the droplets fused together well.

To fabricate freestanding sections of metal by depositing molten metal droplets, it is essential to achieve metallurgical bonding between metal droplets. When compared with wax or polymers, molten metals have much higher values of surface tension, melting temperature, latent heat of solidification, and thermal conductivity. If the temperature at the interface between the existing column and impinging droplet is too low, droplets will bounce off; if it is too high they will not solidify but flow down. There is a fairly narrow window of operating parameters in which metal droplets fuse together and solidify sufficiently and rapidly after impact to form a part.

In this paper, experiments are described in which molten aluminum alloy droplets (0.8 mm in diameter) were sequentially deposited on top of each other to produce vertical columns. Parameters varied included substrate temperature (250–450°C) and deposition frequency (1–8 Hz). The temperature at the base of the column was measured while it was being built. The thermal history of the column was modeled by assuming the column and the substrate to be semi-infinite solids exposed to a periodical heat flux. The objective of this study was to determine conditions under which molten metal droplets can fuse together and form a vertical column.

2 Experimental Procedure

Figure 1 is a schematic diagram of the experimental apparatus used to deposit molten aluminum droplets. Primary components of the system were a droplet generator, translation stages (XYR-1010 and LM-600, Danahar Precision Motion, Chicago, IL), and the control system. More details have been given earlier [20].

A pneumatic droplet generator was used to produce molten aluminum alloy droplets on demand (A380 die casting alloy, Al: 89%, Cu: 4%, Fe: 1.3%, Mg: 0.1%, solidus temperature of 540°C, and liquidus temperature of 590°C). A synthetic sapphire nozzle with an opening of 0.355 mm (0.014 in.) in diameter was used to produce single aluminum droplets of 0.8 mm in diameter. Cheng et al. [21] gave a detailed description of the droplet generator.

Oxidation of molten metal, as it emerged from the nozzle, has a very strong effect on droplet formation. A previous research published [22] shows that oxidation reduces the surface tension of liquid tin and greatly increases its viscosity, hindering molten tin jet break-up and increasing the diameter of droplets ejected from the droplet generator. Similar effects were also present in the generation of molten aluminum droplets. To prevent oxidation as molten metal droplets emerged from the nozzle, inert gas (N_2) was supplied directly to a small enclosed area surrounding the nozzle, maintaining an inert atmosphere. Gas flow was adjusted so as to eliminate oxidation while minimizing the influence on the trajectory of droplets. The inert gas flowed out of this enclosed space through the hole in the bottom of the droplet generator through which the droplet emerged.

The droplet generator was mounted on the single-axis motion stage so that it could move vertically, while an aluminum plate ($50\times50\times12.5$ mm^3) was mounted on the *x-y* stage so that it could be moved in the horizontal plane. Electronic pulses were sent through the computer's printer port to trigger the droplet generator to eject a droplet. By synchronizing droplet generation with the motion of the stages, droplets can be deposited at desired locations on the substrate. The droplet generator was elevated after a layer of material was deposited so as to maintain a constant distance of approximately 5 mm between the top surface of the material deposited and the droplet generator.

Two experimental parameters varied in the experiments: droplet deposition rate and substrate temperature. The initial droplet temperature was held constant at 620°C in all tests. Substrate temperature varied from 250°C to 450°C, and the droplet generation frequency from 1 Hz to 8 Hz.

The temperature variation at the bottom of the columns while they were being built was measured using a K-type (chromel-alumel) thermocouple (0.025 mm, 20 ms response time, TT-K-40-SLE, Omega Inc., Stamford, CT). The thermocouple was positioned on the substrate surface and droplets were deposited on top of it. As droplets landed sequentially on top of each other and a column was built up, the thermal history at the bottom of the column was recorded in real time by a data acquisition system (DAQpad-6020E, National Instrument, Austin, TX). The accuracy of the thermocouples used for measuring temperatures was ±1°C. To ensure repeatability, tests were repeated three times for each set of experimental parameters, and the temperature at the bottom of the column was measured and found to change by less than 10°C for consecutively recorded temperature profiles.

3 Results and Discussion

To build functional parts, it is essential to ensure metallurgical bonding between droplets. However, as droplets land on each other, the rate of heat transfer determines the strength of the bonds formed. Figure 2 shows a 28 mm long column, fabricated by dispensing 50 aluminum droplets at a rate of 2 Hz on a copper substrate held at 200°C. It can be seen that droplets in the upper portion of the column completely coalesced, while those at the lower portion of the column retained their spherical outline. This transition from partial to complete fusion indicates that the temperature at the tip of the column, on which impinging droplets land, increases as the column becomes longer. Thermal resistance to heat conduction from the molten droplet landing on the tip of the column to the substrate increases with column length. Complete coalescence of droplets at the upper portion due to higher tip temperature led to good metallurgical bonding between droplets, while droplets at the lower portion were bonded only through partial melting or mechanical interlock.

To investigate the effect of process parameters on the formation of a column, experiments were conducted in which 20 aluminum alloy A380 droplets (average diameter of 850 μm) were dispensed at one of the four different frequencies (1 Hz, 2 Hz, 4 Hz, and 8 Hz) on an aluminum substrate at varying temperatures (250°C, 350°C, and 450°C) to build a column. Initial droplet temperature was 620°C in all experiments. Columns that were successfully fabricated were collected and photographed, as shown in Fig. 3. At combinations of low deposition rates and substrate temperatures, in the upper left portion of Fig. 3, droplets did not fuse to form columns but instead bounced off the surface of the first solidified droplet. Attempts to build up a column with those process parameters were unsuccessful. Comparatively good fusion between droplets was achieved at a substrate temperature of 250°C when the deposition rate was greater than 4 Hz or 8 Hz. When the substrate temperature was increased to 350°C, a col-

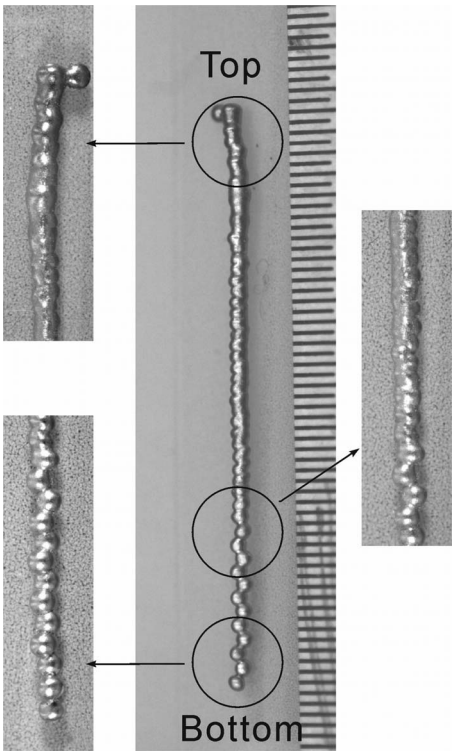

Fig. 2 A column built with 50 droplets deposited at a rate of 2 Hz on a substrate at 200°C. Scale markings are 0.5 mm apart.

umn could be fabricated with a lower deposition rate of 2 Hz. It was possible to build a column with 1 Hz deposition rate by increasing the substrate temperature to 450°C. However, the columns built at a substrate temperature of 450°C did not stand vertically but bent over, since droplets did not freeze rapidly enough after impact but remained in liquid phase long enough to flow down the side of the column. On a substrate at 350°C, the height of the column decreased as the droplet frequency increased. As the droplet deposition rate increases, the tip of the column heats up more and droplets flatten out and spread more upon impact. The resulting columns therefore have greater diameter and lower height.

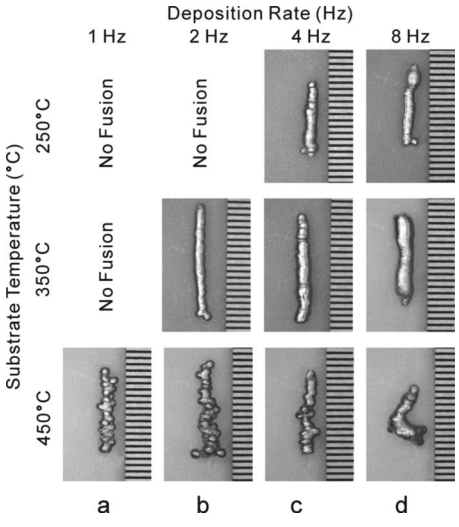

Fig. 3 Columns built by depositing 20 droplets. Substrate temperature and deposition rates were varied. Scale markings are 0.5 mm apart.

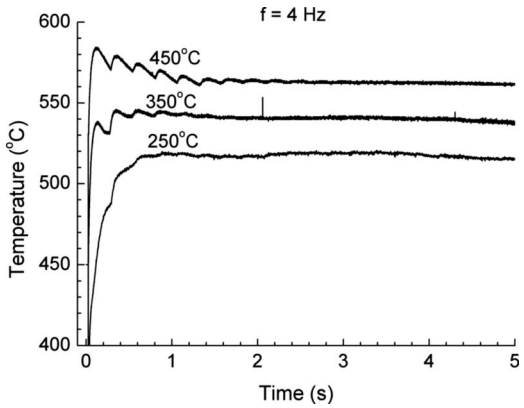

Fig. 4 Temperature variation at base of columns being built by depositing 20 droplets. Substrate temperatures were 250°C, 350°C, and 450°C, respectively, and the deposition rate was 4 Hz for all cases.

To achieve metallurgical bonding between the droplets deposited, it is necessary that the impinging droplets fuse with the solidified material at the column tip. Therefore, the column tip temperature is crucial to the fusion of droplets deposited. The tip temperature is not constant but changes as molten droplets land on it and then cool. To investigate the effect of changing substrate temperature and deposition rate on the temperature variation within a column, the transient temperature at the bottom of a column was measured in real time as it was being built.

Figure 4 shows a set of temperature measurements at the bottom of the columns at substrate temperatures of 250°C, 350°C, and 450°C, respectively, while droplets were deposited at the same rate of 4 Hz. Time $t=0$ corresponds to the impact of the first droplet. The thermocouple did not contact the substrate surface well prior to the arrival of the first droplet, so its temperature was lower than that of the substrate. The first droplet landing and solidifying on the thermocouple bonded it to the aluminum substrate. Subsequent droplets landing on top caused the temperature to rise and then decrease as the droplet cooled. The amplitude of the fluctuations decreased as the column became taller, and the distance between the thermocouple at the bottom of the column and impinging droplets increased. Eventually, the base temperature stabilized at a near-constant value. It is evident that a higher substrate temperature led to a higher bottom temperature when the deposition rate was identical. Increasing substrate temperature from 250°C to 450°C increased the column base temperature by approximately 60°C.

Increasing droplet deposition frequency also increased the column temperature. Figure 5 shows the column base temperature measurements on a substrate at 350°C, for deposition rates of 2 Hz, 4 Hz, and 8 Hz. The steady-state temperature increased by 20°C as deposition frequency was raised from 2 Hz to 8 Hz.

During deposition of droplets on top of each other, the thermal energy carried by each droplet was dissipated into the deposited material and the surrounding. Under typical experimental conditions in these tests, (substrate temperature of 250–450°C, ambient temperature of 520°C, droplet temperature of 620°C, and droplet impact velocity of 1.5 m/s), convective heat transfer was estimated to be less than 10% of the energy conducted to the deposited material and was neglected.

To develop a model of heat transfer in the column being built, all droplets were assumed to have the same size and properties when impinging on the tip of the column (Fig. 6). Other simplifying assumptions made are as follows:

1. Each droplet after impingement flattens into a disk. The spreading time (a few milliseconds) is much less than the

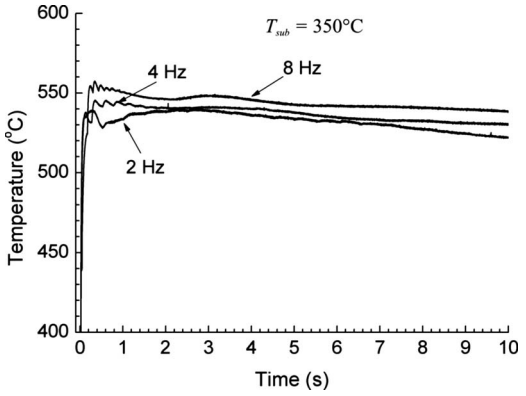

Fig. 5 Temperature variation at the base of columns being built by depositing 20 droplets. The deposition rates were 2 Hz, 4 Hz, and 8 Hz, respectively, and the substrate temperature was 350°C for all cases.

time interval between consecutive droplet impact (125–1000 ms).

2. Heat conduction between an impacting droplet and the existing column is one dimensional.
3. There is no interfacial thermal contact resistance between droplets or between droplets and the substrate.
4. The initial temperature of a droplet prior to impingement is uniform and equal to 620°C.

Assuming the column and the substrate to be a semi-infinite solid system, the heat conduction in the solid is governed by Fourier's equation,

$$\frac{\partial T(x,t)}{\partial t} = \alpha \frac{\partial^2 T(x,t)}{\partial^2 x}, \quad 0 \le x < \infty, \quad t > 0 \tag{1}$$

by initial condition,

$$T(x,0) = T_{\text{sub}}, \quad t = 0 \tag{2}$$

and by boundary conditions,

$$T(\infty,t) = T_{\text{sub}}, \quad x = \infty \tag{3}$$

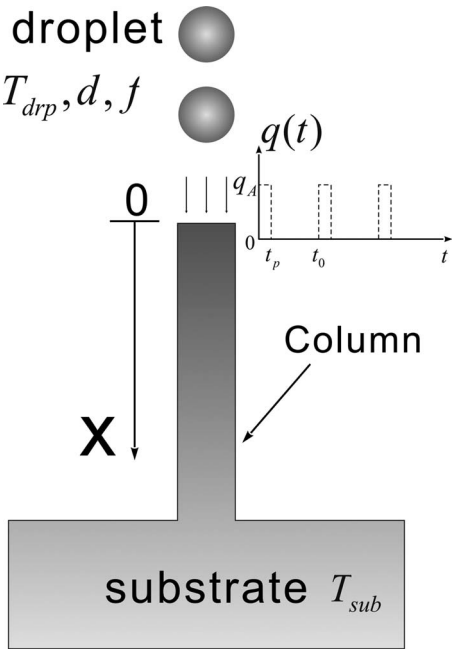

Fig. 6 Geometry of heat conduction model

$$-k\frac{\partial T(x,t)}{\partial x} = q(t), \quad x = 0 \tag{4}$$

where $q(t)$ represents a periodically varying surface heat flux that is produced by the thermal energy carried by impinging droplets being dissipated into the solid. Denoting the deposition rate by f, the heat flux can then be represented by periodic pulses with period $t_0 = 1/f$, and a pulse width of t_p representing the time for the release of the thermal energy.

The pulse width t_p can be estimated based on the three important time scales after a droplet impacts onto a substrate: (1) time to lose its superheat τ_1, (2) time to remove its latent heat τ_2, and (3) time to cool down to target temperature τ_3. In our analysis, the pulse width t_p is equivalent to the postimpact solidification time τ_s, which is equal to $2(\tau_1+\tau_2)$ and is given by [3]

$$t_p = \frac{d^2}{6\alpha}\frac{k}{k_a}\left(\ln\left(\frac{T_o - T_a}{T_{\text{mlt}} - T_a}\right) + \left(1 + \frac{k_t}{2k}\right)\frac{L}{c(T_{\text{mlt}} - T_a)}\right) \tag{5}$$

The postimpact solidification time increases as the substrate temperature increases. Typically, the solidification time is of the order of magnitude ranging from 10 ms to 100 ms when the initial substrate temperature ranges between 200°C and 500°C.

The one-dimensional coordinate system is illustrated in Fig. 6. The origin $x=0$ is set at the tip of the column and extends downwards. As the column becomes larger, the origin of the coordinate system moves at a rate equal to the average growth rate of the column

$$x(t) = \frac{1}{t}\int_0^t f \cdot s \cdot t dt = \frac{1}{2} t \cdot f \cdot s \tag{6}$$

where t is time and s is the splat thickness, which is of the same order of magnitude as the droplet diameter d under aforementioned typical experimental conditions. In our calculations, the droplet diameter was used to estimate the average growth rate.

The surface heat flux $q(t)$ is a periodic series of pulses that can be approximated by a Fourier series

$$q(t) = q_0 + \sum_{n=1}^{\infty} q_a(n)\cos(n\omega_0 t) + \sum_{n=1}^{\infty} q_b(n)\sin(n\omega_0 t) \tag{7}$$

where q_0 is the average heat flux, and $\omega_0 = 2\pi/t_0$ is the frequency.

The thermal energy of an impacting droplet per unit mass, E, includes the superheat and the latent heat of fusion $E = L' + c(T_{\text{drp}} - T_{\text{mlt}})$. Assuming the contact surface area $A = (\pi/4)d^2$, the amplitude of the heat flux q_A is estimated by

$$q_A \cdot t_p \cdot A = \rho \cdot \frac{\pi d^3}{6} \cdot E \tag{8}$$

Then, q_0, which is the average value of the periodically applied heat flux, is

$$q_0 = \frac{1}{t_0}\int_0^{t_0} q(t) dt = \frac{t_p}{t_0} q_A \tag{9}$$

One can also obtain expressions for the coefficients of the sinusoidal terms:

$$q_a(n) = \frac{2}{t_0}\int_0^{t_0} q(t)\cos(n\omega_0 t) dt = \frac{q_A}{n\pi}\sin\left(\frac{t_p}{t_0} 2n\pi\right) \tag{10}$$

$$q_b(n) = \frac{2}{t_0}\int_0^{t_0} q(t)\sin(n\omega_0 t) dt = \frac{q_A}{n\pi}\left(1 - \cos\left(\frac{t_p}{t_0} 2n\pi\right)\right) \tag{11}$$

The general solutions to problems involving a periodic heat flux boundary are provided in a number of references, including Carslaw and Jaeger [23], Myers [24], and Osizik [25]. The solution to governing Fourier's equation is

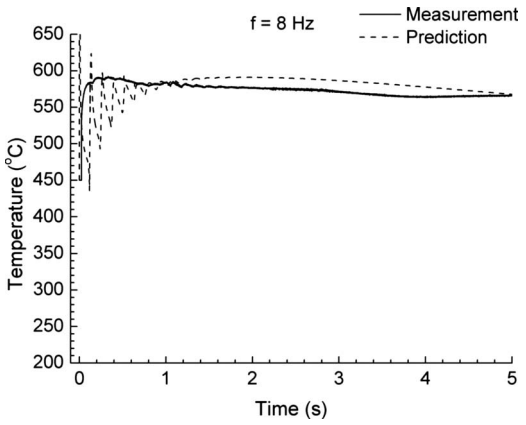

Fig. 7 Comparison of the measured and predicted base temperatures during fabrication of the column on a substrate of 450°C and at 8 Hz deposition rate

$$T(x,t) = T_{\text{sub}} + \frac{2q_0}{k}\left(\sqrt{\frac{\alpha t}{\pi}}e^{-x^2/4\alpha t} - \frac{x}{2}\text{erfc}\left(\frac{x}{2\sqrt{\alpha t}}\right)\right) + \sum_{n=1}^{\infty}\frac{q_a(n)}{k}\sqrt{\frac{\alpha}{n\omega_0}}e^{-x\sqrt{n\omega/2\alpha}}\cos\left(n\omega_0 t - x\sqrt{\frac{n\omega_0}{2\alpha}} - \frac{\pi}{4}\right) + \sum_{n=1}^{\infty}\frac{q_b(n)}{k}\sqrt{\frac{\alpha}{n\omega_0}}e^{-x\sqrt{n\omega/2\alpha}}\sin\left(n\omega_0 t - x\sqrt{\frac{n\omega_0}{2\alpha}} - \frac{\pi}{4}\right) \tag{12}$$

Note that the expression of $T(x,t)$ is an infinite series. In practice, $n=50$ terms offer a good approximation of $q(t)$ and were used in computations.

Using the model developed above, the temperature history at the bottom of the column, where the thermocouple was placed in experiments, can be calculated. Figure 7 shows a comparison of the measured temperature at the bottom of a column and the calculated temperature variation for 450°C substrate temperature and 8 Hz deposition rate. It can be seen in Fig. 7 that the temperature measured rapidly increased to about 590°C after the first droplet impacted. As more droplets arrived, the deposited material experienced several reheating/cooling cycles, indicated by the fluctuations in the temperature measurement curve. The curve eventually flattened out, and a stable temperature of about 570°C was reached. The predicted temperature showed several rapid fluctuations before it stabilizes at approximately 580°C after 1 s. The amplitude of the measured fluctuations was much less because of the relatively slow response time (~20 ms) of the thermocouple used. As the distance between the thermocouples and impacting droplet increased, the lag in response of the thermocouple also increased, making it difficult to detect fast transients.

The solidified portion of a column would have to remelt under an impinging droplet to create a good metallurgical bond. For small times after impact, a single droplet and the deposited material can be assumed to behave as semi-infinite bodies. Neglecting interfacial resistance, the interface temperature T_{int} is [26]

$$T_{\text{int}} = \frac{T_{\text{tip}}\cdot(\sqrt{k\cdot c})_{\text{tip}} + T_{\text{drp}}\cdot(\sqrt{k\cdot c})_{\text{drp}}}{(\sqrt{k\cdot c})_{\text{tip}} + (\sqrt{k\cdot c}_{\text{drp}})} \tag{13}$$

where T_{tip} is the initial temperature at the tip of the column, T_{drp} is the initial temperature of the new incoming droplet, and k and c are the thermal conductivity and specific heat, respectively. Assuming that the interface temperature must be equal to the solidus temperature of the alloy to ensure remelting, Fig. 8 shows combinations of column tip temperature and droplet temperature calculated from Eq. (13). In the case of an impinging droplet at an initial temperature of 620°C, remelting of the previously deposited material occurs when its surface temperature exceeds 480°C.

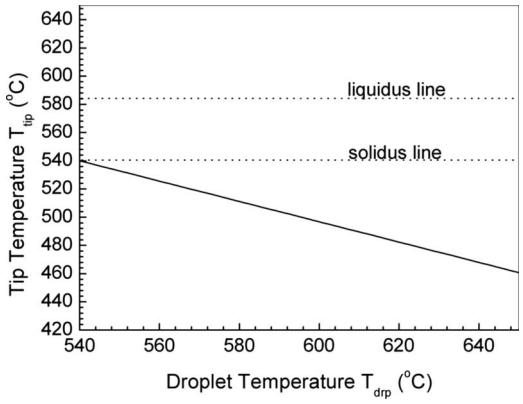

Fig. 8 Variation of T_{drp} with T_{tip}, assuming that T_{int} equals the solidus temperature

We can predict conditions under which remelting will occur by combining predictions of column tip temperature from Eq. (12) with the remelting condition of Eq. (13). Figure 9 shows tip temperature histories of columns as a function of the column length for substrate temperatures of 250°C, 350°C, and 450°C, with 1 Hz deposition rate. At $T_{\text{sub}}=450$°C, the tip temperature monotonically increases as the column grows taller. It reaches 480°C, the critical remelting temperature at 1.5 mm and the solidus temperature (540°C) at 5 mm, and then asymptotically approaches toward the initial droplet temperature (620°C). Inspecting the corresponding sample column shown in Fig. 3(*a*) at a substrate temperature of 450°C, we can see that the droplets began partially fusing together at a height of about 1 mm high, which indicated that remelting took place. The tip temperature was higher than 480°C above this point, allowing subsequent droplets to fuse together. However, for $T_{\text{sub}}=350$°C and $T_{\text{sub}}=250$°C, the tip temperature always remained under 480°C (see Fig. 9), and we were unable to build columns in experiments under these conditions (see Fig. 3). Droplets deposited in experiments bounced off rather than bonding together.

Figure 10 shows the tip temperature predictions for substrate temperatures of 250°C, 350°C, and 450°C, respectively, while the deposition rate increased to 2 Hz. For $T_{\text{sub}}=250$°C, we can see that the tip temperature still remained under the critical remelting temperature, which was not high enough for the droplet to fuse together and form the desired column. As a result, we were not able to fabricate the column with the combination of 250°C

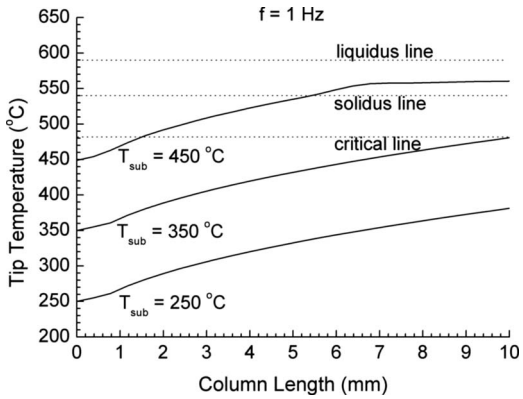

Fig. 9 Predicted variation of tip temperatures during growth of columns at substrate temperatures of 250°C, 350°C, and 450°C. The deposition rate was 1 Hz for all cases.

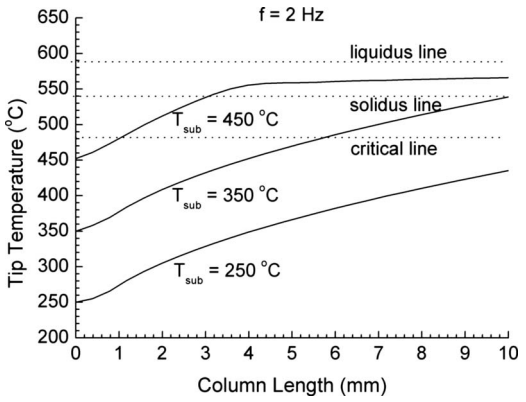

Fig. 10 Predicted variation of tip temperatures during growth of columns at substrate temperatures of 250°C, 350°C, and 450°C, respectively. The deposition rate was 2 Hz for all cases.

substrate temperature and 2 Hz deposition rate. Comparatively, remelting could take place within 5.5 mm and 1 mm for T_{sub} = 350°C and 450°C, respectively, at 2 Hz deposition rate, as indicated in Fig. 10, and columns were successfully built up under these conditions (see Fig. 3).

Increasing the deposition rate of droplets increases the column tip temperature and promotes droplet remelting at a lower position. Figure 11 shows tip temperatures for 1 Hz, 2 Hz, 4 Hz, and 8 Hz deposition rates, respectively, with T_{sub}=450°C. The corresponding remelting locations were predicted to be approximately 1.4 mm, 0.9 mm, 0.6 mm, and 0.5 mm high above the substrate surface, respectively, where the tip temperature reached the critical temperature. This trend can be clearly seen through the column samples shown in Fig. 3 for T_{sub}=450°C. However, too high deposition rate may cause droplets to remain liquid and not freeze sufficiently and rapidly. At a deposition rate of 8 Hz, the tip temperature rose to solidus temperature at a height of about 1.6 mm, leading to complete fusion of the droplets deposited. Inspecting the photograph of the column sample shown in Fig. 3(*d*) at T_{sub} = 450°C, droplets deposited began completely coalescing within 1 mm from the bottom of the column. However, the temperature of the column tip soon exceeded the liquidus temperature of the alloy, above which it remained liquid. The column in Fig. 3(*d*) appears curved, showing that the droplets did not remain attached to the point of impact but flowed down the side.

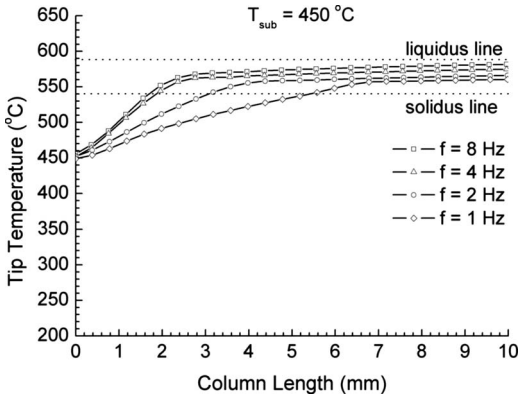

Fig. 11 Predicted variation of tip temperatures during growth of columns at droplet deposition rates of 1 Hz, 2 Hz, 4 Hz, and 8 Hz, respectively. The substrate temperature was 450°C for all cases.

4 Conclusions

Molten aluminum droplets landing sequentially on top of each other can be fused together in order to form vertical columns. To ensure good metallurgical bonding between an impacting metal droplet and a solidified column, the tip of the column should be maintained near the melting point of the metal (solidus temperature for an alloy) to ensure that remelting occurs. If the temperature is much lower than the melting point, droplets will fail to fuse with it; if it is too high, the liquid flows away from the point of impact. Two parameters that have a large influence on column temperature are the substrate temperature and droplet deposition rate. The transient temperature profile of the column was obtained by modeling the column and the substrate as the semi-infinite solid exposed to a pulsating heat flux. The tip temperature of a column constantly increases as it grows. It must exceed the solidus temperature for fusion to occur. However, if the tip temperature exceeds the liquidus temperature, the column may not remain straight since droplets do not freeze upon impact.

Nomenclature

A = area (m^2)
E = energy per unit mass (J/g)
L = latent heat of fusion (J/g)
T = temperature (K)
c = specific heat (J/g K)
d = diameter (m)
f = frequency (Hz)
k = thermal conductivity (W/m K)
q = heat flux (W/m^2)
t = time (s)
s = splat thickness (m)
x = x coordinate (m)

Greek Symbols

α = thermal diffusivity (m^2/s)
ρ = density (kg/m^3)

Subscripts

p = pulse
drp = droplet
int = interface
sub = substrate
mlt = melting
tip = column tip

References

[1] Ashley, S., 1995, "Rapid Prototyping Is Coming of Age," Mech. Eng. (Am. Soc. Mech. Eng.), **117**, pp. 62–68.
[2] Hopkinson, N., and Dickens, P., 2001, "Rapid Prototyping for Direct Manufacture," Rapid Prototyping J., **7**, pp. 197–202.
[3] Gao, F., and Sonin, A., 1994, "Precise Deposition of Molten Microdrops: The Physics of Digital Microfabrication," Proc. R. Soc. London, Ser. A: Math. Phys. Sci. (UK), **444**(1922), pp. 533–554.
[4] Chang, S., Attinger, D., Chiang, F. P., Zhao, Y., and Patel, R. C., 2004, "SIEM Measurements of Ultimate Tensile Strength and Tensile Modulus of Jetted, UV-Cured Epoxy Resin Microsamples," Rapid Prototyping J., **10**, pp. 193–198.
[5] Sui, G., and Leu, M. C., 2003, "Investigation of Layer Thickness and Surface Roughness in Rapid Freeze Prototyping," ASME J. Manuf. Sci. Eng., **125**, pp. 556–563.
[6] Sui, G., and Leu, M. C., 2003, "Thermal Analysis of Ice Walls Built by Rapid Freeze Prototyping," ASME J. Manuf. Sci. Eng., **125**, pp. 824–834.
[7] Amon, C. H., Schmaltz, K. S., and Prinz, F. B., 1996, "Numerical and Experimental Investigation of Interface Bonding Via Substrate Remelting of an Impinging Molten Metal Droplet," ASME J. Heat Transfer, **118**, pp. 164–172.
[8] Orme, M., and Huang, C., 1997, "Phase Change Manipulation for Droplet-Based Solid Freeform Fabrication," ASME J. Heat Transfer, **119**, pp. 818–823.
[9] Tseng, A. A., Lee, M. H., and Zhao, B., 2001, "Design and Operation of a Droplet Deposition System for Freeform Fabrication of Metal Parts," ASME J. Eng. Mater. Technol., **123**, pp. 74–84.
[10] Madejski, J., 1976, "Solidification of Droplets on a Cold Surface," Int. J. Heat Mass Transfer, **19**, pp. 1009–1013.

[11] Bennett, T., and Poulikakos, D., 1993, "Splat-Quench Solidification: Estimating the Maximum Spreading of a Droplet Impacting a Solid Surface," J. Mater. Sci., **28**, pp. 963–970.
[12] Liu, W., Wang, G. X., and Matthys, E. F., 1995, "Thermal Analysis and Measurements for a Molten Metal Drop Impacting on a Substrate: Cooling, Solidification and Heat Transfer Coefficient," Int. J. Heat Mass Transfer, **38**, pp. 1387–1395.
[13] Schiaffino, S., and Sonin, A., 1997, "Molten Droplet Deposition and Solidification at Low Weber Numbers," Phys. Fluids, **9**, pp. 3172–3187.
[14] Rangel, R. H., and Bian, X., 1997, "Metal-Droplet Deposition Model Including Liquid Deformation and Substrate Remelting," Int. J. Heat Mass Transfer, **40**, pp. 2549–2564.
[15] Pasandideh-Fard, M., Bhola, R., Chandra, S., and Mostaghimi, J., 1998, "Deposition of Tin Droplets on a Steel Plate: Simulations and Experiments," Int. J. Heat Mass Transfer, **41**, pp. 2929–2945.
[16] Haferl, S., and Poulikakos, D., 2002, "Transport and Solidification Phenomena in Molten Microdroplet Pileup," J. Appl. Phys., **92**(3), pp. 1675–1689.
[17] Haferl, S., and Poulikakos, D., 2003, "Experimental Investigation of the Transient Impact Fluid Dynamics and Solidification of a Molten Microdroplet Pile-Up," Int. J. Heat Mass Transfer, **46**, pp. 535–550.
[18] Xu, Q., Gupta, V. V., and Lavernia, J., 2000, "Thermal Behavior During Droplet-Based Deposition," Acta Mater., **48**, pp. 835–849.
[19] Ghafouri-Azar, R., Mostaghimi, J., and Chandra, S., 2004, "Numerical Study of Impact and Solidification of a Droplet Over a Deposited Frozen Splat," Int. J. Comput. Fluid Dyn., **18**, pp. 133–138.
[20] Fang, M., Chandra, S., and Park, C. B., 2007, "Experiments on Remelting and Solidification of Molten Metal Droplets Deposited in Vertical Columns," ASME J. Manuf. Sci. Eng., **129**, pp. 311–318.
[21] Cheng, S. X., Li, T., and Chandra, S., 2005, "Producing Molten Metal Droplets With a Pneumatic Droplet-on-Demand Generator," J. Mater. Process. Technol., **159**, pp. 295–302.
[22] Yim, P., 1996, "The Role of Surface Oxidation in the Break-Up of Laminar Liquid Metal Jets," Ph.D. thesis, Massachusetts Institute of Technology, Cambridge, MA.
[23] Carslaw, H. S., and Jaeger, J. C., 1959, *Conduction of Heat in Solids*, 2nd ed., Oxford University Press, Oxford, UK.
[24] Myers, G. E., 1971, *Analytical Methods in Conduction Heat Transfer*, McGraw-Hill, New York.
[25] Ozisik, M. N., 1980, *Heat Conduction*, Wiley, New York.
[26] Incropera, F. P., and Dewitt, D. P., 1996, *Fundamentals of Heat and Mass Transfer*, 4th ed., Wiley, New York.

Convective Heat Transfer for Water-Based Alumina Nanofluids in a Single 1.02-mm Tube

W. Y. Lai

S. Vinod

P. E. Phelan
e-mail: phelan@asu.edu

Department of Mechanical and Aerospace Engineering,
Arizona State University,
Tempe, AZ 85281

Ravi Prasher
Intel Corporation,
CH5-517,
5000 W. Chandler Blvd.,
Chandler, AZ 85226
e-mail: ravi.s.prasher@intel.com

Nanofluids are colloidal solutions, which contain a small volume fraction of suspended submicron particles or fibers in heat transfer liquids such as water or glycol mixtures. Compared with the base fluid, numerous experiments have generally indicated an increase in effective thermal conductivity and a strong temperature dependence of the static effective thermal conductivity. However, in practical applications, a heat conduction mechanism may not be sufficient for cooling high heat dissipation devices such as microelectronics or powerful optical equipment. Thus, thermal performance under convective heat transfer conditions becomes of primary interest. We report here the heat transfer coefficient h in both developing and fully developed regions by using water-based alumina nanofluids. Our experimental test section consists of a single 1.02-mm diameter stainless steel tube, which is electrically heated to provide a constant wall heat flux. Both pressure drop and temperature differences are measured, but mostly here we report our h measurements under laminar flow conditions. An extensive characterization of the nanofluid samples, including pH, electrical conductivity, particle sizing, and zeta potential, is also documented. The measured h values for nanofluids are generally higher than those for pure water. In the developing region, this can be at least partially explained by Pr number effects. [DOI: 10.1115/1.3133886]

Keywords: nanofluid, nanofluid characterization, forced convection, laminar flow

1 Introduction

In recent years, technology development has intensified with the understanding of the physics behind microscale and nanoscale domains. The unprecedented growth in electronics, optical devices, power stations, transportation, etc., has led to a number of applications requiring high heat flux dissipation. This trend is expected to continue unabated for the coming years. To dispel high heat flux, heat transfer liquids such as water, glycol, engine oil, and sodium play an essential part in many diverse industries. However, the performance of these heat transfer liquids is often narrowed by their low thermal properties. Recently, researchers have shown considerable interest in using nanoparticles as additives to alter heat transfer fluids and their performance [1–11].

Fluids with suspended submicron-sized (<100 nm) particles or fibers were named as nanofluids by Choi [1] in 1995. Since then, researchers have attempted to understand and predict the behavior of nanofluids. Compared with base fluids, a number of recent experiments have indicated dramatic improvements in effective static thermal conductivity, and the effective static thermal conductivity depends on the concentration of nanoparticles [1–5]. On the contrary, groups that adopt optical measurement methods [6,7] debated the significant enhancement of nanofluids. Putnam et al. [6] observed that the effective static thermal conductivities of Au-based nanofluids were independent of particle loading. Furthermore, measurements on monodisperse polymer suspensions by Rusconi et al. [7] did not show an anomalous increase in thermal conductivity, but rather followed the classical models for the effective properties of composite media. By virtue of the large number of ongoing investigations, a few groups were able to collect and review published reports on nanofluids [12–16]. Keblinski et al. [12] focused their review on thermal transport in stationary fluids or the understanding and controversy concerning nanofluid static thermal conductivities. Das et al. [13], Wang and Mujumdar [14], and Trisaksri and Wongwises [15] reviewed the literature of general heat transfer characteristics of nanofluids. Daungthogsuk and Wongwises [16] conducted their review that emphasized numerical approaches describing nanofluid convection performance. All of these reviews point out several deficiencies on current nanofluid research: (i) no essential agreement between results from different research groups, (ii) poor or no characterization of nanofluids, and (iii) a shortage of theoretical knowledge of thermal transport mechanisms in nanofluids. Consequently, doubts were raised on nanofluids as future cooling media, making it particularly necessary to investigate convection heat transfer with nanofluids.

Back in 1975, Ahuja [17,18] presented the details of thermal conductivity and heat transfer coefficients of polystyrene water-based solutions in laminar flow. It was shown that, without significantly increasing the friction factor for the flow, the effective thermal conductivity of the colloidal solution was improved by as much as a factor of 2. Also, as the Reynolds number and particle concentration increased, so did the enhancement in the effective thermal conductivity of the suspension. Even with this emphasized melioration of the thermal conductivity of the base fluid, the utilization of suspensions as heat transfer fluids was not adapted for micron-sized dispersed particles. The particles were not stable and were tended to settle out of suspension due to their weight. Therefore, liquids consisting of such coarse-grained particles were not yet widely applied as alternative coolants.

Experimental research on the convective heat transfer performance of nanofluids can be traced back to 1998 [19]. It is remarkable that there are still only relatively few publications of such [19–29]. Table 1 summarizes the nanofluid information, which was used by each of these groups [19–28] in their experimental investigations. Note that since Lee et al. [29] did not report the measured heat transfer coefficient or Nusselt number, those results were not provided in Table 1. The information includes the particle size and geometry, particle material, nanofluid volume frac-

Contributed by the Heat Transfer Division of ASME for publication in the JOURNAL OF HEAT TRANSFER. Manuscript received January 3, 2008; final manuscript received April 16, 2009; published online August 19, 2009. Review conducted by Jayathi Murthy.

Table 1 Summary of recent convection measurements on nanofluids

Ref.	Particle size/geometry	Nanofluids	Flow regime (Re)	Compared measured data with Nu=4.36,[a] D–B equation,[b] or H_2O data[c]
[19]	13 nm/spherical 27 nm/spherical	γ-$Al_2O_3+H_2O$ TiO_2+H_2O	10^4-10^5	$Nu_{measured} > Nu_{D-B}$
[20]	<100 nm/N/A	$Cu+H_2O$	$10^4-2.5\times10^4$	$Nu_{measured} > Nu_{D-B}$ if $\varphi > 0.5\%$
[21]	27–56 nm/spherical	γ-$Al_2O_3+H_2O$	500–2000	$Nu_{measured} > 4.36$
[22]	>100 nm/rodlike	$CNT+H_2O$	800–1200	$h_{nf} > h_{H_2O}$
[23]	20 nm/spherical	TiO_2+H_2O	2000–8000	$h_{nf} > h_{H_2O}$
[24]	d:1–2 μm and δ:20–40 nm/disklike	Graphite+commercial automatic transmission fluid or mixture of two commercial oils with additives	5–80	$h_{nf} > h_{base\ fluid}$
[25]	50–60 nm/N/A	$Cu+H_2O$	650–2050	N/A[d]
[26]	20 nm/spherical	γ-$Al_2O_3+H_2O$	700–2050	$h_{nf} > h_{H_2O}$ and $Nu_{measured} > Nu_{H_2O}$
[27]	36 nm and 47 nm/spherical	$Al_2O_3+H_2O$	$4000-1.6\times10^4$	$h_{nf} > h_{H_2O}$ and $Nu_{measured} > Nu_{H_2O}$
[28]	l:80 nm and w:20 nm/needle	$Cu+H_2O$	$\dot{V}$=10, 15, and 20 ml/min[e]	$performance_{nf} > performance_{H_2O}$

[a]Analytical solution for constant wall heat flux in the laminar flow region.
[b]Dittus–Boelter equation for transient or turbulent flow region.
[c]If the authors did not compare their data with any theoretical prediction.
[d]Did not provide pure water data.
[e]Re numbers were not provided.

tion φ, and the test flow region during experiments. The last column in Table 1 shows that the measured Nusselt number Nu were greater than or equal to Nu=4.36 (analytical result for laminar flow) or the predictions from the Dittus–Boelter correlation (empirical solution for turbulent flow). In addition, if the authors did not provide comparisons between theoretical predictions and their experimental data, the comparison of their measured nanofluids data with the base fluids is reported. Most of the above researches were contributed to relative high Re within large diameter test tubes. More details can be found in Ref. [30].

The main intention of this research is to extend the scope of the measured convective heat transfer behavior of aqueous Al_2O_3-based nanofluids. The focus will be on the convective heat transfer capability of nanofluids in a millimeter-scale tube in the laminar flow regime.

2 Experimental Setup

2.1 Apparatus. An experimental setup was designed and assembled to permit measurements and analysis of heat transfer in both the thermally developing flow region and in the thermally fully developed flow region as shown in Fig. 1. The experimental system included one sample tank, a calibration tank, a pump, a test section, a gauge pressure transducer, a differential pressure transducer, a heating jacket, a cooling jacket, connecting piping, and a single 1.02-mm inner diameter and 50-cm long straight stainless steel tube (AISI 316) that served as the test section. The test tube was heavily insulated by wrapping it in a fiberglass blanket then sandwiching it between two 2-in. thick calcium silicate boards. The portions upstream and downstream of the test section were another two 10-cm long stainless steel tubes, which had the same inner diameter and were insulated in the same way as the test section. The connections between these 10-cm long tubes and the test section also had an inner diameter of 1.02 mm. Based on the flow rates measured in our experiment, the 10-cm long upstream section was sufficient to produce hydraulically fully developed flow at the entrance of the test section.

A polyimide-coated nichrome heater wire (Lakeshore NC-32) was adopted to supply a constant heat flux condition along the test section. The nichrome wire was wrapped around the tube in a noninductive manner to avoid magnetic effects during experiments. The noninductive wrapping is done by doubling the heater wire and then winding the test tube like a solenoid (Fig. 2). Therefore, at every point along the wire there are equivalent currents passing in both directions, thus roughly canceling out any induced magnetic field. The nanofluids were driven by a low pressure microannular gear pump (Micropump Inc., Model 2521) over a volume flow rate capacity of 0.15–9 ml/min. The volume flow rates during the experiments were controlled by a computer through a controller provided by Micropump Inc. The pressure difference across the hydraulically fully developed flow test section was measured by a differential pressure transducer (Setra Inc., Model 230). The input power was confirmed by a digital multimeter. Two T-type thermocouples were inserted into the flow field to measure the nanofluid mean entrance and exit temperatures. Other T-type thermocouples were mounted on the test tube wall as sketched in Fig. 2. The staggered separation of the thermocouple locations was used to carefully monitor the temperature profile in the entrance region.

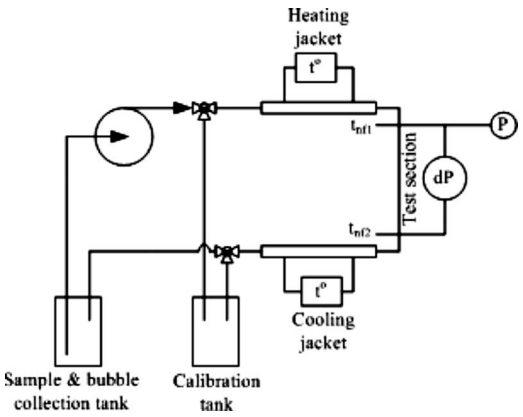

Fig. 1 Experimental apparatus sketch

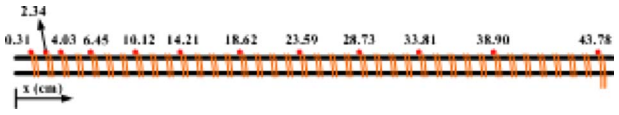

Fig. 2 Sketch of heater wire and thermocouple locations

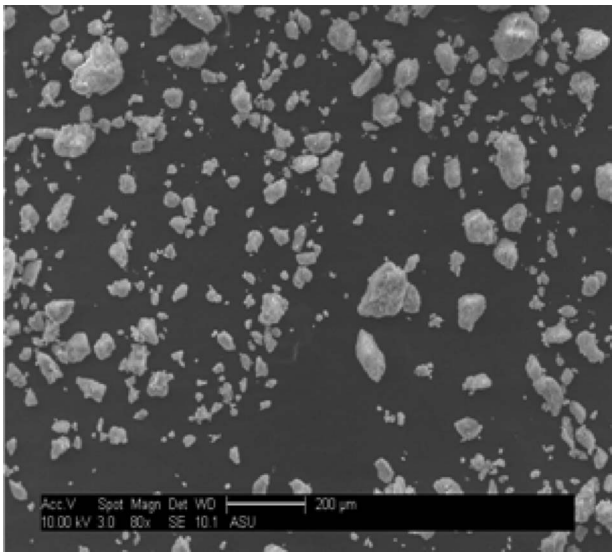

Fig. 3 SEM image for 20-nm dry Al_2O_3 nanopowder

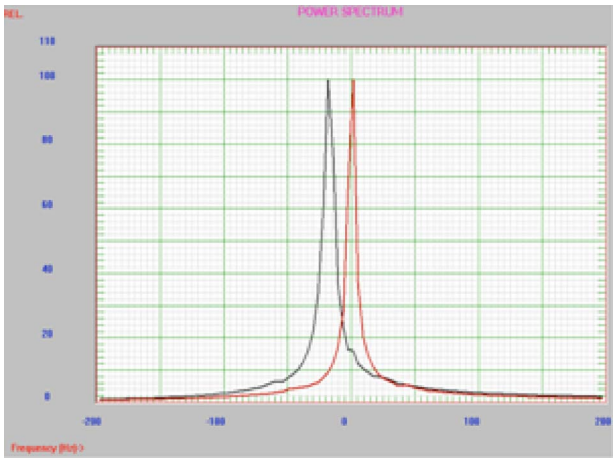

Fig. 4 Example of a good power spectrum during zeta potential measurements for determining nanofluid concentrations for DLS measurement. The curve having a peak at 0 Hz is the reference spectrum while the other curve is the sample spectrum.

2.2 Nanofluids Preparation. We chose the two-step technique as our nanofluids preparation method because the method works well for oxide nanopowders [14]. In this method, the nanoparticles are dispersed in a base fluid by ultrasonification. The nanoparticles we used were purchased from Nanostructured and Amorphous Materials, Inc. The main test samples were 20-nm γ-Al_2O_3 nanoparticles in de-ionized (DI) water. The γ-Al_2O_3 nanoparticles have 99.97% purity and a specific surface area of 180 m^2/g. Starting from a desired volume fraction value, the corresponding mass of γ-Al_2O_3 nanoparticles was calculated and weighed. Finally, the corresponding volume of the base fluid was measured, and the nanoparticles were dispersed into the base fluid via ultrasonification. The ultrasonification (model UP200S from Dr. Hielscher, GmbH) was carried out for 1 h to break up any potential clusters in the dry nanoparticle powder. After ultrasonication, the nanofluids were rested at room temperature for 1 h to eliminate any heating effects from the ultrasonification. The volume fractions of the test samples were 0.5%, 0.75%, and 1%. There was no surfactant used in any of the samples reported here.

2.3 Nanofluids Characterization. Even though there was no official standard introduced for characterizing nanofluids, some parameters have become quite common among the research groups working with nanofluids. Those parameters are the size and shape of nanoparticles or agglomerates, *p*H, electrical conductivity (σ), and zeta potential within the nanofluids. The dry 20-nm Al_2O_3 nanoparticles picture was taken using scanning electron microscopy (SEM) as shown in Fig. 3. The nanoparticle mean diameter of 20 nm was reported by the manufacturer, but Fig. 3 shows some aggregate sizes near 150 μm in the dry nanopowder. When dispersing Al_2O_3 nanoparticles into DI water, the particle surface can acquire electric charge by absorbing or desorbing protons at the particle/liquid interface, since DI water is a polar medium [30,31]. This absorbing and desorbing mechanism forms two layers that surround the particle surface. The inner region is the stern layer where the ions are strongly attached to the particle surface, and for the diffused layer, which is the outer layer, the ions are not that firmly bound. The potential at this electrical double layer (EDL) boundary is known as the zeta potential. The zeta potential and the thickness of the EDL are strongly dependent on the *p*H value. The *p*H values were measured by a *p*H meter (Hach EC10). In the presence of the EDL, the σ of a suspension can be increased due to the surface conductivity of the particles in the EDL region. The nanofluids' σ values were measured using a Hach CO150 conductivity meter.

The particle size and zeta potential in the nanofluids were measured by a dynamic light scattering (DLS) instrument from Particle Sizing Systems, Inc. (Nicomp 380/ZLS). To perform the size and zeta potential measurements using the DLS system, diluted samples were required. We determined the appropriate dilution based on the power spectrum (as shown in Fig. 4) during the zeta potential measurements. The diluted sample concentration for both the size and zeta potential measurements was 0.0006 vol %. In other words, three dispersions with volume fractions of 0.5%, 0.75%, and 1% were first prepared, and then all three samples were diluted to 0.0006 vol %. After dilution, the zeta potential measurement was carried out before the size measurement.

3 Data Analysis

Figure 5 shows the cross-sectional view of the tube. In order to avoid any unwanted uncertainty from thermal conductivities of nanofluids, Nu values are not reported in this work. Instead, we report the local heat transfer coefficient $h(x)$ obtained by

$$h(x) = \frac{q''}{T_w'(x) - T_{nf}(x)} \tag{1}$$

where q'' is the constant heat flux generated by the nichrome heater wire

$$q'' = \frac{Q}{A_h} = \frac{I \cdot V}{\pi D_i L} \tag{2}$$

where I is the measured current, V is the supplied voltage, and L is the heating length.

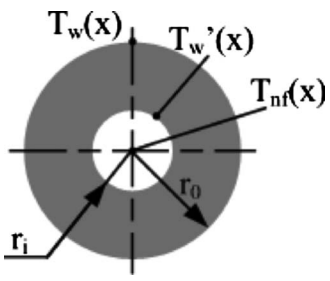

Fig. 5 Cross-sectional view of test tube (not drawn to scale)

$T'_w(x)$ is the inner wall temperature calculated from the steady one-dimensional heat conduction equation in cylindrical coordinates [32], that is,

$$\frac{1}{r}\frac{d}{dr}\left(r\frac{dT}{dr}\right)=0 \tag{3}$$

with constant heat flux boundary condition at the wall q'' (W m^{-2}), hence the solution of $T_w(x)$ becomes

$$T'_w(x)=T_w(x)-\frac{Q\cdot\ln(r_o/r_i)}{2\pi Lk_t} \tag{4}$$

where $T_w(x)$ are the local outer wall temperatures, which were measured by T-type thermocouples mounted on the tube wall. r_i and r_o are the inner and outer tube radii, respectively, and k_t is the thermal conductivity of the tube wall. Typical calculated temperature differences between the inner and outer walls ranged from 0.02°C to 0.05°C. The local fluid temperature $T_{nf}(x)$ is determined by an energy balance,

$$T_{nf}(x)=T_{nf_1}+\frac{Q}{\rho_{nf}c_{nf}\dot{V}}\frac{x}{L} \tag{5}$$

where ρ_{nf} is the nanofluid density, c_{nf} is the nanofluid heat capacity, $\dot{V}$ is the nanofluid volumetric flow rate, and x is the axial distance from the entrance of the test section. The nanofluid density and heat capacity are calculated by $\rho_{nf}=\varphi\rho_p+(1-\varphi)\rho_b$ and $c_{nf}=\varphi\rho_p c_p+(1-\varphi)\rho_b c_b/\rho_{nf}$. Note that all nanofluid thermal properties are determined at the average temperature of the nanofluid, which is justified here over the limited temperature range of our experiments (20–45°C).

4 Calibration and Uncertainty Analysis

The microannular gear pump can maintain the accuracy of volume flow rate to ±0.5%. The differential pressure transducer, which has ±0.25% accuracy, was calibrated by its manufacturer, Setra. The T-type thermocouples were calibrated within a thermostat distilled water bath and the accuracy can reach 0.1%. The accuracy for the *p*H meter is ±0.02 and ±0.5% for the electrical conductivity meter. Extraneous losses from the heater were estimated to be less than 3%, based on measurements for pure water.

Each measured point on the result graphs represents the average of the values obtained from three experimental runs. The uncertainty of experimental data was estimated by the methods described by Figliola and Beasley [33] and were calculated based on 95% confidence level. Student t-distribution used during the precision error calculation for the sample size is three.

5 Results and Discussion

5.1 Nanofluids Characterization. The *p*H and σ values for the original and the diluted samples were measured and are shown in Fig. 6. The *x*-axis labels indicate the volume fractions of the undiluted samples (i.e., the "original" samples), and the "diluted" points represent the diluted samples, which were prepared from the original samples. The results show that with increasing volume fraction, the *p*H has a peak at 0.75% for the original undiluted samples. However, for the diluted samples, the *p*H values were close to 7.4—the base fluid *p*H. For the original undiluted samples, the electrical conductivity data show an increasing trend with increasing particle loading, but σ for the diluted samples reaches a peak at an intermediate volume fraction. The zeta potential as a function of time after sonication is shown in Fig. 7 for the diluted samples. The zeta potential for the 0.75% and 1% volume fractions are at maximum at 20 min, and then decrease, while the zeta potential for the 0.5% samples remains almost constant around 47 mV. At this time, it is not clear why the zeta potential for the higher-volume fraction samples reaches a peak and then declines.

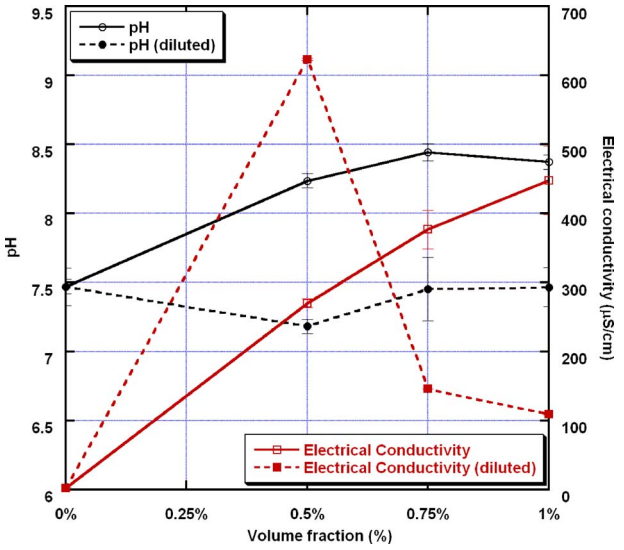

Fig. 6 *p*H and σ values versus volume fraction of the undiluted Al_2O_3-DI water nanofluids

In general, nanoparticle dispersions have a tendency to aggregate due to attractive forces between the particles. Therefore, a given dispersion is likely to exhibit several size distributions over time as a result of different aggregation rates. The Nicomp 380/ZLS is equipped with a software, which allows us to analyze bimodal populations, and an example of which is shown in Fig. 8 for one of our samples. Figure 8 is a volume-weighted distribution, not an intensity-weighted result. Recognizing that larger particles generally scatter more light than smaller particles, using an intensity-weighted distribution may lead to an opposite interpretation of the particle size distribution.

The evolutions of the average aggregate size over time, in diluted samples, are presented in Figs. 9(*a*)–9(*c*). The vol % of each aggregate size population is indicated on the *y*-axis in Fig. 9. Figure 9(*a*) gives the results taken 60 min after sonication, Fig.

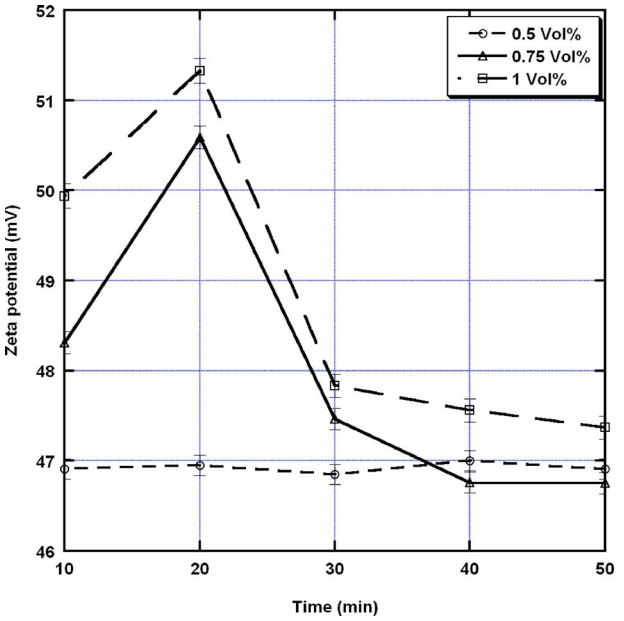

Fig. 7 Zeta potential versus time after sonication for diluted Al_2O_3-DI water nanofluids at different original (undiluted) volume fractions

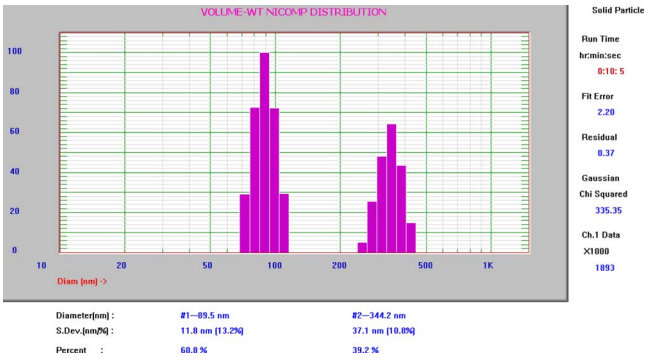

Fig. 8 An example of a particle size distribution measured with the Nicomp 380/ZLS system. Screen shot is the particle sizing result of diluted 20-nm γ-Al_2O_3 nanoparticles in DI water taken 70 min after sonication. The distribution is generated by the Nicomp volume-weighted model.

9(*b*) gives the results 10 min after Fig. 9(*a*), and Fig. 9(*c*) data were taken after another 10 min. Comparing these three graphs, it appears that the 0.5% nanofluid, in particular, manifests a stunning size fluctuation over the measured 30-min time interval. The explanation for this observation may be due to two issues. First, the zeta potential—around 47 mV—did not provide enough repulsive force to avoid aggregation or weak flocculation. Thus, one may see mean aggregate diameters of 100.7 nm and 360 nm initially, and then see three peaks 20 min later. Second, it might be due to the suspiciously high σ as shown in Fig. 6.

5.2 Apparatus Validation. The experimental equipment for measuring convection heat transfer was validated with pure water by measuring the pressure drop (ΔP) and h across the test section. The pressure drop results for pure water are provided in Fig. 10. The measured data points agreed within 3% of the theoretical line; therefore, the assumption of a steady laminar flow is valid. The theoretical line for pure water is calculated by the Hagen–Poiseuille's law [34].

$$\Delta P = \frac{128\mu L\dot{V}}{\pi D_i^4} \tag{6}$$

In the fully developed region with constant surface heat flux, Nu has an analytical solution and is equal to a constant Nu $=4.364$ [34]. The model of Kays and Crawford [34] for Nu(x) in the developing region is frequently cited by many research groups for laminar flow with constant heat flux boundary condition. The theoretical solution for the local Nu number in the thermal entrance region in Ref. [34] is expressed as

$$\mathrm{Nu}(x) = \left[\frac{1}{\mathrm{Nu}_\infty} - \frac{1}{2}\sum_{m=1}^{\infty}\frac{\exp(-\gamma_m^2 x^+)}{A_m\gamma_m^4}\right]^{-1} \tag{7}$$

where $\mathrm{Nu}_\infty = 4.364$, $x^+ = 2x/D_i/\mathrm{Re}\,\mathrm{Pr}$, γ_m, and A_m are corresponding eigenvalues and constants, which are provided in Table 9-5 in

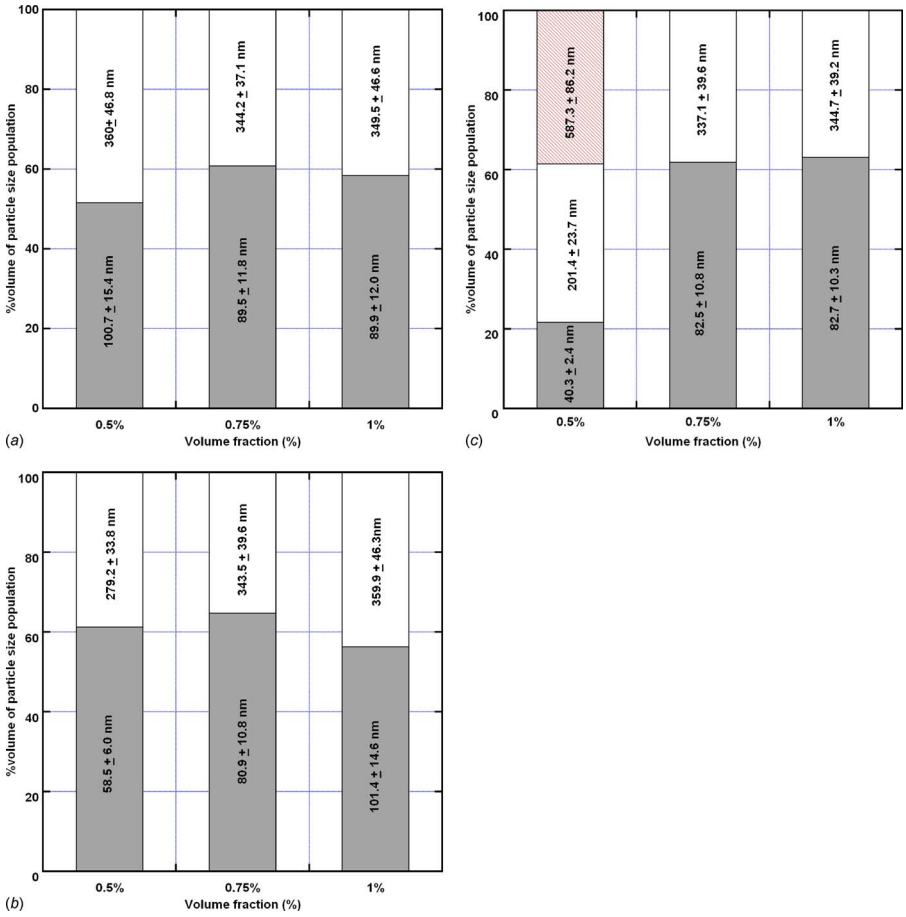

Fig. 9 (*a*) Diluted aggregate mean diameters and vol % versus original nanoparticle volume fraction 60 min after sonication, (*b*) diluted aggregate mean diameters and vol % versus original nanoparticle volume fraction 70 min after sonication, and (*c*) diluted aggregate mean diameters and vol % versus original nanoparticle volume fraction 80 min after sonication

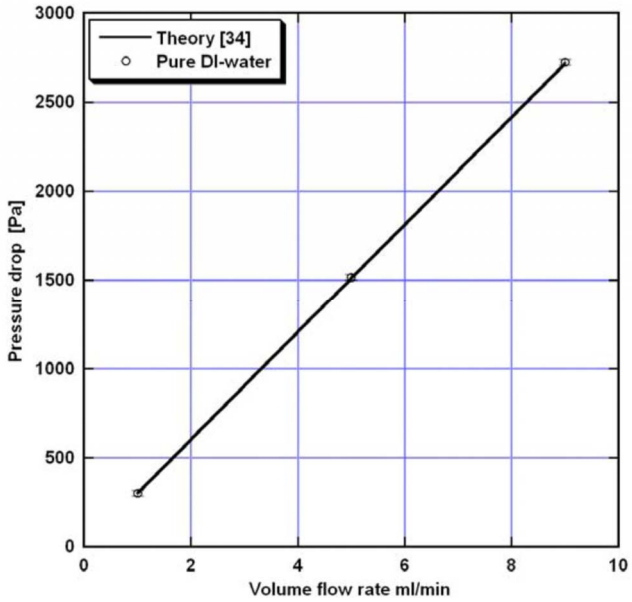

Fig. 10 Pressure drop across the test section using pure DI water (no nanoparticles) as the working fluid

Ref. [34]. Here, for comparison, we calculate $h(x)$ from $\mathrm{Nu}(x)$ as follows:

$$h(x) = \frac{\mathrm{Nu}(x) k_{\mathrm{H_2O}}}{D_i} \tag{8}$$

Figure 11 shows the local h results of pure DI water, in both the thermally developing region and the fully developed region, together with the theoretical solution from the model of Kays and Crawford [34] within the laminar flow regime under constant heat flux boundary condition. In the fully developed region, the calculated and measured h values both vary because of the temperature dependence of $k_{\mathrm{H_2O}}$. The lower the volume flow rate is, the higher the water temperature becomes under the same heat flux. Hence, the higher the water temperature, the higher $k_{\mathrm{H_2O}}$ will be, which results in higher h at the same Nu. The results show that the measured pure water h values for the test section are consistent with the predictions. Furthermore, the experimental data exhibit good agreement with the trend of the classical thermal entry length relation [34]

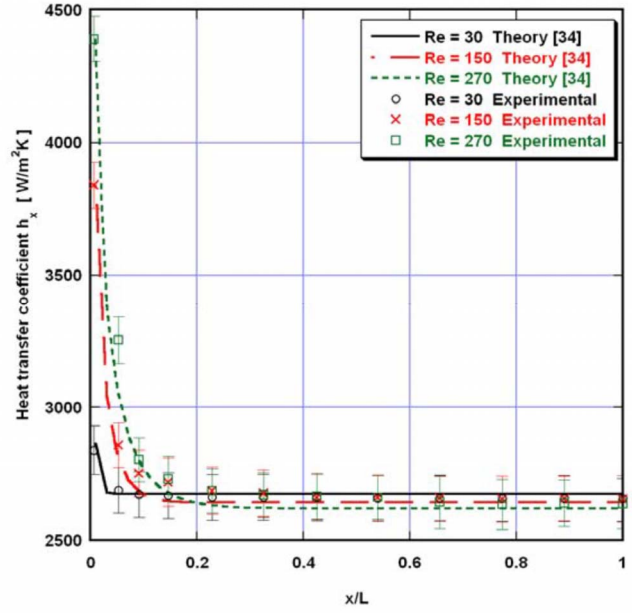

Fig. 11 Comparison between measured and calculated [34] heat transfer coefficients for developing flow, for pure DI water (no nanoparticles)

$$\left(\frac{x}{D_i}\right)_{\text{fully developed}} = 0.05 \cdot \mathrm{Re} \cdot \mathrm{Pr} \tag{9}$$

5.3 Results for Aqueous 20-nm Al_2O_3 Nanofluids. The local heat transfer coefficients in the thermal developing region are presented as a function of axial distance from the test tube entrance, at three different volume flow rates, in Figs. 12(*a*)–12(*c*), respectively. Most h results for the nanofluids are greater than that of pure DI water, except for the nanofluid with a volume fraction of 0.5% at the entrance. In Fig. 12, several trends can be observed. First of all, h decreases with increasing axial distance from the test tube entrance. Second, the h results of the Al_2O_3-DI water nanofluid show that h increases with increasing flow rate and particle volume fraction. Additionally, the enhancements in h near the entrance are greater than the enhancements in h further downstream. Finally, the nanofluids exhibit a longer entrance region than pure DI water.

Figure 13 presents h for nanofluids under different flow rates in the fully developed region. In the fully developed region, the theoretical prediction [34] for pure DI water gives the theoretical h values by using Eq. (8) along with $\mathrm{Nu}(x) = 4.364$ for constant heat flux at the tube surface. These calculated h values for pure DI water show a gradually decreasing trend, which is due to the temperature dependence of $k_{\mathrm{H_2O}}$ as mentioned before. The h results for the nanofluids did not show the same trend. Instead, h for the nanofluids tends to increase with increasing volume flow rate and particle volume fraction. However, at low volume flow rates, the h results for the 0.5% and 0.75% nanofluids are nearly the same. Moreover, the increases in h increased with increasing particle volume fraction.

The overall mechanisms by which the presence of nanoparticles can enhance the static thermal conductivity, relative to its base fluid, were studied by many research groups, but there remains significant debate over both the mechanisms and the extent of enhancement [12]. Furthermore, the exact mechanism that causes the increment in h, i.e., the observed enhancement in convective heat transfer of nanofluids over that of the base liquid, is still unclear. One possibility could be that the observed increases in h are due entirely to increases in the static thermal conductivity of nanofluids k. Another possibility, suggested a number of years ago by Ahuja [17,18] for micron-size particles, is that particle rotation could also lead to convective heat transfer augmentation. Wen and Ding [21] proposed that the enhancement might be due to particle migration within the flow field, especially near the entrance where a larger velocity gradient is expected. Particle size and shape are also parameters, which might affect the heat transfer enhancement because Yang et al. [24] observed only a very small enhancement when using disklike particles.

The observed greater enhancement at the entrance region could be due to how the thermal boundary layer develops for a nanofluid compared with a pure fluid. From Refs. [32,34], h decreases with increasing thermal boundary thickness and remains constant after approaching the fully developed condition. h can be approximated by $h \sim k_{\mathrm{nf}}/\delta$, where k_{nf} is the nanofluid thermal conductivity and δ is the thermal boundary layer thickness. Therefore, either increasing k_{nf} or reducing δ can increase h. Viscosity measurements by Prasher et al. [35] showed that the Prandtl number Pr for nanofluids increases with increasing volume fraction. Per the classic entrance region length given in Eq. (9), a greater Pr means a longer entrance region, or thus a smaller δ at a given location x

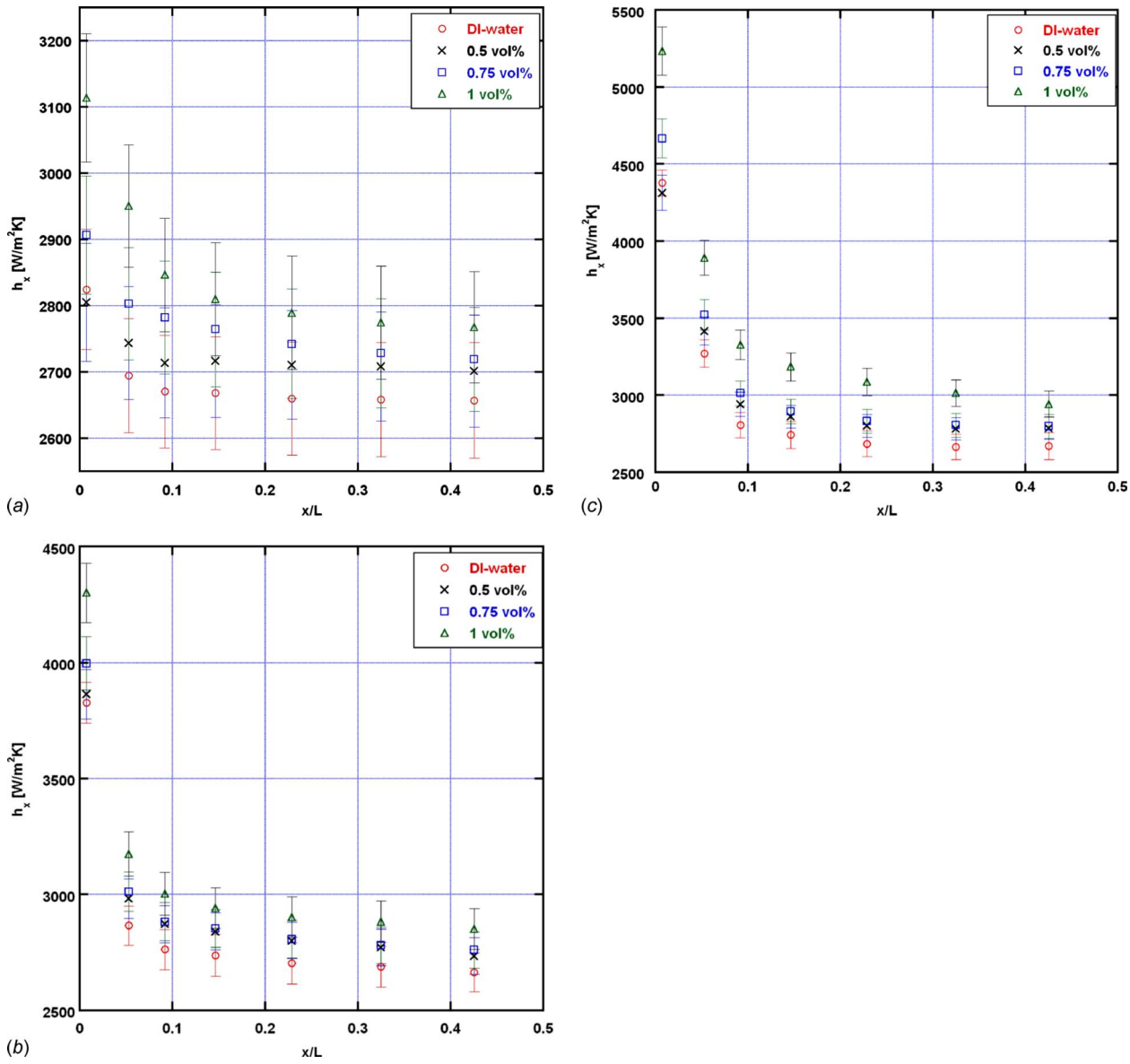

Fig. 12 (*a*) **Local heat transfer coefficients in the thermal developing region for different volume fractions at 1 ml/min volume flow rate,** (*b*) **local heat transfer coefficients in the thermal developing region for different volume fractions at 5 ml/min volume flow rate, and** (*c*) **local heat transfer coefficients in the thermal developing region for different volume fractions at 9 ml/min volume flow rate**

compared with that of the pure liquid. This trend is borne out by the 1 vol % Al_2O_3-DI water nanofluid curves in Fig. 12, which appear to exhibit longer entrance regions than the other curves. Hence, greater enhancement in h in the entrance region for nanofluids can be explained, at least in part, by classic Pr number effects.

The mechanisms responsible for the observed enhancement in h in the fully developed region are unclear. Buongiorno [36] presented a scaling analysis that suggests that any enhancement in convective heat transfer caused by the presence of the nanoparticles must be due only to changes in the effective thermophysical properties (i.e., thermal conductivity and viscosity), and not to nanoparticle dispersion. However, the analysis in Ref. [36] emphasizes the importance of the local nanoparticle distribution within the fluid by including a "nanoparticle continuity" equation. Mills and Snabre [37] studied the particle concentration distribution in the case of Poiseuille flow in a circular pipe. Their results showed that suspensions exhibit a higher concentration core at the center of the channel and the concentration distribution depends on the suspension volume fraction. With a higher concentration core, the nanofluid viscosity around the centerline of the circular tube is greater than the viscosity away from the centerline, the velocity profile is flattened around the centerline, but has a steeper gradient near the wall. Therefore, h increases. Regarding the thermal conductivity distribution along the radial direction, Sohn and Chen [38] correlated the slurry thermal conductivity as a function of shear rate, which is proportional to radial distance, and showed significant enhancement in h even though they assumed a parabolic velocity profile in the first place. Finally, we estimated the Nusselt number Nu for nanofluids in the fully developed region, where we calculated the thermal conductivity of the nanofluids k_{nf} from Ref. [39].

$$k_{nf}(\phi, T) = k_b(T)(1 + 4.5503\phi) \tag{10}$$

The resulting fully developed Nu numbers displayed the same trends as the results for h in Fig. 13, that is, Nu (or h) increases with increasing flow rate and nanoparticle volume fraction, even

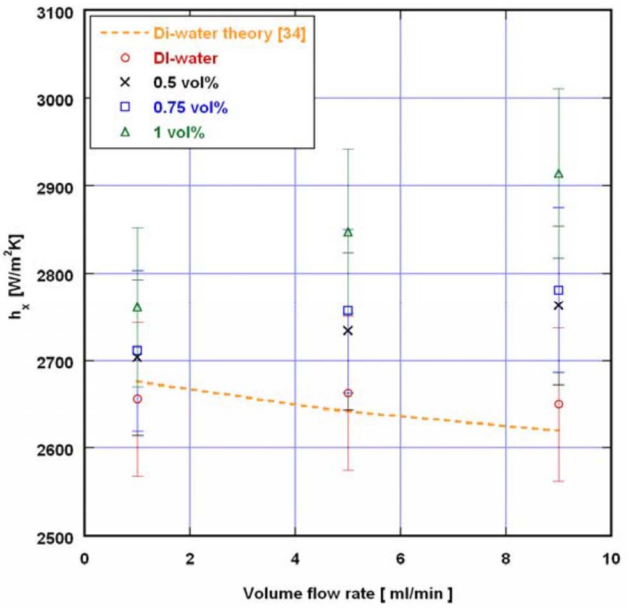

Fig. 13 Heat transfer coefficient of water-based 20-nm Al_2O_3 nanofluids in the fully developed region

in the fully developed region. Our continuing work will probe and hopefully clarify these mechanisms.

6 Conclusions

The convection heat transfer performance of 20-nm, γ-Al_2O_3 water-based nanofluids in a single 1.02-mm inner diameter, constant heat flux stainless steel tube, was experimentally investigated for laminar flow, in both the developing and fully developed regions. Overall, experimental results show that the heat transfer coefficient h increases with volume flow rate and nanoparticle volume fraction. The h enhancements also increased with increasing volume flow rate and nanoparticle volume fraction. In the developing region, the h enhancement decreased with increasing axial distance from the test section entrance. These results also showed that the higher the volume fraction, the longer is the thermal entrance length.

The characterization of the measured nanofluids, including the pH, electrical conductivity, size and shape, and zeta potential were also documented. Further investigations, however, are needed to establish the theoretical relationship between nanoparticle characteristics and the enhancement in the heat transfer coefficient.

Acknowledgment

The authors gratefully acknowledge the support of the National Science Foundation, through a GOALI award (Award No. CTS-0353543), and the direct support provided by the Intel Corporation. This material was based in part on work supported by the National Science Foundation while one of the authors (P.E.P.) was working at the Foundation.

Nomenclature

A = area (m^2)
C = heat capacity per unit volume ($J\ m^{-3}\ K^{-1}$)
D = diameter (m)
H = heat transfer coefficient ($W\ m^{-2}\ K^{-1}$)
I = current
K = thermal conductivity ($W\ m^{-1}\ K^{-1}$)
L = length (m)
Nu = Nusselt number
Pe = Peclect number
Pr = Prandtl number
Q = heat rate (W)
q'' = heat flux ($W\ m^{-2}$)
r = radius (m)
Re = Reynolds number
T = temperature
V = voltage
$\dot{V}$ = volume flow rate ($m^3\ s^{-1}$)
x = axial location

Greek Symbols

δ = thermal boundary layer thickness (m)
σ = electrical conductivity ($\mu S\ cm^{-1}$)
φ = particle volume fraction
ρ = density ($kg\ m^{-3}$)
ν = kinetic viscosity ($m^2\ s^{-1}$)

Subscripts

b = base fluid
i/o = inner/outer
nf = nanofluid
p = particle
t = test tube
w = wall

References

[1] Choi, S. U. S., 1995, "Enhancing Thermal Conductivity of Fluids With Nanoparticles," *Developments and Applications of Non-Newtonian Flows*, ASME, New York, Vol. 231, pp. 99–105.
[2] Lee, S., Choi, S. U. S., Li, S., and Eastman, J. A., 1999, "Measuring Thermal Conductivity of Fluids Containing Oxide Nanoparticles," ASME J. Heat Transfer, **121**, pp. 280–289.
[3] Eastman, J. A., Choi, S. U. S., Li, S., Yu, W., and Thompson, L. J., 2001, "Anomalously Increased Effective Thermal Conductivities of Ethylene Glycol-Based Nanofluids Containing Copper Nanoparticles," Appl. Phys. Lett., **78**(6), pp. 718–720.
[4] Kumar, D. H., Patel, H. E., Kumar, V. R. R., Pradeep, T., and Das, S. K., 2004, "Model for Heat Conduction in Nanofluids," Phys. Rev. Lett., **93**(14), p. 144301.
[5] Hong, K. S., Hong, T. K., and Yang, H. S., 2006, "Thermal Conductivity of Fe Nanofluids Depending on the Cluster Size of Nanoparticles," Appl. Phys. Lett., **88**, p. 031901.
[6] Putnam, S. A., Cahill, D. G., and Braun, P.V., 2006, "Thermal Conductivity of Nanoparticle Suspensions," J. Appl. Phys., **99**, p. 084308.
[7] Rusconi, R., Rodari, E., and Piazza, R., 2006, "Optical Measurements of the Thermal Properties of Nanofluids," Appl. Phys. Lett., **89**, p. 261916.
[8] Prasher, R., Evans, W., Meakin, P., Fish, J., Phelan, P., and Keblinski, P., 2006, "Effect of Aggregation on Thermal Conduction in Colloidal Nanofluids," Appl. Phys. Lett., **89**, p. 143119.
[9] Keblinski, P., and Thomin, J., 2006, "Hydrodynamic Field Around a Brownian Particle," Phys. Rev. E, **73**, p. 010502.
[10] Eapen, J., Williams, W. C., Buongiorno, J., Hu, L. W., and Yip, S., 2007, "Mean-Field Versus Microconvection Effects in Nanofluid Thermal Conduction," Phys. Rev. Lett., **99**, p. 095901.
[11] Sarkar, S., and Selvam, R. P., 2007, "Molecular Dynamics Simulation of Effective Thermal Conductivity and Study of Enhanced Thermal Transport Mechanism in Nanofluids," J. Appl. Phys., **102**, p. 074302.
[12] Keblinski, P., Eastman, J. A., and Cahill, D. G., 2005, "Nanofluids for Thermal Transport," Mater. Today, **8**(6), pp. 36–44.
[13] Das, S. K., Choi, S. U. S., and Patel, H. E., 2006, "Heat Transfer in Nanofluids—A Review," Heat Transfer Eng., **27**, pp. 3–19.
[14] Wang, X. Q., and Mujumdar, A. S., 2007, "Heat Transfer Characteristics of Nanofluids: A Review," Int. J. Therm. Sci., **46**, pp. 1–19.
[15] Trisaksri, V., and Wongwises, S., 2007, "Critical Review of Heat Transfer Characteristics of Nanofluids," Renewable Sustainable Energy Rev., **11**, pp. 512–523.
[16] Daungthongsuk, W., and Wongwises, S., 2007, "A Critical Review of Convective Heat Transfer of Nanofluids," Renewable Sustainable Energy Rev., **11**, pp. 797–817.
[17] Ahuja, A. S., 1975, "Augmentation of Heat Transport in Laminar Flow of Polystyrene Suspensions. I. Experiments and Results," J. Appl. Phys., **46**(8), pp. 3408–3416.
[18] Ahuja, A. S., 1975, "Augmentation of Heat Transport in Laminar Flow of Polystyrene Suspensions. II. Analysis of the Data," J. Appl. Phys., **46**(8), pp. 3417–3425.
[19] Pak, B. C., and Cho, Y. I., 1998, "Hydrodynamic and Heat Transfer Study of Dispersed Fluids With Submicron Metallic Oxide Particles," Exp. Heat Transfer, **11**(2), pp. 151–170.
[20] Xuan, Y., and Li, Q., 2003, "Investigation on Convective Heat Transfer and

Flow Features of Nanofluids," ASME J. Heat Transfer, **125**, pp. 151–155.
[21] Wen, D., and Ding, Y., 2004, "Experimental Investigation Into Convective Heat Transfer of Nanofluids at the Entrance Region Under Laminar Flow Conditions," Int. J. Heat Mass Transfer, **47**, pp. 5181–5188.
[22] Ding, Y., Alias, H., Wen, D., and Williams, R. A., 2006, "Heat Transfer of Aqueous of Carbon Nanotubes (CNT Nanofluids)," Int. J. Heat Mass Transfer, **49**, pp. 240–250.
[23] He, Y., Jin, Y., Chen, H., Ding, Y., Chang, D., and Lu, H., 2007, "Heat Transfer and Flow Behaviour of Aqueous Suspensions of TiO_2 Nanoparticles (Nanofluids) Flowing Upward Through a Vertical Pipe," Int. J. Heat Mass Transfer, **50**, pp. 2272–2281.
[24] Yang, Y., Zhang, Z. G., Grulke, E. A., Anderson, W. B., and Wu, G., 2005, "Heat Transfer Properties of Nanoparticle-in-Fluid Dispersions (Nanofluids) in Laminar Flow," Int. J. Heat Mass Transfer, **48**, pp. 1107–1116.
[25] Heris, S. Z., Esfahany, M. N., and Etemad, G., 2006, "Investigation of CuO/Water Nanofluid Laminar Convective Heat Transfer Through a Circular Tube," J. Enhanced Heat Transfer, **13**(4), pp. 279–289.
[26] Heris, S. Z., Esfahany, M. N., and Etemad, S. Gh., 2007, "Experimental Investigation of Convective Heat Transfer of Al_2O_3/Water Nanofluid in Circular Tube," Int. J. Heat Fluid Flow, **28**(2), pp. 203–210.
[27] Nguyen, C. T., Roy, G., Gauthier, C., and Galanis, N., 2007, "Heat Transfer Enhancement Using Al_2O_3-Water Nanofluid for an Electronic Liquid Cooling System," Appl. Therm. Eng., **27**, pp. 1501–1506.
[28] Chein, R., and Chuang, J., 2007, "Experimental Microchannel Heat Sink Performance Studies Using Nanofluids," Int. J. Therm. Sci., **46**(1), pp. 57–66.
[29] Lee, J., Flynn, R. D., Goodson, K. E., and Eaton, J. K., 2007, "Convective Heat Transfer of Nanofluids (DI Water-Al_2O_3) in Micro-Channels," ASME Paper No. HT2007-32630.
[30] Lai, W. Y., Duculescu, B., Phelan, P. E., Prasher, R., 2006, "A Review of Convective Heat Transfer With Nanofluids for Electronics Packaging," ITHERM 06, pp. 1240–1244.
[31] Hunter, R. J., 2004, *Foundations of Colloid Science*, 2nd ed., Oxford University Press, New York.
[32] Incropera, F. P., and DeWitt, D. P., 1996, *Fundamentals of Heat and Mass Transfer*, Wiley, New York.
[33] Figliola, R. S., and Beasley, D. E., 2005, *Theory and Design for Mechanical Measurements*, 4th ed., Wiley, New York.
[34] Kays, W. M., and Crawford, M. E., 1993, *Convective Heat and Mass Transfer*, McGraw-Hill, New York.
[35] Prasher, R., Song, D., Wang, J., and Phelan, P., 2006, "Measurements of Nanofluids Viscosity and its Implications for Thermal Applications," Appl. Phys. Lett., **89**, p. 133108.
[36] Buongiorno, J., 2006, "Convective Transport in Nanofluids," ASME J. Heat Transfer, **128**, pp. 240–250.
[37] Mills, P., and Snabre, P., 1995, "Rheology and Structure of Concentrated Suspensions of Hard Spheres, Shear Induced Particle Migration," J. Phys. II, **5**, pp. 1597–1608.
[38] Sohn, C. W., and Chen, M. M., 1984, "Heat Transfer Enhancement in Laminar Slurry Pipe Flow With Power Law Thermal Conductivities," ASME J. Heat Transfer, **106**, pp. 539–542.
[39] Williams, W., Buongiorno, J., and Hu, L. W., 2008, "Experimental Investigation of Turbulent and Pressure Loss of Alumina/Water and Zirconia/Water Nanoparticle Colloids (Nanofluids) in Horizontal Tubes," ASME J. Heat Transfer, **130**, p. 042412.

Constructal Design of Particle Volume Fraction in Nanofluids

Chao Bai

Liqiu Wang[1]
e-mail: lqwang@hku.hk

Department of Mechanical Engineering,
The University of Hong Kong,
Pokfulam Road,
Hong Kong

We perform a constructal design of particle volume fraction of four types of nanofluids used for heat conduction in four systems: a circular disk, a sphere, a plane slab, and a circular annulus. The constructal volume fraction is obtained to minimize system overall temperature difference and overall thermal resistance. Also included are the features of the constructal volume fraction and the corresponding constructal thermal resistance, which is the minimal overall resistance to the heat flow. The constructal nanofluids that maximize the system performance are not necessarily the ones with uniformly dispersed particles in base fluids. Nanofluids research and development should thus focus on not only nanofluids but also systems that use them. The march toward micro- and nanoscales must also be with the sobering reminder that useful devices are always macroscopic, and that larger and larger numbers of small-scale components must be assembled and connected by flows that keep them alive. [DOI: 10.1115/1.3155002]

Keywords: nanofluids, effective thermal conductivity, constructal theory, volume fraction distribution, overall thermal resistance

1 Introduction

Nanofluids are fluid suspensions of nanometer-sized particles. They find numerous applications in various fields due to their unique thermal, electronic, magnetic, wetting, and optical properties that can be obtained via engineering particles' structures and properties [1–6]. Recent experiments on nanofluids have shown, for example, up to twofold increases in thermal conductivity [2,6–11], strong temperature dependence of thermal conductivity [3,12], substantial increases in convective heat transfer coefficient [13–16], and threefold increases in critical heat flux (CHF) in boiling heat transfer [1–3,17–20]. State-of-the-art expositions of major advances on the synthesis, characterization, and application of nanofluids are available, for example, in Refs. [1–6].

The very essence of nanofluids research and development is to enhance fluid macroscale properties through manipulating nanoscale physics (structures, properties, and activities). Therefore, the success of nanofluid technology depends very much on how well we can address questions such as how to optimize nanoscale structures and activities for optimal macroscale properties. In the field of nanofluid heat conduction, efforts have been nearly exclusively on correlating thermal conductivity of nanofluids with their nanoscale physics in order to obtain optimal thermal conductivity [1–6]. However, practical applications of nanofluids as the heat-conduction fluids have often with a different ultimate aim such as minimization of system highest temperature and minimization of system overall thermal resistance. Therefore, interest should focus not only on optimizing nanofluid thermal conductivity but also on designing nanofluids for the best system performance.

The present work shows how to design particle volume fraction of four kinds of nanofluids in order to obtain the best performance for four heat-conduction systems. Such an analysis fits well into the design with constructal theory [21–23] so that we term the optimal particle volume fraction distribution as the constructal particle volume fraction. First developed in the late 1990s, the constructal theory holds that flow architecture arises from the natural evolutionary tendency to generate greater flow access in time and in flow configurations that are free to morph [21]. For our problem, the flow is the heat flow and the freedom lies on the distribution of particle volume fraction in nanofluids. The constructal theory unites nature with engineering and helps us generate novel designs across the board [21]. It also complements the march toward micro- and nanoscales with the sobering reminder that useful devices must always be macroscopic, and that larger and larger numbers of small-scale components must be assembled and connected by flows that keep them alive.

2 Optimal Distribution of Particle Volume Fraction

Consider nanofluid heat conduction in four systems: a circular domain of radius R_o (System 1, Fig. 1(*a*)), a sphere of radius R_o (System 2, Fig. 1(*b*)), a plane slab of thickness $R_o - R_i$ (System 3, Fig. 1(*c*)), and a circular annulus of inner radius R_i and outer radius R_o (System 4, Fig. 1(*d*)). The temperature at $r = R_o$ is maintained at a fixed value T_0 for all four systems. The volumetric heat generation rate q''' is constant in Systems 1 and 2, where the disk thickness in System 1 is unit. In Systems 3 and 4, a constant heat flux input q_i occurs at $r = R_i$. For the coordinates shown in Fig. 1, the one-dimensional (along r-direction) steady heat-conduction equation is

$$\frac{1}{r^s}\frac{d}{dr}\left[k_e r^s \frac{dT}{dr}\right] = -tq''' \tag{1}$$

where s and t values are listed in Table 1 for each of the four systems. k_e is the effective thermal conductivity of nanofluids. Here we consider four types of nanofluids whose effective thermal conductivity satisfies Birchak, Landau and Lifshitz, Lichtenecker, and Maxwell formulas, respectively [3]. The first three can be written as

$$k_e = k_f\left\{1 + v\left[\left(\frac{k_p}{k_f}\right)^{1/n} - 1\right]\right\}^n \tag{2}$$

where n values are listed in Table 2 for each of the three types of nanofluids. k_p and k_f are the thermal conductivities of particles and base fluids, respectively, and are assumed to be material constants. v is the particle volume fraction. For the Maxwell nanofluids,

[1]Corresponding author.

Contributed by the Heat Transfer Division of ASME for publication in the JOURNAL OF HEAT TRANSFER. Manuscript received March 11, 2009; final manuscript received April 16, 2009; published online August 26, 2009. Review conducted by Peter Vadasz.

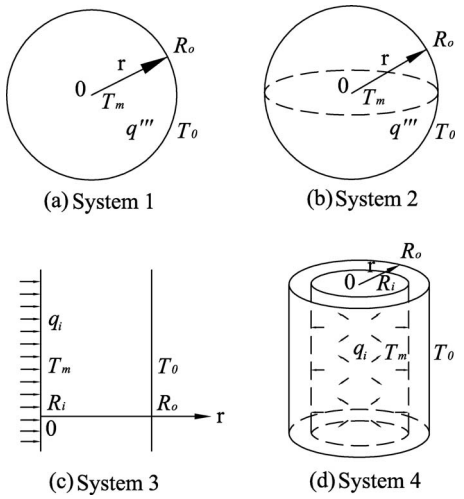

Fig. 1 Heat conduction in four systems of nanofluids: (*a*) a circular disk of radius R_o and unit thickness (System 1), (*b*) a sphere of radius R_o (System 2), (*c*) a plane slab of thickness $R_o - R_i$ (System 3), and (*d*) a circular annulus of inner radius R_i and outer radius R_o (System 4)

$$k_e = k_f + 3k_f \frac{k_p - k_f}{2k_f + k_p - (k_p - k_f)v} v \tag{3}$$

The composition of the nanoparticles and the base fluid is fixed, and is accounted for by the particle volume fraction

$$\phi = \frac{\text{volume of } k_p \text{ material}}{\text{total volume}} \tag{4}$$

Our goal is to search for the constructal $v(r)$ to minimize the system highest temperature T_m that appears at $r=0$ for Systems 1 and 2 and at $r=R_i$ for Systems 3 and 4. We detail the process of finding the constructal $v(r)$ by using Eq. (2) for the effective thermal conductivity. The results for the Maxwell nanofluids can be readily obtained by using a similar approach and are listed directly in the tables.

2.1 Case of $t=1$. By integrating Eq. (1) with respect to r from 0 to r, we obtain

$$\frac{dT}{dr} = \frac{-q'''r}{(s+1)k_e} \tag{5}$$

Substituting Eq. (2) and integrating again with respect to r from 0 to R_o yield

$$T_m - T_0 = \int_0^{R_o} \frac{q'''r}{(s+1)k_f \left\{1 + v(r)\left[\left(\frac{k_p}{k_f}\right)^{1/n} - 1\right]\right\}^n} dr \tag{6}$$

The fixed composition constraint for the case $t=1$ can be written as

Table 1 *s* and *t* values for four systems

Systems	System 1 (Fig. 1(*a*))	System 2 (Fig. 1(*b*))	System 3 (Fig. 1(*c*))	System 4 (Fig. 1(*d*))
s and t values	$s=1$, $t=1$	$s=2$, $t=1$	$s=0$, $t=0$	$s=1$, $t=0$

Table 2 *n* values for the three types of nanofluids

Nanofluids	Value of n
Birchak	$n=2$
Landau and Lifshitz	$n=3$
Lichtenecker	$n\to\infty$

$$\int_0^{R_o} [v(r) - \phi] r^s dr = 0 \tag{7}$$

Minimizing $(T_m - T_0)$ under constraint (7) is the same as minimizing [24]

$$J = \int_0^{R_o} F(r) dr \tag{8}$$

where

$$F(r) = \frac{q'''r}{(s+1)k_f \left\{1 + v(r)\left[\left(\frac{k_p}{k_f}\right)^{1/n} - 1\right]\right\}^n} + \lambda r^s [v(r) - \phi] \tag{9}$$

and λ is the Lagrangian multiplier.

Minimizing J by applying Euler–Lagrange equation [24]

$$F_{v(r)} - \frac{d}{dr} F_{v'(r)} = -\frac{nq'''r\left[\left(\frac{k_p}{k_f}\right)^{1/n} - 1\right]}{(s+1)k_f \left\{1 + v(r)\left[\left(\frac{k_p}{k_f}\right)^{1/n} - 1\right]\right\}^{n+1}} + \lambda r^s = 0 \tag{10}$$

yields

$$v(r) = \left\{\frac{nq'''}{(s+1)\lambda k_f \left[\left(\frac{k_p}{k_f}\right)^{1/n} - 1\right] r^{s-1}}\right\}^{1/(n+1)} - \frac{1}{\left[\left(\frac{k_p}{k_f}\right)^{1/n} - 1\right]} \tag{11}$$

Substituting Eq. (11) into Eq. (7) leads to

$$\lambda = \frac{nq'''}{(s+1)\left[1 + \frac{1-s}{(s+1)(n+1)}\right]^{n+1} k_f \left[\left(\frac{k_p}{k_f}\right)^{1/n} - 1\right]^n \left\{\phi + \frac{1}{\left[\left(\frac{k_p}{k_f}\right)^{1/n} - 1\right]}\right\}^{n+1} R_o^{s-1}} \tag{12}$$

Table 3 Constructal volume fraction distributions

Nanofluids	Systems: System 1 (Fig. 1(*a*))	System 2 (Fig. 1(*b*))	System 3 (Fig. 1(*c*))	System 4 (Fig. 1(*d*))
Birchak	$v_{con}(r)=\phi$	$v_{con}(r)=\frac{8}{9}\left\{\phi+\frac{1}{\left[\left(\frac{k_p}{k_f}\right)^{1/2}-1\right]}\right\}\left(\frac{r}{R_o}\right)^{-1/3}-\frac{1}{\left[\left(\frac{k_p}{k_f}\right)^{1/2}-1\right]}$	$v_{con}(r)=\phi$	$v_{con}(r)=\frac{2\left[1-\left(\frac{R_i}{R_o}\right)^2\right]}{3\left[1-\left(\frac{R_i}{R_o}\right)^{4/3}\right]}\left\{\phi+\frac{1}{\left[\left(\frac{k_p}{k_f}\right)^{1/2}-1\right]}\right\}\left(\frac{r}{R_o}\right)^{-2/3}-\frac{1}{\left[\left(\frac{k_p}{k_f}\right)^{1/2}-1\right]}$
Landau and Lifshitz	$v_{con}(r)=\phi$	$v_{con}(r)=\frac{11}{12}\left[\phi+\frac{1}{\left(\frac{k_p}{k_f}\right)^{1/3}-1}\right]\left(\frac{r}{R_o}\right)^{-1/4}-\frac{1}{\left[\left(\frac{k_p}{k_f}\right)^{1/3}-1\right]}$	$v_{con}(r)=\phi$	$v_{con}(r)=\frac{3\left[1-\left(\frac{R_i}{R_o}\right)^2\right]}{4\left[1-\left(\frac{R_i}{R_o}\right)^{3/2}\right]}\left\{\phi+\frac{1}{\left[\left(\frac{k_p}{k_f}\right)^{1/3}-1\right]}\right\}\left(\frac{r}{R_o}\right)^{-1/2}-\frac{1}{\left[\left(\frac{k_p}{k_f}\right)^{1/3}-1\right]}$
Lichtenecker	$v_{con}(r)=\phi$	$v_{con}(r)=-\frac{\ln(r/R_o)}{\ln(k_p/k_f)}+\phi-\frac{1}{3\ln(k_p/k_f)}$	$v_{con}(r)=\phi$	$v_{con}(r)=\frac{1}{\ln(k_p/k_f)}\left[-2\ln\frac{r}{R_o}-\frac{2\left(\frac{R_i}{R_o}\right)^2}{1-\left(\frac{R_i}{R_o}\right)^2}\ln\frac{R_i}{R_o}+\phi\ln\frac{k_p}{k_f}-1\right]$
Maxwell	$v_{con}(r)=\phi$	$v_{con}(r)=\frac{5}{6}\left[\phi+\frac{2+k_p/k_f}{2(k_p/k_f-1)}\right]\left(\frac{r}{R_o}\right)^{-1/2}-\frac{2+k_p/k_f}{2(k_p/k_f-1)}$	$v_{con}(r)=\phi$	$v_{con}(r)=\frac{1}{2}\left(1+\frac{R_i}{R_o}\right)\left[\phi+\frac{2+k_p/k_f}{2(k_p/k_f-1)}\right]\left(\frac{r}{R_o}\right)^{-1}-\frac{2+k_p/k_f}{2(k_p/k_f-1)}$

Therefore, we obtain the constructal $v(r)$ as follows:

$$v_{con}(r)=\left[1+\frac{1-s}{(s+1)(n+1)}\right]\left\{\phi+\frac{1}{\left[\left(\frac{k_p}{k_f}\right)^{1/n}-1\right]}\right\}\left(\frac{R_o}{r}\right)^{(s-1)/(n+1)}-\frac{1}{\left[\left(\frac{k_p}{k_f}\right)^{1/n}-1\right]} \tag{13}$$

Since

$$F_{v(r)v(r)}-\frac{d}{dr}(F_{v(r)v'(r)})=\frac{n(n+1)q'''r\left[\left(\frac{k_p}{k_f}\right)^{1/n}-1\right]^2}{(s+1)k_f\left\{1+v(r)\left[\left(\frac{k_p}{k_f}\right)^{1/n}-1\right]\right\}^{n+2}}>0 \tag{14}$$

and

$$F_{v'(r)}=0 \tag{15}$$

the $v_{con}(r)$ in Eq. (13) is indeed the constructal distribution of particle volume fraction that minimizes the system highest temperature T_m (Table 3).

Substituting Eq. (13) into Eq. (6) yields the constructal overall temperature difference $(T_m-T_0)_{con}$, which is the minimal (T_m-T_0),

$$(T_m-T_0)_{con}=\frac{q'''R_o^2}{\frac{(ns+n+2)^{n+1}}{(s+1)^{n-1}(n+1)^{n+1}}k_f\left\{1+\phi\left[\left(\frac{k_p}{k_f}\right)^{1/n}-1\right]\right\}^n} \tag{16}$$

which is listed in Table 4 for different combinations of s and n. Table 5 lists the corresponding constructal overall thermal resistance $R_{th,con}$, which is the minimal overall thermal resistance.

2.2 Case of $t=0$. By integrating Eq. (1) with respect to r from R_i to r, we obtain

$$\left(k_e r^s\frac{dT}{dr}\right)_{r=r}-\left(k_e r^s\frac{dT}{dr}\right)_{r=R_i}=0 \tag{17}$$

Since

Table 4 Constructal overall temperature difference

Nanofluids	Systems: System 1 (Fig. 1(*a*))	System 2 (Fig. 1(*b*))	System 3 (Fig. 1(*c*))	System 4 (Fig. 1(*d*))
Birchak	$(T_m-T_0)_{con}=\frac{q'''R_o^2}{4}\frac{1}{k_\phi}$; $k_\phi=k_f\left\{1+\phi\left[\left(\frac{k_p}{k_f}\right)^{1/2}-1\right]\right\}^2$	$(T_m-T_0)_{con}=\frac{81q'''R_o^2}{512}\frac{1}{k_\phi}$; $k_\phi=k_f\left\{1+\phi\left[\left(\frac{k_p}{k_f}\right)^{1/2}-1\right]\right\}^2$	$(T_m-T_0)_{con}=q_i(R_o-R_i)\frac{1}{k_\phi}$; $k_\phi=k_f\left\{1+\phi\left[\left(\frac{k_p}{k_f}\right)^{1/2}-1\right]\right\}^2$	$(T_m-T_0)_{con}=\frac{27(R_o^{4/3}-R_i^{4/3})^3q_iR_i}{16(R_o^2-R_i^2)^2}\frac{1}{k_\phi}$; $k_\phi=k_f\left\{1+\phi\left[\left(\frac{k_p}{k_f}\right)^{1/2}-1\right]\right\}^2$
Landau and Lifshitz	$(T_m-T_0)_{con}=\frac{q'''R_o^2}{4}\frac{1}{k_\phi}$; $k_\phi=k_f\left\{1+\phi\left[\left(\frac{k_p}{k_f}\right)^{1/3}-1\right]\right\}^3$	$(T_m-T_0)_{con}=\frac{2304q'''R_o^2}{14641}\frac{1}{k_\phi}$; $k_\phi=k_f\left\{1+\phi\left[\left(\frac{k_p}{k_f}\right)^{1/3}-1\right]\right\}^3$	$(T_m-T_0)_{con}=q_i(R_o-R_i)\frac{1}{k_\phi}$; $k_\phi=k_f\left\{1+\phi\left[\left(\frac{k_p}{k_f}\right)^{1/3}-1\right]\right\}^3$	$(T_m-T_0)_{con}=\frac{128(R_o^{3/2}-R_i^{3/2})^4q_iR_i}{81(R_o^2-R_i^2)^3}\frac{1}{k_\phi}$; $k_\phi=k_f\left\{1+\phi\left[\left(\frac{k_p}{k_f}\right)^{1/3}-1\right]\right\}^3$
Lichtenecker	$(T_m-T_0)_{con}=\frac{q'''R_o^2}{4}\frac{1}{k_\phi}$; $k_\phi=k_f\left(\frac{k_p}{k_f}\right)^\phi$	$(T_m-T_0)_{con}=\frac{e^{1/3}q'''R_o^2}{9}\frac{1}{k_\phi}$; $k_\phi=k_f\left(\frac{k_p}{k_f}\right)^\phi$	$(T_m-T_0)_{con}=q_i(R_o-R_i)\frac{1}{k_\phi}$; $k_\phi=k_f\left(\frac{k_p}{k_f}\right)^\phi$	$(T_m-T_0)_{con}=\frac{e(R_o^2-R_i^2)q_iR_i}{2R_o^{2R_o^2/(R_o^2-R_i^2)}R_i^{1-(R_o^2+R_i^2)/(R_o^2-R_i^2)}}\frac{1}{k_\phi}$; $k_\phi=k_f\left(\frac{k_p}{k_f}\right)^\phi$
Maxwell	$(T_m-T_0)_{con}=\frac{q'''R_o^2}{4}\frac{1}{k_\phi}$; $k_\phi=k_f\left[1+\frac{3(k_p-k_f)\phi}{2k_f+k_p-(k_p-k_f)\phi}\right]$	$(T_m-T_0)_{con}=\frac{3q'''R_o^2(2k_f+k_p)}{25k_f(k_p-k_f)\left[\phi+\frac{2k_f+k_p}{2(k_p-k_f)}\right]}-\frac{q'''R_o^2}{12k_f}\approx\frac{47q'''R_o^2}{300}\frac{1}{k_\phi}$ (approximation for the case of $\phi\ll1$;) $k_\phi=k_f\left[1+\frac{3(k_p-k_f)\phi}{2k_f+k_p-(k_p-k_f)\phi}\right]$	$(T_m-T_0)_{con}=q_i(R_o-R_i)\frac{1}{k_\phi}$; $k_\phi=k_f\left[1+\frac{3(k_p-k_f)\phi}{2k_f+k_p-(k_p-k_f)\phi}\right]$	$(T_m-T_0)_{con}=\frac{6q_iR_i(R_o-R_i)(2k_f+k_p)}{2(R_o+R_i)k_f[2(k_p-k_f)\phi+2k_f+k_p]}-\frac{q_iR_i\ln\frac{R_o}{R_i}(R_o+R_i)[2k_f+k_p+2(k_p-k_f)\phi]}{2(R_o+R_i)k_f[2(k_p-k_f)\phi+2k_f+k_p]}\approx q_iR_i\ln\frac{R_o}{R_i}\frac{1}{k_\phi}$ (approximation for the case of $\frac{R_i}{R_o}$ from 0.5 to 1); $k_\phi=k_f\left[1+\frac{3(k_p-k_f)\phi}{2k_f+k_p-(k_p-k_f)\phi}\right]$

$$\left(-k_e\frac{dT}{dr}\right)_{r=R_i}=q_i \tag{18}$$

Eq. (17) becomes

$$\frac{dT}{dr}=\frac{-q_iR_i^s}{k_er^s} \tag{19}$$

Substituting Eq. (2) and integrating again with respect to r from R_i to R_o yield

$$T_m-T_0=\int_{R_i}^{R_o}\frac{q_iR_i^s}{r^sk_f\left\{1+v(r)\left[\left(\frac{k_p}{k_f}\right)^{1/n}-1\right]\right\}^n}dr \tag{20}$$

The fixed composition constraint for the case $t=0$ can be written as

$$\int_{R_i}^{R_o}[v(r)-\phi]r^sdr=0 \tag{21}$$

Minimizing (T_m-T_0) under constraint (21) is the same as minimizing [24]

$$J=\int_0^{R_o}F(r)dr \tag{22}$$

where

$$F(r)=\frac{q_iR_i^s}{r^sk_f\left\{1+v(r)\left[\left(\frac{k_p}{k_f}\right)^{1/n}-1\right]\right\}^n}+\lambda r^s[v(r)-\phi] \tag{23}$$

and λ is the Lagrangian multiplier.

Minimizing J by applying Euler–Lagrange equation [24]

$$F_{v(r)}-\frac{d}{dr}F_{v'(r)}=-\frac{nq_iR_i^s\left[\left(\frac{k_p}{k_f}\right)^{1/n}-1\right]}{k_fr^s\left\{1+v(r)\left[\left(\frac{k_p}{k_f}\right)^{1/n}-1\right]\right\}^{n+1}}+\lambda r^s=0 \tag{24}$$

yields

$$v(r)=\left\{\frac{nq_iR_i^s}{\lambda k_f\left[\left(\frac{k_p}{k_f}\right)^{1/n}-1\right]^nr^{2s}}\right\}^{1/(n+1)}-\frac{1}{\left[\left(\frac{k_p}{k_f}\right)^{1/n}-1\right]} \tag{25}$$

Substituting Eq. (25) into Eq. (21) leads to

Table 5 Constructal overall thermal resistance

Systems	Constructal overall thermal resistance
System 1 (Fig. 1(*a*))	$R_{\text{th,con}}=\dfrac{(T_m-T_0)_{\text{con}}}{q'''\pi R_o^2\times 1}=\dfrac{1}{4\pi}\dfrac{1}{k_\phi}$
System 2 (Fig. 1(*b*))	$R_{\text{th,con}}=\dfrac{(T_m-T_0)_{\text{con}}}{q'''\times 4\pi R_o^3/3}=\dfrac{1728}{14641\pi R_o}\dfrac{1}{k_\phi}$ (exact for Landau and Lifshitz nanofluids, with over 98% accuracy for the other three types of nanofluids)
System 3 (Fig. 1(*c*))	$R_{\text{th,con}}=\dfrac{(T_m-T_0)_{\text{con}}}{q_i\times 1\times 1}=(R_o-R_i)\dfrac{1}{k_\phi}$ Birchak: $R_{\text{th,con}}=\dfrac{(T_m-T_0)_{\text{con}}}{q_i\times 2\pi R_i\times 1}=\dfrac{27(R_o^{4/3}-R_i^{4/3})^3}{32\pi(R_o^2-R_i^2)^2}\dfrac{1}{k_\phi}$, Landau and Lifshitz: $R_{\text{th,con}}=\dfrac{(T_m-T_0)_{\text{con}}}{q_i\times 2\pi R_i\times 1}=\dfrac{128(R_o^{3/2}-R_i^{3/2})^4}{162\pi(R_o^2-R_i^2)^3}\dfrac{1}{k_\phi}$, Lichtenecker:
System 4 (Fig. 1(*d*))	$R_{\text{th,con}}=\dfrac{(T_m-T_0)_{\text{con}}}{q_i\times 2\pi R_i\times 1}=\dfrac{e(R_o^2-R_i^2)}{4\pi R_o^{2R_o^2/(R_o^2-R_i^2)}R_i^{1-(R_o^2+R_i^2)/(R_o^2-R_i^2)}}\dfrac{1}{k_\phi}$, Maxwell: $R_{\text{th,con}}=\dfrac{(T_m-T_0)_{\text{con}}}{q_i\times 2\pi R_i\times 1}=\dfrac{\left[\dfrac{6(R_o-R_i)-(R_o+R_i)\ln\dfrac{R_o}{R_i}}{2\pi(R_o+R_i)}\right](2k_f+k_p)-\dfrac{1}{\pi}\ln\dfrac{R_o}{R_i}(k_p-k_f)\phi}{2k_f[2(k_p-k_f)\phi+2k_f+k_p]}\approx\dfrac{1}{2\pi}\ln\dfrac{R_o}{R_i}\dfrac{1}{k_\phi}$ (approximation for the case of $\dfrac{R_i}{R_o}$ from 0.5 to 1)

$$\lambda=\frac{nq_iR_i^s}{\left[\dfrac{ns-s+n+1}{(s+1)(n+1)}\right]^{n+1}k_f\left[\left(\dfrac{k_p}{k_f}\right)^{1/n}-1\right]^n\left\{\phi+\dfrac{1}{\left[\left(\dfrac{k_p}{k_f}\right)^{1/n}-1\right]}\right\}^{n+1}\left[\dfrac{R_o^{s+1}-R_i^{s+1}}{R_o^{(ns-s+n+1)/(n+1)}-R_i^{(ns-s+n+1)/(n+1)}}\right]^{n+1}} \tag{26}$$

Therefore, we obtain the constructal $v(r)$ as follows:

$$v_{\text{con}}(r)=\left\{\phi+\frac{1}{\left[\left(\dfrac{k_p}{k_f}\right)^{1/n}-1\right]}\right\}\left[\frac{R_o^{s+1}-R_i^{s+1}}{R_o^{(ns-s+n+1)/(n+1)}-R_i^{(ns-s+n+1)/(n+1)}}\right]\times\left[\frac{ns-s+n+1}{(s+1)(n+1)}\right]r^{-2s/(n+1)}-\frac{1}{\left[\left(\dfrac{k_p}{k_f}\right)^{1/n}-1\right]} \tag{27}$$

Since

$$F_{v(r)v(r)}-\frac{d}{dr}(F_{v(r)v'(r)})=\frac{n(n+1)q_iR_i^s\left[\left(\dfrac{k_p}{k_f}\right)^{1/n}-1\right]^2}{k_fr^s\left\{1+v(r)\left[\left(\dfrac{k_p}{k_f}\right)^{1/n}-1\right]\right\}^{n+2}}>0 \tag{28}$$

and

$$F_{v'(r)}=0 \tag{29}$$

the $v_{\text{con}}(r)$ in Eq. (27) is indeed the constructal distribution of particle volume fraction that minimizes the system highest temperature T_m (Table 3).

Substituting Eq. (27) into Eq. (20) yields the constructal overall temperature difference $(T_m-T_0)_{\text{con}}$ as follows:

$$(T_m-T_0)_{\text{con}}=\frac{q_iR_i^s(R_o^{(ns-s+n+1)/(n+1)}-R_i^{(ns-s+n+1)/(n+1)})^{n+1}}{\dfrac{(ns-s+n+1)^{n+1}}{(s+1)^n(n+1)^{n+1}}(R_o^{s+1}-R_i^{s+1})^nk_f\left\{1+\phi\left[\left(\dfrac{k_p}{k_f}\right)^{1/n}-1\right]\right\}^n} \tag{30}$$

which is listed in Table 4 for different combinations of s and n. The corresponding constructal overall thermal resistance $R_{\text{th,con}}$ is listed in Table 5.

3 Discussion

Both constructal overall temperature difference $(T_m-T_0)_{\text{con}}$ and thermal resistance $R_{\text{th,con}}$ are proportional to k_ϕ^{-1} for all four systems, where k_ϕ is the effective thermal conductivity evaluated at the overall (average) particle volume fraction ϕ (Tables 4 and 5). The proportional coefficients for $R_{\text{th,con}}$ are either invariant for Systems 1–3 or nearly invariant for System 4 with respect to types of nanofluids (Table 5). Therefore, the constructal thermal resistance $R_{\text{th,con}}$ is indeed an overall property fixed only by the system global geometry and the average thermal conductivity of nano-

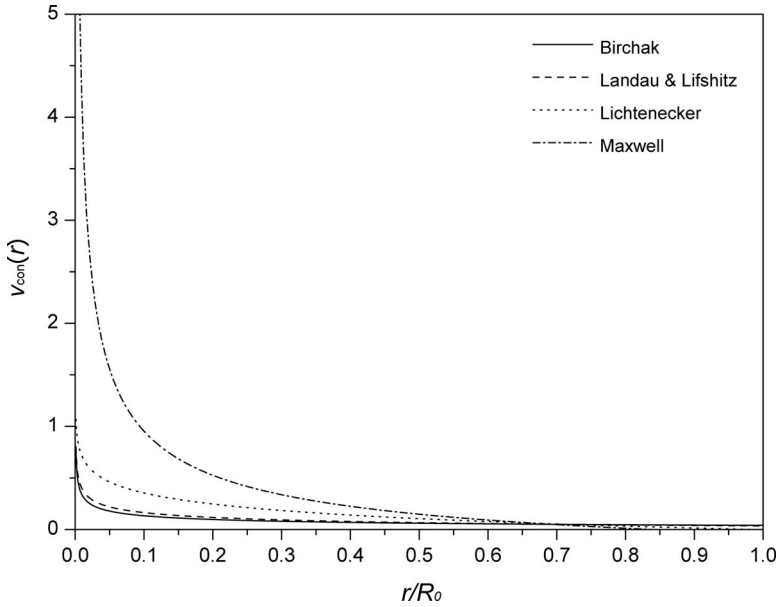

Fig. 2 Distribution of constructal particle volume fraction for System 2 at ϕ=0.05 and k_p/k_f=385/0.6 (thermal conductivity ratio of copper and water)

fluids used in the system. Efforts in upgrading thermal conductivity of nanofluids also do lead to reduction in constructal overall thermal resistance.

However, the constructal particle volume fraction v_{con} (the way by which to realize the constructal thermal resistance) is either a global property invariant with the types and the details of nanofluids for Systems 1 and 3, or a property depending on the types and the details of nanofluids for Systems 2 and 4 (Table 3, Figs. 2 and 3). The march toward synthesizing uniformly dispersed nanofluids [1–6] not necessarily leads to the constructal nanofluids that maximize system overall performance. For example, the constructal nanofluids used in Systems 2 and 4 are with a decreasing particle volume fraction from $r=0$ or $r=R_i$ where the heat flux is high to $r=R_o$ where the heat flux is lower (Figs. 2 and 3); they depend not only on system global geometry (R_i/R_0) and nanofluid global property (ϕ) but also on the types and the details (k_p/k_f) of nanofluids. Therefore, nanofluids research and development should focus on not only nanofluids but also systems that use them.

A uniform distribution of particle volume fraction distribution as the constructal volume fraction is expected for System 3 because the heat flux is uniform everywhere in the system. It comes as a surprise, however, for System 1 in which the heat flux decreases from the center to the periphery. This could represent some kind of new phenomena that demand further study in the future.

4 Concluding Remarks

The constructal overall thermal resistance $R_{th,con}$ is inversely proportional to the effective thermal conductivity evaluated at the global (average) particle volume fraction ϕ for all four systems.

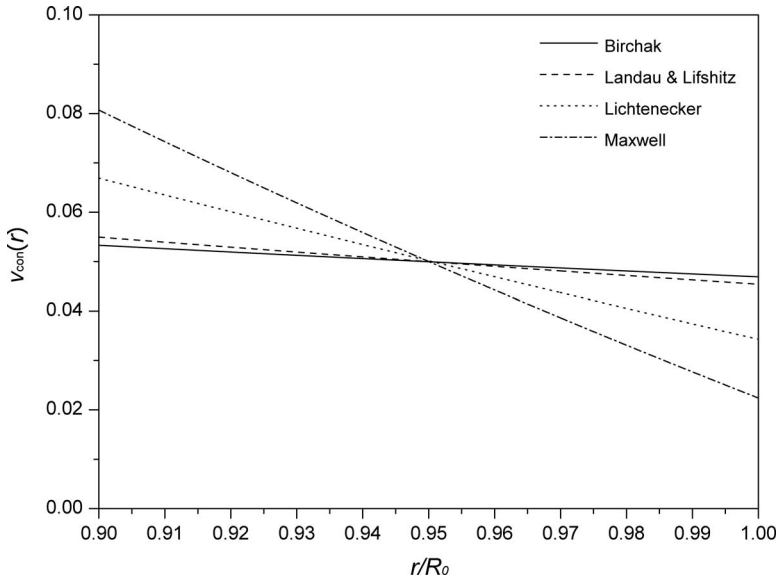

Fig. 3 Distribution of constructal particle volume fraction for System 4 at R_i/R_o=0.9, ϕ=0.05, and k_p/k_f=385/0.6 (thermal conductivity ratio of copper and water)

The proportional coefficients are invariant or nearly invariant with respect to types of nanofluids. The constructal particle volume fraction of nanofluids to materialize this $R_{th,con}$ is a uniform distribution for Systems 1 and 3 (circular disk and plane slab), and a nonuniform distribution with a higher particle volume fraction in the higher heat-flux region for Systems 2 and 4 (sphere and circular annulus).

Therefore, the constructal overall thermal resistance can be reduced through enhancing the thermal conductivity of nanofluids. The constructal nanofluids that maximize the system performance are not necessarily the ones with uniformly dispersed particles in base fluids. Our focus of nanofluids research and development should thus be not only on nanofluids themselves but also on their systems and ultimate goals. The march toward micro- and nanoscales must also be with the sobering reminder that useful devices are always macroscopic, and that larger and larger numbers of small-scale components must be assembled and connected by flows that keep them alive.

Acknowledgment

The financial support from the Research Grants Council of Hong Kong (Grant No. GRF717508) to L.W. is gratefully acknowledged

Nomenclature

F = integrand
J = functional
k = thermal conductivity (W/m K)
n = nanofluid type index
t = heat-source-term index
q = heat flux (W/m^2)
q''' = volumetric heat generation rate (W/m^3)
r = the coordinate (m)
R = radius (m)
R_{th} = thermal resistance (K/W)
s = heat-conduction system index
T = temperature (K)
v = particle volume fraction

Greek Symbols

λ = Lagrangian constant
ϕ = average particle volume fraction

Subscripts

0 = lower temperature
e = effective
f = base fluid
i = inner
m = maximal
o = outer
p = particle
con = constructal

References

[1] Choi, S. U. S., Zhang, Z. G., and Keblinski, P., 2004, "Nanofluids," *Encyclopedia of Nanoscience and Nanotechnology*, Vol. 6, H. S. Nalwa, ed., American Scientific, New York, pp. 757–773.
[2] Peterson, G. P., and Li, C. H., 2006, "Heat and Mass Transfer in Fluids With Nanoparticle Suspensions," Adv. Heat Transfer, **39**, pp. 257–376.
[3] Das, S. K., Choi, S. U. S., Yu, W. H., and Pradeep, T., 2008, *Nanofluids: Science and Technology*, Wiley, Hoboken, NJ.
[4] Wu, D. X., Zhu, H. T., Wang, L. Q., and Liu, L. M., 2009, "Critical Issues in Nanofluids Preparation, Characterization and Thermal Conductivity," Curr. Nanosci., **5**, pp. 103–112.
[5] Choi, S. U. S., 2009, "Nanofluids: From Vision to Reality Through Research," ASME J. Heat Transfer, **131**, p. 033106.
[6] Wang, L. Q., and Wei, X. H., 2009, "Nanofluids: Synthesis, Heat Conduction, and Extension," ASME J. Heat Transfer, **131**, p. 033102.
[7] Li, C. H., Williams, W., Buongiorno, J., Hu, L. W., and Peterson, G. P., 2008, "Transient and Steady-State Experimental Comparison Study of Effective Thermal Conductivity of Al_2O_3/Water Nanofluids," ASME J. Heat Transfer, **130**, p. 040301.
[8] Jang, S. P., and Choi, S. U. S., 2007, "Effects of Various Parameters on Nanofluid Thermal Conductivity," ASME J. Heat Transfer, **129**, pp. 617–623.
[9] Vadasz, P., 2006, "Heat Conduction in Nanofluid Suspensions," ASME J. Heat Transfer, **128**, pp. 465–477.
[10] Lee, S., Choi, S. U. S., Li, S., and Eastman, J. A., 1999, "Measuring Thermal Conductivity of Fluids Containing Oxide Nanoparticles," ASME J. Heat Transfer, **121**, pp. 280–289.
[11] Wei, X. H., Zhu, H. T., and Wang, L. Q., 2009, "$CePO_4$ Nanofluids: Synthesis and Thermal Conductivity," J. Thermophys. Heat Transfer, **23**, pp. 219–222.
[12] Das, S. K., Putra, N., Thiesen, P., and Roetzel, W., 2003, "Temperature Dependence of Thermal Conductivity Enhancement for Nanofluids," ASME J. Heat Transfer, **125**, pp. 567–574.
[13] Tzou, D. Y., 2008, "Instability of Nanofluids in Natural Convection," ASME J. Heat Transfer, **130**, p. 072401.
[14] Tzou, D. Y., 2008, "Thermal Instability of Nanofluids in Natural Convection," Int. J. Heat Mass Transfer, **51**, pp. 2967–2979.
[15] Buongiorno, J., 2006, "Convection Transport in Nanofluids," ASME J. Heat Transfer, **128**, pp. 240–250.
[16] Xuan, Y. M., and Li, Q., 2003, "Investigation on Convective Heat Transfer and Flow Features of Nanofluids," ASME J. Heat Transfer, **125**, pp. 151–155.
[17] Milanova, D., and Kumar, R., 2008, "Heat Transfer Behavior of Silica Nanoparticles Experiment in Pool Boiling," ASME J. Heat Transfer, **130**, p. 042401.
[18] Kim, S. J., McKrell, T., Buongiorno, J., and Hu, L. W., 2008, "Alumina Nanoparticles Enhance the Flow Boiling Critical Heat Flux of Water at Low Pressure," ASME J. Heat Transfer, **130**, p. 044501.
[19] Kim, S. J., McKrell, T., Buongiorno, J., and Hu, L. W., 2009, "Experimental Study of Flow Critical Heat Flux in Alumina-Water, Zinc-Oxide-Water, and Diamond-Water Nanofluids," ASME J. Heat Transfer, **131**, p. 043204.
[20] Kedzierski, M. A., 2009, "Effect of CuO Nanoparticle Concentration on R134a/Lubricant Pool-Boiling Heat Transfer," ASME J. Heat Transfer, **131**, p. 043205.
[21] Bejan, A., and Lorente, S., 2008, *Design With Constructal Theory*, Wiley, Hoboken, NJ.
[22] Reis, A. H., 2006, "Constructal Theory: From Engineering to Physics, and How Flow Systems Develop Shape and Structure," Appl. Mech. Rev., **59**, pp. 269–282.
[23] Bejan, A., and Lorente, S., 2006, "Constructal Theory of Configuration Generation in Nature and Engineering," J. Appl. Phys., **100**, p. 041301.
[24] Wang, L. Q., 1996, "An Approach for Thermodynamic Reasoning," Int. J. Mod. Phys. B, **10**, pp. 2531–2551.

Heat Transfer of Coupled Fluid Flow Within a Channel With a Permeable Base

Rosemarie Mohais[1]
School of Mathematics and Statistics,
University of South Australia,
Mawson Lakes Campus,
5095 South Australia, Australia
e-mail: rosemarie.mohais@unisa.edu.au,
rmohais@gmail.com

Balswaroop Bhatt
Department of Mathematics and Computer Science,
University of the West Indies,
St. Augustine,
Trinidad and Tobago
e-mail: bal.bhatt@sta.uwi.edu,
balswaroopbhatt@hotmail.com

We examine the heat transfer in a Newtonian fluid confined within a channel with a lower permeable wall. The upper wall of the channel is impermeable and driven by an accelerating surface velocity. Through a similarity solution, the Navier–Stokes equations are reduced to a fourth-order differential equation; the analytical solutions of which determined for small Reynolds numbers show dependence of the temperature and heat transfer profiles on the slip parameter based on the properties of the porous channel base. For larger Reynolds numbers, numerical solutions for three main groups of solutions show that the Reynolds number strongly influences the heat transfer profile. However, the slip conditions associated with the porous base of the channel can be used to alter these heat transfer profiles for large Reynolds numbers. The presence of a porous base in a channel can thus serve as an effective means of reducing or enhancing heat transfer performance in model systems. [DOI: 10.1115/1.3154626]

1 Introduction

Flow within a channel with porous walls has been investigated for many years since many natural and industrial processes form the basis of this problem. With applications that range from ground water flow [1], natural transpiration, and the respiratory system to binary gas diffusion, filtration and surface sublimation [2], nuclear waste disposal [3], and oil recovery, many variations in the problem developed. One interesting property of the flow of a fluid within an infinite channel is that it yields an exact solution to the Navier–Stokes equation.

Many authors have examined heat transfer and fluid flow within channels, which may or may not be permeable. Berman [4] was probably the first to study the laminar flow in a channel with a porous wall. He investigated the dependence of key velocity and pressure components in position coordinates, the dimensions of the channel, and the properties of the fluid. Beavers and Joseph [5] later designed experiments, which focused on the boundary condition at the fluid-porous interface. These studies marked the emergence of the famous Beavers–Joseph boundary condition, which states that the velocity gradient at the fluid side is proportional to the slip velocity at the interface [5].

Verma and Bansal [6] later investigated flow and heat transfer profiles in two main geometries. They examined the heat transfer of fluid squeezed between two parallel plates; the lower plate set stationary while the upper plate moves with a constant velocity U. There is a uniform suction at the stationary plate, and both plates are maintained at the same temperature. They also examined laminar flow through a porous pipe of uniform cross section with the pipe walls maintained at constant temperatures. Other researches followed, and an insightful overview by Kuznetsov [7] gives a time-line study of significant contributions to the study of forced convection in a porous media, part of which is occupied by a clear fluid and part by a fluid saturated porous media.

Brady and Acrivos [8] determined the exact solution to the Navier–Stokes equation for the flow inside an infinitely long 2D channel and an axisymmetric tube where the surface velocity of the channel or tube grows linearly with the streamwise coordinate. Using the prescribed form of the flow field, the equations of motion were reduced to an ordinary differential equation for a similarity function. The principal characteristic of the solution is that the presence of reverse flow where the streamwise velocity changes sign in the transverse direction. Some other exact solutions containing regions of reverse flow are the outflow in a diverging channel and the flow between infinite rotating disks. Although Brady and Acrivos [8] discussed that the study was applicable in cases involving porous media, they neglected to elaborate further, probably because their study was predominantly motivated by the flow inside a long slender drop placed in an extensional field, rather than the flow in porous media.

The problem described by Brady and Acrivos [8] is quite useful since flow and heat transfer in a stretching surface have many significant industrial and engineering applications, for instance, cases where heat treated material is manufactured in an extrusion process [9]. Crane [10] was perhaps the first to examine the semi-infinite flow driven by a stretching surface. His work described the process of polymer extrusion from a narrow slit. Wang [11,12] followed up on this work, focusing on the partial velocity slip that occurs on a stretching boundary in the case of particulate fluids such as foams and emulsions.

A heat transfer boundary condition at the fluid-porous interface to account for nonequilibrium between the fluid and solid phases initially suggested by Ochoa-Tapia and Whitakers [13] was extensively used in early work by Kuznetsov [14,15]. Kuznetsov was later concerned with the steady flow in a composite channel bound by two infinite plates. The lower part of the channel is filled with clear fluid while the upper part of the channel comprises a fully saturated porous medium with uniform permeability. While the upper plate and the porous medium remain fixed, the lower plate moves with a constant velocity. The authors used the Brinkman–Forchheimer extended Darcy equation to investigate the flow in the channel and found that for small Darcy number, there is almost no fluid flow in the porous region and the heat transfer is by thermal conductivity only. Also, a decrease in Darcy number leads to a decrease in permeability and to an increased velocity [16]. Extension of the work by Kuznetsov suggested that the majority of practical applications of porous media involved a small Darcy number, implying a small thickness of the momentum boundary layer, much smaller, in fact, than the thickness of the boundary layer itself [7]. He described the four geometrical configurations of parallel plate channels partly filled with porous media. One of the configurations is similar to the one studied in this paper, where

[1]Corresponding author.

Contributed by the Heat Transfer Division of ASME for publication in the JOURNAL OF HEAT TRANSFER. Manuscript received November 2, 2008; final manuscript received April 23, 2009; published online August 19, 2009. Review conducted by Jamal Seyed-Yagoobi.

a lower permeable wall is overlaid by a clear fluid. However, unlike the problem in this paper, the top plate was stationary. Kuznetsov subjected the plates in various configurations and heat fluxes and determined the analytical solutions for the different configurations.

The study was further developed by Xiong and Kuznetsov [17] to include application of uniform heat fluxes to both plates. In a similar manner, they set up a system of four equations, two momentum equations and two energy equations, for the two sections of porous medium and clear fluid. For the boundary conditions, they made use of the dimensionless adjustable coefficient suggested by Ochoa-Tapia and Whitakers [13] describing the jump in the clear fluid at the interface of the porous medium and the clear fluid. Nield and Kuznetsov [18] studied an external convection problem by means of a composite system, which attached a relatively thin porous substrate to the surface of a flat plate in an attempt to build on Vafai and Kim's [19] work. They used the Beavers–Joseph boundary condition, which is used later in this present paper, and found that like Xiong and Kuznetsov [17], the main effects of the porous medium were to introduce slip at the boundary and also to change the value of the thermal conductivity in the domain occupied by the porous medium. The study of forced convection over a wedge with a thin layer of porous material was also explored later on by Kuznetsov and Nield [20], where the wedge angle can be changed. Here, a wedge angle corresponding to zero implies a plane surface and so some of the results obtained can be validated using the previous studies. In all of the above studies, a common thread that existed was the dependence of the heat transfer profile on the Prandtl number and later on in this paper, the relationship is further investigated.

Zhao and Song [3] studied forced convection in a saturated porous medium subject to heating, provided there is a permeable wall placed perpendicular to the flow direction. Analytical solutions show that the heat transfer rate from the permeable wall to the fluid is described by the equality of the Nusselt and Peclet numbers. This is in contrast to the case of boundary layer flow over a flat plate in a porous medium where the Nusselt number is instead equal to the square root of the Peclet number. The results were supported by experimental results using a porous structure consisting of glass beads heated by a finned surface. Zhao and Song [3] suggested that the linear relationship between the Nusselt and Peclet number implies that heat is transferred when the fluid flow is opposite to the direction of the heat flow. They compared their result to those described by Nield and Bejan [21], who showed that in the case of boundary layer flow over a flat plate embedded in a porous medium, where the plate is heated by a constant flux, the relationship of $\mathrm{Nu}=1.329\mathrm{Pe}^{1/2}$ arises.

Zhao and Song [3] described the system they studied as a possible heat exchanger, which may be applied in such technologies as the cooling units of electronic devices, high powered lasers, and X-ray medical devices. The larger surface areas available in porous bodies allow for enhanced heat transfer due to extended surfaces and also the mixing of fluids can be facilitated due to the presence of the porous particles [3]. In later work, motivated by the direct feed methanol fuel cell, a gas-liquid two phase flow in a channel with a fitted permeable sidewall was studied. Liquid was fed into the channel from its entrance and a gas was injected uniformly into the test channel along the sidewall [22].

Zhou and Majdalani [23,24] also determined theoretical solutions for large and moderate injection and suction in a porous channel with expanding or contracting walls. Using similarity transformations, they arrived at symmetric solutions for the flow profiles using linearly varying axial velocity and a uniform wall expansion ratio. These authors found that the velocity profiles were sinusoidal for injection and linear for suction when there is constant wall expansion. Wall contraction tended to increase the Reynolds number and the asymptotic solutions deteriorated when the expansion and contraction values were of the same order as the Reynolds number. A more gradual flow tended to exist when the channel had expanding walls.

This current problem was initially conceived through theoretical considerations of liquid geothermal systems. A geothermal system can be thought of as an area above normal temperature where heat flow involving circulation of hot fluids occurs through natural convection [1]. These systems have been and still continue to be a popular source of alternative energy. Authors like Afzalimehr and Anctil [25] conducted experiments on nonuniform open-channel shear accelerated flow in gravel bed channels, which are naturally permeable surfaces. They determined the existence of a boundary layer when a favorable pressure gradient existed. They neglected to study the heat transfer aspects; however, we realize that conductive and convective heat flow studies are also critical since these mechanisms are the major contributors of most of the heat discharge in geothermal areas. In many volcanic islands in the West Indies such as Nevis and St. Lucia, there are numerous untapped sources of geothermal energy. Those sources, which are constantly being investigated for commercial viability, need to be optimally used. Through the use of a mathematical model involving channel geometry, the processes involved in the system subject to initial and boundary conditions can be described and solved by means of differential equations. We assume that the geothermal sites can be modeled as having an upper wall velocity due to ground deformation by the underlying active volcano and we assume that water moves up over a horizontal fault plane. Mathematical modeling affords a cheap economic alternative to high cost drilling procedures [1]. The solution will aid in the description of the basic phenomenon associated with geothermal sources. There are two main applications: first to investigate geothermal systems, which have not been disturbed by man to evaluate the system before exploitation, and second, to aid in the assessment of available renewable energy and the possible rates of extractions once the systems have been disturbed. The model can be validated through the measurements of cation concentrations in hot spring water, which can provide estimates of temperatures at various depths. The surface acceleration can be determined by geodetic measurements using global positioning system (GPS) measurements.

2 Formulation of the Problem

We examine the flow of a Newtonian fluid of density ρ and viscosity μ within a 2D infinite channel. The upper wall of the channel is impermeable and driven by a surface velocity Ex proportional to the streamwise coordinate. The lower wall comprises a naturally porous surface of permeability K. A naturally porous surface suggests an irregular arrangement of voids and/or particles within the surface (see Fig. 1).

Each channel wall is maintained at distinct isothermal temperatures T_0 and T_1, the former being the temperature at $y=0$ and the latter at $y=a$, the width of the channel. In the geometry, no symmetry exists within the channel along its width because of the existence of the porous base layer.

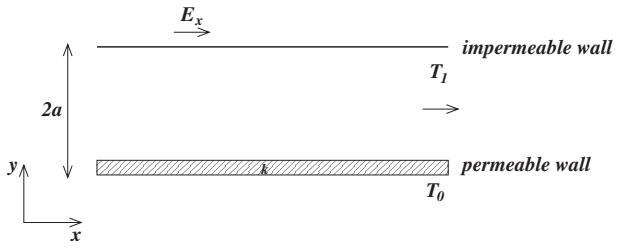

Fig. 1 Channel with a fixed lower porous wall with an upper wall driven by a surface velocity

In the case of an extensional field, for either stretching or compressing flow, the state of stress of the fluid can be fully described by the diagonal tensor $T=ae_1e_1+ae_2e_2-2ae_3e_3$. Here the set $B=e_1,e_2,e_3$ is the basis of three-dimensional space and each vector of this space can be written as a linear combination of $\mathbf{e_1}$, $\mathbf{e_2}$, and $\mathbf{e_3}$. In this problem, the extensional field in 2D is given in terms of $u=Ex$, where u is the velocity in the x-direction.

The flow is considered antisymmetric about the origin $x=0$ so we need to seek a solution only in the semi-infinite domain for the solution $x\geq 0$. The effect of permeability appears through the slip boundary conditions at $y=0$. Using the slip parameter σ, we write $\partial u/\partial y=\sigma u/\sqrt{K}$, $K\neq 0$. We also define the parameter $\lambda=\sigma a/\sqrt{K}$.

We use a similarity parameter f like that of Brady and Acrivos [8] to determine an analytical solution. First, nondimensionalize the variables $y^*=y/a$, $x^*=x/a$, $u^*=u/Ea$, and $v^*=v/Ea$.

Also let $u=xf'(y)$ and $v=-f(y)$. This satisfies the mass continuity equation in two dimensions

$$\frac{\partial u}{\partial x}+\frac{\partial v}{\partial y}=0$$

For the steady state case $\partial u/\partial t=0$ and $\partial v/\partial t=0$, which allows us to write the Navier–Stokes equations as

$$\rho\left(u\frac{\partial u}{\partial x}+v\frac{\partial u}{\partial y}\right)=-\frac{\partial p}{\partial x}+\mu\left(\frac{\partial^2 u}{\partial x^2}+\frac{\partial^2 u}{\partial y^2}\right) \tag{1}$$

$$\rho\left(u\frac{\partial v}{\partial x}+v\frac{\partial v}{\partial y}\right)=-\frac{\partial p}{\partial y}+\mu\left(\frac{\partial^2 v}{\partial x^2}+\frac{\partial^2 v}{\partial y^2}\right) \tag{2}$$

Upon substitution of the transformed variables and the velocity, we arrive at an equation, which incorporates the shear Reynolds number $\mathrm{Re}=\rho Ea^2/\mu$, and a reduced equation (3) with dependence on the pressure and Re is

$$f'''-\frac{\partial p}{\partial x}=\mathrm{Re}((f')^2-ff'') \tag{3}$$

Further examination of Eq. (2) shows that

$$\rho E^2a^2ff'-\eta Ef''=\frac{\partial p}{\partial y} \tag{4}$$

which means that since the left hand side is a function of y only, then $\partial^2 p/\partial y\,\partial x=0$.

We apply this result to Eq. (1) and determine that the equation is satisfied for $\partial p/\partial x=\beta$, where β is a constant of integration. This was first identified by Berman [4]. Later in the work done by Brady and Acrivos [8], they determined that the pressure equation, which can be used to satisfy the problem, can be written as $p=p_0(y)+\frac{1}{2}\beta x^2$, where β is a constant and a slip grouping parameter, and p_0 is a function of y only. We make use of this slip grouping parameter β in our solution below. Later, Ferro and Gnavi [26] defined their pressure term in two dimensions to be $p(x,y)=\pi(y)+(Ax^2/2)$, where their main momentum equation is defined in terms of the channel width only through the transversal Reynolds number.

Barrat and Bocquet [27] determined that for Poiseuille flow, the existence of slip increases the flow rate by a factor of $1+(8\delta/h)$, where h is the pore diameter and δ is the slip length. When extrapolated toward the wall, the parallel velocity component then matches the velocity at the wall at some distance equivalent to the slip length.

Consider now the steady state energy equation, which in rectangular 2D coordinates is written as

$$\rho c\left(u\frac{\partial T}{\partial x}+v\frac{\partial T}{\partial y}\right)=\kappa\left(\frac{\partial^2 T}{\partial x^2}+\frac{\partial^2 T}{\partial y^2}\right) \tag{5}$$

Here we have assumed negligible viscous dissipation and so omitted the viscous terms of the energy equation. κ as used above is the thermal conductivity and c is the heat capacity. Now we use $T^*=(T-T_0)/(T_1-T_0)=xg(y)=a^2x^*g(y^*)$ and making the relevant substitutions and rearrangements to the energy equation we arrive at

$$f'g-fg'=\frac{g''}{\mathrm{Re\,Pr}} \tag{6}$$

where $\mathrm{Pr}=c\mu/\kappa$ defines the Prandtl number.

We have assumed that the lower wall has a small permeability so flow within the porous region can be ignored up to the first order in permeabilities thus the effect of permeability enters only through the slip boundary conditions:

(1) at $y^*=y/a=0$, $\partial u/\partial y=\sigma u/\sqrt{K}$, $v=0$, and $T=T_0$
(2) at $y^*=y/a=1$, $u=Ex$, $v=0$, and $T=T_1$

From these relations, the following boundary conditions emerge: $f'(1)=Ea$, $f(1)=0$, $g(1)=1/(a^2x^*)$, on $y^*=1$. Here a^2x^* is not zero.

3 Analysis and Modeling

We seek to obtain a perturbation solution for small parameter values: $f=f_0+\mathrm{Re}\,f_1+O(\mathrm{Re})^2$ and $g=g_0+\mathrm{Re}\,g_1+O(\mathrm{Re})^2$.

Here, we model our solution after the studies of Hamza and Bhatt [28–31] up to the first order in Reynolds number. The following conditions must be satisfied: $f_0'''=\beta$, $f_1'''-(f_0')^2+f_0f_0'''=0$, $g_0''=0$, and $\mathrm{Pr}(f_0'g_0-f_0g_0')=g_1''$.

Upon solving, the following solutions arise:

$$f_0=\frac{\beta y^3}{6}+y^2(c_1)\left(\frac{\lambda}{\lambda+1}\right)+yc_1\left(\frac{1}{1+\lambda}\right)$$

$$f_1=-\left(\frac{\beta^2}{2520}y^7+\frac{\beta\lambda c_1c_2}{180}y^6+\frac{c_2^2c_1\lambda^2}{30}y^5+\frac{c_2^2c_1^2}{8}\lambda y^4+\frac{c_2^2c_1^2}{6}y^3+c_3y^2+c_4y\right)$$

$$g_0=\frac{y}{a^2x^*}$$

$$g_1=\frac{\mathrm{Pr}}{a^2x^*}\left(\frac{\beta y^5}{60}+\frac{y^4}{12}c_1c_2\lambda+\frac{y}{\mathrm{Pr}}\left(-\frac{\beta}{60}-\frac{\lambda}{12}c_1c_2\right)\right)$$

where

$$c_1=Ea-\frac{\beta}{2}$$

$$c_2=\frac{1}{1+\lambda}$$

$$c_3=\frac{-\beta^2}{840}+\frac{1}{1+\lambda}c_1\left(\frac{c_1}{1+\lambda}\left(\frac{-2\lambda^2}{15}-\frac{3\lambda}{8}-\frac{1}{3}\right)-\frac{\beta\lambda}{36}\right)$$

$$c_4=-\frac{\beta^2}{240}-\frac{\beta}{180}\frac{\lambda}{\lambda+1}c_1-\frac{\lambda^2}{30(1+\lambda^2)}c_1^2-\frac{1}{8}\frac{\lambda}{(1+\lambda)^2}c_1^2-c_1^2\frac{1}{6(1+\lambda)^2}-c_3$$

4 Numerical Solution

The numerical solution proceeds via a simple stretching transformation in accordance with Ref. [8], where Eq. (3) is converted into an initial value problem. Let $f=\mathrm{Re}^{\gamma-1}\,\phi(\zeta)$, where $\zeta=\mathrm{Re}^{\gamma}y$. Evaluating the first three derivatives of the function f, substituting into Eq. (3), and simplifying yield

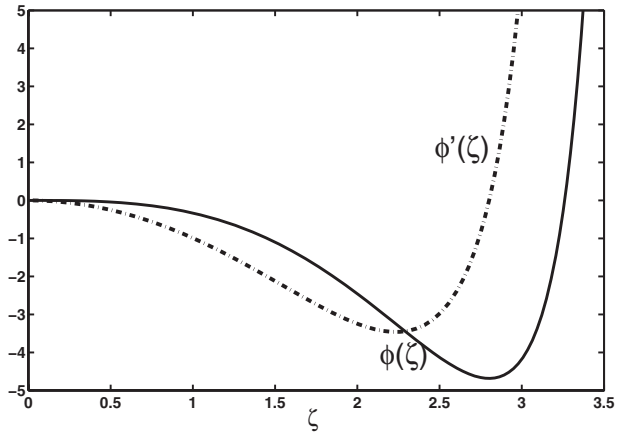

Fig. 2 Plot of ζ versus $\phi(\zeta)$ and $\phi'(\zeta)$

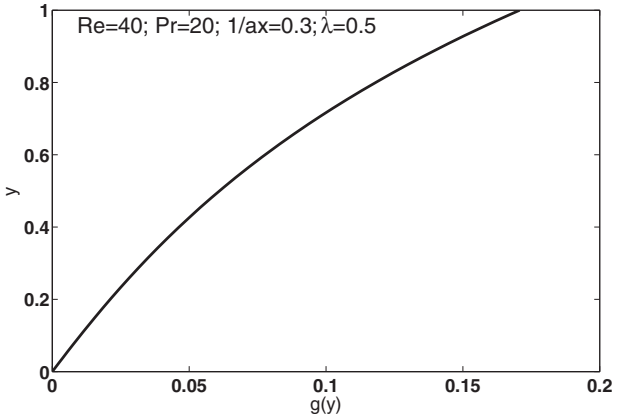

Fig. 4 The temperature profile for Re=40

$$\phi''' - \beta^* = (\phi')^2 - \phi'\phi'' \tag{7}$$

where $\beta^* = \beta/\mathrm{Re}^{4\gamma-1}$. Our new boundary conditions are

$$\phi(0) = 0, \quad \phi(R^\gamma) = 0, \quad \phi'(R^\gamma) = EaR^{1-2\gamma}, \quad \phi''(0) = \lambda R^{-\gamma}\phi'(0)$$

We now have an initial problem with ϕ to be solved with β^* as a parameter. We set $\phi'(0)=0$ as one possibility for fluid velocity along the centerline. Naturally, two other possibilities exist, $\phi'(0)=1$ and $\phi'(0)=-1$, as noted by Brady and Acrivos [8], which flow in opposing directions. We can vary β^* over all possible values and in the first instance we choose a value corresponding to −2. We proceed to integrate Eq. (7) as an initial value problem until a zero of ϕ is encountered at some value of ζ. This value, say, ζ_0, together with the corresponding value of the first derivative of ϕ' evaluated at ζ_0 are used to determine Re and the value of γ. A sample solution is shown in Fig. 2 for a Reynolds number of 40.

We can now evaluate the longitudinal velocity profiles of flow within the channel. These solutions are similar in form to those presented by Brady and Acrivos [8] and the solutions to various Reynolds number designated by these authors as the Group 1 series are presented in Fig. 3. In Brady and Acrivos' solutions, there is evolution from $R=0$ creeping flow profile into a flow having a familiar boundary layer structure. There exists an inviscid core of strength $O(\mathrm{Re}^{-(\frac{1}{2})})$ along with a thin boundary layer of $O(\mathrm{Re}^{-(\frac{1}{2})})$ next to the moving surface. The variation in the longitudinal velocity profiles about the $f'=0$ point is notably different because of the present permeable base layer.

We now proceed to find the numerical solution for the temperature profile and heat transfer profile within the channel. Since we have already evaluated f, we now have a two point boundary value problem to be solved in an effort to determine the g and g' functions within the channel, which represent the temperature and heat transfer profiles, respectively. Using a collocation method, the coupled equations were next expressed as a system of first order differential equations and a residual function, which returns zero at the boundary values, was also defined along with initial guesses. These guesses can be chosen based on the analytical solutions previously derived.

The temperature and heat transfer profiles for a Reynolds number of 40 are shown in Figs. 4 and 5. $g(y)$ is representative of the temperature profile while $g'(y)$ is representative of the heat transfer parameter, the Nusselt number. The profiles were examined for $1/ax=0.3$, and a Prandtl number of 20.

5 Results and Discussion

We built our problem based on an earlier problem developed by Brady and Acrivos [8]. These authors considered the flow profiles within an infinite channel, the surface velocity of which grows linearly with the streamwise coordinate. They found that for Rey-

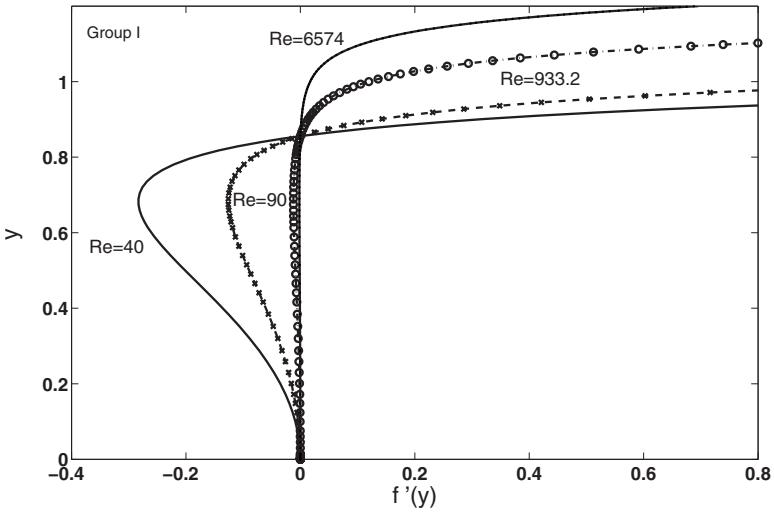

Fig. 3 Longitudinal velocity profiles at Re=40, 90, 933.2, and 6574

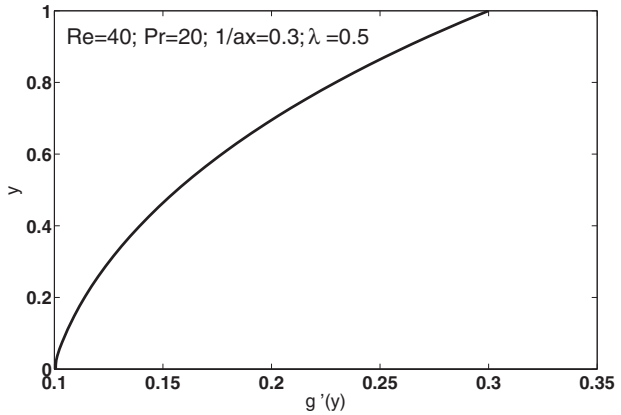

Fig. 5 The heat transfer profile for Re=40

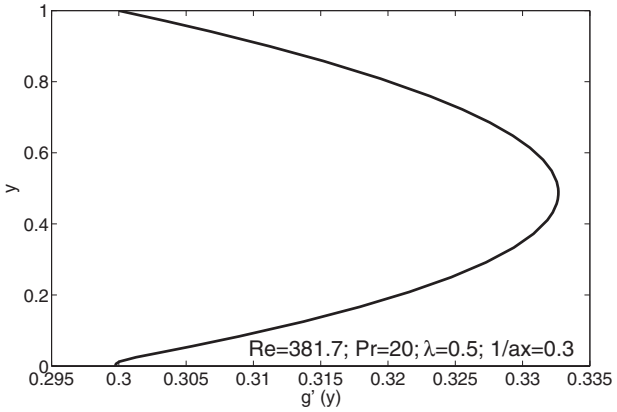

Fig. 7 The heat transfer profile for Re=381.7

nolds numbers less than 310, there existed a single solution to the problem. However, for Reynolds numbers greater than this value, two additional solutions existed, which connected two different asymptotic states for infinite Reynolds number values. This current problem introduces a lower permeable wall and the additional constraint of the upper and lower channel walls being at fixed isothermal temperatures.

The Prandtl number used is significant in problems like these where there a system undergoes simultaneous energy and momentum transfer. We have chosen to examine water Pr=7, air Pr =0.71, an arbitrary fluid of Pr=20, and a highly viscous fluid such as oil with a Prandtl number of 100. Of interest to us is whether the temperature and heat transfer profiles are affected by different values of Reynolds numbers. In order to evaluate this hypothesis, profiles were investigated for other Reynolds numbers of 90, 381.7, and 6574; these are chosen based on the group solutions from Brady and Acrivos [8]. These profiles are shown in Figs. 6–8.

Quite obviously, the heat transfer profiles are different, with an almost linear heat transfer profile between the upper and lower channel walls for small Reynolds numbers such as 40 and 90 the profiles of which appear to be quite similar. We can imagine the fluid as being subdivided into infinitesimally thin layers parallel to the plates. Fluid is dragged by the top plate with the accelerating surface velocity, while the fluid closer to the bottom plate resists the motion. The internal friction in the fluid causes a forward drag in the layer immediately below each fluid layer. The temperature at the upper wall is higher than that of the lower wall and there is no major transfer of heat to the lower permeable wall. As the Reynolds number increases to a value of 381.7, the heat transfer profile appears as a skewed parabola with maximum heat transfer occurring at the midpoint of the channel. At this Reynolds number, the inertial forces are much greater than the viscous forces and the accelerating surface at the top of the channel carries away the top heated fluid layer faster thereby leaving a relatively cold layer of fluid at the top. At the midpoint of the channel, there is heated fluid relative to the fluid at the top of the channel. At the lower part of the channel, the heated fluid is retarded by the slip layer. The higher Reynolds number enables more heat to be transferred to the body of fluid contained within the channel. However, even at this stage there is little heat transfer to the lower channel wall. With an increase in Reynolds number to 6574, there is a maximum heat transfer to the lower wall with the inertial forces overcoming the viscous forces. The effect of permeability is the most pronounced at this Reynolds number. The fluid layers at the top and middle move fast leaving behind cooler fluid. The fluid in the lower region of the channel sticks relative to the lower plate and has a higher relative heat capacity.

Since the above heat transfer variations with Reynolds number were, in fact, evaluated at $1/ax=0.3$, it is of significance that we evaluate these profiles again to ensure that what we have observed are not, in fact, artifacts of the system as a result of these constraints. We do so through the evaluation of the heat transfer profile for a Reynolds number of 40, with an altered value of $1/ax=1$ as opposed to $1/ax=0.3$; all other parameters held constant as in Fig. 5. Comparison of Figs. 5 and 9 shows that the transfer of heat obeys the same profile although the values of the g' parameters are different as can be expected. Similar plots using the other Reynolds numbers provide a similar analysis.

For a Prandtl number of 7, which corresponds to water, the heat transfer profiles are examined for a value of $\lambda=10$ and for Reynolds numbers less than 10. There is a change in the Nusselt

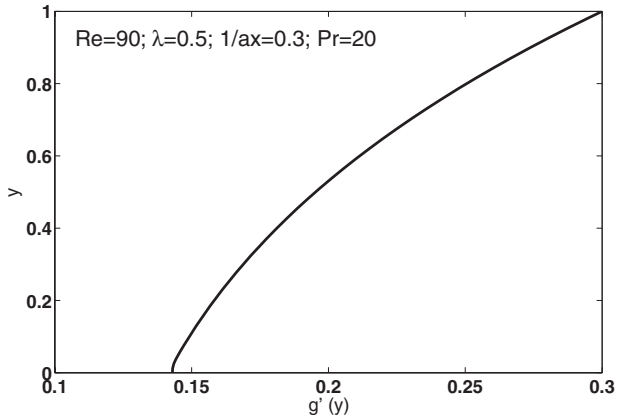

Fig. 6 The heat transfer profile for Re=90

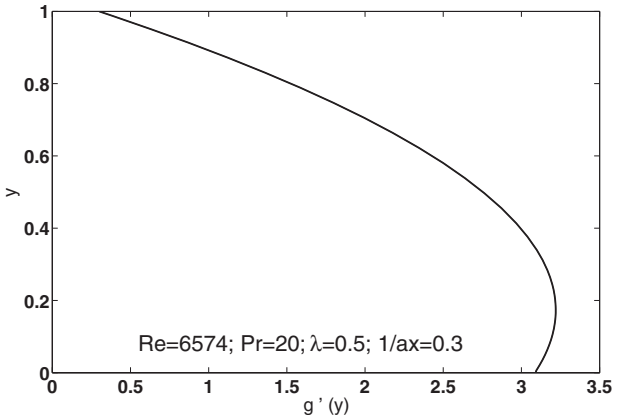

Fig. 8 The heat transfer profile for Re=6574

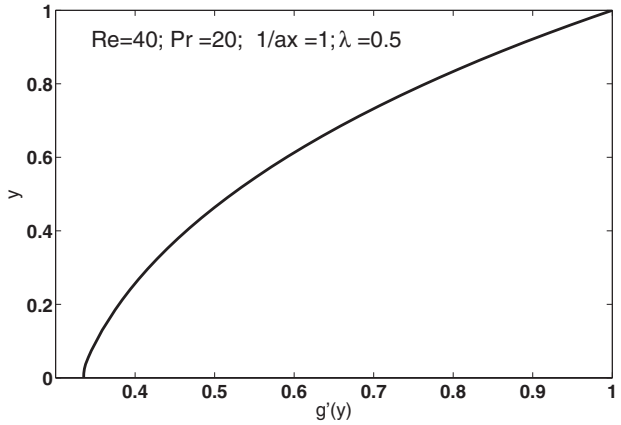

Fig. 9 The heat transfer profile for Re=40 with 1/*ax*=1

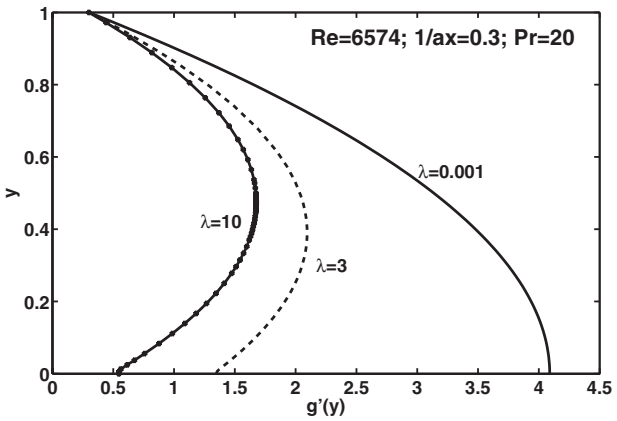

Fig. 11 The heat transfer profile for Re=6574 for values of λ =0.001, 3, and 10

number with small Reynolds number, viz., as the Reynolds number slowly increases, more heat is transferred to the fluid within the channel Fig. 10.

Our prime interest, however, is the evaluation of the heat transfer profiles for various permeabilities. Using a Reynolds number of 6574, we evaluate the changes in the temperature and heat transfer profiles for values of $\lambda = 0$, 0.5, 3, and 10. We first consider a value of $\lambda = 0.001$, in other words a channel, the lower wall of which has an almost infinite permeability (since $\lambda = \sigma a / \sqrt{K}$).

This follows from Fig. 8 where maximum heat transfer occurs at the lower wall. The heat transfer profiles for values of $\lambda = 3$ and 10 are presented in Fig. 11. A reduction in heat transfer is obtained at the lower wall with an increasing value of $\lambda = 3$ with a simultaneous increase in heat transfer at the upper wall. At a value of $\lambda = 10$, there is an almost equal balance of heat at the upper and lower walls, with the maximum heat transfer occurring midway up the channel. This behavior can be thought of in two ways depending on the application in question: either a highly permeable layer can be used as an effective heat transfer agent for high Reynolds number flow or a decrease in permeability facilitates heat transfer throughout the channel, compensating for the high Reynolds number of the fluid used.

Upon examination of the permeable wall for $\lambda = 3$ and $\lambda = 10$, there is evidence of a thin thermal boundary layer close to the wall (see Fig. 12). This does not exist with the almost infinitely permeable wall. In fluid flows of this type, one expects that both a velocity boundary layer and a thermal boundary layer will exist. The relative ratio of the dependence of the two layers depends on the Prandtl number of the fluid used.

Figures 13 and 14 demonstrate the weak effect of the permeable layer for small Reynolds number of 5. The effect of the permeability only affects a thin boundary layer of fluid close to the permeable wall. These plots were done for both air and water because of the initial motivation of the problem to model a geothermal system. However, noting that there was a change in the heat transfer at the porous boundary with different Prandtl numbers and recalling that there was a dependence on heat transfer with changing Prandtl numbers from the papers by Kuznetsov and co-workers [18,17], we also chose to plot the the variation in the

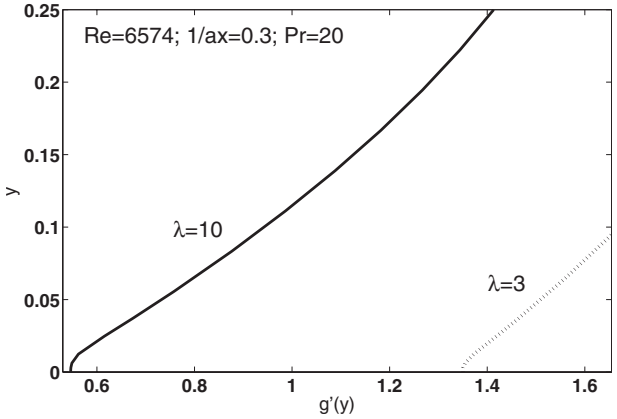

Fig. 12 Existence of thermal boundary layer close to lower permeable wall for high Reynolds number flow

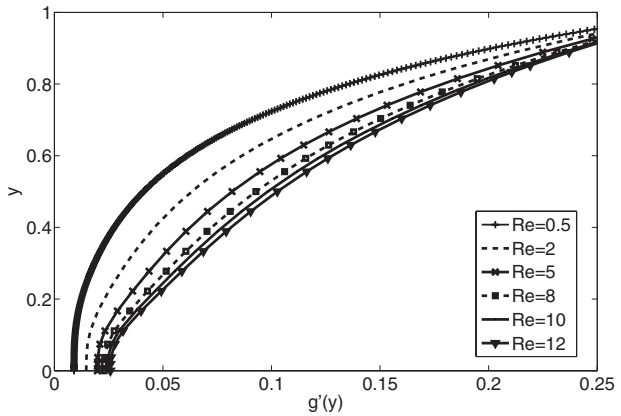

Fig. 10 Variation in the Nusselt number for small Reynolds number for λ=10

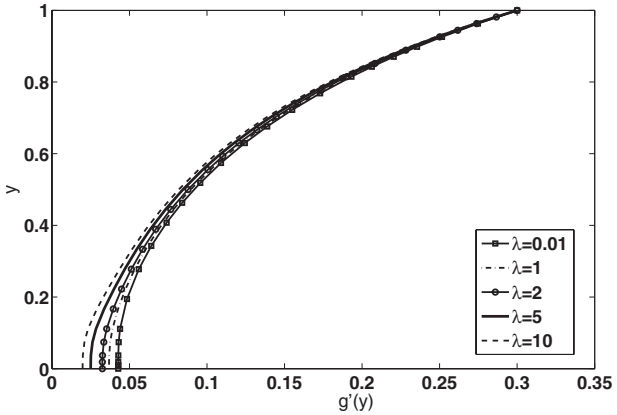

Fig. 13 Variation in $g'(y)$ with permeability for small Reynolds number for water

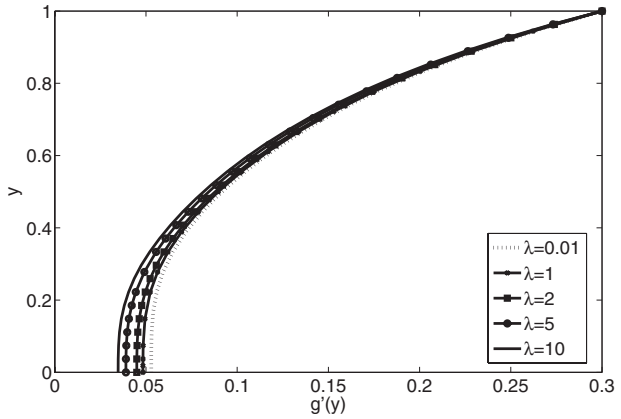

Fig. 14 Variation in $g'(y)$ with permeability for small Reynolds number for air

Nusselt number with an arbitrary fluid of Prandtl number 100 (Fig. 15). The results show, however, that the heat transfer profiles for water and an arbitrary fluid of Prandtl number 100 are quite similar.

6 Conclusions

The heat transfer profiles of a viscous incompressible fluid flowing through a channel with an accelerating surface velocity are examined by means of a similarity solution. The lower channel wall is made permeable, the effect of which is introduced via the slip boundary conditions. The permeability has an influence on the heat transfer profile, the main results being that either a highly permeable layer can be used as an effective heat transfer agent for high Reynolds number flow or alternatively in a channel system where the base can be made less permeable through the addition of some coating substance. A decrease in permeability facilitates heat transfer throughout the channel compensating for the high Reynolds number of the fluid used.

When this system is studied in the context of a geothermal system, once the geology of the sites are explored for small permeable base layers and an average Reynolds number is determined for the contained fluid, then the depth values can be suitably determined to allow for maximum extraction of the high temperature fluid. The study can be developed to include penetration of fluid thorough the porous base layer.

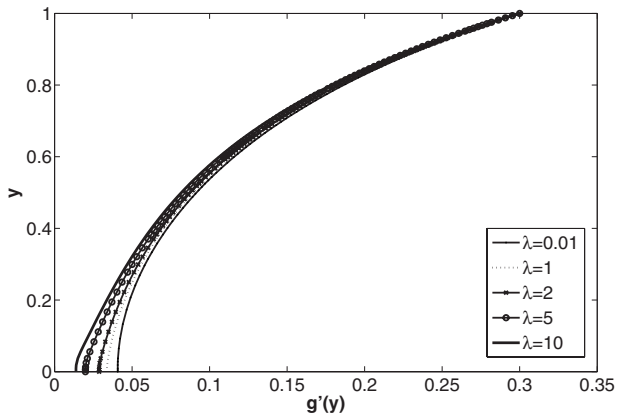

Fig. 15 Variation in $g'(y)$ with permeability for small Reynolds number for an arbitrary fluid of Pr=100

Nomenclature

a = half width of channel
B = basis of 3D space
c = heat capacity of fluid
Ex = surface velocity of fluid
e_1, e_2, e_3 = 3D space vectors
f = similarity parameter
g = similarity parameter
K = permeability
p = pressure
Pr = Prandtl number
Re = shear Reynolds number
t = time
T_0 = temperature at permeable wall
T_1 = temperature at impermeable wall
T_s = stress component
x = streamwise coordinate
y = transverse coordinate
* = dimensionalized variable
β = slip grouping parameter
δ = slip length
κ = thermal conductivity
λ = $\sigma a/\sqrt{K}$
ρ = fluid density
μ = fluid viscosity
σ = slip parameter

References

[1] Sorey, M., 1978, "Numerical Modelling of Liquid Geothermal Systems: Geohydrology of Geothermal Systems," Geophysical Survey Professional Paper, U.S. Government Printing Office, Washington, DC, 1044-d.usgs-pp-1044d and de 83 902181 ed.

[2] Dauenhauer, E., and Majdalani, J., 2003, "Exact Self-Similarity Solution of Navier–Stokes Equation for a Porous Channel With Orthogonally Moving Walls," Phys. Fluids, **15**(6), pp. 1485–1495.

[3] Zhao, T., and Song, Y., 2001, "Forced Convection in a Porous Medium Heated by a Permeable Wall Perpendicular to Flow Direction: Analyses and Measurements," Int. J. Heat Mass Transfer, **44**, pp. 1031–1037.

[4] Berman, A., 1953, "Laminar Flow in Channels With Porous Walls," J. Appl. Phys., **24**(9), pp. 1232–1235.

[5] Beavers, G., and Joseph, D., 1967, "Boundary Conditions at a Naturally Permeable Wall," J. Fluid Mech., **30**, pp. 197–207.

[6] Verma, P., and Bansal, J., 1968, "Forced Convection in Laminar Flow Between Two Parallel Walls and in a Circular Pipe With Suction," Indian J. Pure Appl. Phys., **6**(9), pp. 506–511.

[7] Kuznetsov, A., 2000, "Analytical Studies of Forced Convection in Partly Porous Configurations," *Handbook of Porous Media*, K. Vafai, ed., Dekker, New York, pp. 269–312.

[8] Brady, J., and Acrivos, A., 1981, "Steady Flow in a Channel or Tube With an Accelerating Surface Velocity: An Exact Solution to the Navier–Stokes Equation With Reverse Flow," J. Fluid Mech., **112**, pp. 127–150.

[9] Liu, I. C., and Andersson, H. I., 2008, "Heat Transfer in a Liquid Film on an Unsteady Stretching Sheet," Int. J. Therm. Sci., **47**, pp. 766–772.

[10] Crane, L., 1970, "Flow Past a Stretching Plate," Z. Angew. Math. Phys., **21**, pp. 645–647.

[11] Wang, C., 2006, "Analytic Solutions for a Liquid Film on an Unsteady Stretching Surface," Heat Mass Transfer, **42**, pp. 759–766.

[12] Wang, C., 2009, "Analysis of Viscous Flow Due to a Stretching Sheet With Surface Slip and Suction," Nonlinear Anal.: Real World Appl., **10**, pp. 375–380.

[13] Ochoa-Tapia, J., and Whitaker, S., 1997, "Heat Transfer at a Boundary Between a Porous Medium and a Homogeneous Fluid," Int. J. Heat Mass Transfer, **40**, pp. 2691–2707.

[14] Kuznetsov, A., 1996, "Analytical Investigation of the Fluid Flow in the Interface Region Between a Porous Medium and a Clear Fluid in Channels Partially Filled With a Porous Medium," Appl. Sci. Res., **56**, pp. 53–67.

[15] Kuznetsov, A., 1997, "Influence of the Stress Jump Boundary Condition at the Porous Medium/Clear Fluid Interface in a Flow at a Porous Wall," Int. Commun. Heat Mass Transfer, **24**, pp. 401–410.

[16] Kuznetsov, A., 1998, "Analytical Investigation of Couette Flow in a Composite Channel Partially Filled With a Porous Medium and Partially Filled With a Clear Fluid," Int. J. Heat Mass Transfer, **41**(16), pp. 2556–2560.

[17] Xiong, M., and Kuznetsov, A. V., 2000, "Forced Convection in a Couette Flow in a Composite Duct: An Analysis of Thermal Dispersion and Non-Darcian Effects," J. Porous Media, **3**, pp. 245–255.

[18] Nield, D., and Kuznetsov, A., 2003, "Boundary-Layer Analysis of Forced Convection With a Plate and Porous Substrate," Acta Mech., **166**, pp. 141–148.

[19] Vafai, K., and Kim, S.-J., 1990, "Analysis of Surface Enhancement by a Porous Substrate," ASME J. Heat Transfer, **112**, pp. 700–706.
[20] Kuznetsov, A., and Nield, D., 2006, "A Boundary Layer Treatment of Forced Convection Over a Wedge With an Attached Porous Substrate," J. Porous Media, **9**, pp. 683–694.
[21] Nield, D., and Bejan, A., 1992, *Convection in Porous Media*, 2nd ed., Springer, New York.
[22] Yang, H., Zhao, T., and Cheng, P., 2004, "Gas-Liquid Two Phase Flow Patterns in a Miniature Square Channel With a Gas Permeable Sidewall," Int. J. Heat Mass Transfer, **47**, pp. 5725–5739.
[23] Zhou, C., and Majdalani, J., 2001, "Large Injection and Suction Driven Channel Flows With Expanding and Contracting Walls," 31st AIAA Fluid Dynamics Conference, pp. 1–11.
[24] Majdalani, J., and Zhou, C., 2003, "Moderate to Large Injection and Suction Driven Flows With Expanding and Contracting Walls," Z. Angew. Math. Mech., **83**(3), pp. 181–196.
[25] Afzalimehr, H., and Anctil, F., 2000, "Accelerating Shear Velocity in Gravel Bed Channels," Hydrol. Sci. J., **45**(1), pp. 113–124.
[26] Ferro, S., and Gnavi, G., 2000, "Spatial Stability of Similarity Solutions for Viscous Flows in Channels With Porous Walls," Phys. Fluids, **12**(4), pp. 797–802.
[27] Barrat, J.-L., and Bocquet, L., 1999, "Large Slip Effects at a Non-Wetting Solid-Fluid Interface," Phys. Rev. Lett., **82**(23), pp. 4671–4674.
[28] Hamza, E., 1991, "The Magnetohydrodynamic Effects of a Fluid Film Squeezed Between Two Rotating Surfaces," J. Phys. D, **24**(4), pp. 547–554.
[29] Hamza, E., 1992, "Unsteady Flow Between Two Discs With Heat Transfer in the Presence of a Magnetic Field," J. Phys. D, **25**(10), pp. 1425–1431.
[30] Hamza, E., and Bhatt, B., 1996, "Magnetohydrodynamic Effects of a Fluid Film Squeezed Between Two Rotating Naturally Permeable Discs: Similarity Solutions," Z. Angew. Math. Mech., **76**(10), pp. 583–593.
[31] Bhatt, B., and Hamza, E., 1996, "Similarity Solutions for the Squeezed Film Flow Between Two Rotating Naturally Permeable Discs," Z. Angew. Math. Mech., **76**(5), pp. 291–299.

V. Le Dez
D. Lemonnier
H. Sadat

Laboratoire d'Etudes Thermiques,
UMR 6608,
CNRS-ENSMA,
86960 Futuroscope Cedex, France

Restitution of the Temperature Field Inside a Cylinder of Semitransparent Dense Medium From Directional Intensity Data

The purpose of this paper is to obtain the temperature field inside a cylinder filled in with a dense nonscattering semitransparent medium from directional intensity data by solving the inverse radiative transfer equation. This equation is solved in a first approach with the help of a discrete scheme, and the solution is then exactly obtained by separating the physical set on two disjoint domains on which a Laplace transform is applied, followed by the resolution of a first kind Fredholm equation. [DOI: 10.1115/1.3154622]

1 Introduction

The determination of a temperature field inside an axisymmetric semitransparent medium from optical infrared measurements has been studied many decades ago, especially for gaseous media where the refractive index can be ignored, in the sense where it remains close to one for a large scale of wavelengths. Indeed, the energetic spectral and/or directional radiative flux emerging from such a medium allows the reconstruction of the internal thermal distribution generating this flux. From this basic principle Milne [1] was a pioneer in retrieving the temperature field in the superficial area of the sun from directional and spectral intensities, followed by Chahine [2] who determined atmospheric temperature profiles from spectral outgoing radiances. A similar calculation was performed by Ben Abdallah [3] who studied the gaseous atmosphere of a giant planet from spectral intensities, including an elegant regularization method to take into account the presence of noisy data: in this latter case, a linearization of the Planck function was done to separate the spectral and temperature dependencies. Siewert [4] extended an equivalent approach with the help of orthogonal functions development to the determination of the internal source in an absorbing and scattering sphere from directional emerging intensity data, and Li [5] achieved the restitution of the temperature field inside a cylindrical medium from emerging intensities with a standard functional minimization, ignoring the transmission refractive effects generally induced with specularly transparent reflecting surfaces due here to a constant reflection factor. As mentioned before, in most studies dealing with gaseous atmospheres, the refractive index of the medium is generally taken as 1, from which no reflective and refractive effects can affect the transmitted intensities. In this latter situation, an exact solution can commonly be obtained with the help of a Laplace transform when no scattering occurs. A significant improvement was brought by Kocifaj [6] who took into account the long distance ray deviation due to the continuous refractive effects by solving simultaneously two inverse problems. More specifically devoted to the cylindrical geometry, the study of Liu and Jiang [7] similarly allows the reconstruction of absorption and temperature profiles inside gaseous axisymmetric flames. Considering two distinct but analogous problems, they reconstruct the absorption field by using an Abel equation and perform a standard minimization for the temperature profile, due to the nonconstant absorption, and note that a conjugate gradient method taking into account the sensibility matrix gives, in this special case, accurate results when treating noisy data without any regularization technique. Similar approaches have been explored in retrieving the radiative properties of a given one-dimensional medium by using the observed heat fluxes at the boundaries, for gray gases of unit refractive index in a plane parallel slab [8]: The authors use a standard minimization of an objective function with the help of several efficient techniques, and show that increasing the noise intensity in the input data significantly alters the restitution results obtained with the Levenberg–Marquardt algorithm.

Nevertheless, for dense media, such as glasses, of significantly higher absorption coefficients, the refractive index is much greater than 1 and such effects can no longer be ignored. Although several papers have been devoted to the restitution of the inner temperature field or the radiative source field, for plane dense media parallel slabs, and for Cartesian and cylindrical geometry devices, (see Refs. [9–11] for instances, wherein an objective functional minimization mainly based on the conjugate gradient technique is applied, taking into account the sensibility matrix and looking at the noisy data influence on the numerical procedure) very little literature to our knowledge was interested in retrieving the temperature field inside cylindrical semitransparent nongaseous media, with specularly reflecting surfaces from emerging intensity measurements.

Viskanta et al. [12] used restitution techniques from deep area optical measurements, but due to the particular geometry of the system, only spectral intensities where investigated. Generally devoted to the "best" way in regularizing the experimental data for determining internal sources from emerging intensities, like in Refs. [13,14], these approaches for dense media do not take advantage of the particular properties of the operator governing the problem's physics, which are especially interesting in cylindrical geometry. Ertürk et al. [11] applied three different regularization techniques when retrieving an internal radiative source field inside a three-dimensional device or inverse boundary condition estimation. Since the discrete associated problem often reduces to a linear system of equations resulting from a Fredholm equation of the first kind, they deduced that the corresponding problem is ill-posed and needs to be regularized to avoid error amplifications. They use a truncated singular value decomposition (TSVD) and two related conjugate gradient methods, which produce analogous and relatively accurate results for their problems, and conclude that a simple TSVD of easy computation is generally an efficient technique.

In the case of axisymmetric systems, most of the authors recommend using both spectral and directional measurements; Natterer [15] and Sakami et al. [16] indicated that directional mea-

Contributed by the Heat Transfer Division of ASME for publication in the JOURNAL OF HEAT TRANSFER. Manuscript received June 19, 2008; final manuscript received May 14, 2009; published online August 25, 2009. Review conducted by Ofodike A. Ezekoye.

surements do not allow the complete restitution of the internal temperature field because of refractive effects, and use spectral measurements to perform the complete reconstruction in a so-called "missing data problem." In spite of this, they indicate that such a technique may be limited because of the absorption spectrum sensibility, since dense materials have smooth absorption coefficient spectral fields in the transparency band. This major problem, i.e., a weak sensibility with respect to the absorption for dense media, can only give approximate temperature fields on a few numbers of points, including a priori information on the field. That is why one should prefer directional monochromatic intensities when reconstructing a complete thermal field inside a dense cylinder.

In this paper, we determine the complete temperature field expression inside a cylinder of radius R filled with a dense semitransparent medium of nonunit refractive index n_λ. We first solve the associated inverse problem by using a numerical approach. It is shown that a simple lower and upper (LU) decomposition of the associated matrix gives accurate results only in a restricted area $x \leq R/n_\lambda$ and fails in the complement region, $x > R/n_\lambda$, even for perfect theoretical non-noisy outgoing intensities. This later observation crudely differs from what happens in a media of unit refractive index, such as gaseous atmospheres, where a simple LU decomposition gives exact results everywhere in the cylinder for non-noisy data, and no regularization needs to be applied on the input data. When the refractive index is 1, a simple TSVD [10], for instance, gives accurate results also when adding perturbations in the input data set. Here, for refractive indices strictly greater than 1, a TSVD must be performed even with perfect non-noisy input data to obtain acceptable results in the region, $x > R/n_\lambda$, and only for relatively moderate refractive indices. The results are even accurate when the number of discrete nodes is lower than a threshold value (otherwise the method fails), strongly depending on the medium's refractive index. The scope of this article is then to understand why regularization has to be performed on the global problem even in the presence of perfect input data, contrary to what happens for unit refractive indices. To do so, the input data are considered as perfect non-noisy data obtained from a direct calculation. The exact solution of the integral equation governing the related temperature field is proposed by separating the whole problem into two disjoint calculations on two separate sets. This allows us to finally show that the problem does not belong to the missing data problems, as frequently mentioned, although a discussion on the eigenvalues of the operator's kernel demonstrate why this solution is impossible to obtain in a practical way.

2 Geometrical and Physical Model

One considers a cylinder of radius R filled with dense absorbing-emitting but nonscattering semitransparent medium (STM), such as glass or crystal, mainly characterized by its spectral absorption coefficient κ_λ and its spectral refractive index n_λ. The medium (amorphous or not), assumed to be made of dense bulk material without heterogeneity, is weakly or not scattering, and its absorption and refraction fields do not strongly depend on the inner temperature for relatively large temperature scales. Furthermore, the absorption (and refraction) spectrum of most of dense media being generally extremely smooth on the major part of the semitransparency band, spectral measurements of the emerging intensities emitted by the body will present an extremely bad sensitivity relatively to the wavelength. Also, angular collected monochromatic (simulated) data have been preferred to a spectral intensities set, at a wavelength where the lateral surface of the cylinder is not opaque.

The directional intensities are collected in a tomographic plane perpendicular to the cylinder's axis at a given z, which allows the problem to be considered to be one-dimensional, i.e., the emerging intensities at a given z only depend on the geometric variable x due to the revolution symmetry.

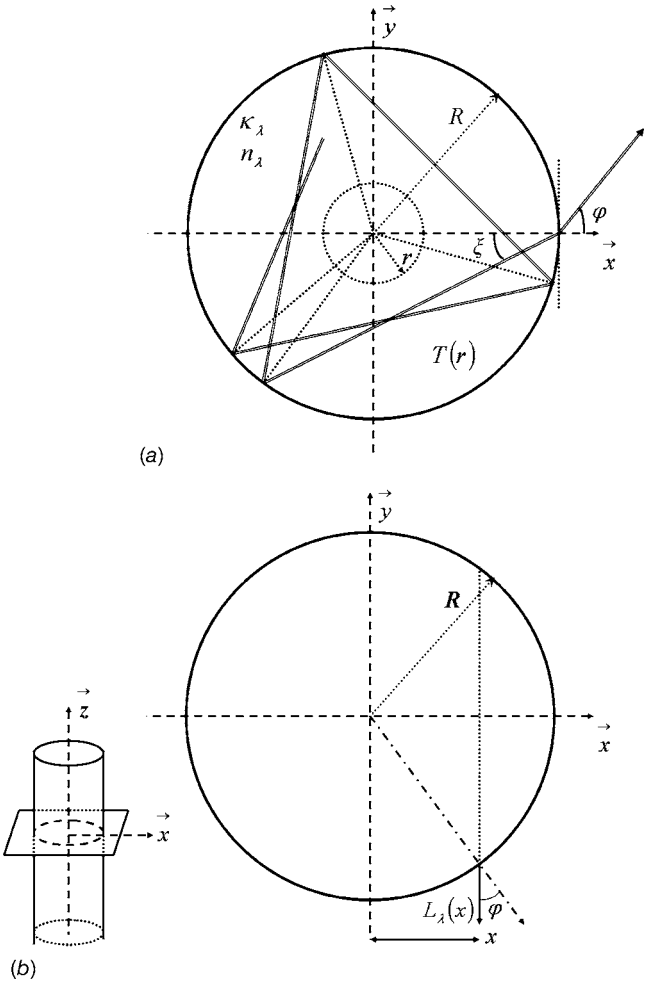

Fig. 1 (*a*) Internal trajectory of a ray emerging in the tomographic plane and (*b*) schematic description of the emerging intensities at local position $0 \leq x \leq R$

Since the refractive index is assumed to be strictly greater than 1, the reflection coefficients at the lateral specular surface between the semitransparent medium and the surrounding environment, given by the Fresnel formulas, are functions of the local position x. The geometrical path in the tomographic plane for a particular emerging ray consists in a complete series of broken lines, as illustrated on Fig. 1(*a*).

The outgoing intensity $L_\lambda(x)$ at position x is given by the classical expression [17]

$$L_\lambda(x) = \frac{2\kappa_\lambda[1-\rho(x)]\exp(-\kappa_\lambda R\cos\xi)}{1-\rho(x)\exp(-2\kappa_\lambda R\cos\xi)} \times \int_{r=R\sin\xi}^{R} \frac{rL_\lambda^0[T(r)]}{\sqrt{r^2R\sin^2\xi}}\cosh(\kappa_\lambda\sqrt{r^2-R^2\sin^2\xi})dr \quad (1)$$

In this expression, $L_\lambda(x)$ is the directional monochromatic intensity emerging from the cylinder in a plane $(\boldsymbol{x},\boldsymbol{y})$ orthogonal to the cylinder's axis $\boldsymbol{z}$, for a given angle φ (between the emerging ray at abscissa x and the normal to the lateral surface of the cylinder at this point), simply related to the spatial position x by $x=R\sin\varphi$, as depicted on the schematic in Fig. 1(*b*). The spectral absorption coefficient is assumed to be known and spatially constant, and the reflection factors $\rho(x)$, either parallel or perpendicular, are classically given by the Fresnel formulas for transparent media, considering that the imaginary part of the complex refractive index is much lower than the real one in the semitransparent band. $T(r)$ is

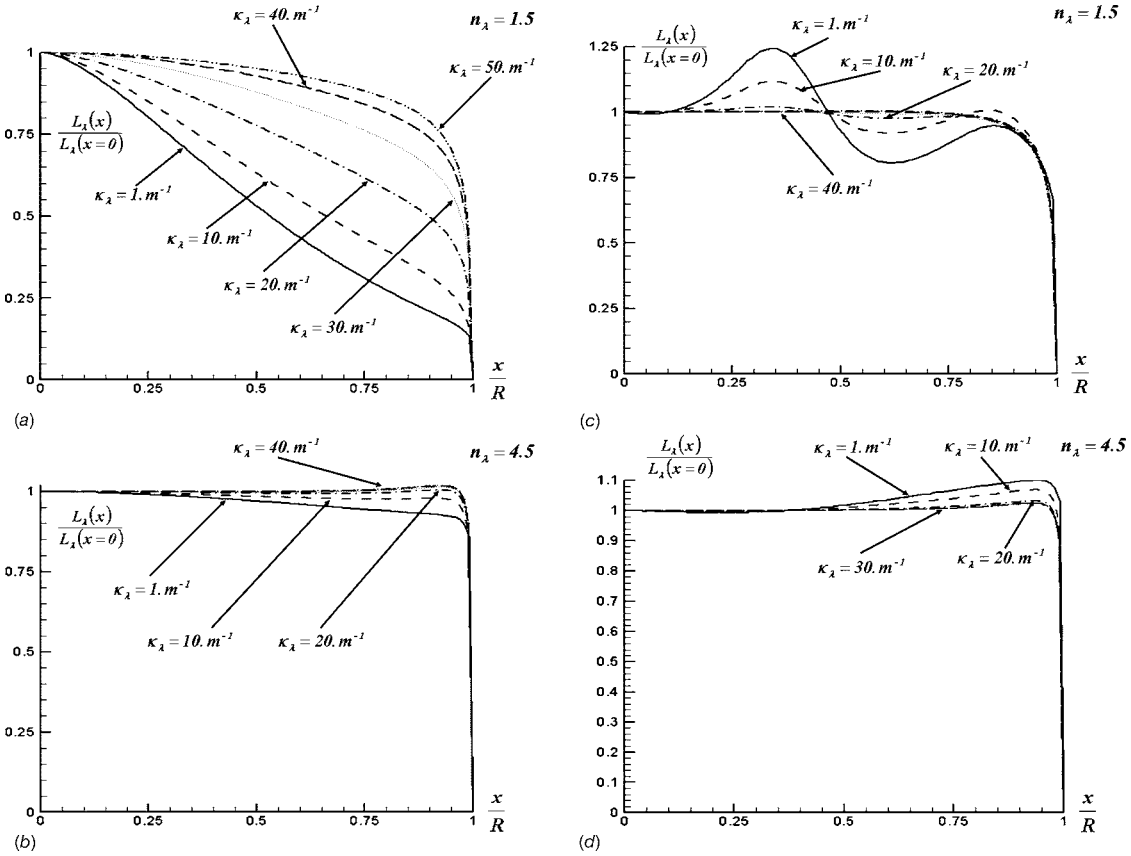

Fig. 2 (*a*) **Intensity for a linear temperature field,** $n_\lambda = 1.5$, (*b*) **intensity for a linear temperature field,** $n_\lambda = 4.5$, (*c*) **intensity for a sinusoidal temperature field,** $n_\lambda = 1.5$, **and** (*d*) **intensity for a sinusoidal temperature field,** $n_\lambda = 4.5$

the spatial temperature field to be reconstructed and L_λ^0 is the Planck function. Noticing that from Descartes' law $\sin\varphi = n_\lambda \sin\xi$, it obviously becomes $x = n_\lambda R \sin\xi$, and Eq. (1) is equivalent to the following integral equation:

$$\int_{r=\frac{x}{n_\lambda}}^{R} \frac{r\kappa_\lambda L_\lambda^0[T(r)]}{\sqrt{r^2 - \frac{x^2}{n_\lambda^2}}} \cosh\left(\kappa_\lambda \sqrt{r^2 - \frac{x^2}{n_\lambda^2}}\right) dr = \frac{\left[1 - \bar{\rho}(x)\exp\left(-2\kappa_\lambda \sqrt{R^2 - \frac{x^2}{n_\lambda^2}}\right)\right] L_\lambda(x)}{2[1 - \bar{\rho}(x)]\exp\left(-\kappa_\lambda \sqrt{R^2 - \frac{x^2}{n_\lambda^2}}\right)} = g(x) \quad (2)$$

The unknown function is $L_\lambda^0[T(r)]$, the useful data being the discrete set $g(x)$, where the mean reflection factor is defined by $\bar{\rho}(x) = \frac{1}{2}[\rho_\perp(x) + \rho_\parallel(x)]$. In the previous expression, the subscript $\perp$ stands for the reflection factor related to the perpendicular polarization, while the subscript $\parallel$ denotes the parallel polarization.

The behavior of the directional emerging intensity with respect to the local position x inside a cylinder of radius $R = 24$ cm has been reported in Figs. 2(*a*)–2(*d*), when the internal temperature field is assumed linear, with $T(x) = 273.15 + 200(2 - (x/R))$, and when the internal temperature field inside the cylinder is a decaying sine function, with $T(x) = 573.15 + 100[1 - \exp(-5x/2R)]\sin(11\pi x/2R)$, for an observation wavelength $\lambda = 1.5$ μm, with $n_\lambda = 1.5$ and $n_\lambda = 4.5$. It appears from these results that increasing the refractive index apparently acts on the emerging intensities as increasing the absorption coefficient for a fixed lower refractive index, and that the shape of the emerging intensities strongly depends on the internal temperature field inside the cylinder for moderate refractive indices.

The physical model being fully described, Sec. 3 shall be now devoted to the numerical discretization of Eq. (2) to obtain the temperature field $T(r)$.

3 Discrete Numerical Solution of the Integral Equation

3.1 Numerical Scheme. The continuous equation (2) is transformed into a linear system of N equations by using a spatial discretization. One defines N control volumes (cells) of depth, Δr, labeled i and whose center is characterized by $x_i = i - 1/N - 1R = (i-1)\Delta r$ for $1 \le i \le N$. In each cell, the temperature is supposed constant, with $T = T_1$ on $[x_1 = 0, \Delta r/2[$, $T = T_i$ on $[x_i - \Delta r/2, x_i + \Delta r/2[$ for $2 \le i \le N-1$, and $T = T_N$ on $[R - \Delta r/2, x_i = R]$.

For a refractive index strictly greater than 1, $x_i/n_\lambda < x_i$, and it exists one and only one integer p strictly lower than i, i.e., $p \in \{1, \ldots, i-1\}$, such that $x_p \le x_i/n_\lambda < x_{p+1}$. This simply means that for a refractive index very close to 1, $x_i/n_\lambda \approx x_i$ and this point belongs to the cell that contains x_i, i.e., $x_{i-1} \le x_i/n_\lambda < x_i$, and $p = i-1$. On the other hand, for large refractive indices, the point characterized by its position x_i/n_λ is much closer to the cylinder's center than x_i and belongs to a cell far from the one that contains x_i. As an example, let us choose a cylinder of radius $R = 24$ cm and $n_\lambda = 6$, with $N = 25$ for $i = 13$, $x_i = 12$ cm, while $x_i/n_\lambda = 2$ cm, from which $x_i/n_\lambda = x_3$ and $p = 3$.

A simple analysis shows that the corresponding integer p is

defined by $p=1+E(i-1/n_\lambda)$, where E stands for the integer part of a positive real number x, with $E(x)=m$ and $m\leq x<m+1$. Hence defining the index

$$q=\begin{cases} p & \text{if } x_p\leq \dfrac{x_i}{n_\lambda}<x_p+\dfrac{\Delta r}{2} \\ p+1 & \text{if } x_p+\dfrac{\Delta r}{2}\leq \dfrac{x_i}{n_\lambda}<x_{p+1} \end{cases}$$

the discrete form of Eq. (2) can be formulated by the following system for $1\leq i\leq N-1$:

$$g(x_i)=L^0_\lambda(T_q)\sinh\left[\kappa_\lambda\sqrt{\left(x_q+\frac{\Delta r}{2}\right)^2-\frac{x_i^2}{n_\lambda^2}}\right]+\sum_{k=q+1}^{N-1}L^0_\lambda(T_k)\times\left\{\sinh\left[\kappa_\lambda\sqrt{\left(x_k+\frac{\Delta r}{2}\right)^2-\frac{x_i^2}{n_\lambda^2}}\right]-\sinh\left[\kappa_\lambda\sqrt{\left(x_k-\frac{\Delta r}{2}\right)^2-\frac{x_i^2}{n_\lambda^2}}\right]\right\}+L^0_\lambda(T_N)\times\left\{\sinh\left(\kappa_\lambda\sqrt{R^2-\frac{x_i^2}{n_\lambda^2}}\right)-\sinh\left[\kappa_\lambda\sqrt{\left(R-\frac{\Delta r}{2}\right)^2-\frac{x_i^2}{n_\lambda^2}}\right]\right\} \tag{3}$$

The case $i=N$ is a particular case, since, although $L_\lambda(x_N)=L_\lambda(R)=0$ is known, $g(x_N)$ is nonequal to 0 (except for a unit refractive index) and undetermined because $\rho(x_N)=\rho(R)=1$, then $g(x_N)$ has to be extrapolated, for instance, from the other values.

Defining the index

$$t=\begin{cases} j_{\max} & \text{if } x_{j_{\max}}\leq \dfrac{R}{n_\lambda}<x_{j_{\max}}+\dfrac{\Delta r}{2} \\ p+1 & \text{if } x_{j_{\max}}+\dfrac{\Delta r}{2}\leq \dfrac{R}{n_\lambda}<x_{j_{\max}+1} \end{cases}$$

where $j_{\max}=1+E(N-1/n_\lambda)$, the discrete form of Eq. (2) for $i=N$ is identical to Eq. (4) if $t\leq N-1$, while if $t=N$, it reduces to

$$g(x_N)=L^0_\lambda(T_N)\sinh\left(\kappa_\lambda R\sqrt{1-\frac{1}{n_\lambda^2}}\right) \tag{4}$$

Hence Eqs. (3) and (4) can be transformed into the following linear system whose solution gives the unknown intensities:

$$CL^0_\lambda(T)=g \tag{5}$$

3.2 Numerical Results. In all that follows, the numerical applications will be done for a cylinder of radius $R=24$ cm, filled with a semitransparent medium characterized by its refractive index $n_\lambda=1.5$ or $n_\lambda=4.5$, and its spectral absorption coefficient $\kappa_\lambda=10$ m^{-1} at a given wavelength $\lambda=1.5$ μm, the temperature field being expressed by $T(x)=573.15+100[1-\exp(-5x/2R)]\sin(11\pi x/2R)$.

The numerical results obtained by solving to the former linear system are presented in Figs. 3(*a*) and 3(*b*) for $N=50$ and 500 cells. A simple direct LU decomposition of matrix C has been used. It can be seen that the Planck function is correctly determined for $x\leq R/n_\lambda$. The method fails, however, in the area $x>R/n_\lambda$, even with exact non-noisy data. The results are oscillatory and inaccurate with an error increasing rapidly with the grid refinement. However, the complete temperature field is correctly evaluated for N lower than 27 in this particular situation. For $N\leq 26$ and perfect data, the retrieved Planck function field cannot be distinguished from the exact Planck function at all internal points inside the medium, while as soon as $N\geq 27$, the retrieved field is of poor quality in the neighborhood of the lateral surface of the cylinder.

This threshold value of the number of cells, below which the reconstructed field is correctly determined for perfect data, is strongly depending on the refractive index of the medium, as clearly shown in Figs. 4(*a*) and 4(*b*). In these examples, the number of cells is set to $N=27$. For $n_\lambda=1.5$, the number of cells equals the threshold value, and the reconstructed field is extremely close to the exact one, except in a small neighborhood of the lateral surface. On the contrary, when $n_\lambda=4.5$, the reconstructed field is correctly estimated only in the range $x\leq R/n_\lambda$ and of extremely bad quality for $x>R/n_\lambda$. In this case the threshold value is $N=9$ and is lower than the number of cells used in the calculation.

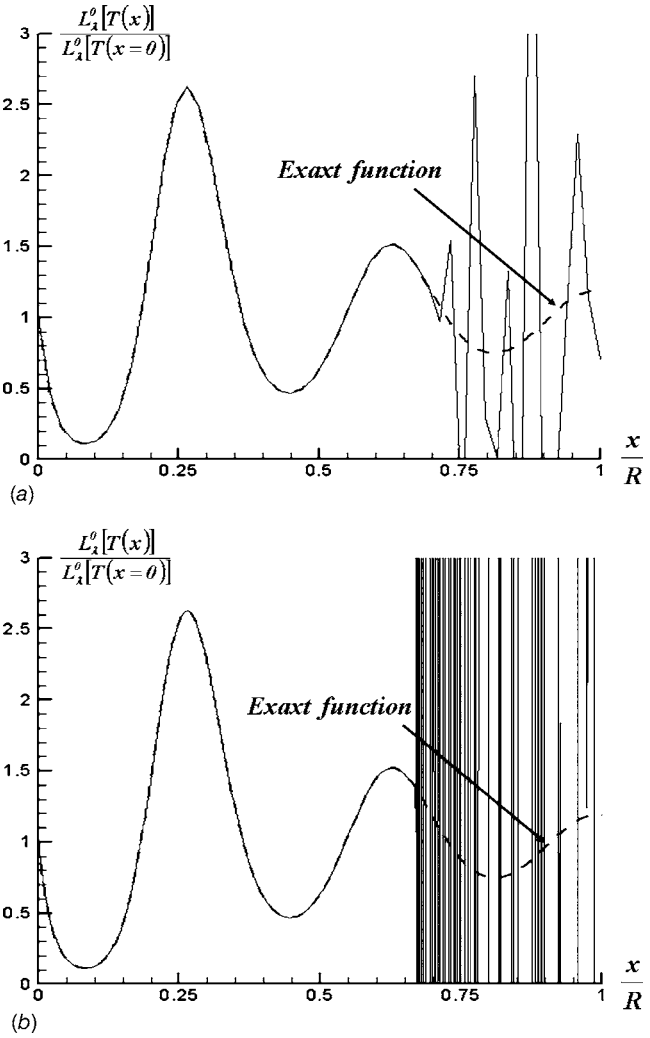

Fig. 3 (*a*) Retrieved Planck function for $N=50$ and (*b*) retrieved Planck function for $N=500$

Hence it appears that for refraction indices greater than 1, an excellent approximation of the temperature field cannot be retrieved everywhere inside the whole cylinder, even for perfect data without any noise. And for a relatively large refractive index, typically in the range $n_\lambda\in[1.5,3]$ for many dense media, the temperature field cannot be estimated in an important area of the cylinder when using a simple LU decomposition. This is particularly true for internal temperature fields of complex shape inside highly refracting media, when using a consequent number of data.

The previous numerical inversion procedure has been then applied to a noisy data set with $g(x)=\bar{g}(x)(1+\delta\langle r\rangle)$, where $\bar{g}(x)$ is a perfect non-noisy data set obtained from a direct calculation, $\langle r\rangle$ is a random number such that $-1\leq\langle r\rangle\leq 1$, and δ is a parameter characterizing the noise intensity. The corresponding results, for the same internal temperature field and thermophysical constants,

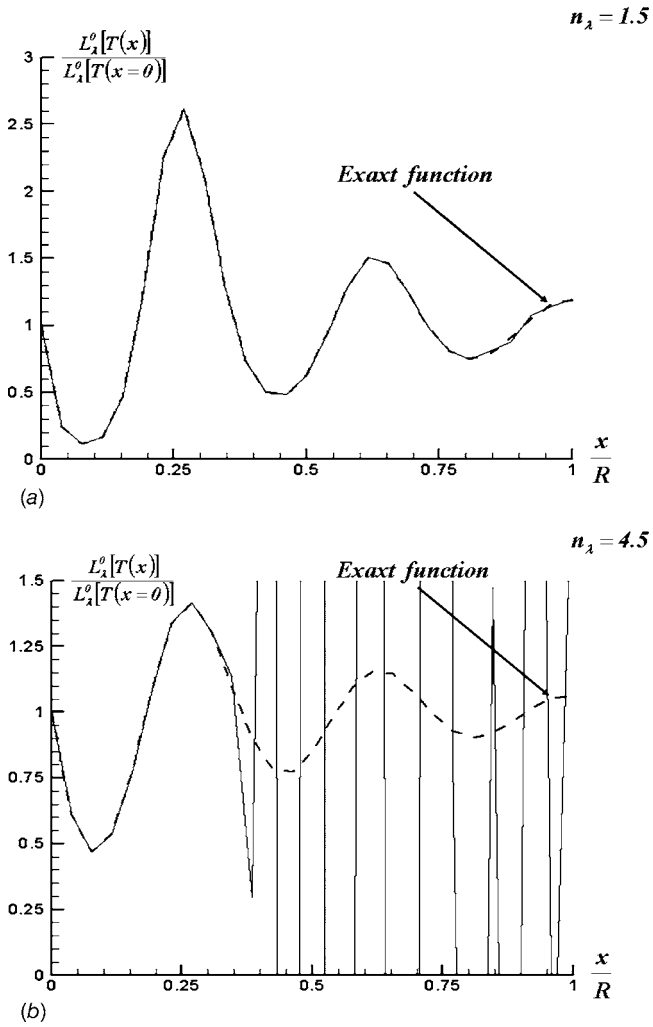

Fig. 4 (*a*) Retrieved Planck function for *N*=27 and (*b*) retrieved Planck function for *N*=27

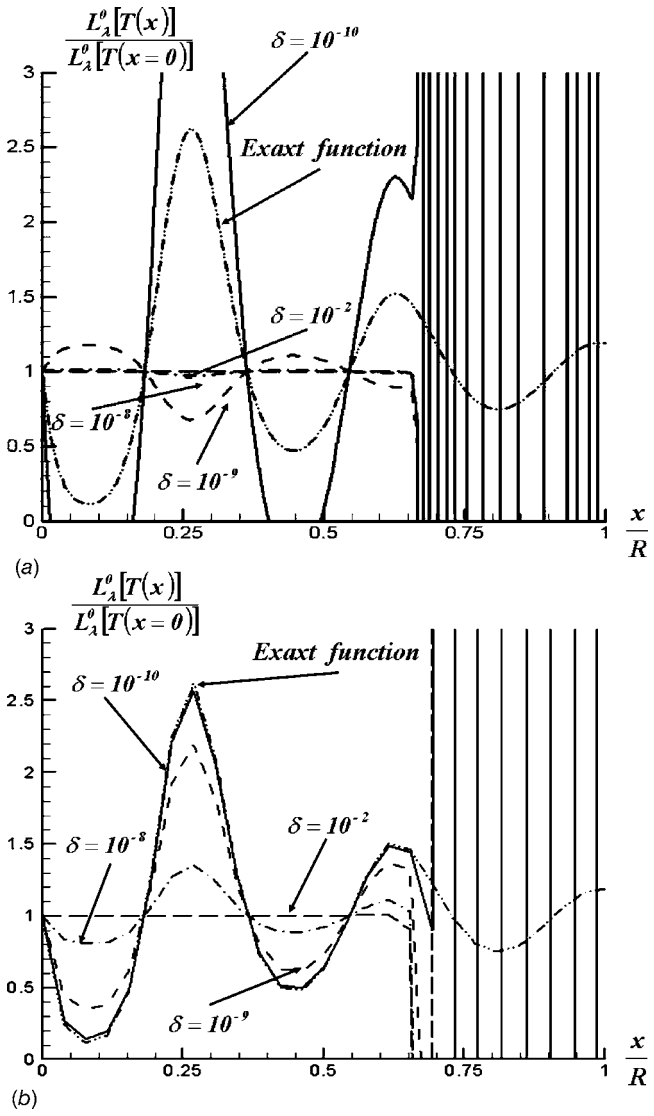

Fig. 5 (*a*) Retrieved Planck function with noisy data for *N*=100 and (*b*) retrieved Planck function with noisy data for *N*=27

are depicted in Figs. 5(*a*) and 5(*b*) for various noise intensity parameters, when the number of cells is 100 and 27, corresponding to the above determined threshold value. For a large number of cells, the numerical procedure is unable to produce satisfactory results even for an insignificant value of the noise intensity, while for a number of cells close to the threshold value, the results are acceptable on the partial area $x \leq R/n_\lambda$ for very small additive perturbations. In all cases, however, the temperature field cannot be obtained in the particular area $x > R/n_\lambda$.

One has to decide then, before dealing with noisy input g values representing a real experimental set of data, if Eq. (2) has a solution for any $x \in [0, R]$ or if, as suggested by the previous numerical study, Eq. (2) can only be inverted in the range $x \leq R/n_\lambda$ and belongs then to the class of missing data problems.

3.3 Solution by the SVD Decomposition. Applying a singular value decomposition (SVD) of matrix C, i.e., $C = U\,\mathrm{diag}(w_i)V^T$, where U and V are two orthogonal matrices, the solution of Eq. (5) writes

$$L^0_\lambda(T) = V\left[\mathrm{diag}\left(\frac{1}{w_i}\right)\right]U^T g \tag{6}$$

Then, introducing the C matrix condition number cond $C = \sup|w_i| / \min|w_i|$, leads for this example ($n_\lambda = 1.5$) to the results presented in Table 1. These results indicate that matrix C is highly ill-conditioned for a large number of cells greater than the step number. Since C is ill-conditioned, a powerful way widely used to obtain an approximate solution is to minimize the residual $|C - L^0_\lambda(T) - g|$ by zeroing the small eigenvalues [11,14,18]. To do so, one chooses a regularization parameter α such that if $|w_j| \leq \alpha \sup|w_i|$, then $w_j = 0$. For the numerical chosen example, the direct calculation gives a correct solution for $\min|w_i| \geq 10^{-12}$, so that the optimal α is about $\alpha \approx 10^{-12}$.

The approximate solution obtained with a regularization parameter $\alpha = 10^{-12}$ is depicted in Figs. 5(*a*) and 5(*b*). For refractive indices that are not too high, exemplified here in Fig. 6(*a*) when $n_\lambda = 1.5$, the approximate solution with a regularization parameter

Table 1 Condition number

No. of cells	$\min\|w_i\|$	$\sup\|w_i\|$	cond C
10	9.783×10^{-6}	5.598	5.722×10^{5}
20	1.132×10^{-12}	5.648	4.990×10^{12}
50	2.447×10^{-17}	5.673	2.318×10^{16}
100	9.697×10^{-17}	5.681	5.858×10^{16}
500	2.420×10^{-17}	5.687	2.350×10^{17}

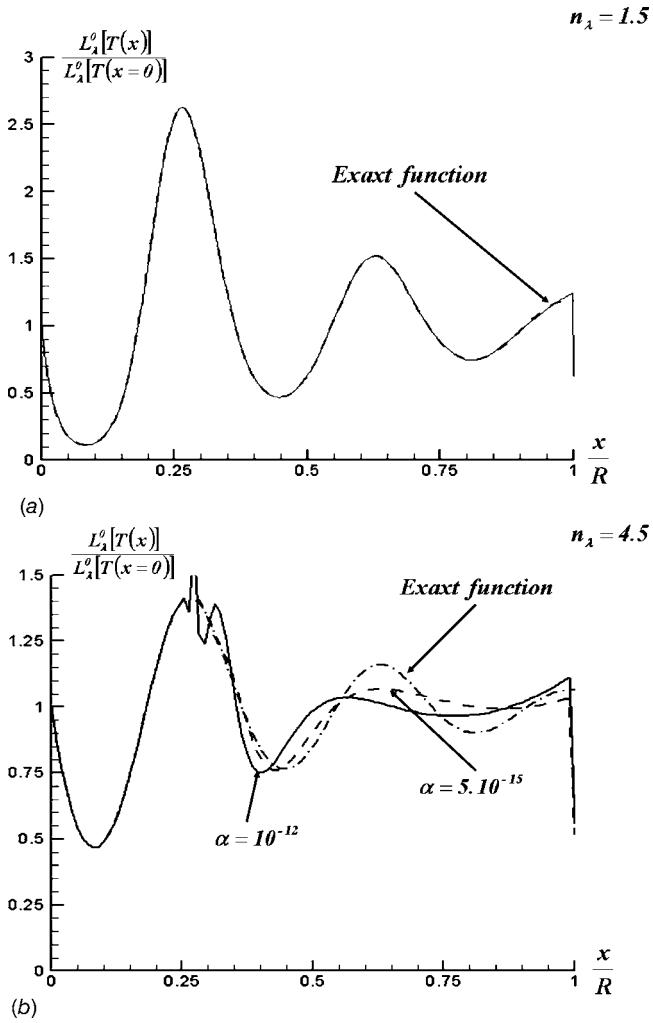

Fig. 6 (*a*) Retrieved Planck function when using a regularization: $\alpha=10^{-12}$, $n_\lambda=1.5$, and $N=500$ and (*b*) retrieved Planck function when using a regularization parameter, $n_\lambda=4.5$, $N=100$

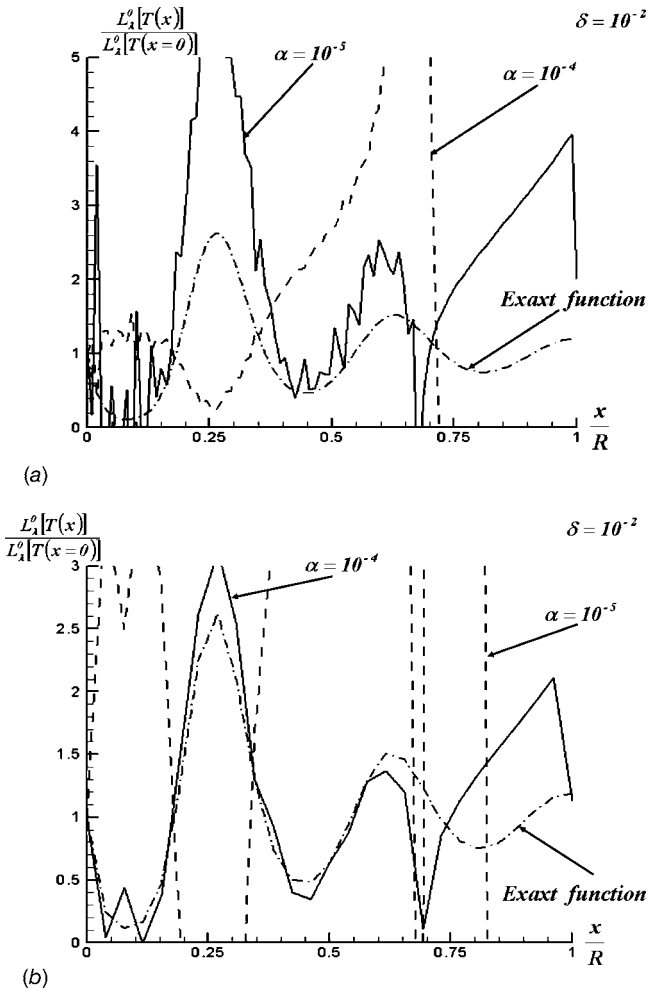

Fig. 7 (*a*) Retrieved Planck function when using a regularization parameter, $N=100$, and (*b*) retrieved Planck function when using a regularization parameter, $N=27$

is very close to the exact one, even for a large number of cells (500) on the range $r \leq R/n_\lambda$ and also on the set $[R/n_\lambda, R]$, except at the single point $r=R$. This allows us to admit that, from a practical point of view, a simple discretization of Eq. (2) followed by a singular value decomposition of matrix C and zeroing the small eigenvalues lead to a satisfactory solution by using only directional and no spectral intensities. However, for important refractive indices, and/or important absorption coefficients, as illustrated in Fig. 6(*b*) when $n_\lambda=4.5$, a regularization procedure gives a good approximation for $r \leq R/n_\lambda$, as when a single LU decomposition is performed and fails to obtain a satisfactory solution on $[R/n_\lambda, R]$ even for large scales of the regularization parameter when the number of cells is important (500). But for moderate cell numbers (100 for instance in this case), the results are of acceptable accuracy for very small regularization parameters. This zeroing procedure works well enough when the number of cells is not too important, which is generally the case in practical cases. However, for cylinders of large dimensions with internal temperature fields of complex shapes, for which a significant number of data may be necessary, and if the refractive index is relatively high, the proposed numerical scheme will produce sometimes poor quality approximations of the temperature field.

A SVD has also been performed for a cylinder of 24 cm radius filled with a STM of absorption coefficient $\kappa_\lambda=10\ \mathrm{m}^{-1}$ and refractive index $n_\lambda=1.5$ submitted to a sinusoidal temperature field, with noisy data for two different cells numbers when the noise intensity is 1% (i.e., $\delta=10^{-2}$). As illustrated in Figs. 7(*a*) and 7(*b*), a SVD gives poor quality results even for relatively high regularization coefficients, especially for a large number of cells. When this number tends toward the threshold value, the results are more accurate and acceptable; also for important regularization factors in the range $x \leq R/n_\lambda$, but remain of poor quality when $x > R/n_\lambda$. This latter remark enhances that the restitution of the temperature field inside a cylinder of dense STM with high refractive indices suffers from two major restrictions: (1) due to the nonunit refractive index, the restitution cannot be performed on the range $x > R/n_\lambda$ without any regularization procedure on the governing operator, even for perfect non-noisy data, and (2) the presence of weakly noisy data significantly alters the above operator regularization procedure in such a way that it necessarily implies an initial preconditioning of the useful perturbed data.

To avoid at this stage a discussion on the possible techniques of data conditioning, such as filtering, and, moreover, to understand why such an operator regularization (even for non-noisy data) is necessary, i.e., why a direct LU decomposition gives only a good solution on the range $r \leq R/n_\lambda$, we shall determine in Sec. 4.1 the exact solution of the integral equation (2), when no perturbation is added to a perfect set of emerging intensity data. If, as suggested by a simple SVD for perfect non-noisy data, there is an exact theoretical solution on the whole set $0 \leq r \leq R$, this opens the way to studies whose scope is the complete restitution of a temperature

field inside a cylinder filed with a dense STM in presence of noisy directional emerging intensity data from an experimental apparatus.

4 Exact Solution of the Integral Equation

4.1 Formal Exact Solution. By using the following variables change:

$$u = \tau^2, \quad y = \frac{\kappa_\lambda^2 x^2}{n_\lambda^2}$$

$$v = \tau_0^2 - u, \quad z = \tau_0^2 - y \tag{7}$$

and introducing functions F and G defined by

$$F(v) = L_\lambda^0\left[T\left(\frac{\sqrt{\tau_0^2 - v}}{\kappa_\lambda}\right)\right], \quad G(v) = 2g\left(\frac{n_\lambda\sqrt{\tau_0^2 - z}}{\kappa_\lambda}\right) \tag{8}$$

one obtains

$$\int_{v=0}^{z} F(v)\frac{\cosh(\sqrt{z-v})}{\sqrt{z-v}}dv = G(z) \tag{9}$$

In Eq. (9), $z \in [z_1, z_2] = [(1-1/n_\lambda^2)\tau_0^2, \tau_0^2]$ can never reach zero if the refraction index is different from 1, and the classical theorems on the Laplace transform can no longer be applied. To avoid this difficulty, an origin translation is applied by introducing $z^* = z - z_1 \in [z_1^*, z_2^*] = [0, \tau_0^2/n_\lambda^2]$, from which one deduces

$$\int_{u^*=0}^{z^*} J(u^*)\frac{\cosh(\sqrt{z^*-u^*})}{\sqrt{z^*-u^*}}du^* = \tilde{H}(z^*) \tag{10}$$

with $u^* = v - z_1$, $F(u^* + z_1) = J(u^*)$, and $\tilde{H}(z^*) = G(z) - \int_{u^*=0}^{z_1} J(-u^*) \times (\cosh(\sqrt{z^*+u^*})/(\sqrt{z^*+u^*}))du^*$.

The boundary values of these functions can be written explicitly

$$J(0) = L_\lambda^0\left[T\left(\frac{R}{n_\lambda}\right)\right], \quad J(z_2^*) = L_\lambda^0[T(0)]$$

$$\tilde{H}(0) = 0, \quad \tilde{H}(z_2^*) = 2\kappa_\lambda\int_{r=0}^{R/n_\lambda} L_\lambda^0[T(r)]\cosh(\kappa_\lambda r)dr \tag{11}$$

Equation (10) is a Faltung convolution equation of kernel $K(t^*) = cosh(\sqrt{t^*})/\sqrt{t^*}$, whose Laplace transform is $[L(K)](p^*) = (\sqrt{\pi/p^*})\exp(1/4p^*)$. Applying a Laplace transform to Eq. (10) leads to

$$L_\lambda^0\left[T\left(\frac{x}{n_\lambda}\right)\right] = \frac{1}{\pi}\int_{v=0}^{z^*}\tilde{H}'(v)\frac{cos(\sqrt{z^*-v})}{\sqrt{z^*-v}}dv \tag{12}$$

With the help of the previous variables and functions changes, the right member of Eq. (10) can be reformulated under the exact form

$$\int_{v=0}^{z^*}\tilde{H}'(v)\frac{\cos(\sqrt{z^*-v})}{\sqrt{z^*-v}}dv = -\frac{1}{\kappa_\lambda}\int_{r=x^*/n_\lambda}^{R}\frac{d}{dr}\{\tilde{H}[\kappa_\lambda^2(R^2-r^2)]\}\frac{\cos\left(\kappa_\lambda\sqrt{r^2 - \frac{x^{*2}}{n_\lambda^2}}\right)}{\sqrt{r^2 - \frac{x^{*2}}{n_\lambda^2}}}dr \tag{13}$$

where $x^*/n_\lambda = \sqrt{(x^2/n_\lambda^2) + (1-1/n_\lambda^2)R^2}$. Replacing $\tilde{H}$ by its value in terms of g and L_λ^0 functions and using the two successive variables changes defined by $r^* = \sqrt{r^2 - (1-1/n_\lambda^2)R^2}$ and $s = n_\lambda r^*$, finally lead to (after a straightforward calculation)

$$L_\lambda^0\left[T\left(\frac{x}{n_\lambda}\right)\right] - \frac{2n_\lambda^2}{\pi}\int_{y=\frac{R}{n_\lambda}}^{R}\frac{yL_\lambda^0[T(y)]}{y^2 - \frac{x^2}{n_\lambda^2}}\left[\begin{array}{l}\frac{\sqrt{R^2-x^2}}{n_\lambda\sqrt{y^2 - \frac{R^2}{n_\lambda^2}}}\cos\left(\frac{\kappa_\lambda}{n_\lambda}\sqrt{R^2-x^2}\right)\cosh\left(\kappa_\lambda\sqrt{y^2 - \frac{R^2}{n_\lambda^2}}\right) \\ -\sin\left(\frac{\kappa_\lambda}{n_\lambda}\sqrt{R^2-x^2}\right)\sinh\left(\kappa_\lambda\sqrt{y^2 - \frac{R^2}{n_\lambda^2}}\right)\end{array}\right]dy$$
$$= -\frac{2n_\lambda}{\pi\kappa_\lambda}\int_{s=x}^{R} g'(s)\frac{\cos\left(\frac{\kappa_\lambda}{n_\lambda}\sqrt{s^2-x^2}\right)}{\sqrt{s^2-x^2}}ds \tag{14}$$

where g' is the derivative of the data set g. Equation (14) is the exact inverse solution of Eq. (2).

Note that the complete data set g on the whole set $[0, R]$ must be used to compute the temperature field in the zone $[0, R/n_\lambda]$, and that this field depends on the temperature field in the region $[R/n_\lambda, R]$. Under this form, Eq. (14) looks like a second kind Fredholm equation, however, it is not an integral equation.

Indeed, the previous equation is strictly equivalent to the analogous form

$$\Phi(r) - \lambda\int_{y=R/n_\lambda}^{R}\Phi(y)K(r,y)dy = F(r) \tag{15}$$

where Φ is the unknown function defined on $r \in [0, R/n_\lambda]$ for the first left-hand side member, while the definition interval of the integral is $[R/n_\lambda, R]$. One can notice that from the exact definition of the g function given by Eq. (2), Eq. (14) can be replaced by the strictly equivalent equation

$$L_\lambda^0\left[T\left(\frac{x}{n_\lambda}\right)\right] = -\frac{2n_\lambda}{\pi\kappa_\lambda}\int_{s=x}^{R} h'(s)\frac{\cos\left(\frac{\kappa_\lambda}{n_\lambda}\sqrt{s^2-x^2}\right)}{\sqrt{s^2-x^2}}ds \tag{16}$$

where the h function is defined by

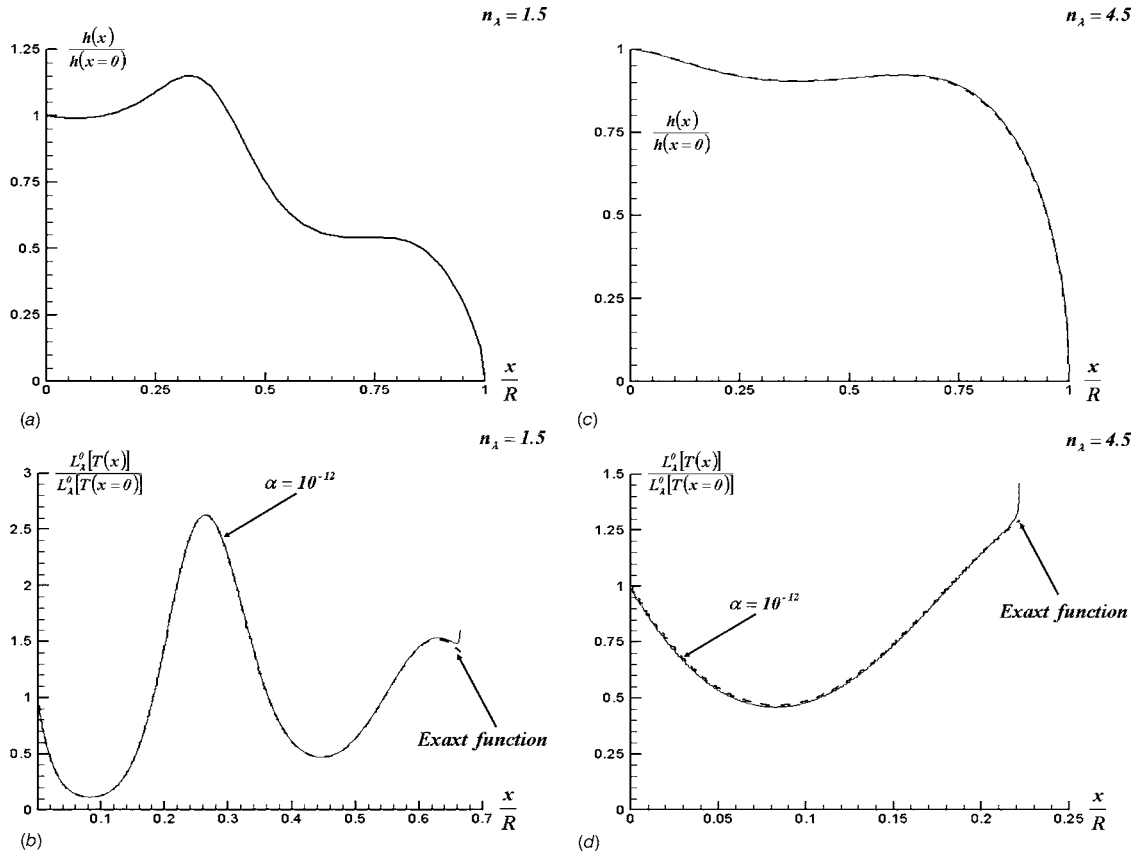

Fig. 8 (*a*) Evolution of h for $x \leq R$, $n_\lambda = 1.5$, (*b*) retrieved Planck function with Eq. (14) on the range $[0, R/n_\lambda]$ for $n_\lambda = 1.5$, (*c*) evolution of h for $x \leq R$, $n_\lambda = 4.5$, and (*d*) retrieved Planck function with Eq. (14) on the range $[0, R/n_\lambda]$ for $n_\lambda = 4.5$

$$h(x) = \int_{r=x}^{R} \frac{r\kappa_\lambda L_\lambda^0\left[T\left(\frac{r}{n_\lambda}\right)\right]}{n_\lambda\sqrt{r^2 - x^2}} \cosh\left(\frac{\kappa_\lambda}{n_\lambda}\sqrt{r^2 - x^2}\right) ds \qquad (17)$$

The h function is the generalized g function for $n_\lambda \neq 1$ and is equivalent to g when $n_\lambda = 1$.

Under this latter form, it is therefore obvious that the inversion of Eq. (2) only leads to a partial temperature field on $[0, R/n_\lambda]$. Note also that the function h cannot be simply related to the experimental set g and cannot be applied at this stage from a practical point of view to determine the temperature field.

4.2 Numerical Verification. From the exact expression (17) of the function h, it is easy to prove that Eq. (14) is verified at $x = R$. We present in this section the results obtained by solving numerically Eq. (14) with the numerical scheme presented in Appendix A.

The restitution of the temperature field, as well as the evolution of the function h, analogous to the data g set for unit refractive indices, are presented in Figs. 8(*a*)–8(*d*) for $n_\lambda = 1.5$ and $n_\lambda = 4.5$ with $N = 500$ and $\kappa_\lambda = 10$ m^{-1}, for exact h data and for "data" obtained from a calculated g set by a SVD of matrix C, followed by a simple zeroing with $\alpha = 10^{-12}$, when no perturbation is done on the exact g data. The numerical computation of Eq. (14) gives excellent results compared with the exact ones, even if the temperature field is not correctly estimated in the neighborhood of $x = R/n_\lambda$, due to the fact that h'_N is forced to have a finite value.

The main interest of this operation here is not to obtain the temperature field on $[0, R/n_\lambda]$, but to calculate the generalized h function on $[0, R]$, from which the partial temperature field on $[R/n_\lambda, R]$ is governed by the integral equation

$$\int_{r=R/n_\lambda}^{R} \frac{r\kappa_\lambda L_\lambda^0[T(r)]}{\sqrt{r^2 - \frac{x^2}{n_\lambda^2}}} \cosh\left(\kappa_\lambda\sqrt{r^2 - \frac{x^2}{n_\lambda^2}}\right) dr = g(x) - h(x) = \Psi(x) \qquad (18)$$

The function Ψ is completely known on $[0, R]$, and Eq. (18) can be considered to be a first kind Fredholm equation for $x \in [R/n_\lambda, R]$, where Ψ is the data function of the equation, $K(r,x) = r\cosh(\kappa_\lambda\sqrt{r^2 - (x^2/n_\lambda^2)})/\sqrt{r^2 - (x^2/n_\lambda^2)}$ is the kernel of the integral equation, and $L_\lambda^0[T(r)]$ is the unknown function to determine on $[R/n_\lambda, R]$. Equation (18) only depends on the unknown part of the temperature field, which means that if this latter equation has a solution, then the global problem summed up by the general Eq. (2) does not belong to the class of missing data problems, as frequently mentioned, and there is hope to find approximate numerical procedures allowing the restitution of the complete temperature field on the whole set $[0, R]$. If, however, Eq. (18) has no physical admissible solution, directional intensities data are unable to give a complete description of the temperature field inside the cylinder.

4.3 Discussion on the Kernels of the Operator. The detailed behavior of the exact Ψ function with respect to the absorption coefficient is depicted in Figs. 9(*a*)–9(*d*). Figures 9(*a*) and 9(*b*) detail the relative behavior of the three functions g, h, and Ψ on the whole set $[0, R]$ for two refractive indices ($n_\lambda = 1.5$ and $n_\lambda = 4.5$) when $\kappa_\lambda = 10$ m^{-1}. In both cases, Ψ is an approximately linear slowly decaying function for this absorption coefficient on the major part of the set $[0, R]$, and it increases near the lateral surface of the cylinder. The influence of the absorption coefficient

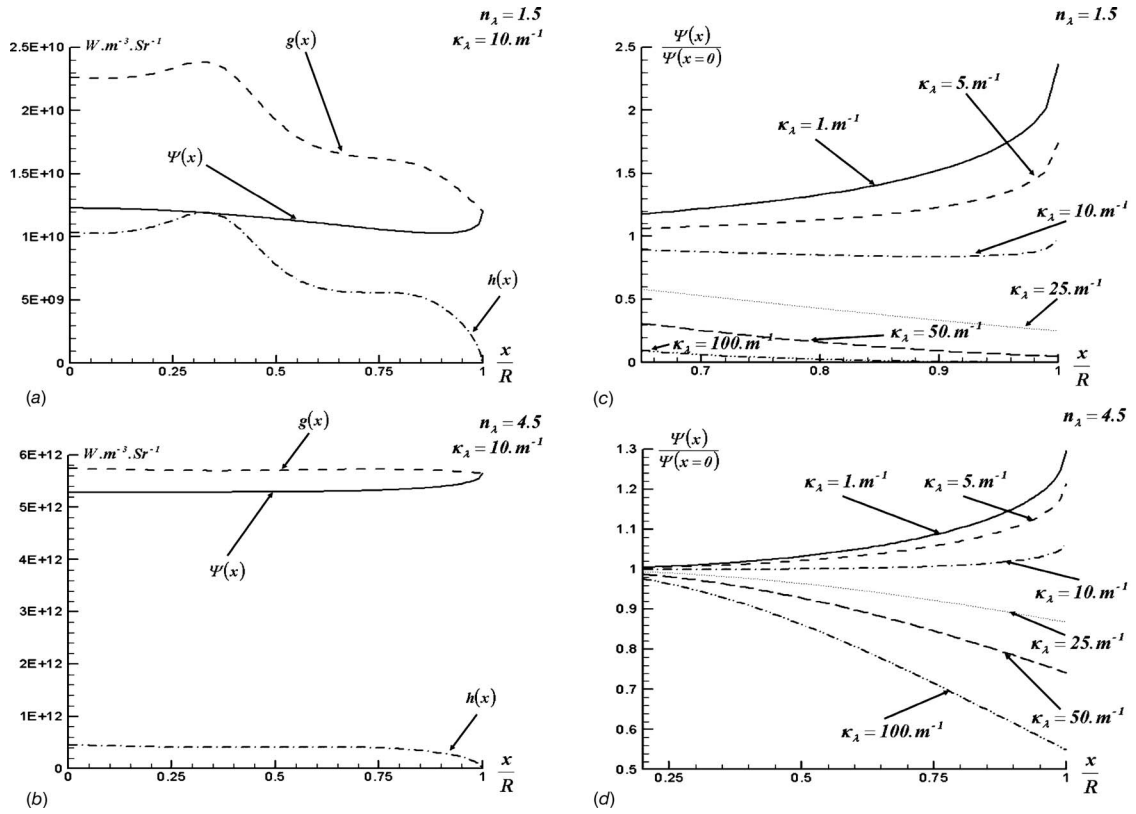

Fig. 9 (*a*) Evolution of *g*, *h*, and Ψ on [0,*R*], (*b*) evolution of *g*, *h*, and Ψ on [0,*R*], (*c*) evolution of function Ψ on $[R/n_\lambda, R]$ for various absorption coefficients, $n_\lambda = 1.5$, and (*d*) evolution of function Ψ on $[R/n_\lambda, R]$ for various absorption coefficients, $n_\lambda = 4.5$

for a given refractive index has been reported in the two last figures: It shows, whatever the refractive index is, that Ψ is a decaying function for absorption coefficients higher than a critical value depending on the refractive index and the cylinder's radius, and Ψ increases as soon as the absorption coefficient is lower than this threshold value.

Nevertheless, the sensibility of Ψ on the useful set $[R/n_\lambda, R]$ is relatively poor with respect to the internal position *x*, especially for high refractive indices for which the amplitude of Ψ is low.

Before examining the particular properties of Eq. (18), it is worth noting that its discrete form is as follows.

If $t \le N-1$

$$L_\lambda^0(T_t)\left[\sinh\left(\kappa_\lambda\sqrt{r^2-\frac{x_j^2}{n_\lambda^2}}\right)\right]_{R/n_\lambda}^{x_t+\Delta r/2} + \sum_{k=t+1}^{N-1} L_\lambda^0(T_k) \times\left[\sinh\left(\kappa_\lambda\sqrt{r^2-\frac{x_j^2}{n_\lambda^2}}\right)\right]_{x_k-\Delta r/2}^{x_k+\Delta r/2} + L_\lambda^0(T_N) \times\left[\sinh\left(\kappa_\lambda\sqrt{r^2-\frac{x_j^2}{n_\lambda^2}}\right)\right]_{R-\Delta r/2}^{R} = \Psi(x_j) \tag{19}$$

If $t=N$,

$$L_\lambda^0(T_N)\left[\sinh\left(\kappa_\lambda\sqrt{r^2-\frac{x_j^2}{n_\lambda^2}}\right)\right]_{R/n_\lambda}^{R} = \Psi(x_j), \quad 1 \le j \le N$$

For $j=N$ the solution is

$$L_\lambda^0(T_N) = \frac{g(R)}{\sinh\left(\kappa_\lambda R\sqrt{1-\frac{1}{n_\lambda^2}}\right)}$$

When n_λ is very close to 1, or equivalently when the number of cells is small, Eq. (19) gives the exact value T_N. Since one must seek the exact solution on $[R/n_\lambda, R]$, the discrete numerical approach involves the grid labeled $t \le j \le N$ and leads to the resolution of a linear system of $N-t+1$ equations with $N-t+1$ unknown quantities, formally written as $\tilde{C}L_\lambda^0(T)=\Psi$. We present in Figs. 10(*a*) and 10(*b*) the numerical results of such a calculation, when a SVD followed by a zeroing is performed on the matrix $\tilde{C}$ and when the number of cells is exactly $N-t+1$, with $N=100$ and $\kappa_\lambda = 10\ m^{-1}$. For a refractive index $n_\lambda = 1.5$, this leads to $N-t+1 = 34$, and for $n_\lambda = 4.5$, one has $N-t+1 = 78$. As it can be seen, there is a slight improvement (relatively to a global discretization of Eq. (2)) when Eq. (18) is discretized and a SVD is applied. A numerical solution, although of poor quality, can be exhibited, which let us believe that the integral equation on the partial set $[R/n_\lambda, R]$ has an exact solution.

With the notations used for the Laplace transform, Eq. (18) can be rewritten under the following form:

$$\int_{\upsilon=R/n_\lambda}^{(1-1/n_\lambda^2)\tau_0^2} L_\lambda^0\left[T\left(\frac{\sqrt{\tau_0^2-\upsilon}}{\kappa_\lambda}\right)\right]\frac{\cosh(\sqrt{z-\upsilon})}{\sqrt{z-\upsilon}}d\upsilon = 2\Psi\left(\frac{n_\lambda}{\kappa_\lambda}\sqrt{\tau_0^2-z}\right) \tag{20}$$

The variable *z* is such that $z \in [(1-1/n_\lambda^2)\tau_0^2, (1-1/n_\lambda^4)\tau_0^2] \not\subset [0,(1-1/n_\lambda^2)\tau_0^2]$. Introducing the new parameter and variables $\alpha^* = \tau_0\sqrt{1-1/n_\lambda^2}$, $w = 1-\upsilon/\alpha^{*2} \in [0,1]$, and $z' = n_\lambda^2(z/\alpha^{*2}-1) \in [0,1]$, as well as the two following functions: $F(w) = L_\lambda^0\{T[R\sqrt{1/n_\lambda^2+(1-1/n_\lambda^2)w}]\}$ and $\bar{\Psi}(z') = \Psi[R\sqrt{1-(1-1/n_\lambda^2)z'}]$, easily lead to the simplified equation

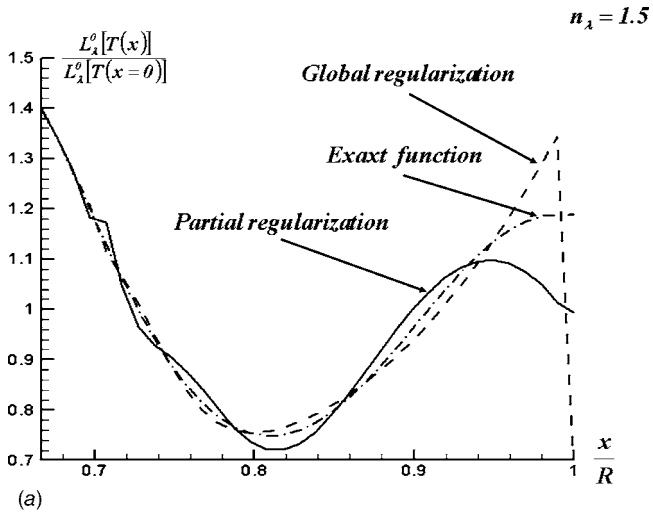

Fig. 10 (*a*) retrieved Planck function when using a regularization parameter $\alpha=10^{-9}$ and $n_\lambda=1.5$, and (*b*) retrieved Planck function when using a regularization parameter, $\alpha=10^{-9}$ and $n_\lambda=4.5$

$$\int_{w=0}^{1} F(w)\frac{\cosh\left(\alpha^*\sqrt{w+\frac{z'}{n_\lambda^2}}\right)}{\sqrt{w+\frac{z'}{n_\lambda^2}}}dw=\bar{\Psi}(z'),$$

$$(w,z')\in[0,1]\times[0,1] \tag{21}$$

Equation (21) is a first kind Fredholm equation of data $\bar{\Psi}$ on $[0,1]$ and unknown function F on the same range, with a nonsymmetric kernel $K(w,z')=\cosh(\alpha^*\sqrt{w+(z'/n_\lambda^2)})/\sqrt{w+(z'/n_\lambda^2)}$, where $K(w,z')\neq K(z',w)$. The two symmetric left K_G and right K_D associated kernels are defined by

$$K_G(w,z')=\int_{v=0}^{1}K(v,w)K(v,z')dv$$

$$K_D(w,z')=\int_{v=0}^{1}K(w,v)K(z',v)dv \tag{22}$$

It can be shown that they can be expressed as follows:

$$K_G(w,w)=\mathrm{Chi}\left(\frac{2\tau_0\sqrt{n_\lambda^2-1}}{n_\lambda^2}\sqrt{w+n_\lambda^2}\right)-\mathrm{Chi}\left(\frac{2\tau_0\sqrt{n_\lambda^2-1}}{n_\lambda^2}\sqrt{w}\right)+\frac{1}{2}\ln\left(\frac{w+n_\lambda^2}{w}\right),\quad w\neq 0$$

$$K_G(w,z')=\mathrm{Chi}\left[\frac{\tau_0\sqrt{n_\lambda^2-1}}{n_\lambda^2}(\sqrt{w+n_\lambda^2}+\sqrt{z'+n_\lambda^2})\right]-\mathrm{Chi}\left[\frac{\tau_0\sqrt{n_\lambda^2-1}}{n_\lambda^2}(\sqrt{w}+\sqrt{z'})\right]+\mathrm{Chi}\left(\frac{\tau_0\sqrt{n_\lambda^2-1}}{n_\lambda^2}|\sqrt{w}-\sqrt{z'}|\right)-\mathrm{Chi}\left(\frac{\tau_0\sqrt{n_\lambda^2-1}}{n_\lambda^2}|\sqrt{w+n_\lambda^2}-\sqrt{z'+n_\lambda^2}|\right),\quad z'\neq w \tag{23}$$

and

$$K_D(w,w)=n_\lambda^2\left[\mathrm{Chi}\left(\frac{2\tau_0\sqrt{n_\lambda^2-1}}{n_\lambda}\sqrt{w+\frac{1}{n_\lambda^2}}\right)-\mathrm{Chi}\left(\frac{2\tau_0\sqrt{n_\lambda^2-1}}{n_\lambda}\sqrt{w}\right)+\frac{1}{2}\ln\left(\frac{w+\frac{1}{n_\lambda^2}}{w}\right)\right],\quad w\neq 0$$

$$K_D(w,z')=n_\lambda^2\left\{\begin{array}{l}\mathrm{Chi}\left[\frac{\tau_0\sqrt{n_\lambda^2-1}}{n_\lambda}\left(\sqrt{w+\frac{1}{n_\lambda^2}}+\sqrt{z'+\frac{1}{n_\lambda^2}}\right)\right]-\mathrm{Chi}\left[\frac{\tau_0\sqrt{n_\lambda^2-1}}{n_\lambda}(\sqrt{w}+\sqrt{z'})\right]\\ +\mathrm{Chi}\left(\frac{\tau_0\sqrt{n_\lambda^2-1}}{n_\lambda}|\sqrt{w}-\sqrt{z'}|\right)-\mathrm{Chi}\left(\frac{\tau_0\sqrt{n_\lambda^2-1}}{n_\lambda}\left|\sqrt{w+\frac{1}{n_\lambda^2}}-\sqrt{z'+\frac{1}{n_\lambda^2}}\right|\right)\end{array}\right\},\quad z'\neq w \tag{24}$$

where $\mathrm{Chi}(x)=1/2[Ei(x)-E_1(x)]=\gamma+\ln x+\Sigma_{k=1}^{+\infty}x^{2k}/(2k(2k)!)$ is the hyperbolic cosine integral [19].

Since chi is a strictly growing function for $x>0$, $K_D(w,z')$ (respectively, $K_G(w,z')$) is a strictly positive function on $]0,1]\times]0,1]$ and from the previous definition of chi, $K_D(w,z')$ (respectively, $K_G(w,z')$) is obviously a continuous function on $]0,1]\times]0,1]$. Furthermore, a simple analysis shows that if $K_{D,G}$ reaches a minimal value, where $K_{D,G}$ stands indifferently either for K_D or K_G, this value is located on the straight line $w=z'$.

Then for the right kernel K_D, noting $\Omega=1.1996787$ the solution of $\tanh\Omega=1/\Omega$, it is possible to prove that if $\tau_0\leq(n_\lambda\Omega)/\sqrt{n_\lambda^2-1}$, $K_D(w,w)$ is a strictly positive decaying function on $]0,1]$ with $\lim_{\tau_0\to 0}[\min_{w\in}]0,1]K_D(w,w)]=n_\lambda^2\ln(1+1/n_\lambda^2)$, and if $\tau_0>(n_\lambda\Omega)/\sqrt{n_\lambda^2-1}$, $K_D(w,w)$ is a strictly positive function that reaches a minimal value at a given $u_0(\tau_0)\in]0,1[$ with $\lim_{\tau_0\to+\infty}u_0(\tau_0)=0$ and $\lim_{\tau_0\to+\infty}[\min_{w\in}]0,1]K_D(w,w)]=+\infty$. The

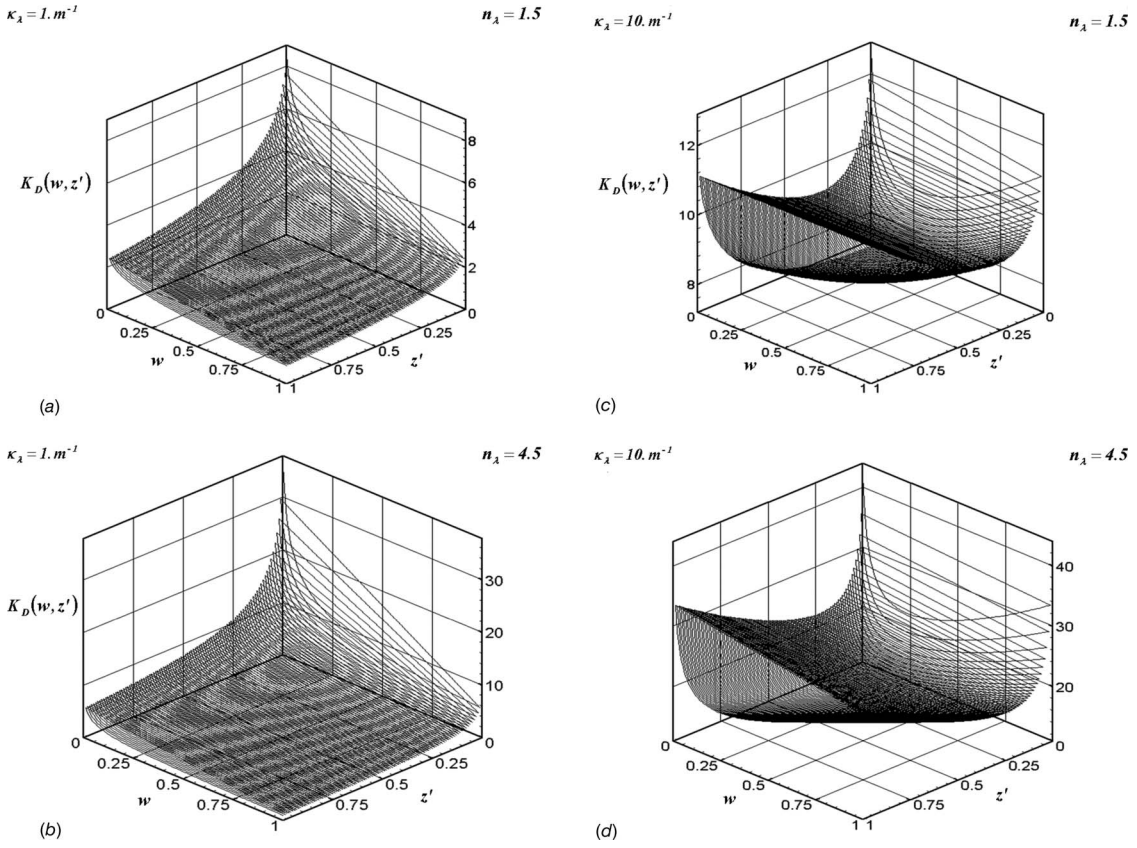

Fig. 11 (*a*) evolution of K_D for $\tau_0 \leq n_\lambda \Omega / \sqrt{n_\lambda^2 - 1}$, (*b*) evolution of K_D for $\tau_0 \leq n_\lambda \Omega / \sqrt{n_\lambda^2 - 1}$, (*c*) evolution of K_D for $\tau_0 > n_\lambda \Omega / \sqrt{n_\lambda^2 - 1}$, and (*d*) evolution of K_D for $\tau_0 > n_\lambda \Omega / \sqrt{n_\lambda^2 - 1}$

evolution of $K_D(w,z')$ is depicted in Figs. 11(*a*)–11(*d*) for two absorption coefficients (1 m^{-1} and 10 m^{-1}) and two refractive indices (1.5 and 4.5).

In the first case (Figs. 11(*a*) and 11(*b*)), $\tau_0 \leq (n_\lambda \Omega)/\sqrt{n_\lambda^2 - 1}$ and the minimal value of $K_D(w,z')$ is $K_D(1,1)$, (0.860 for $n_\lambda = 1.5$ and 1.032 for $n_\lambda = 4.5$). When the refractive index increases, the values taken by the right kernel significantly increase, but the global behavior remains unchanged. For $\tau_0 > n_\lambda \Omega / \sqrt{n_\lambda^2 - 1}$ the minimal value of the kernel grows rapidly (Figs. 11(*c*) and 11(*d*)) when the absorption coefficient increases, since $\min_{w \in]0,1]} K_D(w,w) = 7.498$ for $n_\lambda = 1.5$ and $\min_{w \in]0,1]} K_D(w,w) = 12.480$ for $n_\lambda = 4.5$.

The two symmetric kernels are such that $\|K_{D,G}\|_2^2 = \int_{w=0}^1 \int_{z'=0}^1 K_{D,G}^2(w,z')dz'dw = \Lambda_1^{D,G}(\alpha^*, n_\lambda) < +\infty$, where $\Lambda_1^{D,G}(\alpha^*, n_\lambda)$ (related either to the right or left kernel) is a complicated function in terms of power, logarithm, exponential, and product of Chi and Shi (hyperbolic sine integral) functions of finite value for $\alpha^* \neq 0$, which is the case since $n_\lambda \neq 1$.

Hence $K_{D,G}(w,z')$ are L_2-kernels on $[0,1] \times [0,1]$. Obviously, $\bar{\Psi}$ is a L_2-function on $[0,1]$, which guaranties [20] the existence of a solution for Eq. (21), whose formal expression is

$$F(z') = \operatorname*{lem}_{n \to +\infty} \sum_{k=1}^{n} \lambda_k \alpha_k \mu_k(z') \Leftrightarrow \lim_{n \to +\infty} \int_{z'=0}^{1} \left[F(z') - \sum_{k=1}^{n} \lambda_k \alpha_k \mu_k(z') \right]^2 dz' = 0 \tag{25}$$

where lem commonly stands for the usual limit in mean [20]. The $(\lambda_n)_{n \in |N}$ are the eigenvalues associated to the system $(\mu_n)_{n \in |N}$ of the right kernel eigenfunctions, that is, $\mu_n(z') = \lambda_n^2 \int_{w=0}^1 K_D(w,z')\mu_n(w)dw$, and $(\alpha_n)_{n \in |N}$ are the Fourier coefficients of $\bar{\Psi}$ relative to the system $(\mu_n)_{n \in |N}$, i.e., $\bar{\Psi}(z') = \sum_{n=1}^{+\infty} \alpha_n \mu_n(z')$ with $\alpha_n = \int_{z'=0}^1 \bar{\Psi}(z')\mu_n(z')dz'$.

Considering one-normed eigenfunctions, i.e., functions such that $\int_{u=0}^1 \mu_n^2(u)du = 1$, the eigenvalues associated to the right kernel are such that $\lambda_n^2 \geq 1/\|K_D\|_2$.

The exact eigenfunctions and eigenvalues cannot be obtained in an analytical way, and we shall only determine a numerical approximation of the solution by using the method presented in Appendix B.

As an example, the first ten eigenvalues of the right kernel are listed in Table 2, with respect to the numerical quadrature (Gauss quadrature) order M, in the case where $R = 0.24$ m, $\kappa_\lambda = 10$ m^{-1}, and $n_\lambda = 1.5$, with $\mathrm{tr}(K_D) = 8.805$ and $\|K_D\|_2 = 8.743$, $\mathrm{tr}(K_D)$ being the trace of the kernel K_D.

One can see that $\lim_{M \to +\infty} 1/\lambda_1^2 = \|K_D\|_2$; this result has been obtained for a very large spectrum of various situations, so that one may here postulate that $1/\lambda_1^2 = \|K_D\|_2$. Hence, since it is observed that $\mathrm{tr}\, K_D \approx \|K_D\|_2$, one deduces that all the ordered eigenvalues $1/\lambda_n^2$, except the first one, quickly tends toward zero with n. This main result is strongly amplified when the refractive index increases. Since $\lim_{\kappa_\lambda \to +\infty} \|K_D\|_2 = +\infty$, the first eigenvalue $1/\lambda_1^2$ has a high magnitude for large absorption coefficients, while the other eigenvalues rapidly tend toward zero. It is then not surprising that the convergence of the eigenvalues is extremely slow. For the considered example, the convergence is only reached for the four first eigenvalues with a 4000 point quadrature. At such an order, because of multiple round-off errors, a Given, Householder, or Jacobi reduction completely fails in finding the eigenelements,

Table 2 Eigenvalues of the right kernel

	$\frac{1}{\lambda_n^2}$				
n	$M=10$	$M=100$	$M=1000$	$M=2000$	$M=4000$
1	8.740	8.743	8.743	8.743	8.743
2	5.167×10^{-2}	5.821×10^{-2}	5.822×10^{-2}	5.822×10^{-2}	5.822×10^{-2}
3	1.295×10^{-3}	3.840×10^{-3}	3.876×10^{-3}	3.876×10^{-3}	3.876×10^{-3}
4	1.520×10^{-5}	4.393×10^{-4}	4.806×10^{-4}	4.807×10^{-4}	4.807×10^{-4}
5	6.152×10^{-8}	5.589×10^{-5}	8.250×10^{-5}	8.267×10^{-5}	8.269×10^{-5}
6	2.870×10^{-8}	6.438×10^{-6}	1.727×10^{-5}	1.750×10^{-5}	1.754×10^{-5}
7	1.754×10^{-8}	6.426×10^{-7}	4.030×10^{-6}	4.259×10^{-6}	4.312×10^{-6}
8	1.344×10^{-8}	5.548×10^{-8}	9.668×10^{-7}	1.124×10^{-6}	1.178×10^{-6}
9	8.018×10^{-9}	2.315×10^{-8}	2.261×10^{-7}	3.043×10^{-7}	3.347×10^{-7}
10	5.692×10^{-9}	1.865×10^{-8}	5.063×10^{-8}	8.107×10^{-8}	1.028×10^{-7}

and a SVD appears to be the best technique in finding the complete eigenelements. Nevertheless, due to the extremely slow convergence of the eigenvalues up to a very high quadrature order, the partial sum $f(z)=\Sigma_{k=1}^{n}\lambda_k\alpha_k\mu_k(z)$ is not correctly evaluated in most cases.

4.4 Final Remarks. Now, one knows that an exact solution of the problem exists and that no spectral intensities theoretically need to be added to the directional ones to obtain a complete solution on the set $r\in[0,R]$. This means that determining the temperature field inside a cylinder with only directional intensity data does not belong to the class of missing data problem, and that it has a theoretical exact solution. However, from a practical point of view, this exact solution is unreachable for at least two reasons: the experimental data are never perfect, and particularly in this case, the problem is extremely ill-posed because of the intrinsic properties of the kernel governing the Fredholm equation on the set $[R/n_\lambda,R]$, contrary to what happens on the set $[0,R/n_\lambda]$, where a smooth regularization is most often powerful. Even with sophisticated filtering treatments applied to experimental data, or at the limit case of perfect non-noisy data, a numerical approximate solution is very hard to obtain on $[R/n_\lambda,R]$, even when using a discretization of the integral equation, followed by a SVD of the discrete operator and zeroing of its too small singular values. This limitation is essentially critical for media with high refractive indices and of internal temperature fields of complex shape. On the other hand, for usual dense media with indices not too far from 1.5 and smooth internal temperature fields, a SVD and zeroing work very well in practice with no noisy data.

Finally, we can note that a little refinement can be provided to the search of the temperature field on $[R/n_\lambda,R]$ by adding spectral measurements. Indeed, integrating Eq. (18) on $x\in[R/n_\lambda,R]$ gives for the first order moment

$$\int_{x=R/n_\lambda}^{R} x\int_{r=R/n_\lambda}^{R}\frac{r\kappa_\lambda L_\lambda^0[T(r)]}{\sqrt{r^2-\frac{x^2}{n_\lambda^2}}}\cosh\left(\kappa_\lambda\sqrt{r^2-\frac{x^2}{n_\lambda^2}}\right)dr\,dx = \int_{x=R/n_\lambda}^{R} x\Psi(x)dx \tag{26}$$

That is, after a simple integration

$$\int_{x=R/n_\lambda}^{R} x\left[\cosh\left(\kappa_\lambda\sqrt{x^2-\frac{R^2}{n_\lambda^4}}\right)\times-\cosh\left(\kappa_\lambda\sqrt{x^2-\frac{R^2}{n_\lambda^2}}\right)\right]L_\lambda^0[T(x)]dx = \int_{x=R/n_\lambda}^{R} x\Psi(x)dx \tag{27}$$

which is an integral equation of the form $\int_{r=R/n_\lambda}^{R}K(r)L_\lambda^0[T(r)]dr=G$, where G is a constant for a given wavelength, and K is the kernel depending only on one variable for the same wavelength. Then a discrete form of Eq. (27) can easily be obtained, for several wavelengths where the absorption sensibility is significant.

5 Conclusion

In this paper, we proved than an exact solution of the problem, which consists in determining the temperature field inside a cylinder filled with a dense semitransparent medium of nonunit refractive index only from directional emerging intensity data, can be theoretically found in the complete domain $[0,R]$, when the useful intensity measurements are perfect non-noisy data. A partial solution on the set $[0,R/n_\lambda]$ can easily be found from a Laplace transform extension applied to the convolution equation governing the problem, and allows the exhibition of the generalized "data function h," from which the auxiliary function Ψ is determined on the complete set. This latter function is the datum of the first kind Fredholm equation, for which an exact formal solution on $[R/n_\lambda,R]$ can be proposed. However, even with perfect intensity data, this exact theoretical solution cannot simply be reached on $[R/n_\lambda,R]$ because of the intrinsic properties of the kernel governing the integral equation to be solved to obtain the corresponding temperature field. Indeed, the ordered eigenvalues of the symmetrized right kernel are such that the first one corresponds to the operator's norm, from which all the other ones quickly tend toward zero, since their sum equals the operator's trace minus its norm, a quantity extremely close to zero for all absorption coefficients and refractive indices. Then, due to a very slow convergence in the eigenvalues' computation, high order quadratures have to be used, leading to extremely ill-conditioned discrete operators, for which standard Householder reductions fail in determining the associate eigenfunctions and solution. That particular behavior of the kernel and its eigenelements also explains why a SVD followed by a zeroing of the smallest singular values generally gives poor approximate solutions for high refractive indices and/or absorption coefficients. This means, in other practical

words, that in spite of sophisticated filtering and/or regularization procedures on noisy experimental data, an acceptable approximate solution of the initial problem on the whole set $[0,R]$ cannot be exhibited unless a judicious regularization of the governing operator itself is applied.

Acknowledgment

We greatly appreciated the helpful advice of Professor Anouar Soufiani.

Nomenclature

R = radius of the cylinder (m)
κ_λ = spectral absorption coefficient (m^{-1})
n_λ = spectral refractive index
T = temperature (K)
$L_\lambda(x)$ = directional monochromatic intensity (W m^{-3} Sr^{-1})
$L_\lambda^0(T)$ = Planck function (black body intensity)
$g(x)$ = data set
$\rho(x)$, $\rho_\perp(x)$, and $\rho_\parallel(x)$ = mean reflection factor, perpendicular, and parallel polarization reflection factors
$h(x)$ = generalized data set
$\psi(x)$ = data function on the range $x > R/n_\lambda$
x_i = center of a discrete cell labeled i
N = number of discrete cells in the cylinder
Δr = depth of a cell (m)
$E(x)$ = integer part of a real number x
Ci, Chi = cosine integral, hyperbolic cosine integral
Ei, E_1 = exponential integral, exponential integral of first order
α = regularization parameter
δ = noise intensity factor
$\tau=\kappa_\lambda r$ and $\tau_0=\kappa_\lambda R$ = optical depths
γ = Euler–Mascheroni constant
$K(w,z')$ = nonsymmetric kernel of a first kind Fredholm integral equation
K_G and K_D = symmetric left and right kernels
$(\lambda_n)_{n\in|N}$ and $(\mu_n)_{n\in|N}$ = eigenvalues and eigenfunctions of the right kernel K_D

Appendix A

Writing

$$\int_{s=x_i}^{R} \frac{h'(s)\cos\left(\frac{\kappa_\lambda}{n_\lambda}\sqrt{s^2-x_i^2}\right)}{\sqrt{s^2-x_i^2}}ds = \sum_{k=i}^{N-1} I_{ki}$$

$$\frac{I_{ki}}{\Delta r} = \int_{t=0}^{1} \frac{h'(\Delta r t + x_k)\cos\left[\frac{\kappa_\lambda}{n_\lambda}\sqrt{(\Delta r t + x_k)^2 - x_i^2}\right]}{\sqrt{(\Delta r t + x_k)^2 - x_i^2}}dt$$

for $2\le i\le N-1$ and $H_k(t)=h(\Delta r t+x_k)$, leads to $H'_k(t)=\Delta r h'(\Delta r t + x_k)=a_k+b_k t+c_k t^2+d_k t^3$, with a development of the $H'_k(t)$ function in cubic splines, $H'_k(0)=a_k=\Delta r h'_k$, $H'_k(1)=a_k+b_k+c_k+d_k=\Delta r h'_{k+1}$, and $H''_k(0)=b_k=D_k$, where D_k is obtained from the linear system

$$\sum_{k=1}^{N-1} A_{1,k}D_k = 3\Delta r(h'_2 - h'_1)$$

$$\sum_{k=1}^{N-1} A_{i,k}D_k = 3\Delta r(h'_{i+1} - h'_{i-1}) \quad 2\le i\le N-1$$

$$\sum_{k=1}^{N-1} A_{N,k}D_k = 3\Delta r(h'_N - h'_{N-1}) \tag{A1}$$

with

$$A_{i,k} = \begin{pmatrix} 2 & 1 & 0 & \dots & & & 0 \\ 1 & 4 & 1 & 0 & \dots & & 0 \\ 0 & 1 & 4 & 1 & 0 & \dots & 0 \\ \dots & & & & & & \\ 0 & \dots & 0 & 1 & 4 & 1 & 0 & 0 \\ \dots & & & & & & \\ 0 & \dots & & & 0 & 1 & 4 & 1 \\ 0 & 0 & 0 & 0 & 0 & 0 & 1 & 2 \end{pmatrix}$$

the coefficients a_k, b_k, c_k, and d_k being related to the D_k by $a_k=\Delta r h'_k$, $b_k=D_k$, $c_k=3\Delta r(h'_{k+1}-h'_k)-2D_k-D_{k+1}$, and $d_k=2\Delta r(h'_k-h'_{k+1})+D_k+D_{k+1}$. Hence previous integrals I_{ki} become

$$I_{ki} = \frac{n_\lambda}{\kappa_\lambda \Delta r}\left\{\left[\tilde{B}_k + \tilde{D}_k\left(v^2 + x_i^2 - \frac{2n_\lambda^2}{\kappa_\lambda^2}\right)\right]\sin\left(\frac{\kappa_\lambda v}{n_\lambda}\right) + \frac{2n_\lambda \tilde{D}_k}{\kappa_\lambda} v\cos\left(\frac{\kappa_\lambda v}{n_\lambda}\right)\right\}_{v=\sqrt{x_k^2-x_i^2}}^{\sqrt{x_{k+1}^2-x_i^2}} + \frac{\alpha_{ki}}{\Delta r}\int_{u=0}^{1}[\tilde{A}_k + \tilde{C}_k x_i^2 ch^2(\alpha_{ki}u+\beta_{ki})] \times\cos\left[\frac{\kappa_\lambda}{n_\lambda}x_i \sinh(\alpha_{ki}u+\beta_{ki})\right]du \tag{A2}$$

The different quantities appearing in the I_{ki} integrals are defined by the following relations:

$$\tilde{A}_k = a_k - \frac{b_k x_k}{\Delta r} + \frac{c_k x_k^2}{\Delta r^2} - \frac{d_k x_k^3}{\Delta r^3},$$

$$\tilde{B}_k = \frac{b_k}{\Delta r} - \frac{2c_k x_k}{\Delta r^2} + \frac{3d_k x_k^2}{\Delta r^3} = -\frac{d\tilde{A}_k}{dx_k},$$

$$\tilde{C}_k = \frac{c_k}{\Delta r^2} - \frac{3d_k x_k}{\Delta r^3} = \frac{1}{2}\frac{d^2\tilde{A}_k}{dx_k^2}$$

$$\tilde{D}_k = \frac{d_k}{\Delta r^3} = -\frac{1}{6}\frac{d^3\tilde{A}_k}{dx_k^3},$$

$$\alpha_{ki} = \ln\left[\frac{k+\sqrt{k^2-(i-1)^2}}{k-1+\sqrt{(k-1)^2-(i-1)^2}}\right], \quad \text{and}$$

$$\beta_{ki} = \ln\left[\frac{k-1+\sqrt{(k-1)^2-(i-1)^2}}{i-1}\right]$$

The integral in I_{ki} being nonanalytical is computed numerically with a Gauss quadrature. For $i=1$, the integral I_{k1} simply reduces to

$$I_{k1} = \frac{n_\lambda}{\kappa_\lambda \Delta r}\left\{\left[\widetilde{B}_k + \frac{n_\lambda \widetilde{C}_k}{\kappa_\lambda} + \widetilde{D}_k\left(v^2 - \frac{2n_\lambda^2}{\kappa_\lambda^2}\right)\right]\sin\left(\frac{\kappa_\lambda v}{n_\lambda}\right) + \left(\frac{2n_\lambda \widetilde{D}_k}{\kappa_\lambda} - \widetilde{C}_k\right) v\cos\left(\frac{\kappa_\lambda v}{n_\lambda}\right)\right\}_{v=x_k}^{x_{k+1}} + \frac{\widetilde{A}_k}{\Delta r}\left[\mathrm{Ci}\left(\frac{\kappa_\lambda x_{k+1}}{n_\lambda}\right) - \mathrm{Ci}\left(\frac{\kappa_\lambda x_k}{n_\lambda}\right)\right] \tag{A3}$$

where $\widetilde{A}_1 = 0$, $\widetilde{B}_1 = b_1/\Delta r$, $\widetilde{C}_1 = c_1/\Delta r^2$, and $\widetilde{D}_1 = d_1/\Delta r^3$ for $k=1$.

Ci stands for the integral cosine [18], with $\mathrm{Ci}(x) = 1/2[\mathrm{Ei}(ix) + \mathrm{Ei}(-ix)] = \gamma + \ln x + \Sigma_{k=1}^{+\infty}(-1)^k x^{2k}/2k(2k)!$, γ being the Euler–Mascheroni constant and Ei being the exponential integral. The local derivatives of h are then obtained from a centered finite differences scheme, with $h'_1 = 0$, $h'_i = h_{i+1} - h_{i-1}/2\Delta r$ for $2 \le i \le N-1$, and $h'_N = 3h_N - 4h_{N-1} + h_{N-2}/2\Delta r = h_{N-2} - 4h_{N-1}/2\Delta r$. Note here that for the numerical calculation h'_N is forced to have a finite value since one should have $h'_N = -\infty$.

Appendix B

With the help of a numerical quadrature, the eigenelements are the solution of the discrete equation $\mu_i^n = \lambda_n^2 \Sigma_{j=1}^M \omega_j \hat{K}_{ij}^D \mu_j^n \Leftrightarrow \mu^n = \lambda_n^2 \hat{K}^D \mathrm{diag}(\omega)\mu^n$, with $\hat{K}^D$ being the discrete form of the continuous operator K_D, with $\hat{K}_{ij}^D = K_D(w_i, w_j)$. Hence the eigenvalues for the discrete problem are the solution of $[\hat{K}^D \mathrm{diag}(\omega) - 1/\lambda_n^2 I]\mu^n = 0$, where $0 < 1/\lambda_n^2 \le \|K_D\|_2$. Since $\|K_D\|_2$ quickly tends toward important values as soon as κ_λ increases, one writes $1/\lambda_n^2 = \alpha_n \|K_D\|_2$ and $\hat{K}_{ij}^D = \|K_D\|_2 \widetilde{K}_{ij}^D$, from which the previous problem is equivalent to $\widetilde{K}^D \mathrm{diag}(\omega)\mu^n = \alpha_n \mu^n$ with $0 < \alpha_n \le 1$, where $\widetilde{K}^D$ is a square $M \times M$ matrix and μ^n is an M vector.

The global matrix $\widetilde{K}^D \mathrm{diag}(\omega)$ of eigenvalues α_n is nonsymmetric, contrary to the matrix $\mathrm{diag}(\omega)\widetilde{K}^D \mathrm{diag}(\omega)$, from which the initial discrete problem is equivalent to $A\mu^n = \alpha_n B\mu^n$, where $A = \mathrm{diag}(\omega)\widetilde{K}^D \mathrm{diag}(\omega)$ is a symmetric matrix, and $B = \mathrm{diag}(\omega)$ is obviously a nonsingular positive definite matrix, with $B = \mathrm{diag}(\sqrt{\omega})\mathrm{diag}(\sqrt{\omega})$. Then the eigenvalues α_n are the ones of the matrix $D = \mathrm{diag}(1/\sqrt{\omega})A\,\mathrm{diag}(1/\sqrt{\omega}) = \mathrm{diag}(\sqrt{\omega})\widetilde{K}^D \mathrm{diag}(\sqrt{\omega})$, and the eigenvectors are determined by $\mu^n = \mathrm{diag}(1/\sqrt{\omega})\nu^n$. The condition for the set $(\mu^n)_{n\in|N}$ to be an orthonormal basis in the sense of the L_2-scalar product leads to $\int_{u=0}^1 \mu^n(u)\mu^m(u)du = \delta_{nm} = \Sigma_{j=1}^M \omega_j \mu_j^n \mu_j^m = \Sigma_{j=1}^M \nu_j^n \nu_j^m$, where ν^n are the orthonormed eigenvectors (in the usual sense of the scalar product for vectors) of the matrix D, so that $\mu^n = \mathrm{diag}(1/\sqrt{\omega})\nu^n$ are the orthonormed eigenfunctions for the L_2-scalar product of the operator $\hat{K}^D$.

Furthermore, since $\Sigma_{j=1}^M \alpha_j = \mathrm{tr}[\widetilde{K}^D \mathrm{diag}(\omega)] = \Sigma_{j=1}^M \omega_j \widetilde{K}_{jj}^D$, it obviously comes that $\lim_{M\to+\infty} \Sigma_{j=1}^M \alpha_j = \lim_{M\to+\infty} \Sigma_{j=1}^M \omega_j \widetilde{K}_{jj}^D = \int_{u=0}^1 \widetilde{K}^D(u,u)du = \mathrm{tr}(\widetilde{K}^D)$ and the series $(\Sigma\alpha_n)_{n\in|N^*}$ is absolutely convergent since $\mathrm{tr}(\widetilde{K}^D) < +\infty$.

Since matrix D is real and symmetric, its eigenelements can be both obtained thanks to a Jacobi transformation, or it can be reduced to a tridiagonal form with the help of a Given's or Householder's reduction to calculate the eigenvalues and vectors. However matrix D is extremely ill-conditioned, with $\lim_{M\to+\infty}(\det D) = 0$, and even for small Ms, only a few eigenvalues are of significant magnitude when the absorption coefficient is moderate. Then Jacobi, Given, or Householder reductions fail in finding the eigenelements even at low orders. However, since D is real and symmetric, its eigenvalues equal its singular values obtained by a SVD, the eigenvectors of D being contained in the orthogonal matrix U given by the SVD, such that $D = U\,\mathrm{diag}(1/\lambda_i^2)U^T$.

References

[1] Milne, A. E., 1966, "Thermodynamics of Stars," *Selected Papers in Radiation Transfer*, D. H. Menzil, ed., Dover Publication, New York.

[2] Chahine, M. T., 1968, "Determination of the Temperature Profile in an Atmosphere From Its Outgoing Radiance," J. Opt. Soc. Am., **58**, pp. 1634–1637.

[3] Ben-Abdallah, P., 1998, "A Variational Method to Inverse the Radiative Transfer Equation: Application to Thermal Sounding of Atmospheres of Giant Planets," J. Quant. Spectrosc. Radiat. Transf., **60**(1), pp. 9–15.

[4] Siewert, C. E., 1994, "A Radiative Inverse-Source Problem for a Sphere," J. Quant. Spectrosc. Radiat. Transf., **52**(2), pp. 157–160.

[5] Li, H. Y., 1994, "Estimation of the Temperature Profile in a Cylindrical Medium by Inverse Analysis," J. Quant. Spectrosc. Radiat. Transf., **52**(6), pp. 755–764.

[6] Kocifaj, M., 1994, "The Inversion Problem of Interaction of Shortwave Direct Solar Radiation With Small Dust Particles in the High Atmosphere," Contributions of the Astronomical Observatory Skalnate Pleso, **24**, pp. 57–64.

[7] Liu, H. G., and Jiang, J., 2001, "Inverse Radiation Problem for Reconstruction of Temperature Profile in Axisymmetric Free Flames," J. Quant. Spectrosc. Radiat. Transf., **70**(2), pp. 207–215.

[8] Deiveegan, M., Balaji, C., and Venkateshan, S. P., 2006, "Comparison of Various Methods for Simultaneous Retrieval of Surface Emissivities and Gas Properties in Gray Participating Media," ASME J. Heat Transfer, **128**(8), pp. 829–837.

[9] Park, H. M., and Lee, W. J., 2002, "The Solution of Inverse Radiation Problems Using an Efficient Computational Technique," J. Quant. Spectrosc. Radiat. Transf., **73**(1), pp. 41–54.

[10] Kim, K. W., and Baek, S. W., 2007, "Inverse Radiation-Conduction Design Problem in a Participating Concentric Cylindrical Medium," Int. J. Heat Mass Transfer, **50**, pp. 2828–2837.

[11] Ertürk, H., Ezekoye, O. A., and Howell, J. R., 2002, "Comparison of Three Regularised Solution Techniques in a Three-Dimensional Inverse Radiation Problem," J. Quant. Spectrosc. Radiat. Transf., **73**, pp. 307–316.

[12] Viskanta, R., Hommert, P. J., and Groninger, G. L., 1975, "Spectral Remote Sensing of Temperature Distribution in Semitransparent Solids Heated by an External Radiative Source," Appl. Opt., **14**(2), pp. 428–437.

[13] Zhou, H. C., Hou, Y. B., Chen, D. L., and Zheng, C. G., 2002, "An Inverse Radiative Transfer Problem of Simultaneously Estimating Profiles of Temperature and Radiative Parameters From Boundary Intensity and Temperature Measurements," J. Quant. Spectrosc. Radiat. Transf., **74**(5), pp. 605–620.

[14] Kudo, K., Kuroda, A., Eid, A., Saito, T., and Ogurna, M., 1995, "Solution of the Inverse Radiative Load Problems by the Singular Value Decomposition," *Proceedings of the First International Symposium on Radiative Transfer*, Kusadasi, Turkey.

[15] Natterer, F., 1983, "Exploiting the Ranges of Radon Transforms in Tomography in Numerical Treatment of Inverse Problems in Differential and Integral Equations," *Progress in Scientific Computing*, Vol. 2, P. Deuflhard and E. Hairer, eds., Birkhauser, Stuttgart, pp. 290–303.

[16] Sakami, M., Le Dez, V., and Lallemand, M., 1991, "Retrieval of Temperature Profiles in Cylinders of Semi-Transparent Media," Fourth Annual Inverse Problems in Engineering Seminar, Michigan State University, Jun.

[17] Le Dez, V., Huclin, J. C., and Lallemand, M., 1993, "Directional Emissivities of Semi-Transparent Media. Cases of Dihedron, Infinite Cylinder and Cone," Glastech. Ber., **66**(5), pp. 127–137.

[18] Press, W. H., Teukolsky, S. A., Vetterling, W. T., and Flannery, B. P., 2007, "Numerical Recipies in Fortran 77," *The Art of Scientific Computing*, 2nd ed., Cambridge University Press, New York.

[19] Abramowitz, M., and Stegun, I. A., eds., 1972, *Handbook of Mathematical Functions*, National Bureau of Standards, Washington, DC.

[20] Tricomi, F. G., 1985, *Integral Equations*, Dover, New York.

Effect of Geometry on the Conjugate Heat Transfer of Wall Jet Flow Over a Backward-Facing Step

P. Rajesh Kanna[1]
Former Research Scholar

Manab Kumar Das[2]
Former Associate Professor

Department of Mechanical Engineering,
Indian Institute of Technology Guwahati,
Guwahati 781039, India

Conjugate heat transfer study of a backward-facing step cooled by a two-dimensional laminar incompressible wall jet has been carried out. The study is performed to find the isotherm patterns, conjugate interface temperature, local Nusselt number and average Nusselt number by varying the geometry of the solid slab. Different step length, step height, and slab thickness are considered for conjugate heat transfer study. [DOI: 10.1115/1.2717251]

Keywords: Laminar plane wall jet, flow over step, conjugate heat transfer, effect of geometry, Nusselt number

1 Introduction

The flow emanating from a two-dimensional (2D) plane wall jet over backward-facing step is shown in Fig. 1 where the main features and regions of interest are depicted. Fluid is discharged from a slot along the horizontal wall into the ambient near a horizontal solid boundary parallel to the inlet jet direction. The jet flow features are different in various regions. In the near-field up to the step from the point of discharge, the jet behaves like a plane wall jet. Further, the jet expands across the step. Due to the entrainment between the solid wall and the jet, there is a reduction of pressure in this region, forcing the jet to deflect toward the boundary and eventually attach to it. This is called the Coanda effect [1]. Wall jet flow over a step occurs in many engineering applications such as environmental discharges, heat exchangers, fluid injection systems, cooling of combustion chamber wall in a gas turbine, automobile demister, and others. In electronics cooling, the prediction of the Nusselt number distribution along the step is very important from a thermal design point of view.

Similarity the solution for a plane wall jet as well as a radial wall jet for both the laminar and the turbulent cases are presented by Glauert [2]. Schwarz and Caswell [3] have investigated the heat transfer characteristics of a two-dimensional laminar incompressible wall jet. They have found an exact solutions for both the constant wall temperature and the constant heat flux cases. Yang and Patel [4] have presented an analysis of mixed natural and forced convection in a two-dimensional wall jet along a vertical isothermal wall. In the case of the aiding flow, the buoyancy force acts like a favorable pressure gradient and increases the temperature gradient at the wall, which results in a higher heat-transfer rate. The problem of turbulent convection with a wall jet is studied by Nizou [5]. Previous results for the relationships between heat transfer and skin friction are supplemented, pointing out differences between this situation and the classical boundary layer. Angirasa [6] has studied a laminar buoyant wall jet and reported the effect of velocity and the width of the jet during convective heat transfer from the vertical surface.

Recently, Bhattacharjee and Loth [7] have simulated the laminar and transitional cold wall jets and have investigated the significance of three different inlet profiles, viz. parabolic, uniform, and ramp. They have presented the detailed results of time-averaged wall jet thickness and temperature distribution with Reynolds averaged Navier–Stokes approach (RANS) for higher Reynolds number and direct numerical simulation (DNS) approach for the three-dimensional wall jet. Kanna and Das [8] have studied the conjugate plane wall jet flow and reported close form solutions for conjugate interface temperature, local Nusselt number distribution, and average Nusselt number. Their analytical solution for a low Pr case matches well the numerical solution. However, their analytical solution for high Pr case is unable to produce results close to the numerical solution.

Conjugate heat transfer study on the offset jet is carried out by Kanna and Das [9]. They have studied the conjugate heat transfer characteristics with four parameters, viz. Re, Pr, S, and $k=k_s/k_f$. They have found that the fluid properties are affecting the heat transfer in the solid slab. When Re is increased, the slab temperature is reduced. At low Pr, the heat transfer across the slab is greater. It is decreased when the slab thickness is increased. The conjugate interface temperature is decreased up to the recirculation region and further increased close to a developed condition. Kanna and Das [10] have reported in detail the flow characteristics of a wall jet flow over a step. Reattachment length and local u velocity decay, are reported for different step geometry. The heat

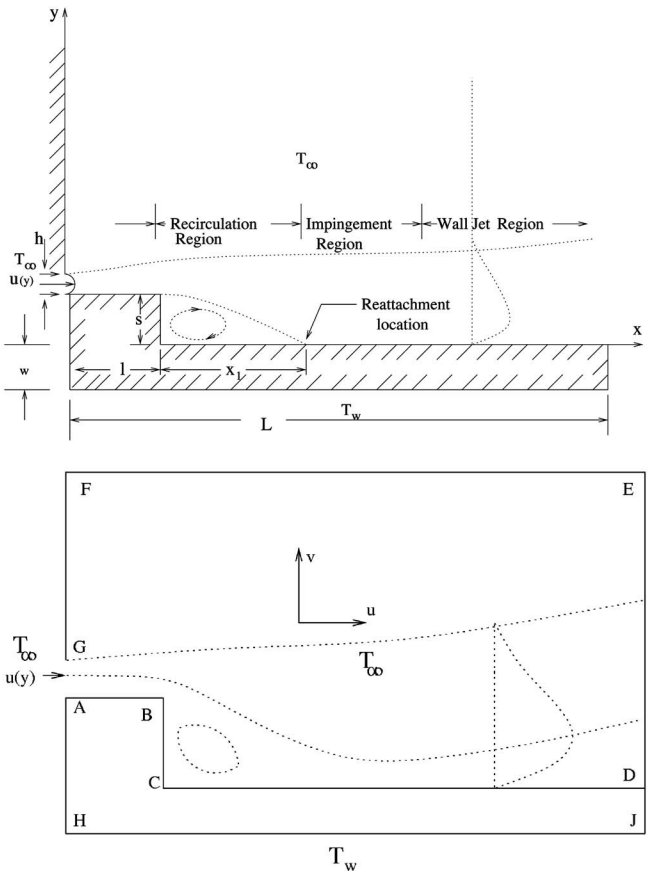

Fig. 1 Schematic diagram and boundary conditions

[1]Present address: Associate Professor, Department of Mechanical Engineering, Kalasalingam University, Krishnankoil, India; e-mail: prkanna@gmail.com

[2]Corresponding author. Present address: Associate Professor, Department of Mechanical Engineering, India Institute of Technology Kharagpur, Kharagpur 721302, India; e-mail: manab@mech.iitkgp.ernet.in

Contributed by the Heat Transfer Division of ASME for publication in the JOURNAL OF HEAT TRANSFER. Manuscript received July 14, 2006; final manuscript received January 3, 2007; published online August 19, 2009. Review conducted by Ranga Pitchumani.

transfer study is also carried out by the same authors [11]. They have found that the peak Nusselt number occurs due to entrainment as well as recirculation. Step height enhances the average Nusselt number. Similarity velocity profiles from different downstream locations are presented.

The same authors [12] have numerically investigated the effect of properties involved in the conjugate heat transfer in a wall jet flow over a backward-facing step. The conjugate heat transfer characteristics are studied with flow property (Re), fluid property (Pr), and solid to fluid conductivity ratio (k). They have noticed that the fluid properties are affecting the heat transfer in the solid slab. The conjugate interface temperature decreases along the step. Two peak Nusselt numbers occur due to the entrainment and the recirculation eddy. As k is increased, the average Nusselt number is increased and at a higher k, it approaches a nonconjugate value. It is worthwhile to note that the conjugate heat transfer is affected by the geometry of the solid slab involved in heat transfer with the fluid medium.

Although many studies have been conducted on the wall jet, the available literature suggests that the study concerning the effect of geometry on a wall jet flow over a backward-facing step as the conjugate case has not been carried out by any researcher. In the present paper, conjugate heat transfer study is focused on finding the effect of the step length, step height, and the bottom wall thickness on the isotherm, conjugate interface temperature, local Nusselt number distribution, and average Nusselt number distribution.

2 Governing Equations and Boundary Conditions

The governing equations for the wall jet fluid flow are solved by the stream function-vorticity method. The energy equations in the fluid and the conduction equation in the solid slab are solved by finite-difference method. The equations are given below.

stream function equation

$$\nabla^2 \psi = -\omega \tag{1}$$

vorticity equation

$$\frac{\partial \omega}{\partial t} + \frac{\partial (u\omega)}{\partial x} + \frac{\partial (v\omega)}{\partial y} = \frac{1}{\mathrm{Re}} \nabla^2 \omega \tag{2}$$

energy equation in fluid region

$$\frac{\partial \theta_f}{\partial t} + \frac{\partial (u\theta_f)}{\partial x} + \frac{\partial (v\theta_f)}{\partial y} = \frac{1}{\mathrm{Re\,Pr}} \nabla^2 \theta_f \tag{3}$$

energy equation in solid region,

$$\frac{\partial \theta_s}{\partial t} = \frac{\alpha_s}{\alpha_f} \frac{1}{\mathrm{Re\,Pr}} \nabla^2 \theta_s \tag{4}$$

where ψ=stream function; $u=\partial\psi/\partial y$, $v=-\partial\psi/\partial x$; and $\omega=(\partial v/\partial x)-(\partial u/\partial y)$; $k=k_s/k_f$.

The details of the boundary conditions are given in Karma and Das [12].

3 Numerical Procedure

The unsteady vorticity transport equation (Eq. (2)) in time is solved by the alternate direction implicit (ADI) scheme. The central differencing scheme is followed for both the convective as well as the diffusive terms [13]. The energy equation (Eq. (3)) is solved by the ADI method. ADI is first-order accurate in time and second-order accurate in space $O(\Delta t, \Delta x^2, \Delta y^2)$, and is unconditionally stable. The Poisson Eq. (1) is solved explicitly by five point Gauss–Seidel methods. For the computation, a time step 0.01 is used for Pr=1.0,100.0, whereas for Pr=0.01, a time step 0.0001 is used. Here computation is terminated when the sum of temperature difference from consecutive time marching steps is reduced to the convergence criteria ε. The convergence condition is given by the expression

$$\sum_{i,j=1}^{i_{\max},j_{\max}} [(\theta_{s,i,j}^{t+\Delta t} - \theta_{s,i,j}^{t}) + (\theta_{f,i,j}^{t+\Delta t} - \theta_{f,i,j}^{t})] < \varepsilon \tag{5}$$

Details of the numerical procedure are given in Kanna and Das [12].

4 Validation of the Code

For validation and comparison study of the present situation, the backward-facing step flow and the plane wall jet flow problems have been chosen. The fundamental features of the present problem like expansion of the jet, recirculation of the eddies formed, entrainment from the free shear layer, and heat transfer are common with them. The computed results have shown excellent agreement with them. Two split domain problems, viz. the L-shape lid driven cavity problem as solved by Oosterlee et al. [14] and backward-facing step flow with upstream channel [15] are solved and the results are compared. The energy equation solution of the backward-facing step flow is compared with that of Dyne and Heinrich [16]. Excellent agreement has been obtained with the benchmark solutions reported in the above references. The laminar plane wall jet problem has been solved and the computed velocity profiles are compared with the similarity solutions of Glauert [2] and the experimental results of Quintana et al. [17] in a similar way as represented by Seidel [18]. Details of the validation for hydrodynamic solution as well as energy solution as the nonconjugate case are given in Kanna and Das [8,10,12].

5 Grid Independence Study

The grid numbers 61×51, 71×61, 97×85, and 127×125 are used to obtain the average Nusselt number for grid independence study. The average $\overline{\mathrm{Nu}}$ values are given in Kanna and Das [12]. The variation in $\overline{\mathrm{Nu}}$ is less than 1.5% for the last two grid system. So the grid 97×85 is used for the entire computation.

6 Results and Discussion

The conjugate heat transfer characteristics, systematically studied for flow property (Re), fluid property (Pr), and the conductivity ratio (k), are reported in details in Ref. [12]. In the present investigation, the effect of geometry on the conjugate heat transfer has been studied with three parameters considered here. They are: the length of the step (l), the height of the step (s), and the thickness of the solid slab (w). Results are presented for different geometry sizes. Flow property, fluid property, and thermal property are fixed as follows: Re=400, Pr=1, and k=5. The detailed conjugate heat transfer results are presented in terms of interface temperature, Nusselt number (Nu) and the average Nusselt number ($\overline{\mathrm{Nu}}$).

6.1 Effect on Interface Temperature. The effect of the geometry on the interface temperature is presented in Figs. 2–4. The interface is divided into three lengths, viz. AB (step length), BC (step height), and CD ($L-l$) (Fig. 1(b)). The interface temperature decreases gradually up to a certain length followed by a sharp drop (Fig. 2(a)). The temperature at midstep length is θ=0.83 for l=1, θ=0.92 for l=2, and θ=0.95 for l=3. It is observed that when l increases, the interface temperature is increased. As k_s is greater than k_f, more heating processes take place when l is increased. The interface temperature decrement is continued along BC and is shown in Fig. 2(b). For all three cases, the variations are close to each other with maximum difference of θ=0.031 at y=0 (i.e., point C). Along CD, the interface temperature decreases to a minimum value and finally it reaches an asymptotic value in the downstream direction (Fig. 2(c)). This trend is due to the recirculation eddy and development of the wall jet after the reattachment point. The effect of step height on the interface temperature is presented in Fig. 3. The interface temperature decreases gradually and becomes minimum near the convex corner of the

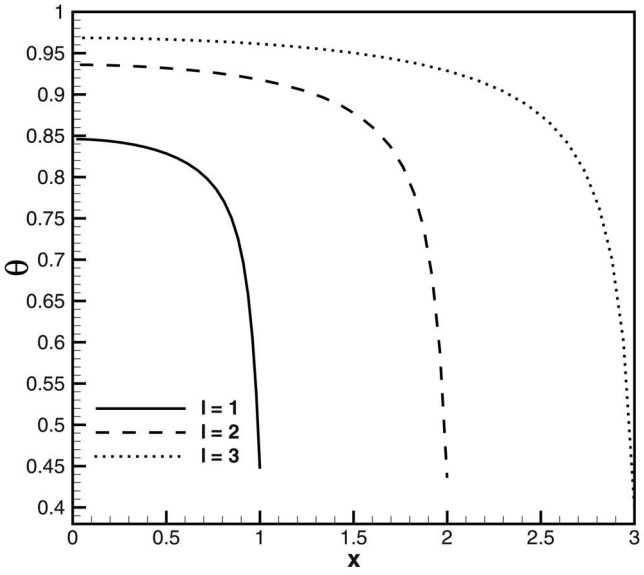

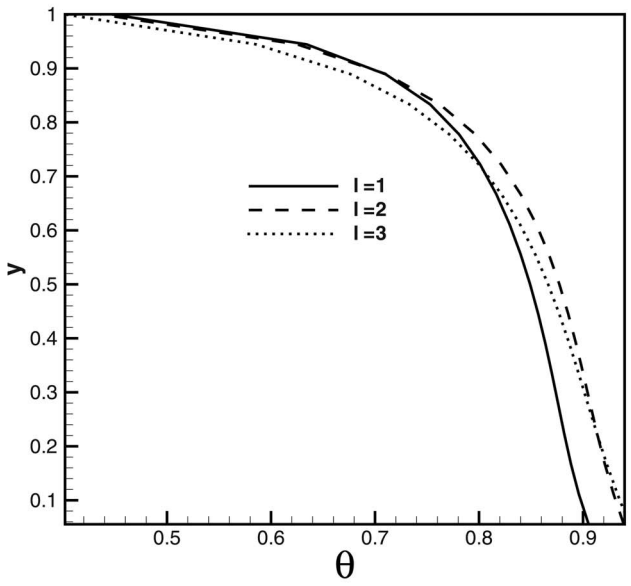

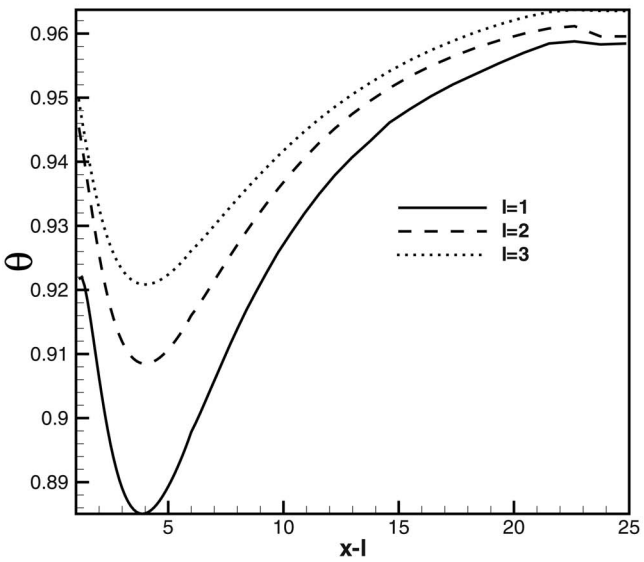

Fig. 2 Conjugate interface temperature: effect of *l* (Re =400, Pr=1, *k*=5, *s*=1, *w*=1)

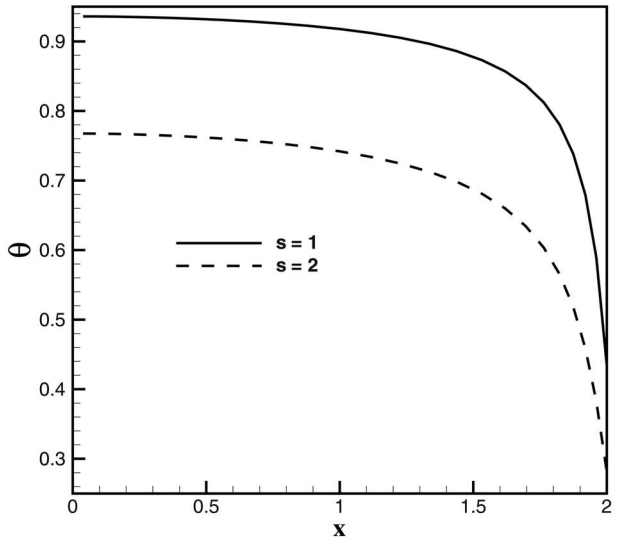

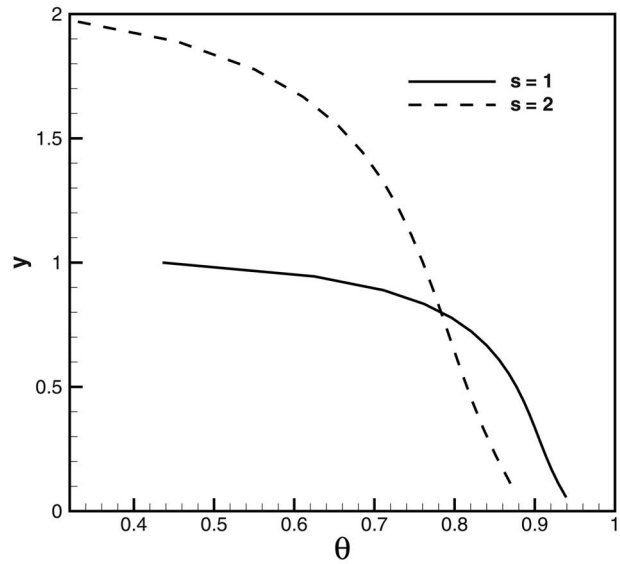

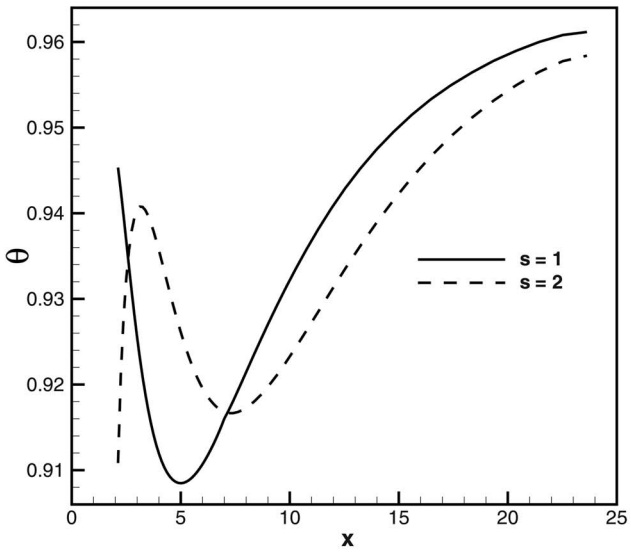

Fig. 3 Conjugate interface temperature: effect of *s* (Re =400, Pr=1, *k*=5, *l*=2, *w*=1)

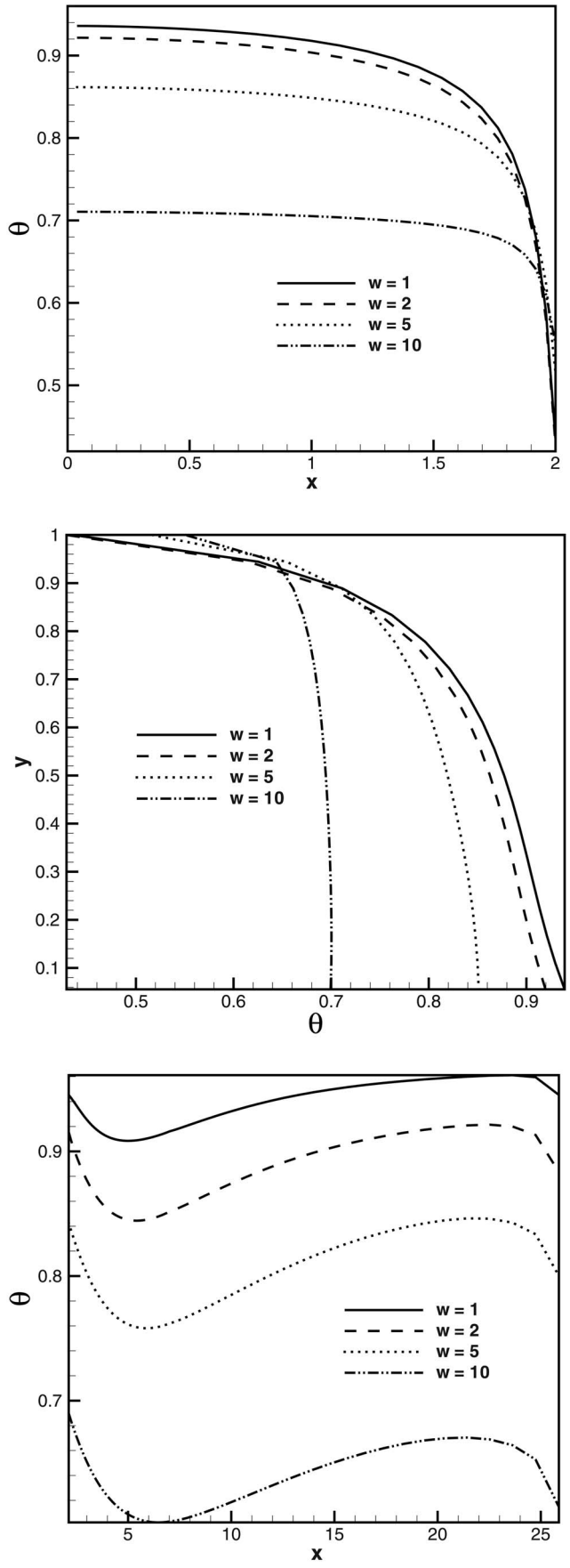

Fig. 4 Conjugate interface temperature: effect of *w* (Re =400, Pr=1, *k*=5, *l*=2, *s*=1)

step (Fig. 3(*a*)). When *s* is increased, the interface temperature value is reduced since the size of the recirculation eddy is increased. Figure 3(*b*) shows the interface temperature along the step height *BC*. It decreases through the entire length in a nonlinear pattern. The interface temperature along *CD* is shown in Fig. 3(*c*). When $s=1$, it decreases to a local minimum value and further downstream it increases to a near asymptotic value. For $s=2$, it increases to a local maximum value and decreases to a local minimum value; finally it attains a steady value of $\theta=0.96$. The effect of the slab thickness *w* on the interface temperature is shown in Fig. 4. Along *AB* (Fig. 4(*a*)), the interface temperature decreases in the streamwise direction. When *w* increases, interface temperature value is decreased. This is due to reduction of temperature inside the slab at higher slab thickness. A boundary layer type profile is observed where the interface temperature from an asymptotic value drops sharply near the location at $x=2$. Along *BC* it increases with an opposing nature to that of *AB* (Fig. 4(*b*)). Along *CD* the interface temperature is shown in Fig. 4(*c*). It decreases to a local minimum value and further increases in the downstream direction. It is noticed that when *w* is increased, the interface temperature is decreased. It is observed that the minimum value is shifted in the downstream direction when *w* is increased (for $w=1$, $x=5.01$, $w=2$, $x=5.49$, $w=5$, $x=6.05$, $w=10$, and $x=6.54$).

6.2 Effect on Nusselt Number Distribution. The effect of the step length on the local Nusselt number is shown in Fig. 5. Along *AB*, due to the entrainment, Nu is very large and it decreases in the downstream direction. When *l* is increased, a small increment in Nu is observed (for $l=1$, Nu=46.93; for $l=2$, Nu =51.62, and for $l=3$, Nu=53.31 at $x=0.5$) (Fig. 5(*a*)). This is caused due to the variation in the entrainment near the inlet. However this variation is reduced along the downstream of the step length. Figure 5(*b*) shows the Nu distribution along *BC*. Nu increases to a maximum value and decreases in the direction of *B* to *C* (negative *y* direction). When *l* is increased, the maximum value is decreased ($l=1$, Nu=13.865; $l=2$, Nu=10.903; $l=3$, Nu =8.365). Nu distribution along CD is presented in Fig. 5(*c*). Nu increases to a maximum value and then decreases to a near-steady value in the downstream direction. It is noticed that when *l* is increased, the magnitude is decreased and the peak Nu value is shifted ($l=1$, $x=3.679$, Nu=11.769; $l=2$, $x=4.746$, Nu=9.352; $l=3$, $x=5.678$, Nu=8.501) in the downstream direction. The effect of step height is shown in Fig. 6(*a*). Along AB, Nu is decreased in the downstream direction. When *s* is increased, Nu is decreased (for $s=1$, Nu=51.66 and for $s=2$, Nu=42.16 at $x=0.5$). Along *BC*, Nu is decreased to a certain height and increases to a maximum value and then further it is decreased (Fig. 6(*b*)). This trend is magnified at a higher step height. Along *CD*, Nu is increased to a maximum value and decreases to a near-steady value (Fig. 6(*c*)). When *s* is increased, Nu is decreased and the peak value is shifted downstream (for $s=1$, Nu=9.35 at $x=4.76$ and $s=2$, Nu=8.43 at $x=7.25$). This is attributed to the large size of recirculation eddy. The effect of the slab thickness is presented in Fig. 7. Along *AB*, Nu is sensitive to *w* (for $w=1$, Nu=51.66; for $w=2$, Nu=50.87; for $w=5$, Nu=47.62 and for $w=10$, Nu=39.35 at $x=0.5$). It is observed that when *w* is increased, Nu is decreased (Fig. 7(*a*)). Along *BC* (Fig. 7(*b*)), Nu is increased to a maximum value and is decreased and further increased (for $w=1$, 2, and 5). At higher slab thickness (at $w=10$), the trend is slightly different such that near the corner it is decreased. Along *CD*, Nu increases to a maximum value (at $x=4.73$ for $w=1$, Nu=9.35; $w=2$, Nu=8.35; $w=5$, Nu=7.10, and $w=10$, Nu=5.28) and decreased gradually to a near-steady value. When *w* is increased Nu is decreased. It is observed that the peak value location does not vary for different *w* (Fig. 7(*c*)). It is observed from the entire study that the singularity is arisen at step corner *B* and the buffer zone effect is reflected at the exit region results [18].

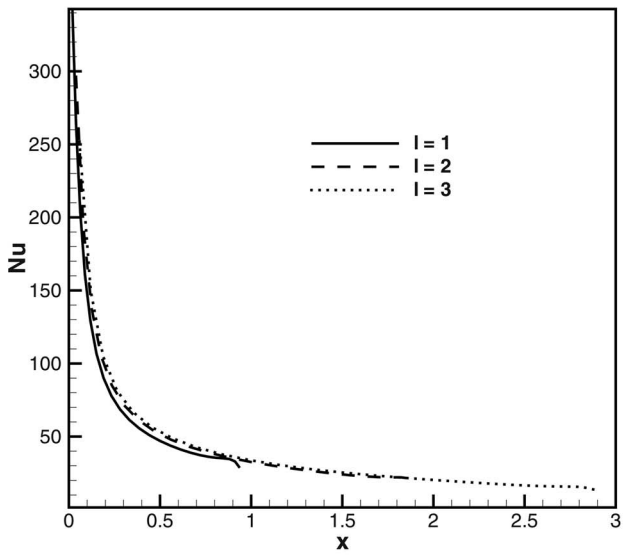

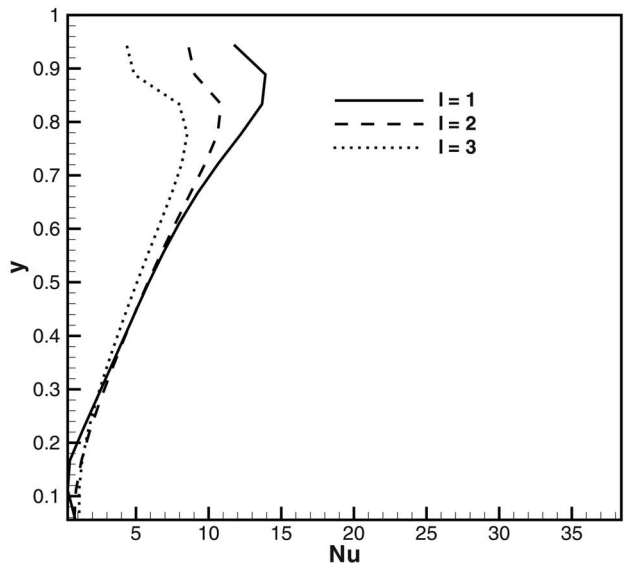

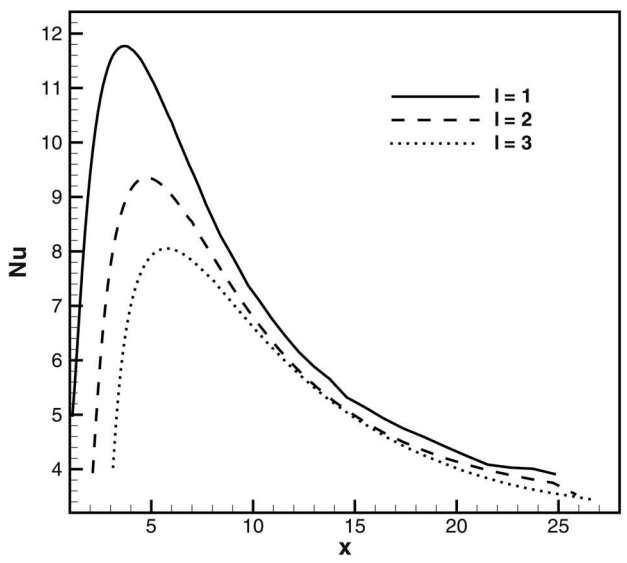

Fig. 5 Local Nusselt number distribution: effect of *l* (Re =400,Pr=1,*k*=5,*s*=1,*w*=1)

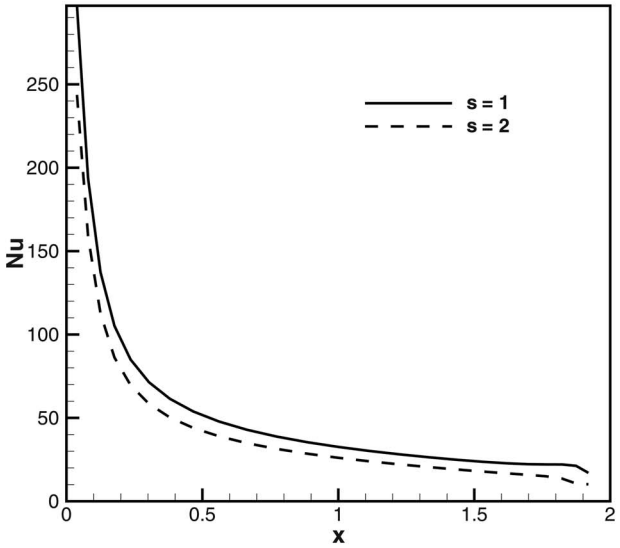

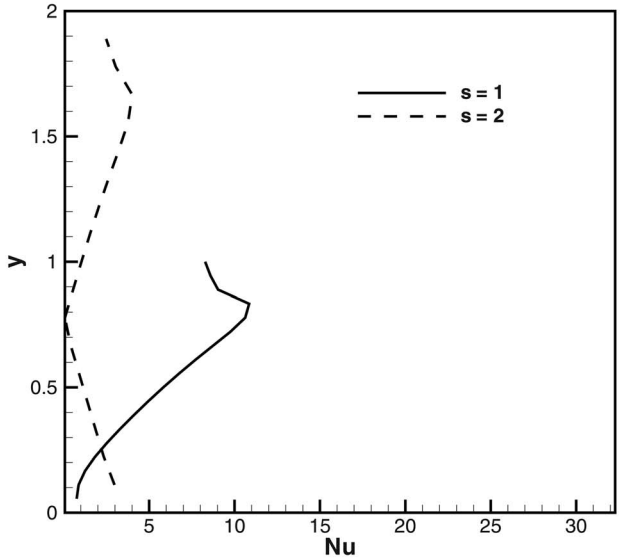

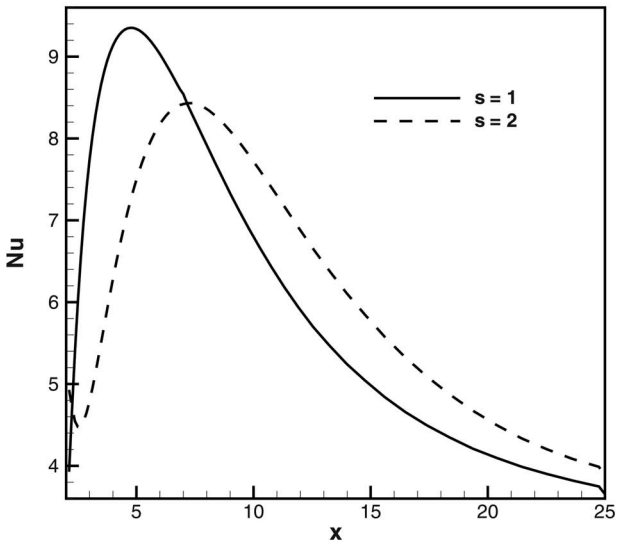

Fig. 6 Local Nusselt number distribution: effect of *s* (Re =400,Pr=1,*k*=5,*l*=2,*w*=1)

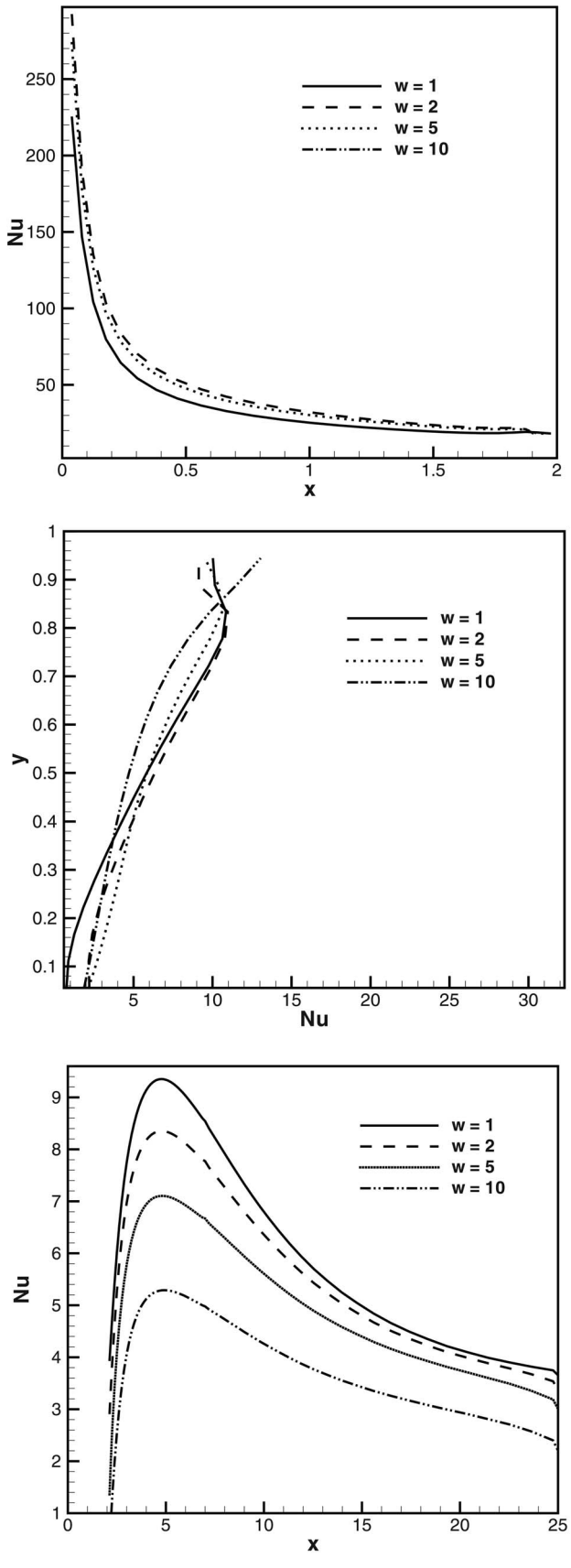

Fig. 7 Local Nusselt number distribution: effect of *w* (Re =400, Pr=1, *k*=5, *l*=2, *s*=1)

Table 1 Average Nusselt number: effect of *l* (Re=400, Pr=1, *k*=5, *s*=1, *w*=1)

l	$\overline{\text{Nu}}$	% change
1	8.675	—
2	7.645	−11.88
3	6.909	−20.35

Table 2 Average Nusselt number: effect of *s* (Re=400, Pr=1, *k*=5, *l*=2, *w*=1)

s	$\overline{\text{Nu}}$	% change
1	7.645	—
2	7.066	−7.57

Table 3 Average Nusselt number: effect of *w* (Re=400, Pr=1, *k*=5, *l*=2, *s*=1)

w	$\overline{\text{Nu}}$	% change
1	7.645	—
2	7.239	−5.30
5	6.683	−12.57
10	5.400	−29.35

6.3 Effect on Average Nusselt Number. The bulk mean property in terms of the average Nusselt number ($\overline{\text{Nu}}$) are presented in Tables 1–3. When length of the step is increased from 1 to 3, the average Nusselt number is decreased by 20% (Table 1). At a higher step height of 2, the average Nusselt number is decreased by 7.6% (Table 2). Table 3 shows the effect of slab thickness in $\overline{\text{Nu}}$. It is noticed that when slab thickness is increased to 10, the average Nusselt number is decreased by 29%.

7 Conclusions

Conjugate heat transfer study of a two-dimensional incompressible nonbuoyant wall jet over a backward-facing step flow problem is carried out by solving the vorticity transport equation and energy equation using stream function and vorticity formulation for the fluid region and conduction equation for the solid region. Parametric study is carried out for step length, step height, and slab thickness. Results are presented in terms of conjugate interface temperature, local Nusselt number, and average Nusselt number. This study is carried with Re=400, Pr=1, and $k=5$. The following conclusions are drawn.

1. Conjugate interface temperature is decreased in the downstream direction and further increases to a near-steady value. When the length of the step is increased, interface temperature value is increased. When the step height is increased the interface temperature is decreased. However within the reattachment length the effects are reversed. When the slab thickness is increased the interface temperature is decreased in the downstream direction and further it is increased.
2. Near the inlet, the Nusselt number is larger due to entrainment and further it is decreased. Along *CD* it is increased to a maximum value and further decreases to a near-steady value monotonically. When *l* is increased, it is decreased. Similarly, as *w* is increased Nu is decreased.
3. Average Nusselt number is decreased up to 20.35% when the length of the step is increased to 3. It is observed that higher step height ($s=2$) reduces the $\overline{\text{Nu}}$ by 7.5%. The increment in slab thickness from 1 to 10 reduces the average Nusselt number by 29.35%.

Acknowledgment

The authors are grateful to the reviewers for various suggestions on the manuscript.

Nomenclature

h = inlet slot height, m
k = thermal conductivity ratio, k_s/k_f
n = normal direction
Nu = local Nusselt number
$\overline{\mathrm{Nu}}$ = average Nusselt number
Pr = Prandtl number, ν/α
Re = Reynolds number for the fluid, $\bar{U}h/\nu$
s = height of the step, m
T = dimensional temperature, °C
$\bar{t}$ = dimensional time, s
t = nondimensional time
$\bar{u},\bar{v}$ = dimensional velocity components along (x,y) axes, m/s
u,v = dimensionless velocity components along (x,y) axes
$\bar{U}$ = inlet mean velocity, m/s
w = solid wall thickness, m
$\bar{x},\bar{y}$ = dimensional Cartesian coordinates along and normal to the plate, m
x,y = dimensionless Cartesian coordinates along and normal to the plate

Greek Symbols

α = thermal diffusivity (m^2/s)
ε = convergence criterion
θ = dimensionless temperature
θ_b = dimensionless average boundary temperature
κ = clustering parameter
ν = kinematic viscosity
ψ = dimensionless stream function
ω = dimensionless vorticity

Subscripts

f = fluid
$\max$ = maximum
s = solid
w = wall
∞ = ambient condition

References

[1] Tritton, D. J., 1977, *Physical Fluid Dynamics*, Von Nostrand Reinhold, New York, U.K., pp. 284–286.
[2] Glauert, M. B., 1956, "The Wall Jet," J. Fluid Mech., **1**, pp. 625–643.
[3] Schwarz, W. H., and Caswell, B., 1961, "Some Heat Transfer Characteristics of the Two-Dimensional Laminar Incompressible Wall Jet," Chem. Eng. Sci., **16**, pp. 338–351.
[4] Yang, J. W., and Patel, R. D., 1973, "Effect of Buoyancy on Forced Convection in Two-Dimensional Wall Jet Along a Vertical Wall," Trans. ASME, Ser. C: J. Heat Transfer, **95**, pp. 121–123.
[5] Nizou, P. Y., 1981, "Heat and Momentum Transfer in a Plane Turbulent Wall Jet," Trans. ASME, Ser. C: J. Heat Transfer, **103**, pp. 138–140.
[6] Angirasa, D., 1999, "Interaction of Low-Velocity Plane Jets With Buoyant Convection Adjacent to Heated Vertical Surfaces," Numer. Heat Transfer, Part A, **35**, pp. 67–84.
[7] Bhattacharjee, P., and Loth, E., 2004, "Simulations of Laminar and Transitional Cold Wall Jets," Int. J. Heat Fluid Flow, **123**, pp. 32–43.
[8] Kanna, P. R., and Das, M. K., 2005, "Conjugate Forced Convection Heat Transfer from a Flat Plate by Laminar Plance Wall Jet Flow," Int. J. Heat Mass Transfer, **48**, pp. 2896–2910.
[9] Kanna, P. R., and Das, M. K., 2005, "Conjugate Heat transfer Study of Two-Dimentsional Laminar Incompressible Offset Jet Flows," Numer. Heat Transfer, Part A, **48**, pp. 671–691.
[10] Kanna, P. R., and Das, M. K., 2006, "Numerical Simulation of Two-Dimensional Laminar Incompressible Wall Jet over backward-facing step flows," ASME Trans. J. Fluids Eng., **128**, pp. 1023–1035.
[11] Kanna, P. R., and Das, M. K., 2006, "Heat Transfer Study of Two-Dimensional Laminar Incompressible Wall Jet Flow over Backward-Facing Step," Numer. Heat Transfer, Part A, **502**, pp. 165–187.
[12] Kanna, P. R., and Das, M. K., 2007, "Conjugate Heat Transfer Study of Two-Dimensional Laminar Incompressible Wall Jet over Backward-Facing Step," ASME J. Heat Transfer, **129**(2), pp. 220–231.
[13] Roache, P. J., 1998, *Fundamentals of Computational Fluid Dynamics*, Hermosa, Albuquerque, NM, Chap. 3.
[14] Oosterlee, C. W., Wesseling, P., Segal, A., and Brakkee, E., 1993, "Benchmark Solutions for the Incompressible Navies–Stokes Equations in General Coordinates on Staggered Grids," Int. J. Numer. Methods Fluids, **17**, pp. 301–321.
[15] Barton, I. E., 1997, "The Entrance Effect of Laminar Flow over a Backward-Facing Step Geometry," Int. J. Numer. Methods Fluids, **25**, pp. 633–644.
[16] Dyne, B. R., and Heinrich, J. C., 1992, "Flow Over a Backward-Facing Step: A Benchmark Problem for Laminar Flow with Heat Transfer," *Benchmark Problems for Heat Transfer Codes*, B. Blackwell and D. W. Pepper, eds., ASME, New York, pp. 73–76.
[17] Quintana, D. L., Amitay, M., Ortega, A., and Wygnanski, I. J., 1997, "Heat Transfer in the Forced Laminar Wall Jet," Trans. ASME, Ser. C: J. Heat Transfer, **119**, pp. 451–459.
[18] Seidel, J., 2001, "Numerical Investigations of Forced Laminar and Turbulent Wall Jets over a Heated Surface," Ph.D. thesis, Faculty of the Department of Aerospace and Mechanical Engineering, The Graduate College, The University of Arizona, Tucson, AZ.